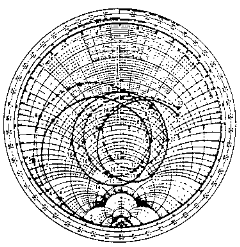

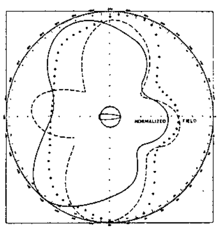

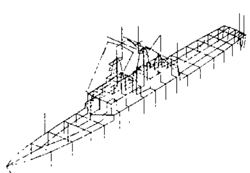

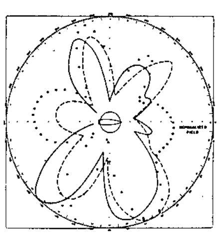

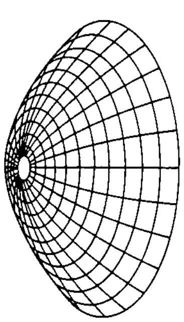

8th Annual Review of Progress in

APPLIED COMPUTATIONAL ELECTROMAGNETICS

at the

Naval Postgraduate School

Monterey, CA

March 16-20, 1992

CONFERENCE PROCEEDINGS

CONFERENCE PROCEEDINGS

8th Annual Review of Progress in

APPLIED

COMPUTATIONAL

ELECTROMAGNETICS

at the

Naval Postgraduate School

Monterey, CA

March 16-20, 1992

SYMPOSIUM PROGRAM COMMITTEE CHAIRMAN

Pat Foster

Sponsored by

The Applied Computational Electromagnetics Society

and DOD/USA ECOM, USAISEC, NCCOSC,NPS, DOE/LLNL

THE NAVAL POSTGRADUATE SCHOOL

1993 **CALL FOR PAPERS** 1993

The 9th Annual Review of Progress in Applied Computational Electromagnetics

March 22-26, 1993

SUBMISSION OF PAPERS

Suggested topics for papers include

NUMERICAL METHODS	CODE DEVELOPMENT	APPLICATIONS
Differential methods	EM Field Codes	Antenna analysis
Integral methods	NEC	EMC/EMI
Method of Moments	GEMACS	EMP/shielding/radiation effects
Finite Element methods	System Compativility Codes	Impulse and transient analysis
Finite Difference methods	IEMCAP	Propagation and scattering
GTD/FTD methods	SEMCAP	Microwave, mm-wavecomponents
Spectral Domain techniques	AAPG	EM machines and devices
Low/High frequency issues	COEDS	Power transmission
Time Domain techniques	Time Domain codes	Accelerator design
Hybrid techniques	Code validation	Biological interpretation
Perturbation multipole methods	Cad/automesh generation	Data interpretation
New algorithms	Graphical I/O techniques	Code studies of basic physics

TIMETABLE

October 1st 1992:- Submission deadline. Submit four copies of a 300-500 word summary to the Symposium Chairman.

November 17th 1992: Authors notified of acceptance.

January 15 1993: Submission of camera-ready copy, not more than 8 pages including figures. All submissions become the property of the SYMPOSIUM and will not be returned. The author of each paper accepted for publication will be required to provide Copyright Releases from the author and the sponsoring organization to the Symposium. Copyright Release forms will be supplied at time of acceptance. The author and sponsoring organization will retain the right to free use of the copy protected material. For both summary and final paper, please supply the following data for the lead author - Full name, address, telephone and FAX number for both work and home and a brief professional biography.

SHORT COURSES

These will cover numerical techniques, computational methods, surveys of EM analysis and code usage instruction. Full details will be published by November 1992.

DEMONSTRATIONS

These will cover computer demonstrations, software demonstrations; poster papers and key-note speakers.

VENDOR BOOTHS

These will cover product distribution, small company capabilities, new commercial codes.

The Applied Computational Electromagnetics Society

1993 **CALL FOR PAPERS** 1993

The 9th Annual Review of Progress in Applied Computational Electromagnetics

March 22-26, 1993

Naval Postgraduate School, Monterey, California

Share your knowledge and expertise with your colleagues
at the Applied Computational Electromagnetics Society's
8th Annual Review of Progress

The Annual ACES Symposium is an ideal opportunity to participate in a large gathering of EM analysis enthusiasts. Whether your interest is to learn or to share your knowledge, this Symposium is aimed at you. In addition to technical publication, the Symposium organizes live demonstrations and short courses. All aspects of electromagnetic computational analysis are represented.

The purpose of the Symposium is to bring analysts together to share information and experience about the practical application of EM analysis using computational methods. There are four areas, Symposium papers, short courses, demonstrations and vendor booths. Contact Perry Wheless for details.

1993 ACES Symposium Chairman
Perry Wheless
Dept. of Electrical Engineering
University of Alabama
Box 870286
Tuscaloosa, AL 35487-0286
Tel (205-348-1757)
Fax (205-348-8573)
e-mail: wwheless@ualvm.ua.edu

Symposium Administrator
Richard W. Adler
Naval Postgraduate School
Code EC/AB
Monterey, CA 93943

Tel (408-646-2352)
Fax (408-646-2955)

1993 ACES Symposium Co--Chairman
Andy Terzuoli
Air Force Institute of Technology
PO Box 3402
Dayton, OH 45401-3402

Tel (513-255-3576/252-3133)
Fax (513-476-4055)

1993 ACES Symposium
Sponsored by: ACES, USAIESA, NCCOSC, NPS, DOE/LLNL, DOD/USA CECOM
In cooperation with: The IEEE Antennas and Propagation Society, the IEEE Electromagnetic Compatibility Society and USNC/URSI

1992 Symposium Program Committee
for the
8th Annual Review of Progress in
APPLIED COMPUTATIONAL ELECTROMAGNETICS
at the
Naval Postgraduate School
Monterey, CA

Symposium Chairman:	Pat Foster Microwave and Antenna Systems 16 Peachfield Road Great Malvern, Worcestershire, UK WR14 4AP Phone: 0684 574057
Symposium Administrator:	Dr. Richard W. Adler Naval Postgraduate School Code EC/AB Monterey, CA. 93943 (408) 646-2352
Symposium Short Course Chairman:	Dr. John Rockway NCCOSC/Code 805 San Diego, CA. 92152-5000 (619) 553-3791
CAEME Director:	Dr. Magdy Iskander Electrical Engineering Dept. University of Utah Salt Lake City, UT. 84112 (801) 581-6944
1993 Symposium Chairman:	Perry Wheless Dept. of Electrical Engineering University of Alabama Box 870286 Tuscaloosa, AL 35487-0286 (205) 348-1757
Conference Secretary:	Mrs. Pat Adler
Advisory Committee:	Dr. Ed Miller, Los Alamos Labs. Dr. Robert Bevensee, Consultant Dr. Harold Sabbagh, Sabbagh Assoc., Inc. Jim Logan, NCCOSC Dr. Ray Luebbers, Penn State Univ. Dr. Andrew Peterson, Georgia Inst. of Tech.

CONFERENCE CHAIRMAN'S SUMMARY

As in 1991, we are publishing the Conference Proceedings in time for distribution at the conference. The time schedule for this to happen has been very tight and would not have been successful if all the authors and Session Coordinators had not responded in a timely manner. The major burden of getting the volume organized and to the printer in time has fallen on Dick and Pat Adler to whom we are all very grateful.

Next year, Professor Perry Wheless, Jr., of the University of ALabama, will be Symposium Chairman. He has been a tower of strength as Co-Chairman to this year's Symposium Chairman. Perry's Co-Chairman will be Dr. Andy Terzuoli, Jr., of the Air Force Institute of Technology, who will also be 1994 Symposium Chairman. ACES hopes by this arrangement to have continuity in the Symposium organization.

There is growing participation in the ACES Symposium by authors from outside North America. This year, they account for 25 papers out of a total of 80 which is an indication of ACES's growing international role

Professor Magdy Iskander, CAEME director, has again organized a CAEME session and there will be additional CAEME demonstrations during the Symposium.

This year, we are breaking new ground by having a variety of events all running in parallel on Tuesday afternoon. In the Banquet Hall, the technical events are Poster Sessions on code applications and CAEME, a session for demonstrating CAEME software, and booths for software vendors. On site, there will be a discussion led by Dr. Hal Sabbagh on "Canonical Problems". The afternoon will culminate in a cheese and wine party in the Banquet Hall. The events in the Banquet Hall should prove a good forum for informal discussion and I urge all Symposium attendees to go, prepared to engage in argument.

Dr. John Rockway has again done a wonderful job of putting together the short courses. These are now spread over three days, Monday, Tuesday and Friday. We are very grateful to him for carrying out this piece of organization which is so beneficial to the EM community.

It only remains for me to welcome you to the 1992 ACES Symposium and hope that you make useful contacts amongst those participating in order to advance your knowledge in the field of computational electromagnetics.

Pat Foster
1992 Symposium Chairman

ACES PRESIDENT'S STATEMENT

Welcome to the 8th Annual Review of Progress in Computational Electromagnetics! On behalf of our society, I take great pleasure in greeting you at this most important yearly event in the tchnical life of our society. I do hope that the spring beauty of the Monterey Peninsula and the hospitality of the Naval Postgraduate School will make this an occasion of intellectual and professional growth for you as well as a restful change of pace from your everyday responsibilities.

It is our intention to continue to strive to make this yearly conference the single event where you can obtain the most up-to-date information on techniques in Computational Electromagnetics and their applications. As you see from these proceedings, Pat Foster and her team have put on the richest program yet of technical papers, short courses, and display booths. We continue to support the innovative program in Computer Applications in Electromagnetics Education (CAEME) directed by Magdy Iskander. We are hoping that this mix of technical activity will be exposed to you in a congenial and convivial atmosphere that will make it a most productive as well as a pleasant experience for you. If it works, let us know. Your reactions are important to us as we learn and strive to improve.

On behalf of the officers and directors of ACES, I also wish to thank you for your participation in these difficult economic times. In this way you are attesting the importance of the mission of our society in the dissemination of practical information in Applied Computational Electromagnetics. To the authors, instructors, and chairman go my special thanks for your efforts and willingness to play this vital role in our conference. I hasten to suggest that you consider the elaboration of your presentations as papers for either our Newsletter or our Journal.

The conference also presents the opportunity for our members to renew their links with our technical committees. I should hope that you will seek out your respective chairman or join the committee meetings that will be taking place at this time. This occasion for code users and developers to have face-to-face sharing of ideas, information and organization of committee tasks is essential for progress between conferences. I hope that you can join in and see your devotion of time and energy bear fruit.

Finally, as you participate, please plan ahead for 1992 and tell your colleagues of your experiences and useful encounters.

Dr. Stan Kubina
ACES President

1993 CONFERENCE CHAIRMAN'S STATEMENT

The advances presented at the first eight Annual Review of Progress in Applied Computational Electromagnetics are notable, and bear witness to the pervasive influence of applied electromagnetics in latter twentieth century life. The need to solve Maxwell's equations, subject to boundary conditions, by numerical methods continues to increase, as devices and systems involving more arbitrary geometry and complex media proliferate. In this atmosphere of maturation, particularly within the past ten years, researchers and applications engineers have both developed and extended numerous methodologies for successful treatment of a wide variety of different problem types. The ACES Symposium provides a unique forum for the electromagnetics community to report and pursue significant progress in matters of numerical methods, code development, and applications. ACES members enjoy a society which operates in a collegial manner, and encourages future breakthroughs through the healthy inclusion of meritorious experimental studies and reports of failure among the Symposium papers.

You are invited to help the 1993 Technical Program serve the full and free exchange of knowledge and experience. A broad base of participation, especially by special session organizers and authors, will ensure that the important analysis methods and tools are appropriately present in the technical sessions. A conscientious effort will be made to offer an informative slate of Short Courses on timely topics. Commercial exhibitors can be a valuable information resource, and we will attempt to advance the exhibition component of the Symposium. An important tradition of ACES is that newcomers to the field of applied computational electromagnetics are made to feel welcome and comfortable, in both the technical program and the short courses, by the experienced veterans and advanced practitioners; every effort will be made to preserve and protect the distinctive ACES spirit and environment.

W. Perry Wheless, Jr.
1993 Symposium Chairman

SHORT COURSES

MONDAY MARCH 16 **FULL-DAY COURSE:** (Approximately 6 hour Course)

0830 "Time Domain Modeling of Guiding and Radiating Structures with TLM"
by Wolfgang J.R. Hoefer, Professor, University of Ottawa.

MONDAY MARCH 16 **MORNING HALF-DAY COURSE**

0830 "An Introduction to FDTD and Its Applications"
by Dr. K. Kunz and Dr. R. Luebbers, Pennsylvania State University

MONDAY MARCH 16 **AFTERNOON HALF-DAY COURSE**

1300 "Signal Representation and Model-based Parameter Estimation Applications in Computational EM"
by E.K. Miller, Los Alamos National Laboratory and G.J. Burke, Lawrence Livermore National Laboratory

MONDAY MARCH 16/TUESDAY MARCH 17 **SPLIT FULL-DAY COURSE**
(Monday 0830-1130 am - Tuesday 1300-1630 pm)

0830 "Antenna Radiation in Natural Environments - Special Topics"
by Dr. Robert N. Bevensee, BOMA Enterprises

MONDAY MARCH 16/TUESDAY MARCH 17 **SPLIT FULL-DAY COURSE**
(Monday 1300-1630 pm - Tuesday 1300-1630 pm)

1300 "UTD and its Practical Applications"
by Dr. R.J. Marhefka, The Ohio State University Electroscience Laboratory

FRIDAY MARCH 20 **FULL-DAY COURSE** (Approximately 6 hour Course)

0830 "Using GEMACS to Solve Practical Problems"
by Buddy Coffey, Advanced Electromagnetics

0830 "Electromagnetic Microwave Design"
by Dr. James C. Rautio, Sonnet Software, Inc.

FRIDAY MARCH 20 **MORNING HALF-DAY COURSE**

0830 "The 3D MMP Code for Computational Electromagnetics on PCs"
by Ch. Hafner, Swiss Federal Institute of Technology"

MONDAY 16 MARCH

1800 - 2030	REGISTRATION	Ingersoll Lobby
1600 - 1800	ACES BOARD OF DIRECTORS MEETING (Members invited to observe)	122 Ingersoll
1830	ACES BOARD OF DIRECTORS DINNER	Fifi's Restaurant

TABLE OF CONTENTS

KEY:

DOMAINS

TD	Time Domain
SD	Spectral Domain
MM	Millimeter wave (microwave, microstrip, antennas)
LF	Low Frequency (power systems)

METHODS

MOM	Method of Moments
FE	Finite Element method
FD	Finite Difference method
BV	Boundary Value method
TLM	Transmission Line Modeling
WG	Wire Grid modeling
ASY	Asymptotic solution applications
NM	New Method
UTD	Uniform Theory of Diffraction
PO	Physical Optics
GO	Geometrical Optics
PWS	Plane Wave Spectrum

APPLICATIONS

SC	Scattering (RCS)
MAT	Materials
BIO	Biological applications
ANT	Antenna analysis
MMIC	Monolithic Microwave Integrated Circuitry
EMC	Electromagnetic Compatibility, Electromagnetic Interference (EMC/EMI)
V	Validation
I/O	Input/Output interfaces
PC	Personal Computer applications

CODES

NEC	Numerical Electromagnetics Code (NEC)
GEM	GEMACS/GAUGE

SESSION 1- "MOMENT METHOD THEORY"

Moderator: Allen W. Glisson

Electromagnetic Scattering by Bodies with Complete or Partial Material Coatings of Varying Thickness

Allen W. Glisson, Paul M. Goggans, and Ahmed A. Kishk
Department of Electrical Engineering
University of Mississippi
University, MS 38677

Abstract

The numerical solution of electromagnetic scattering problems involving perfectly conducting bodies coated either partially or completely with a material coating of arbitrary thickness is investigated. A general surface integral equation approach is used to model geometries for which specialized thin-coating formulations may not be directly applicable or may not be expected to work well. In particular, cases are considered in which the material coating on the body changes continuously from a very thin coating to a relatively thick coating. Results are presented comparing data obtained for a coating that varies smoothly from a thin coating to a thick one with data obtained for a similar geometry in which the coating is simply terminated when it becomes very thin. Results are also presented which demonstrate the effects of using codes which do not accurately compute some elements of the moment matrix for very thin coatings.

I. Introduction

The ability to model electromagnetic scattering from objects coated with one or more thin material layers has become increasingly important in recent years as improved materials are developed. Such coatings may find uses, for example, in the protection of equipment from the environment and in the reduction or enhancement of radar cross section. The method of moments has been widely used to model scattering by combinations of conducting and material objects [1-8]. Relatively thin coatings have also been investigated via the method of moments for two-dimensional bodies and bodies of revolution [9,10]. Some standard method of moment formulations have been observed to fail for very thin coatings and a special formulation valid only for thin coatings has been developed to overcome this difficulty [11]. The formulation of [11] has also been applied to the case of conductors partially coated with thin material layers [12]. Other specialized formulations valid only for thin coatings have also been developed [13-15].

The formulations developed especially to treat thin coatings have the advantage of reducing the number of unknowns required in the numerical model, and they may be very useful for situations in which they are applicable. They may not be directly applicable, or may not be expected to work well, however, for cases in which the coating thickness becomes thick. Since "thick" is a relative term and one cannot always be certain of the circumstances for which a thin-coating formulation will fail to accurately model the scattering problem, it is desirable to have a general formulation available that is capable of modeling both thick and thin coatings simultaneously.

In previous work the authors have demonstrated that the well-known surface integral equation formulations and the method of moments can be employed to model coatings of arbitrary thickness,

This work was supported in part by the National Science Foundation under Grant No. ECS-9015328.

including thin coatings, when the elements of the moment matrix are calculated accurately [16,17]. In this work a general surface integral equation approach is employed to investigate problems involving electromagnetic scattering by perfectly conducting bodies coated either partially or completely with a material coating of arbitrary thickness. Configurations studied include conductors which are completely or partially covered with material coatings which vary substantially in thickness, from a very thin coating to a thick coating. Numerical results are presented comparing data obtained for a coating that varies smoothly from a thin coating to a thick one with data obtained for a similar geometry in which the coating is simply terminated when it becomes very thin. Results are also presented which demonstrate the effects of using codes which do not accurately compute some elements of the moment matrix for very thin coatings. A very brief description of the formulation used in this work is given in Section II. Numerical results are presented in Section III for several cases, and a summary is given in Section IV.

II. Formulation

A representative geometry for a perfectly conducting scatterer coated with a dielectric and/or magnetic material is shown in cross section in Fig. 1. The region exterior to the scatterer is assumed to have constitutive parameters (ϵ_0,μ_0) and the total fields in the exterior region are denoted by $(\mathbf{E}_0,\mathbf{H}_0)$. The material coating region is characterized by constitutive parameters (ϵ_1,μ_1) and the total fields in this region are denoted by $(\mathbf{E}_1,\mathbf{H}_1)$. The perfect electric conductor (PEC) surface and the dielectric/free space interface are denoted as S_c and S_d, respectively. The excitation is arbitrary, but is here assumed to be a plane wave which produces the incident field $(\mathbf{E}^i,\mathbf{H}^i)$. The equivalence principle [18] is applied to obtain equivalent representations of the fields in the two regions in terms of equivalent surface currents defined on S_c and S_d.

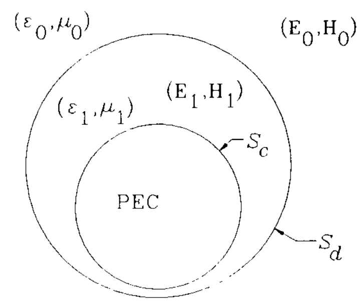

Figure 1. Geometry of a coated body.

Expressions for the scattered fields at a point $\mathbf{r}$ in the exterior region may be written in terms of potential functions and the equivalent currents as

$$\begin{aligned} \mathbf{E}_0^s(\mathbf{r}) &= -j\omega\mathbf{A}_0(\mathbf{r};\mathbf{J}_d) - \nabla\Phi_0(\mathbf{r};\rho_d^e) - \frac{1}{\epsilon_0}\nabla\times\mathbf{F}_0(\mathbf{r};\mathbf{M}_d) \\ \mathbf{H}_0^s(\mathbf{r}) &= -j\omega\mathbf{F}_0(\mathbf{r};\mathbf{M}_d) - \nabla\Psi_0(\mathbf{r};\rho_d^m) + \frac{1}{\mu_0}\nabla\times\mathbf{A}_0(\mathbf{r};\mathbf{J}_d) \end{aligned} \tag{1}$$

where $\mathbf{A}$ and $\mathbf{F}$ are the usual homogeneous-region magnetic and electric vector potential functions, Φ and Ψ are electric and magnetic scalar potential functions, $\mathbf{J}_d$ and $\mathbf{M}_d$ are the electric and magnetic surface current densities on S_d, and ρ_d^e and ρ_d^m are the electric and magnetic surface charge densities related to the surface current densities through the appropriate continuity equations. The subscript 0 on the potential quantities indicates that the constitutive parameters of the exterior region are used in the potential expressions. The total fields in the exterior region are then obtained by adding the scattered and incident fields. In a similar manner the expressions for the total fields in the material coating region are given by

$$
\begin{aligned}
\mathbf{E}_1(\mathbf{r}) &= -j\omega\mathbf{A}_1(\mathbf{r};\mathbf{J}_c) - \nabla\Phi_1(\mathbf{r};\rho_c^e) + j\omega\mathbf{A}_1(\mathbf{r};\mathbf{J}_d) + \nabla\Phi_1(\mathbf{r};\rho_d^e) + \frac{1}{\epsilon_1}\nabla\times\mathbf{F}_1(\mathbf{r};\mathbf{M}_d) \\
\mathbf{H}_1(\mathbf{r}) &= \frac{1}{\mu_1}\nabla\times\mathbf{A}_1(\mathbf{r};\mathbf{J}_c) + j\omega\mathbf{F}_1(\mathbf{r};\mathbf{M}_d) + \nabla\Psi_1(\mathbf{r};\rho_d^m) - \frac{1}{\mu_1}\nabla\times\mathbf{A}_1(\mathbf{r};\mathbf{J}_d)
\end{aligned} \tag{2}
$$

where the subscript c denotes the electric current source on the conductor surface.

A set of coupled integral equations that can be solved for the unknown surface current densities $\mathbf{J}_c$, $\mathbf{J}_d$, and $\mathbf{M}_d$ are obtained by application of the boundary conditions at the surfaces S_c and S_d. Various sets of integral equations can be obtained in this manner. In this work the boundary conditions enforced are that the tangential electric field is zero on the conductor surface S_c and that the tangential electric and magnetic fields are continuous across the dielectric/free space interface S_d. The resulting set of equations can be expressed succinctly as

$$\mathbf{E}_{1_{\tan}}(\mathbf{r}) = \mathbf{0} \quad , \qquad \text{on } S_c \tag{3}$$

$$\mathbf{E}_{1_{\tan}}(\mathbf{r}) - \mathbf{E}^s_{0_{\tan}}(\mathbf{r}) = \mathbf{E}^i_{\tan}(\mathbf{r}) \quad , \qquad \text{on } S_d \tag{4}$$

$$\mathbf{H}_{1_{\tan}}(\mathbf{r}) - \mathbf{H}^s_{0_{\tan}}(\mathbf{r}) = \mathbf{H}^i_{\tan}(\mathbf{r}) \quad , \qquad \text{on } S_d \tag{5}$$

This set of equations has been referred to as the E-PMCHW formulation, indicating that the EFIE is used on the conductor surface, whereas the PMCHW formulation (continuity of tangential fields) has been used at the material boundary.

III. Discussion of Results

In this section results for several geometrical configurations are presented to illustrate the effects of thin coatings on the scattering cross sections of objects. Some of the configurations studied include conductors which are completely or partially covered with material coatings which vary substantially in thickness, from a very thin coating to a thick coating. All of the geometries studied are rotationally symmetric, and the numerical results are obtained using a modified version of the computer code used in [19]. Some examples of the coated bodies studied are shown in cross section in Fig. 2. In the figure the dashed lines represent a conducting sphere surface, while the solid line represents the surface of the material coating. Fig. 2a represents a PEC sphere with dimension $k_0a=1.5$ that is coated with a material layer of thickness t, which varies linearly along the generating contour of the sphere from a thickness of $t=0.001\lambda_0$ at $\theta=180°$ to $t=0.01\lambda_0$ at $\theta=0°$, where θ is the usual spherical coordinate angle. Fig. 2b shows the same sphere, but with a coating that varies logarithmically instead of linearly (*i.e.*, $\log(t)$ varies linearly). Fig. 2c shows the same sphere and coating variation as in Fig. 2a, but the coating is truncated at $\theta=90°$. The truncation is accomplished by reducing the thickness of the coating layer linearly from its normal value to zero over the distance of one segment of the generating arc model. The same PEC sphere is again shown in Fig. 2d, where the coating thickness varies logarithmically from $\log(t)=-4.8$ to $\log(t)=-0.8$, with $\lambda_0=1$ meter.

Results are shown in Fig. 3 comparing the monostatic scattering cross section of several geometries similar to that shown in Fig. 2b. The different curves in the figure represent coatings of different thicknesses on the sphere of dimension $k_0a=1.5$. The relative constitutive parameters of the coating in each case are $\epsilon_{1_r}=3\text{-}j4$ and $\mu_{1_r}=5\text{-}j6$. The coatings all vary logarithmically in thickness around

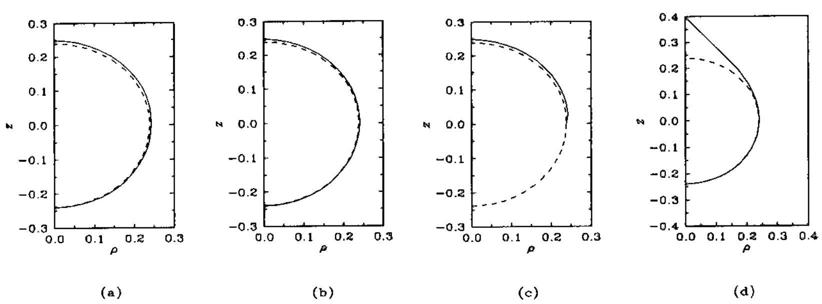

Figure 2. Examples of coated bodies: (a) linear coating taper, (b) log coating taper, (c) truncated linear taper, and (d) log taper with a larger range.

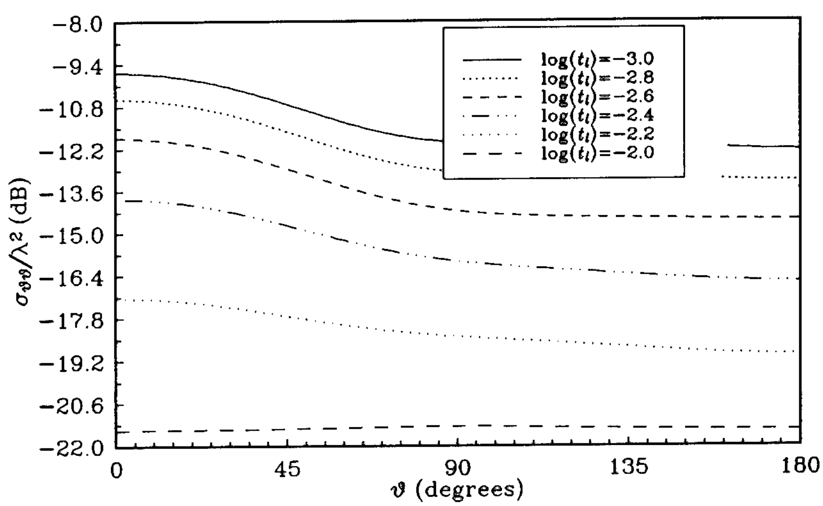

Figure 3. Monostatic scattering cross sections of spheres with log-taper coatings of varying minimum thickness.

the generating contour from a minimum thickness of t_l to a maximum thickness t_u=0.01λ_0. Each curve is for a different value of t_l. The solid curve in Fig. 3 corresponds to the geometry illustrated in Fig. 2b. One observes that there is a fairly substantial change in the scattering cross section as the minimum thickness is increased. The lowest curve in the figure is for the case in which the coating is uniform with

thickness $t=t_l=t_u=0.01\lambda_0$. Not shown on the figure, but useful for comparison, is the case in which the coating is uniform with thickness $t=0.001\lambda_0$; the scattering cross section is approximately -8.5 dB for this case.

Fig. 4. shows monostatic scattering cross section results for a geometry similar to that shown in Fig. 2d, where the coating thicknesses varies over a wide range. The basic geometry for the results of Fig. 4 is again the PEC sphere of radius $k_0a=1.5$. The relative constitutive parameters of the coating

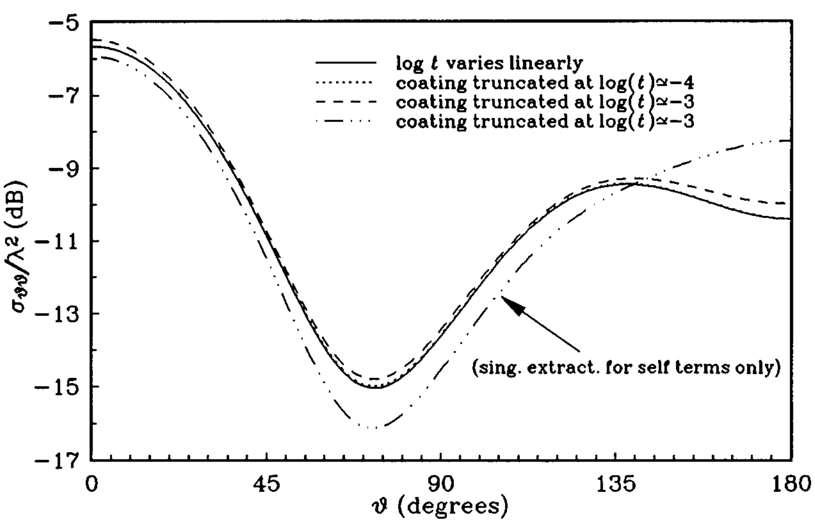

Figure 4. Monostatic scattering cross section for a sphere with a log-taper coating with a wide thickness range and comparison to cases for truncated coatings.

are $\epsilon_{1r}=3\text{-}j4$ and $\mu_{1r}=5\text{-}j6$. The coating thickness varies logarithmically from $\log(t)=-5$ at $\theta=180°$ to $\log(t)=-1$ at $\theta=0°$. The results for this basic geometry are shown as a solid line. Results shown as a dotted line are obtained if the coating is simply removed over the portion of the sphere where the coating thickness would be less than approximately $0.0001\lambda_0$. The results for this case are essentially indistinguishable from those of the basic geometry, as one might expect. A small difference in the cross section is observed if the coating is removed over the region where its thickness would be less than about $0.001\lambda_0$ (dashed line). The results shown as the dash-dot line are for the same configuration as those of the dashed line, but the careful evaluation of the singularity [16,17] has not been performed when the source and observation segments are not on the same surface. The results for this case show significant variation from the other curves even though no adjacent-surface segments in the model are closer than $0.001\lambda_0$ (except for the segment which connects the dielectric surface to the conductor surface in the truncation procedure). While other data was not available for comparison, the validity of the results shown is suggested both by past experience with uniform coatings [17] and by the agreement between

the complete-coating and the truncated-coating data, for which the numerical model is very different.

Results are shown in Fig. 5 for the monostatic scattering cross section of the same PEC sphere and coating material for the case in which the coating has a linear taper such as shown in Fig. 2a and for the case in which the linear-taper coating is truncated at $\theta=90°$ as depicted in Fig. 2c. The dimensions

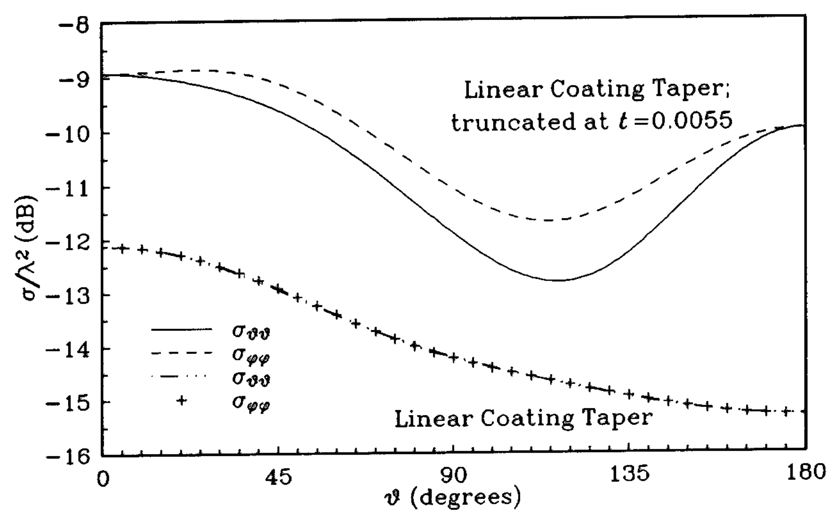

Figure 5. Monostatic scattering cross sections for a sphere with a linear-taper coating and a truncated linear-taper coating.

described for Fig. 2a are correct for the linear-taper case; in particular, the thickness of the coating varies linearly from $t=0.001\lambda_0$ at $\theta=180°$ to $t=0.01\lambda_0$ at $\theta=0°$. The results clearly demonstrate that truncating the coating in this case has a substantial effect on the scattering cross section.

Fig. 6 shows results for the geometry shown in Fig. 2d, where the coating thickness varies from $\log(t)=-4.8$ to $\log(t)=-0.8$, with $\lambda_0=1$ meter. Comparison results are shown in the figure for the case in which careful evaluation of the singularity in the integrands is performed only for source and observation segments on the same surface. Significantly different results are obtained when the integrations are not performed accurately. While no firm conclusion can be drawn, it seems that less error results (for the scattering cross section) as fewer very nearby segments exist on adjacent surfaces, if the integrations are not performed accurately. See Fig. 4 for comparison, where less overall error seems to occur when the coating is truncated if the coating is too thin.

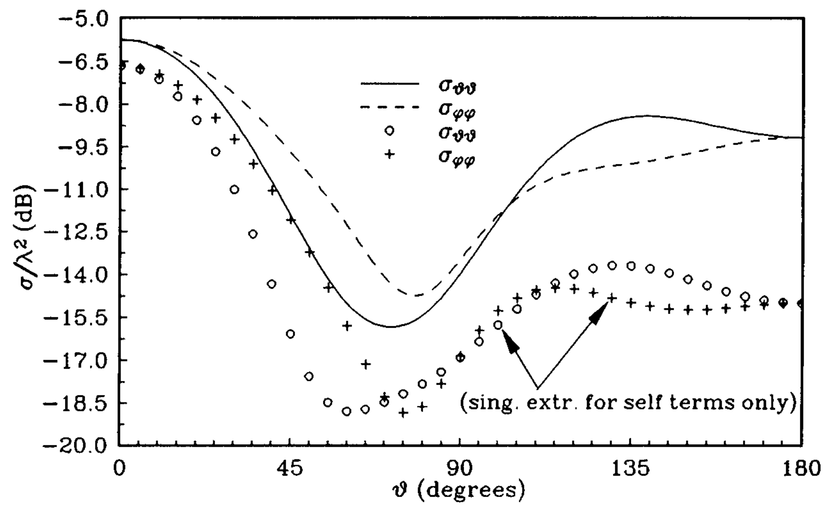

Figure 6. Monostatic scattering cross section for the geometry of Fig. 2d, with and without singularity extraction on adjacent-surface integrations.

IV. Summary

A general surface integral equation approach is employed in this work to investigate problems involving electromagnetic scattering by perfectly conducting bodies coated either partially or completely with a material coating of arbitrary thickness. The surface integral equation approach is used to model geometries for which specialized thin-coating formulations may not be directly applicable or may not be expected to work well. The geometrical configurations studied include conductors which are completely or partially covered with material coatings which vary in thickness over a large range, from a very thin coating to a thick coating. Numerical results are presented for structures with a coating that varies smoothly from a thin coating to a thick one and for similar geometries in which the coating is simply terminated when it becomes very thin. Results are also presented which illustrate the effects of using codes which do not accurately compute some elements of the moment matrix for very thin coatings. It is observed that substantial variation in the scattering cross section can be produced by very thin coatings with varying thickness.

References

[1] P. M. Goggans and T. H. Shumpert, "CFIE MM solution for TE and TM incidence on a 2-D conducting body with a dielectric filled cavity," *IEEE Trans. Antennas Propagat.*, vol. AP-38, pp. 1645-1649, 1990.

[2] E. Arvas, Y. Qian, T. K. Sarkar, and F. Alan, "TM scattering from a conducting cylinder of arbitrary cross-section covered by multiple layers of lossy dielectrics," *IEE Proceedings - Part H*, vol. 135, pp. 226-230, 1988.

[3] S. M. Rao, E. Arvas, and T. K. Sarkar, "Combined field solution for TM scattering from multiple conducting and dielectric cylinders of arbitrary cross section," *IEEE Trans. Antennas Propagat.*, vol. AP-35, pp. 447-451, 1987.

[4] E. Arvas and T. K. Sarkar, "RCS of two-dimensional structures consisting of both dielectrics and conductors of arbitrary cross section," *IEEE Trans. Antennas Propagat.*, vol. AP-37, pp. 546-554, 1989.

[5] L. N. Medgyesi-Mitschang and C. Eftimiu, "Scattering from axisymmetric obstacles embedded in axisymmetric dielectrics: The method of moments solution," *Appl. Phys.*, vol. 19, pp. 275-285, 1979.

[6] S. Govind, D. R. Wilton, and A. W. Glisson, "Scattering from inhomogeneous penetrable bodies of revolution," *IEEE Trans. Antennas Propagat.*, vol. AP-32, pp 1163-1173, 1984.

[7] A. A. Kishk and L. Shafai, "Numerical solution of scattering from coated bodies of revolution using different integral equation formulations," *Inst. Elec. Eng. Proc.*, vol. 133, pt. H. pp. 227-232, 1986.

[8] J.R. Mautz and R.F. Harrington, "Electromagnetic coupling to a conducting body of revolution with a homogeneous material region," *Electromagn.*, vol. 2., pp 797-806, 1984.

[9] L. N. Medgyesi-Mitschang and J. M. Putnam, "Electromagnetic scattering from electrically large coated flat and curved strips: entire domain galerkin formulation," *IEEE Trans. Antennas Propagat.*, vol. AP-35, pp. 790-801, 1987.

[10] P. L. Huddleston, "Scattering from conducting finite cylinders with thin coatings," *IEEE Trans. Antennas Propagat.*, vol. AP-35, pp. 1128-1136, 1987.

[11] J. M. Putnam, "Combined field formulation for conducting bodies with thin coatings," *ACES J.*, vol. 4, no. 2, pp. 15-26, 1989.

[12] A. A. Kishk, A. W. Glisson, and P. M. Goggans, "Scattering from conductors partially coated by thin materials," *Symposium on Antenna Technology and Applied Electromagnetics 1990 Conference Proceedings*, pp. 246-252, August, 1990.

[13] S. U. Hwu and D. R. Wilton, "Electromagnetic scattering from arbitrary cylinders with thin material coatings," *1989 IEEE AP-S International Symposium Digest*, vol. II, pp. 1112-1115, June 1989.

[14] X. Min, W. Sun, W. Gesang, and K.M. Shen, "An efficient formulation to determine the scattering characteristics of a conducting body with thin magnetic coating," *IEEE Trans. Antennas Propagat.*, vol. AP-39, pp. 448-454, 1991.

[15] A. Sadigh and E. Arvas, "Electromagnetic scattering from arbitrarily shaped conducting bodies coated with a thin layer of lossy magnetic material," in press, *IEE Proceedings Part H*, 1992.

[16] P. M. Goggans, A. A. Kishk, and A. W. Glisson, "A systematic treatment of conducting and dielectric bodies with arbitrarily thick or thin features using the method of moments," submitted to *IEEE Trans. Antennas Propagat.*

[17] A. A. Kishk, A. W. Glisson, and P. M. Goggans, "Scattering from conductors coated with materials of arbitrary thickness," in press, *IEEE Trans. Antennas Propagat.*

[18] R. F. Harrington, *Time Harmonic Electromagnetic Fields*. New York: McGraw-Hill, 1961.

[19] A. W. Glisson and D. R. Wilton, "Simple and efficient numerical methods for problems of electromagnetic radiation and scattering from surfaces," *IEEE Trans. Antennas Propagat.*, vol. AP-28, pp. 593-603, 1980.

CLASP—A NEW, GENERAL-PURPOSE METHOD OF MOMENTS SCATTERING CODE

by

P. Kirby, D.W. Lizius, A.J. Marrison, J.G. Morgan and J.C. Wood

Radio Frequency Effects Department, Culham Laboratory,
Abingdon, Oxfordshire, OX14 3DB, United Kingdom

This paper describes the construction of *CLASP* (Culham Laboratory Advanced Scattering Program), which is a new, general-purpose computer program for the solution of problems of electromagnetic scattering at low frequency. The program uses the boundary element method to calculate the currents that are induced on a scattering body, from which the radiated fields follow directly. A fundamental feature of the program is that the scattering body may be of general shape and may be composed of conducting, dielectric and magnetic material, in the form of wires, surfaces and volumes. This means that the program has many possible applications.

1. INTRODUCTION

This paper describes the construction of *CLASP* (Culham Laboratory Advanced Scattering Program), which is a new, general-purpose computer program for the solution of problems of electromagnetic scattering at low frequency. The construction of the program has been an ambitious project and has required much effort, in both mathematical analysis and computer programming. A fundamental feature of the program is that the scattering body may be of general shape and may be composed of conducting, dielectric and magnetic material, in the form of wires, surfaces and volumes. This means that the program has many possible applications.

The program is based on the integral solutions in the frequency domain for the scalar and vector electromagnetic potentials, together with the method of boundary finite elements (also known as the Method of Moments), in a rigorous Galerkin formulation. The analytical expressions for the electromagnetic fields and the boundary conditions are converted into a system of linear algebraic equations, which are solved to find the current density at the given frequency on all parts of the scattering body. The scattered fields are then calculated directly once these currents are known. At present, the program calculates scattering cross-sections, that is, it calculates the out-going far fields that correspond to an impressed in-coming plane wave. The program will be enhanced in the near future to allow local electromagnetic sources, such as voltage sources on wires, so that the radiation from antennas may also be modelled.

The method of boundary finite elements is particularly useful in practical scattering problems, first because it can treat realistic geometries, and secondly because it includes the radiation condition at infinity by construction. For these reasons, very accurate results may be obtained. The fundamental disadvantage of the method is that, by definition, every

boundary element interacts with every other boundary element, so that the system of linear equations is dense, and the computational effort for its solution increases as N^3, in which N is the number of unknowns. This behaviour means that the method is impractical if the scattering body is large compared with the wave-length of the incident electromagnetic wave. Nevertheless, a wide variety of useful calculations may be performed within this constraint, especially as powerful computers are now widely available.

The subject area that *CLASP* addresses has a large literature. The program has been built upon this knowledge (described for instance by Moore and Pizer [1], and Wang [2]), and the wide-spread practical success of existing computer codes such as *NEC* of Burke and Poggio [3]. The particular features that characterize *CLASP* are: the flexibility and generality of its capabilities; the rigorous approach to the evaluation of the Galerkin integrals; and the care that has been taken in the design and implementation of the software. A central feature of *CLASP*, as of several other recent computer codes (for instance *FERM* [4], *EASOGS* [5], and the MoM code at MATRA [6]), is the use of plane triangular patches to model conducting surfaces. This provides an improvement in accuracy and flexibility over the traditional representation of a surface by a mesh of thin wires.

As indicated above, the range of objects that *CLASP* may model is large and includes many items of practical importance, such as: open and closed structures that are composed of thin wires and metallic surfaces, including connections between wires and surfaces; volumes of inhomogeneous dielectric material; bulk volumes of homogeneous dielectric and magnetic material; and dielectric and magnetic material attached to conducting surfaces.

2. THEORY

If an electromagnetic wave is incident upon a body, the total electric field at any point in space may be written as the sum of the known incident field $\mathbf{E}^i$ and the unknown scattered field $\mathbf{E}^s$, so that

$$\mathbf{E}(\mathbf{r}) = \mathbf{E}^i(\mathbf{r}) + \mathbf{E}^s(\mathbf{r}). \tag{1}$$

The scattered field may be derived in the usual way from its electromagnetic potentials in the form

$$\mathbf{E}^s(\mathbf{r}) = -i\omega\mathbf{A}(\mathbf{r}) - \nabla\phi(\mathbf{r}), \tag{2}$$

$$\mathbf{A}(\mathbf{r}) = \frac{\mu}{4\pi}\int_{V'} \mathbf{j}(\mathbf{r}')\frac{\exp(-ikR)}{R}\,dv', \tag{3}$$

$$\phi(\mathbf{r}) = \frac{1}{4\pi\epsilon}\int_{V'} \rho(\mathbf{r}')\frac{\exp(-ikR)}{R}\,dv', \tag{4}$$

in which $\mathbf{j}$ is the unknown current density in the scattering body, ρ is the corresponding electric charge density, and $R \equiv |\mathbf{r} - \mathbf{r}'|$ is the distance between the source point $\mathbf{r}'$ and the field point $\mathbf{r}$. Here, the harmonic time-dependence $\exp(+i\omega t)$ has been assumed. The permittivity ϵ and permeability μ, which are assumed to be uniform and constant, refer to the infinite medium in which all the currents and fields are assumed to be embedded. The quantity k is the wave-number in that medium and is given by $k \equiv \omega\sqrt{\mu\epsilon}$. In the treatment for metallic bodies, for which the skin depth is negligibly small, the integrals over volumes in (3) and (4) may be reduced to integrals over surfaces of a surface charge density and a surface current density $\mathbf{J}$. When augmented by the appropriate boundary conditions,

(1)-(4) constitute a set of integral equations for the electric and the magnetic field. In particular, for a metallic conductor of surface impedance Z_s, the boundary condition on the tangential component of the field, namely

$$\mathbf{E}_{\tan} = Z_s \mathbf{J}, \tag{5}$$

gives the Electric Field Integral Equation. The surface impedance is zero for a perfect conductor.

3. BASIS FUNCTIONS

CLASP works in terms of the currents that flow in the scattering body because this choice provides the most natural and convenient description. In the boundary element method, these currents are represented approximately by a linear superposition of suitable basis functions in the form

$$\mathbf{J}(\mathbf{r}) = \sum_{n=1}^{N} J_n \mathbf{f}_n(\mathbf{r}), \tag{6}$$

in which N is the total number of basis functions, the scalar quantities J_n are unknown constants to be determined, and the vector quantities $\mathbf{f}_n(\mathbf{r})$ are the individual basis functions, which are given functions of position.

In order to allow a range of geometry, *CLASP* contains four different types of basis function. Each basis function has compact support and corresponds to one of the four geometrical elements from which any numerical model is to be constructed, namely: the thin wire, the plane triangular patch, the junction between a wire and a patch, and the tetrahedron. The basis functions are linear functions of position, except for the singular part of the basis function for the junction.

The thin wire is represented by a chain of piece-wise straight, conical segments of finite or infinite conductivity. A roof-top basis function exists on each pair of connected wires and describes the surface current density on those wires. The current density is assumed to be zero at all free ends. The wires are assumed to be very thin, that is, they are regarded as idealized conductors of radius a and length h such that $a/h \ll 1$ and $ka \ll 1$. This hypothesis allows the poloidal current to be ignored, and allows the axial current to be taken as independent of the poloidal angle around each wire. It also allows the boundary condition on the electric field to be imposed only along the length of each wire. These approximations constitute the usual thin-wire approximation of electromagnetic modelling [1]. In *CLASP*, thin wires are intended to model actual wires only; as described above, the use of triangular patches supersedes the use of a wire mesh to model a solid metallic surface.

The triangular patch is of central importance in the program. Triangular patches are used to model metallic surfaces using the Electric Field Integral Equation, and to model volumes of homogeneous dielectric and magnetic material using a Combined Field Integral Equation in a surface source treatment that is described by Harrington [7]. The basis function that is used in *CLASP* for triangular patches is that introduced by Rao, Wilton and Glisson [8]. A basis function of this type exists on each pair of triangles that have a common edge. The basis function has the desirable property that the normal component

of current density is continuous at this edge, thus avoiding spurious line charges in the numerical model.

The mathematical properties of such basis functions (linear elements defined over a plane triangle) have been examined formally by Bendali [9], who shows that the results from the numerical model may not converge as the size of the patches is reduced. However, successful results already in the literature and those from *CLASP* show that this potential difficulty does not seem to be important in practice. Nevertheless, an element of Bendali's result appears in the empirical fact that considerable care must be taken in the representation of curved surfaces by plane patches if results of high accuracy are to be obtained.

The junction is the geometrical element that allows the connection of thin wires to triangular patches. The basis function is similar to that described by Hwu, Wilton and Rao [10], but differs in that here a separate basis function is assigned to each connection between one wire and one patch; in Ref. [10] a basis function is assigned to each wire and all the patches to which it is connected. The present approach has the disadvantage that it uses more basis functions, but given that the number of junctions in a numerical model is likely to be small, this is likely to be unimportant in practice. Conversely, the present approach has the advantage that it makes no assumption about the relative distribution of the current that flows from a wire on to several patches. The basis function has a singular part that represents the concentration of the current at the point of attachment of the wire. This point is restricted to be a vertex of the patch.

The tetrahedron is the geometrical element that is used to represent volumes of inhomogeneous dielectric material. This is done by a piece-wise constant approximation, by filling the volume with a set of tetrahedra that each have a constant permittivity. The basis function is that introduced by Schaubert, Wilton and Glisson [11] and is simply the analogue in three dimensions of the basis function for the triangular patch. The polarization current in the material is treated as an unknown current density and is described in terms of a ratio of permittivities and a modified electric displacement vector.

These basis functions are mathematically satisfying in that, with the exception of the singular part of the junction, they are the same essential object (a certain linear function defined over a simplex), but specified in either one, two or three space dimensions.

4. GALERKIN PROCEDURE

A rigorous Galerkin formulation has been adopted in *CLASP*. This is based on the symmetric integral

$$\langle \mathbf{f}, \mathbf{g} \rangle \equiv \int \mathbf{f} \cdot \mathbf{g} \, dv, \tag{7}$$

in which $\mathbf{f}$ is a basis function, $\mathbf{g}$ is a testing function, and v is the volume of the scattering body. In the Galerkin method, the function $\mathbf{g}$ is taken from the set of basis functions $\mathbf{f}$. When (5), for instance, is tested in this way, the result may be written as

$$\langle \mathbf{E}^i, \mathbf{f}_m \rangle = i\omega \langle \mathbf{A}, \mathbf{f}_m \rangle + \langle \nabla \phi, \mathbf{f}_m \rangle + \langle Z_s \mathbf{J}, \mathbf{f}_m \rangle, \tag{8}$$

in which $\mathbf{f}_m$ is the mth basis function in the numerical model. The potentials $\mathbf{A}$ and ϕ are then expressed in terms of the unknown currents from (3) and (4), so that (8) may be

written as a matrix equation in the form

$$ZI = V, \tag{9}$$

in which Z is a known, dense, complex $N \times N$ matrix (the impedance matrix), I is a vector of N unknown currents, and V is a vector of N known right-hand sides. The Galerkin method ensures that the reciprocal nature of the electromagnetic field is represented in the numerical approximation; in particular, for metallic conductors, Z is a symmetric matrix. The advantages of a Galerkin treatment are discussed and promoted in Ref. [2].

A large part of the mathematical analysis that is needed to implement the boundary element method occurs in the evaluation of the two terms $i\omega\langle \mathbf{A},\, \mathbf{f}_m\rangle$ and $\langle \nabla\phi,\, \mathbf{f}_m\rangle$. These terms represent singular integrals in two dimensions for wires, four dimensions for patches, five and six dimensions for tetrahedra, and three, four and five dimensions for cross-terms. Their accurate evaluation is no small matter, especially as only a few calculations of the integrand are permitted, owing to the potentially huge number of integrals to be treated. A feature of the present approach is that it is formally correct and involves no arbitrary simplifications.

The method of evaluation of the integrals may be illustrated by the treatment for triangular patches. The quantity to be evaluated takes the form

$$\int_S \int_{S'} (k^2 \mathbf{x} \cdot \mathbf{x}' - 4)\, \frac{\exp(-ikR)}{kR}\, dS'\, dS, \tag{10}$$

in which $\mathbf{x}$ and $\mathbf{x}'$ are local position vectors in the surfaces S and S' of the field and source patch respectively. First, the divergent term $1/R$ is subtracted out, as discussed by Davis and Rabinowitz [12], and the regular part of the four-dimensional integral is integrated numerically.

This integration uses a product rule that is based on a standard rule for the two-dimensional simplex, from Stroud [13] and Dunavant [14]. The code allows a choice of rule so that convergence tests may be performed and the best compromise between speed and accuracy may be obtained. Secondly, the divergent term is integrated analytically over the source triangle, using the expressions given by Wilton et al. [15], and is then integrated numerically over the field triangle.

From a mathematical point of view, the use of adaptive integration would provide a more rigorous calculation, for then each integral could be found to a specified accuracy, regardless of the difficulty of the integrand. Such a scheme has not been adopted here because of concern for the unacceptably large amount of computing time that it might consume. Experience so far with *CLASP* suggests that the present method is perfectly adequate.

The integrals over tetrahedra are evaluated in exactly the same way, using the Gaussian rules over the three-dimensional simplex that are given by Keast [16]. The integrals over wires are treated similarly, but the calculation includes more analytical integration and is therefore more accurate.

The integrals over junctions provide a further difficulty in that there is a fixed-point singularity at the point of attachment of the wire to the patch, in addition to the usual $1/R$ singularity. This has been treated by a series of transformations and dissections of the region of integration, such that the Jacobians of the transformations cancel the singularities in the integrand.

5. IMPLEMENTATION

The construction of CLASP has been a substantial task. The computer program is written in FORTRAN 77 and comprises roughly 60 000 lines of code in 300 subroutines. It was developed on UNIX workstations, but is intended to be readily portable to other machines. It is constructed from well-defined modules so that maintenance is relatively easy. Considerable care has been taken in the design of the software and the standard of coding.

The fundamental geometrical entity in the program is the node, which is a point in space that is specified by its three Cartesian coordinates. Wires, patches and tetrahedra are then defined as ordered sets of nodes and are stored as lists of integer node numbers. The connections between these elements, and the positions of the basis functions, are found by sorting these lists and then identifying those elements with common node numbers. This operation is fast because it requires only of order $N \log N$ integer operations for N elements. The use of node numbers is particularly convenient in the evaluation of the Galerkin integrals because it gives a sure method of finding the relative positions of any two basis functions, in particular whether they are separated, touching or overlapping.

The manipulation of the impedance matrix and the solution of the system of linear equations is a major item in the program. The most important feature of the design, as found in existing codes such as *NEC* [3], is that the impedance matrix is allowed to be larger than the memory of the computer on which the program is run. If this occurs, the entire impedance matrix is stored only on disk (as a direct access file), and only a small sub-set of it is held in memory at any one time. This facility increases greatly the utility of the program, but at the expense of considerable extra complexity in the software. The impedance matrix is treated as a set of small square sub-blocks, and each sub-block is filled element by element and is then written on disk. In this way, the process of storing the matrix is largely uncoupled from the calculation of the matrix elements.

The solution of the linear system in (9) is found by conventional LU factorization, which is refined here by the use of row-equilibration. The factorization has been implemented in a way that minimizes the number of disk accesses, by careful manipulation of the square sub-blocks. A further refinement of the solution process is that it treats multiple right-hand sides. This provides an efficient solution of problems in which many different scattering angles are required.

If the scattering body has reflection or rotational symmetry, the impedance matrix is circulant in blocks that correspond to each symmetry cell, and the matrix may therefore be diagonalized in blocks by a unitary transformation. The program then constructs and stores only these diagonal blocks, with the corresponding reduction in the necessary storage and computing time. The program allows rotational and reflection symmetry to be used simultaneously.

A further feature of the program, as in *NEC* [3], is that it allows additions to the geometry of a structure for which the factored impedance matrix already exists. This facility allows the effects of different small additions to a large primary structure to be found without the need to solve the full problem each time. It makes use of a simple 2×2 partitioning of the impedance matrix in the form

$$Z = \begin{pmatrix} A & B \\ C & D \end{pmatrix},$$

in which block A represents the large primary structure, block D represents the additional structure, and blocks B and C represent the interactions between the primary structure and the additional structure.

CLASP takes the form of a batch program. The input file contains the specification of the geometry and composition of the scattering body, and the calculation to be performed, as a sequence of tagged records. These data are read by the program and the four elements of the scattering matrix are calculated and are written on the output file for each scattering angle that has been requested. The user of the program is allowed to specify monostatic and bistatic calculations by a single line in the input file. By design, *CLASP* is purely an electromagnetics code and does not include facilities for mesh generation or the graphical display of the results; these operations are assumed to be provided by other programs.

6. RESULTS

CLASP has been applied successfully to several different types of scattering body, such as: conducting wires, spheres, disks, cubes, cylinders with hemispherical end-caps, dielectric spheres, and conducting spheres that are coated with dielectric material. The results of these calculations are presented in a separate paper, *Benchmark Calculations with CLASP*, in these proceedings. A further paper, *The Regular Tetrahedron—A Canonical Scattering Problem*, in these proceedings, presents various numerical and experimental results for the scattering from a conducting tetrahedron of edge 3λ, and proposes this as a new canonical problem for ACES.

An indication of the accuracy that may be obtained from *CLASP* is given here by the calculation of the scattering from a perfectly conducting sphere.

The numerical model of the sphere is constructed from 320 triangles that are obtained by the recursive refinement of the 20 faces of an icosahedron. The size of the icosahedron is chosen so that the mean radius of the model is exactly equal to the radius of the true sphere. (This constitutes a modelling rule for triangulated spheres.) Comparison of the numerical and analytical results for the bistatic radar cross-section of a sphere of size $ka = 8$ shows that for angles less than 90° there are local deviations of about 0.4 dB, but at angles greater than 90° the results are almost coincident. This result is obtained for a patch size of 0.38λ, that is, larger than $\lambda/3$, which is rather coarse. When the size of each patch is reduced, the accuracy of the numerical calculation increases; when the patch size is $\lambda/20$, the error is less than 0.01 dB.

Acknowledgement

This work was done under contract to the Electronics Division of the Defence Research Agency (RSRE Malvern). The authors are grateful for permission to publish this paper.

REFERENCES

1. J. Moore and R. Pizer (Eds), *Moment Methods in Electromagnetics*, Research Studies Press, Letchworth, England, 1984.
2. J.J.H. Wang, *Generalized Moment Methods in Electromagnetics*, John Wiley & Sons, Inc., New York, USA, 1991.
3. G.J. Burke and A.J. Poggio, *Numerical Electromagnetics Code (NEC)—Method of Moments*, Lawrence Livermore National Laboratory, USA, Report UCID 18834, 1981.

4. D.A. Shnidman and S. Lee, *The Finite Element Radiation Model (FERM) Program*, Proc. *3rd Annual Review of Progress in Applied Computational Electromagnetics*, Monterey, USA, Applied Computational Electromagnetics Society, 1987.
5. E. Michielssen, K. Libbrecht and H. Pues, *EASOGS: A General-Purpose Method of Moments Electromagnetic Computer Modeling Code*, Newsletter of the Applied Computational Electromagnetics Society, USA, Vol. **4**, no. 3, pp. 13–15, 1989.
6. J.P. Estienne, J.G. Ferrante, A. Baradat and J. Seille, *Comparison of Numerical Simulation Techniques Applied to EMC/ESD Analysis*, Proc. *2nd ESA Workshop on Electromagnetic Compatibility and Electromagnetic Modelling for System EMC Analysis*, European Space Agency, ESTEC, Noordwijk, The Netherlands, 1990.
7. R.F. Harrington, *Boundary Integral Formulation for Homogeneous Material Bodies*, J. E.M. Waves and Appl., Vol. **3**, no. 1, pp. 1–15, 1989.
8. S.M. Rao, D.R. Wilton and A.W. Glisson, *Electromagnetic Scattering by Surfaces of Arbitrary Shape*, IEEE Trans. on Antennas and Propagat., Vol. AP-30, no. 3, pp. 409–418, 1982.
9. A. Bendali, *Numerical Analysis of the Exterior Boundary Value Problem for the Time-Harmonic Maxwell Equations by a Boundary Finite Element Method, Part 2: The Discrete Problem*, Mathematics of Computation, Vol. **43**, no. 167, pp. 47–68, 1984.
10. S.U. Hwu, D.R. Wilton and S.M. Rao, *Electromagnetic Scattering and Radiation by Arbitrary Conducting Wire / Surface Configurations*, IEEE Symposium Digest *Antennas and Propagation*, Syracuse University, USA, Vol. 2, pp. 890–893, 1988.
11. D.H. Schaubert, D.R. Wilton and A.W. Glisson, *A Tetrahedral Modeling Method for Electromagnetic Scattering by Arbitrarily Shaped Inhomogeneous Dielectric Bodies*, IEEE Trans. on Antennas and Propagat., Vol. AP-32, no. 1, pp. 77–85, 1984.
12. P.J. Davis and P. Rabinowitz, *Methods of Numerical Integration*, Academic Press, New York, USA, 1975, section 2.12.4.
13. A.H. Stroud, *Approximate Calculation of Multiple Integrals*, Prentice-Hall, Inc., New Jersey, USA, 1971.
14. D.A. Dunavant, *High Degree Efficient Symmetrical Gaussian Quadrature Rules for the Triangle*, Int. j. numer. methods eng., Vol. **21**, pp. 1129–1148, 1985.
15. D.R. Wilton, S.M. Rao, A.W. Glisson, D.H. Schaubert, O.M. Al-Bundak and C.M. Butler, *Potential Integrals for Uniform and Linear Source Distributions on Polygonal and Polyhedral Domains*, IEEE Trans. on Antennas and Propagat., Vol. AP-32, no. 3, pp. 276–281, 1984.
16. P. Keast, *Moderate-Degree Tetrahedral Quadrature Formulas*, Comput. Meths. Appl. Mech. Engrg., Vol. **55**, pp. 339–348, 1985.

Hybrid Optics/Numerical Approach to Electromagnetic Scattering

Colin Sillence. British Aerospace PLC. Sowerby Research Centre. FPC267. PO Box 5. Filton. Bristol BS12 7QW. UK. Work funded by BAe, Military Aircraft Ltd, Warton, Lancs, UK

The use of current basis functions of electrically large support over wide tracts of a target's surface away from sharp edges, small excrescences, gaps etc., is a natural way to vastly reduce the size of linear problem arising from the discretization of a boundary integral equation. The problem reduces to getting the correct forms for the large-support functions over arbitrary 3-D geometries. As a step towards this, an attempt is made to simplify the formulation of a 2-D problem. A hybrid optics/method of moments approach is applied to electromagnetic scattering from a conducting semi-cylinder, much as in previously published work. A 2-D integral equation for surface current is solved by a standard moment method, but using a mixed set of current basis functions, together with "known" optics components. A significant simplification of the optics functions is made, with no consequent loss of accuracy of the solution. Convergence with pure optics solutions is demonstrated for semi-cylinders, as their size increases up to 30λ in diameter. The effect of using approximations to the optics functions on the accuracy of solutions is demonstrated.

1 Introduction

The hybrid method discussed in this report is seen as having potential for development into general application computer codes for the analysis of electromagnetic problems involving electrically large bodies. This could cover RCS prediction, EMC, and antenna performance problems. There is currently a wide regime of electrical size for which no existing technique can be used with confidence; numerical methods require too much computation, and optical methods are inaccurate. The hope is that methods which hybridize these two approaches might succeed where the pure methods fail.

One major technique in CEM is the Moment Method (MM) [1,2]. An exact integral equation for unknown induced currents, is solved approximately by a discretization which results in a large system of linear equations. The method can yield results of excellent quality, but the high computational demand of matrix inversion currently limits the application of the technique to relatively small bodies; a few wavelengths in maximum dimension is typical. With the largest supercomputers, the limit of practical turn-around times is reached for objects smaller than 20 λ.

For structures many wavelengths in size, optical methods can be applied [3]. These make approximations appropriate to the domain, and a very much simpler problem results. Unfortunately, the scattering mechanisms relevant to many objects of interest, particularly those which are "global" in nature such as substructure resonances and surface wave phenomena, often lie outside the scope of current optical methods. Also, optical methods often involve very crude approximations to surface currents, and this is naturally of little use for EMC purposes.

A natural line of research for CEM is to combine the MM and optical methods in some "Hybrid" scheme, which improves the accuracy of purely optical methods, whilst avoiding the massive computational load of the MM. This paper covers work concentrated on one such technique; the use of high-frequency (optical) basis functions (HFBF) within the framework of an integral equation solution of an electromagnetic scattering problem. [4,5,6,7]. Briefly, the use of optics basis functions defined over large areas of the surface of a complex structure, together with small-domain basis functions around "difficult" regions such as small excrescences and sharp edges, greatly reduces the size of the linear system to be solved. This is achieved at the expense of the time taken to calculate each element of the matrix.

We first reproduce results of [4] for 2-D scattering from a conducting semi-cylinder. The optics basis functions are derived from the unified theory of diffraction (UTD) and involve diffraction coefficients and Fock functions. [3,8]. Small domain pulse functions are used close to the sharp corners. It has been found possible to simplify significantly the published work, with no loss of accuracy, and with improved computational efficiency. This increases the likelihood of future application of the method to arbitrary 3-D geometries.

2 The HFBF Method

2.1 General Formulation

In the usual formulation of the MM, the unknown current J is expanded in a series of basis functions $\mathbf{J}_1, \mathbf{J}_2, ..., \mathbf{J}_N$ with coefficients I_n: $\mathbf{J} = \sum_{n=1}^{N} I_n \mathbf{J}_n$. The $\mathbf{J}_n$ are in the domain of an operator $\mathcal{L}$ associated with the integral equation defining the problem, $\mathcal{L}\mathbf{J} = \mathbf{E}^{\mathbf{i}}$, where $\mathbf{E}^{\mathbf{i}}$ is the impressed field. Introducing a set of weighting functions $\{\mathbf{W}_m\}$ and assuming that we have available a suitable inner product, $\langle \mathbf{A}, \mathbf{B} \rangle$, we can form the generalized impedance matrix, $Z_{mn} = \langle \mathbf{W}_m, \mathcal{L}\mathbf{J}_n \rangle$, so that the problem becomes $[\mathbf{Z}](I) = (V)$, where (I) is the column vector of I_n's and (V) is the column vector of V_n's, where $V_n = \langle \mathbf{W}_n, \mathbf{E}^{\mathbf{i}} \rangle$.

The solution entails inversion of the generalized impedance matrix, or, for each particular incidence case, solving the inhomogeneous system. The essential part of the HFBF approach is to incorporate current forms based on known high-frequency solutions of generic problems into the set of basis functions. Whereas standard basis functions have supports small compared to a wavelength, the high-frequency forms are not so limited. This reduces the number of basis functions, and hence the size of the linear system.

2.2 The Semi-Cylinder Problem

In [4], the 2-D problem of scattering from a semicircular cylinder was studied for both TE and TM excitation by a line source. MM pulse currents of electrically small support were employed around the two edge discontinuities, and UTD optics forms, elsewhere. Coefficients for the pulses and UTD currents were found by a standard point-matching MM procedure.

The problem is ideal for testing various forms of the HFBF method as it involves most of the canonical electromagnetic problems; diffraction around a curved surface, surface waves on a flat surface, current discontinuities at sharp edges, and sharp-edge diffraction. A diagram of the semi-cylinder and coordinate system is given in Figure 1. The axis is aligned with the z-direction. The perimeter is split into four connected regions: Region 1, the region of the right hand corner, where currents are represented as a sum of disjoint pulses; Region 2, the majority of the curved part of the object, where currents are represented as sums of various optical functions sharing the same domain; Region 3, the region of the left hand corner, treated the same as the right corner; and Region 4, the majority of the flat surface, where a different set of optics functions are used. Tx and Rx stand for Transmitter (source) and Receiver (field point) respectively.

We restrict attention to a single polarization case, that of a magnetic current line source which yields an electromagnetic field in which H is everywhere aligned with z, and E is purely orthogonal to z. In 2-D parlance, this is the transverse electric or TE case. Currents on the object are in consequence purely circumferential, and we may write scalar equations relating circumferential currents and z-directed **H** fields.

Rather than carry the arbitrary strength of the line source through all equations, we prefer to follow [4], assume a source of strength 1 volt, and adjust the dimensions of currents and fields. Surface currents and magnetic fields should then both have dimensions of amps per metre per volt or $(\text{ohms})^{-1}\ \text{m}^{-1}$. In what follows, expressions for known currents will have these dimensions. The dimensions of current basis functions are arbitrary, as only their mathematical form is of consequence.

Induced currents satisfy the 2-D TE integral equation (a 2-D specialization of the MFIE).

$$\mathcal{L}J(\rho) = \frac{J(\rho)}{2} - \frac{k}{4j} \int_C J(\rho')\, \mathrm{H}_1^{(2)}(k \mid \rho - \rho' \mid)\, \hat{\mathrm{n}}.(\widehat{\rho - \rho'})\, ds' = -H_z^i \tag{1}$$

Where H_z^i is the z (only) component of the incident magnetic field, ρ and ρ' are shown in Figure 1, $k = 2\pi/\lambda$, λ is the wavelength, $\mathrm{H}_1^{(2)}$ is a Hankel function, and $\hat{\mathrm{n}}$ is the outward normal at ρ.

We suppose the unknown current J to be a complex linear combination of current functions as follows.

$$J = J_{KC} + J_{KF} + \alpha_1 J_{C1} + \alpha_2 J_{C2} + \alpha_3 J_{F1} + \alpha_4 J_{F2} + \sum_{n=5}^{N} \alpha_n J_{Pn} \tag{2}$$

where J_{KC} is a "known" optics component of the induced current in Region 2, J_{KF} is a "known" optics component of the induced current in Region 4, J_{C1} and J_{C2} are optics basis current forms in Region 2, J_{F1}

and J_{F2} are optics basis current forms in Region 4, $J_{Pn}, n = 5, ..., N$ are pulse basis functions with supports in Regions 1 and 3, and the $\alpha_n, n = 1, ..., N$ are unknown complex coefficients. The known and basis currents are taken to be zero except in their relevant regions. Thus the optical current forms are not used close to the corners of the cylinder, where they might be inaccurate, or in some cases singular.

The optics current forms are as follows. Refer to Figure 2 for definition of the geometrical terms.

$$J_{C_{\substack{1\\2}}}(\rho) = \mathbf{g}\left(\left[\frac{ka}{2}\right]^{1/3} \frac{t_{\substack{r\\l}}}{a}\right) \exp\left(-jkt_{\substack{r\\l}}\right) \tag{3}$$

g is the hard Fock function. These two terms represent currents supporting fields due to disturbances at the corners. The first (with subscripts 1 and r) is associated with an anticlockwise creeping wave, and the second with a clockwise creeping wave.

$$J_{F_{\substack{1\\2}}}(\rho) = \frac{\exp\left(-jks_{\substack{l\\r}}\right)}{\sqrt{s_{\substack{l\\r}}}} \tag{4}$$

These terms represent surface waves travelling right and left respectively across the flat due to disturbances at the corners. The expressions for the known current components are considerably more complex.

For points ρ in Region 2 which are directly illuminated by the line source, we have,

$$J_{KC}(\rho) = -\frac{C_0}{Z_0}\,\mathbf{g}\left(-\left[\frac{ka}{2}\right]^{1/3} \hat{\mathbf{n}}.\hat{\mathbf{s}}\right) \exp\left(\frac{jka}{6}(\hat{\mathbf{n}}.\hat{\mathbf{s}})^3\right) \frac{\exp\left(-jks\right)}{\sqrt{s}} \tag{5}$$

where $Z_0 = 4\pi c \times 10^{-7}$ ohms is the impedance of free space, and $C_0 = -\sqrt{k/(8\pi)}\,\exp(j\pi/4)$. For points which are not directly illuminated, we have,

$$J_{KC}(\rho) = -\frac{C_0}{Z_0}\,\mathbf{g}\left(\left[\frac{ka}{2}\right]^{1/3} \frac{t}{a}\right) \exp(-jkt)\,\frac{\exp(-jks_b)}{\sqrt{s_b}} \tag{6}$$

There will be two shadow regions and two terms of this form if both $T_x < a$ and $T_y > 0$.

We now define the known flat region currents. If the flat is lit,

$$J_{KF}(\rho) = \frac{\omega\varepsilon_0}{4}\{L_1 + L_2 + L_3\} \tag{7}$$

where

$$L_1 = 2\,\mathrm{H}_0^{(2)}(ks), \tag{8}$$

and

$$L_{\substack{2\\3}} = \frac{\exp(-jkc_{\substack{r\\l}})}{\sqrt{c_{\substack{r\\l}}}}\,\mathbf{D}_{\substack{r\\l}}\,\mathrm{H}_0^{(2)}(ks_{\substack{r\\l}}) \tag{9}$$

Here ω is the angular frequency, and ε_0 is the permittivity of free space (8.854×10^{-12} farads per metre). $\mathbf{D}_r$ and $\mathbf{D}_l$ are edge diffraction coefficients with units of $m^{1/2}$ [9]. Physically, L_1 gives the physical optics current, L_2 represents a surface wave excited by direct illumination of the right corner and travelling left across the flat, and L_3 gives a surface wave excited by direct illumination of the left corner, and travelling right.

If the flat is in shadow, then

$$J_{KF}(\rho) = \frac{\omega\varepsilon_0}{4}\{S_1 + S_2 + S_3 + S_4\} \tag{10}$$

where

$$S_{\substack{1\\2}} = \frac{\exp(-jkc_{\substack{l\\r}})}{\sqrt{c_{\substack{l\\r}}}}\,\mathbf{D}_{\substack{l\\r}}\,\mathrm{H}_0^{(2)}(ks_{\substack{l\\r}}) \tag{11}$$

$$S_{\substack{3\\4}} = \frac{\exp(-jks_{\substack{b1\\b2}})}{2\sqrt{s_{\substack{b1\\b2}}}}\,\mathrm{g}\left(\left[\frac{ka}{2}\right]^{1/3} t_{\substack{1\\2}}\right)\,\exp(-jkt_{\substack{1\\2}})\,\mathrm{D}_{\substack{l\\r}}\,\mathrm{H}_0^{(2)}(ks_{\substack{l\\r}}) \tag{12}$$

We now substitute the current forms into the integral equation and rearrange to get

$$\sum_{j=1}^{N} \alpha_j \mathcal{L}J_j = -H_z^i - \mathcal{L}J_{KC} - \mathcal{L}J_{KF} \tag{13}$$

where now the J_j stand for the total set of basis functions, optical and pulse, $J_1 = J_{C1}$ etc. We choose N match points, ρ_i, one at the centre of each pulse, and one for each optics basis function, close to the end of its support which is nearest the launching point (ie. corner) for the corresponding surface wave.

Put $a_{ij} = \mathcal{L}J_j(\rho_i)$, $h_i = -H_z^i - \mathcal{L}J_{KC}(\rho_i) - \mathcal{L}J_{KF}(\rho_i)$, $[A] = \{a_{ij}\}$, $[\alpha] = \{\alpha_j\}$, and $[h] = \{h_i\}$. An approximate solution to the integral equation can then be found by solving the linear system $[A][\alpha] = [h]$ for $[\alpha]$. The total induced current J can be reconstituted from Equation (2). The magnetic field anywhere outside the semi-cylinder due to the induced currents (ie. the scattered field) can be found from

$$H_z^s = -\frac{k}{4\pi}\int_C J(s)\,\mathrm{H}_1^{(2)}(kr)\,\hat{\mathbf{n}}.\hat{\mathbf{r}}\,ds \tag{14}$$

where the arguments and vectors are shown in Figure 1. The scattering width of the semi-cylinder is proportional to the squared modulus of the scattered field. The radiation pattern of the line-source/semi-cylinder combination may be found by adding the direct field,

$$H_z^d = -\frac{\omega\varepsilon_0}{4}\,\mathrm{H}_0^{(2)}(kr_d) \tag{15}$$

where r_d is the distance from source to field point.

Results were calculated for all 6 cases of [4], to validate our implementation, and study current phasors, which are a more stringent test of accuracy than radiation patterns. Figures 3 and 4 compare an all-pulse result using 82 0.05λ pulses with a hybrid result using 16 0.07λ pulses for Case 1. Agreement for the other 5 cases was of a similar order. Note that $\lambda = 1m$ is assumed in all results.

3 Simplification of Published Method

The key to the simplification lies in noting that the six most complicated terms of the known current on the flat of the semicylinder (J_{KF}) are of essentially the same form as the basis functions J_{F1} and J_{F2}. The former can therefore be deleted from the definition, as any component of these forms required to satisfy the integral equation, can be provided by the coefficients of the basis functions. This possibility is slightly obfuscated in the cited work because Hankel functions are used in the definitions of the known functions, whereas their large-argument asymptotic forms are used in the basis functions. Referring to Equations (7) to (12), terms $L_2, L_3, S_1, S_2, S_3, S_4$ are all of the form of a complex number times a Hankel function with argument ks_l or ks_r where s_l and s_r are distances from the left and right corners to the evaluation point. The complex numbers involve diffraction coefficients and Fock functions, but these all have arguments which do not depend on the evaluation point.

For large arguments,

$$\mathrm{H}_0^{(2)}(x) \simeq \sqrt{\frac{2}{\pi x}}\,\exp(-j[x - \pi/4]) \tag{16}$$

and so

$$\mathrm{H}_0^{(2)}(ks) \simeq z\,\frac{\exp(-jks)}{\sqrt{s}} \tag{17}$$

for some complex constant z. For large arguments therefore, the six terms above are all of the same form as the basis functions $J_{F1}(\rho)$ and $J_{F2}(\rho)$. The expansion can be used with impunity for arguments greater than 2, i.e. for s further than about $\lambda/3$ from the corners. In the hybrid method, pulses are used out to about $\lambda/3$ from the corners. The six terms above are never evaluated with small Hankel function arguments,

because such regions lie outside the supports of the optics functions. We are at liberty therefore to replace the Hankel functions with their large argument expansions.

Thus we simply delete the six terms from the definition of J_{KF} leaving,

$$J_{KF}(\rho) = \frac{\omega\epsilon}{2}\,\mathrm{H}_0^{(2)}(ks) \tag{18}$$

The simplification is significant since the six terms are the only places where diffraction coefficients are used in the solution. The 6 cases of [4] were recalculated and the resulting current phasors compared with those from the original formulation. Results were indistinguishable graphically, and agreed numerically up to the 6th significant figure. Having established that the simplification incurred no loss of accuracy, the simplified formulation was extensively tested.

It was considered important to examine the behaviour of the hybrid method as the electrical size of the semi-cylinder was increased. It was also of interest to try cases where both transmitter and receiver were in the far field, and hopefully observe convergence to the familiar optics-dominated scattering width pattern. Figures 5, 6, and 7 show far-field scattering width patterns for a 30 λ case for PO, UTD, and Hybrid solutions, each compared with the all-pulse result. The accuracies of the three approximate solutions may be judged. 616 pulses were used for the all-pulse calculation, whereas the hybrid method required only 16, and resulted in a 20×20 system. Hybrid run times were about one tenth of the all-pulse times for a 30λ target.

4 Approximate Basis Functions

A major incentive for this work is to assess the use of hybrid techniques for the calculation of the RCS of arbitrary 3-D bodies. While it is clear that the size of linear problem will be significantly reduced, it is likely that the effort required to fill the matrix could be dominant. The 3-D case will require multiple integration of 2-D optics basis functions, and so any simplification of the evaluation of these functions will be very beneficial. Such simplification entails some loss of accuracy, and it is therefore of interest to test the robustness of the HFBF method to relaxation of the accuracy of the optics functions.

Within the special case studied, the most complex function required is the hard Fock function $\mathbf{g}$. This complex valued function of a real variable can be evaluated as follows [3]. For $x < -3$, a trivial complex exponential asymptotic form can be used. For $x > 1$, a ten term truncation of a residue series expansion will suffice. In both these ranges, the evaluation of the function is rapid. The problems arise in the central range, $-3 \leq x \leq 1$, where accurate evaluation is only possible by numerically performing the contour integration of an expression involving Airy functions, which defines the Fock function. Over this range, the real and imaginary parts of the function can be approximated with arbitrarily small mean square error, by a truncated series of Chebyshev polynomials, $P_n^{R/I} = \sum_{i=0}^{n} a_i^{R/I} T_i$, $P_n = P_n^R + jP_n^I$. The error as a function of the order n of the Chebyshev series is shown in Figure 8.

Many cases have been tried, and 15th order approximation has been found to be universally adequate. The d_∞ error of this approximation is 1% of the maximum modulus of the function.

5 Conclusions

A significant simplification of the published formulation has been achieved with no loss of accuracy. This results in reduced run-times, and makes the future generalisation of the method to 3-D geometries more likely. Convergence with a sophisticated optics solution has been demonstrated as the target becomes electrically large. No problems have been encountered over many hundreds of runs against a range of illumination conditions and target sizes. The hybrid method is superior in accuracy to the UTD solution, at least for targets up to 30 wavelengths in diameter, and greatly superior in accuracy to physical optics. It has been shown that moderate-order polynomial approximations to the basis functions can be used and result in negligible loss of accuracy. These can therefore be used to speed up function evaluations and integrations. This may be particularly significant in future 3-D applications.

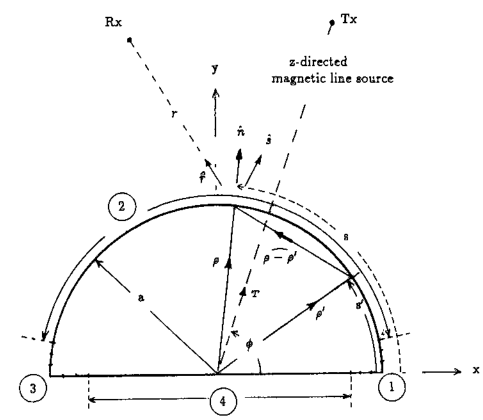

Figure 1: Semi-cylinder Geometry

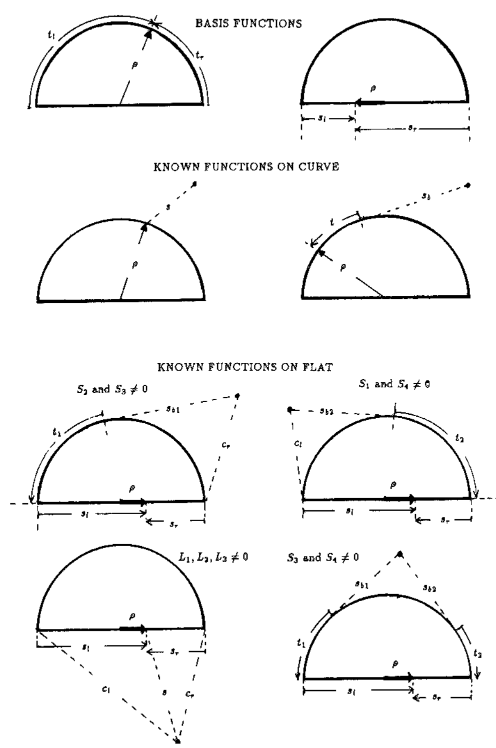

Figure 2: Geometry for Optics Functions

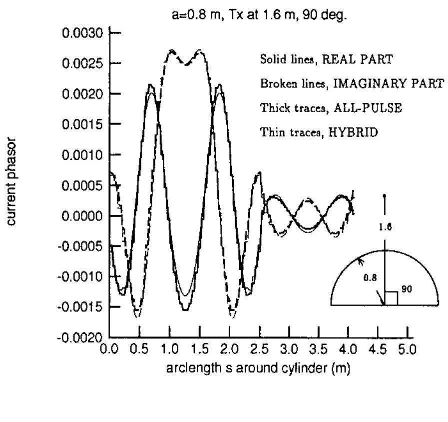

Figure 3: Current Phasor for Case 1: HYBRID AND ALL PULSE SOLUTION

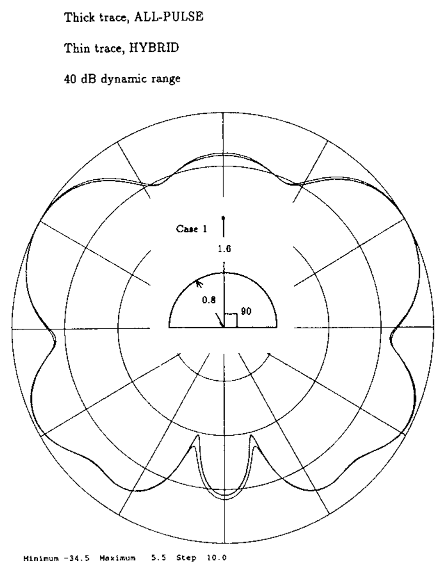

Figure 4: Radiation pattern for Case 1:HYBRID AND ALL PULSE SOLUTION

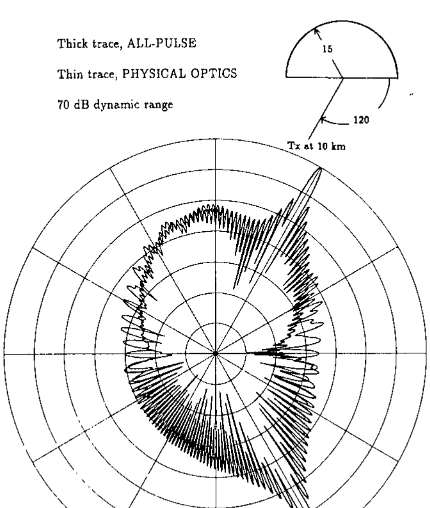

Figure 5: Scattering Width for 30 λ Target: PO AND ALL-PULSE SOLUTIONS

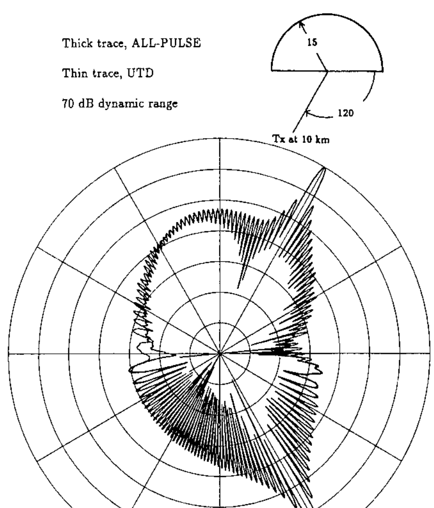

Figure 6: Scattering Width for 30 λ Target: UTD AND ALL-PULSE SOLUTIONS

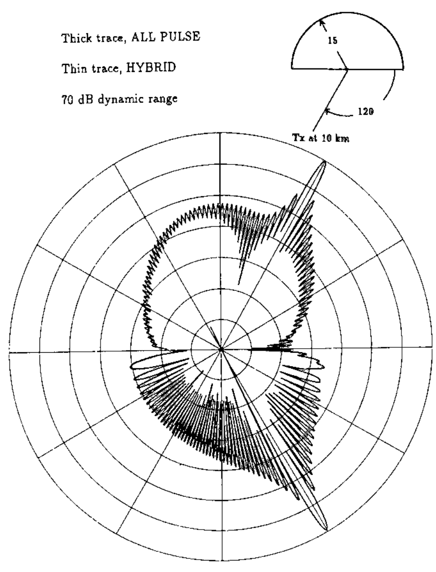

Figure 7: Scattering Width for 30 λ Target: HYBRID AND ALL-PULSE SOLUTIONS

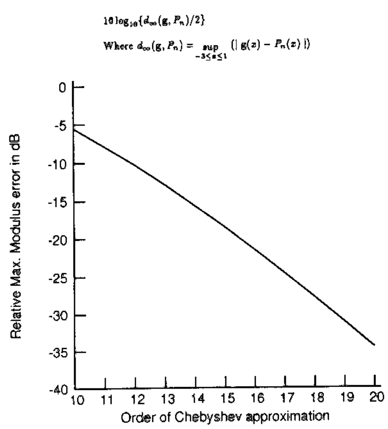

Figure 8: Maximum Modulus Error in Chebyshev Approximation to Hard Fock Function

6 References

1. Harrington RF, "Field computation by moment methods" Krieger, Malabar Fla. 1968.
2. Glisson AW, "On the development of numerical techniques for treating arbitrary-shaped surfaces" Ph.D. Thesis, Univ. Mississippi 1978.
3. James GL, "Geometrical theory of diffraction for electromagnetic waves" IEE Electromagnetic waves Series 1. Peter Perigrinus, 1976.
4. Shrikanth S, Pathak PB, Chuang CW, "Hybrid UTD-MM analysis of the scattering by a perfectly conducting semicircular cylinder" IEEE Trans AP-34. No 10, pp 1250-1257, Oct 1986.
5. Medgyesi-Mitschang LN, Wang DS, "Hybrid solutions for scattering from perfectly conducting bodies of revolution" IEEE Trans. AP-34, No 10, pp 570-583, Oct 1986.
6. Sahalos JN, Thiele GA, "On the application of the GTD-MM technique and its limitations" IEEE Trans. AP-29, No 5, pp 780-786, Sep 1981.
7. Burnside WD, Yu CL, Marhefka RJ. "A technique to combine the geometrical theory of diffraction and the moment method" IEEE Trans. AP-23, pp 551-558, July 1975.
8. Goodrich RF, "Fock Theory- an appraisal and exposition" IRE Trans. AP-7 pp 528-536, 1959.
9. Kouyoumjian RG, Pathak PH, "A uniform geometrical theory of diffraction for an edge in a perfectly conducting surface." Proc. IEEE, Vol 62, pp 1448-1461, Nov 1974.

REALISTIC FEED REGION MODELS FOR USE IN THE NUMERICAL ANALYSIS OF WIRE ANTENNAS

D.J.Janse van Rensburg[1] and D.A.McNamara

Department of Electronic & Computer Engineering

University of Pretoria, Pretoria, South Africa 0002.

ABSTRACT : A source modelling technique allowing arbitrary rotationally symmetric wire antenna source regions to be analysed is presented. The technique which relies on a quasi-static approximation employs a numerical solution procedure to obtain an equivalence magnetic surface current which emulates the actual antenna feed region. This approach provides much more flexibility for the analysis of wire antenna feeds. Measured and computed values are shown to illustrate the validity of the method.

INTRODUCTION

The necessity of accurate modelling of wire antenna source regions is nowhere better illustrated than when terminal impedance and antenna near-fields are computed. From such computations it soon becomes clear that it is required to develop detailed source models for wire antennas, if accurate input impedance computations are to be made. In this paper results obtained using this source modelling technique is presented. The technique, which relies on the surface equivalence theorem, as well as the quasi-static approximation, allows modelling of arbitrary, rotationally symmetric source regions.

DESCRIPTION OF THE APPROACH

Feed regions of antennas are generally very complex structures and therefore difficult to analyse using numerical methods. If the fields in the region close to such a feed are however quasi-static, existing techniques for determining static fields may be used to obtain them. This process, which is considerably simpler than the full electrodynamic one [1], then allows a complicated feed region to be replaced by surface equivalence currents. These currents may then be used as the source illuminating the antenna.

The source model described here allows the analysis of rotationally symmetric feed regions

[1] Corresponding author

and is valid for wire only feed regions as well as wire groundplane feed regions. In order to solve for the quasi-static fields in the source region the rotationally symmetric laplacian operator implementations described in [2, 3] and [4] are used. The numerical nature of this process allows accurate representation of the source region. The possibility of dielectric material in a coaxial cable may also be taken into account. The application of the source model may be illustrated by considering the following two examples.

Consider firstly the dipole with feed configuration shown in Fig. 1(a). In this case the antenna is fed by a source in the gap of the dipole antenna. Using the surface equivalence theorem an equivalence magnetic current density (illuminating the structure) can be found from the total electric field existing in the gap as shown in Figure 1(b). Since this gap is small in terms of wavelength and due to it's capacitive nature [5], the quasi-static potentials can be used to find this electric field [6]. Using this electric field the equivalence magnetic current density may then be computed and the problem reduced to that shown in Figure 1(b).

Consider secondly the monopole antenna shown in Figure 2(a). For this antenna, through the application of the surface equivalence theorem and the quasi-static approximation, an equivalence current may be computed along the dotted line as shown in Figure 2(b). Using this surface current as the new antenna source and applying image theory the current distribution on a solid wire (with no step) may be computed.

The current induced on the solid wire represents the contour integral of the magnetic field on the equivalence surface. Since this is exterior to the equivalence surface, this integral will also be equal to the actual terminal conduction current plus a displacement current term. The displacement current represents the difference between the contour integral of the magnetic field on the equivalent surface and the same integral on the actual wire (the thin-section). The integral of the time derivative of the axial electric field in the gap region of the monopole represents the displacement current. This displacement current term may be computed by using the quasi-static field in the source region. This approach provides a correction factor for the induced current, which will supply the actual terminal current. The integration of the time derivative of the axial electric field (the displacement current term) is performed numerically, and the result then subtracted from the computed induced current. The complex

source region geometry is thus accounted for in the static solution process (with the displacement current compensation), where the step in wire radius is not as difficult to treat as in the electrodynamic case.

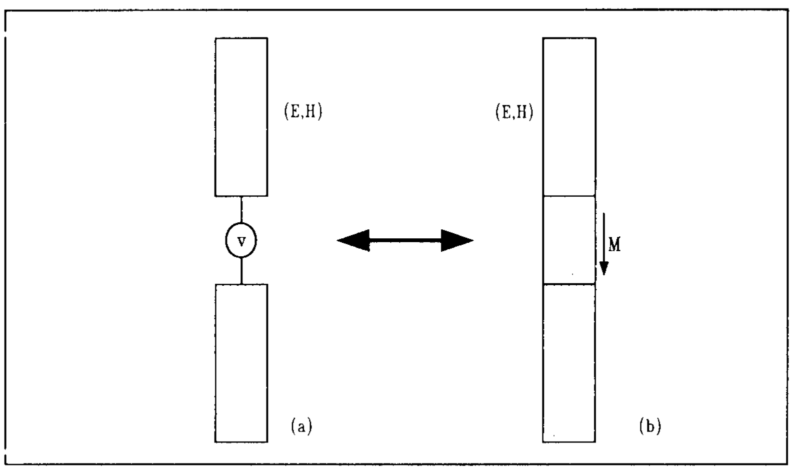

Figure 1: A dipole antenna with wire-only feed region is shown in (a). This problem may be reduced to that shown in (b) through the application of the surface equivalence theorem.

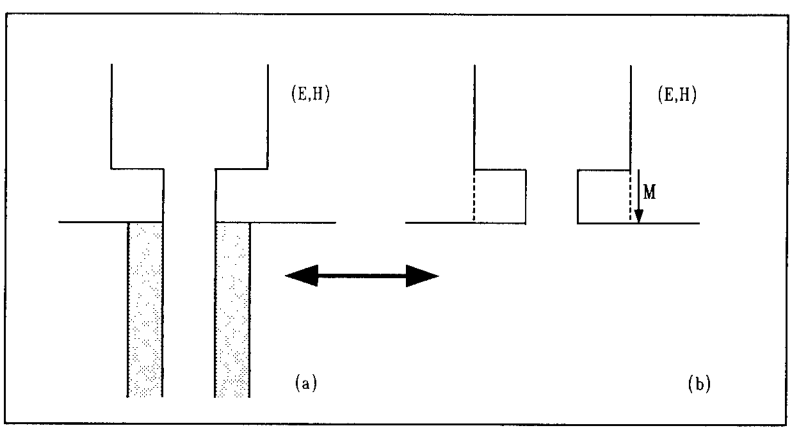

Figure 2: A monopole antenna with wire-groundplane feed region is shown in (a). This problem may be reduced to that shown in (b) through the application of the surface equivalence theorem.

COMPARISON OF COMPUTED AND MEASURED INPUT IMPEDANCE RESULTS

The monopole antenna considered is 76.0mm long and contains a step in wire radius. The thick wire radius is 2.0mm and the thin wire radius is 0.45mm. The source region is as shown in Figure 2(a). The antenna is simplified to a dipole antenna through image theory and then analyzed using a Galerkin method [7] and the quasi-static source model. The relative permittivity of the dielectric in the coaxial cable is 2.03 and the radius of the dielectric section is 1.49mm.

Table 1 shows computed impedance values for the monopole antenna at a frequency of 3.0 Ghz. The impedance values shown have been obtained using the quasi-static source model, with and without displacement current compensation. Also shown is a measured impedance value [7]. Error terms are shown in Table 1 indicating the error between the real and imaginary parts of each computed value with respect to the measured value. From these error values (which decrease when displacement current compensation is performed) it may be concluded that this source modelling techniques provides an accurate mechanism for wire antenna source modelling. It also illustrates that the technique allows complicated source regions to be treated without having to perform full electrodynamic analyses.

Frequency	3.0 GHz
Measured	$34.3 + j16.4\Omega$
Quasi-static (Uncompensated) Error	$32.4 + j13.4\Omega$ $5.5\% + j18.3\%$
Quasi-static (Compensated) Error	$33.6 + j14.8\Omega$ $2.0\% + j9.8\%$

Table 1: Measured and computed input impedance results for the monopole antenna described above at a frequency 3.0 Ghz. Error terms shown indicate the error between the real and imaginary parts of each computed value with respect to the measured value.

CONCLUSIONS

Impedance results obtained using a new source model providing a more accurate representation of wire-groundplane source regions, has been presented. The source model is general and caters for different rotationally symmetric source region geometries. The

model relies on the quasi-static potentials and a numerical formulation is used for the solution of the electrostatic fields in the source region. Although only specific geometries are presented here other rotationally symmetric source geometries can be treated without difficulty. The results shown are for a monopole antenna fed through an infinite groundplane. These computations indicate that the source modelling technique is reliable and allows modelling of complicated source regions geometries. The source modelling technique described here addresses a topic which has been discussed frequently in the literature and represents the first contribution towards the accurate representation of arbitrary wire antenna source regions for improved impedance computation.

REFERENCES

[1] D. G. Dudley, "Error minimization and convergence in numerical methods", Electromagnetics, Vol. 5, No. 2-3, pp. 89-97, 1985.

[2] J. R. Mautz and R. F. Harrington, "Computation of rotationally symmetric laplacian potentials", Proc. IEE, Vol. 117, No. 4, pp. 850-852, April 1970.

[3] J. Daffe and R. G. Olsen, "An integral equation technique for solving rotationally symmetric electrostatic problems in conducting and dielectric material", IEEE Trans. Power Apparatus and Systems, Vol. PAS-98, No. 5, pp. 1609-1615, Sept/Oct 1979.

[4] R. F. Harrington and T. K. Sarkar, "Boundary elements and the method of moments", Boundary Elements, Proc. Of The Fifth International Conference, pp. 31-40, Hiroshima, Japan, Nov 1983.

[5] R. G. Olsen, G. L. Hower and P. D. Mannikko, "A hybrid method for combining quasi-static and full-wave techniques for electromagnetic scattering problems", IEEE Trans. Antennas Propagat., Vol. AP-36, No. 8, pp. 1180-1184, Aug 1988.

[6] R. Plonsey and R. E. Collin, **Principles And Applications Of Electromagnetic Fields**, (McGraw-Hill, 1961).

[7] D. J. Janse Van Rensburg, **On The Computational Of Electromagnetic Observables Of Conducting Thin-Wire Radiators**, Ph D. Dissertation, University of Pretoria, Pretoria, South Africa, 1990.

SESSION 2- "GENERAL MULTIPOLE EXPANSION"

Moderator: Robert Bevensee

On the Application of Line Multipoles in the MMP-Program

P. Leuchtmann and F. Bomholt
Electromagnetics group, ETH Zurich
CH-8092 Zurich, Switzerland

Abstract: *The use of line multipoles in the MMP-program reduces the number of unknowns compared with a modelling using only spherical multipoles. This is shown at two examples for which the field has been simulated. A: An absorbing clamp used in EMC-test arrangements and B: the scattering of a square conductive plate of moderate thickness.*

1. Introduction

The MMP-program package [1,2] developed by the Electromagnetic Field Research Group is an excellent tool for calculating electromagnetic fields. It is possible to perform rigorous calculation of coupling through apertures, influence of cable layout relative to cabinets etc. It has been used for calculating EMC test arrangements [3] and other complicated structures.

The newly developed expansion functions for long structures (the line multipoles) [4] have been used for modeling different arrangements, in particular a high-frequency absorbing clamp described in details in section 3 of this paper, and a thick square plate with a sidelength of one wavelength, described in section 4.

In section 2, general remarks are given on how to expand an unknown field function with the MMP program, when the line multipoles are used.

2. On the Expansion of an Unknown Field

Let F denote the electromagnetic field, consisting of six components (electric field $\vec{E}$ and magnetic field $\vec{H}$). The MMP-code uses a direct expansion of the electromagnetic field F:

$$F = F_0 + \sum_{k=1}^{N} a_k F_k,$$

where each F_k is a solution of the homogeneous Maxwell equations and F_0 is a given solution (excitation). The N parameters a_k are determined using boundary conditions.

2.1 General Remarks

The behaviour of the (unknown) field solution F has a direct influence on the optimal choice of the expansion functions F_k. An appropriate choice of the set of F_k is necessary for obtaining solutions with a minimum number of unknowns N. There are different requests for the set of expansion functions:

- The expansion set should cover a wide range of possible solutions.
- The set should be adapted to the particular case so that as few unknowns as possible must be used.
- The F_k should be linearly independent in order to obtain regular matrices.
- Each ('two vector valued') F_k should be calculable in a cheap and easy way.

The first two points are contradictory in a certain sense: The more a priori knowledge on the solution is available, the more can the set of expansion functions be restricted to those functions which are useful to represent the solution.

2.2 'Normal' Multipoles vs. Line Multipoles: General Behaviour of the Functions

A 'normal' multipole forms a complete set of expansion functions on a sphere in a similar way as the functions $\cos nx$, $\sin nx$ form a complete set on the interval $[0,2\pi]$ (Fourier series). Due to the local behaviour of the 'normal' multipole functions (their values decrease apart from the origin), multiple multipoles (MMP) can be used to form a general expansion for domains differing from spheres. The positioning of the origins of 'normal' multipoles reduces to a geometric problem and is highly automated [5].

In opposite to the 'normal' multipoles, which are adapted to a *spherical domain*, the line multipoles are adapted to a *circular cylinder of finite length*. This fact allows a significant reduction of the number of expansion functions for all that cases, where relatively long structures (wires, edges etc.) are involved. The important point is, that a 'normal' multipole function varies in any direction on the sphere in a similar way, whereas the variation of a line multipole function is different along the cylinder axis and along the circumference of the cylinder. The longitudinal behaviour is like $\cos kz$, $\sin kz$, (k is the constant(!) wave number of the medium and z is the longitudinal coordinate) where the azimuthal variation is like $\cos n\varphi$, $\sin n\varphi$ (φ is the angle around the cylinder and n is the arbitrary (integer) order of the line multipole). This means, that the longitudinal behaviour is generally much smoother than that around the cylinder. This is useful in all that cases, where it is a priori known, that the solution has the same behaviour. E.g., in thin wires, a row of many 'normal' multipoles placed along the wire axis may be replaced by a single line multipole.

If the longitudinal variation is expected to be different from $\cos kz$, $\sin kz$, a *segmentation* can be made, where each segment has a length $l \leq \lambda/10 = \pi/(5k)$. In this case, each segment consists its own line multipole, and in a first approximation, the $\cos kz$-term can be considered as constant along z, where the $\sin kz$-term is linear. Hence, the longitudinal variation results in a segmentwise linear behaviour.

3. Example A: The Absorbing Clamp

The absorbing clamp is an equipment for measuring the common mode current on a cable at frequencies up to 100 MHz. It mainly consists of a highly absorbing ferrite tube, through which the cable is lead (see fig. 1).

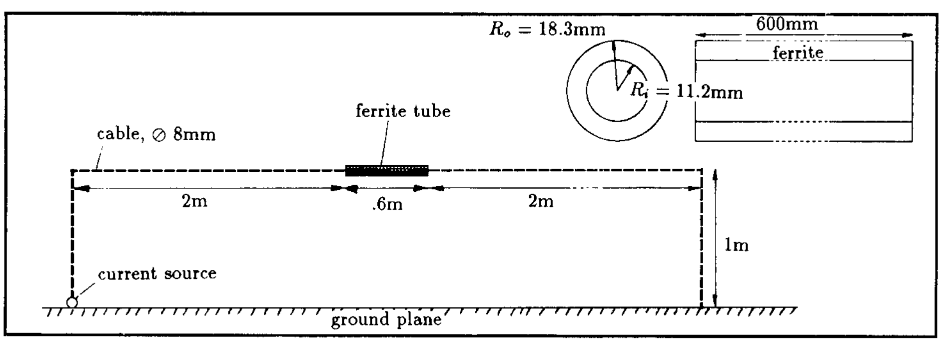

Figure 1 **The absorbing clamp (modelled as a ferrite tube) has a strong influence on the (common mode) current distribution on the cable. This figure shows the arrangement which has been simulated using line multipoles.** At the right top corner, the dimensions of the ferrite tube are shown in detail. At 30 MHz, the ferrite has a relative permeability $\mu_{\mathrm{rel}} = 160 + 37i$, a relative permittivity $\epsilon_{\mathrm{rel}} = 15$ and a conductivity $\sigma = 10^{-5}\frac{1}{\Omega\mathrm{m}}$.

The MMP-model for the analysis of the arrangement shown in fig. 1 uses three different field domains:

- the ferrite region with the shape of a hollow circular cylinder,
- the inner air region between the ferrite tube and the cable, and
- the outer air region.

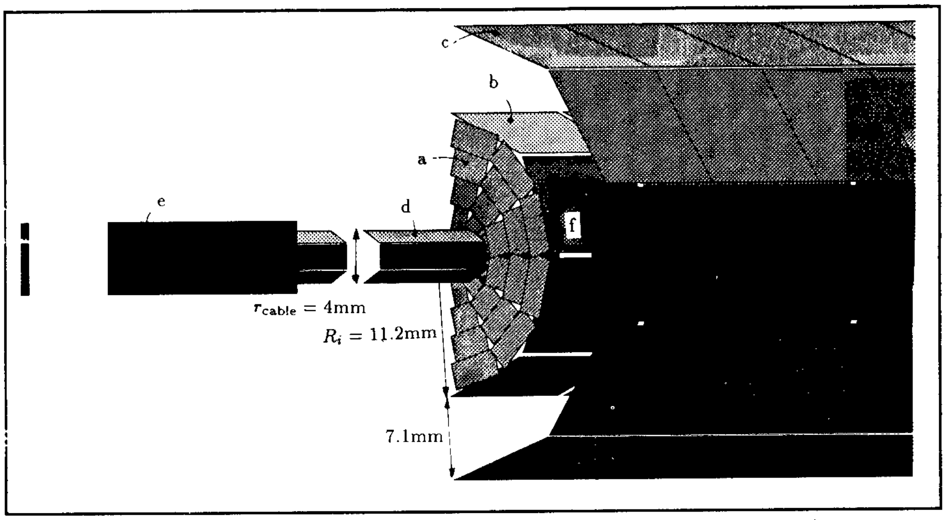

Figure 2 This picture shows some details on the modeling of the ferrite tube and the cable. At the center of each rectangle (matching points), appropriate boundary conditions are fulfilled. It is: a) artificial boundary inner air – outer air, b) boundary inner air – ferrite, c) boundary ferrite – outer air, d) boundary cable – outer air at the influence of the line multipole, e) boundary cable – outer air at the influence of the long wire expansion, f) boundary cable – inner air (almost hidden). The distribution of the matching points is chosen according to the rules discribed in [6]. Due to symmetry, only one half of the arrangement must be modelled. Only the part at the front of the ferrite tube is shown.

The inner and the outer air region are separated by an artificial boundary at the front ends of the ferrite tube (see fig. 2). This is done in order to allow different expansions for these two regions.

For the modelling of the outer air field around the cable, 4 thin wire expansions [7] with totally 66 segments (=69 unknowns) are used, while close to the clamp and for the inner air field and the ferrite field, three sets of 14 line multipoles are used. Each of these line multipoles is placed on the cable axis and its singularity is 5 cm long. The order of all the line multipoles is one and therefore, each has 6 unknowns. This gives a total number N of 321 unknowns for the full problem. The influence of the ground plane is taken into account by using image principle (odd symmetry with respect to the ground plane in MMP). Results are shown in figs. 3 and 4.

4. Example B: Square Plate Illuminated by a Plane Wave

A square metal plate of moderate thickness is exposed to an incident plane wave. The frequency is chosen in such a way that the wavelength equals the side length of the plate. The ratio side length to thickness is 9:1. The illumination is normal to the plate, with the polarization parallel to one side (see fig. 5). The discretization is based on a modeling using 'normal' (spherical) multipole expansions and has not been changed for the use of the new line multipoles. In the following two subsections, both the conventional modeling and the new modeling using line multipoles are described.

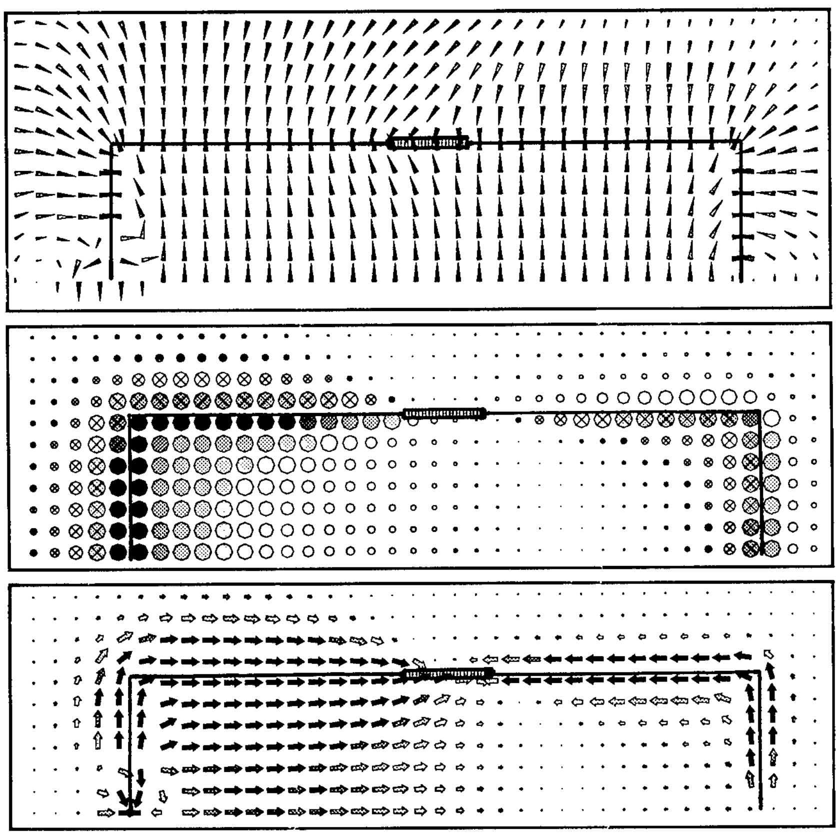

Figure 3 These pictures show the instantaneous value of the electric (top), the magnetic (middle) and the Poynting field (bottom) in the loop plane. The frequency is 30 MHz, and the width of the pictures is approximately half a free space wave length.

4.1 Modeling of the Scattered Field Using 'Normal' Multipoles

Due to the geometric symmetry of the object, only one octant has to be modeled. The number of equations (boundary conditions) can thus be reduced to one eighth of the full size. Since the incident plane wave matches the symmetry of the plate, only two of the symmetry components of the field exist (the incident wave has an even and an odd part with respect to any wave front), and therefore only two subproblems of reduced size must be solved.

In this case, the scattered field can be modeled using 'normal' multipoles. Due to the moderate thickness of the plate, the 'normal' multipoles are placed on the center plane of the plate, arranged in a regular square array (see fig. 7).

The procedure for choosing the right expansion positions resembles filling up the inside of the plate with spheres [5]. For a thinner plate, the sphere radii would become smaller, and the number of multipoles increases rapidly. As the variation of the field along the edge is much smaller than the variation from the top to the bottom side (around the edge), some type of 'stretched' expansion functions would be more appropriate and would reduce the required number of expansion functions.

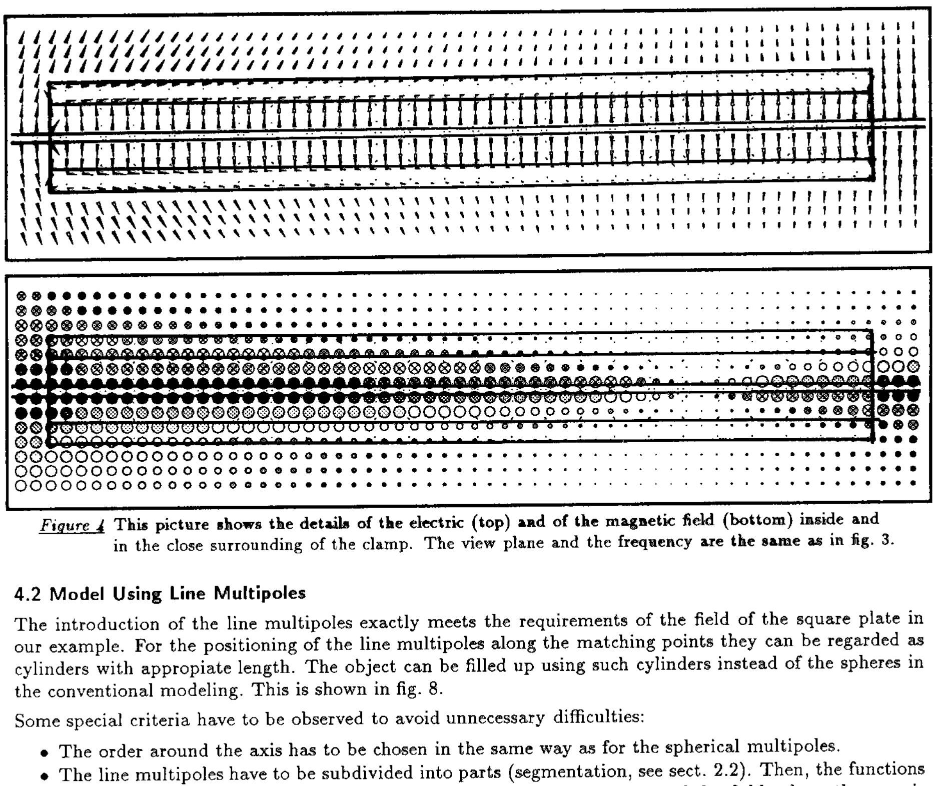

Figure 4 This picture shows the details of the electric (top) and of the magnetic field (bottom) inside and in the close surrounding of the clamp. The view plane and the frequency are the same as in fig. 3.

4.2 Model Using Line Multipoles

The introduction of the line multipoles exactly meets the requirements of the field of the square plate in our example. For the positioning of the line multipoles along the matching points they can be regarded as cylinders with appropiate length. The object can be filled up using such cylinders instead of the spheres in the conventional modeling. This is shown in fig. 8.

Some special criteria have to be observed to avoid unnecessary difficulties:

- The order around the axis has to be chosen in the same way as for the spherical multipoles.
- The line multipoles have to be subdivided into parts (segmentation, see sect. 2.2). Then, the functions behave approximately like a segmentwise linear function. The change of the fields along the axes is modeled using this approximation. Especially at short wavelengths the required segments may become quite short. The angle of incidence of the excitation may additionally influence the number of segments.
- Numerical dependencies may appear. The singularity on the axis may interfere with parallel line multipoles or with 'normal' multipoles which are able to produce a similar scattered field as the line multipoles. For this reason, the 'normal' multipole is separated from the end of the two adjoining line multipoles by one radius, as shown in fig. 8. Otherwise instabilities may result.

Due to the length of the line multipole segments not all fields can be approximated along the axes and at the end. The behaviour at the end around the axis is similar to a 'normal' multipole of the same order, and like a point charge (order 0) in the other directions. Using only line multipoles the field around the corner of the plate could not be modeled. The 'normal' multipole has to be introduced for this purpose. Further details of modeling edges are explained in [8].

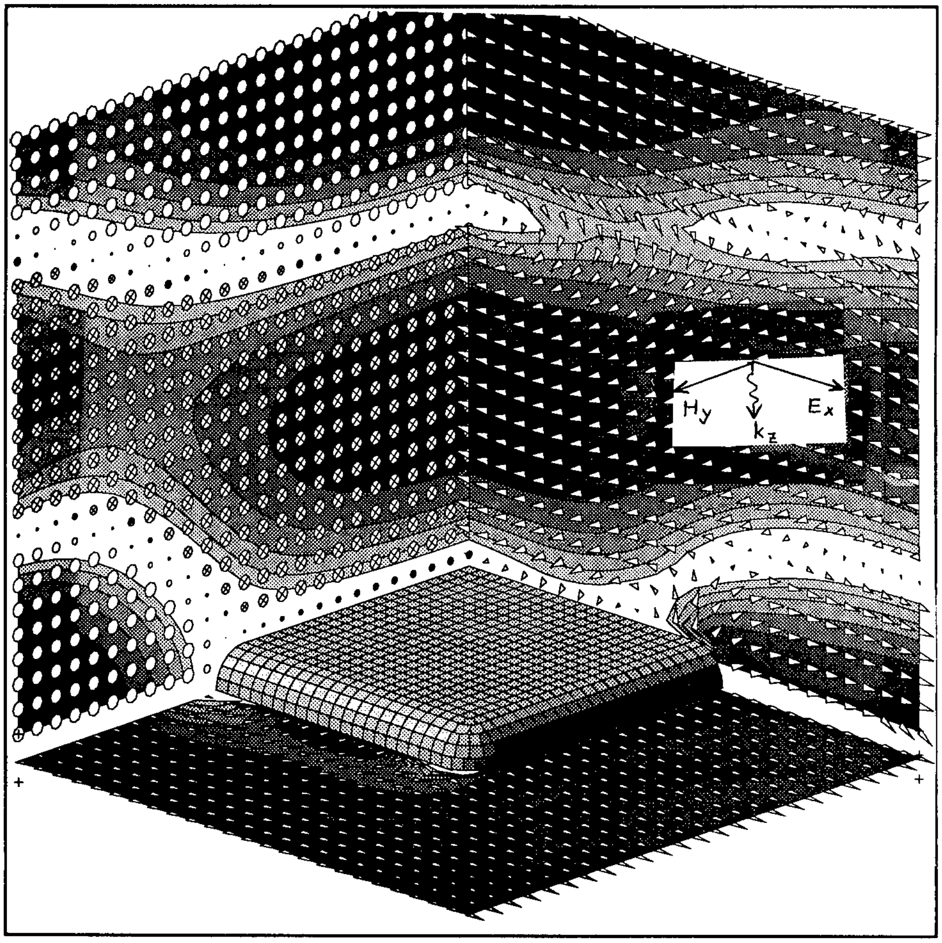

Figure 5 A square plate is exposed to a plane wave coming from top. The picture shows the arrangment (one quarter only) as well as the resulting electric field. The underlied gray areas increase the range of representation: Their borders are equilines for the absolute value of the instantaneous electric field.

Summary

The use of the line multipoles in the MMP-program allows the modeling of the electromagnetic field of various structures with less unknowns than the normal multipoles would require. The reduction is higher, when the structures to be modeled are 'thin and flat'. The placing of the line multipoles could be automated following a similar strategy than that used for 'normal' multipoles (filling up by *cylinders* rather than *spheres*). The two examples — scattering at a one wavelength plate of moderate thickness and simulation of the influence of an absorbing clamp in an almost resonant loop — show the wide range of application of the line multipole concept.

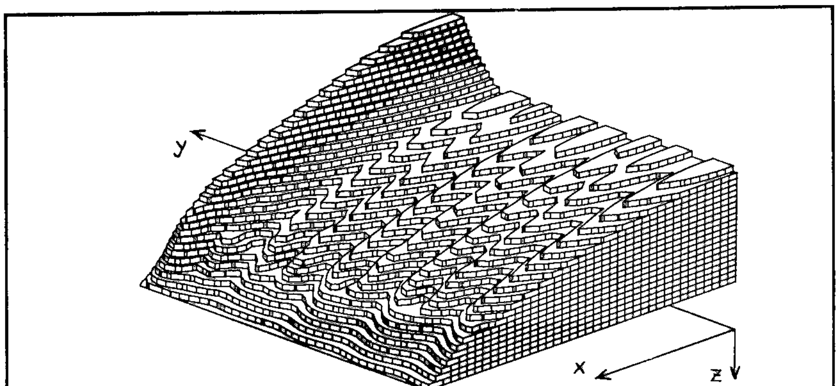

Figure 6 **The surface current varies along the surface of the plate. The picture shows the absolute value** of the surface current density on one quarter of the upper surface of the plate. The ripples are due to the matching errors and are correlated with the line pole modeling of the field. Note the **cahnge of the view point compared with fig. 5.**

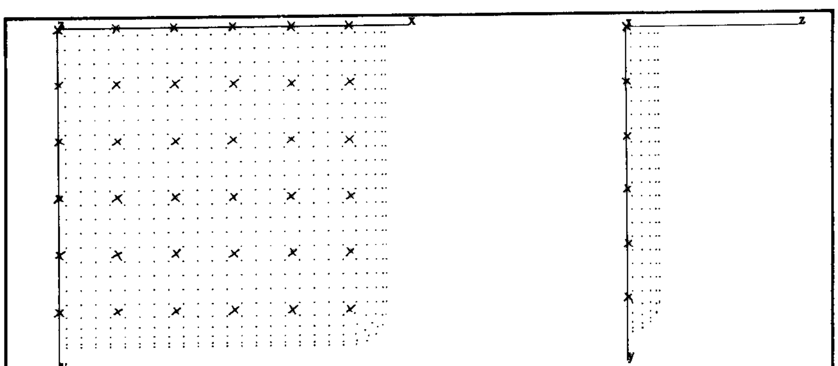

Figure 7 **The modeling with 'normal' multipoles requires 616 matching points and 36 multipoles** (×) of order 4. Due to symmetry, only one octant hat to be discretized.

References

[1] Ch. Hafner, *The generalized multipole technique for computational electromagnetics*, Artech House Books, 1990.

[2] L. Bomholt, P. Regli, Ch. Hafner, and P. Leuchtmann, "MMP-3D: A package for computation of 3D electromagnetic fields on PC's and workstations," in *6th Annual Review of Progress in Applied Computational Electromagnetics (ACES), Conference Proceedings*, (Monterey), Mar. 1990.

[3] P. Leuchtmann, "On the modelling of the electromagnetic field of EMC test arrangements with the MMP-code," in *9th International Zurich Symposium on Electromagnetic Compatibility, Conference Proceedings* (Zürich), 1991.

[4] P. Leuchtmann, "New expansion functions for long structures in the MMP-code," in *7th Annual Review of Progress in Applied Computational Electromagnetics (ACES), Conference Proceedings*, (Monterey), Mar. 1991.

[5] P. Regli, "Automatic Expansion Setting for the 3D-MMP Code," in this Conference, (Monterey), Mar. 1992.

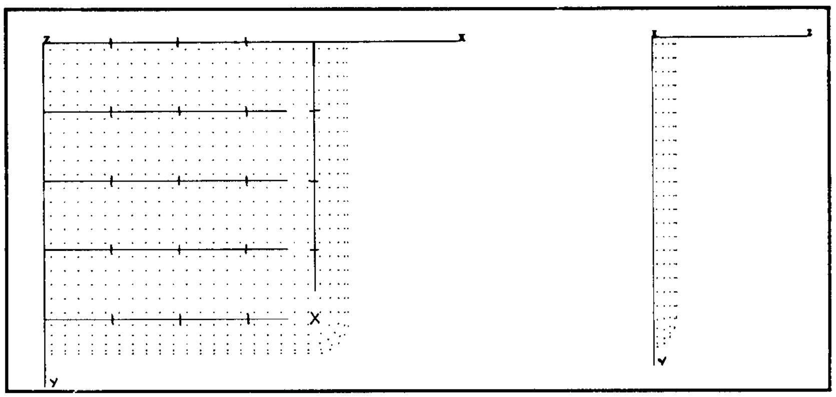

Figure 8 **Model using 24 line multipoles (6 lines with 4 segments each) along the edges and for filling up the remaining inner of the plate. This type of expansion functions** would allow a considerable reduction of matching points, which has not yet been realized. Note the 'normal' multipole (×) at the outer corner.

[6] P. Leuchtmann, "Optimal location for matching points for wire modelling with MMP," in *Applied Computational Electromagnetics (ACES) Journal*, Vol. 6, Dec. 1991.

[7] P. Leuchtmann, "Thin wire feature for the MMP-code," in *6th Annual Review of Progress in Applied Computational Electromagnetics (ACES), Conference Proceedings*, (Monterey), Mar. 1990.

[8] F. Bomholt, "Die Einkopplung elektromagnetischer Wellen in Schaltungsgehäuse; Berechnung mit der MMP-Methode", GRD Project No. 64'099, Final report. Available at Electromagnetics group, ETH Zürich.

Iterative and Block Iterative Solutions of Overdetermined Systems of Equations in the MMP Code

Ch.Hafner and N.Kuster, Swiss Federal Institute of Technology, Zurich

Abstract

In this paper, different iterative schemes are applied to typical MMP matrices. It is shown that the results depend very much on both the type of problem and the type of MMP expansion. Relatively simple models, which may already lead to a very slow convergence, have been studied in detail. These models illustrate the problems of iterative algorithms in the MMP code. When pure mathematics fails, some physical reasoning can be very helpful. The MMP code provides some features that allow a given problem to be split into several subproblems. This directly leads to a block iterative technique. It is shown that this technique is reliable and advantageous, at least when the splitting of the problem into subproblems is physically reasonable. Even in cases where no reduction of the computation time is achieved, block iteration is helpful because of its numerical advantages and significant benefits for modeling and validation.

Introduction and Basic Considerations

The solution of linear systems of equations is the most time consuming task in many numerical codes. The tendency towards faster computers with larger memories causes a bias towards larger systems of equations and this causes a trend to iterative matrix solvers such as Conjugate Gradient (CG) algorithms. When the CG was first proposed by Hestenes and Stiefel, only small problems were solved (the largest one that could be calculated on a computer at the Swiss Federal Institute of Technology had 106 unknowns!). Although CG was applied for solving dense matrices at that time as well, most modern iterative schemes are designed for sparse matrices whereas direct solvers are still preferred for dense matrices.

At the time of MMP's code's inception, only a relatively small computer was available at the Swiss Federal Institute of Technology. The fact that relatively small, dense systems were obtained was of major importance (for problems with more than 150 unknowns, special permission was required!). Today, the number of unknowns in the MMP code exceeds 1000, even on PCs. Thus, it is reasonable to look for iterative techniques that can handle the relatively dense, rectangular matrices, which occur in the MMP code. Unfortunately, both dense and rectangular matrices have not been extensively studied by those who developed iterative matrix solvers.

Although the MMP code has a strong mathematical background, physical reasoning has often proved to be helpful in improving the performance of the code. In many cases, mathematical problems could be avoided or solved with some physical knowledge. The procedure used in classical physics for solving complex problems is 1) to split the problems into smaller subproblems, 2) to solve the subproblems alone, and 3) to study the interactions between the subproblems. This procedure is equivalent to block iterative matrix solvers. It is shown below that the pure mathematical approach to solving the MMP matrices iteratively has important drawbacks and may converge very slowly even in simple applications, whereas (physically reasonable) block iterative techniques are helpful, at least for problems of higher complexity.

Although the MMP code runs on PCs, it looks rather like a camera system than an instant camera. I.e., its virtue is flexibility rather than simplicity. Consequently, new ideas can often be introduced and tested in the code with some minor modifications or even without any modification. Although the solution of the linear system of equations is usually much more time consuming than everything else in the code, it is done in a few statements in a few, simple subroutines. Thus, implementing a new matrix solver requires only the replacement of a small part of the code and is easily done.

Large scattering and eigenvalue problems can be solved with the existing 2D MMP code [1]. Since only the boundary is discretized, the term "large" refers to the size of the surface with respect to the wavelength. Useful results are obtained in most cases with five unknowns per wavelength. Consequently, scatterers with a surface that exceeds 100 wavelengths can be easily computed on a fast PC. Although solving systems of equations with more than 500 unknowns with the Givens algorithm used in the 2D MMP code becomes time consuming, there is no real need for a faster iterative technique in the 2D code. The situation is completely different in the 3D MMP code. To obtain similar accuracy, 25 unknowns per square wavelength are necessary and therefore a scatterer with a surface of 20 square wavelengths is already large for 3D MMP. Overdiscretization is advantageous in 2D MMP modelling because it usually leads to useful results already in the first approach, whereas in 3D MMP modelling one is often forced to work with a relatively small number of unknowns per square wavelength, which in many cases leads to ill-conditioned or near rank-deficient matrices. Thus, the 3D MMP code is the better suited candidate for iterative and block-iterative matrix solvers. Nonetheless, iterative techniques have been implemented and tested in the 2D code because this code is simpler and allows the study of a much larger number of different examples. To test block-iterative techniques, no modification of the code is required because this can be done with the MMP feature called "connection." Since "connections" have been implemented in the 3D MMP code [2] in a much more flexible and general way, block-iterative techniques have been studied in 3D.

As in most numerical codes for electrodynamics, the field is approximated by a linear combination of basis function in the MMP code. Unlike in many other codes, the basis functions are selected in such a way that the field is an analytic solution of the time-harmonic Maxwell equations in each domain with linear, homogeneous, isotropic material properties. Each basis function affects one column of the MMP matrix. The appropriately weighted boundary conditions are fulfilled in the least-squares sense by a Generalized Point Matching (GPM) technique that has been shown to be numerically equivalent with error minimization and projection techniques – provided that 1) appropriate testing functions are used, 2) the integrals are approximated numerically by trapezoidal integration, and 3) $A^*Ac = A^*b$ is solved in the GPM [3]. When the overdetermined system of equations $Ac = b$ is solved directly with an appropriate algorithm, GPM is even superior. In the MMP, codes $Ac = b$ is solved directly with an improved Givens updating procedure that is well-known from LINPACK. This procedure is more time-consuming than other matrix solvers but it has the advantage that only an upper triangular matrix U must be stored. U has the same number of columns as A. Since A usually has 3 to 20 times more rows than columns, one can solve problems with 2.5 to 6 times more unknowns with the updating procedure, which is very important on machines with limited memory. Another important advantage of GPM is that each boundary condition of a matching point affects exactly one row of A. Thus, the meaning of the rows and columns of A can be easily understood.

CG applied to 2D MMP

One of the most important advantages of CG for solving a linear system of equations $Ax = b$ iteratively is the fact that the matrix A remains unchanged. For us, this is an important drawback of CG (and of other iterative techniques) compared with the Givens updating procedure that requires the storage of U only. A is usually a square, positive definite matrix. Moreover, today A is assumed to be sparse in most cases. Thus, one might believe that CG cannot be applied to the dense, rectangular matrices obtained in the MMP code. Already in the original paper [4], however, a CG algorithm for solving such systems is given. This algorithm has been implemented in the 2D MMP code.

The most simple testing example for the 2D MMP code is the scattering of a plane wave at a circular conducting cylinder. In this case, one easily can select the MMP expansion in such a way that the basis functions are orthogonal. Consequently, a simple iterative technique such as Gauss-Seidel converges to the exact solution in only one step. When the CG algorithm was applied to a circular cylinder with a diameter of five wavelength leading to 81×29 matrix A, 80 iterations were required to reach the same accuracy as the Givens updating procedure. This disappointing result can be explained by the fact that A has not been preconditioned. As there is not much literature about the preconditioning of rectangular matrices, one might be tempted to solve the normal equations with the symmetric, positive definite matrix A^*A and to take advantage of the immense literature for such matrices. However, we do not want to lose the numerical advantage of the direct solution of $Ax = b$. Moreover, the computation of A^*A is very time-consuming ($mn(n+1)/2$ complex multiplications!).

From analyzing the MMP matrices, it seems to be reasonable to compute the square norm of each column and to divide all elements by the corresponding norm, i.e., to generate a matrix A_n with columns of unit norm instead of A. Applying this method to the example of the circular cylinder, we already obtain an exact result after the first iteration. Unfortunately, we get much worse results when we study more complicated structures. It is an important advantage of the MMP code that the system $Ax = b$ easily can be interpreted physically. The excitation is contained in the right hand side, i.e., the vector b. When the excitation affects only a few matching points, most of the elements of b are zero, and the completely wrong solution $x = 0$ leads to relatively small integral values of the absolute errors on the boundaries. Thus, we expect that such cases are difficult for iterative techniques that usually start with the approximation $x = 0$. The MMP computations of waveguide discontinuities [5] always lead to such problems. The most simple case is the computation of a "fictitious" inhomogeneity, i.e., a part of a waveguide that is not inhomogeneous but is computed as if it would be inhomogeneous. This has the advantage that the solution is known analytically, which is most helpful for testing.

As expected, the convergence of the CG method turns out to be poor and becomes worse the longer the "fictitious" inhomogeneity of the waveguide. In the following, a piece that is twice as long as its width is considered. As the ratio 2:1 is not at all large, and the MMP matrix with 117 rows and 31 columns is small, the convergence is disappointing. After the first iteration the average of the absolute error on the boundaries computed by the MMP program is 0.55 and the field (cf. Figure 1a) looks somewhat as expected: it is relatively strong near the fictitious boundary where the wave comes in and small where the wave goes out. Surprisingly, the error increases in the second iteration to 1.67.

After 117 iterations, i.e., as many iterations as equations, the error is still 0.31 and the result is still quite inaccurate. To obtain the same accuracy as the Givens algorithm, i.e., an error smaller than 0.0025, about 1500 iterations are required.

It should be mentioned that different simple preconditioners have been tried without success. The first example shows that we can easily find applications demonstrating the efficiency of the properly preconditioned CG algorithm. This would allow to present some impressive benchmark results of the MMP code. However, the second example shows that there are much more important and interesting classes of problems that cannot be efficiently solved by this CG implementation – except when a much better preconditioner is found. Since the results of other point iterative techniques, such as Gauss-Seidel, were not encouraging as well, the use of the direct Givens updating procedure is still recommended. Nonetheless, better techniques to solve large MMP matrices are being sought. One of them is presented in the following section.

Block-Iterative Techniques in the 3D MMP Code

For the application of block iterative methods, the original system of equations $Ax = b$:

$$\sum_{k=1}^{n} a_{ik}x_k = b_i \quad (i = 1, ..., m) \tag{1}$$

is partitioned into blocks. One can formally write the same equation as (1):

$$\sum_{K=1}^{N} A_{IK}X_K = B_I \quad (I = 1, ..., M) \tag{2}$$

where A_{IK} is a rectangular matrix containing a part of A, X_K and B_I are column vectors containing parts of x and b respectively. Usually one has $N = M$ in the block system. A Gauss iteration step requires the solution of

$$A_{II}C_I^{(l+1)} = B_I - \sum_{J=1;\ J\neq I}^{N} A_{IJ}X_J^{(l)} \quad (I = 1, ..., N). \tag{3}$$

In the MMP code, A and at least the diagonal blocks A_{II} are rectangular. Thus, the system of equations to be solved in each step of (3) is overdetermined and can be solved with the Givens algorithm implemented in the MMP code. This block-iterative technique is equivalent to the solution of $P^*Ax = c$ instead of $Ax = c$, where P is a block diagonal matrix with the blocks A_{II} as diagonal elements. I.e., the solution is different from the solution of the original system in the least squares sense which is obtained when P is replaced by A. It is interesting to observe that the Gauss block iteration applied to $A^*Ax = c$ is similar to (3) but more expensive. It minimizes the norm of the residual vector $r = b - Ax$ of the entire system, whereas (3) minimizes the residual vectors of the subsystems separately.

Both types of block iterations have been studied in [6]. As might be expects from well-known point iterative solutions of square systems ($m = n$, block size 1, i.e., $A_{IK} = a_{ik}$), the block iterative solution of $A^*Ax = c$ does converge when (3) does not, but it converges much slower when (3) can be applied (cf. Figure 3). The success of (3) strongly depends on the partitioning of A. Since the MMP matrices can easily be interpreted, there usually is no difficulty to find appropriate blocks from physical reasoning.

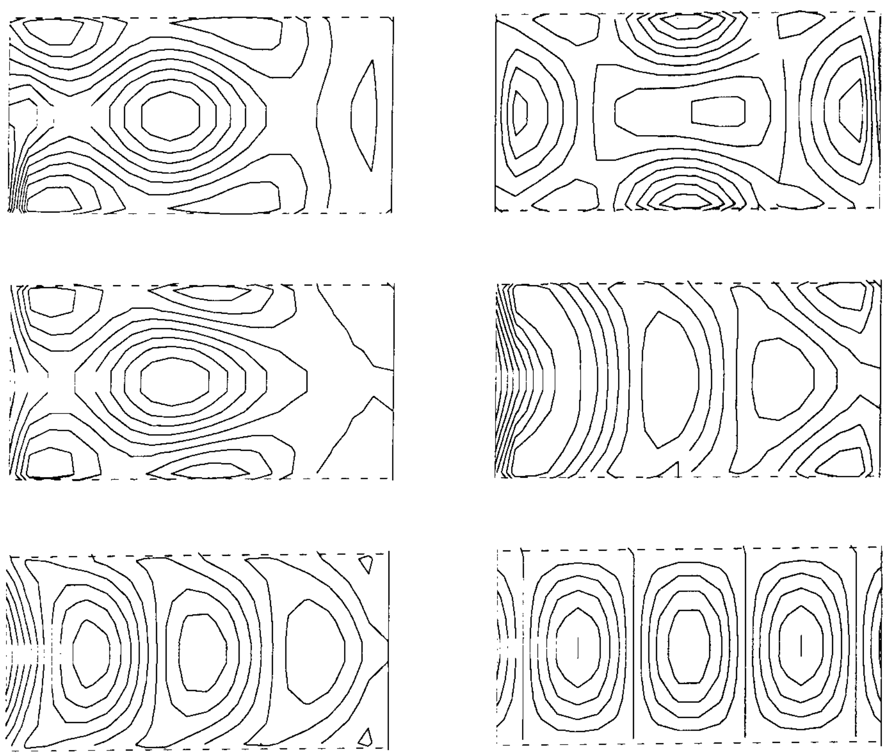

Figure 1 Magnetic field lines in a "fictitious" inhomogeneity of a rectangular waveguide computed with a preconditioned CG algorithm after 1,2,6,7,117,1500 iterations respectively.

This can be understood when one recognizes that a smaller error does not necessarily mean that the solution is closer to the correct solution because a small absolute error can be achieved when the field itself is small. It seems as if the CG algorithm would now try a solution with a stronger field near the fictitious boundary where the wave goes out (see Figure 1b). After the second iteration, the average error continuously decays and one obtains a more reasonable result after six iterations (see Figure 1c). The algorithm finds almost identical solutions in the following six iterations and the average error is reduced from 0.679 to 0.678. Thus, one might expect that one is close to the correct solution and that one should stop the iteration and generate a better MMP model because the result is too inaccurate. However with the performance of more iteration, a considerably better result is suddenly obtained (see Figure 1d) with an error 0.426. Afterwards, the error remains almost constant for several iterations. I.e., the convergence of the CG algorithm typically looks like a stair. This is very annoying because one newer knows whether it is worth continuing the iteration or not. After 30 iterations, the error is 0.36, which is smaller than the error after the first iteration.

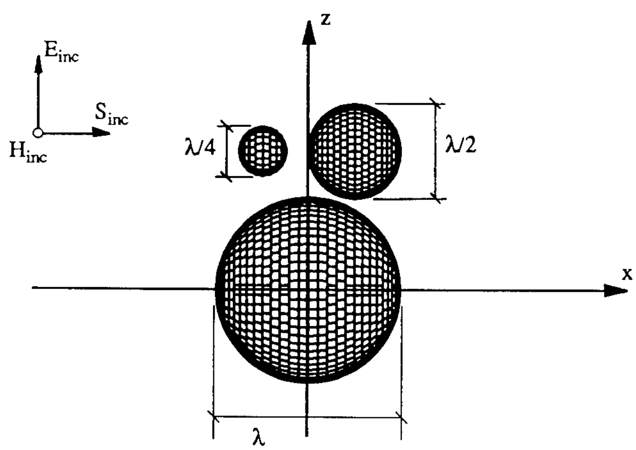

Figure 2 Example consisting of 3 perfectly conducting self-contained spheres of different size: small (s), medium (m) and large(l).

A typical example consists of three perfectly conducting self-contained spheres (cf. Figure 2). A subdivision of A into 3×3 blocks is obvious. With an appropriate arrangement of the columns and rows of the matrix A, the three diagonal blocks represent the scattering of the three scatterers in absence of the others and the off-diagonal blocks represent the interaction between the scatterers. Needless to say, the convergence is very fast when the interaction is weak. However, the convergence of (3) is good even when the distance between the spheres is quite small (cf. Figure 2). Depending on the arrangement of the rows and columns, the large sphere (l) first is computed, then the medium sphere (m), and finally the small one (s), or the large one (l), then the small one (s) and finally the medium one (m), and so on. In Figure 3 three of the total number of six arrangements are depicted. Good convergence is obtained in all cases. Moreover, it should be noted that the iterative solution of $A^*Ax = c$ is much slower.

Since (3) fails in more complicated cases and the iterative solution of $A^*Ax = c$ usually converges too slowly, a solution in between the two can be considered. This is achieved by the following generalization of (3): The blocks can be replaced in (3) by larger and therefore "overlapping" blocks. In our example, the parameters corresponding to the multipoles in each sphere are computed using the equations obtained from the matching points on this sphere only when (3) is applied, whereas all equations are used at the same time when $A^*Ax = c$ is solved instead. For larger, non-spherical scatterers, several multipoles are generaly used inside the body for approximating the scattered field. Despite the local behavior of the multipoles, the correlation of matching points to multipoles is not as simple and unique as when there are several scatterers. In this case, (3) fails and the method of "overlapping" blocks is reasonable: For computing the parameters of one multipole or of a set of neighbor multipoles, one will use all matching points near these multipoles. Since some matching points will be near different sets of multipoles, "overlapping" blocks are directly obtained. For more information, see [6].

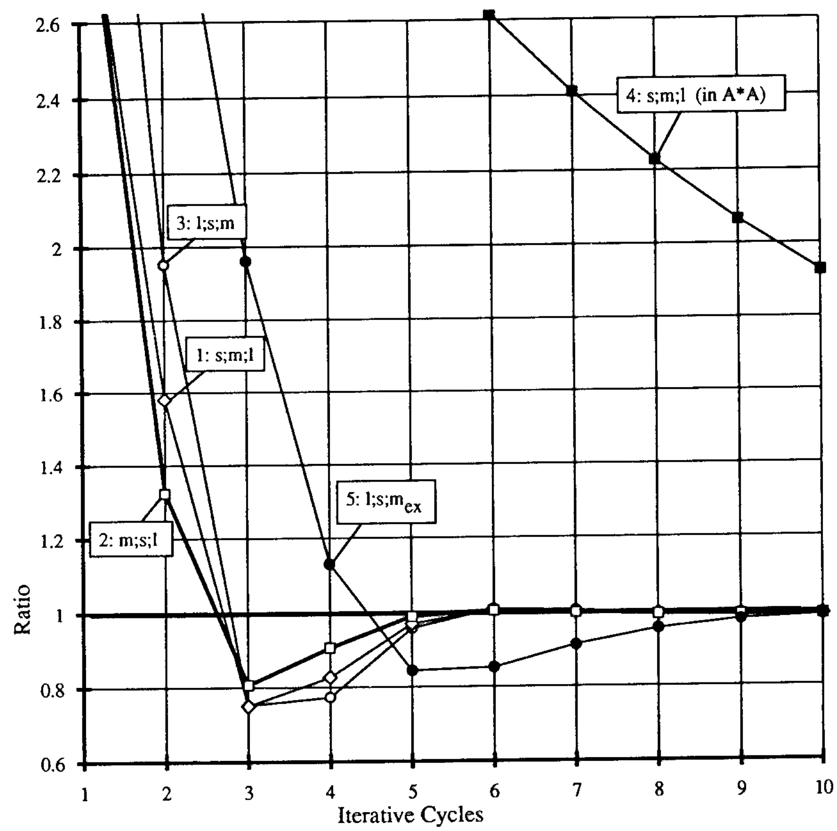

Figure 3 Convergence diagram for the Gauss-Seidel algorithm applied to the first example. Reference is the absolute value of the backscattered field at point $(-1000, 0, 1000)$; the ratio to the correct solution is shown. Curves 1,2 and 3 result from a matrix A that is partitioned in such a way that each diagonal block represents one of the spheres (s,m,l). The sequence in which the subproblems are calculated is indicated. Curve 4 results, if Gauss-Seidel is applied to A^*A and Curve 5, if some matching points of the large sphere, which are closest to the medium sphere, are aditionally evaluated in the subproblem (m_{ex}), which represents the medium sphere, i.e., some of the rows of A are common to two different blocks.

In order to improve the convergence rate of block iterative techniques, Successive Block Overrelaxation (SBOR) could be applied. It has been shown in [6], however, that when the blocks are physically reasonable, optimal overrelaxation factor is close to 1, i.e., SBOR is not necessary.

It should be pointed out that block iterative techniques have been very useful for solving more complex problems than the ones considered here. Above all, for large and complicated structures, useful results have been found even when the direct method

failed because of the ill-conditioned matrices. Moreover, the technique removes some of the problems that occur when – in addition to the multipole expansions – other types of basis functions, e.g., "thin-wire expansions" [7] are used. Examples for these cases are discussed in [6].

Conclusions

Although point iterative techniques are not well suited to solve the system of equations obtained by the MMP approach, block iterative techniques provide important advantages in many respect. A subdivision of many problems of higher complexity can be performed by physical considerations in such a way that a convergence within 3 to 10 steps is achieved by applying a "generalized" Gauss-Seidel algorithm. The numerical advantages are more important than those regarding speed. The most significant benefits, however, are for the modeling and the solution validation so that the spectrum of problems to which the MMP code can be applied is considerably extended by this block iterative technique.

References

[1] Hafner, Ch., *2D-MMP; Two Dimensional Multiple Multipole Software and User's Manual*, Norwood, MA: Artech House, 1990.

[2] Hafner, Ch. and L. Bomholt, *The 3D MMP Codes for Personal Computers*, to be published, Demo version available from the authors.

[3] Hafner, Ch., *The Generalized Multipole Technique for Computational Electromagnetics*, Norwood, MA: Artech House, 1990.

[4] Hestenes, M. R. and E. Stiefel, "Methods of Conjugate Gradients for Solving Linear Systems" *Journal of Research of the National Bureau of Standards*, Vol. 49, No. 6, Dec. 1952.

[5] Hafner, Ch., "Multiple Multipole (MMP) Computations of Guided Waves and Waveguide Discontinuities" *Int. J. of Numerical Modelling*, Vol. 3, pp. 247-257, 1990.

[6] Kuster, N. and L. Bomholt, "A Block Iterative Technique to Expand MMP's Applicability to EM Problems of Higher Complexity" *IEEE Trans. on AP* , submitted.

[7] Leuchtmann, P. and L. Bomholt, "Thin wire feature for the MMP-code" *Conference Proc., 6th Annual Review of Progress in Applied Computational Electromagnetics (ACES)*, Monterey, March, 1990.

Automatic Expansion Setting for the 3D-MMP Code

Peter Regli

Electromagnetics Group
Swiss Federal Institute of Technology ETH
8092 Zurich, Switzerland

Abstract

This paper presents the structure and some details of an algorithm which automatically creates and initializes a robust set of 3D-MMP expansions from the given domain properties and boundary data. The algorithm works for domains of arbitrary shape with edges and corners, considers reflective symmetries, was successfully tested and is implemented in the graphical MMP user interface *mmptool*.

Introduction

The MMP-Method uses - among others - the spherical solutions of the time harmonic Maxwell equations to expand the unknown fields in piecewise linear, homogeneous and isotropic domains and is mainly used to simulate near-field scattering problems in the presence of dielectric and lossy materials [1][3].

All spherical field components are derived from two scalar "potentials" of the form

$$\Psi(r, \vartheta, \varphi) = \sum_{n=1}^{N} b_n(kr) \sum_{m=0}^{M} S_n^m(\vartheta, \varphi) \quad ; \qquad M \le n, \tag{1}$$

where $b_n(kr)$ stands for one of the spherical Bessel functions

$$b_n(kr) \in \{j_n(kr), y_n(kr), h_n^{(1)}(kr), h_n^{(2)}(kr)\} \tag{2}$$

and $S_n^m(\vartheta, \varphi)$ are the spherical harmonics. Due to their radial behavior, these expansion functions divide into four different types, corresponding to the four different kinds of spherical Bessel functions. Three of them are mainly used as single multipole expansions, i.e., they are only applied to nearly spherically shaped domains. The fourth (radial functions of $h_n^{(1)}$-type) can be used multiply with different origins and is therefore appropriate for domains of arbitrary shape. The location and orientation of each expansion as well as the minimum and maximum degree and order must be defined properly with respect to the boundary shape and discretization. Insufficient expansion sets cause bad convergence rates and result in inaccurate solutions. Another potential problem may arise from numerical dependencies between expansion functions. These must be avoided carefully, as they lead to badly conditioned matrices or even to wrong results.

Region of influence

Multipole functions of the $h_n^{(1)}$-type decay with the distance from the origin and thus hardly influence remote parts of the boundary. Conversely, the unknown function coefficients are mainly determined by the nearest boundary elements. We therefore define the *region of influence* I_p of a multipole Ψ_p being the part of the boundary inside a sphere centered at the origin of the multipole with the radius

$$R = \rho R_0 , \tag{3}$$

where R_0 denotes the distance to the nearest boundary element and ρ is a control variable with normal values between 1.2 and 1.5.

Dependency tests

From a numerical point of view, we distinguish between three main reasons for dependencies between expansion functions:

- Dependencies between multipoles with different origins: Expansions must be far enough apart from each other. Otherwise they act on the same section of the boundary where they supply similar function sets.
- Dependencies between "orthogonal" functions of a single multipole expansion: Although the multipole expansions are orthogonal in the whole space or on a spherical surface, this is generally not true for arbitrary subspaces like non-spherical surfaces or parts of spherical surfaces. Non-orthogonalities of this kind are introduced if the region of influence - seen from the origin of a spherical expansion - appears under a solid angle which is significantly less than 4π.
- Dependencies between different expansion types: The MMP code offers other types of expansions, e.g., plane waves, 2D-expansions, waveguide modes etc. Combinations with spherical expansions always imply non-orthogonalities which may cause dependency problems.

We use the following two conditions to decide if the numerical dependencies between two multipole expansions can be neglected (Figure 1):

- *Boundary test*: Two expansions are sufficiently independent, if the corresponding two re-

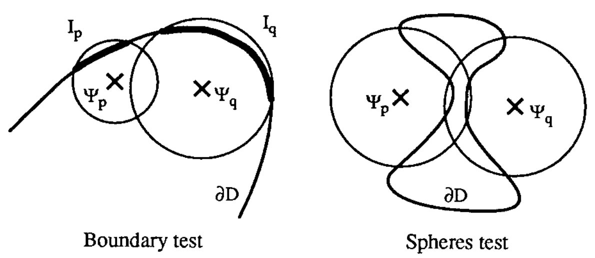

Figure 1: Dependency tests are used to avoid numerical dependencies between expansions. Both pictures show sufficiently independent expansions. I_p and I_q denote the regions of influence of the corresponding expansions.

gions of influence do not overlap. This test is safe but sometimes too restrictive. It is extendable to arbitrary expansions if only an appropriate region of influence can be defined. Conversely, this condition may be used as a general definition of the region of influence.

- *Spheres test*: A spherical expansion Ψ_p is sufficiently independent from a second expansion Ψ_q, if its origin is exterior to a sphere centered at the origin of Ψ_q and containing the region of influence of Ψ_q. This test is very efficient and actually applied in the algorithm.

Both statements should be understood as *sufficient* but not *necessary* conditions, i.e., they may be violated in some cases. They obviously rely on the definition of the region of influence and are therefore dependent on and controllable by the variable ρ in (3).

Algorithm

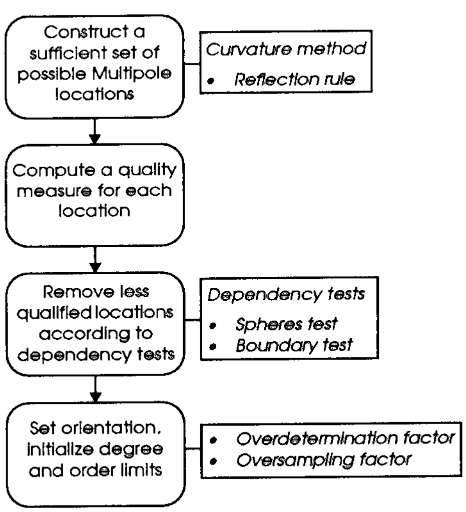

Figure 2: The basic idea is to create a sufficiently large set of good multipole locations and then remove as many locations as necessary to avoid numerical dependencies between expansion functions. A quality measure guarantees the survival of the better locations in this elimination process. The remaining expansions are oriented with respect to the boundary discretization and initialized with maximum limits of degree and order. A few control variables enable the user to adapt the rules and tests according to requirements of robustness, exactness or size of the generated model.

Construction of multipole locations

Since the sphere is the most natural domain for a spherical expansion, we can imagine a multipole as a ball of variable size. Domains of arbitrary shape should be tightly covered with such balls and each one should fit the boundary as smoothly as possible. A simple geometric method - we call it the *curvature method* - is used to construct the center $\boldsymbol{r}_i$ of a "best fit sphere" for each surface element S_i of the discretized boundary. It is based on the following definition of the "discrete curvature" of a surface element:

- Given two surface elements S_i and S_k with their locations and unit normal vectors $(\boldsymbol{s}_i, \boldsymbol{n}_i)$ and $(\boldsymbol{s}_k, \boldsymbol{n}_k)$, the center of curvature of the element S_i with respect to S_k is the point $\boldsymbol{r}_{ik}$ on

the straight line $g_i(t) = s_i + tn_i$ which has the same distance to both s_i and s_k.

This point results from a simple geometric construction (see Figure 3) and can be computed efficiently by:

$$r_{ik} = g_i(t_{ik}) \quad \text{with} \quad t_{ik} = \frac{d_{ik}^2}{2n_i d_{ik}} \quad \text{and} \quad d_{ik} = s_k - s_i. \tag{4}$$

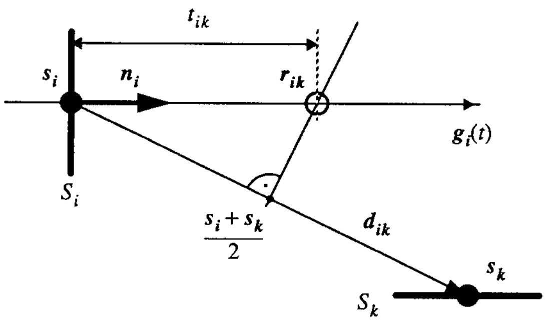

Figure 3: Two-dimensional illustration of the "discrete curvature" of a surface element S_i with respect to a second surface element S_k.

If s_i and s_k are points on a smooth surface and $s_k \to s_i$, then $\frac{1}{t_{ik}}$ is equal to the corresponding normal curvature at the point s_i.

The curvature method is now defined by the following algorithm (see Figure 4):

- Take a single surface element S_i and compute t_{ik} for all $k \neq i$, i.e., for all the remaining surface elements of a domain boundary.
- Take the minimum of all positive t_{ik} and the maximum of all negative t_{ik} and call them t_i^+ and t_i^- respectively. Choose the corresponding points $r_i^+ = g_i(t_i^+)$ and $r_i^- = g_i(t_i^-)$ as possible multipole locations produced by S_i.
- If any of these locations is inadmissible (e.g., because of a singularity of the corresponding expansion), take the "reflected" location $\bar{r}_i = 2s_i - r_i$ instead of it.
- Repeat these steps for all surface elements S_i of the domain.

This algorithm produces at least one and at most two multipole locations for each surface element of a domain boundary.

Quality measures

We define the quality of an expansion's location with regard to the ideal case of a spherical domain. Two simple measures are introduced to penalize deviations from this case:

- *Solid angle measure*: The solid angle Ω, under which the region of influence is seen from the origin of the expansion should be as large as possible to minimize dependencies between

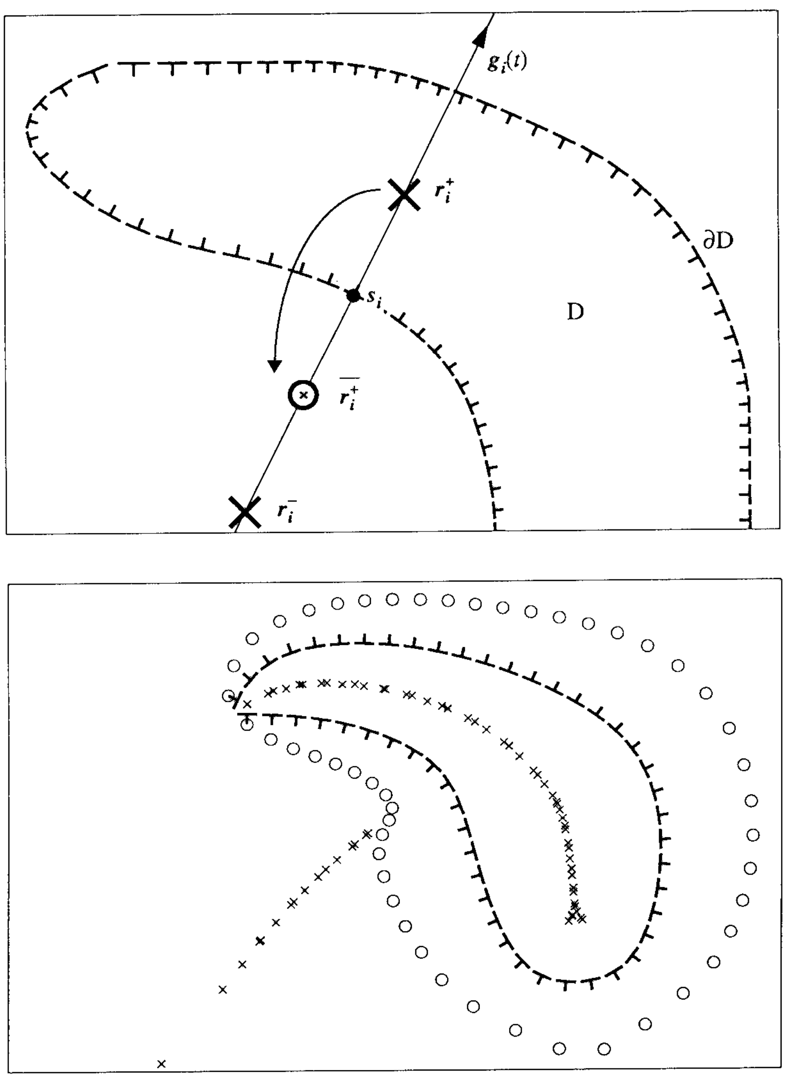

Figure 4: Construction of multipole locations with the curvature method. Each surface element of the boundary generates at least one and at most two possible multipole locations. Locations that are inside the domain are inadmissible and therefore reflected to the outside. The second picture shows the whole set of possible multipole locations. Points that are produced by the reflection rule are drawn as small circles.

functions of similar degree and order.

- *Sphericity measure*: To achieve maximum convergence rate, the surface elements in the region of influence should be tangential to a sphere centered at the origin $\boldsymbol{r}$ of the expansion, i.e., the angles α_i between the radius vectors $\boldsymbol{s}_i - \boldsymbol{r}$ and the respective surface normal vectors $\boldsymbol{n}_i$ should be zero. Considering all surface elements S_i in the region of influence, we use the quantity $T = \min(\cos^2\alpha_i)$ to express sphericity in this sense.

If one of two similar locations is on a symmetry plane, it is preferred because symmetries reduce the number of unknowns. If a location is near a symmetry plane, it is moved into the symmetry plane. The above measures and a few other quantities are combined to a scalar valued function that defines a quality for each location.

Orientations, degrees and orders

Full-order spherical expansions ($M = N$ in (1)) are invariant with respect to rotations, i.e., the orientation of their local coordinate system is irrelevant. Sometimes however, we know in advance that the solution to be found varies only slightly along one of the two orthogonal directions which can be defined on the boundary surface and therefore the number of unknowns can be reduced significantly by taking partial order expansions, e.g., expansions with $M < N$. These are not invariant to arbitrary rotations and must therefore be oriented properly.

Upper limits for the maximum degree N and the maximum order M of an expansion can be derived from two different conditions:

1) The number b of independent boundary conditions in the region of influence of the expansion Ψ should be greater than the number p of unknown expansion coefficients. For a full-order expansion, the number of unknowns is $p = 2N(N+2)$ and hence we set

$$N \le \sqrt{\frac{b}{2\gamma} + 1} - 1\,, \tag{5}$$

where $\gamma \ge 1$ is a user definable control variable with the meaning of an "overdetermination" factor.

2) N and M are limited by a sampling theorem which is similar to the two-dimensional Shannon sampling theorem. Supposing a spherical domain with a regular parametric boundary discretization, it states that

$$N \le \frac{\pi}{\Delta\vartheta} \quad \text{and} \quad M \le \frac{\pi}{\Delta\varphi}, \tag{6}$$

where $\Delta\vartheta$ and $\Delta\varphi$ are the (positive) angles between adjacent boundary elements in the spherical coordinates of the expansion. The generalization to arbitrarily shaped domains with an irregular boundary discretization requires an appropriate definition of the sampling angles

$\Delta\vartheta$ and $\Delta\varphi$. Let

$$\begin{aligned} \boldsymbol{s}_i &= [r, \vartheta, \varphi] \\ \boldsymbol{u}_i &= [u_r, u_\vartheta, u_\varphi] \\ \boldsymbol{v}_i &= [v_r, v_\vartheta, v_\varphi] \end{aligned} \tag{7}$$

be a surface element located at $\boldsymbol{s}_i$ with the two tangent vectors $\boldsymbol{u}_i$ and $\boldsymbol{v}_i$ described in the coordinate system of the expansion Ψ. The length of the tangent vectors is supposed to reflect the real size of the surface element. Then, a safe definition of the sampling angles with regard to (5) is

$$\Delta\vartheta_i = \frac{\sqrt{u_r^2 + v_r^2 + u_\vartheta^2 + v_\vartheta^2}}{R_0} \quad \text{and} \quad \Delta\varphi_i = \frac{\sqrt{u_r^2 + v_r^2 + u_\varphi^2 + v_\varphi^2}}{R_0 \sin\vartheta}, \tag{8}$$

where R_0 denotes the distance between the origin and the nearest boundary element. Considering all surface elements in the region of influence of Ψ, we define the limiting sampling angles used in (5) as

$$\Delta\vartheta = \min(\Delta\vartheta_i) \quad \text{and} \quad \Delta\varphi = \min(\Delta\varphi_i). \tag{9}$$

Again, a control variable is introduced to modify the degree and order limits according to an oversampling rate.

After N and M are computed from the sampling condition, the first condition is also checked and the limits are lowered if necessary.

Example

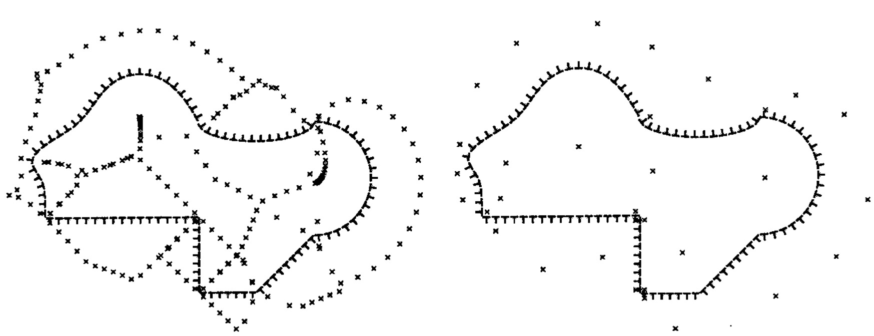

Figure 5: The picture on the left shows the set of multipole locations generated with the curvature rule. The set was restricted to only one location per boundary element (the one which was nearer to the boundary). The remaining best locations after the evaluation of dependency tests and quality measures are shown in the right picture. Note that some locations near corners can not really be used since their region of influence does not supply enough boundary conditions. This problem would not be removed by a refinement of the boundary discretization. It is rather a manifestation of the difficulties, which naturally arise for the computation of the electromagnetic field near discontinuities of the boundary tangents.

Conclusions

The algorithm generates a good set of multipole expansions for arbitrary closed 3D-domains with edges, corners and holes, provided that the boundary discretization is adequate. In special situations, it is advantageous to use other expansions like plane waves, 2D-expansions, wire expansions, etc. In this cases, the algorithm can still be used to create a full set of spherical expansions from which the superfluous expansions are deleted manually.
The overall computing time is, roughly speaking, proportional to $\sum n_i^2$, where n_i is the number of matching points of the domain D_i. This is acceptable if compared with the time needed for the solution of the equation system, which is about m^3, where m denotes the total number of matching points.

Availability

The presented algorithm is implemented in the graphical user interface *mmptool.* Demo-versions of this program are available for Sun workstations (SunView) [2][4]. The MMP kernel program is available for Sun workstations and PC's.

References

[1] L.H. Bomholt, *A Computer Code for Electromagnetic Scattering Based on the GMT.* Diss. ETH Nr. 9225, Zürich, 1990.

[2] L.H. Bomholt, P. Regli, Ch. Hafner, P. Leuchtmann, *A Package for Computation of 3D Electromagnetic Fields on PCs and Workstations*, 6th Annual Review of Progress in Applied Computational Electromagnetics (ACES), Conference Proceedings, 1990.

[3] Ch. Hafner, *The Generalized Multipole Technique for Computational Electromagnetics.* Artech House, 1990.

[4] P. Regli, Ch. Hafner, N. Kuster, *Graphic Output Routines of the MMP Program Package on PCs and Workstations*, 5th Annual Review of Progress in Applied Computational Electromagnetics (ACES), Conference Proceedings, 1989.

FD Schemes, Particles, Cellular Automata, and other Exotic Features of the 3D MMP Graphics

Ch.Hafner, Swiss Federal Institute of Technology, Zurich

Abstract

In this paper the implementation of some iterative algorithms in the graphic plot program of the 3D MMP code for PCs is presented. The algorithms cover a wide range from classical electrodynamics (finite differences, FDTD schemes, and moving particles) to concepts of chaos theory (cellular automata and fractals). These features have been implemented to test the graphic capabilities of the code, for tutorial and educational reasons, and for a future combination of the MMP code with FDTD and similar algorithms.

Introduction

The MMP code is based on the Generalized Multipole Technique (GMT) [1]. It was first designed for purely scientific purposes. When PCs became available, a new version including powerful graphic front ends, was developed with a more educational intention [2,3]. Because of the limited memory of PCs, the code was split into 1) a graphic editor, 2) a kernel without graphics, and 3) a graphic plot program. The latter allows 2D and 3D scalar and vector fields with harmonic or general time dependences to be depicted. The program can also compute energy densities, power densities, etc. from the given fields provided that the material properties are piecewise homogeneous, linear and isotropic. The kernel program can compute the field either on a regular 2D or 3D grid, or in an arbitrary set of field points anywhere in 2D or 3D space. Needless to say the plot file can handle all types. In most cases regular grids are preferred because this reduces the amount of data and allows nice graphic representations like iso lines. Since data are transferred between the different parts via ASCII files, the plot program can be used to represent the electromagnetic field computed with any code that is able to generate appropriate files. In order to work reasonably fast, the plot program stores the amplitudes of the E and H field in all field points and computes other quantities from E and H upon request. Thus, it is quite natural to allow the plot program to compute its own plot data instead of reading them from files.

The most important concept in the early days of the MMP code was the generalization of both the multipole expansions (also called spherical expansions in 3D) and the point matching technique [1]. The process of generalization is something like breathing. It starts with an inflation that allows a code to solve more complex problems more efficiently and widens the range of applications. At the same time, the code becomes more difficult to handle and the user requires a lot of know-how to obtain useful results. The know-how can be built into the code in the form of rules and the user can be supported by automated procedures. This reduces the amount of input and is a kind of deflation required for getting a user-friendly code. Comparisons with different techniques are helpful during inflation to obtain new ideas and during deflation to find useful rules. This process has been applied several times to the MMP code. The most important

concepts are: 1) "normal" expansions that are similar to multipoles but have no singularities, 2) "special" expansions that have either no singularities or singularities that are not concentrated on a single point, 3) "connections" that are a linear combination of different expansions, 4) additional or "special" boundary and continuity conditions, 5) surface impedances, and 6) "fictitious" boundaries. Some of these concepts can be interpreted as a combination of the MMP code with other techniques. For example, the "thin-wire" approximation [4] and all other expansions known from MoM codes [5] are "special" expansions for the MMP code and "fictitious" boundaries lead to MMP models that look similar to finite element models [6]. Useful rules for the MMP code have been found above all from the derivation of numerical equivalences between different techniques. For example, the generalized point matching technique with appropriate weighting is numerically equivalent to the projection technique known from MoM with appropriate testing functions. Thus, the process of generalization leads automatically to a kind of combination of different techniques. Consequently, all numerical techniques are potential candidates for improving the MMP code. Even techniques that have a background that is completely different from the MMP background can be useful. For example, ideas known from geometric optics have been used for handling scattering at large objects with the MMP code.

Finite Differences and Cellular Automata

The Cellular Automata (CA) concept [7] is known to fit very well to computers whereas the continuous space used throughout in good old Maxwell theory cannot be handled by computers without an appropriate discretization, i.e., a numerical technique that translates Maxwell's language into computer language. It is well known that "old" Finite Differences (FD) is one of the methods winning back a growing interest. FD can easily be interpreted as a result of the generalization process applied to CA. It is a generalized CA, specialized for computing electromagnetic and other fields. Since the MMP code is very close to the analytic solution of Maxwell equations, it is relatively far away from FD codes. Although a combination FD-MMP is expected to be useful (the FD part might handle non-linear materials, whereas the MMP part could easily compute the field in infinite domains), this seems to be much less trivial than the combinations that have been implemented up to now. For getting more experience a code that allows playing with CA rules and FD schemes is very desirable. This is the most important reason for the implementation of CA and FD in the 3D MMP plot program.

Both FD and CA usually work iteratively on regular grids. In the 3D MMP plot program they are implemented in a relatively simple and flexible way, i.e., for tutorial rather than for scientific use. In addition to some famous algorithms, the user easily can add his own algorithm in standard FORTRAN. Both CA and FD algorithms consist of 1) a general rule defining how the field in a point on the grid has to be computed from the information in this point and in its neighbors and 2) boundary conditions, i.e., a second rule that replaces the first one when the point is on the boundary of the grid. In CA codes, the information stored in each grid point is an integer [7,8] or even a logical value. Moreover, the rule usually does not depend on the location of the point. In electrostatics and similar applications, FD codes usually store a real number for the scalar potential and eventually some additional numbers for the material properties. In FDTD algorithms for electrodynamics one has to store several real numbers in every point defining the components of the field and the material properties. From this point of view, FD algorithms are more general than CA. The 3D MMP plot program provides

arrays for storing the real and imaginary parts of the electric and magnetic field, of the vector potential, of the scalar potential, and an integer array for storing some additional information about a field point, for example, a domain number. The material properties of the different domains are stored in separate arrays. I.e., one has 20 real and an integer number per grid point. In most of the algorithms far fewer numbers are required. Usually the real and imaginary parts are used for storing the "new" and "old" values of a computation respectively. Several variables remain unused in most cases. Moreover, the plot program always works on the whole electromagnetic field vectors in 3D space even when one has a 2D CA or an 1D CA. Thus, the computation time and the drawing time considerably exceed those of specialized codes like [7,8]. But the user is free to implement very complicated, generalized CA with different rules acting on different points.

Particles and Fictitious Worlds

As soon as an iterative scheme had been implemented for CA and FD algorithms, it was quite natural to introduce particles in the program because the computation of moving particles is done with iterative algorithms as well. The MMP implementation allows to study the interaction of particles, the movement of particles in a field computed either with the MMP kernel or with the plot program itself.

Since Maxwell theory is the origin of Einstein's theory of relativity, it seems to be obvious that relativistic particles should also be implemented. But when trying to do this, one will recognize the following: It is well known that in the Newtonian world one can compute the location and velocity of all particles for all times after a time t provided that the location and velocity of all particles is known at the time t. Although Einstein's world is deterministic as well, a similar computation is not possible: at the time t the force acting on any of the particles cannot be computed because the fields take time to propagate. Thus, one should not only know the location and velocity of all particles but also the (gravitational and electromagnetic) field everywhere in space at the time t. This clearly shows that the theory of relativity is a field theory. However, the particles implemented in the MMP code are non-relativistic.

The computation of the movement of particles requires a discretization of the time. To computing the location and velocity of a particle after a time step, one has to compute first the force acting on the particle. In the MMP code, electric, a magnetic, and a gravitational force are considered. In addition, friction can be introduced. The electric and the magnetic force each split into two parts: one arising from the interaction between the particles and another one due to an external field that is computed, for example, from FD or CA algorithms.

It is well known that the simple step by step computation of the location of particles is inaccurate after a large time interval even if the time step is relatively short. For example, when one computes the most simple interaction between two mass points with zero charges, one expects exact elliptic orbits when the initial positions and velocities are properly set. But one obtains only approximatively elliptic orbits. The major effect of the discretization is a slow rotation of the axis of the ellipse. Incidentally, the general theory of relativity predicts a similar rotation as well but this does not depend on the selection of something like the time step. The elliptic orbit with a stable axis is a direct result of Newton's "one over the square of the distance" law for the gravitational force. When the exponent in this law is changed slightly, a rotation of the axis follows as well. To verify this, the user of the MMP code can modify Newton's law. I.e., he can

generate and study "fictitious" worlds – which does not mean that the author considers Newtonian world to be "real" at all.

Fractals and Chaos Theory

When one is designing a graphic plot program, one always needs a large number of different examples in order to find appropriate representations. It is clear that the graphic representation of smooth fields is simple and requires no further investigation. In order to make the code more powerful, complicated structures have been searched for testing the different graphic procedures. It is well known, that fractals like the Mandelbrot set are geometrically most complicated. From fractals one easily construct complicated fields. This is shown in the examples below. Although the pure mathematical definition of fractals can be complicated, very simple algorithms lead to fractals, i.e., their implementation is extremely simple and very useful for testing. Moreover, fractal algorithms allow students to get experience not only with Maxwell theory and modern algorithms for computational electromagnetics, but although with post-modern concepts like chaos theory [8]. It is hoped that this finally will lead to more powerful and useful codes and that it will widen the mathematic and computational description of what we call the world.

Examples

One of the most simple, but interesting CA is John Conway's 2D "Live". In this game, each cell is either living or dead. I.e., one has a logical field on a regular 2D grid. The 2D Live rule is: 1) A living cell remains alive when two or three of its eight neighbors are living, otherwise it dies and 2) a dead cell remains dead except when three neighbors are living. It is interesting to see that this rule leads to a strange world of very different objects consisting of a certain number of cells. One can find stable objects, moving objects called gliders, and complicated objects like glider guns that are generating one glider after another. Theoretically, one can simulate with 2D Live all components of a computer or even a computer – provided that a sufficiently, i.e., extremely large grid is available.

There are several ways to formulate boundary conditions for 2D Live and other CA. Usually, the left boundary is simply connected with the right one and the upper boundary is connected with the lower one. I.e., one has the topology of a hypercube. This has the advantage that objects like gliders are neither reflected nor destroyed at a boundary: They simply exit one boundary and enter on the opposite boundary again.

The 2D Live rule can be generalized either on 2D, or on 3D grids, or even on n-dimensional grids: One simply has to state how many neighbors of a cell are necessary to keep it living or dead. Most of the generalized Live algorithms seem to be not very interesting because either all cells die or stay living after very few iterations. In the 3D MMP plot program a generalized 3D Live algorithm characterized by an integer with four digits d1, d2, d3, d4 is implemented: A living cell remains alive when d1 up to d2 of its eight neighbors are living, otherwise it dies and 2) a dead cell remains dead except when d3 up to d4 neighbors are living. This algorithm includes Conway's 2D Live that is characterized by the number 2333. The most interesting 3D Lives seem to be characterized by the numbers 5766 and 4555. In both one can find stable objects, gliders, and so on. Gliders look completely different in 3D Live 5766 and 3D Live 4555.

A 5766 glider does not survive in 3D Live 4555 and vice versa (see figures 1 and 2). Incidentally, a 5766 glider looks like a sandwich of two 2333 gliders.

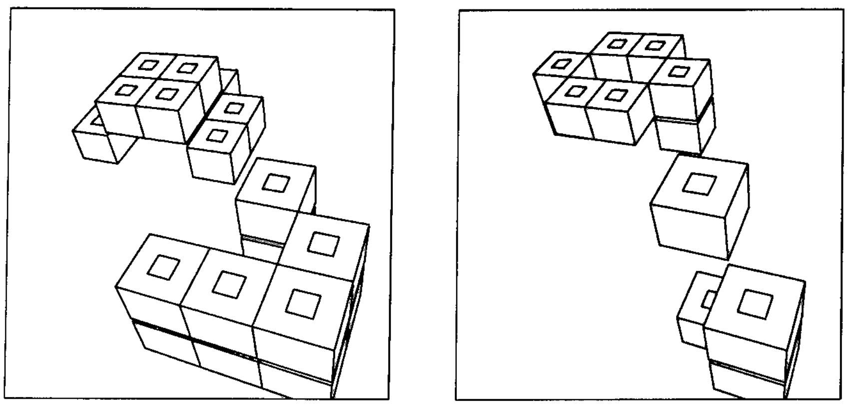

Figure 1 Left hand side: Initial placement of a 4555 glider in the background and a 5766 glider in the foreground. Right hand side: After one 3D Live 4555 iteration the 4555 glider is moved and the 5766 glider is partially destroyed (nothing of this glider will be left after the next iteration).

In all Live algorithms only a logical value in each grid point has to be represented. On a monochrome screen one can simply represent each cell of 2D Live by a pixel that is either black or white. In 3D Live the graphic representation is a bigger problem because one has to avoid that the information of a cell is hidden behind other cells. In the 3D MMP plot program, the so-called manager representation is most useful. This allows to represent living cells by cubes and to suppress dead cells. Usually, perspective projection is convenient. Needless to say that this kind of representation is much more time consuming than the 2D Live representation. Since time plays an important role in 2D and 3D Live, the user certainly prefers to watch movies. The 3D MMP plot programs allows to generate movies but unfortunately they cannot be shown in a report.

Unlike many CA algorithms FD and FDTD schemes are of interest in computational electromagnetics. Several 2D and 3D FD and FDTD schemes have been implemented in the 3D MMP plot program. The algorithms that have been used till now are very simple but a combination of the MMP code with schemes that are able to handle nonlinear materials is planned. A computation of a 2D capacitor with two rectangular electrodes (one of them surrounded by a rectangular dielectric) is shown in figure 3. The FD and FDTD algorithms allow a comparison with results obtained by the MMP kernel. A good agreement could be obtained although the boundary conditions that have been implemented are simple and lead to errors when the boundaries are not far away from the structure that is to be studied.

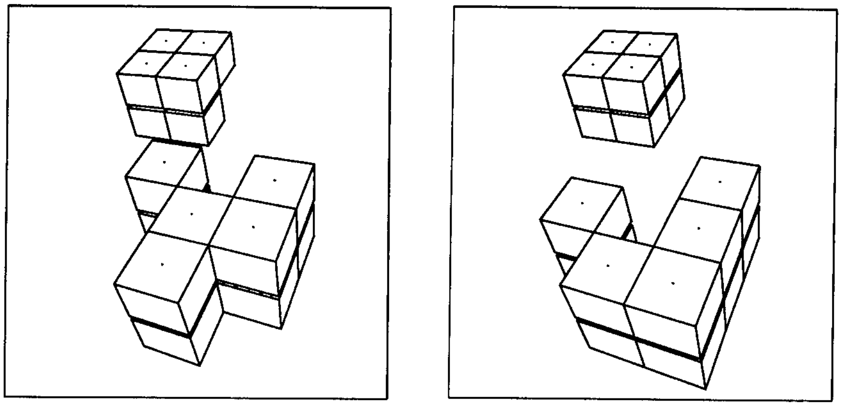

Figure 2 Left hand side: Situation after one 3D Live 5766 iteration applied to the initial placement (see figure 1). The 4555 glider is partially destroyed, the 5766 glider has moved. Right hand side: After another iteration, the 5766 glider is moved again and instead of the 4555 glider one has obtained a stable cube.

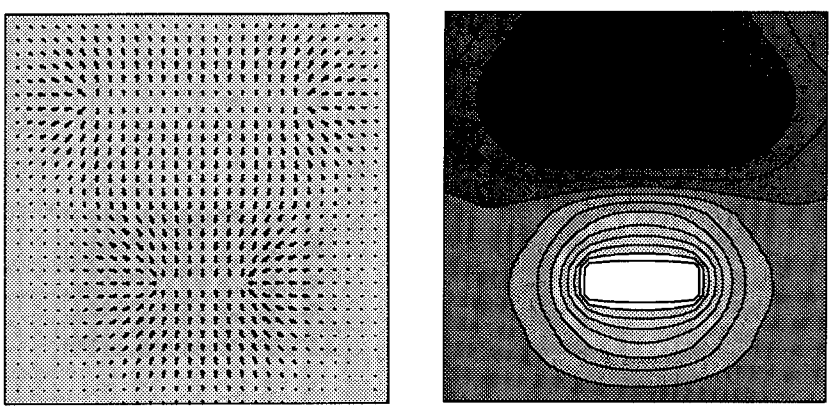

Figure 3 2D capacitor with two rectangular electrodes. The lower one is surrounded by a rectangular dielectric. Left hand side: electric field vectors. The dielectric is represented by a different fill pattern. Right hand side: Lines of constant potential. One can easily recognize that the boundary conditions used in this computation cause errors.

The following fractals have been implemented in the 3D MMP plot program to test the graphic capabilities: 1) the Mandelbrot set (figure 4), 2) the Julia set, 3) the Newton set (figure 4). All these fractals are defined in the complex plane that can easily be mapped onto the 2D real plane. In the Mandelbrot and Julia set each point belongs

to the set or it does not. This seems to be a trivial statement but it makes obvious that one can associate a boolean value to each point in the complex z plane. Thus, one imlicitely has a boolean field defined on the z plane. When one sets the value 0 for "false" and 1 for "true" one has already an integer field that can be depicted with the graphic plot program. Each value is obtained by an iterative process. On a computer the process has to be stopped after a finite number of iterations. When this number is too small, the result can be wrong in certain points. In the Mandelbrot and Julia algorithms the process is defined by $z := z^2 + c$ and the point obtains the value 0 when one knows that the process diverges, for example, when the absolute value of z exceeds 2. In the Julia set c is a complex parameter and z is initialized to the location of the point in the complex plane that is to be tested. The Mandelbrot set is obtained when one initially sets $z = c$ and considers c no longer as a parameter. I.e., somebody who is not an experienced programmer might obtain the Mandelbrot set when he tries to implement the Julia set.

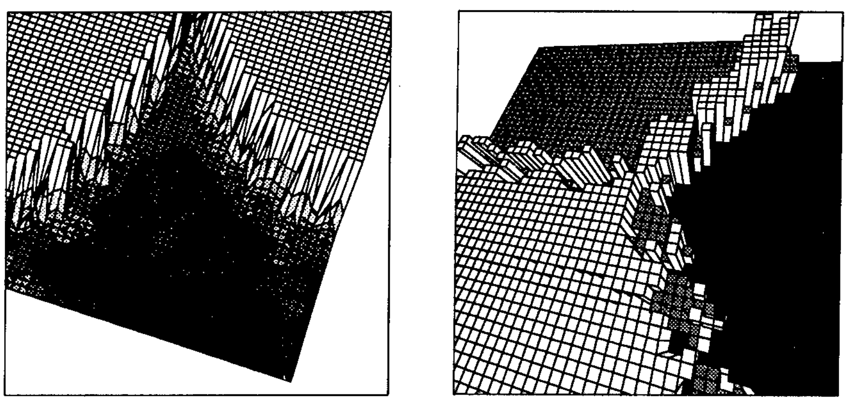

Figure 4 Left hand side: 3D representation with iso lines, grid lines and different fill patterns of a part of the Mandelbrot set. Right hand side: Manager representation of the Newton solution of the equation $z^3 - 1 = 0$ in the complex plane. The three solutions of this equation are represented by rectangular rods of different height with different fill patterns of the top side. One can recognize some wrong lines in this figure. These lines are due to the imperfect hiding procedure used in the plot program.

Since pictures of boolean fields look not very nice, one usually makes the pictures more beautiful by depicting the number of the iterations that have been required to detect whether a point does not belong to the set, i.e., whether the process diverges. The Newton fractal is obtained when the well-known Newton algorithm is used to iteratively search the solutions of the complex equation $z^n - 1 = 0$. Starting from a point z_0 in the complex plane, this algorithm converges to one of the n solutions of $z^n - 1 = 0$ after a sufficient number of iterations. When one represents each of the n solutions by an integer number from 1 to n, one has an integer field defined on the z_0 plane. For $n > 2$ one obtains fractals. In figure 4 the solution for $n = 3$ is shown. In

this case one has only three different values in each point which is not much more than a boolean field of the Mandelbrot set. Nonetheless, one can obtain nice pictures when either colors or 3D representations are used.

Codes written for depicting fractals [8] usually perform a sufficient number of iterations one point after another. As soon as the iteration is terminated, the value in the corresponding point is visualized and the iteration for the next point is started. Thus, no array is required for storing the field defined on the complex plane and the user can see how the picture is growing on the screen. Since the MMP code is not specialized for this purpose, each iteration is applied to the entire field at the same time. The drawing of the field is started when all requested iterations have been performed. Thus, the user does not see anything on the screen during the iteration. This procedure has an interesting advantage: It allows to generate movies that show how the fractal "grows" or "shrinks" when the number of iterations is increasing.

References

[1] Hafner, Ch., *The Generalized Multipole Technique for Computational Electromagnetics*, Norwood, MA: Artech House, 1990.

[2] Hafner, Ch., *2D-MMP; Two Dimensional Multiple Multipole Software and User's Manual*, Norwood, MA: Artech House, 1990.

[3] Hafner, Ch. and L. Bomholt, *The 3D MMP Codes for Personal Computers*, to be published, Demo version available from the authors.

[4] Leuchtmann, P. and L. Bomholt, "Thin wire feature for the MMP-code" *Conference Proc., 6th Annual Review of Progress in Applied Computational Electromagnetics (ACES)*, Monterey, March, 1990.

[5] Hafner, Ch., "On the Relationship between the MoM and the GMT" *IEEE AP-S Magazine*, Vol. 32, December, 1990.

[6] Hafner, Ch., "On the Implementation of FE and GTD concepts in the MMP Code" *Archiv für Elektronik und Übertragungstechnik*, Vol. 45, September, 1991.

[7] Rucker, R. and J. Walker, *CA Lab: Rudy Rucker's Cellular Automaton Laboratory*, Sausalito, CA: Autodesk, Inc., 1989.

[8] Gleick, J., *Chaos: The Software*, Sausalito, CA: Autodesk, Inc., 1991.

SESSION 3- "INVERSE SOLUTIONS"

Moderator: Andrew J. Terzuoli, Jr.

Target Discrimination Based On
High-Range-Resolution (HRR) Transient-Radar Returns
Computed From Triangular-Patch Aircraft Models

Lloyd S. Riggs
Electrical Engineering Department
200 Broun Hall
Auburn University, Alabama 36849

C. Ray Smith
Research, Development, and Engineering Center
AMSMI-RD-AS-RA
U.S. Army Missile Command
Redstone Arsenal, Alabama 35898-5253

Abstract

The task of discriminating among a set of N known targets based on their high-range-resolution (HRR) transient radar returns is viewed as a problem of information processing, calling for a full application of probability theory. In this paper an expression for the back-scattered field from a triangular-patch model of a perfectly conducting radar target (without apertures) is derived using the usual physical optics (PO) approximation for the currents induced on the target by the incident field. The frequency domain expression for the target's HRR radar return is inverse Fourier transformed to obtain the target's HRR transient radar return. Bayesian probability theory is used to discriminate among a four target library consisting of an SR-71, YB-49, B2 and a "flying wing". The performance of the Bayesian discrimination algorithm is discussed for the case when the HRR returns are contaminated with noise and when the "unknown" target signature is computed at an angle distinct from the angles for which the target library was constructed.

I. Calculating the High Range Resolution (HRR) Transient Radar Signature From a Triangular Patch Model of a Target

Figure 1 depicts an electromagnetic plane wave incident upon a perfectly conducting target with no apertures. The task at hand is to derive a reasonably accurate means of representing the field scattered by the target. It is usually assumed that the incident wave excites currents on the scatterer and that these currents give rise to the electromagnetic field reradiated (or scattered) by the target. An expression for the reradiated or target scattered field will be computed in the frequency domain and then inverse Fourier transformed to time domain so that the target's transient high-range resolution radar signature can be computed. Actually, it is the envelope of the target's time domain scattered field which is of interest here.

For the problem of interest here, that of determining the the HRR signature of an aircraft, high-frequency scattering methods (approximations) are valid since most HRR radar systems operate in

X-band (8.0 to 12.5 GHz) and typical military aircraft are on the order of 10 meters or so in length. In short, the targets of interest have major dimensions which are literally hundreds of wavelengths.

As a compromise between accuracy and ease of use, a high-frequency method known as physical optics (PO) was chosen to compute the HRR profiles for this study. For perfectly conducting bodies, it is probably the most widely used of all methods for estimating scattering, and it is particularly convenient for machine computation. According to Beckmann [1],

> "The term "physical optics" denotes an approximate method for the determination of the field scattered by an object through an assumption about the specific form of the field distribution on the surface. Explicitly, it is assumed that the field there is the geometrical optics surface field, implying that at each point on the geometrically illuminated side of the body the scattering at the surface takes place as though from an infinite tangent plane at the point, whereas over the shadowed portion of the body the surface field is zero. For a perfectly conducting body the postulated current distribution is therefore
>
> $$\mathbf{J} = \begin{cases} 2\hat{n} \times \mathbf{H}_{inc} & \text{on the illuminated side, } S_I \\ 0 & \text{on the shadowed side} \end{cases} \tag{1}$$
>
> where $\hat{n}$ is a unit vector normal drawn outwards as regards the body, . . . etc."

Equation (1) yields an expression for the current on the target in terms of the known incident field ($\mathbf{H}_{inc}$), and as usual, potential theory [2] can be employed to derive an expression for the vector component of the backscattered far-field in the direction of polarization of the incident field

$$\mathbf{E}_{scat} = jk\ 2\mathbf{E}_0 \frac{e^{-jkr}}{4\pi r} \left[\hat{n}_I \cdot \iint\limits_{\substack{\text{illuminated}\\ \text{surface of}\\ \text{scatterer}}} \hat{n} \exp(-jk\ 2\hat{n}_I \cdot \mathbf{r}')\, ds' \right] \hat{a}_E \tag{2}$$

Here, k is the wavenumber, $\mathbf{E}_0$ is the amplitude of the incident field, r is the distance from the radar to the target, $\hat{n}_I$ is a unit vector in the direction of propagation of the incident wave, $\mathbf{r}'$ is a vector from the coordinate origin to the source current, and $\hat{a}_E$ is a unit vector in the direction of the incident electric field.

Thus far, the task of calculating the back-scattered far-field from a perfectly conducting closed (i.e. no apertures) target has been reduced to computing the physical optics integral given in (2) above. As shown in Figure 1, it is possible to further simplify the problem by approximating the target of interest using triangular patches. Brand [3] has shown that it is possible to compute the integral in (2) exactly for

a planar triangular patch. Once the exact expression for the PO integral of a triangular patch is known, it is a simple matter to write an efficient computer algorithm to sum the contribution to the backscattered field from each triangular patch on the illuminated (or lit) portions of the target.

Equation (2) explicitly defines the back-scattered electric field from a triangular-patch model of a perfectly conducting target in the frequency domain. As previously mentioned, the quantity of interest here is the target's high-range resolution radar signature, which requires that (1) be inverse Fourier transformed to the time domain. More precisely, the envelope of the target's time-domain return is desired. The block diagram in Figure 2a follows directly from (1) and relates the target's "output" scattered field, the "input" incident waveform, and transfer function (e.g. $\mathbf{E}_{scat}(\omega) = \mathbf{E}_0(\omega)\ \mathbf{H}(\omega)$). According to Cohen et. al. [3], a typical HRR input waveform might consist of an X-band (8-12.5 GHz) carrier modulated by a 1 to 13 microsecond square wave with a 30 KHz pulse repetition frequency (Figure 2b). It will suffice for our purposes to compute the envelope of the target's return for an input waveform of the form

$$E_0 = f_1(t)\ \cos(\omega_0 t) \tag{3}$$

where $\omega_0 = 2\pi f_0$ is some X-band carrier frequency (say $f_0 = 10$ GHz) and

$$f_1(t) = \begin{cases} 1 & -a/2 \le t \le a/2 \\ 0 & \text{otherwise} \end{cases} \tag{4}$$

has a low frequency spectrum

$$f_1(\omega) = a\ \frac{\sin(\omega a/2)}{\omega a/2} \tag{5}$$

The target's transfer function $\mathbf{H}(\omega)$ is unsymmetrical [4] and can be written as a sum

$$\mathbf{H}(\omega) = \mathbf{H}_1(\omega) + \mathbf{H}_2(\omega) \tag{6}$$

where $\mathbf{H}_1(\omega)$ and $\mathbf{H}_2(\omega)$ are as shown in Figure 3a and ω_0 is the radar's carrier frequency. Next define

$$\begin{aligned} \mathbf{H}_{11}(\omega) &= \mathbf{H}_1(\omega + \omega_0) \\ \mathbf{H}_{12}(\omega) &= \mathbf{H}_2(\omega - \omega_0) \end{aligned} \tag{7}$$

which are obtained by shifting $\mathbf{H}_1(\omega)$ and $\mathbf{H}_2(\omega)$ to the left and right respectively, by ω_0 (see Figure 3b). Now, as shown in Figure 3c, define in-phase and quadrature system functions

$$\begin{aligned} \mathbf{H}_p(\omega) &= \frac{\mathbf{H}_{11}(\omega) + \mathbf{H}_{12}(\omega)}{2} \\ \mathbf{H}_q(\omega) &= \frac{\mathbf{H}_{12}(\omega) - \mathbf{H}_{11}(\omega)}{2j} \end{aligned} \tag{8}$$

Denote the response of the filters $\mathbf{H}_p(\omega)$ and $\mathbf{H}_q(\omega)$ to the envelope $f_1(t)$ of $E_0(t)$ by $q_p(t)$ and $q_q(t)$ respectively (see Figure 4a). Finally, as shown in Figure 4b, the response $E_{scat}(t)$ of the target (unsymmetrical filter) to a modulated input, $E_0(t)\ \cos(\omega_0 t)$, is given by

$$E_{scat}(t) = q_p(t)\cos(\omega_0 t) + q_q(t)\sin(\omega_0 t)$$

or

$$E_{scat}(t) = \sqrt{q_p^2(t) + q_q^2(t)}\ \cos\left\{\omega_0 t - \tan^{-1}\frac{q_q(t)}{q_p(t)}\right\} \tag{9}$$

where $\sqrt{q_p(t) + q_q(t)}$ is the desired <u>envelope</u> of the target's HRR return!

II. Bayesian Probability Theory Applied to the Problem of Target Discrimination Based on HRR Radar Returns

In this chapter the problem of identifying a target based on its (HRR) return is discussed. The reader should refer to a paper by Bretthorst et. al. [5] for a rigorous derivation of the final expression for the posterior probability of the object as only a brief explanation of each term in this expression, as it applies to the problem at hand, will be presented here.

Figures 5a-5d show triangular patch models of four aircraft, denoted as the wing, YB-49, B2 and SR-71 respectively. Note that although the models contain some quadrilateral patches, the computer program used to compute the HRR returns subdivides each quadrilateral patch into two triangular patches. Figure 6a-6d present typical HRR returns for the targets of Figure 5. HRR returns for each target were computed for the incident wave in the plane of the target ($\theta = 90^0$) for azimuthal angles of $\phi = 0^0, 2^0, \ldots, 30^0$. In every case the excitation waveforms consist of a 5.0 nanosecond duration 10 GHz carrier (see equation (4)). Furthermore, parameters were chosen in the fast Fourier transform algorithm [6] in such a way as to provide 2,048 time samples with a sampling increment Δt of $375 \times 10^{-9}/2047 = 183.19492 \times 10^{-9}$ seconds for a total HRR return duration (window) of 375×10^{-9} seconds. These transform parameters insured a response of sufficient duration (375×10^{-9} seconds) so that the entire return from the target with greatest length was completely captured in the observation window.

The problem of interest here may be stated as follows: given a set of S objects (here, 4 triangular-patch aircraft models: the wing, YB-49, B2 and SR-71) and a set of data D (similar to the data shown in Figure 6) sampled at discrete times t_i such that $D = (d_1, d_2, \ldots, d_n)$ (as described in the proceeding paragraph), which object f_j ($j = 1,2,3,4$) is most probable in view of the data and all one's prior information. The posterior probability distribution will be designated as $P(f_j|D,I)$, where f_j is the object to be identified, D is all of the data, and I represents a set of assumptions that must be made to solve the problem (The notation $P(f_j|D,I)$ is read: the probability that f_j is the true target given the data D and any prior information I. That is, "$|D,I)$" means conditional on the truth of the data D and prior information).

In this problem the HRR return is postulated to consist of the return from an object plus noise (As discussed later, Gaussian noise was added to the return to test the robustness of the discrimination algorithm). The basic model is: a discrete data set $D = \{d_1, \ldots, d_n\}$

has been recorded; it is sampled from y(t) at discrete times $\{t_1, \ldots, t_n\}$; with modal equation,

$$d_i = y(t_i) + e_i \quad (1 \le i \le N) \tag{10}$$

where e_i represents the numerical value of the noise at time t_i, and $f_j(t)$ represents the numerical value of the true radar return. The HRR return from each object may be written

$$f_j(t_i) = B\, G_j\, (\theta = 90^0,\ \phi,\ t_i - t) \tag{11}$$

where B is an amplitude, t is the position of the object in the data, $t_i - t$ is the relative position of the return in the observation window, and ϕ is the backscattered direction (see Figures 5a through 5d). In the calculation of the posterior probability of the object $(P(f_j|D,I))$, it will be assumed that $G_j \; (\theta = 90^0,\ \phi,\ t_i)$ has been determined by imaging a number of object at a finite number of angles (for this problem, $\phi = 0^0, 2^0, 4^0, \ldots, 30^0$). Thus the angular variable ϕ will be restricted to α discrete angles. Additionally, it will be assumed that the noise associated with the determination of $G_j\ (\theta = 90^0,\ \phi,\ t_i)$ is much less than that in the data, and so this noise will be ignored.

Employing Bayes' theorem and the rules of probability theory (the so-called product rule and the sum rule), the desired posterior probability of the object becomes

$$P(f_j/D,I) = \frac{P(D|f_j,I)}{\sum_{k=1}^{s} P(D|f_k,I)} \tag{12}$$

Further application of the rules of probability theory allows one to obtain the following expression which is proportional to the global-likelihood of the data (i.e. $f(D|f_j,I)$

$$P(D|f_j,I) \propto \sum_{k=1}^{\alpha} \sum_{l=1}^{N} \left[\frac{(G_j \cdot d)^2}{G_j \cdot G_j} \right]^{-\frac{1}{2}} \cdot \exp\left(- \frac{(t' - t_l)^2}{2\delta^2} + \frac{(G_j \cdot d)^2}{2\sigma^2\ (G_j \cdot G_j)} \right) \tag{13}$$

It should be noted that the G_j functions depend on both the orientation angle ϕ and the relative position of the HRR return in the observation window t_l.

In the development of (13) it was assumed that the HRR returns from the objects are located in the observation window at a position t′ and that the position is known to some error δ,

$$t = t' \mp \delta$$

at one standard deviation. In effect, this is saying that it is not necessary to look over the entire data set to locate the HRR return. Furthermore, the noise e_i (see (10)) will be assumed to be white

Gaussian noise with expected square σ^2; therefore the probability of a given noise function (e) becomes

$$P(e|\sigma) = (2\pi\sigma^2)^{-N/2} \exp\left\{ -\sum_{j=1}^{N} \frac{e_j^2}{2\sigma^2} \right\} \tag{14}$$

Equation (13) when used in (12) reflects the assumptions made and represents an optimal answer to the question: Given a set of S objects, what is the probability of the jth target (f_j) given the data, the variance of the noise and the approximate location of the HRR return in the data? There are three important factors in (12) and (13). The first factor (i) is the relative position of the HRR return in the observation window. The factor effectively allows us to program the computer in such a way that one looks over only a restricted portion of the data. This will save time and effort in the identification process, and is effectively exactly what our intuition would have told us to do. After all, if we know the HRR return begins near the one-hundredth data value, it makes little sense to start looking at the back of the data. The exponential factor $\exp\{-(t' - t_l)^2/2\delta^2\}$ is just probability theories way of quantifying the conclusion our intuition draws naturally. The second term (ii) represents how well the data fits the model and is essentially the likelihood of the data. In order for a particular model to be preferred, the normalized projection to the data onto the model must be large. The third term (iii) is essentially the prior probability of the amplitude, and expresses the assumption that the signal should have finite total power. Each model is effectively penalized by a factor which is the inverse of the expected amplitude: the bigger the expected total power the less probable the model becomes!

The functional form of equation (13) is so simple as to be deceptive. Indeed one's intuition might have led one to the likelihood of the data (the third term in (13)). Additionally one's intuition might have led one to modify this by the probability of the target being at location t' (the second term in (13)). But it is unlikely that any ones intuition would have been led to the prior probability of the magnitude factor (the first term in (13)), nor is it likely that one's intuition would have told one to sum over all possible angles of incidence and location. But despite the simplicity of these equations, the numerical simulations presented in the next chapter indicate that target identification should be possible.

III. Numerical Results

The probability that an unknown target return is from each of the targets in the library has been calculated and compiled in tables 1-3 for various library data bases, unknown returns, and signal-to-noise ratios. In all of the cases considered below, the library data base consisted of representations of the field scattered from all four aircraft models over an azimuthal scan from zero to thirty degrees. Furthermore, the threshold used to determine the effective length of each library file was chosen to be 0.01% of the maximum entry in that file. The signal-to-noise ratio given in each table refers to that of the unknown target return, while no noise has been added to the library returns.

In generating Tables 1a and 1b, the library consisted of fields scattered from the four aircraft models with the entries calculated at azimuthal increments of ten degrees (0°, 10°, 20°, and 30°). The unknown returns were chosen as the fields scattered from the same models used to generate the library data base, but at angular locations of five, fifteen, and twenty-five degrees (5°, 15°, and 25°).

In generating Tables 1a and 1b, the signal-to-noise ratio for the unknown target return was chosen as 10.0 dB and 1.0 dB respectively. If it is assumed that a target is correctly identified when its calculated probability is greater than 0.99, then from these tables the identification rates can be determined as

$$\text{Correct ID Rate} = (7/12) * 100\ \% = 58.3\ \%$$

$$\text{False ID Rate} = (4/12) * 100\ \% = 33.3\ \%$$

$$\text{Indeterminate ID Rate} = (1/12) * 100\ \% = 8.3\ \%$$

seemingly independent of the signal-to-noise ratio. (As will be shown later, the identification rates are not independent of signal-to-noise ratio, and, in fact, as the signal-to-noise ratio increases, so does the rate at which an unknown target can be correctly identified, just as one would expect.)

As a further investigation of this technique, the probabilities for each target were once again calculated, but in this instance, the library data base consisted of 16 azimuthal angular bins per target model (0°, 2°, ..., 30°) while the unknown target returns were calculated as the responses of the target models in between the angular bins used in the library base (1°, 3°, ..., 29°). The results of this investigation are shown in Tables 2a-2d and 3a-3d when the signal-to-noise ratio of each unknown return was 10.0 dB and 1.0 dB, respectively.

From Tables 2a-2d the identification rates for the complete set of data are calculated to be

$$\text{Correct ID Rate} = (44/60) * 100\ \% = 73.3\ \%$$

$$\text{False ID Rate} = (11/60) * 100\ \% = 18.3\ \%$$

$$\text{Indeterminate ID Rate} = (5/60) * 100\ \% = 8.3\ \%$$

Notice however that the identification rate is model dependent, perhaps suggesting that the ability to correctly identify a target model depends on how different it is from the other models in the library. Decreasing the signal-to-noise ratio down to 1.0 dB yields the results shown in Tables 3a-3d and the identification rates shown below.

$$\text{Correct ID Rate} = (32/60) * 100\ \% = 53.3\ \%$$

$$\text{False ID Rate} = (21/60) * 100\ \% = 35.0\ \%$$

$$\text{Indeterminate ID Rate} = (7/60) * 100\ \% = 11.7\ \%$$

Observe that as the signal-to-noise ratio decreases so does the correct

identification rate.

In the last example to be considered, the library data base again consists of the 4 target models with 16 angular entries per target model (0°, 2°, ..., 30°). Unlike the previous examples, in this case the unknown return is the same as one of the library files except for the addition of noise in the unknown return. A curve expressing the correct identification rate versus signal-to-noise ratio has been constructed and is shown in Figure 7, where the unknown target is assumed correctly identified when its calculated probability is at least 0.99. The "knee" of the resulting curve appears to occur at a signal-to-noise ratio of approximately 1.0 (0.0 dB) with the ID rate falling rapidly for smaller values and slowly approaching 100 % for larger values.

IV. References

[1]. P. Beckman, *The Depolarization of Electromagnetic Waves.*

[2]. R.F. Harrington, *Field Computation by Moment Methods,* Krieger, 1968.

[3]. M.N. Cohen, et. al., "Vulnerability Assessment of Multiple Frequency High Range Resolution Radars", Final Tech. Report, GTRI Project A-8656, Prepared for U.S. Army, MICOM, Redstone Arsenal.

[4]. A. Papoulis, *The Fourier Integral and its Applications,* McGraw-Hill, 1962.

[5]. G.L. Bretthorst, et. al., "Radar Target Discrimination Using Probability Theory," First Annual Symposium on Ultra-Wideband Radar, CRC Publishing Company, 1991.

[6]. W.H. Press, et. al., *Numerical Recipes (Fortran Version),* Press Syndicate, University of Cambridge, 1990.

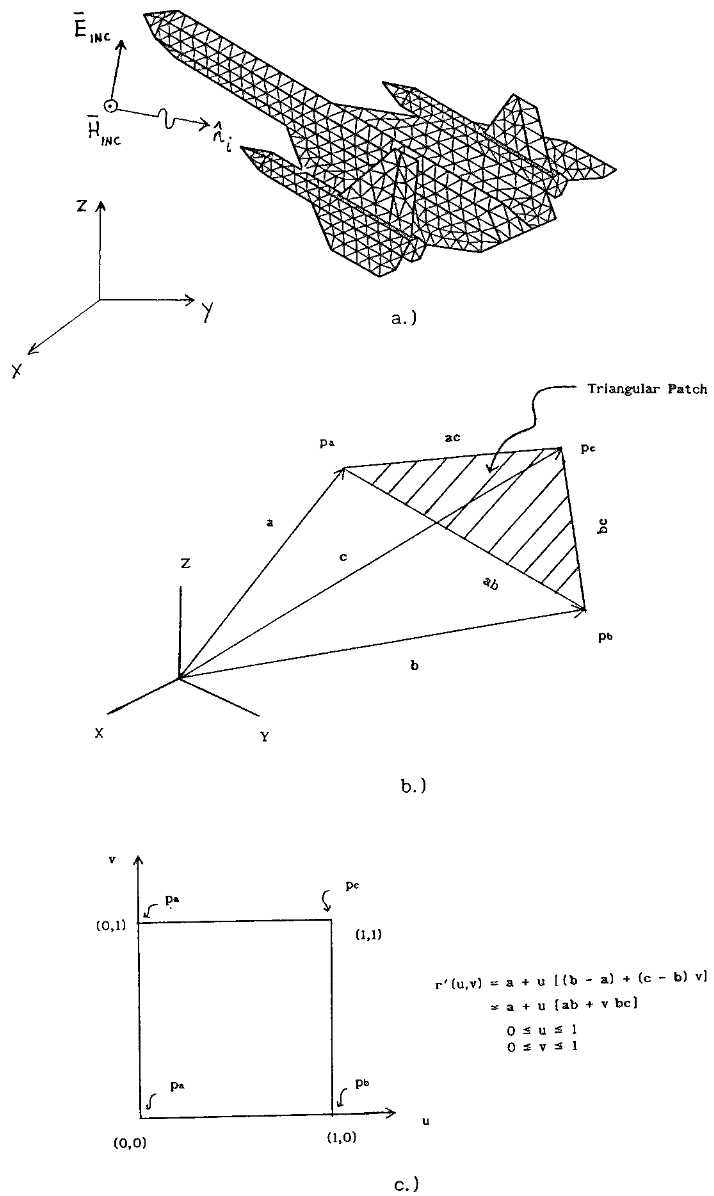

Figure 1 a.) Arbitrary Surface Modeled by Triangular Patches. b.) General Triangular Patch with Vertices at p_a, p_b, and p_c. c.) A Two-Parameter Representation for the Source Vector $\mathbf{r}'$ Over the Triangular Patch.

$$E_o(\omega) \longrightarrow \boxed{H(\omega)} \longrightarrow E_{scat}(\omega)$$

$E_{scat}(\omega) = E_o(\omega)\ H(\omega)$

$E_{scat}(\omega)$ = Target's "Output" Scattered Field

$E_o(\omega)$ = "Input" Incident Waveform

$H(\omega)$ = Target "Transfer" Function

$$H(\omega) = 2jk\ \frac{\exp(-jkr)}{4\pi r} \left[\hat{n}_i \cdot \iint_{\substack{\text{illuminated} \\ \text{surface of} \\ \text{scatterer}}} \hat{n}\ \exp(-jk\ 2\hat{n}_i \cdot r')\ ds' \right]$$

a.)

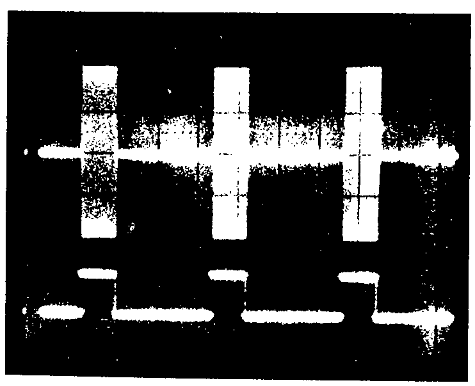

b.)

Figure 2 a.) Block Diagram Which Relates the Target's "Output" Scattered Field ($E_{scat}(\omega)$), "Input" Incident Waveform ($E_o(\omega)$), and Target Transfer Function ($H(\omega)$). b.) Typical High Range Resolution Waveform ($E_o(\omega)$) Consisting of an X-Band (8.0 - 12.5 GHz) Carrier Modulated by a 1 to 13 Micosecond Square Wave Which has a 30 KHz Pulse Repetition Frequency.

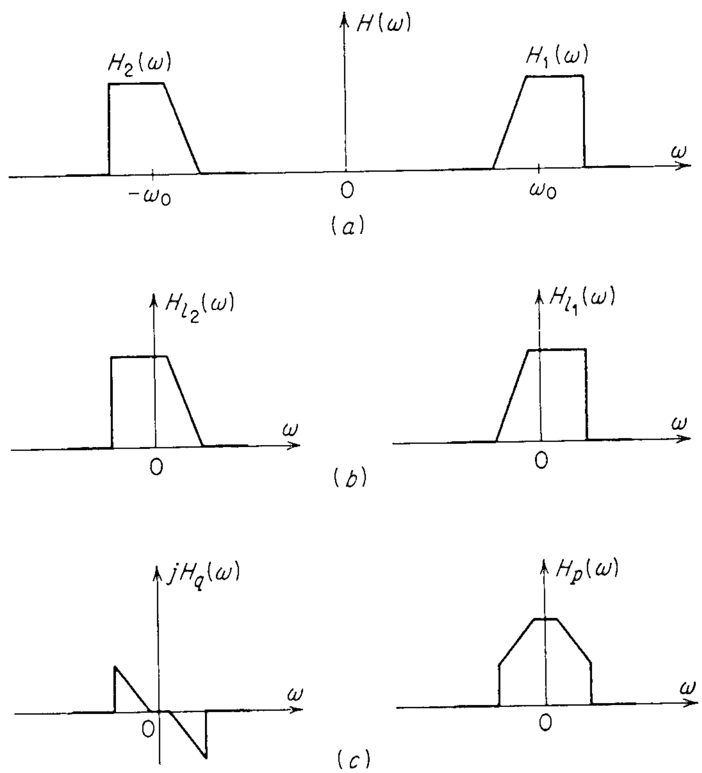

Figure 3 The Target Transfer Function Written as a Sum of Two Other Transfer Functions $H(\omega) = H_1(\omega) + H_2(\omega)$ b.) Transfer Function $H_{l1}(\omega)$ and $H_{l2}(\omega)$ Obtained by Shifting $H_1(\omega)$ and $H_2(\omega)$ to the left and right Respectively, by ω_0. c.) In Phase Quadrature System Function $H_p(\omega) = 0.5\ (H_{l1}(\omega) + H_{l2}(\omega))$, $H_q(\omega) = -0.5j\ (H_{l2}(\omega) - H_{l1}(\omega))$.

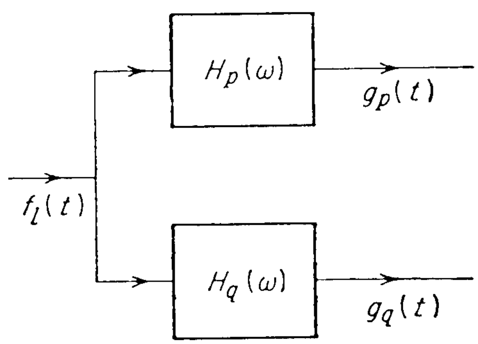

a.)

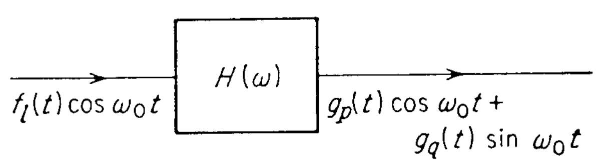

b.)

Figure 4 a.) Block Diagram Showing the Response of the Filters $\mathbf{H_p}(\omega)$ and $\mathbf{H_q}(\omega)$ to the Envelope $f_l(t)$ of $E_0(t)$. b.) The Response (the Scattered Field From the Target, $E_{scat}(t)$) of the Target (Unsymmetrical Filter) to a Modulated Input, $E_0(t) = f_l(t) \cos(\omega_0 t)$. The desired envelope of the Target's HRR Return is Given by $\sqrt{q_p^2(t) + q_q^2(t)}$.

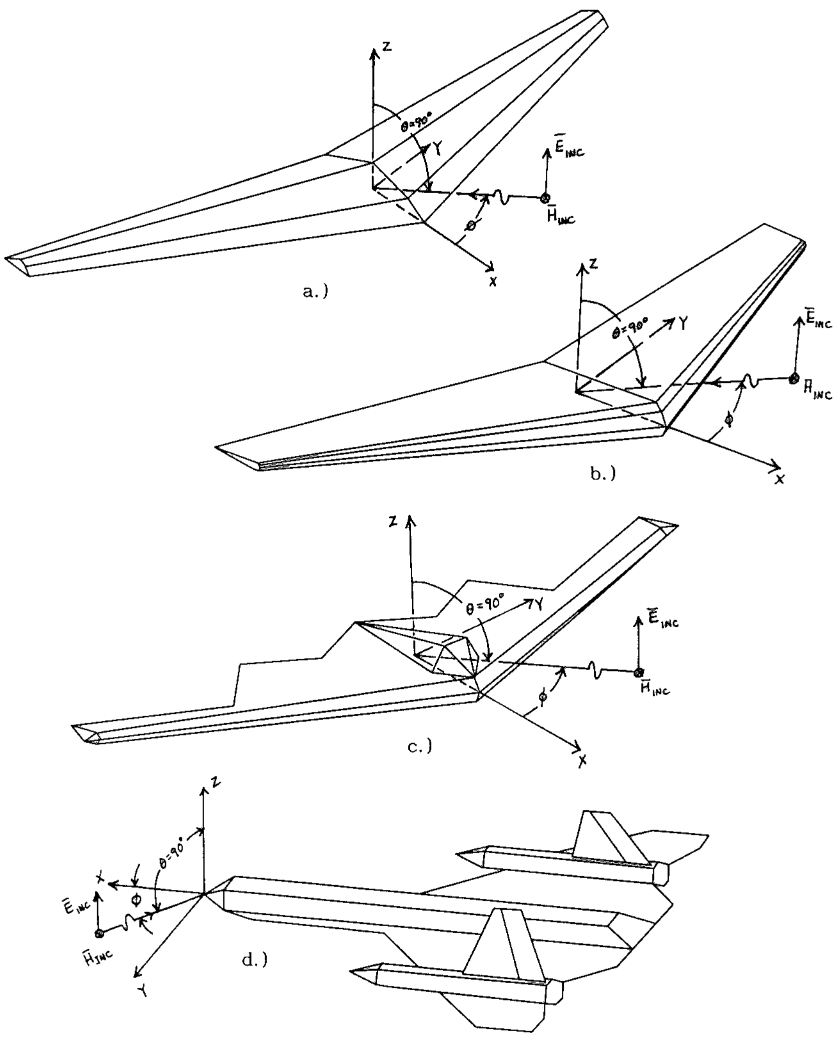

Figure 5. Triangular Patch Model of a.) Wing, b.) YB-49, c.) B2, and d.) SR-71 Aircraft HRR Return Were Computed for the Incident Wave in the Plane of the Wing ($\theta = 90^0$) for $\phi = 0^0$, (nose on), $\phi = 2^0$, . ., $\phi = 30^0$.

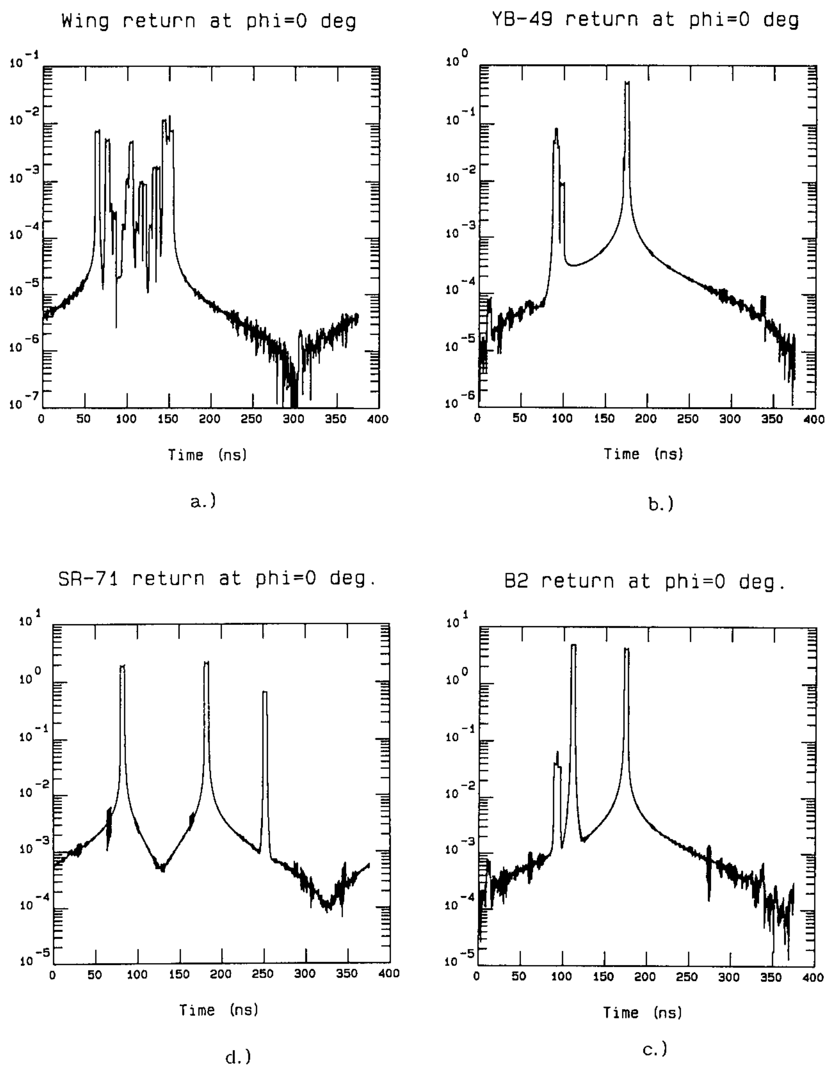

Figure 6. HRR Return From a.) Wing, b.) YB-49 c.) B2, and d.) SR-71 Aircraft at $\theta = \phi = 0^0$ (nose on). The Excitation Waveform is a 5.0 Nanosecond Duration Pulse with a 10 GHz Carrier (see Equation 8 in Text).

Table 1a. Illustration of probabilities when the target library consists of 4 targets with 4 angle entries per target (0°, 10°, 20°, and 30°), and the unknown target return has a signal-to-noise ratio of 10.0 dB (S/N = 10.0).

Unknown Target	P(SR-71)	P(B2)	P(YB-49)	P(Wing)
SR-71 @ 5°	1.000	0.000	0.000	0.000
SR-71 @ 15°	1.000	0.000	0.000	0.000
SR-71 @ 25°	1.000	0.000	0.000	0.000
B2 @ 5°	0.000	1.000	0.000	0.000
B2 @ 15°	0.000	1.000	0.000	0.000
B2 @ 25°	0.000	0.000	0.000	1.000
YB-49 @ 5°	1.000	0.000	0.000	0.000
YB-49 @ 15°	0.046	0.552	0.399	0.004
YB-49 @ 25°	0.000	0.000	0.000	1.000
Wing @ 5°	0.000	0.000	0.000	1.000
Wing @ 15°	0.000	1.000	0.000	0.000
Wing @ 25°	0.000	0.000	0.000	1.000

Table 1b. Illustration of probabilities when the target library consists of 4 targets with 4 angle entries per target (0°, 10°, 20°, and 30°), and the unknown target return has a signal-to-noise ratio of 1.0 dB (S/N = 1.259)

Unknown Target	P(SR-71)	P(B2)	P(YB-49)	P(Wing)
SR-71 @ 5°	1.000	0.000	0.000	0.000
SR-71 @ 15°	1.000	0.000	0.000	0.000
SR-71 @ 25°	1.000	0.000	0.000	0.000
B2 @ 5°	0.000	1.000	0.000	0.000
B2 @ 15°	0.000	1.000	0.000	0.000
B2 @ 25°	0.000	0.000	0.000	1.000
YB-49 @ 5°	1.000	0.000	0.000	0.000
YB-49 @ 15°	0.026	0.460	0.513	0.001
YB-49 @ 25°	0.000	0.000	0.000	1.000
Wing @ 5°	0.000	0.000	0.000	1.000
Wing @ 15°	0.000	1.000	0.000	0.000
Wing @ 25°	0.000	0.000	0.000	1.000

Table 2a. Illustration of probabilities when the target library consists of 4 targets with 16 angle entries per target (0°, 2°, 4°, ..., 30°), and the unknown target return has a signal-to-noise ratio of 10.0 dB (S/N = 10.0).

Unknown Target	P(SR-71)	P(B2)	P(YB-49)	P(Wing)
SR-71 @ 1°	0.000	0.000	0.000	1.000
SR-71 @ 3°	1.000	0.000	0.000	0.000
SR-71 @ 5°	1.000	0.000	0.000	0.000
SR-71 @ 7°	1.000	0.000	0.000	0.000
SR-71 @ 9°	1.000	0.000	0.000	0.000
SR-71 @ 11°	1.000	0.000	0.000	0.000
SR-71 @ 13°	1.000	0.000	0.000	0.000
SR-71 @ 15°	1.000	0.000	0.000	0.000
SR-71 @ 17°	1.000	0.000	0.000	0.000
SR-71 @ 19°	1.000	0.000	0.000	0.000
SR-71 @ 21°	1.000	0.000	0.000	0.000
SR-71 @ 23°	1.000	0.000	0.000	0.000
SR-71 @ 25°	1.000	0.000	0.000	0.000
SR-71 @ 27°	1.000	0.000	0.000	0.000
SR-71 @ 29°	1.000	0.000	0.000	0.000

Table 2b. Illustration of probabilities when the target library consists of 4 targets with 16 angle entries per target (0°, 2°, 4°, ..., 30°), and the unknown target return has a signal-to-noise ratio of 10.0 dB (S/N = 10.0).

Unknown Target	P(SR-71)	P(B2)	P(YB-49)	P(Wing)
B2 @ 1°	0.000	0.000	0.000	1.000
B2 @ 3°	0.000	0.000	1.000	0.000
B2 @ 5°	0.000	0.000	1.000	0.000
B2 @ 7°	0.000	1.000	0.000	0.000
B2 @ 9°	0.000	1.000	0.000	0.000
B2 @ 11°	0.000	1.000	0.000	0.000
B2 @ 13°	0.000	1.000	0.000	0.000
B2 @ 15°	0.000	1.000	0.000	0.000
B2 @ 17°	0.000	1.000	0.000	0.000
B2 @ 19°	0.000	1.000	0.000	0.000
B2 @ 21°	0.000	1.000	0.000	0.000
B2 @ 23°	0.000	1.000	0.000	0.000
B2 @ 25°	0.000	1.000	0.000	0.000
B2 @ 27°	0.000	0.000	0.000	1.000
B2 @ 29°	0.372	0.089	0.037	0.502

Table 2c. Illustration of probabilities when the target library consists of 4 targets with 16 angle entries per target (0°, 2°, 4°, ..., 30°), and the unknown target return has a signal-to-noise ratio of 10.0 dB (S/N = 10.0).

Unknown Target	P(SR-71)	P(B2)	P(YB-49)	P(Wing)
YB-49 @ 1°	0.000	0.000	0.000	1.000
YB-49 @ 3°	0.000	0.000	1.000	0.000
YB-49 @ 5°	0.000	0.000	1.000	0.000
YB-49 @ 7°	0.000	0.000	1.000	0.000
YB-49 @ 9°	0.000	0.000	1.000	0.000
YB-49 @ 11°	0.000	0.000	1.000	0.000
YB-49 @ 13°	0.000	0.000	1.000	0.000
YB-49 @ 15°	0.000	0.000	0.000	1.000
YB-49 @ 17°	0.000	0.000	1.000	0.000
YB-49 @ 19°	0.000	0.000	1.000	0.000
YB-49 @ 21°	0.000	1.000	0.000	0.000
YB-49 @ 23°	0.000	0.000	1.000	0.000
YB-49 @ 25°	0.000	0.000	0.000	1.000
YB-49 @ 27°	0.000	0.000	0.000	1.000
YB-49 @ 29°	0.000	0.000	0.000	1.000

Table 2d. Illustration of probabilities when the target library consists of 4 targets with 16 angle entries per target (0°, 2°, 4°, ..., 30°), and the unknown target return has a signal-to-noise ratio of 10.0 dB (S/N = 10.0).

Unknown Target	P(SR-71)	P(B2)	P(YB-49)	P(Wing)
Wing @ 1°	0.000	0.000	0.000	1.000
Wing @ 3°	0.000	0.000	0.000	1.000
Wing @ 5°	0.000	0.000	0.000	1.000
Wing @ 7°	0.000	0.000	0.000	1.000
Wing @ 9°	0.000	0.000	0.000	1.000
Wing @ 11°	0.000	0.000	0.000	1.000
Wing @ 13°	0.000	0.000	0.000	1.000
Wing @ 15°	0.000	0.000	0.000	1.000
Wing @ 17°	0.000	0.000	0.000	1.000
Wing @ 19°	0.000	0.000	0.000	1.000
Wing @ 21°	0.000	0.000	0.000	1.000
Wing @ 23°	0.658	0.055	0.039	0.248
Wing @ 25°	0.188	0.071	0.075	0.666
Wing @ 27°	0.012	0.043	0.730	0.216
Wing @ 29°	0.256	0.148	0.045	0.551

Table 3a. Illustration of probabilities when the target library consists of 4 targets with 16 angle entries per target (0°, 2°, 4°, ..., 30°), and the unknown target return has a signal-to-noise ratio of 1.0 dB (S/N = 1.259).

Unknown Target	P(SR-71)	P(B2)	P(YB-49)	P(Wing)
SR-71 @ 1°	0.000	0.000	0.000	1.000
SR-71 @ 3°	0.000	0.000	0.000	1.000
SR-71 @ 5°	1.000	0.000	0.000	0.000
SR-71 @ 7°	1.000	0.000	0.000	0.000
SR-71 @ 9°	1.000	0.000	0.000	0.000
SR-71 @ 11°	1.000	0.000	0.000	0.000
SR-71 @ 13°	1.000	0.000	0.000	0.000
SR-71 @ 15°	1.000	0.000	0.000	0.000
SR-71 @ 17°	1.000	0.000	0.000	0.000
SR-71 @ 19°	1.000	0.000	0.000	0.000
SR-71 @ 21°	0.000	0.000	1.000	0.000
SR-71 @ 23°	0.000	0.000	1.000	0.000
SR-71 @ 25°	0.000	0.000	1.000	0.000
SR-71 @ 27°	0.000	0.000	1.000	0.000
SR-71 @ 29°	1.000	0.000	0.000	0.000

Table 3b. Illustration of probabilities when the target library consists of 4 targets with 16 angle entries per target (0°, 2°, 4°, ..., 30°), and the unknown target return has a signal-to-noise ratio of 1.0 dB (S/N = 1.259).

Unknown Target	P(SR-71)	P(B2)	P(YB-49)	P(Wing)
B2 @ 1°	0.000	0.000	0.000	1.000
B2 @ 3°	0.000	0.000	1.000	0.000
B2 @ 5°	0.000	0.000	1.000	0.000
B2 @ 7°	0.000	1.000	0.000	0.000
B2 @ 9°	0.000	1.000	0.000	0.000
B2 @ 11°	0.000	1.000	0.000	0.000
B2 @ 13°	0.000	0.000	0.000	1.000
B2 @ 15°	0.000	1.000	0.000	0.000
B2 @ 17°	0.000	1.000	0.000	0.000
B2 @ 19°	0.000	1.000	0.000	0.000
B2 @ 21°	0.000	1.000	0.000	0.000
B2 @ 23°	0.000	0.000	0.000	1.000
B2 @ 25°	0.000	1.000	0.000	0.000
B2 @ 27°	0.000	0.000	0.000	1.000
B2 @ 29°	0.331	0.114	0.048	0.508

Table 3c. Illustration of probabilities when the target library consists of 4 targets with 16 angle entries per target (0°, 2°, 4°, ..., 30°), and the unknown target return has a signal-to-noise ratio of 1.0 dB (S/N = 1.259).

Unknown Target	P(SR-71)	P(B2)	P(YB-49)	P(Wing)
YB-49 @ 1°	0.000	0.000	0.000	1.000
YB-49 @ 3°	0.000	0.000	0.000	1.000
YB-49 @ 5°	0.000	0.000	1.000	0.000
YB-49 @ 7°	0.000	0.000	1.000	0.000
YB-49 @ 9°	0.000	0.000	0.000	1.000
YB-49 @ 11°	0.000	0.000	1.000	0.000
YB-49 @ 13°	0.000	0.000	1.000	0.000
YB-49 @ 15°	0.008	0.814	0.171	0.007
YB-49 @ 17°	0.000	0.000	0.000	1.000
YB-49 @ 19°	0.000	0.000	0.000	1.000
YB-49 @ 21°	0.000	1.000	0.000	0.000
YB-49 @ 23°	0.000	0.000	0.000	1.000
YB-49 @ 25°	0.000	0.000	0.000	1.000
YB-49 @ 27°	0.000	0.000	0.000	1.000
YB-49 @ 29°	0.630	0.235	0.060	0.075

Table 3d. Illustration of probabilities when the target library consists of 4 targets with 16 angle entries per target (0°, 2°, 4°, ..., 30°), and the unknown target return has a signal-to-noise ratio of 1.0 dB (S/N = 1.259).

Unknown Target	P(SR-71)	P(B2)	P(YB-49)	P(Wing)
Wing @ 1°	0.000	0.000	0.000	1.000
Wing @ 3°	0.000	0.000	0.000	1.000
Wing @ 5°	0.000	0.000	0.000	1.000
Wing @ 7°	0.000	0.000	0.000	1.000
Wing @ 9°	0.000	0.000	0.000	1.000
Wing @ 11°	0.000	0.000	0.000	1.000
Wing @ 13°	0.000	0.000	0.000	1.000
Wing @ 15°	0.000	0.000	0.000	1.000
Wing @ 17°	0.000	0.000	0.000	1.000
Wing @ 19°	0.000	0.000	0.000	1.000
Wing @ 21°	0.000	0.000	0.000	1.000
Wing @ 23°	0.665	0.076	0.034	0.225
Wing @ 25°	0.484	0.089	0.032	0.395
Wing @ 27°	0.298	0.090	0.035	0.577
Wing @ 29°	0.281	0.169	0.046	0.504

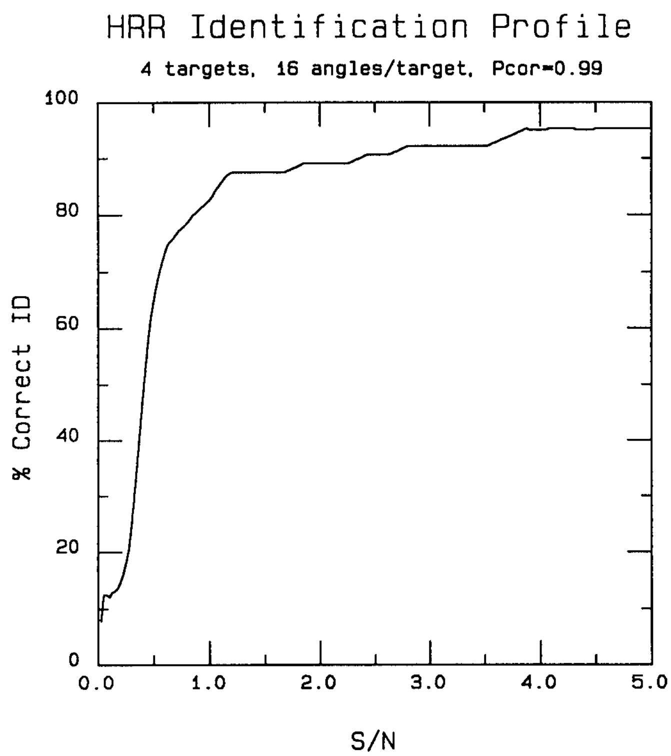

Figure 7 Correct ID Rate vs. Signal-to-Noise Ratio. The Library Data Base (the Model) Consists of the 4 Targets With 16 Angular Entries per Target Model ($\theta = 0^0, 2^0, \ldots, 30^0$) (See Figures 8-11 for Definitions of Target Geometry). The Unknown Return is the Same as One of the Library Files Except for the Addition of Noise. The Ordinate is Computed by Counting the Numbers of Times the 64 Possible Returns Were Associated With the Correct Target With a Probability Greater Then or Equal to 0.99. Ordinate Values Were Computed for Signal-to-Noise Ratios From 0.025 to 5.0 in Steps of 0.025.

Scattered/Internal Intensity for Dielectric Objects With Gaussian Beam Illumination

E. Esam M. Khaled, Steven C. Hill* and Peter W. Barber

Department of Electrical and Computer Engineering,

Clarkson University, Potsdam, NY 13699-5720.

* U.S. Army Atmospheric Sciences Laboratory, White Sands Missile Range, NM 88002.

Abstract

The scattered and internal intensity are calculated for a spherical object illuminated with an arbitrary laser beam. A simple expression for expanding any physically realizable laser beam, including those which may not have a mathematical representation, into vector spherical harmonics is given through the use of the plane-wave spectrum technique. The interaction of an arbitrarily-located off-axis Gaussian beam with a spherical object is treated by the T-matrix method. The combination of the plane-wave spectrum technique and the T-matrix method can be extended to solve the interaction problem for an arbitrary laser beam incident upon some arbitrarily-shaped axisymmetric homogeneous or layered object.

[I] Introduction

The interaction of a focused laser beam with a spherical object is of interest in areas such as object characterization, nonlinear optics in droplets, optical levitation, and laser-induced breakdown.

In this paper we have used the plane-wave spectrum technique,[1] to model a physically-realizable Gaussian beam. This technique can be used to model an arbitrary beam even if it does not have an exact mathematical representation. The electromagnetic interaction with the spherical object has been solved using the T-matrix method.[2,3] This combination of the plane wave spectrum technique and the T-matrix method has been used before, but with a different formulation which involves a complicated process for calculating the far-field scattering,[4,5] and numerical results were obtained only for small spheres. Here we have developed a simple formula, taking advantage of the linearity of the T-matrix method and the angular spectrum of plane waves. Although the T-matrix method is applicable to nonspherical objects, its use here is restricted to spherical objects. However, the T-matrix formalism provides the framework for future modeling of nonspherical objects.

[II] Gaussian Beam Modeling

The Gaussian beam propagates in the z-direction and is polarized in the x-z plane. The total incident electric field vector, in the right-handed Cartesian coordinate system (x, y, z), is

$$\mathbf{E}^{\mathrm{i}}(x,y,z) = E_x^{\mathrm{i}}(x,y,z)\mathbf{i}_x + E_z^{\mathrm{i}}(x,y,z)\mathbf{i}_z \tag{1}$$

where $\mathbf{i}_x$ and $\mathbf{i}_z$ are unit vectors in the x and z directions.

We choose a Gaussian beam for which the spatial distribution of the amplitude of E_x has a Gaussian distribution, i.e., the transverse component of the electric field is

$$E_x^{\mathrm{i}}(x,y,z) = E_0^{\mathrm{i}}\, g(x,y,z), \tag{2}$$

where for purposes of illustration, we begin by using $g(x,y,z)$ for a lowest-order Gaussian beam with its focal point at the origin,[6]

$$g(x,y,z) = \frac{w_0}{w(z)}\, exp\left[-\frac{x^2+y^2}{w^2(z)}\right]\; exp\left[ik\frac{x^2+y^2}{2R(z)}\right]\; exp\left\{i\left[kz - \tan^{-1}(\frac{z}{z_0})\right]\right\}, \tag{3}$$

where w_0 is the spot size at the beam waist (spot size at $z = 0$), $k = \dfrac{2\pi}{\lambda}$ is the wave number, λ is the wavelength, and $z_0 = \dfrac{\pi w_0^2}{\lambda}$. The spot size, $w(z)$, and radius of curvature, $R(z)$, of the phase front of the beam are,

$$\begin{aligned} w(z) &= w_0\left[1+(\frac{z}{z_0})^2\right]^{1/2} \\ R(z) &= z\left[1+(\frac{z_0}{z})^2\right]. \end{aligned} \tag{4}$$

In the $z = 0$ plane, where $w(z) = w_0$ and $R(z) = \infty$, $E_x^{\mathrm{i}}(x,y,z)$ is

$$E_x^{\mathrm{i}}(x,y,0) = E_0^{\mathrm{i}}\, exp(-\frac{x^2+y^2}{w_0^2}). \tag{5}$$

The electric field at any point, $\mathbf{E}^{\mathrm{i}}(x,y,z)$, can be expressed as a sum of plane waves.[1] The first step is to take the two-dimensional Fourier transform[7] of both sides of (5),

$$\mathcal{F}[E_x^{\mathrm{i}}(x,y,0)] = \pi w_0^2 E_0^{\mathrm{i}}\, exp\left[-\frac{w_0^2}{4}(k_x^2+k_y^2)\right], \tag{6}$$

where $k_x = k\cos\xi = k\sin\theta\cos\phi$, $k_y = k\cos\zeta = k\sin\theta\sin\phi$ and $k_z = k\cos\theta$. The wave vector is $\mathbf{k} = k_x\mathbf{i}_x + k_y\mathbf{i}_y + k_z\mathbf{i}_z$, $k = |\,\mathbf{k}\,| = \left[k_x^2+k_y^2+k_z^2\right]^{1/2} = \dfrac{2\pi}{\lambda}$, and the angles ξ, ζ and θ are the angles of the direction cosines of $\mathbf{k}$. The transverse electric field at any point, $E_x^{\mathrm{i}}(x,y,z)$ is obtained by multiplying (6) by $exp(ik_z z)$ and taking the inverse Fourier transform,[7]

$$\begin{aligned} E_x^{\mathrm{i}}(x,y,z) &= \frac{E_0^{\mathrm{i}}}{4\pi^2}(\pi w_0^2)\int_{k_x=-\infty}^{\infty}\int_{k_y=-\infty}^{\infty} exp\left[-\frac{w_0^2}{4}(k_x^2+k_y^2)\right] \\ &\quad \times exp\left[i(k_x x + k_y y + k_z z)\right]\; dk_x dk_y, \end{aligned} \tag{7}$$

which can be written as

$$E_x^{\mathrm{i}}(x,y,z) = \frac{E_0^{\mathrm{i}} w_0^2}{4\pi} \int_{k_x=-\infty}^{\infty} \int_{k_y=-\infty}^{\infty} exp\left[-\frac{w_0^2}{4}(k_x^2+k_y^2)\right] \; exp[i(\mathbf{k}\cdot\mathbf{r})] \;\; dk_x dk_y, \tag{8}$$

where $\mathbf{r} = x\mathbf{i}_x + y\mathbf{i}_y + z\mathbf{i}_z$ is a position vector. The term within the integral in (8) is a uniform plane wave having a propagation vector $\mathbf{k}$.

The z-component of the electric field can be obtained from the relation, $\mathbf{E}^{\mathrm{i}} \cdot \mathbf{k} = 0$. Therefore, when the focal point is at the origin, the electric field of the incident Gaussian beam at any point is

$$\mathbf{E}^{\mathrm{i}}(x,y,z) = \int_{k_x=-\infty}^{\infty} \int_{k_y=-\infty}^{\infty} E_o(k_x,k_y)\, \mathbf{e}_o(k_x,k_y)\, exp[i(\mathbf{k}\cdot\mathbf{r})] \;\; dk_x dk_y \;, \tag{9}$$

where

$$E_o(k_x,k_y) = \left(\frac{E_0^{\mathrm{i}} w_0^2}{4\pi}\right) \left[\frac{(k_x^2+k_z^2)^{1/2}}{k_z}\right] \;\; exp\left[\frac{-w_0^2}{4}\left(k_x^2+k_y^2\right)\right], \tag{10}$$

and $\mathbf{e}_o(k_x,k_y)$ is a unit vector given by

$$\mathbf{e}_o(k_x,k_y) = \frac{k_z}{(k_x^2+k_z^2)^{1/2}} \left[\mathbf{i}_x - \left(\frac{k_x}{k_z}\right)\mathbf{i}_z\right]. \tag{11}$$

For a Gaussian beam with the focal point located at a point (x_0, y_0, z_0) the incident electric field can be written as

$$\begin{aligned} \mathbf{E}^{\mathrm{i}}(x,y,z) \;\; &= \;\; \frac{E_0^{\mathrm{i}} w_0^2}{4\pi} \int_{k_x=-\infty}^{\infty} \int_{k_y=-\infty}^{\infty} \left[\mathbf{i}_x - (\frac{k_x}{k_z})\mathbf{i}_z\right] \; exp\left[-\frac{w_0^2}{4}(k_x^2+k_y^2)\right] \\ &\quad \times exp\left\{i\left[k_x(x-x_0)+k_y(y-y_0)+k_z(z-z_0)\right]\right\} \;\; dk_x dk_y. \end{aligned} \tag{12}$$

This can be written in terms of the direction cosine angles ξ and ζ as

$$\mathbf{E}^{\mathrm{i}}(x,y,z) = \int_0^{\pi} \sin\xi \left[\int_0^{\pi} \sin\zeta \; E_o(\xi,\zeta)\, \mathbf{e}_o(\xi,\zeta)\, exp[ik(\mathbf{s}\cdot\mathbf{r})]\, d\zeta\right] d\xi \;, \tag{13}$$

where

$$\begin{aligned} E_o(\xi,\zeta) \;\; &= \;\; \left(\frac{E_0^{\mathrm{i}} k^2 w_0^2}{4\pi}\right) \left[\frac{\sin\zeta}{(1-s^2)^{1/2}}\right] exp[-ik\,(\mathbf{s}\cdot\mathbf{v})]\, exp\left[-\left(\frac{w_0 k s}{2}\right)^2\right] \\ \mathbf{e}_o(\xi,\zeta) \;\; &= \;\; \left[\frac{(1-s^2)^{1/2}}{\sin\zeta}\right] \left[\mathbf{i}_x - \frac{\cos\xi}{(1-s^2)^{1/2}}\mathbf{i}_z\right] \;, \end{aligned} \tag{14}$$

$s^2 = \cos^2\xi + \cos^2\zeta$, and the vectors $\mathbf{s}$ and $\mathbf{v}$ are

$$\begin{aligned} \mathbf{s} \;\; &= \;\; \cos\xi\mathbf{i}_x + \cos\zeta\mathbf{i}_y + (1-s^2)^{1/2}\mathbf{i}_z \\ \mathbf{v} \;\; &= \;\; x_0\mathbf{i}_x + y_0\mathbf{i}_y + z_0\mathbf{i}_z \,. \end{aligned} \tag{15}$$

This can be written in discrete plane-wave spectrum form as

$$\mathbf{E}^{\mathrm{i}}(x,y,z) \approx p^2 \sum_i \sin\xi_i \sum_j \sin\zeta_j E_{o_{ij}}(\xi_i,\zeta_j) \mathbf{e}_{o_{ij}}(\xi_i,\zeta_j) exp\left[ik\,(\mathbf{s}_{ij}\cdot\mathbf{r})\right] \;, \tag{16}$$

where p is the integration step size using the trapezoidal rule and the index ij refers to the plane wave having propagation constants k_{x_i} and k_{y_j} in the x and y directions, respectively. The amplitude and polarization of the $ij^{\underline{th}}$ plane wave are

$$\begin{aligned} E_{o_{ij}}(\xi_i,\zeta_j) &= \left(\frac{E_0^i k^2 w_0^2}{4\pi}\right)\left[\frac{\sin\zeta_j}{(1-s_{ij}^2)^{1/2}}\right] exp[-ik(\mathbf{s}_{ij}\cdot\mathbf{v})]\, exp\left[-\left(\frac{w_0 k s_{ij}}{2}\right)^2\right] \\ \mathbf{e}_{o_{ij}}(\xi_i,\zeta_j) &= \left[\frac{(1-s_{ij}^2)^{1/2}}{\sin\zeta_j}\right]\left[\mathbf{i}_x - \frac{\cos\xi_i}{(1-s_{ij}^2)^{1/2}}\mathbf{i}_z\right], \end{aligned} \tag{17}$$

where $\mathbf{s}_{ij} = \cos\xi_i \mathbf{i}_x + \cos\zeta_j \mathbf{i}_y + (1-s_{ij}^2)^{1/2}\mathbf{i}_z$.

[III] Expansion of the Beam in Vector Spherical Harmonics

The expansion of the incident Gaussian beam in vector spherical harmonics(VSH) can be obtained by expanding each of the plane waves in (16) as[8]

$$\begin{aligned} \mathbf{E}_{ij}(k\mathbf{r}) &= E_{o_{ij}}(\xi_i,\zeta_j)\mathbf{e}_{o_{ij}}(\xi_i,\zeta_j) exp[ik(\mathbf{s}_{ij}\cdot\mathbf{r})] \\ &= E_{o_{ij}}(\xi_i,\zeta_j)\sum_m\sum_n D_{mn}\left[a^t_{emn_{ij}}\mathbf{M}^1_{emn}(k\mathbf{r}) + a^t_{omn_{ij}}\mathbf{M}^1_{omn}(k\mathbf{r})\right. \\ &\quad \left. + b^t_{emn_{ij}}\mathbf{N}^1_{emn}(k\mathbf{r}) + b^t_{omn_{ij}}\mathbf{N}^1_{omn}(k\mathbf{r})\right] \end{aligned} \tag{18}$$

where D_{mn} is a normalization factor; ϵ_m is equal to 1 for $m = 0$ and is equal to 2 for $m > 0$, $\mathbf{M}^1_{emn}$, $\mathbf{M}^1_{omn}$, $\mathbf{N}^1_{emn}$ and $\mathbf{N}^1_{omn}$ are the VSH of the first kind, $a^t_{emn_{ij}}$, $a^t_{omn_{ij}}$, $b^t_{emn_{ij}}$ and $b^t_{omn_{ij}}$ are the VSH expansion coefficients of the $ij^{\underline{th}}$ constituent plane wave in the medium of interest,[9] e and o denote even and odd modes and m and n are integers.

Finally, the total electric field of the Gaussian beam at any point can be written

$$\begin{aligned} \mathbf{E}^i(k\mathbf{r}) &= \left(p^2\frac{E_0^i w_0^2 k^2}{4\pi}\right)\sum_m\sum_n D_{mn}\left[a^t_{emn}\mathbf{M}^1_{emn}(k\mathbf{r}) + a^t_{omn}\mathbf{M}^1_{omn}(k\mathbf{r}) + \right. \\ &\quad \left. b^t_{emn}\mathbf{N}^1_{emn}(k\mathbf{r}) + b^t_{omn}\mathbf{N}^1_{omn}(k\mathbf{r})\right], \end{aligned} \tag{19}$$

where, a^t_{emn}, a^t_{omn}, b^t_{emn}, and b^t_{omn} are the incident field expansion coefficients for the Gaussian beam which are given by

$$a^t_{emn} = \sum_i \sin\xi_i \sum_j a^t_{emn_{ij}} \left[\frac{\sin^2\zeta_j}{(1-s_{ij}^2)^{1/2}}\right] exp\left[-\left(\frac{w_0 k s_{ij}}{2}\right)^2\right] exp[-ik(\mathbf{s}_{ij}\cdot\mathbf{v})], \tag{20}$$

with identical expressions for a^t_{omn}, b^t_{emn} and b^t_{omn} in terms of $a^t_{omn_{ij}}$, $b^t_{emn_{ij}}$ and $b^t_{omn_{ij}}$, respectively.

[IV] Internal and Scattered Field Calculations

The electric field inside an arbitrary object, illuminated with a Gaussian beam, can be calculated from[8]

$$\mathbf{E}^{int}(\sqrt{\epsilon_r}k\mathbf{r}) = \left(p^2\frac{E_0^i w_0^2 k^2}{4\pi}\right)\sum_{m'}\sum_{n'}\left[c^t_{em'n'}\mathbf{M}^1_{em'n'}(\sqrt{\epsilon_r}k\mathbf{r}) + c^t_{om'n'}\mathbf{M}^1_{om'n'}(\sqrt{\epsilon_r}k\mathbf{r})\right.$$

$$+ \quad d^t_{em'n'}\mathbf{N}^1_{em'n'}(\sqrt{\epsilon_r}k\mathbf{r}) + d^t_{om'n'}\mathbf{N}^1_{om'n'}(\sqrt{\epsilon_r}k\mathbf{r})\Big] \tag{21}$$

where ϵ_r is the dielectric constant of the object. The $c^t_{em'n'}$ $c^t_{om'n'}$ $d^t_{em'n'}$ and $d^t_{om'n'}$ are VSH expansion coefficients for the internal electric field. The expansion coefficients for the internal field are related to the incident field expansion coefficients for each azimuthal mode, m, by[9]

$$-i\begin{bmatrix} a^t_{emn} \\ a^t_{omn} \\ b^t_{emn} \\ b^t_{omn} \end{bmatrix} = \begin{bmatrix} A_{11} & A_{12} & A_{13} & A_{14} \\ A_{21} & A_{22} & A_{23} & A_{24} \\ A_{31} & A_{32} & A_{33} & A_{34} \\ A_{41} & A_{42} & A_{43} & A_{44} \end{bmatrix} \begin{bmatrix} c^t_{em'n'} \\ c^t_{om'n'} \\ d^t_{em'n'} \\ d^t_{om'n'} \end{bmatrix}.$$

The A_{lp} submatrices each have a dimension $n \times n'$ and the submatrix elements are integrals over the surface of the object. For axisymmetric objects the A-matrix is block diagonal [8] where each block is a full matrix with $m = m'$. In the case of spherical objects, the A-matrix is diagonal[9] and the nonzero elements are the diagonal elements of A_{11}, A_{22}, A_{33} and A_{44} with $m' = m$ and $n' = n$.

The scattered electric field is[8]

$$\begin{aligned} \mathbf{E}^s(k\mathbf{r}) \; = \; & \left(p^2 \frac{E^i_0 w_0^2 k^2}{4\pi}\right) \sum_m \sum_n D_{mn} \Big[f^t_{emn}\mathbf{M}^3_{emn}(k\mathbf{r}) + f^t_{omn}\mathbf{M}^3_{omn}(k\mathbf{r}) \\ & + g^t_{emn}\mathbf{N}^3_{emn}(k\mathbf{r}) + g^t_{omn}\mathbf{N}^3_{omn}(k\mathbf{r}) \Big] \ , \end{aligned} \tag{22}$$

where $\mathbf{M}^3(k\mathbf{r})$ and $\mathbf{N}^3(k\mathbf{r})$ are VSH of the third kind (for outgoing waves). The expansion coefficients for the scattered field f^t_{emn}, f^t_{omn}, g^t_{emn} and g^t_{omn} are related to the incident field expansion coefficients for each azimuthal mode, m, by[9]

$$\begin{bmatrix} f^t_{emn} \\ f^t_{omn} \\ g^t_{emn} \\ g^t_{omn} \end{bmatrix} = - \begin{bmatrix} B_{11} & B_{12} & B_{13} & B_{14} \\ B_{21} & B_{22} & B_{23} & B_{24} \\ B_{31} & B_{32} & B_{33} & B_{34} \\ B_{41} & B_{42} & B_{43} & B_{44} \end{bmatrix} \begin{bmatrix} A_{11} & A_{12} & A_{13} & A_{14} \\ A_{21} & A_{22} & A_{23} & A_{24} \\ A_{31} & A_{32} & A_{33} & A_{34} \\ A_{41} & A_{42} & A_{43} & A_{44} \end{bmatrix}^{-1} \begin{bmatrix} a^t_{emn} \\ a^t_{omn} \\ b^t_{emn} \\ b^t_{omn} \end{bmatrix}.$$

The elements of the B_{lp} submatrices are the same as the corresponding elements of the A_{lp} submatrices except that the Hankel function $h_n(kr)$ is replaced by the Bessel function $j_n(kr)$ in all of the surface integrals. For spherical objects, the B-matrix is diagonal.[9] The matrix equation for the scattered field expansion coefficients can be written as[8]

$$\begin{bmatrix} f^t_{emn} \\ f^t_{omn} \\ g^t_{emn} \\ g^t_{omn} \end{bmatrix} = - \begin{bmatrix} T_{11} & T_{12} & T_{13} & T_{14} \\ T_{21} & T_{22} & T_{23} & T_{24} \\ T_{31} & T_{32} & T_{33} & T_{34} \\ T_{41} & T_{42} & T_{43} & T_{44} \end{bmatrix} \begin{bmatrix} a^t_{emn} \\ a^t_{omn} \\ b^t_{emn} \\ b^t_{omn} \end{bmatrix},$$

where, $T_{lp} = \sum_q [B]_{lq}[A]^{-1}_{qp}$ are the elements of the T-matrix. In the case of spherical objects the T-matrix is diagonal [9] and its elements are given by $T_{ll} = B_{ll}/A_{ll}$.

Details of the theoretical development in section II, III, and IV may be found in a previous publication.[9]

[V] Numerical Results

Energy density distributions inside and near a sphere of radius a located at the origin and illuminated with an arbitrary Gaussian beam are calculated. The dielectric constant of the sphere is $\epsilon_r = 1.85$. The sphere is illuminated with a Gaussian beam having a spot size at the beam waist, $w_0 = 4\mu m$. Energy density distributions on and near the $TE_{94,2}$ resonance are considered. This corresponds to a size parameter of $x = 79.6279518$ ($x = \frac{2\pi a}{\lambda}$, where λ is the incident wavelength). If $\lambda = 1.06\mu m$, this resonant size parameter corresponds to a sphere radius of $a \approx 13.43\mu m$.

Figure 1 shows the electric energy density distribution in the yz-plane with the incident beam focused at the origin in the absence of the sphere. The surface of the sphere is only shown for reference. This illustrates that the calculated plane-wave spectrum representation of the incident beam is a smooth Gaussian function. Figure 2 shows a contour plot of the normalized electric energy density in the yz-plane inside and near a sphere with a size-parameter of $x = 79.6279518$, which corresponds to the $TE_{94,2}$ resonance. The quality factor of this resonant mode is $Q \approx 1.8 \times 10^7$, ($Q = \frac{x}{\Delta x}$, where Δx is the linewidth, full width at half maximum). The beam axis is shifted along the y-axis by a distance, $y_0 = 0.75a$ and the spot-size at the beam's waist is $w_0 \approx 0.149a$. Figure 2 shows that this position of the incident beam does not induce a resonant distribution of electric energy density within the sphere, even when the radius-to-wavelength ratio corresponds to a resonant mode. Indeed, a resonance distribution of electric energy density is not excited when the Gaussian beam is incident anywhere inside the surface of the sphere, i.e., $y_0 < a$. This is true if the ratio of the spot-size at the beam's waist to the sphere's radius is less than one, that is $w_0/a < 1$. If $w_0/a \approx 1$ the focal point position will have less influence on the resonance excitation because the Gaussian beam in this case behaves approximately like a plane wave. This implies that in the case of tightly-focused Gaussian beam illumination inside the surface of the sphere the energy is distributed among all the modes and none of them dominate the internal or external energy distribution.

Figure 3 shows the normalized electric energy density in the yz-plane inside and near the sphere at the $TE_{94,2}$ resonance for the incident Gaussian beam axis at $y_0 = a$. The results clearly show a resonant distribution with two radial maxima as expected for a $TE_{94,2}$ mode. The incident Gaussian beam does not appear in Fig. 3 because its energy density is negligible compared to the resonant energy values inside the sphere.

Figure 4 shows the normalized electric energy density in the yz-plane for a near-resonance sphere with a size parameter of 79.62 which is 1767 linewidths away from the $TE_{94,2}$ resonance. All other parameters are the same as in Fig. 3. When illuminated at $y_0 = a$, the internal distribution approximates that of a resonant mode, even when the incident beam is not at a resonant frequency. Illumination by this tightly-focused Gaussian beam clearly shows the reflected and refracted components which are normally only observed by geometrical optics ray-tracing analysis.

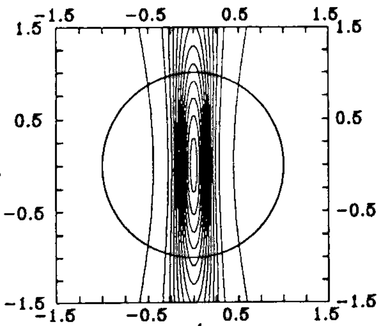

Figure 1 Contour plot of the electric energy distribution in the yz-plane of the incident Gaussian beam for beam axis coincident with the z-axis and the beam focal point at $z = 0$. The location of the beam axis and focal point are arbitrary. The outline of the sphere of radius a is shown for reference.

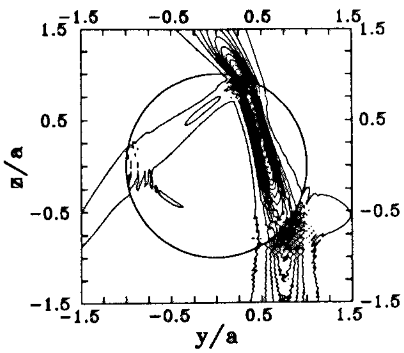

Figure 2 Contour plot of the electric energy density in the yz-plane inside and near a sphere illuminated with an off-axis Gaussian beam propagating along the $+z$ direction. The parameters are: $x = 79.6279518$ (the resonance frequency of the $TE_{94,2}$ mode), $\epsilon_r = 1.85$, $w_0 \approx 0.149a$, $x_0 = 0$, $y_0 = 0.75a$ and $z_0 = 0$. The outline of the sphere of radius a is shown for reference.

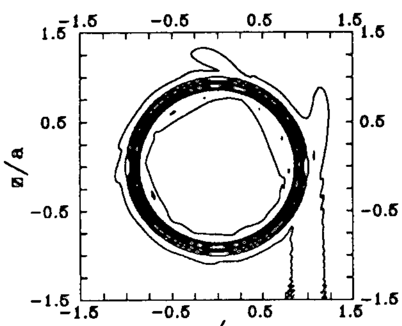

Figure 3 Contour plot for the same case as in Fig. 2 except $y_0 = a$.

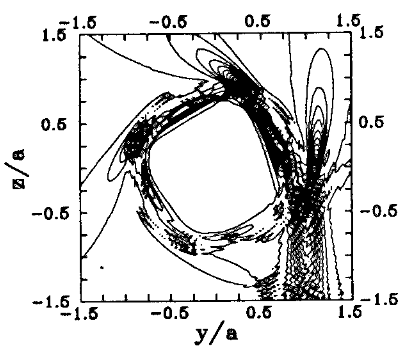

Figure 4 Contour plot of the electric energy density in the yz-plane inside and near an off-resonance sphere with a size parameter of 79.62 which is 1767 linewidths away from the resonance location of the mode $TE_{94,2}$. All other parameters are the same as in Fig. 3.

References

[1] P. C. Clemmow, *The Plane Wave Spectrum Representation of Electromagnetic Fields* (Pergamon Press, 1966).

[2] P. C. Waterman, " Symmetry, unitarity, and geometry in electromagnetic scattering, " Phys. Rev. D **3**, 825-839 (1971).

[3] P. Barber and C. Yeh, " Scattering of electromagnetic waves by arbitrarily shaped dielectric bodies," Appl. Opt. **14**, 2864-2872 (1975).

[4] S. Colak, C. Yeh and L. W. Casperson, "Scattering of focused beams by tenuous particles," Appl. Opt. **18**, 294-302 (1979).

[5] C. Yeh, S. Colak and P. Barber, "Scattering of sharply focused beams by arbitrarily shaped dielectric particles: an exact solution," Appl. Opt. **21**, 4426-4433 (1982).

[6] Amnon Yariv, *Optical Electronics*, 4th ed. (Holt, Rinehart and Winston, New York, USA, 1991).

[7] Partha P. Banerjee and Ting-Chung Poon, *Principles of Applied Optics* (Aksen Associates, Homewood, IL and Boston, MA, USA, 1991).

[8] P. W. Barber and S. C. Hill, *Light Scattering by Particles: Computational Methods* (World Scientific, Singapore, 1990).

[9] E. E. M. Khaled, S. C. Hill and P. W. Barber "Scattered and internal intensity of a spherical particle illuminated with a Gaussian beam," J. Opt. Soc. Am. A, submitted, 1992.

SOLUTION OF INVERSE SCATTERING PROBLEMS USING A METHOD OF MOMENTS APPROACH

David C. Jenn
Naval Postgraduate School
Monterey, CA 93943
Code EC/Jn
(408) 646-2254

Abstract

A procedure is described that yields the surface impedance at every point on the surface of a body for a specified RCS pattern. The solution parallels the standard method of moments (MM) technique in that the surface impedance is expanded into a series of basis functions with unknown coefficients. An approximate impedance function is obtained by assuming a current (e.g., physical optics) and solving the integral equation for the expansion coefficients. A rigorous solution to the problem requires that both the surface current and impedance be expanded into series. In the first case, the approximation for the current and the properties of the basis functions will determine whether the resulting set of simultaneous equations will be linear or not. In the second, a nonlinear set of simultaneous equations must be solved.

I. INTRODUCTION

In most cases, identification of a completely unknown target from the characteristics of its radar return has proven to be difficult [ref. 1]. A restricted form of this problem is considered here: given that the shape of a body and its scattered field are known, what are the boundary conditions at its surface? This is the problem that must be addressed when the radar cross section (RCS) of a target is to be synthesized. If the scattered field of a particular body is specified, the inverse problem can be solved to provide the surface impedance at each point on the surface. Once it is known, estimates of the equivalent ϵ and μ can be obtained that satisfy the same boundary conditions. The RCS engineer can then use these estimates to establish guidelines for the design of low observable targets, including treatments to suppress 'hot spots.' Such a procedure would be of great practical interest, since to date there does not exist a reliable RCS synthesis method. The usual reduction techniques of shaping, materials selection and cancellation are primarily based on intuition and past experience [ref. 2].

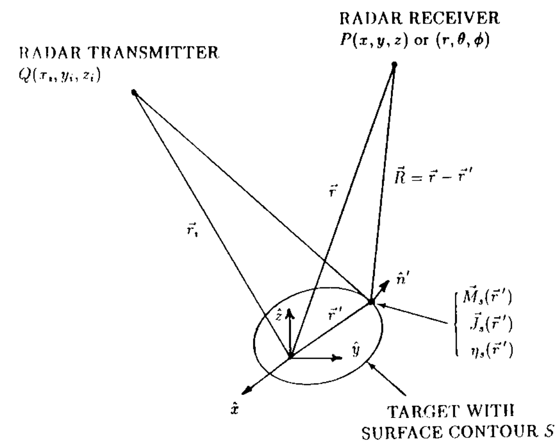

Figure 1: Definition of geometry and notation.

II. DESCRIPTION OF THE SOLUTION METHOD

An integral equation for the surface impedance can be derived from the integral solutions of Maxwell's equations (the radiation integrals) and the appropriate boundary conditions. The procedure requires that the shape of the body be known (denoted S), and to simplify the following discussion, it will be assumed that the target is surrounded by free space. Furthermore, the electrical properties of the body will be approximated by a surface impedance, η_s, which is normalized to the impedance of free space, η_o. The surface impedance relates the tangential components of the electric and magnetic fields on S [ref. 3]

$$\vec{E}_{tan} = \eta_s \eta_o \vec{H}_{tan}. \tag{1}$$

$\vec{E}$ and $\vec{H}$ are the total electric and magnetic fields on the surface of the body, the geometry of which is shown in Figure 1. In general, all of the quantities in (1), except η_o, can vary from point to point. This positional dependence can be expressed explicitly by writing these quantities as a function of an argument $\vec{r}'$, which is the position vector to a current element (x', y', z') on the surface.

When a target is illuminated by a wave as in Figure 1, currents are induced on its surface. Let the total fields be ($\vec{E} = \vec{E}_i + \vec{E}_s$, $\vec{H} = \vec{H}_i + \vec{H}_s$) so that the electric surface current on S is $\vec{J}_s = \hat{n} \times \vec{H}$ [ref. 4] and the magnetic surface current is $\vec{M}_s = -\hat{n} \times \vec{E}$. By using (1)

$$\vec{M}_s = -\eta_s \eta_o \hat{n} \times \vec{J}_s. \tag{2}$$

At an observation point P, the scattered electric field that arises from the currents $\vec{J}_s$

and $\vec{M}_s$ radiating in free space is

$$\vec{E}_s(P) = -jk\eta_o \iint_S \left[\vec{J}_s G + \frac{\vec{M}_s \times \nabla' G}{j\omega\mu} - \frac{\nabla' \cdot \vec{J}_s}{k^2} \nabla' G \right] ds' \tag{3}$$

where

$$G = \frac{e^{-jkr}}{4\pi r}, \quad r = \sqrt{(x-x')^2 + (y-y')^2 + (z-z')^2}, \quad k = \frac{2\pi}{\lambda}.$$

In the above equations λ is the wavelength and the primed quantities refer to a current source point while the unprimed quantities to the observation point. Using (2) in (3) eliminates the magnetic current from the integrand

$$\vec{E}_s(P) = -jk\eta_o \iint_S \left[\vec{J}_s G + \frac{j\eta_s}{k}(\hat{n}' \times \vec{J}_s) \times \nabla' G - \frac{\nabla' \cdot \vec{J}_s}{k^2} \nabla' G \right] ds'. \tag{4}$$

For the synthesis problem, $\vec{E}_s(P)$ is known and η_s is desired at every point on S. This can be accomplished in either of two ways:

(1) an estimate of $\vec{J}_s$ is specified at every point on the surface and the integral equation solved for η_s, or
(2) additional boundary conditions must be provided and the integral equation solved for both $\vec{J}_s$ and η_s.

In subsequent discussion these are referred to method 1 and method 2 respectively.

The additional information needed to solve the problem rigorously can be obtained from an impedance boundary condition integral equation that can be derived by moving the observation point P onto the surface S in (4) [ref. 5]. Thus two integral equations must be solved simultaneously for the unknown quantities η_s and $\vec{J}_s$

$$\vec{E}_s(P) = -jk\eta_o \iint_S \left[\vec{J}_s G + \frac{j\eta_s(\vec{r}\,')}{k}(\hat{n}' \times \vec{J}_s) \times \nabla' G - \frac{\nabla' \cdot \vec{J}_s}{k^2} \nabla' G \right] ds' \tag{5}$$

$$\begin{aligned} \frac{\vec{E}_i(\vec{r})|_{tan}}{\eta_o} - \eta_s(\vec{r})\hat{n} \times \vec{H}_i(\vec{r}) &= \eta_s(\vec{r})\hat{n} \times \Bigg[\nabla \times \iint_S \vec{J}_s G ds' \\ &+ jk \iint_S \eta_s(\vec{r}\,')(\hat{n}' \times \vec{J}_s) G ds' + \frac{j}{k} \iint_S \nabla' \cdot [\eta_s(\vec{r}\,')\hat{n}' \times \vec{J}_s] \nabla G ds' \Bigg] \\ &+ \left[jk \iint_S \vec{J}_s G ds' + \frac{j}{k} \iint_S (\nabla' \cdot \vec{J}_s) \nabla G ds' - \nabla \times \iint_S \eta_s(\vec{r}\,')(\hat{n}' \times \vec{J}_s) G ds' \right]_{tan} \end{aligned} \tag{6}$$

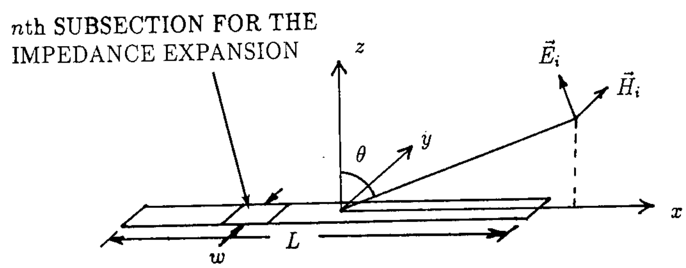

Figure 2: TM_z polarized plane wave incident on a thin strip.

In (5) P denotes an observation point off of S and in (6) $\vec{r}$ the location of an observation point on S.

III. APPROXIMATE SOLUTION FOR A THIN STRIP

Consider the special case of bistatic scattering from the thin strip shown in Figure 2. Only TM_z polarization need be considered because the current is restricted to the x axis

$$\vec{H}_i = \hat{\phi}\frac{E_o}{\eta_o}e^{-j\vec{k}\cdot\vec{R}}. \tag{7}$$

An estimate of the impedance is obtained by specifying $\vec{J}_s$ and solving (4) for η_s. Since the shape of the body is known, an intuitive guess at $\vec{J}_s$ can be made. For large bodies a modified form of the the physical optics approximation can be used. The current is set to

$$\vec{J}_s \approx 2\Gamma\hat{n}\times\vec{H}_i \tag{8}$$

on the illuminated part of the target and zero on the shadowed part, where Γ is the reflection coefficient of the impedance surface. This reduces to the standard physical optics approximation for a perfect electric conductor ($\eta_s = 0$)[ref. 4]. Using the current obtained from (7) and (8) in (4), restricting the observation point to the far field $\phi = 0$ plane, and assuming near-normal incidence for the reflection coefficient ($\theta = \theta_i = 0$) gives

$$E_\theta(\theta) = \frac{-jke^{-jkr}}{2\pi r}E_o\cos\theta\int_{-L/2}^{L/2}\frac{\eta_s^2 - 2\eta_s + 1}{\eta_s + 1}e^{jkx'(\sin\theta+\sin\theta_i)}dx'. \tag{9}$$

To solve this equation the impedance is expanded into a series with unknown coefficients

$$\eta_s(x') = \sum_{n=1}^{N} a_n f_n(x'). \tag{10}$$

Let the wire be divided into N segments of equal length Δ, and the basis functions be pulses

$$f_n(x') = \begin{cases} 1, & \text{if } x' \text{ on } S_n \\ 0, & \text{otherwise} \end{cases} \tag{11}$$

where S_n signifies the area occupied by the nth segment. Using the last two equations in (9) and rescaling to remove the leading constants gives

$$E_\theta(\theta) = \cos\theta F(\theta) \sum_{n=1}^{N} b_n e^{jkx_n \sin(\theta+\theta_i)} \tag{12}$$

where x_n is the center point of the nth segment and

$$F(\theta) = \frac{w\Delta \sin[\frac{k\Delta}{2}(\sin\theta + \sin\theta_i)]}{\frac{k\Delta}{2}(\sin\theta + \sin\theta_i)} \tag{13}$$

is the PO scattering pattern for a single patch. A new coefficient b_n has been defined for convenience

$$b_n = \frac{a_n^2 - 2a_n + 1}{a_n + 1}. \tag{14}$$

Now equation (15) can be enforced in M directions for which the RCS is known $(\theta_1, \theta_2, ..., \theta_M)$ yielding M equations. In matrix notation this set of equations becomes

$$\mathbf{E} = \mathbf{A}\mathbf{b} \tag{15}$$

where $E_m = E_\theta(\theta_m)$ and denoting $F(\theta_m)$ by F_m the elements of $\mathbf{A}$ are

$$A_{mn} = \cos\theta_m F_m e^{jkx_n(\sin\theta_m + \sin\theta_i)}. \tag{16}$$

The vector of coefficients $\mathbf{b}$ can be solved for using standard matrix methods if $M = N$, or by using a generalized inverse if $M < N$ [ref. 6]. The coefficients a_n can be determined from the b_n numerically using root finding routines, or directly by making some approximations in equation (14). Thus, when E_θ is given in N directions, the surface impedance on N subsections can be determined.

IV. RIGOROUS SOLUTION FOR A THIN STRIP

In principle the impedance can be determined exactly by expanding both η_s and $\vec{J}_s$ into series and solving for the expansion coefficients. For the special case of the strip

shown in Figure 2 with constant current across its width, these two integral equations reduce to

$$E_\theta(\theta) = \frac{-jkwe^{-jkr}}{4\pi r}\left[\cos\theta \int_{-L/2}^{L/2} J_{sx} e^{jkx'(\sin\theta+\sin\theta_i)}dx' + \int_{-L/2}^{L/2} \eta_s J_{sx} e^{jkx'(\sin\theta+\sin\theta_i)}dx'\right] \quad (17)$$

$$\frac{E_o}{\eta_o} e^{jkx\sin\theta_i}[\cos\theta_i - \eta_s(x)] = -\eta_s(x) w \int_{-L/2}^{L/2} \eta_s J_{sx} G(x,x')dx'$$

$$+jkw \int_{-L/2}^{L/2} J_{sx} G(x,x')dx' - \frac{jw}{k}\int_{-L/2}^{L/2} (\hat{r}\cdot\hat{x})\left(\frac{d}{dx'}J_{sx}\right)\left(\frac{1+jkr}{r}\right) G(x,x')dx' \quad (18)$$

with $r = |x - x'|$. To solve this set of equations the series representation in (10) along with

$$\vec{J}_s(x') = \sum_{n=1}^{N} I_n \vec{J}_n(x') = \sum_{n=1}^{N} I_n \frac{f_n(x')}{w}\hat{x} \quad (19)$$

are substituted into (17) and (18) and a Galerkin testing procedure applied [ref. 7]. Each side of (18) is multiplied by $w\vec{J}_m(x)$ and integrated with respect to x. The same assumptions with regard to the incident wave, geometry and basis functions hold as in Section III. For the derivative of the current in (18) a delta function representation is used. Finally, after enforcing (17) at N far field points and testing (18) at N points on the strip, two sets equations result, each with N unknowns

$$E_\theta(\theta_m) = \sum_{n=1}^{N} I_n (W_{mn} - a_n H_{mn}) \quad (20)$$

$$U_n(\cos\theta_i - a_m) = \sum_{n=1}^{N} I_n \left[(jk - a_m a_n)G_{mn} + \frac{j}{k} Q_{mn}\right]. \quad (21)$$

The quantities in (20) and (21) are defined as follows:

$$G_{mn} = \int_{\Delta_m}\int_{\Delta_n} G(x,x')dxdx', \qquad Q_{mn} = \int_{\Delta_m} [Q(x,x_n^-) - Q(x,x_n^+)]dx$$

$$Q(x,x') = (\hat{x}\cdot\hat{r})\left(\frac{1+jkr}{r}\right)G(x,x'), \qquad x_n^{\pm} = x_n \pm \frac{\Delta}{2}$$

$$U_n = \frac{E_o}{\eta_o}\frac{\Delta\sin(\frac{k\Delta}{2}\sin\theta_i)}{\frac{k\Delta}{2}\sin\theta_i} e^{jkx_n\sin\theta_i}$$

$$H_{mn} = \frac{E_o}{\eta_o}\cos\theta_m \frac{\Delta\sin(\frac{k\Delta}{2}\sin\theta_m)}{\frac{k\Delta}{2}\sin\theta_m} e^{jkx_n\sin\theta_m}, \qquad W_{mn} = H_{mn}\cos\theta_m.$$

In matrix notation these two sets of equations become

$$\mathbf{E} = \mathbf{WI} - \mathbf{H}(\mathbf{a} \otimes \mathbf{I}) \tag{22}$$

$$\mathbf{U} \otimes [\mathbf{1}\cos\theta_i - \mathbf{a}] = jk[\mathbf{G} - \frac{1}{k^2}\mathbf{Q}^T]\mathbf{I} - [(\mathbf{a}\mathbf{a}^T) \otimes \mathbf{G}]^T\mathbf{I}. \tag{23}$$

The symbols $\otimes$ and T denote the Hadamard product [ref. 8] and the transpose. $\mathbf{1}$ is a diagonal matrix of ones and $\mathbf{I}$ and $\mathbf{a}$ are vectors containing the expansion coefficients for the unknown current and impedance.

V. CALCULATED RESULTS AND DISCUSSION

The approximate method for the thin strip developed in Section III has been verified by using the RCS computed from a known surface impedance. Typical results are shown in Figure 3. A trianglular impedance distribution was used to calculate the field scattered from the strip using the PO approximation. The resulting points were used as input for the synthesis procedure (i.e., formed the vector $\mathbf{E}$ in (12)), which was solved for the vector $\mathbf{b}$, and subsequently for $\mathbf{a}$. The result is virtually identical to the original impedance distribution in spite of the approximation $\eta_s << 1$ which was used to simplify (14).

The far field synthesis procedure was found to give generally accurate results, but as expected, the synthesized distribution was sensitive to several parameters. Among them are the sampling increment in angle, range of impedance values synthesized, symmetry conditions, approximations made to linearize the equations, and the accuracy of the assumed current distribution. In cases where the target impedance distribution did not support surface waves, the PO approximation for the current gave excellent results.

IV. REFERENCES

[1] D. Dudley, 'Progress in Identification of Electromagnetic Systems,' IEEE AP-S Newsletter, August 1988, p. 5.

[2] Knott, et. al., Radar Cross Section, Artech House, 1989.

[3] T. Senior, 'Impedance boundary condition for imperfectly conducting surfaces,' Appl. Sci. Res., sec. B, vol. 8, 1960, p. 414.

[4] R. F. Harrington, Time-Harmonic Electromagnetic Fields, McGraw-Hill.

[5] L. N. Mitschang, 'Integral equation formulations for imperfectly conducting scatterers,' IEEE Trans. on Antennas and Prop., AP-33, no. 2, February 1985, p. 206.

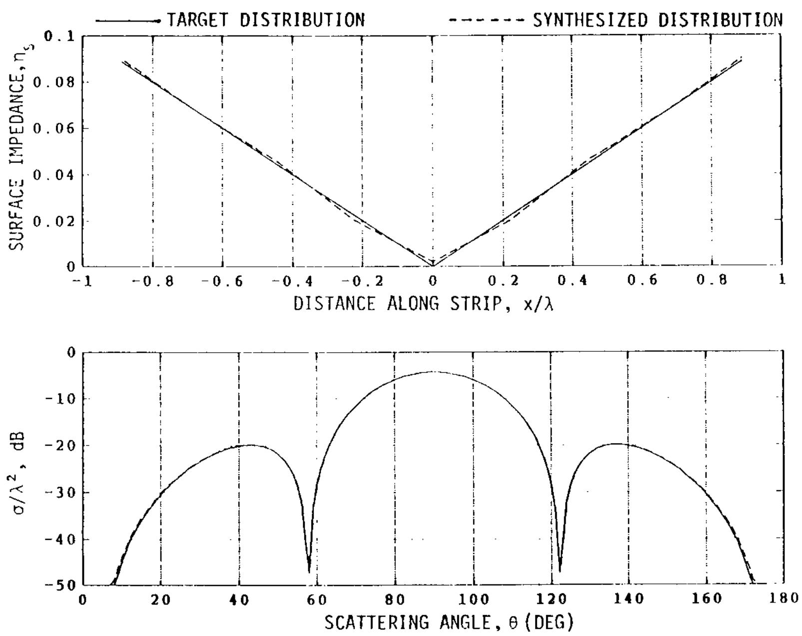

Figure 3: Target and synthesized impedance distributions and scattering patterns for a strip ($w = .1\lambda$, $L = 2\lambda$, $\theta_i = \phi_i = 0$)

[6] Rao and Mitra, Generalized Inverse of Matrices and its Applications, Wiley.

[7] R. F. Harrington, Field Computation by Moment Methods, Macmillan.

[8] R. A. Horn, 'The Hadamard product,' Proc. of Symp. in Appl. Math., vol. 40, 1990, p. 87.

ASYMPTOTIC SCATTERING CENTER MODEL AND NUMERICAL SOLUTION FOR SCALAR SCATTERING BY TWO SOFT CYLINDERS

ROBERT W. SCHARSTEIN

The University of Alabama
Department of Electrical Engineering
317 Houser Hall, Box 870286
Tuscaloosa, Alabama 35487-0286
205-348-1761

ABSTRACT. The back-scattered scalar field due to two parallel circular cylinders illuminated by a plane wave is approximated by a simple pair of noninteracting scattering centers. The individual scattering center fields are the geometrical optics fields from a single cylinder, which are also the first term in the asymptotic evaluation from the Kirchoff approximation. As a reference solution for model validation, an accurate numerical solution is formulated in terms of outgoing cylindrical waves emanating from each cylinder. Dirichlet boundary conditions are enforced on each cylindrical surface. Graf's addition theorem for cylindrical harmonics enables the closed-form evaluation of the coefficients in two infinite, coupled sets of linear equations for the unknown modal coefficients. An inverse Fourier transformation to the time domain is used to calculate the aspect dependent signature of this coupled pair of cylinders. The time domain excitation is taken to be a Gaussian signal of effective duration less than the propagation time for a cylinder diameter, resulting in the "smoothed pulse" response functions.

I. PHYSICAL SCATTERING CENTER MODEL FOR BACKSCATTER

The one-term asymptotic ($ka \to \infty$) expression for the specular reflection back toward the source from a single soft cylinder is derived by geometrical optics or by the stationary phase evaluation of the physical optics (Kirchoff) integral. This specular reflection, expressed in a coordinate system centered on the cylinder of radius a, is

$$\psi_{bs}^{\text{cyl}} = -\sqrt{\frac{a}{2\rho}}e^{ik\rho}e^{-i2ka}. \tag{1}$$

This work was supported by the MICOM Research, Development, and Engineering Center (Dr. C. Ray Smith) under the auspices of the U.S. Army Research Office Scientific Services Program administered by Battelle (Delivery Order 2332, Contract No. DAAL03-86-D-0001).

Phase reference for the incident wave of unit amplitude is at the origin. The phase factor $\exp[-i2ka]$ is interpreted as the shortening of the round trip path length by twice the cylinder radius, since the physical reflection point is a distance a closer to the plane wave source.

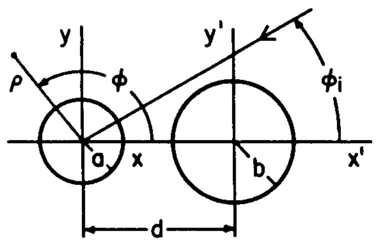

FIG. 1. Two Parallel Cylinders

The equivalent line-source scattering center could be placed at the physical reflection point on the cylinder surface, but this reflection point migrates around the cylinder circumference as ϕ_i changes. Probably the simplest scattering center model imaginable for the cylinder-pair geometry of Fig. 1 consists of two *stationary* line sources, one at the location of each cylinder center. Inclusion of on/off shadowing and the phase factor to refer the scattered field of cylinder (b) to the origin gives

$$\psi_{bs}^{sc}(\rho,\phi_i) = -\sqrt{\frac{2}{\pi k\rho}}e^{ik\rho} \cdot \frac{\sqrt{\pi}}{2}\left\{u_a(\phi_i)\sqrt{ka}e^{-i2ka} + u_b(\phi_i)\sqrt{kb}e^{-i2(kb+kd\cos\phi_i)}\right\} \quad (2)$$

for this particular scattering center model. Digital functions u_a and u_b are one or zero, depending on whether or not the reflection point of the respective cylinder is visible from the far-field location ϕ_i. From Fig. 1, the on/off function for cylinder (a) is

$$u_a(\phi_i) = \begin{cases} 1, & \sin^{-1}(\frac{b}{d}) < \phi_i < 2\pi - \sin^{-1}(\frac{b}{d}) \\ 0, & \text{otherwise} \end{cases} \quad (3)$$

and the shadowing function for cylinder (b) is

$$u_b(\phi_i) = \begin{cases} 0, & \pi - \sin^{-1}(\frac{a}{d}) < \phi_i < \pi + \sin^{-1}(\frac{a}{d}) \\ 1, & \text{otherwise}\,. \end{cases} \quad (4)$$

The multiplicative factor on the right side of (2) is written in anticipation of the cylindrical wave factor in (21). When both cylinders are fully visible, (2) is the "round-trip array factor" of a two-element scatterer, with element amplitudes determined by cylinder size.

II. Boundary Value Problem

In the two-dimensional geometry of Fig. 1, coordinate system (x, y) is centered on cylinder (a) of radius a and coordinates (x', y') are centered on cylinder (b) of radius b. The center-to-center spacing along the x-axis is d, resulting in

$$x = x' + d \qquad \text{and} \qquad y = y'. \tag{5}$$

In terms of the time-harmonic convention $\exp[-i\omega t]$, the plane wave incident from the angle ϕ_i propagates in the unit vector direction

$$\hat{s}_i = -\hat{x}\cos\phi_i - \hat{y}\sin\phi_i. \tag{6}$$

The complex phasor expression is

$$\psi_i(\vec{\rho}) = e^{ik\hat{s}_i\cdot\vec{\rho}} \tag{7}$$

for this unit amplitude incident field, where the position vector to the field point in un-primed coordinates is $\vec{\rho}$. This scalar field ψ represents the $\hat{z}$-component of electric field intensity for a TM polarized electromagnetic wave. In acoustic wave studies, ψ can be taken to be the scalar pressure field.

The total field external to the cylinders of Fig. 1 is written as the sum of the incident plus scattered fields. Incident field is defined to be the field of the incident plane wave, in the absence of the cylinders (a) and (b). The scattered field is further decomposed into two parts, resulting in

$$\psi(\vec{\rho}) = \psi_i(\vec{\rho}) + \psi_a(\vec{\rho}) + \psi_b(\vec{\rho}). \tag{8}$$

Each of these three partial fields individually satisfies the scalar Helmholtz equation. The usual plane-to-cylindrical wave transformation is used to write the incident plane wave as a sum of cylindrical eigenfunctions of the Helmholtz equation:

$$\psi_i(\rho, \phi) = e^{-ik\rho\cos(\phi-\phi_i)} = \sum_{n=-\infty}^{\infty} i^{-n} J_n(k\rho) e^{in(\phi-\phi_i)}. \tag{9}$$

The two components of the scattered field are expressed in forms that anticipate the application of boundary conditions and automatically satisfy the Sommerfeld radiation condition,

$$\psi_a(\rho, \phi) = \sum_{n=-\infty}^{\infty} a_n H_n^{(1)}(k\rho) e^{in\phi} \tag{10}$$

$$\psi_b(\rho', \phi') = \sum_{n=-\infty}^{\infty} b_n H_n^{(1)}(k\rho') e^{in\phi'} \tag{11}$$

in terms of unknown mode coefficients a_n and b_n.

Physical justification for these a priori functional forms is that on the circular surface of each cylinder, the equivalent surface current or layer distribution (ala potential theory) can be expressed as a complex Fourier series in the azimuthal angles ϕ and ϕ'. Note that the partial fields ψ_a and ψ_b are not interpreted as existing alone. In other words, the coefficients a_n and b_n in each series are very definitely a function of *both* cylinders.

The addition theorem [1] for cylindrical harmonics is used to express the individual wave function (mode) of each coordinate system as an infinite sum of wave functions in the other coordinate system (see also [5]–[9]):

$$H_n^{(1)}(k\rho')e^{in\phi'} = \begin{cases} \sum_{m=-\infty}^{\infty} J_{m-n}(kd)H_m^{(1)}(k\rho)e^{im\phi}, & \rho > d \\ \sum_{m=-\infty}^{\infty} H_{m-n}^{(1)}(kd)J_m(k\rho)e^{im\phi}, & \rho < d \end{cases} \tag{12}$$

$$H_n^{(1)}(k\rho)e^{in\phi} = \begin{cases} \sum_{m=-\infty}^{\infty} J_{n-m}(kd)H_m^{(1)}(k\rho')e^{im\phi'}, & \rho' > d \\ \sum_{m=-\infty}^{\infty} H_{n-m}^{(1)}(kd)J_m(k\rho')e^{im\phi'}, & \rho' < d \end{cases} . \tag{13}$$

The Dirichlet boundary condition satisfied on the surface of each soft cylinder is the vanishing of the total field

$$\psi(\rho = a, \phi) = 0 \quad ; 0 \le \phi \le 2\pi \tag{14}$$

$$\psi(\rho' = b, \phi') = 0 \quad ; 0 \le \phi' \le 2\pi. \tag{15}$$

Orthogonality of the $\exp[im\phi]$ functions over each circular boundary results in the pair of infinite, linear, coupled algebraic equations

$$a_p \quad + \quad \frac{J_p(ka)}{H_p^{(1)}(ka)} \sum_{n=-\infty}^{\infty} b_n H_{p-n}^{(1)}(kd) = -i^{-p} \frac{J_p(ka)}{H_p^{(1)}(ka)} e^{-ip\phi_i} \tag{16}$$

$$\frac{J_p(kb)}{H_p^{(1)}(kb)} \sum_{n=-\infty}^{\infty} a_n H_{n-p}^{(1)}(kd) \quad + \quad b_p = -i^{-p} \frac{J_p(kb)}{H_p^{(1)}(kb)} e^{-ip\phi_i}\, e^{-ikd\cos\phi_i} \tag{17}$$

$$\text{with} \qquad p = 0, \pm 1, \pm 2, \ldots . \tag{18}$$

Note that all coefficients in the above are finite for all real non-zero values of ka and kb, since there are no real zeros of the Hankel function. Furthermore, in the case where $J_p(ka) = 0$, then the coefficient $a_p = 0$ and similarly, if $J_p(kb) = 0$, then $b_p = 0$.

Infinite equations (16) and (17) are simply truncated at $|n| = |p| = N$, resulting in a pair of coupled matrix equations

$$[a] + [X][b] = [c] \tag{19}$$

$$[Y][a] + [b] = [d]. \tag{20}$$

The continuous surface layer distributions represented by Fourier series (10) and (11), evaluated on the *smooth* surfaces $\rho = a$ and $\rho' = b$, respectively, are necessarily uniformly convergent, indicating that any "relative convergence" [2] phenomena should not be too serious.

The principal asymptotic form of the Hankel function is used to evaluate the far scattered field as the sum of (10) and (11) as $k\rho \to \infty$:

$$\psi_s(\rho, \phi) = \sqrt{\frac{2}{\pi k \rho}} e^{-i\pi/4} e^{ik\rho} \sum_{n=-N}^{N} \left[a_n(\phi_i) + e^{-ikd\cos\phi} b_n(\phi_i)\right] (-i)^n e^{in\phi}. \tag{21}$$

The functional dependence upon incidence angle ϕ_i of the coefficients a_n and b_n is explicitly shown as a reminder that the set of linear equations (16) and (17) must be solved for each ϕ_i of interest.

III. Smoothed Pulse Response of Cylinder Pair

The transient signature of the soft cylinder pair of Fig. 1 is computed via the FFT algorithm applied to the frequency domain result of section II. Incident Gaussian waveform is

$$\Psi_{0i}(t) = \exp\left\{-\beta\left(\frac{ct}{b}\right)^2\right\} \tag{22}$$

in terms of the pulse-width parameter β. The three time-domain signatures of Figs. 2–4 are all computed for $\beta = 10$; that is the effective duration of the incident pulse is less than the time for a free-space wave to propagate a distance b.

Normalized space-time coordinate $(ct - \rho)/b$ is used as the abscissa in Figs. 2–4, where 0 is the value at which a reflection occurs at ρ due to a scattering center at the $x - y$ coordinate origin. This $x - y$ origin of Fig. 1 is at the center of cylinder (a) on the left. Therefore, when viewed from the aspect angle $\phi_i = 0$ (Fig. 2), the initial, specular flash from cylinder (b) occurs at the space-time value -10. Recall that one unit is the time for the wave to propagate a distance b. The reflection point of (b) is a distance of $d + b = 5b$ closer (hence the minus sign) to the source than the origin. Round-trip path length doubles the -5 to yield the -10. Even though cylinder (a) is half the size of cylinder (b) and is completely shadowed (in the geometrical optics sense) from any direct illumination, there is a small reflection off of cylinder (a) at $(ct - \rho)/b = -1$. A small reflection in Fig. 2 that occurs in the neighborhood of

$(ct-\rho)/b \approx 5$ is likely due to a triple bounce between the two cylinders. The pulse widths of successively higher order bounces are wider owing to the dispersion caused by interaction of wavefronts with the diffracting surfaces. It is plausible that this dispersion is a function of surface curvature and polarization (boundary condition). All single bounce, specular reflections presented here are negative, as required by the Dirichlet boundary condition.

When this cylinder-pair is illuminated from an aspect angle of $\phi_i = \pi$, the transient signature of Fig. 4 is scattered back to the source. The initial flash in Fig. 4 is smaller than the initial flash in Fig. 2 approximately by the factor $1/\sqrt{2}$, as predicted by the individual element factors of the scattering center model of (2). Smaller cylinder (a) cannot shield as effectively as its larger partner (b), and so the second flash from cylinder (b) in Fig. 4 is considerably stronger than the second flash from cylinder (a) in Fig. 2. The intermediate aspect angle represented by Fig. 3 exhibits a strong positive double reflection plus additional wave shapes caused by the strong interaction (multiple bounces) between the coupled cylinders.

All transient reflections in this paper are calculated for a two-dimensional scatterer, and therefore exhibit the trailing tail or wake of the time-domain Green's function in $\mathbb{R}^2$ [3] and [4]. This tail is an artifact of the infinite two-dimensional geometry, and is not present in the signatures of three-dimensional targets.

The dashed curve in each of Figs. 2–4 is the transient response of the two-element scattering center model. Inverse Fourier transformation of the frequency domain expression (2) results in a Dirac delta function representation of the specular flash from each visible cylinder

$$\Psi_{bs}^{sc}(\rho,\phi_i,t) = \\ -\frac{1}{\sqrt{2}\rho}\left\{\sqrt{a}u_a(\phi_i)\,\delta\left(t-\frac{\rho-2a}{c}\right)+\sqrt{b}u_b(\phi_i)\,\delta\left(t-\frac{\rho-2(b+d\cos\phi_i)}{c}\right)\right\}, \tag{23}$$

which upon convolution with the incident Gaussian pulse (22), yields delayed Gaussian signals.

Summary and Conclusions

A simple, two-element scattering center model for a pair of coupled soft cylinders is heuristically assembled from the asymptotic physics of the isolated soft cylinder. Resultant backscatter signatures are contrasted with accurate time domain data from a Fourier transformation of the convergent solution to the real boundary value problem. Some combinations of cylinder geometries (cylinder radii and separation), excitation aspect angle, and waveform (spectrum) are modeled reasonably well by the very simple "scatter array factor." In other instances, when the coupling or

multiple bouncing between the individual scatterers makes substantial contributions to the backscatter, the electromagnetic modeling performance of the approximation is highly deficient. Performance of this and other scattering center models remains to be tested as part of an actual target identification algorithm. Availability of the accurate signatures developed in the present research is an asset for the testing of target identification schemes.

REFERENCES

1. W.C. Chew, *Waves and Fields in Inhomogeneous Media*, Van Nostrand Reinhold, New York, 1990, p. 591.
2. M. Leroy, *On the Convergence of Numerical Results in Modal Analysis*, IEEE Trans. Antennas Propagat. **AP-31** (1983), 655–659.
3. E. Zauderer, *Partial Differential Equations of Applied Mathematics*, Second Edition, Wiley, New York, 1989, pp. 277–278, 475.
4. P.M. Morse and H. Feshback, *Methods of Theoretical Physics*, Part I, McGraw-Hill, New York, 1953, pp. 687, 842.
5. J.W. Young and J.C. Bertrand, *Multiple Scattering by Two Cylinders*, J. Acoust. Soc. Am. **58** (1975), 1190–1195.
6. G.O. Olaofe, *Scattering by Two Cylinders*, Radio Science **5** (1970), 1351–1360.
7. A.Z. Elsherbeni and M. Hamid, *Scattering by Parallel Conducting Circular Cylinders*, IEEE Trans. Antennas Propagat. **AP-35** (1987), 355–358.
8. C. Liang and Y.T. Lo, *Scattering by Two Spheres*, Radio Science **2** (1967), 1481–1495.
9. Ye. A. Ivanov, *Diffraction of Electromagnetic Waves on Two Bodies*, Translated as NASA TT F-597, Nauka i Tekhnika, Minsk, 1968.

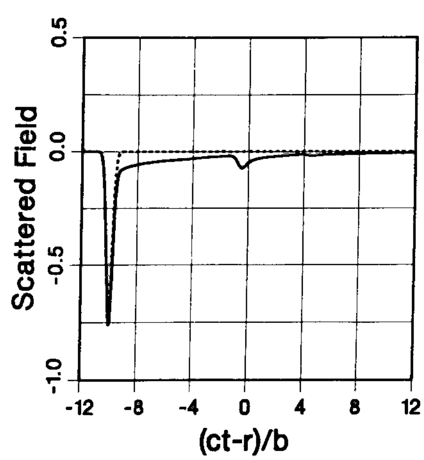

FIG. 2. Smoothed Pulse Response of Soft Cylinder Pair: $\phi_i = 0$, $\beta = 10$, $a/b = 1/2$, $d/b = 4$ (solid–accurate; dashed–2 scattering centers)

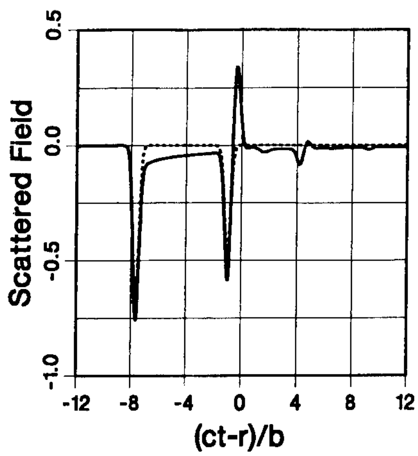

FIG. 3. Smoothed Pulse Response of Soft Cylinder Pair: $\phi_i = \pi/4$, $\beta = 10$, $a/b = 1/2$, $d/b = 4$ (solid–accurate; dashed–2 scattering centers)

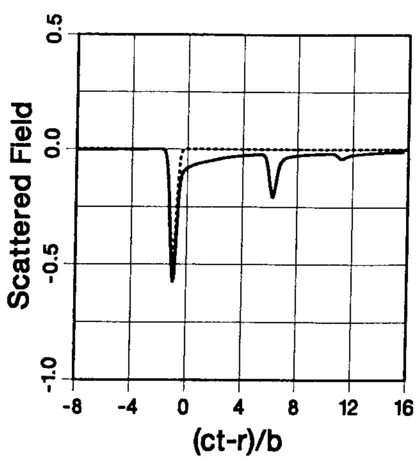

FIG. 4. Smoothed Pulse Response of Soft Cylinder Pair: $\phi_i = \pi$, $\beta = 10$, $a/b = 1/2$, $d/b = 4$ (solid–accurate; dashed–2 scattering centers)

Time and Frequency Domain Evaluation of Asymptotic Methods for Computing the Electromagnetic Scattering From Jet Engines[1]

Dennis J. Andersh, Jeffrey L. Fath, Andrew J. Terzuoli, Jr.
School of Engineering
Air Force Institute of Technology
Wright-Patterson AFB, Ohio 45433

Abstract

For several reasons, jet engines are important high frequency electromagnetic scatterers that require special attention. For example, several new military airplanes require a reduced radar cross section to improve mission survivability, and conversely, there is a desire to detect and identify airborne targets using noncooperative means such as radar. To fully understand the electromagnetic scattering by, and evaluate a particular design of an aircraft engine, sophisticated analysis tools or extensive measurements of full and/or scale models are required. Measurements, however, are expensive, time consuming, and are only valid over a limited range of frequencies and aspect angles. For these reasons, it is advantageous to be able to analytically model the electromagnetic scattering from engines using numerical techniques. This paper documents a procedure for validation, and the results from the evaluation of some of the existing high frequency electromagnetic scattering prediction codes for jet engines in the time and frequency domains. In particular, the hybrid asymptotic modal techniques, and "shooting and bouncing ray" techniques developed at The Ohio State University and the University of Illinois are evaluated.

I. Introduction

The jet engine depicted in Figures 1 is a more complex geometry than a simple cylinder terminated with a flat shorting plate. A simple accurate numerical method is required to predict the electromagnetic scattering from jet engines to enhance the design process of jet engines and predict, in near real time, a radar signature for detection and identification purposes. Given that the engine return is one of the major contributors to an aircraft's overall radar cross section (RCS) each aircraft type will have a unique signature based upon the engine cavity return [1]. This is true for nose-on aspect angles as well as tail on aspect angles. The tail-on aspect is often neglected because it is difficult to predict the radar signatures since the exhaust geometries contain rough surfaces, jagged edges and dynamic control surfaces. These requirements are the motivation for this paper.

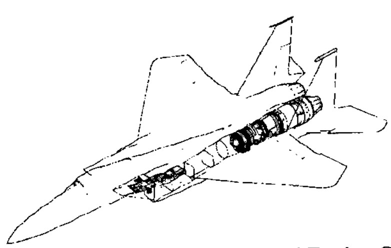

Figure 1. Diagram of F-15 Jet Engine Duct and Engine Compartment [2].

[1] This work was sponsored by the U. S. Air Force Wright Laboratory, Avionics Directorate, Mission Avionics Division, Target Recognition Branch.

II. Engine Cavity Problem Definition

The total high frequency approximated backscattered electric field strength of an engine is defined as [3]:

$$\vec{E}_{scat} = \vec{E}_{rim} + \vec{E}_{cav} + \vec{E}_{ext} \tag{1}$$

where $\vec{E}_{scat}$ is the total backscattered electric field strength (V/m), $\vec{E}_{rim}$ is the scattered electric field due to the cavity rim (V/m), $\vec{E}_{cav}$ is the scattered electric field due to the cavity (V/m), and $\vec{E}_{ext}$ is the scattered electric field from the cavity exterior (V/m).

The rim scattering $\vec{E}_{rim}$ is generally found by using the equivalent current method combined with GTD or PTD. The exterior scattered field $\vec{E}_{scat}$ resulting from the engine housing is generally dominate beyond about 70° off axial incidence and is generally calculated using PO and PTD. Most engine cavity prediction codes do not include the exterior scattered field and are only valid from 0° to approximately 70°. The cavity exterior calculations are generally accomplished with a full aircraft scattering code [3].

The cavity scattered electric field $\vec{E}_{cav}$ is calculated by several methods. Integral techniques are used in the low frequency regime where the engine cavity opening dimensions are about a wavelength or less. The method of moments, finite elements and finite difference techniques are some of the available low frequency analysis techniques.

High frequency techniques, the primary focus of this paper, are applicable when the engine cavity opening dimensions are several wavelengths large. There are several high frequency analytical techniques available for analyzing the electromagnetic scattering from engine inlet and exhaust ducts. The existing techniques are grouped into three basic categories: ray techniques, modal techniques, and hybrid techniques.

A. Ray Techniques. The predominate ray method used for calculating the RCS of a cavity is called the shooting and bouncing rays (SBR) technique. This technique is based on shooting a dense grid (5 to 15 rays/λ) of parallel geometric optic (GO) rays into a cavity. The rays, representing a plane wave, enter the cavity opening and are then traced through the opening bouncing along the cavity walls, reflecting from the engine cavity termination and finally exiting at the cavity opening. As the rays exit the cavity, the individual ray contributions to the backscattered field are found by summing all the rays incident at a specific observation point. A variant of this technique is to calculate an equivalent backscattered field at the opening of the cavity using Kirchoff's approximation. Either technique predicts the total backscattered aperture field from the cavity opening and the radar cross section (RCS) of the cavity [4].

B. Modal Techniques. Waveguide modal analysis provides an exact representation of the field interaction in smooth simple cylindrical and rectangular cavities. The backscattered fields are determined by expanding all the known active modes in a cavity geometry. For high frequencies, this may consist of several hundred modes. The incident field on the cavity is expanded as propagation modes into the cavity. The total field at the cavity entrance is then equal to the modes incident on the cavity and those modes reflected by the cavity. Given the total field, the backscattered fields were then calculated using the Stratton-Chu integral formulation performed by Witt and described by Moll [5].

C. Hybrid Techniques. This hybrid asymptotic modal method combines the modal solutions with the asymptotic methods of geometrical theory of diffraction (GTD), uniform theory of diffraction (UTD), physical theory of diffraction (PTD), and the equivalent current method (ECM) [6]. The combination of these methods is accomplished by a generalized scattering matrix. The modal solution defines the electromagnetic scattering for the separable waveguide sections and the asymptotic methods are used to calculate the diffractions from the junctions of the separable waveguide sections [6] Other hybrid techniques are described in an article by Pathak [3].

III. Codes Evaluated

This research evaluated current theoretical electromagnetic scattering prediction codes, summarized in Table 1, using primitive engine ducts and various fan blade configurations. The codes were evaluated by comparing simple primitive geometry results to existing exact theoretical

models and experimental data. The evaluation of complex geometries was made with comparisons of one code to another. The accuracy analysis of each of these codes was done for temporal, spatial and spectral signatures of primitive and complex geometries.

Table 1. Computer Simulation Codes Analyzed

CODE NAME AND TYPE	CODE DEVELOPER	APPLICABILITY
LARGECIRC Hybrid Asymptotic Modal	Ohio State University Columbus Ohio	Uncoated Circular ducts with flat plate and blade like terminations for diameters < 9.6λ
SBR Single Frequency Domain Ray Tracing	University of Illinois Champaign Urbana Illinois	Straight circular uncoated ducts with flat plate terminations
SBRI Single Frequency Domain Ray Tracing	University of Illinois Champaign Urbana Illinois	All classes of rectangular and circular ducts with flat plate terminations
JET Time Domain Ray Tracing	General Dynamics Pomona California	All classes of circular coated and uncoated ducts with blade like terminations
XTUBE Multiple Frequency Domain Ray Tracing	University of Illinois Champaign Urbana Illinois	All classes of rectangular and circular coated and uncoated ducts with flat plate terminations
MCCW & CYLSC Hybrid Asymptotic Modal	University of Texas Austin Texas University of Illinois Champaign Urbana Illinois	Uncoated circular ducts with flat plate terminations with no limitations
WG4 Hybrid Asymptotic Modal	Ohio State University Columbus Ohio	Uncoated and coated rectangular ducts with flat plate terminations for duct opening areas < 100λ^2
GRE Single Frequency Domain Ray Tracing	Ohio State University Columbus Ohio	All classes of rectangular coated and uncoated ducts with flat plate and actual fan blade terminations terminations

IV. Limitations

This research used existing measured frequency domain data for the comparisons to predicted results. While the measured data has been reported in several reports [6,7] this author cannot verify 100% that the data is accurate for all situations. The validation frequency range was 8 to 12 gigahertz (GHz) with the primary emphasis at 10 GHz. The accuracys of these predications are based on comparative results from the SUN™ workstation even though some codes were developed on a VAX™ and subsequently ported to the SUN™.

The hybrid asymptotic modal solutions were used for validation of primitive shapes when measured data was not available. For complex non-separable geometries where a modal solution was not possible, SBRI, GRE, and XTUBE were used as the comparative baseline.

The results beyond approximately 70°, off-axial incidence of the engine opening, do not properly reflect the external scattering from the engine duct.

V. Frequency Domain Results

The hybrid asymptotic modal solution was used as a truth baseline for comparison to the ray method results. Figure 2 is a comparison of the hybrid asymptotic modal results versus OSU measured data [7]. As Figure 2 clearly illustrates, the hybrid asymptotic modal solution and the measured data agree very well.

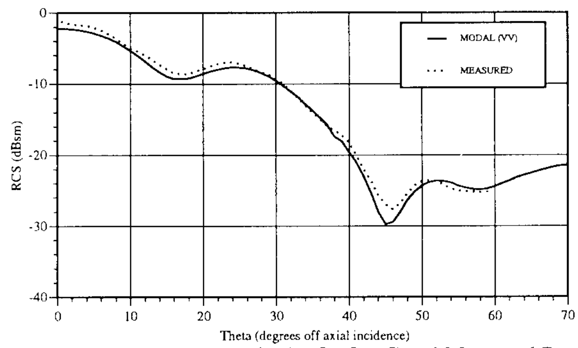

Figure 2. Comparison of LARGECIRC and Measured Data for a Cylindrical Duct Terminated with a Short, f = 10 GHz, VV Pol, $\phi = 0°$, d = 3.92 in, L = 20 in

A. Circular Disk Result. The next test used a larger circular flat plate that more closely approximated the dimensions of an actual engine face. This disk geometry was approximated by shrinking the duct length to 1 μm. As Figure 3 illustrates, the SBR and SBRI techniques perform fairly well at approximating the PO solution for a flat plate.

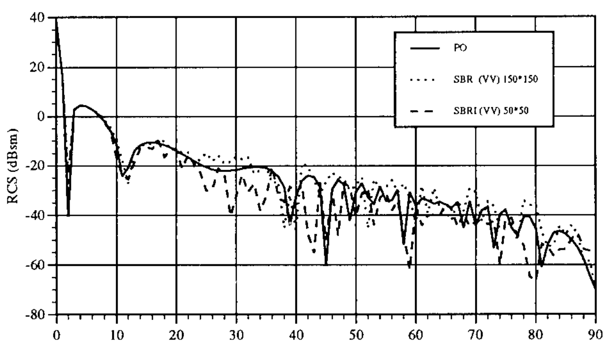

Figure 3. Comparison of SBR and SBRI using Different Ray Densities with PO Solution for a Circular Flat Plate, f = 10 GHz, VV Pol, $\phi = 0°$, d = 37.795 in

Neither SBR, nor SBRI includes diffraction calculations, therefore, neither of these techniques will predict the exact solution off broadside incidence, where the dominant scattering mechanism is edge diffraction. However, the ray methods should approximate the PO solution fairly accurately as is shown in Figure 3. To predict the edge scattering, either the physical theory of diffraction

(PTD), the geometric theory of diffraction (GTD) or the uniform theory of diffraction (UTD) must be used to account for the edge diffracted fields.

B. Small Cylindrical Duct Results. The next sets of results were for a small cylindrical duct. Even though ray methods are only valid for ducts with an opening diameter >10λ the smaller ducts are excellent test cases to evaluate the general RCS trends and because the computation time is significantly faster. The decreasing JET RCS trend demonstrated in Figure 4 was determined to be caused by the improper calculation of the geometric optic divergence factor for curved surfaces.

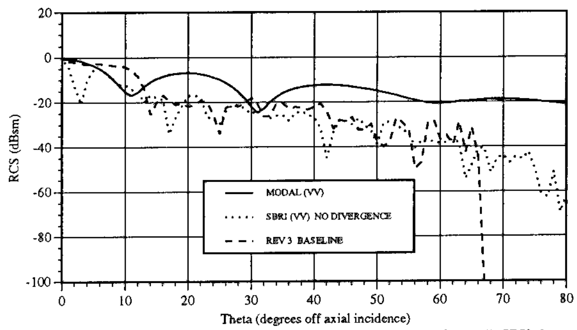

Figure 4. Comparison of JET REV3 and SBRI Without the Divergence Factor against LARGECIRC for a Shorted Cylindrical Duct, f = 10 GHz, VV Pol, $\phi = 0°$, d = 3.92 in, L = 20 in

The divergence factor for SBRI is calculated at each bounce point. In JET, the divergence factor is only determined by the calculating the exiting ray tube solid angle as the ray tube exits the duct. Inclusion of the divergence factor for cured surface produces the improved results in Figure 5.

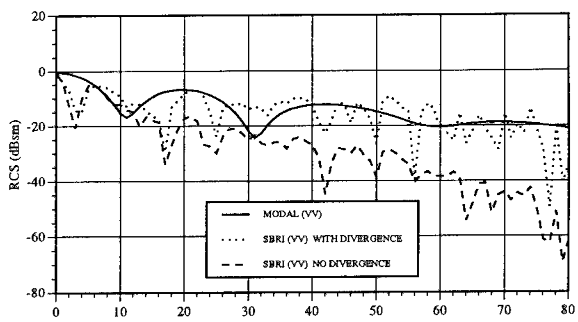

Figure 5. Comparison of SBRI With and Without the Divergence Factor against LARGECIRC for a Shorted Cylindrical Duct, f = 10 GHz, VV Pol, $\phi = 0°$, d = 3.92 in, L = 20 in

As shown in Figure 6, similar results are obtained for larger ducts. Most cavity ray tracing codes do not account for the ray tube divergence factor at each bounce point, but as illustrated here it significantly affects the RCS amplitude. While this factor is very pronounced in the cylindrical duct, similar errors are not expected in a rectangular duct because there is no curvature to the rectangular duct surface.

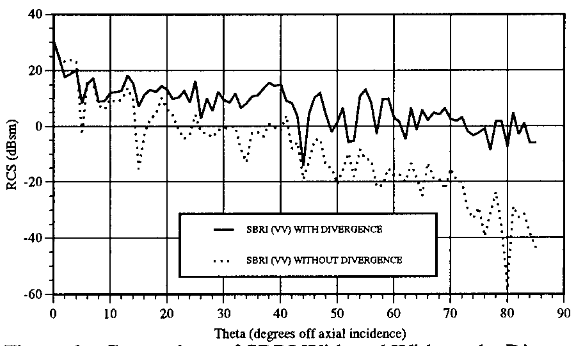

Figure 6. Comparison of SBRI With and Without the Divergence Factor against LARGECIRC for a Shorted Cylindrical Duct, f = 10 GHz, VV Pol, $\phi = 0°$, d = 23.622 in, L = 177.17 in

C. Large Duct Results. The results shown in Figure 7, illustrate that the ray methods are capable of predicting a very accurate RCS estimate from 0° to 40° for ducts with openings dimensions greater than 20λ.

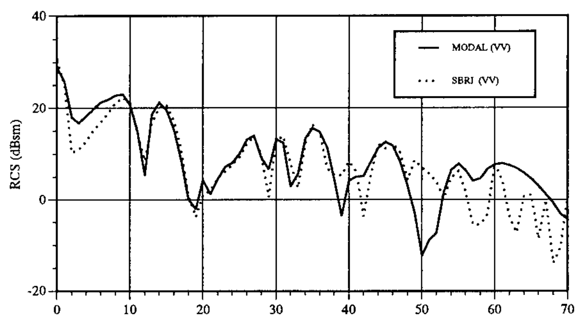

Figure 7. Comparison of SBRI with CYLSC for a Shorted Cylindrical Duct, f = 10 GHz, VV Pol, $\phi = 0°$, d = 23.622 in, L = 70.866 in

The next geometry tested was for a rectangular duct. Figure 8 shows that the results for the GRE method agree with the asymptotic modal solution very well. In comparing the SBRI results to the GRE results it shows that the GRE produces more exact results as compared to the modal solution at 0° incidence as well as other aspect angles. This is because GRE inherently includes the rim diffraction where JET and SBRI do not.

VI. Time domain Results

The next series of test results are inverse FFT results for 2^n frequency domain RCS calculations using the program XTUBE developed by the University of Illinois. The frequency domain RCS values were calculated over a band of 8 -12 GHz and then inverse FFT'd to the time domain. A comparison of the MCCW modal results to the XTUBE results are also provided in Figure 9.

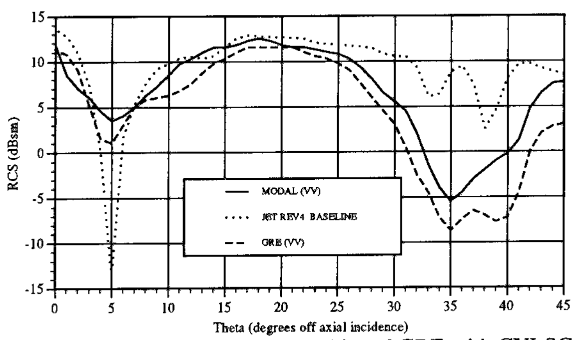

Figure 8. Comparison of JET REV4, and GRE with CYLSC for a Shorted Rectangular Duct, f = 10 GHz, VV Pol, $\phi = 90°$, H = 0.18 m, L = 0.6m, W= 0.24 m

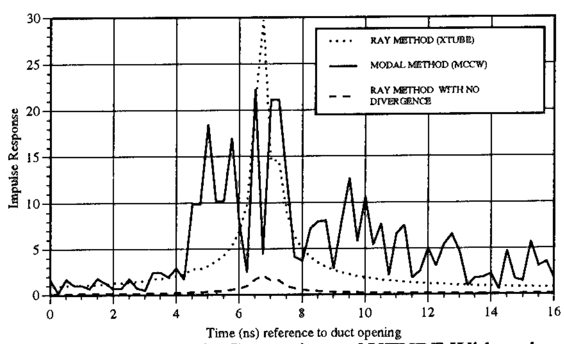

Figure 9. Time Domain Comparison of XTUBE With and Without Divergence against MCCW for a Shorted Cylindrical Duct, VV Pol, $\phi = 0°$, incident $\theta = 60°$, d = 3.92 in, L = 20 in

The XTUBE results in Figure 9 with and without the divergence factor again illustrate the effect on the amplitude for this time domain signature. The location of this time domain pulse is defined by the length of the geometry multiplied by (2/cos θ). The estimated propagation time round trip time through the duct for axial incidence is approximately 6.7 ns. This is the approximate time delay predicted by XTUBE, and MCCW.

Another feature depicted in Figure 9 is the spreading out of the modal time domain response beyond approximately 40°. This is due to the excitation of higher order modes in the duct at large aspect angles off axial incidence. These modes are not exited near axial incidence. They are excited as the energy propagation in the duct changes from a pure modal or ray energy tube at axial incidence to a dispersive propagation tube path at broad aspect angles.

VII. Conclusions

The ray methods are an excellent first order approximation to the RCS and resultant radar signature for engine ducts. Given that the ray methods are applicable to a wide range of geometries, they appear to be the best all purpose method to predict the radar signature of engine ducts at this time. There are deficiencies in the prediction accuracy using ray methods that must be

ducts at this time. There are deficiencies in the prediction accuracy using ray methods that must be considered when this method is used for calculating the RCS or radar signature of engine ducts. As discussed in this paper, the ray methods cannot predict the absolute amplitude and waveshape of the radar signature of engine ducts for four reasons. First, the ray method results for duct diameters smaller than 20λ typically have large peaks and valleys that perturb the time and frequency domain amplitude. Second, the rim diffraction and proper scattering from a complex engine face have not been incorporated in a general purpose computer code. The third reason is that the ray methods have problems in predicting the correct response at caustics. Finally, the ray propagation inside the duct is purely based on the geometric optics theory that does not include the diffraction effects. Over a long duct and/or a wide incidence angle, the diffraction effect on the propagation may be important. This effect was illustrated in the time domain results by the spreading out of the time domain signatures at broad aspect angles.

An evaluation methodology of computer simulation codes was an outgrowth of this research. As was demonstrated that if computer simulation codes are not capable of predicting the response of simple geometries there is no possibility of being able to predict the correct response of ducts for complex geometries. Although, the ability to predict the correct response for simple ducts is no guarantee that the correct response is being predicted for complex geometries.

To validate the complex geometries requires either full scale measurements or scale model measurements. This is mandatory in evaluation of different RCS prediction techniques. The general process should begin with simple geometries and gradually increase to more complex ones, using measurements as a baseline for all phases of the code performance evaluation. The use of full scale complex geometries, as the initial validation, is not a sound scientific process. Without the progression of analysis outlined here, the signature synthesis effort is doomed for failure.

References

[1] E. Heyman, G. Friedlander and L. Felsen, "Ray-Mode Analysis of Complex Resonances of an Open Cavity," *Proceedings of the IEEE,* vol 77: pp. 780-787, May 1989.

[2] R. E. Ball, *The Fundamentals of Aircraft Combat Survivability Analysis and Design,* New York: AIAA Education Series, 1985.

[3] P. H. Pathak and R. J. Burkholder, "High-Frequency Electromagnetic Scattering by Open-ended Waveguide Cavities," *Radio Science,* vol. 26, pp. 211-218, Jan-Feb. 1991.

[4] H. Ling, R. Chou, and S. W. Lee, "Shooting and Bouncing Rays: Calculating the RCS of an Arbitrarily Shaped Cavity," *IEEE Transactions on Antennas and Propagation,* vol. 37, pp. 194-205, Feb. 1989.

[5] J. W. Moll and R. G. Seecamp, "Calculation of Radar Reflecting Properties of Jet Engine Intakes Using a Waveguide Model," *IEEE Transactions on Aerospace and Electronic Systems,* vol. 6, pp. 675-683, Sept. 1970.

[6] R. J. Burkholder and P. H. Pathak, "High-Frequency Asymptotic Methods for Analyzing the EM Scattering by Open-Ended Waveguide Cavities," Technical Report TR 719630-3. ElectroScience Laboratory, The Ohio State University, Columbus OH, Sept. 1989, NASA-CR-186244 (N90-16103).

[7] P. H. Pathak, C. W. Chuang, and M. C. Liang, "Inlet Modeling Studies," Technical Report TR 717674-1. ElectroScience Laboratory, The Ohio State University, Columbus OH, Oct. 1986, (AD-A222908).

SESSION 4- "CAEME"

Moderator: Magdy Iskander

REFLECTIONS ON THE FIRST CAEME BOOK AND A DESCRIPTION OF FUTURE DIRECTIONS

Magdy F. Iskander
Electrical Engineering Department
University of Utah
Salt Lake City, UT 84112

Abstract

The NSF/IEEE Center for Computer Applications in Electromagnetics Education (CAEME) has been in operation for two years. It funded 19 software development projects, organized several workshops and special sessions, and recently published its first book that includes diskettes and videos of the developed software. This paper provides an overview of the CAEME software book and describes avenues for its use in classroom teaching. Specific examples of the use of modern technologies such as interactive video to help integrate the developed software in electromagnetics curriculum will be described. Remaining challenges and future directions in areas of additional software developments, fundraising, and dissemination of the Center's products are also discussed.

I. Overview of the CAEME Software Book

The CAEME book contains 17 chapters that provide broad coverage of an introductory course in electromagnetics. Table 1 lists the contents of the CAEME book while Table 2 lists universities whose faculty contributed to the book. From Table 1 it may be seen that

1. The book provides broad and comprehensive coverage of an introductory course in electromagnetics. Topics covered range from fundamentals of electromagnetics, including vector differential and integral operations, to undergraduate senior-level-type topics such as waveguides, antennas, and numerical techniques.

2. It is important to indicate that all the software is interactive and provides simulation, problem solving, and visualization capabilities that may be exciting and motivating to students.

3. Many of the software packages contain tutorials and adequate input/output interfaces.

Copies of the CAEME book are available to ACES members at cost [1].

II. Integration of Developed Software in Electromagnetics Curriculum

The availability of this extensive collection of software for introductory electromagnetics, however, raises the following interesting questions:

1. Would undergraduate students be able to fully understand underlying physical principles independently and just by running the software?

2. What are the most adequate modalities for integrating this software in electromagnetics curriculum and classroom teaching?

Table 1. Table of Contents.

Table 2. List of participating institutions.

Massachusetts Institute of Technology	University of California, Davis
Naval Postgraduate School	University of Illinois, Urbana-Champaign
New York Institute of Technology	University of Iowa
Polytechnic University of New York	University of Mississippi
Rose-Hulman Institute of Technology	University of Utah
Syracuse University	Virginia Polytechnic Institute & State University

These are clearly difficult questions with no simple or unique answers. CAEME, however, is addressing these issues in its ongoing developments and the following are examples of the ongoing activities:

1. Development of open-ended design problems and homework assignments based on the available CAEME software. Examples of these efforts include development of quiz sessions based on a series of electrostatic simulations, design of a coupled transmission-line system with practical size, substrate properties, and maximum cross-talk requirements, and the design of a wire antenna array with a specified pattern requirement.

2. Use of interactive video applications using commercially available authoring software to develop quiz sessions, simulated laboratory experiments, and other materials for classroom teaching. In an interactive video application, students may access a video based on experimental measurements [2] or a computer-generated movie [3], or they may work with one of the available CAEME software packages. After reviewing background information and carrying out a carefully selected list of simulations, students are asked a series of questions aimed at emphasizing a specific principle. Depending on the student's answers, the interactive video application directs the student to one of several available options. For example, the student may be directed to perform additional simulations, view additional segments of a video, or continue with the quiz. At the end of the quiz session, the student's performance is evaluated and reported. CAEME has developed two such applications, and the results will be demonstrated in the presentation.

III. Additional Challenges and Future Developments

The objective of the CAEME Center is to stimulate and accelerate the use of computers and software tools to boost electromagnetics education. The Center has certainly stimulated software development by

1. Providing seed funds for software development projects at universities across the U.S.A.

2. Sponsoring and organizing workshops and special sessions in conjunction with international symposia. These forums are important for the exchange of ideas, stimulating discussion, increasing awareness of available challenges and encountered problems, and for providing a very effective forum for testing the developed software.

3. With the publication of the CAEME catalog of available software and the software book, the Center has effectively accelerated the use of computers and software tools in education. This is because with the availability of this information and the established effective mechanism for distribution, the Center has facilitated sharing, minimized duplication, and certainly helped focus future developments on software that either enhances or complements available software.

To this end, it may be concluded that the Center has certainly succeeded in achieving its objective and far exceeded its initial expectations.

There are, however, remaining challenges that need to be carefully addressed in this third year of its NSF funding. The first is technical and is related to trends in future software developments, while the second is related to the financial future of the Center and its fundraising activities. The other issue is related to the dissemination of CAEME information and products and available avenues for the CAEME faculty to publish their work. In the following, each of these issues will be discussed.

A. Future Software Developments

CAEME intends to continue support of development of new software for electromagnetics education. To help expand the CAEME software library, however, focus will be placed on supporting new software developments that complement existing applications. Examination of needs of a comprehensive introductory course in electromagnetics and the available CAEME software reveals that areas of interest for future developments include (a) simulation of EM interactions with materials, (b) simulation of some interesting EM-based applications such as xerography, optical fibers, doppler radar, etc., and (c) suitably developed software for simulating laboratory experiments and for complementing hardware experiments routinely included in microwave courses. This issue of developing software for simulating laboratory experiments has been addressed by chemical engineering colleagues in the NSF-funded center at Purdue University [4], and some aspects of their work will be reviewed in this presentation.

B. Fundraising Activities

One of CAEME's objectives is to be active and self supporting after the three-year NSF funding. The NSF grant ends in 1993, and CAEME has thus far been very successful in its fundraising efforts. To date, CAEME has five corporate sponsors including Hewlett Packard, Motorola, Lockheed, Texas Instruments, and Martin Marietta Energy Systems. In addition, both Hughes and Boeing sent representatives to the CAEME Policy Board meeting and are expected to join the Center soon. Each corporate sponsor pays a membership fee of $10,000. CAEME also has four participating societies including IEEE AP-S, IEEE MTT-S, IEEE EMC-S, and ACES. Distribution of the CAEME products, including the software book, is limited to members of the CAEME sponsoring societies and companies. Reviewing the fundraising activities of the CAEME Center, it may be seen that with the continued support from the present member corporations and technical societies, an annual income of over $70,000 is expected. This is equivalent to the NSF annual support, and it may be stated that CAEME has achieved the self-supporting status even before the end of NSF grant.

C. Dissemination of CAEME Information

An important aspect of the CAEME Center is to provide an effective mechanism for distribution of its products and also avenues for its faculty to share and cross examine their ideas and also to publish their work. As stated on many occasions, CAEME uses the NEEDHA list for distributing its products to electrical engineering departments across the U.S.A. and Canada. Regarding the exchange of ideas, presentation of faculty work, and testing of CAEME software, the Center organized several special sessions and workshops in conjunction with IEEE and ACES symposia. CAEME is also publishing a special issue of the *ACES Journal* (deadline for paper submission is April 30, 1992). The Center is also very pleased to announce the publication of a new archival journal on *Computer Applications in Engineering Education.* This new journal is to be published

by John Wiley & Sons, Inc., who also decided to provide special subscription rates for students and members of societies who are participating in the CAEME Center. The new Wiley journal will also include with each issue diskettes of educational software. This quarterly journal and the CAEME special sessions and workshops are expected to provide ample opportunities for faculty to exchange ideas and share their work with colleagues in the U.S.A. and abroad.

IV. Concluding Remarks

In this paper, features of the first CAEME software book were reviewed and avenues for enhancing its use in teaching electromagnetics were discussed. While the book provides a comprehensive software package for introductory electromagnetics, additional efforts are required to develop educational aids (homework assignments, design and simulation problems, etc.) to facilitate the use of the software in classroom teaching. The financial status of the CAEME Center was also reviewed and its successful fundraising effort was discussed. It is indicated that with the continued support from the present member corporations and societies, CAEME has successfully achieved its self-supporting status. CAEME will also publish a special issue of the *ACES Journal*, and has arranged in collaboration with John Wiley & Sons, Inc. the publication of an archival journal on *Computer Applications in Engineering Education*, to be published quarterly starting July 1992.

V. References

1. *NSF/IEEE CAEME Center Software Book*, Volume I, edited by M. F. Iskander, September 1991. The book is available from the Center at the Electrical Engineering Department, University of Utah, Salt Lake City, UT 84112.

2. M. Zahn, J. R. Melcher, and H. A. Haus, "Experimental Demonstrations for Teaching Electromagnetic Fields and Energy," Chapter 7 of the *CAEME Software Book* referenced in [1].

3. V. Cable, "Simulation of Some Basic Concepts in Electromagnetics," a video prepared by Lockheed Corporation for distribution by the CAEME Center.

4. R. G. Squires, G. V. Reklaitis, N. C. Yeh, J. F. Mosby, I. A. Karimi, and P. K. Anderson, "Purdue-Industry Computer Simulation Modules -- The Amoco Resid Hydrotreater Process," *Chemical Engineering Education*, Vol. XXV, No. 2, Spring 1991.

ROLE OF COMPUTATIONAL TOOLS IN THE LEARNING CYCLES OF A PRACTICING ENGINEER

SHASHI SANZGIRI, PHILIP B.GREEN, AND RICHARD SMITH

ANTENNA DEPARTMENT
TEXAS INSTRUMENTS INCORPORATED, McKINNEY, TEXAS

Abstract

This paper describes the role of electromagnetic computer simulation tools in the design cycle time reduction of antenna systems. The importance of computer applications in the electromagnetic education of practicing engineers is emphasized.

1. Introduction

In today's highly competitive global environment, design cycle time reduction is becoming very important. This is particularly true in today's declining defense business where more contractors are going after fewer business opportunities and profitability is key to survival. Commitment to Total Quality Management demands design cycle time reduction as part of the continuous improvement process. The key factors in design cycle time reduction are: training, availability of design tools, concurrent engineering, and a knowledge base driven by cycles of learning or experience.

This paper reviews shortcomings in today's design and learning process and how new simulation tools are being used in the industry for reducing design cycle times. The discussion is focused on the antenna system design and on electromagnetic simulation and visualization tools. As an example, use of the Transmission Line Matrix (TLM) method for design cycle time reduction of a phased array antenna element is given.

This paper also discusses the role CAEME can play in continuing education by providing electromagnetic visualization and animation tools to make wave interactions, propagation, and radiation understandable and intellectually satisfying to the various segments of engineering professionals and technicians.

2. Traditional Design and Learning Process

Most of the current design processes are serial and iterative. Figure 1 illustrates the traditional design process for antenna systems. As shown in this Figure, the fabrication and test are in the design iteration loop and no flexibility exists to eliminate design flaws before costs are incurred. Learning is a trial and error process and does not translate into well defined design rules that can be used in the next similar product design. Figure 2 illustrates the current learning process and its weak coupling to the design cycles. The dissipative medium represents the inefficient processes which lead to the gradual loss of knowledge base or design "recipes". The inefficient processes include such things as lack of documentation, lack of information storage or a retrieval facility, lack of parametric design data base, and design by word of mouth.

The key impediments in minimizing the design iterations have been lack of generalized electromagnetic solvers, common electrical and mechanical three dimensional modeling tools, fast computers, large memory and graphics work stations for interactive design, and visualization of the input and output data sets. The availability of commercial EM solvers, emergence of powerful computers using parallel processing, and a host of graphical tools are transforming today's electromagnetic engineering work environment.

3. Impact of Computational Tools in the Design and Learning Process

Computational tools facilitate concurrent engineering design and concurrent learning. The concurrent engineering includes evaluating various aspects of product performance (electrical, mechanical, environmental, producibility, reliability, installation etc.) and arriving at a design that best meets customer requirements with a minimum number of design iterations. Concurrent learning is enhanced by the use of learning aids that guide the design engineer during the design process.

Figure 3 shows a concurrent engineering design process as applied to the antenna system design. The new computational and geometric modeling tools enable this process. Three key features in this design process are:

- A common geometrical data base for mechanical and electrical performance evaluation
- Computer simulation of various subsystem level and installed antenna level performances
- Use of centralized design resource or knowledge base.

A common geometrical data base allows rapid transition from design to fabrication. We use various commercial, University developed, and in-house developed analysis software packages. The challenge has been the development of a common graphical user interface for display of the input and output data for each of the software packages. A centralized design resource is envisioned as a data base of design aids (parametric curves), visualization aids for certain electromagnetic interactions, and a collection of scattering matrices for certain building blocks such as power dividers, couplers, etc.

Figure 4 shows a concept for a centralized design resource being pursued in the Antenna Department of Texas Instruments. The electromagnetic training aids as supplied through CAEME are part of this design resource center. An engineer undertaking a new design problem, for example, can go through the applicable lessons to gain an understanding of relevant physics and behavior of the electromagnetic fields. This concurrent training, i.e., learning when you need it, we are sure, will help in the design cycle time reduction.

4. Example of a Computational Tool in the Design Cycle Reduction

Although numerous examples are available in the design cycle reduction using modern computational electromagnetic tools, a specific example is given here of how a generalized EM solver was used to analyze the radiating element performance embedded in a large phased array. The radiating element used in this application was a stripline fed flared slot (notch) element shown in Figure 5. It is well known that the input impedance of such an element in an array environment is dependent on both the frequency and beam scan angle. An experimental

approach of evaluating the input impedance consists of using a small subarray (one or more elements) in a waveguide which simulates an infinite array (image theory) and the dominant waveguide propagating mode simulates addition of two plane waves impinging on the array at angles symmetrical with respect to the array normal.

The development of moment method based code using an integral equations approach would have taken several years. Instead of developing a special code, we used a generalized EM solver based on the three dimensional TLM method. The actual waveguide simulator geometry was gridded as shown in Figure 6. It took about one month for an engineer familiar with the TLM code to develop the TLM nodes, impose appropriate boundary conditions, specify material types, and provide appropriate terminations at the two ends of the waveguide. Figure 7 shows a comparison between the measured and computed return loss of an element in a waveguide simulator as a function of frequency. It should be noted that each frequency point also corresponds to a unique scan angle. The agreement between the computed and measured data is excellent.

A traditional empirical design process would have taken more than six man-months of efforts to arrive at the phased array element design. With an electromagnetic simulation tool such as TLM, we have been able to accomplish the design in less than two man-months.

One of the advantages of the numerical electromagnetic solvers is the availability of the electric and magnetic field data over the computational domain. The display of these fields can provide valuable information on the manner in which various boundaries and materials affect the flow of the fields. Figure 8, for example, shows a four flared notch element array in which one of the elements is excited while others are terminated in 50 ohm loads. Figure 9 displays the E_x and E_y components of the field in the cross-sectional planes defined in Figure 8. The fields within the slotline and between the ground planes of the notch elements, as well as in the space between the notch elements, are shown in this Figure. The coupling between elements can be visualized by assessing the strengths of the slotline fields in the neighboring elements relative to those in the excited element. Such display of the fields in different cross-sectional planes gives the designer a new visual tool with which to manipulate the geometrical and material properties of the radiating structures to achieve the desired results.

5. Role of CAEME in the Electromagnetic Training

As a corporate sponsor of CAEME, Texas Instruments plans to work with other members of the advisory council in recommending software development projects beneficial not only in the traditional classroom, but also in the corporate engineering environment. The availability of this training software is important not only for design cycle time reduction, but in maintaining the technical currency and vitality of the engineering group. Another important benefit of the electromagnetic educational software is in exposing other members of the concurrent engineering team such as producibility, reliability, and manufacturing engineers to the basic electromagnetic concepts using visual electromagnetics.

Table 1 shows a matrix of electromagnetic training needs in an Antenna Laboratory. Training extends from simple visualization to the use of advanced design and analysis tools. The training appropriate to each segment of the engineering population is shown in this Table. In partnership with CAEME, the training aids to meet the needs of various engineering population segments will be developed and will form a part of our design resource center.

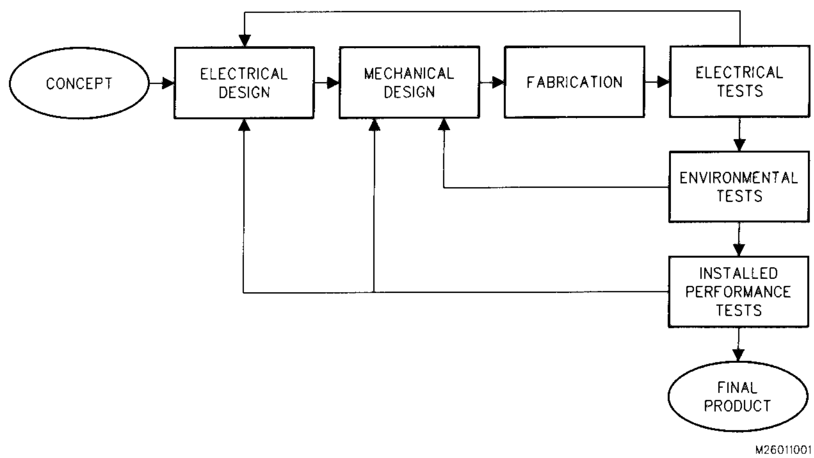

Figure 1. Conventional Design Model for Antenna Systems

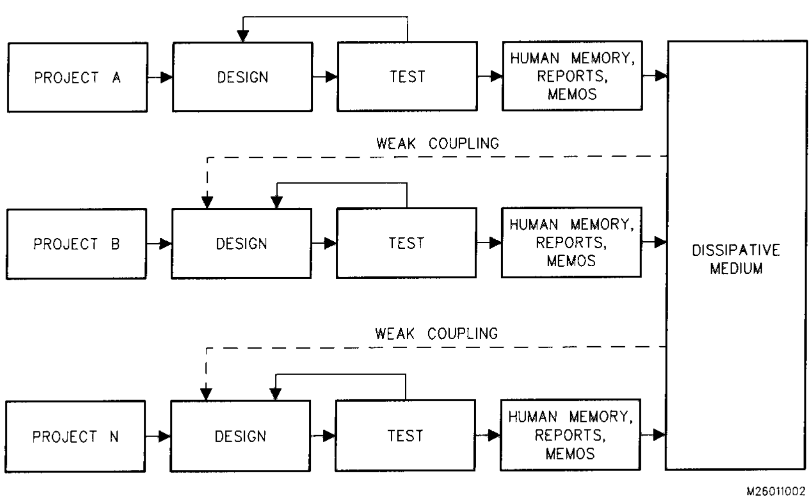

Figure 2. Conventional Learning Cycles and Coupling to the Design Process

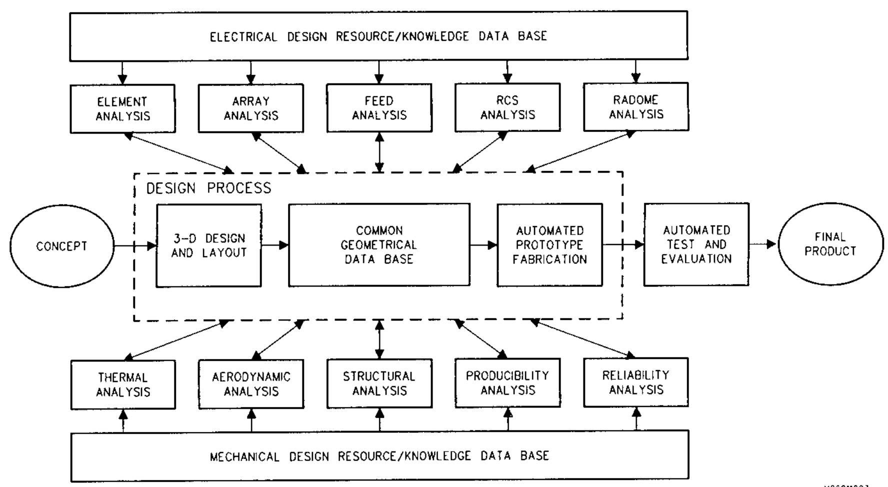

Figure 3. Desired Concurrent Design Model for Antenna Systems

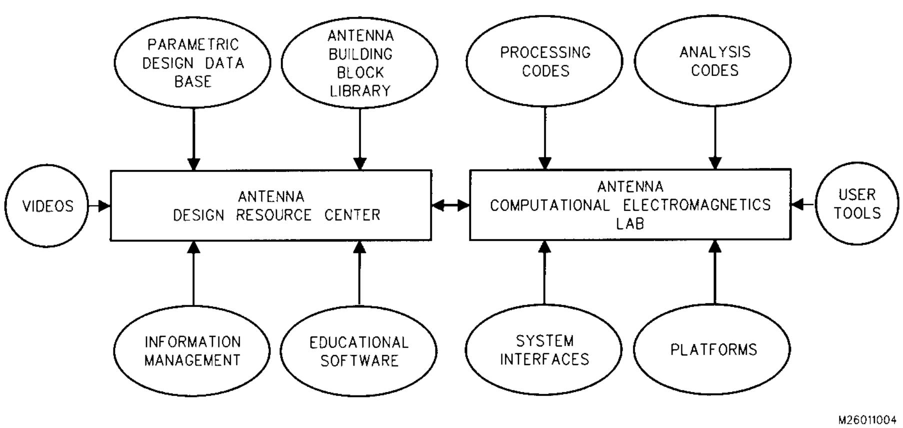

Figure 4. Future Antenna Engineering Work Environments

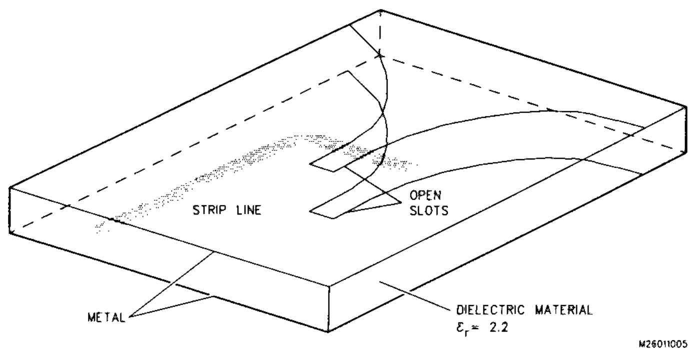

Figure 5. Stripline Fed Flared Slot Antenna Geometry

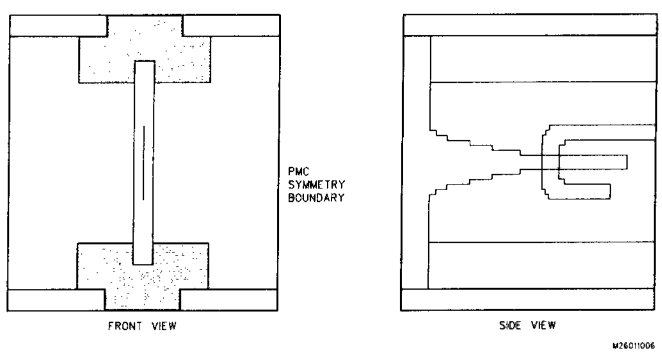

Figure 6. Element Model Geometry for TLM Analysis

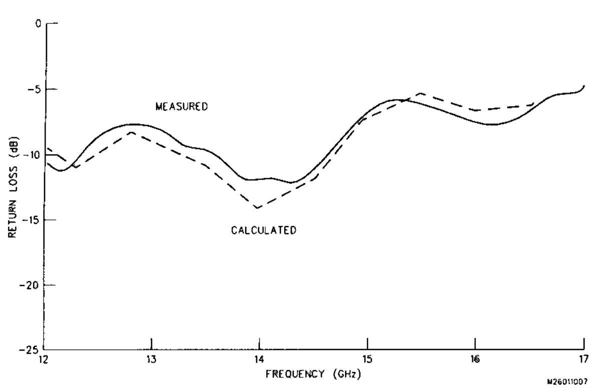

Figure 7. Comparison of Measured and Calculated Data for Notch Element in an Infinite Array Environment

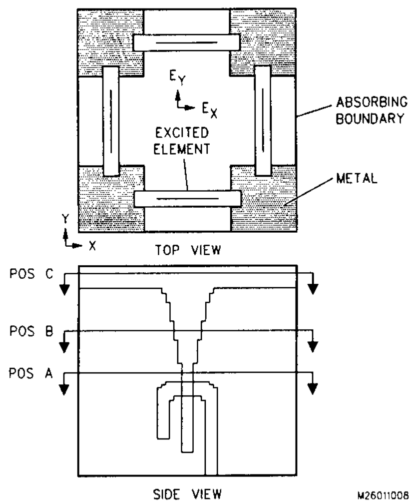

Figure 8. Four Element Array Geometry Modeled Using TLM Code to Evaluate Coupling Between Elements

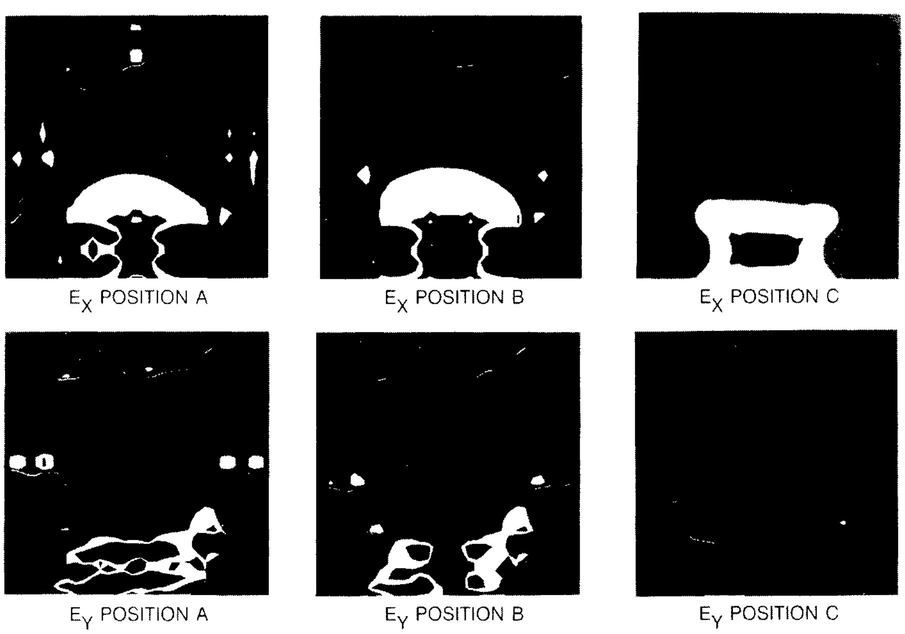

Figure 9. Electric Field Maps at Different Cross-sections Within Four Element Array Cell Shown in Figure 8

TABLE 1. ELECTROMAGNETIC TRAINING MATRIX

EM TRAINING AREA	RF TECH	SUPPORT ENGRS	JUNIOR ENGRS	SENIOR ENGRS
EM PHENOMENA UNDERSTANDING/ VISUALIZATION				
- RADIATION	X	X	X	
- GUIDED WAVE PROPAGATION	X	X	X	
- REFLECTION, DIFFRACTION AND SCATTERING	X	X	X	
- POLARIZATION	X	X	X	
RF CIRCUIT/RADIATING STRUCTURE DESIGN				
- VISUALIZATION OF FIELDS/CURRENTS ON FEED AND RADIATING ELEMENTS			X	X
- VISUALIZATION OF REFLECTION AND RADIATION AT CIRCUIT DISCONTINUITIES			X	X
- IMPEDANCE MATCHING	X		X	
- MICROWAVE NETWORK ANALYSIS			X	
- COMMERCIAL DESIGN TOOLS			X	X
- IN-HOUSE DESIGN TOOLS			X	X
RADIATION/SCATTERING ANALYSIS				
- VISUALIZATION OF COMPLEX FUNCTIONS				X
- VISUALIZATION OF DIFFERENTIAL AND INTEGRAL OPERATIONS ON VECTOR FIELDS			X	X
- VISUALIZATION OF GREEN'S FUNCTIONS				X
- VISUALIZATION OF GEODESIC PATHS				X
- MODAL ANALYSIS			X	X
- MOMENT METHODS			X	X
- GTD, PTD, UTD			X	X
- FEM, FDTD, TLM			X	X
- TRANSVERSE MODAL ANALYSIS			X	X

Simple Techniques for Effortless Desk-Top Production of Computer Movies to Help Students Visualize Time-Varying Phenomena in Electromagnetics

by

F.E. Vermeulen, F.S. Chute, and E. Sumbar

Department of Electrical Engineering
University of Alberta
Edmonton, Alberta, Canada
T6G 2G7

Abstract

The comprehension of electromagnetic phenomena requires students to develop an ability to visualize four-dimensional fields represented by vectors that depend on the spatial coordinates and time. Often the complexity of the fields makes it extremely difficult for the beginning student to correctly interpret the wide range of fundamental abstractions and principles which form the basis of time varying electromagnetism. For example, few students ever gain proper appreciation of the radial wave nature and attendant phase reversals of something supposedly as straightforward as axial current flow in a round wire at power frequencies. Nor do they readily comprehend the nature of the instantaneous electromagnetic fields in simple wave reflection problems. Using combinations of readily available software on Apple Macintosh® computers the authors have developed computer animations that effectively illustrate fundamental concepts. The production of such movies is effortless and requires only a small investment in time. The methodology, typical movie preparation, and the software and hardware requirements are discussed.

Introduction

The use of computer movies can greatly enhance classroom presentation of electromagnetic phenomena [1,2,3,4], but movies to address the full range of fundamental concepts that must be dealt with in typical electromagnetics courses are not widely available to individual instructors. This paper presents a very simple — yet flexible — approach to the preparation of computer movies. Using Apple Macintosh® computers equipped with typical office productivity and desk-top presentation software, an individual instructor can personally author a sophisticated movie and tailor it to his or her needs. A typical movie can be planned and prepared at the instructor's desk in a matter of a few hours at most, and classroom presentation will be seen to be as simple as using an overhead projector. The basic methodology for preparation and presentation of a movie, and the software and hardware requirements are discussed.

Preparation of a movie

The phenomena that are to be displayed in a movie are time-varying, though not necessarily time-harmonic. The period of time over which the phenomena are to be observed is divided into equally spaced time intervals. The objective is to choose a sufficient number of intervals so that the phenomena change only marginally from frame to frame, but not so many as to incur unnecessary labor in the preparation of additional frames. For time-harmonic phenomena, 24 frames per cycle are generally satisfactory, while the number of frames can vary widely for non-harmonic cases. One image of a phenomenon is produced for the beginning of each time interval. These images, or frames, are then recorded and played back sequentially as a movie.

For time-harmonic phenomena it is convenient to loop the sequence into an endless display. The speed at which the movie runs may be varied for optimal effect, or the movie can be advanced a single frame at a time. Such film strips, with

explanations supplied by the instructor during presentations, are generally adequate. However, several filmstrips can easily be assembled to form a completely self-explanatory composite movie with titles and equations. All the steps that are necessary to produce a movie are implemented in "off the shelf" software packages so that no intricate programming is required. Even novice computer users who have a basic familiarity with the Macintosh environment can quickly become proficient at creating their own movies.

In all cases an equation or several equations have to be established that describe the curve or surface which is characteristic of the phenomena that are to be graphically displayed, such as a distribution of field amplitude or the location of lines of force. These equations contain one or more spatial variables and time. The equations must first be evaluated at the beginning of each time interval for the coordinate locations that define the space in which the phenomenon is to be viewed. There are a number of software programs available for the Macintosh computer that can display curves and surfaces with as little effort as typing in the equation or equations. Such programs as *Matlab* [5], *Systat* [6], *Theorist* [7], and *Mathview Professional* [8] present the data in a variety of graphical formats. The images so created can be stored in the *Scrapbook*, a standard feature of the Macintosh operating system.

Alternately, spread sheet programs, such as *Microsoft Excel* [9], or user programs written in Fortran or other languages, can be used to evaluate the equations and to write tables of coordinates as text files. Raw numerical data produced in this way can be easily imported into a suitable graphing program, such as *Excel's* Chart window, *Cricket Graph* [10], or indeed into one of the programs previously mentioned, such as *Matlab* or *Systat*, where the images can be rendered and stored as before.

The approach selected is largely a matter of choosing the desired level of sophistication of the graphical output. Programs such as *Cricket Graph* provide elaborate 2-D graphics with control of axes, labelling, line width, font and so on, but

cannot be used in the numerical evaluation of the equations. On the other hand, programs such as *Matlab* provide basic 2D and 3D images, but with little editing control of the images.

The final assembly of images into film strips can be achieved with any one of a number of animation programs [11]. The authors have found *Video Works II* [12] entirely satisfactory (Macromind, Inc., makers of *Video Works II,* have a more powerful program called *Director*). It is extremely easy to use and incorporate a basic drawing capability that permits the editing and enhancement of graphical images, as well as the addition of text.

The general approach outlined above can be thought of in terms of four separate steps, namely, formulate, calculate, graph and assemble. Thus, for example, preparation of a simple film strip to represent plane wave reflection at a dielectric interface could proceed as follows:

1. *Formulate*

The electric fields are expressed in the two regions by the standard expressions

$$e_1 = E_o e^{-\alpha_1 z}\cos(\omega t - \beta_1 z) + E_o|\Gamma| e^{+\alpha_1 z}\cos(\omega t + \beta_1 z + \phi)$$
$$e_2 = E_o|\mathrm{T}| e^{-\alpha_2 z}\cos(\omega t - \beta_2 z + \theta)$$

where $\Gamma = |\Gamma|\angle\phi$ is the reflection coefficient

and $\mathrm{T} = |\mathrm{T}|\angle\theta$ is the transmission coefficient.

The objective is to present this *e*-field information in a conventional 2-D graphical format with the horizontal axis coinciding with z, the direction of propagation, and with the vertical axis representing the instantaneous field amplitude.

2. *Calculate*

A convenient way to evaluate these expressions the several thousand times necessary to provide values for the field at each of 100 to 200 axial locations for 24 separate instances of time is with a spreadsheet program, such as *Excel* by *Microsoft*. The mechanics of the construction of the spread sheet will be obvious to anyone familiar with this type of program. The complete construction of this spread sheet, which will contain the data for the entire filmstrip, can be accomplished in well under an hour. *Excel* permits storage of the results in text format, allowing other programs, such as *Cricket Graph*, to read the data directly. Alternately, these calculations could be made using a matrix based program, such as *Matlab*, using its own high level formula-like command language.

3. *Graph*

The next step is to prepare the 24 individual graphical images that will comprise the filmstrip. A graphing program such as *Cricket Graph* can directly open and read the data stored in step 2, and organize it into a row and column format identical to that of *Excel*. A two-dimensional graph of any of the electric field quantities versus axial position can then be produced, and in addition *Cricket Graph* permits the axes to be labelled with any desired font, the image to be resized, and additional text, legends, arrows, and so on, to be added. Using this method, all of the 24 individual frames are created. They are then stored by copying them to the *Clipboard* and then into the *Scrapbook* (standard features of the *Macintosh* operating system). Figure 1 illustrates one frame from such a wave reflection movie. Steps 2 and 3 are combined into a single step if *Matlab* is used, but the graphical presentation is less flexible.

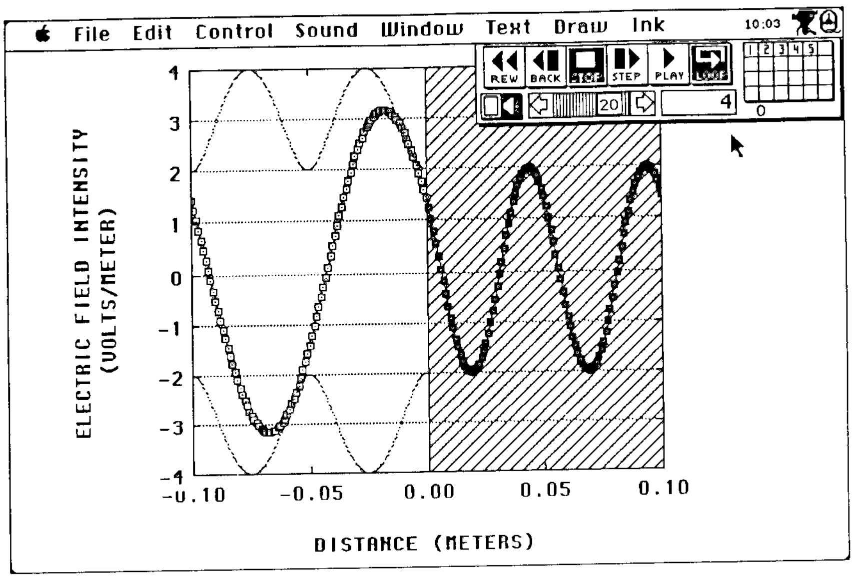

Figure 1: *Instantaneous electric field amplitude of a wave in free space, normally incident on a dielectric half-space of relative dielectric constant 4. The standing wave pattern is designated by lightly dotted lines.*

4. *Assemble*

The 24 frames are now assembled to form a filmstrip that will run as a continuous loop depicting the instantaneous field variations in the vicinity of the dielectric interface by using any one of a number of animation programs [11]. For example, using *Video Works II*, the process is as simple as copying the stored images to a "cast window". From the cast window, cast members are moved onto the "stage" in the order in which they are to be shown, simultaneously creating a movie "score". Assembly of a movie, once the graphical images have been created and stored (steps 2 and 3), rarely takes more than a few minutes.

The authors have produced, and incorporated into their classroom presentations, many such filmstrips designed to illustrate specific conceptual points on such topics as

- wave reflections (normal and oblique incidence)
- total internal reflection and Brewster angle
- wave polarizations
- phase and group velocities
- distribution and propagation of fields in waveguides
- eddy currents in metal strips and round wires
- skin depth
- current and charge distributions on wire antennas
- electric lines of force in dipole radiation
- phased arrays

Projection

While small classes may view the movie on the computer monitor itself, some means of projecting the image will generally be required. One could for instance, prior to class time, photograph the computer screen as the movie runs with a conventional movie camera for later projection. One could also record the movie on videotape. There are several commercially available systems for large screen projection of such video images. A much simpler and more flexible approach (and used exclusively by the authors) is to use the *Kodak Datashow HR/M Projection Pad* with an overhead projector.

System Requirements

Most of the software mentioned above for the preparation of a filmstrip can be used on any currently available Macintosh computer. However, the professional versions of *Systat* and *Matlab* require a math coprocessor. Moreover, systems without coprocessors are limited to rather low frame speeds when running *Video Works II*. A

hard disk is necessary. The authors have been using a Mac SE/30 system with 8 MB RAM and an internal 80 MB hard disc.

Conclusions

Movies for the visualization of electromagnetic phenomena are easy to prepare, can be easily structured to reflect an instructors preferred style of teaching, and can be integrated into a lecture as easily as any other overhead illustration, using readily commercially available hardware and software. The movies produced by the authors have been well received in the classroom. They have helped students to clarify important concepts, have stimulated student thought, and have heightened student interest in the study of electromagnetics.

References

1. *TLS: Transmission Line Simulator* is available from Kinko's Academic Courseware Exchange, 4140 State St., Santa Barbara, CA 93110.
2. R.W. Cole, E.K. Miller, S. Chakrabarti and S. Gogineni, "Learning About Fields and Waves Using Visual Electromagnetics", *IEEE Trans. Educ.*,Vol.33, pp.81-94, 1990.
3. E.K. Miller, R.D. Merrill and R.W. Cole, "Computer Movies for Education", *IEEE Trans. Educ.,* Vol.31, pp.58-68, 1988.
4. M.F. Iskander, "CAEME: An Exciting Opportunity to Make a Difference in Electromagnetics Education", *IEEE Ant. and Prop. Soc. Newsletter,* Vol.31, No.5, pp.41-43, 1989.
5. *Matlab:* The Math Works, Inc., 20 North Main St., Suite 250, Sherborn, MA 01770, (617) 653-1415.
6. *Systat:* Systat Inc., 2902 Central St., Evanston, IL 60201, (321) 864-5670.
7. *Theorist:* Prescience, 814 Castro St., San Francisco, CA 94114, (415) 282-5864.
8. *Math View Professional:* Brain Power Inc., 24009 Ventura Blvd., Suite 250, Calabasas, CA 91302.
9. *Excel:* Microsoft Corporation, 16011 NE 36th Way, Box 97017, Redmond, WA 98073-9717.
10. *Cricket Graph*: Cricket Software, 40 Valley Stream Parkway, Malvern, PA 19355, (215) 251-9890.
11. S. Cudlitz, "Move It", *Macworld*, pp. 108-115, June 1989.
12. *VideoWorksII:* MacroMind Inc., 1028 W. Wolfram, Chicago, IL 60657, (312) 871-0987.

A Computer Algebra Approach to Laplace's Equation

by

Joseph M. Crowley
Electrostatic Applications
16525 Jackson Oaks Dr.
Morgan Hill, California 95037
(408) 779-7774

Abstract

Computer algebra operates on symbolic expressions, rather than numbers, to obtain solutions to problems. This allows solutions to be derived using the classical analytical techniques, and gives answers as formulas. The use of computer algebra offers all the traditional advantages of symbolic methods. The effect of parameter changes is easy to determine, derivatives can be obtained exactly, and three dimensional problems can be solved in reasonable times and memories.

The principal drawback of analytical techniques has been the difficulty in carrying out the steps in the solution, and the resulting scarcity of available solutions. This paper describes the development of computer algebra methods for the systematic derivation of solutions of Laplace's equation for a wide variety of geometries and materials. These solutions are then entered into a database which can be accessed by a user in terms of the geometry of the problem, the nature of the sources, and the types of materials. The solution is presented as a formula in a computer text document. The formula appears as a symbolic expression, which can also be evaluated numerically or plotted, if desired.

INTRODUCTION

Packages which carry out computer aided solutions of the electric and magnetic field equations are usually considered as combinations of three separate parts. The fundamental section in the solution engine, which performs the mathematical operations needed to produce the solutions. The other two parts, often called the preprocessor and the postprocessor, are concerned with gathering information about the problem , and explaining the result to the user.

Currently, a number of solution engines are popular in electromagnetic solvers. In general, each is based on a single formula (or algorithm) which is applied to a large number of points in the

region of interest. For example, a finite difference engine might be based on the relaxation technique, in which the potential and every grid point is continually approximated as the average of potentials at the surrounding points. More complicated algorithms which allow non-uniform spacing of the points are normally used in finite element methods. In all of these numerical solution engines, the computer's main contribution is the solution of a large number of equations of the same form, but applied to different points or regions.

This set of equations represents an approximation to the actual situation, since they are formed by breaking the continuum of space into discrete elements or cells, and then taking some kind of average over each cell. Once these equations are obtained, they can be solved as accurately as the computer allows, but the equations are themselves only an approximation. In practice, extra care is needed when the fields can vary significantly over the extent of the cells. Some examples of problem areas are sharp points, combinations of very large and very small objects, and the need to calculate derivatives of the solution. Such problems are normally attacked by reducing the cell size, but this also increases the number of equations to be solved. For many problems, the size and speed of the computer needed to solve the equations becomes a serious limitation, especially in three dimensions.

The work described in this paper offers an alternative to the traditional numerical solution engine. Instead of solving large sets of similar equations, it uses a single analytical expression which is the exact solution for the problem at every point. This is the same technique taught in introductory courses. This approach removes the difficulties associated with the discretization of the region of interest, but it replaces it with a need to supply a different analytical solution for each problem of interest. The present paper describes one approach to a computer aided analytical solution of Laplace's equation, which is intended for student use in undergraduate electromagnetics courses.

INTERFACE

Although the primary thrust of this research is the development of the analytical solution engine, there are a number of requirements which are easier to understand in terms of the user interface. In the current version [Crowley 1991b], the student selects a problem by interacting with the preprocessor through a window like that shown in Figure 1. The selection process consists of a two step procedure. The first is selecting a general geometrical description of the problem. The choices are listed in a popup menu shown in the upper left of the figure. In this example, spherical geometry has been selected, but others, such as lines, circular cylinders, and dipoles, are also available.

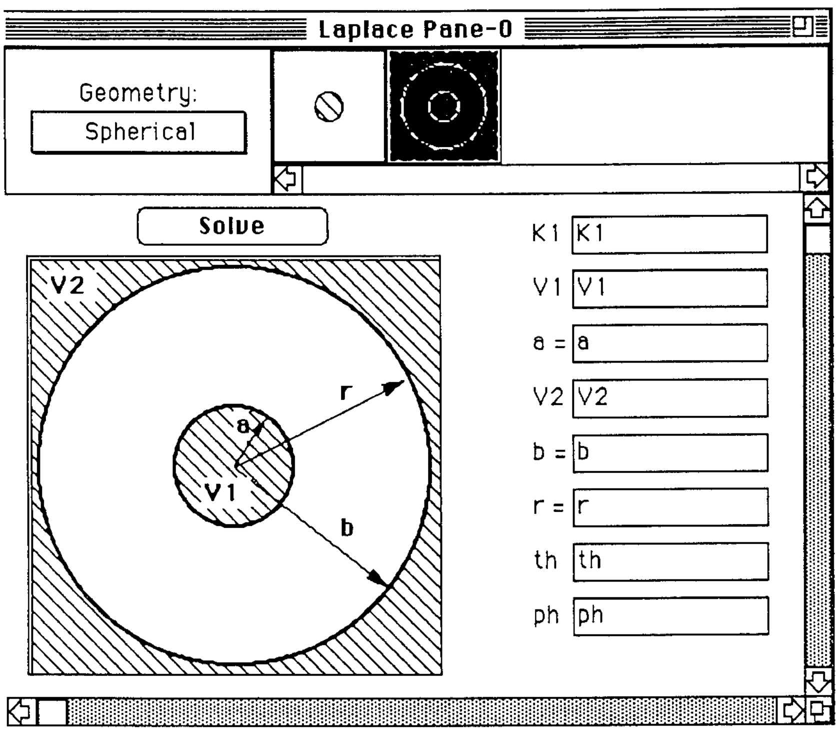

Fig. 1. The problem definition window

Once the user selects a geometry class, the program displays a selection bar of icons representing the various problems in its database. Figure 1 shows the problem of two concentric electrodes. A selection of the other available problems is shown in Figure 2. These are the problems most likely to be encountered by a student taking the Junior level course in electromagnetism in the standard Electrical Engineering curriculum, using textbooks like Hayt [1989] or Rao [1991]. The problems involve , electrodes, point charges, line charges, surface charges, and dipoles in relatively simple arrangements. The electrodes must be flat, circular, or spherical, and arranged so that the symmetry of the problem leads to a solution that is a function of one variable.

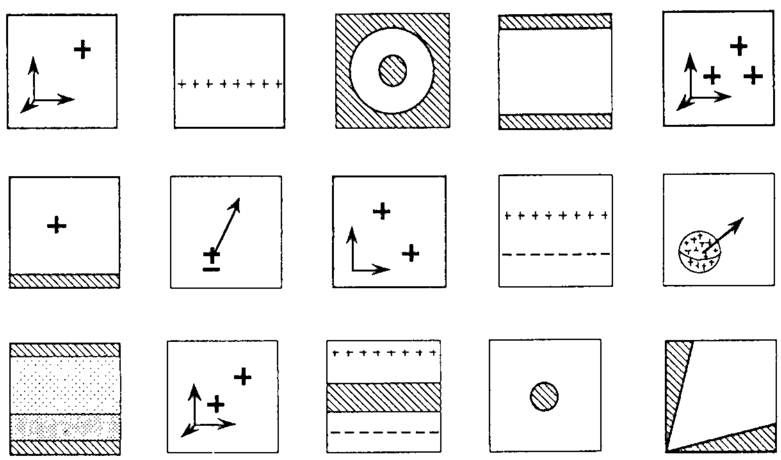

Figure 2. Selected problems in the database

After the geometry of the problem has been selected, the user can enter new values for any of the parameters, to bring the general solution into accord with the problem at hand. For example, an electrode can be grounded by setting its potential to zero, or a circular electrode can be enlarged by changing its diameter. At this point, the user's job is finished. The rest of the solution will be carried out by the program as soon as the 'Solve' button on the input window (Figure 1) is pressed.

In presenting the completed solution, the program performs the following steps:

1) Create the general solution from the canonical form which is stored in a database;

2) Substitute the user parameters in the appropriate places;

3) Simplify the resulting expression;

4) Format the expression for legible output.

The output of the solution process is presented as a computer 'notebook', which contains the boundary conditions and other descriptive material on the problem, as well as the expressions for the solution. A part of a typical notebook, is shown in Figure 3. This window has standard text editing capabilities, so that notes, comments, or longer descriptions of the problem can be added by the user. The text can be saved in a file, and individual portions can be copied and pasted using the standard Macintosh techniques. For example, the formatted equation can be copied from the output window and pasted into a standard word processor.

```
                    Untitled
================================================
PROBLEM: concentricSphere
Dielectric constant
    K1 = K1

Condition #1:
    V1 = V1
  when
    a = a

Condition #2:
    V2 = V2
  when
    b = b

Evaluate at:
    r = r
    th = th
    ph = ph

------------------------------------------------
SOLUTION


Region #1:
V =
        b            b     b
 -1 + ---           --- - ---
        r            a     r
---------- V1 + ----------- V2
        b                b
 -1 + ---          -1 + ---
        a                a

Er =
                         /                    \
        b                |          b         |
--------------- V1 +     |- ---------------   | V2
 /          \            |   /          \     |
 |       b  | 2          |   |       b  | 2   |
 |-1 + ---| r            |   |-1 + ---| r     |
 |       a  |            |   |       a  |     |
 \          /            |   \          /     |
                         \                    /
```

Fig. 3. The solution notebook

COMPUTER-AIDED SOLUTION

The heart of the solution engine in this appoach is the database of canonical solutions for different problems. For student use, this database could be constructed by hand from the solutions in

standard texts, but a computer-aided technique was developed and used here so that the engine can be later extended to a much larger selection of problems. The computer program, written in Mathematica, includes the following steps:

1) The problem specification structure file is read;

2) Starting with a general form of the solution, the boundary conditions are applied to find the arbitrary constants in the potential expression;

3) The metric coefficients are calculated from the definition of the coordinate system;

4) The gradient of the potential (electric field) is calculated from the potential expression and the metric coefficients;

5) The divergence and curl of the gradient are calculated to ensure that the field solution satisfies Laplace's equation;

6) The newly derived expressions for potential and electric field are written to a new problem specification file.

As an illustration of the method, the program fragment used to perform step 2 is described below. The general solution form contains several arbitrary constants, which are needed to match the boundary conditions. For two parallel electrodes, the general solution for the potential can be written as

$$\Phi = A + B u$$

The constants A and B are determined by evaluating the general solution at all the boundaries. For a one-dimensional problem with two electrodes, this gives the two equations

$$\begin{aligned} V_1 &= A + B u_1 \\ V_2 &= A + B u_2 \end{aligned}$$

which are to be solved for the unknown constants A and B. Substituting the values back into the general equation gives the solution for the potential. The program which carries out these steps is shown in Figure 4. The program statements are shown in bold face, and the output of the program is shown immediately following each statement.

This example is the simplest process to be carried out. Others, such as evaluation of the metric coefficients in arbitrary geometries

$$g_{uu}(u, v, w) = \left(\frac{\partial x}{\partial u}\right)^2 + \left(\frac{\partial y}{\partial u}\right)^2 + \left(\frac{\partial z}{\partial u}\right)^2$$

or the evaluation of the electric field

$$\mathbf{E} = -\nabla\Phi = -\frac{1}{\sqrt{g_{uu}}}\frac{\partial\Phi}{\partial u}\hat{i}_u - \frac{1}{\sqrt{g_{vv}}}\frac{\partial\Phi}{\partial v}\hat{i}_v - \frac{1}{\sqrt{g_{ww}}}\frac{\partial\Phi}{\partial w}\hat{i}_w$$

```
ab
V := A + B u
eq1 := (V1 == A + B u) /. u -> u1
eq1
V1 == A + B u1
eq2 := (V2 == A + B u) /. u -> u2
eq2
V2 == A + B u2
soln = Solve [{eq1, eq2}, {A, B}]
            V2 u1         V1 u2               V1          V2
{{A -> -(--------) + --------, B -> -(--------) + --------}}
          -u1 + u2      -u1 + u2          -u1 + u2     -u1 + u2
genSoln = (A + B u) /. soln
    V2 u1         V1 u2                V1          V2
{-(--------) + -------- + u (-(--------) + --------)}
   -u1 + u2      -u1 + u2          -u1 + u2     -u1 + u2
genSoln /. V1 -> 0
   V2 u       V2 u1
{-------- - --------}
 -u1 + u2   -u1 + u2
```

Figure 4. Mathematica code to evaluate constants in general solution

require more complicated Mathematica programs which can deal with derivatives, trigonometric relations, and the like. The output of these Mathematica programs is a data file which contains all the information needed to specify a problem and construct its solution. Details of these files have been presented in an earlier paper [Crowley 1991a]

SUMMARY OF RESULTS

The version described here was tested in an undergraduate class at the University of Illinois. Assessments performed by the students indicate that this approach is helpful in carrying out assignments, and in exploring new areas, but that more work needs to be done to expand the solution database and provide explanations of the solution process to aid in learning the subject.

The entire Macintosh program, including the solution database and graphical resources for the user interface, is only 265 Kbytes in size. The program can also run in a very small memory partition, on the order of 300K. This is an important result for a program intended for student use, since students rarely own computers with large memories. It is especially encouraging because no effort was made to optimize the memory usage for the program in the current version.

Another beneficial result was the ability of the test program to return a simplified analytical expression for the solution in a fairly short time (on the order of seconds) for most problems. Along with the modest memory requirement, this auspicious result can be traced to the decision to use a solution database, rather than to attempt to perform the entire solution on demand.

Acknowledgements

Thanks are due to Paul Klock and N. Narayana Rao for their cooperation in evaluating the program in a class situation.

Most of the Macintosh interface for the test version of the program was developed by Edward J. Devinney, Jr.

The research was supported in part by NSF Grant No. ISI-9060714.

References

Crowley, J. M. [1991a], "Computer-aided analytical solutions of Laplace's equation," *IEEE-IAS 1991 Annual Meeting Conference Record*, Dearborn, MI, October 5-9, 1991, 7 pages.

Crowley, J. M. [1991b], *Potentials...*, Computer program, Electrostatic Applications, Morgan Hill, CA, 1991.

Hayt, W. H. [1989], Engineering Electromagnetics, McGraw-Hill, New York, fifth edition.

Rao, N. N. [1991], *Elements of Engineering Electromagnetics,* Prentice-Hall, Englewood Cliffs, NJ, third edition.

SESSION 5 A- "CODE APPLICATIONS (POSTERS)

Moderator: James K. Breakall

THE EFFECT OF MODELING RESOLUTION ON ANTENNA PATTERN SENSITIVITY USING GEMACS V5.0

Mr. Jeffrey A. Evans
Mr. Harry F. Bascom

Decision-Science Applications, Inc.
1300 Floyd Avenue
Rome, NY 13440
(315) 339-6184

ABSTRACT

The objective of this paper is to provide insight to the sensitivity of antenna patterns to the resolution of the scattering platform using GEMACS Version 5.0. GEMACS uses the uniform geometric theory of diffraction (GTD) for analysis of electrically large objects. The GTD modeling elements available in GEMACS consist of flat plats and elliptic cylinders with endcaps as shown in the following figure. A full structure can be built by using combinations of these elements. The essential question to ask is how much fine detail do I build into my model and how will this affect the resultant output data. This paper will address this issue as it pertains to a study that was performed.

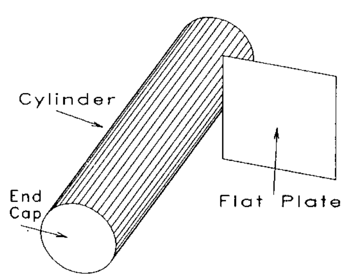

Figure 1. GEMACS GTD Modeling Elements

1.0 INTRODUCTION

The study recently completed was to analyze the performance of UHF blade antennas on the E-8A aircraft for air-to-ground and air-to-air communications. The GEMACS V5.0 code was used to perform the analysis. The desired results were to maximize the coverage of the antenna and to minimize any coupling from other UHF blades in the antenna group. This paper concentrates on the modeling and validation of the antenna and aircraft.

The antenna under analysis is a SENSOR dual UHF/L band blade antenna with vertical polarization. Its patterns are Omni/az and Cos/El. The antenna model was validated against measured monopole antennas over finite ground planes.

This work was sponsered by Rome Laboratory under contract F30602-90-D-0120

The aircraft model was constructed using GTD cylinders and flat plates. Figure 2 shows the full model of the aircraft. Different versions of this model were used for the different antenna locations.

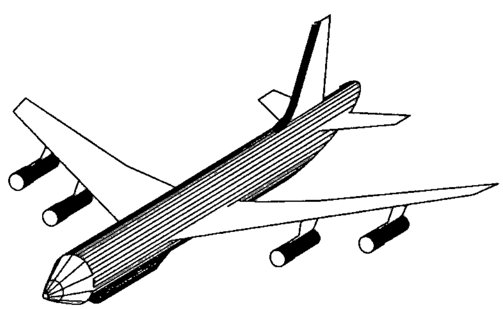

Figure 2. E-8A GTD Model

The aircraft/antenna combination was validated by using data measured from a 1/20 scale model by Grumman Corp., Melbourne, FL.

2.0 AIRFRAME MODELING

2.1 Basic Airframe

The basic GTD model of the E-8A was obtained from Rome Laboratory (RL). It was constructed by Dr. Edgar L. Coffey of Advanced Electromagnetics for the ADI support program at RL. This model was used as the jumping-off point for the analysis effort. Initially the aircraft model was used without engine nacelles or pylons and the wings were perpendicular to the fuselage. This was done for simplicity to get a first cut view of how good the model was. The model is shown in Figure 3.

The dimensions of the fuselage, wings and stabilizers were compared with measurements taken from the 1/20 scale model E8-A at RL. 1/20 scale drawings of the aircraft fuselage were also obtained from RL later in the effort and the GTD model was compared to these as well. Based on these comparisons the GEMACS GTD model was found to accurately represent the E-8A airframe.

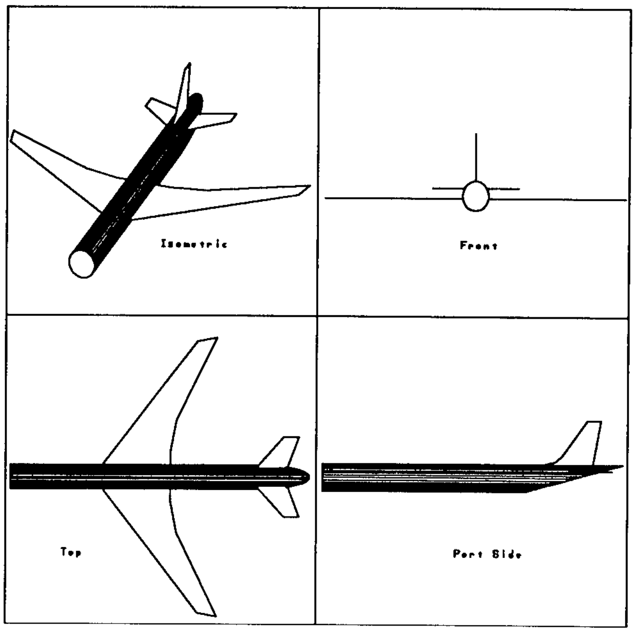

Figure 3. Basic E-8A GTD Model

2.2 Modifications to the Basic Airframe Model

As stated, the model was modified during the initial stages of the analysis effort. These modifications involved adding detail to the model to make it more closely replicate the actual aircraft in a physical and an electrical sense. The following list is a brief summary of the evolutionary modifications done to the basic model:

- Attached engine nacelles and supports
- Attached a simplistic nose cone
- Canted the wings and engines up by 7^{0}
- Constructed a more realistic nose section
- Smoothed the leading edge of the vertical stabilizer
- Added the radome on the belly of the fuselage.

Each of these modifications is now discussed in relation to its contribution to the antenna analyses.

2.2.1 Addition of Engine Nacelles

After the initial analyses with the basic model, the engine nacelles and their supporting pylons were added to the wings. The nacelles are a set of collinear cylinders with radii that closely match that of the actual engine. The support pylon is a simple flat plate to make the connection between the engine and the wing. The following figure shows the GEMACS model of the engines.

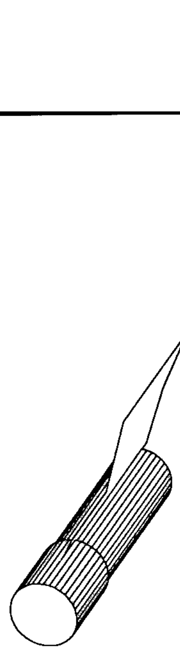

Figure 4. Engine Nacelle with Mounting Pylon

The following figure shows the resulting GEMACS model after the engines have been added. The resulting model now consists of nine (9) cylinders and nine (9) plates.

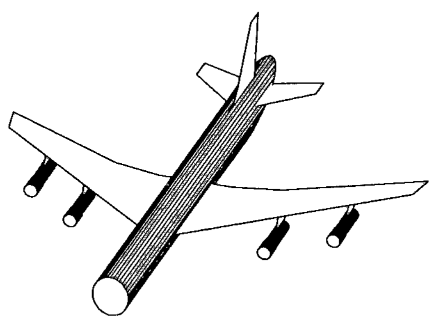

Figure 5. Model with Engines and Pylons

2.2.2 Simple Nose Cone

The next area of concern in analyzing the preliminary analysis results was the area covering the nose of the model. In the basic model the nose had been the truncated cylinder with a flat endcap. The pitch plane patterns in this area (theta from 80 to > 90 degrees) were sharply truncated. The data obtained from measurements showed that the pattern actually slowly tapered off as theta went down past the nose. This was attributed to the pattern creeping down around the rounded nose of the actual aircraft. Figure 6 shows the airframe model with the simple nose cone attached.

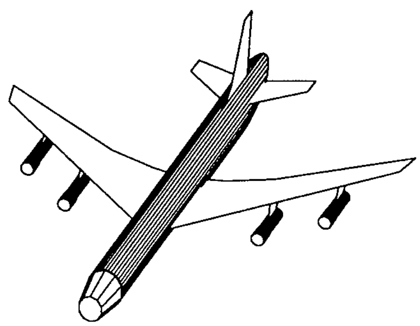

Figure 6. Model with Simple Nose Cone

2.2.3 Canted Wings

The basic model of the E8-A airframe was built using flat plates for the wings that were kept in the X-Y plane. The actual wings on the aircraft have an upward cant of approximately 7°. This cant was applied to the GEMACS model to assess the impact on the antenna patterns. The resulting geometry is shown in Figure 7.

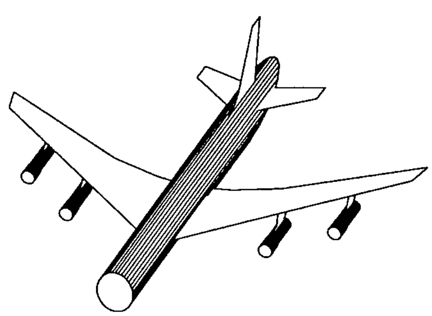

Figure 7. Model with Canted Wings

The major difference in the antenna patterns was that lobing in the patterns was emphasized with the cant added to the wings. This enhanced lobing structure more closely followed the measured data that was supplied by Grumman and Rome Laboratory. Figure 8 shows the difference in the antenna roll pattern for the flat versus canted wing model.

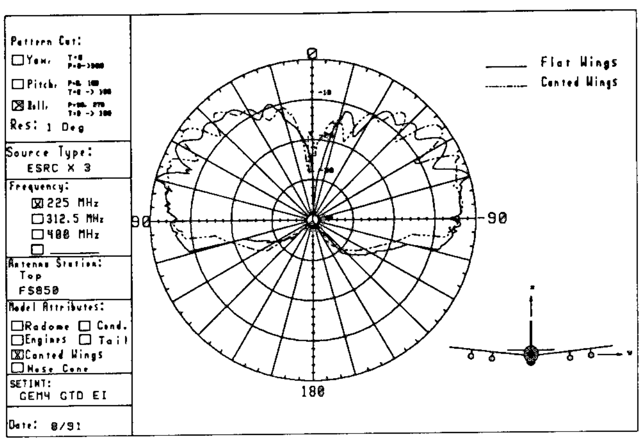

Figure 8. Comparison of Patterns for Flat vs Canted Wings

2.2.4 More Complex Nose Section

The simple nose that was described earlier was an attempt to see the trend in the antenna pattern if the nose section was modified. Since the results were encouraging, a more complex nose section was built. This section has a tandem set of plates tapered at different angles to simulate two sections of the real aircraft, 1) just over the cockpit, and 2) from in front of the cockpit to the tip of the nose. Also, the cylinder for the fuselage was shortened an appropriate amount to account for the added nose section. Figure 9 shows the GEMACS model with this new nose section added. Figure 10 is the new pitch plane pattern that was obtained by using the more complex nose cone.

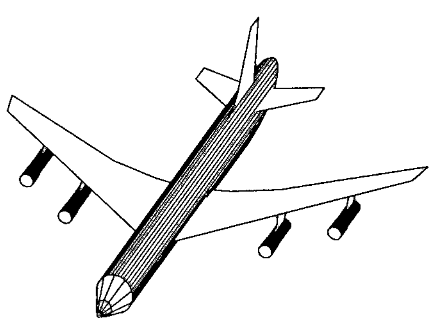

Figure 9. Model with Complex Nose Section

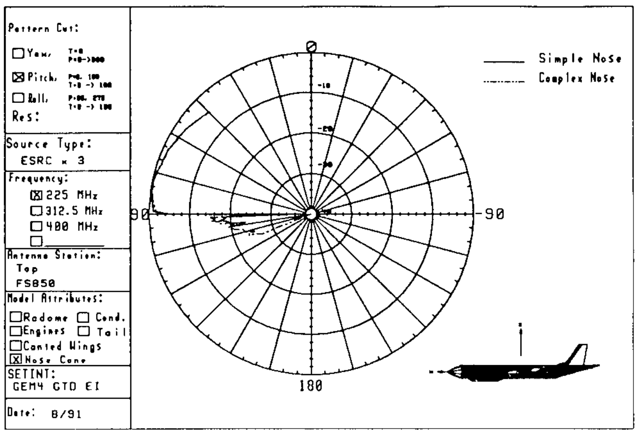

Figure 10. Pitch Plane Patterns for Complex Nose Addition

2.2.5 Vertical Stabilizer Modification

In the baseline antenna analyses it was noted that for the antennas on the top of the fuselage there was a deep null in the rear portion of the pitch plane pattern (Figure 11).

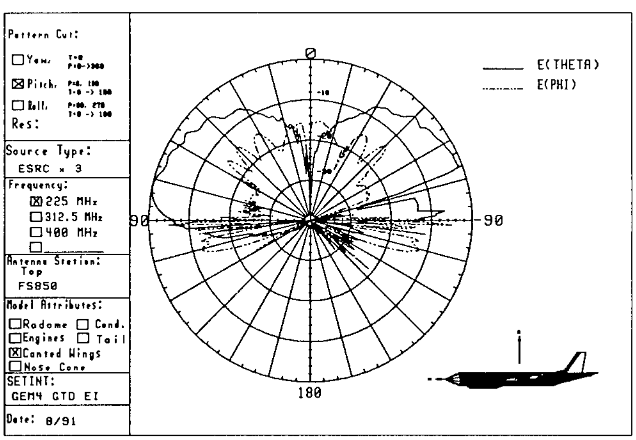

Figure 11. Pitch Plane Pattern with Null

After some investigation it was determined that the model of the vertical stabilizer was causing the null. The stabilizer was made of a flat GTD plate and in the x-z plane looked like a knife edge, whereas the real stabilizer has an elliptic airfoil shape. In order to approximate this airfoil

shape, a series of flattened cylinders was molded to the leading edge of the stabilizer as shown in Figure 13. The full model with the modified stabilizer is shown in Figure 14.

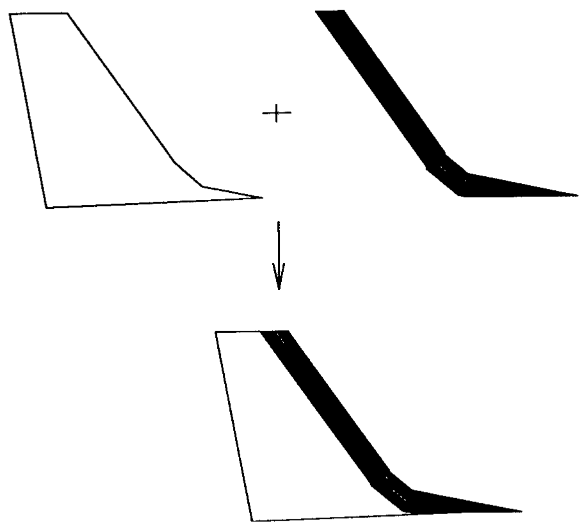

Figure 13. Vertical Stabilizer Modification Steps

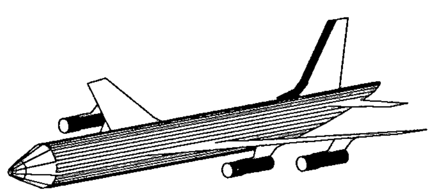

Figure 14. Model with Modified Vertical Stabilizer

The same pattern cuts were performed using this new model of the vertical stabilizer. The resulting pattern has a much shallower null than without the modified tail (Figure 15).

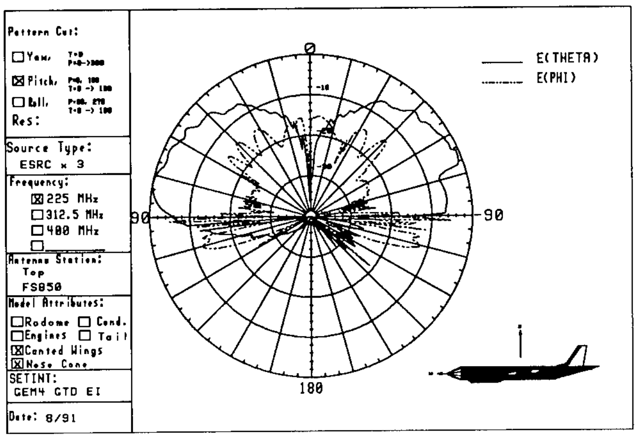

Figure 15. Pitch Plane Pattern after Tail Modifications

3.0 SUMMARY

As shown, the accuracy of a GEMACS model has direct bearing on the analysis being performed. This paper touched on some of the ways in which an aircraft model can be enhanced to more closely replicate the actual structure. For any modeling and analysis effort this job will entail different details but the overall thought process should be relatively the same. Identify weaknesses in the model via anamolies in the patterns and refine the model in that area. One other thing that must be kept in mind when developing a model is that the process is never quite complete. Rather, it is an iterative process in which a model is developed then run through an analysis and then the model is refined based on the results of the analysis. It should be understood that there is a point of diminishing return for the effort that is put into the model. This will be different for each modeling effort. On top of this, for any given analysis several different models may need to be built that provide the necessary resolution to give accurate results for different situations in the analysis.

In performing this analysis we found that using plates to replicate a curved surface introduced errors in the patterns generated. One feature that could be added to the GEMACS code that would further enhance this type of model would be the ability to selectively turn GTD element edges ON or OFF. In this way, the plates used to build a curved surface such as the nose cone could more closely mimic that actual surface.

4.0 REFERENCES

Bensman, D. and R. J. Marhefka. *SATCOM Antenna Siting Study on a P-3C Using the NEC-BSC V3.1.,* The Ohio State University Technical Report No. 721711-2 (April 1990).

Coffey, E.L., and D.L. Kadlec, *General Electromagnetic Model for the Analysis of Complex Systems (GEMACS), Version 5.0,* Advanced Electromagnetics, RADC-TR-90-360, Volumes I, II and III.

Coffey, E.L., and D.L. Kadlec, *GEMACS Source Book,* Advanced Electromagnetics, RADC-TR-87-102 (February 1988).

Lockyer, A. L., and P. Tulyathan, E.L. Coffey III, M. J. Grage, G. Upshaw, *Graphical Aids for the Users of GEMACS (GAUGE),* Northrup Corp., RADC-TR-88-316 (February 1989).

Stutzman, W.L., and G.A. Thiele, *Antenna Theory and Design,* Wiley, New York (1981).

VALIDATION OF THE *CROSS SECTION AND GLINT EVALUATION SYSTEM*[1]

Michael T. Husar, Andrew J. Terzuoli, Jr.
School of Engineering
Air Force Institute of Technology
Wright-Patterson AFB, Ohio 45433

Abstract

The *Cross Section and Glint Evaluation System* (CAGES) is a Radar Cross Section (RCS) prediction software package[2], which provides both time and frequency domain output. This simulation package has potential uses in target identification as well as signature prediction of air targets. CAGES uses primitive targets such as flat plates, cylinders and truncated cones to model complicated targets. The electromagnetic theory is based on Physical Optics (PO) and Geometrical Optics models. This paper compares the RCS predictions of CAGES primitives to a Uniform Theory of Diffraction (UTD) model and measurement data. Assessments are made on the domain of applicability of CAGES to perform accurate RCS prediction for the target identification role. In general CAGES matches both UTD and measurements in the regions where the specular return is the prominent contributor of the total RCS. The error increases as the aspect angle moves away from the specular return. Time domain problems are pointed out where they are relevant to the target recognition role.

Introduction

General Issue. High confidence aircraft identification is a chronic problem in the tactical Air Force. Radar Cross Section (RCS) is rapidly becoming more important as a means of classifying and identifying a target. An identification system based on the RCS of the target requires an RCS data base of potential targets. One such model, Cross Section and Glint Evaluation System (CAGES), is under development to provide all-aspect synthetic time domain RCS data.

RCS Modeling Using Primitives. CAGES uses simple shapes (primitives) to simulate each major scattering center on a target. Example primitives include truncated cones, ogives and cylinders. A generic aircraft could be modeled as in the following example. The wings could be truncated elliptical cones, the fuselage a series of cylinders and truncated cones, the engines as cavities, the radome as a dielectric ogive, the antenna a circular plate, the cockpit a combination of flat plates and the edges as cylinders, thin wires or wedges. Whether a particular feature such as the rear stabilizer is a source of scattering depends on the orientation of the target.

Scope. CAGES (Version 7) is used in this study and is capable of computing the RCS in both time and frequency domains. The validation focuses on the accuracy with which CAGES predicts the most significant scattering centers of primitives with the radar receiver and transmitter collocated (monostatic). Assessments are made on the accuracy of the time domain impulse response. Results include comparisons with theoretical techniques, measured data, and a reference RCS code.

[1]Sponsored by the U.S. Air Force Wright Laboratory, Avionics Directorate, Mission Avionics Division, Target Recognition Branch.

[2]written by General Dynamics, Pomona Division [5]

Validation

Validation Baseline. Numerous theoretical techniques are available for predicting the RCS of the primitive shapes used by CAGES. The Uniform Theory of Diffraction (UTD) was used as the baseline for comparing the electromagnetic scattering from edges. RCS-Basic Scattering Code (RCS-BSC) version 2.0 is based on UTD and written by The Ohio State University ElectroScience Laboratory [1]. RCS-BSC has been tested and validated against a variety of primitive shapes which are common to CAGES.

Validation Procedure. The following steps were tailored to this problem using steps recommended in the tutorial by Sargent of the Simulation Research Group [2]. Form an agreement with the sponsor on what is to be validated and what techniques are considered appropriate. Examine the assumptions and theories underlying the model. Consult with knowledgeable people in the RCS modeling community about the techniques used and the reasonableness of the input/output data. Compare model output with a standard for various aspect angles, polarizations, primitive sizes etc. Document the tests performed and justify the conclusions drawn.

Theory

The concept of RCS refers to the effective echoing area of a target [3]. First assume the radar is at the center of a spherical surface containing the target. The RCS of the target is the area on the sphere's surface that isotropically reradiates all of its incident power at the same power per unit solid angle as the target reradiates toward the radar receiver. RCS is a far field expression with respect to the scatterer and mathematically may be described as:

$$\sigma(m^2)=4\pi R^2\frac{|E^s|^2}{|E^i|^2} \tag{1}$$

with the range (R) in meters and other terms the incident electric field E^i and scattered electric field E^s.

High Range Resolution Radar. The definition must be modified for High Range Resolution (HRR) radar since individual scattering centers on a target are detectable. The target's RCS as described by equation (1) is the coherent sum of these individual returns. The RCS is modified by retaining the time each return arrives at the receiver with respect to some reference point on the target. The magnitude may be saved in (m^2) or any convenient units. CAGES directly obtains the time domain RCS by geometrically calculating the down range scattering center position based on the location of the primitive in the model file. This target impulse response is convolved with the radar impulse response and then measured data noise samples are added to obtain the final synthesized signature [4].

Results

RCS with respect to aspect angle for CAGES, RCS-BSC and measured data is presented and discussed for square and rectangular plates, circular plates, truncated cones, finite cones and circular cylinders. Sizes and incident angles are varied to show the domain of each CAGES primitive tested. The RCS is plotted verse azimuth angle (ϕ).

Square Plates. Plates are used in the cockpit and for flat surfaces on the body of aircraft. Double diffractions occur when the electric field has a component perpendicular to the plate and in the plane of incidence, which is horizontal polarization for this geometry (see Figure 1). The plot in Figure 2 shows excellent agreement between RCS-BSC and measurements for plates. An equivalent plot of vertical polarization would look like the RCS-BSC trace seen in Figure 3. . CAGES is polarization independent because of the physical optics solution used in this version. Future versions of CAGES are scheduled to include diffraction effects based on the Physical Theory of Diffraction (PTD). For target recognition only the regions near specular are useful, and therefore CAGES is accurate where it needs to be. In the time domain, second order returns would not effect the position or magnitude of first order peaks unless both peaks were within the same resolution cell of the radar. Two first order time domain returns originate from the vertical edges and are separated by about one nanosecond at $\phi=10°$ for a one meter wide plate. CAGES predicts only one return originating from the center of the plate. The plot in Figure 4 shows that the same conclusions apply to a 50λ electrically large plate.

Circular Plate. The circular plate is used primarily to model antennas and therefore the incident field would pass through a radome adding frequency selective attenuation. The radome and attenuation effects were not addressed in this study. The results were similar to those of square plates with the exception that sidelobe levels drop-off faster for circular plates. In the regions near specular, no polarization dependencies exist and only vertical

polarization is presented in this paper. The geometry is displayed in Figure 5 along with the locations of the two time domain returns. RCS-BSC matches measurements within two dB as shown in Figure 6. The plots in Figures 7 and 8 compare RCS-BSC to CAGES for 5λ and 50λ diameter plates. The same conclusions apply to both; however, for the larger plate the same time domain error in square plates is present. The magnitudes of the actual radar returns would spread out in the time domain due to the finite bandwidth of the radar. The two pulses would be resolved only if the separation in time is greater than the resolution of the HRR radar.

Truncated Cones. Truncated Cones (TC) are useful for sections of the fuselage. Two subsets of the TC are the Elliptical TC (ETC) and the finite cone The TC has three first order scattering centers visible at one time as seen in Figure 9. TCs are constructed with three primitives in CAGES (TC, and two circular plate endcaps). The scattering center for a CAGES circular plate is in the center of the endcap so scattering centers 1 and 4 are shifted to the center of the endcaps. This time error is the same as for circular plates however the problem goes away in most target recognition situations since scattering points 1 and 4 are typically shadowed by other primitives.

As the plot approaches the broadside peak (120°) in Figure 10, CAGES agrees exactly for the mainlobe and is within 3 dB for the first sidelobe. The agreement is better because PO is very accurate near specular. The final region from 135° to 180° is influenced by three contributors. The disagreement at 180° is attributed to the lack of a diffracted field off the back rim in CAGES. This return is adding out of phase with the circular plate and shows up in RCS-BSC where the diffracted field is accounted for.

The TC model was found to give inconsistent results as the electrical size increases. The plot in Figure 11 shows excellent agreement in the region from ϕ=90° to 180°. The agreement at ϕ=180° is better because the back rim and the front endcap are no longer out of phase. The problem manifests when the endcaps are increased to 10λ and 20λ. The CAGES sidelobes are approximately 5 dB higher than RCS-BSC. At the mainlobe (ϕ=110°) a 9 dB null appears in the CAGES trace while the RCS-BSC trace is smooth. This problem appears to be related to a problem found when looking at elliptical truncated cones. General Dynamic found an error in the CAGES source code which reportedly corrects the problem. This is a prime example of the need to revalidate the primitive models after each release to insure new errors are not introduced.

Finite Cone. The Finite Cone is a special case of the truncated cone in CAGES and RCS-BSC. There are many higher order effects on a cone which include interactions between the tip and rim, and creeping waves cross the back circular plate of the cone. These effects are not included in CAGES and this is assumed to be correct considering how the cone is used. The creeping wave across the back of the cone is eliminated when the cone is connected to another primitive such as a cylinder. The tip-rim interactions are significantly reduced when the cone/cylinder connection 1st derivatives match. Nose-on is at ϕ = 180° for the finite cone plots.

The measurement plotted in Figure 13. compares an electrically small cone to RCS-BSC. Because the cone dimensions are less than 5λ, the modeling assumptions are violated. This and the fact that many higher order effects are included in the measurement make this plot less conclusive. The tip-on peak in Figure 14. is at ϕ = 180° and shows CAGES is 23 dB below the measurement and 20 dB below RCS-BSC. The tip and rim returns are in phase at this incidence.

Agreement between the side lobes of the measurement were not expected to match the computer simulations because of the small electrical size and missing higher order terms, and they do not. The region from ϕ = 280° to 360° degrees is unimportant for this study since this region is dominated by the circular plate. A more involved study of the cone would include combinations with other primitives that may be used with a cone on an actual target. This would assess the reduction in the rim scattering for different configurations.

The broadside peak from CAGES shifts by about 5° when R1 is small. Increasing the tip radius to at least 0.6 cm puts the CAGES broadside peaks in the correct location as seen in Figure 14. This modeling rule should be documented in the CAGES user manual [4]. Overall CAGES works well near broadside after the modeling rule is followed. CAGES is significantly lower than it should be at tip-on incidence. The problem at tip-on incidence will be improved with the addition of diffraction terms based on PTD.

Circular Cylinder. The plot in Figure 15. compares RCS-BSC with measurements for vertical polarization with broadside to the length at ϕ=90°. The agreement in the specular regions is excellent considering the electrical size of the endcaps is on the order of a wavelength. Agreement in the lower level regions is of minimal importance because the return magnitude is insufficient for target ID purposes. This regions are dominated by the diffractions from the edges. In typical ID applications, the cylinder edges are rounded or changed in some way by the

connection of other primitives. For these reasons and the fact that the lower returns away from broadside offer little target recognition potential, the cylinder model appears adequate. Solving for the time domain returns at $\phi = 80°$ on Figure 15 showed that the difference between the two scattering points is less than 1 dB. CAGES uses a closed form PO solution and divides the magnitude in two equal returns. This approximation is accurate to within about one dB near broadside where the cylinder model is useful.

Recommendations

Recommendations that follow are intended to document the features this author feels would benefit CAGES. Addition of triangular plate primitives would allow closer approximation to flat surface areas. This would also better account for the edge effects as the aspect angle moves away from specular. Add a graphical interface. For complex models it is difficult to insure that the correct geometry has been input into the model file. Documentation of modeling rules so that more standardized model files will be generated. Simplify the geometry definitions. Currently there are or four coordinate systems in use and translation is accomplished by CAGES. The problem is that modelers must input boundary and shadowing angles in one coordinate system that does not match the incident field or target coordinate system. Complete PTD improvements to extend the range for which primitives are valid.

Conclusions

CAGES is very accurate in regions near a specular return which are the most important regions of primitives for the purpose of target identification. The inclusion of diffraction coefficients based on the Physical Theory of Diffraction (PTD) will improve the performance in regions away from specular returns. The time domain returns from flat plates will continue to be in error even with the addition of PTD due to the inherent modeling techniques used in CAGES. Correcting this error requires distributing the Physical Optics (PO) return form the center of the plate to the correct edge or corners. An alternative is changing the technique of obtaining the time domain return to the inverse Fourier transform.

The use of primitives for RCS modeling is generally considered a first order approximation. Primitives allow rough estimates to be made of a complex target in a minimum amount of time. The estimates are generally considered good for finding relative RCS differences between targets. Primitives do not match complex target surfaces with as high a degree of fidelity as faceted models. This has pushed the RCS community to move aggressively towards faceted models and today there are numerous such models in use. The faceted model has the ability to account for partial shadowing of target features. The faceted model also lends itself to automated shadowing algorithms and many of the models in use today have this feature built in [6].

References

1. Marhefka, R.J. *RADAR CROSS SECTION - BASIC SCATTERING CODE RCS-BSC (VERSION 2.0) USER'S MANUAL,* Ohio State University ElectroScience Laboratory Technical Report 718295-15, Contract F33615-86-K-1023. Aeronautical Systems Division, Wright-Patterson AFB OH, February 1990.

2. Sargent, R.G. "A Tutorial on Validation and Verification of Simulation Models" *Proceedings of the 1988 Winter Simulation Conference,* 33-38, December 1988.

3. Wehner, D.R. *High Resolution Radar.* Norwood, MA: Artech House, 1987.

4. Wright Laboratories/AARA, Aeronautical Systems Division. *Signature Synthesis User's Manual, Automatic Radar Target Identification (ARTI) Phase III-A,* Contract F33615-89-C-1099. Wright-Patterson AFB OH,19 May 1991.

5. Wright Laboratories/AARA, Aeronautical Systems Division. *Description/Specifications/Work Statement Automatic Radar Target Identification (ARTI) Phase III-A,* Contract F33615-89-C-1099. Wright-Patterson AFB OH, 1989.

6. Youssef, N.N. "Radar Cross Section of Complex Targets," *Proceedings of the IEEE Special Issue on Radar Cross Sections of Complex Objects,* 77:720-734, May 1989.

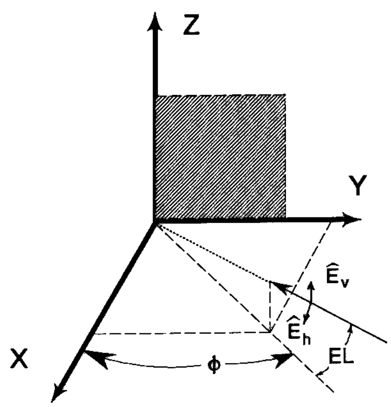

Figure 1. Square Plate Orientation

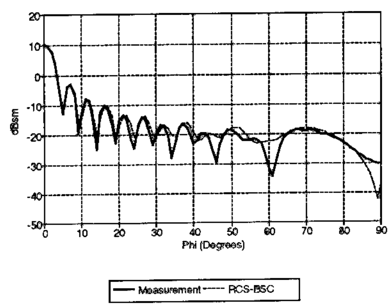

Figure 2. Square Plate, 6.1λ, H-Pol, EL=0°

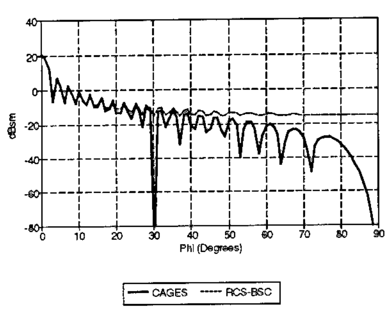

Figure 3. Square Plate, 10λ, V-Pol, EL=0°

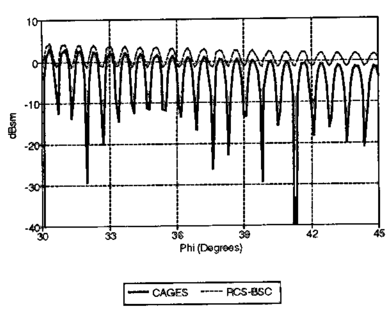

Figure 4. Square Plate, 50λ, V-Pol, EL=0°

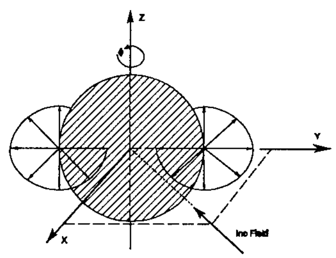

Figure 5. Circular Plate Orientation

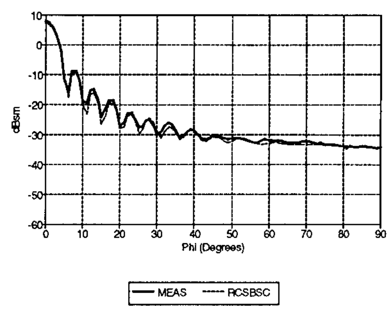

Figure 6. Circular Plate, Dia.=6.1λ, V-Pol, EL=0°

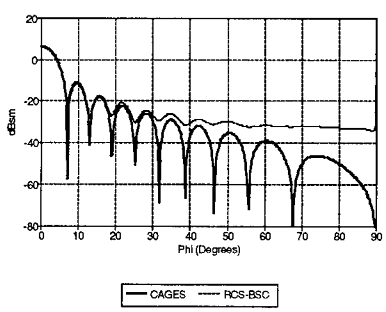

Figure 7. Circular Plate, Dia.=5λ, V-Pol, EL=0°

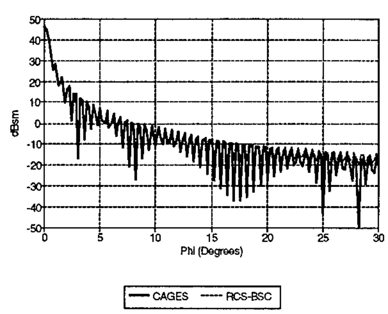

Figure 8. Circular Plate, Dia.=50λ, V-Pol, EL=0°

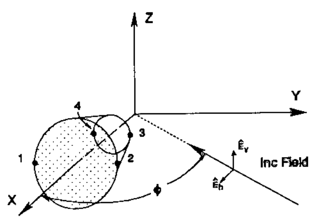

Figure 9. Truncated Cone Orientation

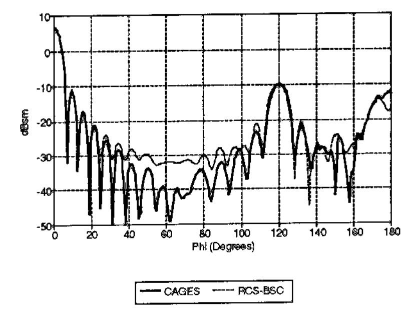

Figure 10. Truncated Cone, R1=0.85λ, R2=2.54λ, V-Pol, α=30°, EL=0°

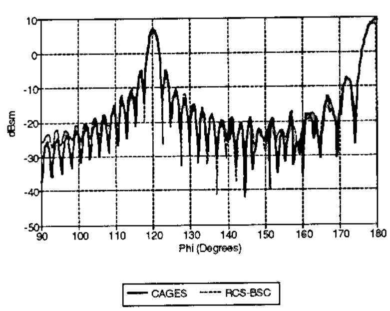

Figure 11. Truncated Cone, R1=3λ, R2=9λ, V-Pol, α=30°, EL=0°

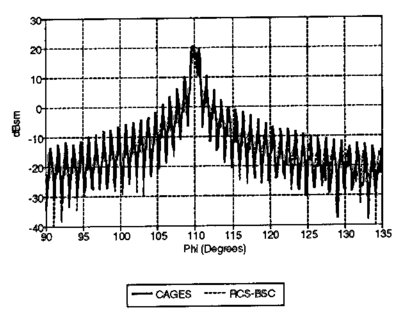

Figure 12. Truncated Cone, R1=10λ, R2=20λ, V-Pol, α=20°, EL=0°

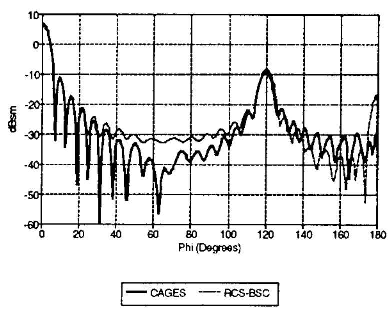

Figure 13. Finite Cone, R2=2.54λ, V-Pol, EL=0°

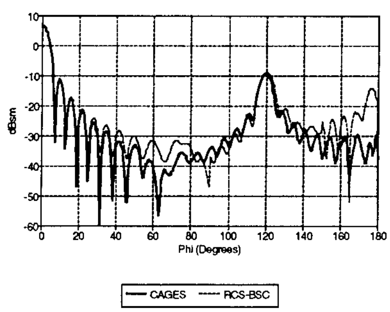

Figure 14. Finite Cone, R2=2.54λ, H-Pol, EL=0°

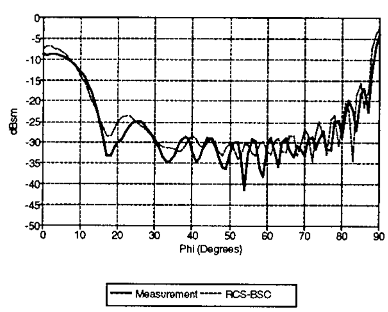

Figure 15. . Circular Cylinder, L=8.13λ, r=1.02λ, V-Pol, AZ=0°-90°, EL=0°

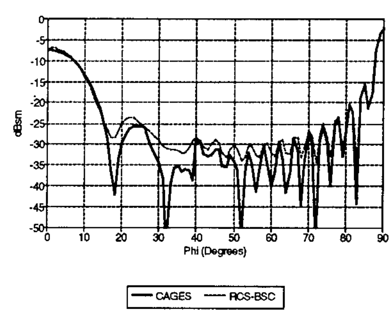

Figure 16. Circular Cylinder, L=8.13λ, r=1.02λ, V-Pol, EL=0°

WIDE BAND OPTIMIZATION OF YAGI ARRAYS USING NEC

R.W. O'Connor and J.P. Scherer
Loral Randtron Systems
130 Constitution Drive
Menlo Park, California 94025

ABSTRACT

The wide band optimization of a Yagi-Uda array is described. A general constrained non-linear optimization program was interfaced with NEC-81 which is a PC version of the NEC-2 code. Next, a cost function was chosen that would tend to produce desired pattern, gain and matching network characteristics. The Yagi-Uda array configuration was then optimized over a 20% frequency band using a 486/33 PC. In addition, both the Yagi array and a matching circuit were simultaneously optimized over the same frequency band. Both equality and inequality configuration constraints were used.

An optimized thick wire Yagi-Uda array was fabricated and tested. Calculated results are compared to measured.

INTRODUCTION

A Yagi-Uda array with matching circuit is illustrated in Figure 1. Element 1 is a reflector, element 2 is a driven dipole, elements 3 to N are parasitic directors and the matching circuit matches the dipole impedance ZD to the source impedance ZS.

A problem with Yagi-Uda arrays for wide band applications is that the maximum gain bandwidth is usually on the order of 2%. Larger bandwidths require making trade offs between gain, input impedance, beamwidth, sidelobe level and front-to-back ratio.

The objective of this study was to show that NEC can be used both to increase the bandwidth of Yagi-Uda arrays and to make the necessary trade offs between electrical parameters.

The approach taken for this study was to first interface a general constrained non-linear optimization program with NEC-81. Next, a cost function was chosen that was suitable for making trade offs between electrical parameters. Configuration constraints were established and a 6 element Yagi-Uda array without matching circuit was optimized over a 20% frequency. Next, the array and matching circuit were simultaneously optimized over the same frequency band. Finally, an optimized thick wire Yagi-Uda array was fabricated and measured results were compared with NEC calculated results.

NEC OPTIMIZATION PROGRAM

A flow chart of the program is given in Figure 2. The program reads in initial parameters and then minimizes a cost function by iteratively varying the matching network parameters and/or the

Yagi-Uda array dimensions. For each iteration, a NEC-81 input file is created, the array is analyzed using NEC-81 and a cost function is created using both the NEC-81 output file and the matching circuit equivalent circuit. The program stops when the change in the cost function is less than a specified value.

The program has three main parts: NEC-81, Flexible Tolerance optimization method and the cost function.

NEC-81

NEC-81 [1] is a double precision PC version of NEC-2 [2] that was modified as follows: the program was made a subroutine of the Flexible Tolerance optimization program, numerous STOP statements were replaced with RETURN statements and the location of permanent I/O files was changed from the hard disk to a memory resident ramdisk.

Flexible Tolerance

Flexible Tolerance [3] is a general constrained non-linear optimization method that will minimize a linear or non-linear cost function of N variables subject to linear and/or non-linear equality and inequality constraints. The program is well suited for interfacing with NEC since it does not require derivatives of the cost function with respect to the N variables as required by many optimization programs. The derivatives are not available when using NEC. In addition, the NEC model geometry can be constrained so that NEC modeling guide lines are not violated during optimization.

Cost Function

Kajfez [4] used a cost function containing both average gain and the deviation of gain from the average to optimize a Yagi-Uda array for flat gain over a 33% frequency band. The cost function chosen for this study extends the reference 4 cost function to also include input impedance, beam shape, sidelobe level and front to back ratio. The cost function is as follows:

$$C = -W_1 \times S_1 + W_2 \times S_2 + W_3 \times S_3 + \sum_{i=1}^{6} W_{i+3} \times T_i \tag{1}$$

where W_i are weights and S_i and T_i are average and rms values respectively given by

$$S_i = (1/(FH-FL)) \int_{FL}^{FH} G_i(f)\, df \tag{2}$$

$$T_i = [(1/(FH-FL)) \int_{FL}^{FH} [G_i(f) - GSPEC_i(f)]^2 df]^{1/2} \tag{3}$$

where f is the frequency, FL and FH are the band edge frequencies and G_i and $GSPEC_i$ are given in Table 1.

For front-to-back ratio or sidelobe level, the equation 3 integral is only over frequencies where the F/B or SLL is less than the specified minimum values given in Table 1.

Table 1 Cost Function G Values

S/T	G_i	$GSPEC_i$
S_1	NEC gain	0
T_1	NEC gain	S_1
T_2	Input resistance RIN or RD *	Specified
T_3	Input reactance XIN or XD*	Specified
T_4, T_5, T_6	F/B, AZ SLL, ELEV SLL	Minimum Values
S_2, S_3	RMS error between calculated and specified az/elev patterns	0

*Matching network or driven dipole

NEC YAGI ARRAY OPTIMIZATION

In this section, the N=6 element Yagi-Uda array illustrated in Figure 1 is optimized over a 20% frequency band by making trade offs between gain, input impedance and front-to-back ratio. One of our goals was to show that specified trade-offs can easily be made. The approach taken was to first establish constraints on the optimization and then optimize an array without matching circuit for maximum gain and for various flat responses. Finally, the array and a matching circuit were simultaneously optimized. Representative results are given.

Constraints

Constraints were placed on the Yagi-Uda array configuration and on the matching circuit parameters. The Figure 1 array was constrained during optimization to satisfy both NEC modeling guidelines and specified maximum dimensions. The following inequality constraints were used:

Element Diameter D:	$D < 0.066\ \lambda_{MIN}$
Element Length L:	$1.5\ D < L < 0.55\ \lambda_{MID}$
Element Spacing S:	$S > 2.5\ D$

It was difficult to specify a maximum value for D. The NEC Users Guide [2] recommends making $PI*D/\lambda << 1$ or $D << 0.318\ \lambda$. Trueman [5] recommends making D less than $\lambda/15 = 0.067\ \lambda$. But, in the literature, Yagi-Uda array analytical designs usually use element diameters $D << 0.01\ \lambda$. One exception is Millican's 10% bandwidth design [6] which used $0.01\ \lambda$ diameter elements. A maximum $D = 0.066\ \lambda_{MIN}$ was chosen for this study.

It was also difficult to specify a minimum value for element spacing. The NEC Users Guide [2] recommends that "wires be several radii apart" but larger spacing may be required since the NEC extended thin wire kernel was used. A minimum spacing S = 2.5 D was chosen which corresponds to a 3 radii wire separation.

Equality constraints were also successfully used to make the array length a specified value. This constraint may be useful when comparing the gain of NEC designs with that of published designs.

The matching circuit had three stubs which were constrained to have lengths less than a quarter of the midband wavelength and characteristic impedances between 20 and 120 ohms.

NEC Gain Optimized (W/O Matching Circuit)

The purpose for these trials was to find an upper bound for NEC average gain over a 20% frequency band. Several gain maximums were observed during optimization depending on the initial values for the variables and the number of variables. Maximum NEC gain over the 20% frequency band was between 10.26 and 13.13 db as shown in Figure 3a. Mismatch loss is not included. The front-to-back ratio F/B and dipole resistance RD and reactance XD distributions are also as shown in Figure 3b, 3c, and 3d respectively. The configuration dimensions are given in Table 2.

TABLE 2 - OPTIMUM CONFIGURATIONS FOR A
6-ELEMENT YAGI-UDA ARRAY - $d/\lambda_{MID} = 0.06$

OPTIMIZATION	LENGTHS IN MIDBAND WAVELENGTHS										
	L_1	L_2	L_3	L_4	L_5	L_6	S_1	S_2	S_3	S_4	S_5
MAX NEC GAIN	.491	.518	.341	.325	.325	.325	.150	.239	.323	.323	.323
LEVEL RESPONSE											
a) $RD = RD_{AV}$ $XD_{MID} = 0$	.552	.417	.344	.330	.326	.314	.151	.173	.283	.287	.310
b) RD = 50 Ω XD = 0	.539	.434	.331	.332	.307	.291	.183	.149	.292	.293	.317
c) GAIN	.524	.548	.183	.303	.303	.303	.222	.274	.403	.403	.403
d) $RD = RD_{AV}$ + XD = 0	.548	.507	.286	.313	.216	.311	.344	.150	.325	.348	.346

Flat Response Optimized (W/O Matching Circuit)

In order to show the wide range of trade offs that can be made, weights W1, W4, W5, W6 and W7 were varied to make gain, RD and both RD and XD level across the 20% frequency band. The other weights were set equal to 0. Representative level results are given in Figure 3 and the configuration dimensions are given in Table 2.

Array + Matching Circuit Optimized

Our goal was to show feasibility of simultaneously optimizing the

array and it's matching circuit. This may result in better gain, pattern characteristics and impedance than if the Yagi-Uda array and the matching circuit are optimized separately.

An array and matching circuit consisting of a split tube coax balun and two matching stubs was simultaneously optimized over a 20% band. A typical optimization of all variables for 5 frequencies took about 1 hour on a 486/33 PC but length of time was dependent on variable initial values. There were 17 variables consisting of 6 element lengths, 5 element spacings, 3 stub lengths and 3 stub impedances. There were also 29 configuration constraints consisting of 12 on element lengths, 5 on element spacings, 6 on stub lengths and 6 on stub impedances. Results were similar to the Rd=50 ohm case given in Figure 3 except RIN varied from 48.5 to 53.5 ohms.

EXPERIMENTAL MEASUREMENTS

A 6 element Yagi-Uda array optimized to a 50 ohm source impedance was fabricated and tested over a 20% bandwidth. The elements were made from 0.25" diameter metal rods with lengths and spacings in midband wavelengths given in Table 2 under the heading "LEVEL RESPONSE b) RD=50 XD=0". The midband frequency was 2.83 GHz and thus multiply the lengths by 4.1707 to get the lengths in inches.

Figure 4 shows a comparison between measured and NEC calculated E and H plane patterns at normalized frequencies of 0.929, 1.0 and 1.071. The close agreement between measured and calculated performance is typical of that over the entire frequency band.

Measured gain with respect to isotropic varied from about 8.8 dB at the lower band edge to 12.3 dB at the upper band edge. Gain values include dipole mismatch loss but do not include matching circuit loss. The measured gain agrees well with calculated gain which varied from 9.3 dB to 12.1 dB across the frequency band. Calculated gain is NEC gain per Figure 3a curve "FLT RD=50, XD=0" minus dipole mismatch loss of 0.18 dB maximum.

CONCLUSIONS

In conclusion, the following major goals have been achieved:

1. Developed a NEC optimization program with a cost function that allows making a wide range of trade-offs during wide or narrow bandwidth optimization. In addition, the NEC model geometry can be constrained during optimization so that a desired configuration is achieved or so that NEC modeling guidelines are not violated. We are not aware of a program with similar capabilities that uses NEC.

2. Demonstrated that the optimization program can be used to design Yagi-Uda arrays over wide bandwidths by making design trade-offs. In addition, the array and a matching circuit can simultaneously be optimized with the program. Element diame-

ters and the minimum spacing between elements were near the limits that modeling guidelines generally recommend: $0.066\lambda_{MIN}$ diameter elements were used with a minimum spacing between elements of 3 radii.

3. Over a 20% bandwidth, demonstrated good agreement between measured and calculated performance of a Yagi-Uda array with element diameters as large as $0.066\lambda_{MIN}$ and with a minimum spacing between elements of 3 radii.

REFERENCES

1. Pinion, P.E., "NEC-81", V 2.2, 13 DEC88, Part of "NEEDS - The Numerical Electromagnetic Engineering Design System (Version 2)", June 1989, Distributed by ACES - The Applied Computational Electromagnetic Society.
2. Burke, G.J., Poggio, A.J., "Numerical Electromagnetic Code(NEC) - Method of Moments, Parts I, II and III, January 1981, UCID-18834, Lawrence Livermore National Laboratory
3. Himmelblau, D.M., "Applied Nonlinear Programming", McGraw-Hill, New York, 1972
4. Kajfez, D., "Nonlinear Optimization Extends The Bandwidth of Yagi Antenna", IEEE Trans. Antennas Propagation, Vol. AP-23, No. 2, March 1975, PP 287-289
5. Trueman, C. W. and S. J. Kubina, "Verifying Wire - Grid Model Integrity with Program Check", ACES Journal, Winter 1990, Vol. 5 No. 2.
6. Millican, T.A., "Modern Antenna Design", McGraw-Hill, New York, 1985, pp 335-338

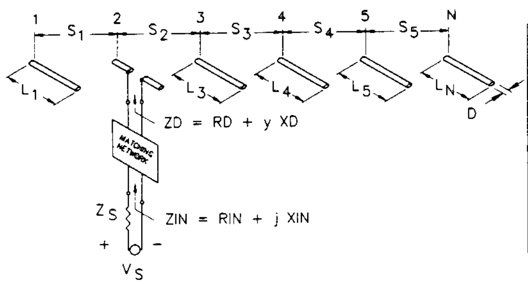

FIGURE 1 YAGI-UDA ARRAY

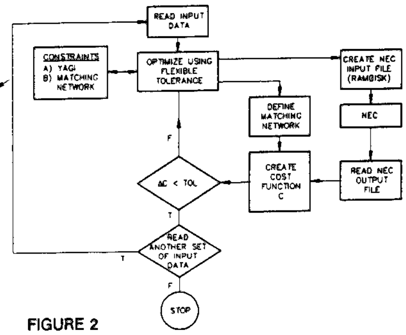

FIGURE 2
FLOW CHART OF NEC OPTIMIZATION PROGRAM

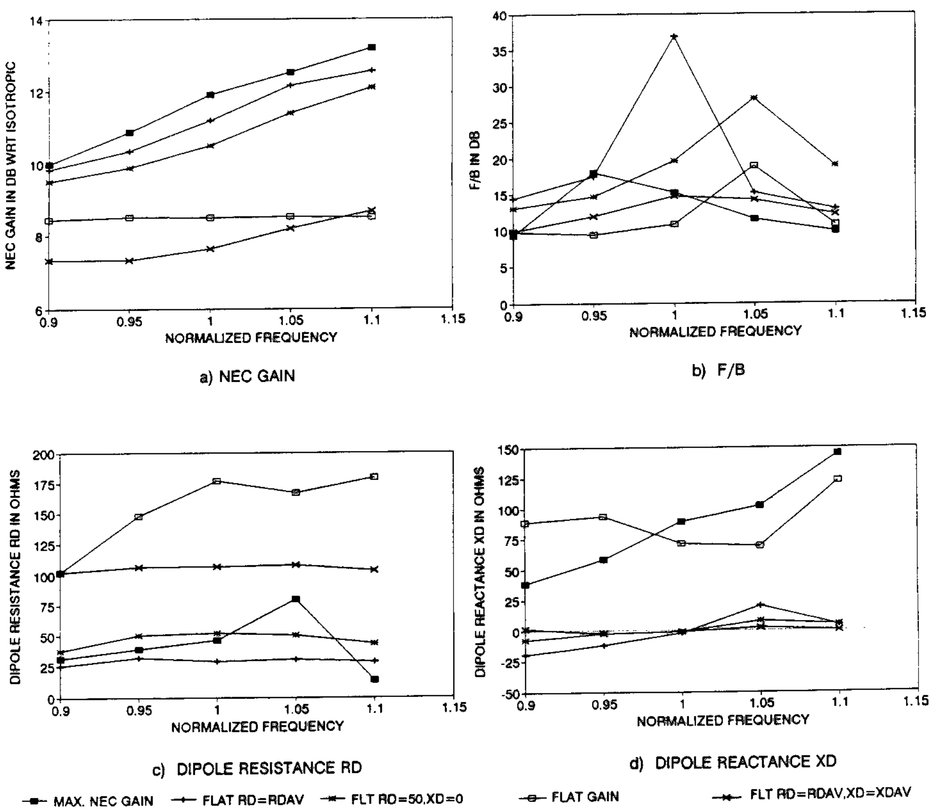

FIGURE 3 - OPTIMIZED 6 ELEMENT YAGI-UDA ARRAYS W/O MATCHING CIRCUITS

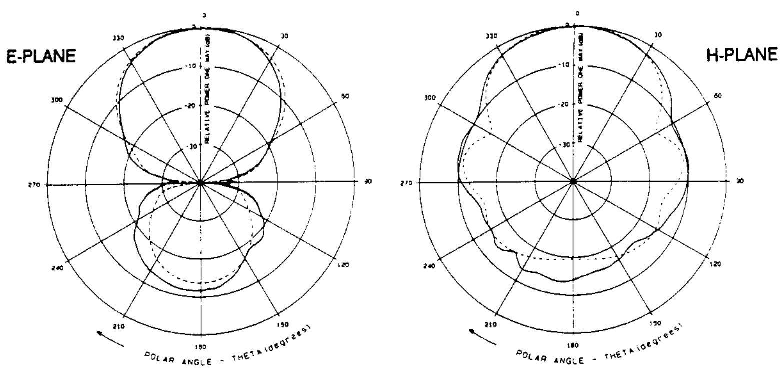

NORMALIZED FREQUENCY = 0.929
D/λ = 0.056

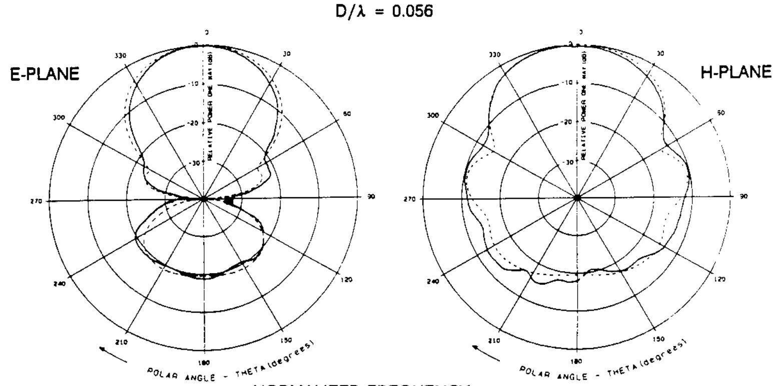

NORMALIZED FREQUENCY = 1.0
D/λ = 0.06

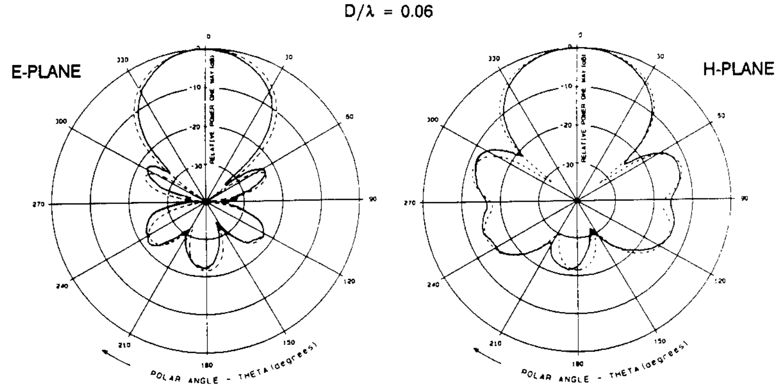

NORMALIZED FREQUENCY = 1.071
D/λ = 0.064

—— MEASURED   - - - - NEC CALCULATED

FIGURE 4 - ANTENNA PATTERNS OF A 6 ELEMENT YAGI-UDA ARRAY OPTIMIZED TO A 50 Ω SOURCE IMPEDANCE

A COMPARISON OF SOLUTIONS FOR WIRES OVER GROUND *

G. J. Burke
Lawrence Livermore National Laboratory
P.O. Box 5504, L-156, Livermore, CA 94550

Abstract

Validation of the NEC–2 and 3 antenna modeling codes for wires over ground has been a problem of continuing concern due to the lack of independent numerical or analytical solutions and the difficulty of obtaining measured data of high accuracy and for known ground parameters. In this paper, the complex propagation constants for wires of varying height above ground are obtained from the NEC solution by analyzing the computed current distribution, and the values are compared with analytic and approximate solutions for infinite wires over ground. The results support the accuracy of NEC for horizontal wires over ground and also demonstrate the relative accuracy of approximate transmission-line formulas as a function of the index of refraction of the ground.

Introduction

The solution for conducting bodies over ground in the codes NEC–2 and NEC–3 [1, 2] is a numerical implementation of the rigorous solution for the ground problem. However, the approximations necessary for the numerical solution introduce many possible sources of error, and hence have required careful validation. One basic source of error is in the accuracy of the fields over ground. The field values over ground are initially obtained by numerical evaluation of the Sommerfeld integrals, and the accuracy of this evaluation has been well established by comparison with independent evaluations. In order to reduce the computation time in the moment-method solution in NEC, the field values are obtained from lookup tables generated from the Sommerfeld integral evaluations. The field values are obtained by interpolation and model-based parameter estimation [2], with the table parameters chosen with relative errors of 10^{-3} to 10^{-4} as a goal. The required accuracy of the field values is relaxed by subtracting a quasistatic component of the field in analytic form. However, the accuracy of the fields are a primary concern in determining the solution accuracy. Other possible sources of error are the validity of the thin-wire approximation for wires near ground, the treatment of wire junctions in close proximity to the ground and wires penetrating the ground surface, particularly at oblique angles.

The NEC ground model has undergone extensive testing to establish its accuracy and limitations. Relatively easy and valuable confirmation was provided by internal checks such as integrating the total radiated power for a dielectric ground and comparing it with the computed input power. Numerical checks on boundary conditions along wires or across the interface also provided very useful validation. NEC–3 was shown to be in good agree-

* Work performed under the auspices of the U. S. Department of Energy by the Lawrence Livermore National Laboratory under Contract W-7405-Eng-48.

ment with an independent moment-method code for a vertical cylinder passing through the interface [3].

The propagation constant for current on a horizontal wire over the ground provides a test that is sensitive to the accuracy of the field evaluation in NEC and can conveniently be compared with analytic solutions. The propagation constants determined from NEC solutions were compared in [4] with the transmission-line approximation of King, Wu and Shen [5] and showed excellent agreement. However, this comparison was limited to grounds with large index of refraction due to the limitations of the transmission-line approximation for the wire over ground.

A solution for the current on an infinite wire over ground, with no limitations on the ground constants, has been developed by Chang, Olsen and Kuester [6, 7, 8]. Their analysis leads to a modal expansion of the current on the wire in which they found two discrete modes and also continuous-spectrum components associated with radiation. The component termed the transmission line mode in this solution is dominant near the source on a wire close to the ground. In the results that follow, this solution for the transmission line mode is used as a standard of accuracy to check the NEC solution for wires near ground, and also to determine the accuracy of the transmission line approximation in [5] as a function of the index of refraction of the ground.

Solutions for a Wire Over Ground

In [6], an integral equation for the current on an infinite horizontal wire along the x axis, with radius a and at height $z = h$ over a ground plane, is solved for a delta-function source located at $x = 0$. The solution for current is

$$I(x) = \frac{2}{\pi\zeta_0}\int_{-\infty}^{\infty}\frac{\exp(ikx\alpha)}{M(\alpha)}\,d\alpha \tag{1}$$

where $M(\alpha)$ is the Fourier transform of the integral equation kernel. For a perfectly conducting wire this function is [8]

$$M(\alpha) = \zeta^2\left[H_0^{(1)}(\zeta A) - J_0(\zeta A)H_0^{(1)}(2\zeta H)\right] + P(\alpha, 2H) - \alpha^2 Q(\alpha, 2H) \tag{2}$$

where $H = k_1 h$ and $A = k_1 a$, with k_1 the free-space wavenumber, and $\zeta = (1-\alpha^2)^{1/2}$ with $\mathrm{Im}\ \zeta \geq 0$. The functions P and Q are given by the integrals

$$P(\alpha, Z) = \frac{2}{i\pi}\int_{-\infty}^{\infty}\frac{e^{-u_1 Z}}{u_1 + u_2}\,d\lambda$$

$$Q(\alpha, Z) = \frac{2}{i\pi}\int_{-\infty}^{\infty}\frac{e^{-u_1 Z}}{n^2 u_1 + u_2}\,d\lambda$$

where $n = (\epsilon_r + i\sigma/\omega\epsilon_0)^{1/2}$ for ϵ_r and σ the relative dielectric constant and conductivity of the ground and

$$u_1 = (\lambda^2 - \zeta^2)^{1/2}, \qquad u_2 = (\lambda^2 - \zeta_n^2)^{1/2}, \qquad \mathrm{Re}\ u_1, u_2 \geq 0$$
$$\zeta_n = (n^2 - \alpha^2)^{1/2}, \qquad \mathrm{Im}\ \zeta_n \geq 0.$$

Evaluating (1) for many x values would be time consuming, due to the double infinite integrations. Some results for specific ground parameters are given in [6]. The discrete modes can be found much more easily. Chang, Olsen and Kuester have shown that there are two discrete modes in the solution, corresponding to zeros of $M(\alpha)$, and two continuous-spectrum components from branch cuts. One of the discrete modes is termed the structure-attached mode, or transmission line mode, and the other is a surface-attached mode. The surface-attached mode is mainly important for large h, and generally has a smaller attenuation rate than the transmission line mode. However, the transmission line mode is dominant near the source on wires close to the ground. It is this mode that will be compared with the NEC solution and the result of the transmission line approximation.

The discrete modes were found here by taking the symbolic derivative of (2). A code was then written to evaluate P and Q and their symbolic derivatives with respect to α by numerical integration. The zeros of $M(\alpha)$ were then found by applying Newton's method. The iteration usually converged in four or five iterations from any reasonable distance from the zero. With large h, two solutions may be found, for the transmission line mode and the surface-attached mode. However, for h less than about 0.1λ the structure-attached mode becomes very hard to find, and the solution always converged to the transmission line mode.

A frequently used approximate result for the propagation constant of the transmission line mode is that given by King, Wu and Shen [5]. This result gives the wavenumber for current propagating on the wire as

$$\begin{aligned} k_L = &k_0\left\{1 + \frac{2}{\ln(2h/a)}\left[\frac{1}{(2k_2h)^2} - \frac{K_1(2k_2h)}{2k_2h} + i\pi\frac{I_1(2k_2h)}{4k_2h}\right.\right. \\ &\left.\left. - i\left(\frac{2k_2h}{3} + \frac{(2k_2h)^3}{45} + \frac{(2k_2h)^5}{1575} + \cdots\right)\right]\right\}^{1/2} \end{aligned} \tag{3}$$

where $k_0 = \omega\sqrt{\mu_0\epsilon_0}$ is the wave number in free space, and $k_2 = k_0(\epsilon_r + i\sigma/\omega\epsilon_0)^{1/2}$ is the wavenumber in the ground. As before, a is the wire radius and h is the height. I_1 and K_1 are modified Bessel functions of first and second kind. Alternate forms of (3), that should be used for large or small heights, are given in [5]. Equation (3) is expected to be accurate for $|k_2| \gg |k_0|$.

To compare the results of NEC with these solutions for the current modes on a wire over ground, a wire with length $6\lambda_0$ was modeled at various heights over ground. The wire was fed with a voltage source at about $\lambda_0/4$ from one end, and terminated at a similar distance from the other end with a resistive load. The load resistance was adjusted by trial to minimize the reflected wave. The required load resistance was most sensitive to the wire radius, so a constant value was used with varying height and ground parameters. The complex propagation constant was then determined from a least-squares fit of a line to the log of magnitude and the phase of current, with the current evaluated at five points over each segment using the sinusoidal current expansion in NEC.

The NEC solution is expected to be accurate for wires at least $10^{-6}\lambda_0$ above the ground surface. The height is also restricted by the thin-wire approximation in NEC, which is also

used in (2) and (3). The errors due to the thin-wire approximation have not been well determined, but the solution might be expected to be good for heights greater than about two to three times the wire radius. The NEC solution should be accurate over a wide range of ground parameters, for $|k_2/k_0|$ ranging from 1.0 to very large values. When $|k_2/k_0|$ is extremely large, as may occur with highly conducting ground and very low frequencies, the relative errors from the table-lookup algorithms may increase. Such errors, which are magnified in the finite-difference solution for magnetic field, have been pointed out by Haack [9].

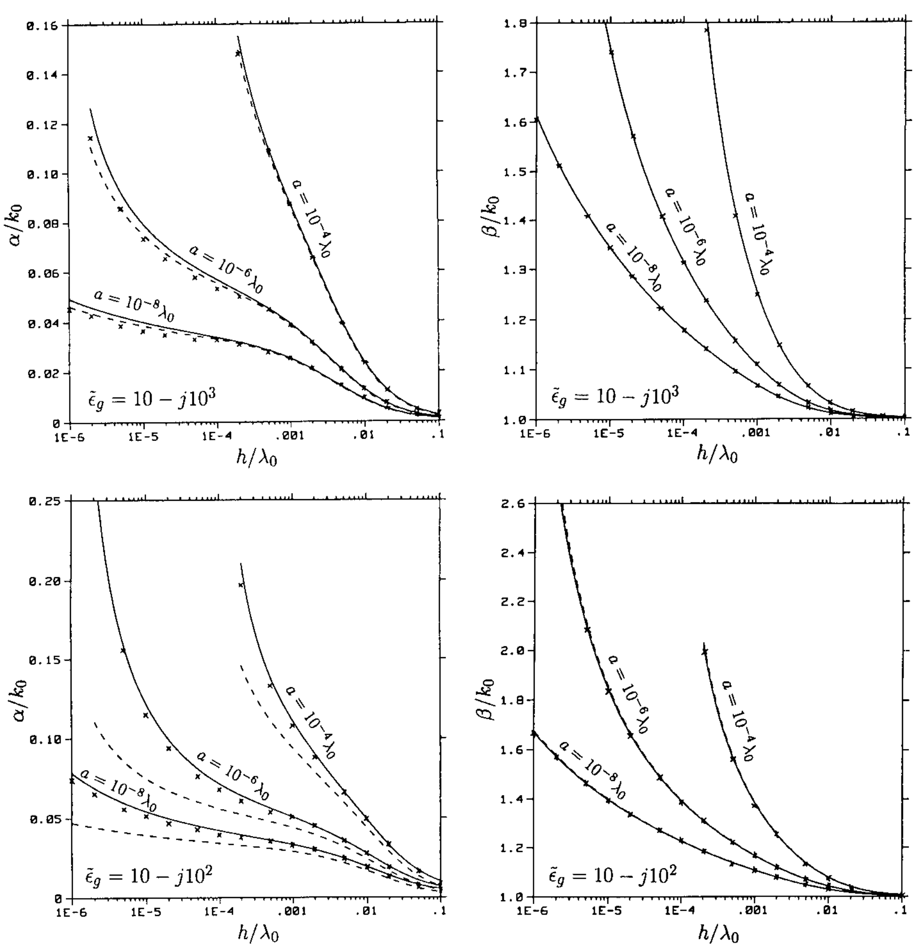

Fig. 1. Complex propagation constant on a wire with radius a and height h over ground. Results shown are the transmission-line mode from Eq. (2) (————), the transmission-line approximation of Eq. (3) (- - - - - - -) and NEC-2 (× ×).

Results

Propagation constants on wires over ground were computed for wire heights ranging from a minimum of $10^{-6}\lambda_0$ or two times the wire radius to at least $0.1\lambda_0$. The ground constants are shown by $\tilde{\epsilon}_g = n^2 = \epsilon_r - j\sigma/\omega\epsilon_0$. Note that equations (2) and (3) are written for $e^{-j\omega t}$ time convention, as in the sources referenced, while in the rest of this paper $e^{+j\omega t}$ is assumed, as in NEC. Results obtained by solving for zeros of equation (2), directly from equation (3) and from the NEC–2 solution for current are shown in Figures 1 and 2. The α/k_0 and β/k_0 shown are respectively the imaginary and real parts of k_L/k_0 and the α_t

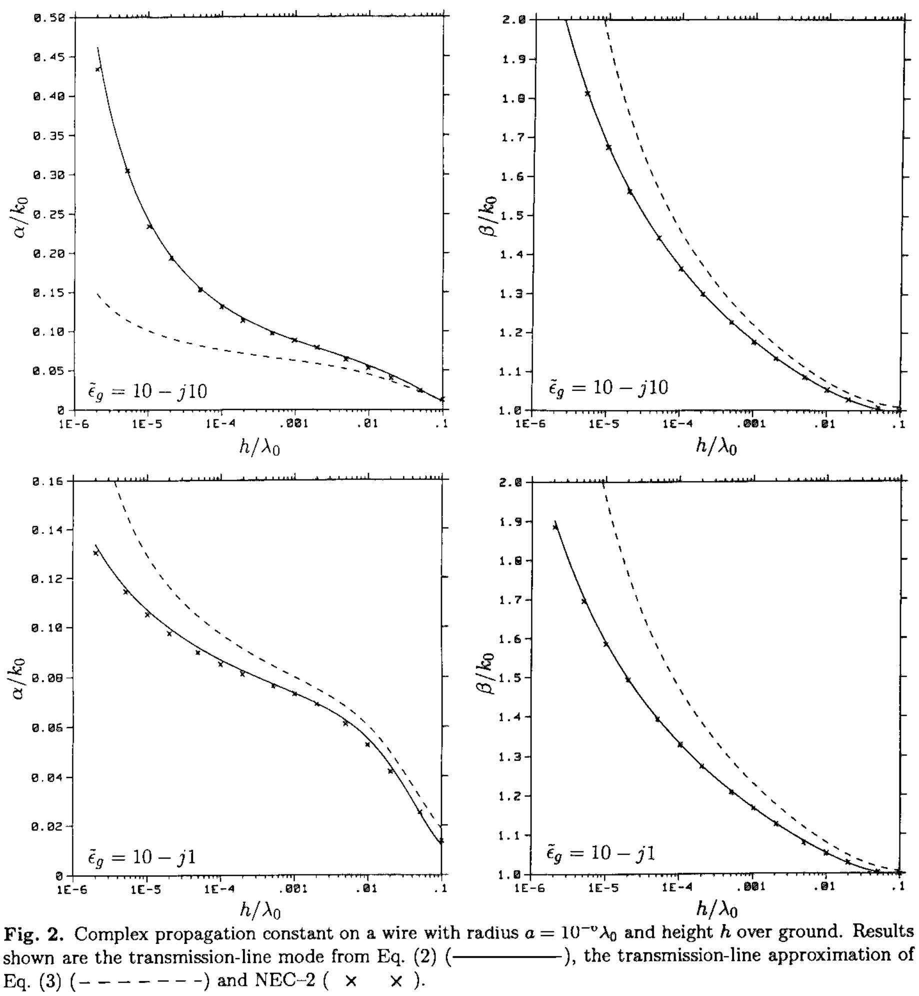

Fig. 2. Complex propagation constant on a wire with radius $a = 10^{-6}\lambda_0$ and height h over ground. Results shown are the transmission-line mode from Eq. (2) (————), the transmission-line approximation of Eq. (3) (- - - - - - -) and NEC–2 (× ×).

satisfying $M(\alpha_t) = 0$. All of the results are seen to be in good agreement for large $|\epsilon_g|$. For smaller $|\epsilon_g|$, NEC and the transmission line mode remain in good agreement, while the transmission line approximation shows increasing errors, as expected.

In some cases, the slight oscillation of the NEC result with respect to the transmission line mode may be the result of other modes in the full NEC solution interfering with the numerical determination of the transmission line mode. This is particularly true for h approaching $0.1\lambda_0$, where the NEC solution for current showed a partially algebraic decay characteristic of a branch cut contribution. More sophisticated processing of the NEC current data would be necessary to separate the modes.

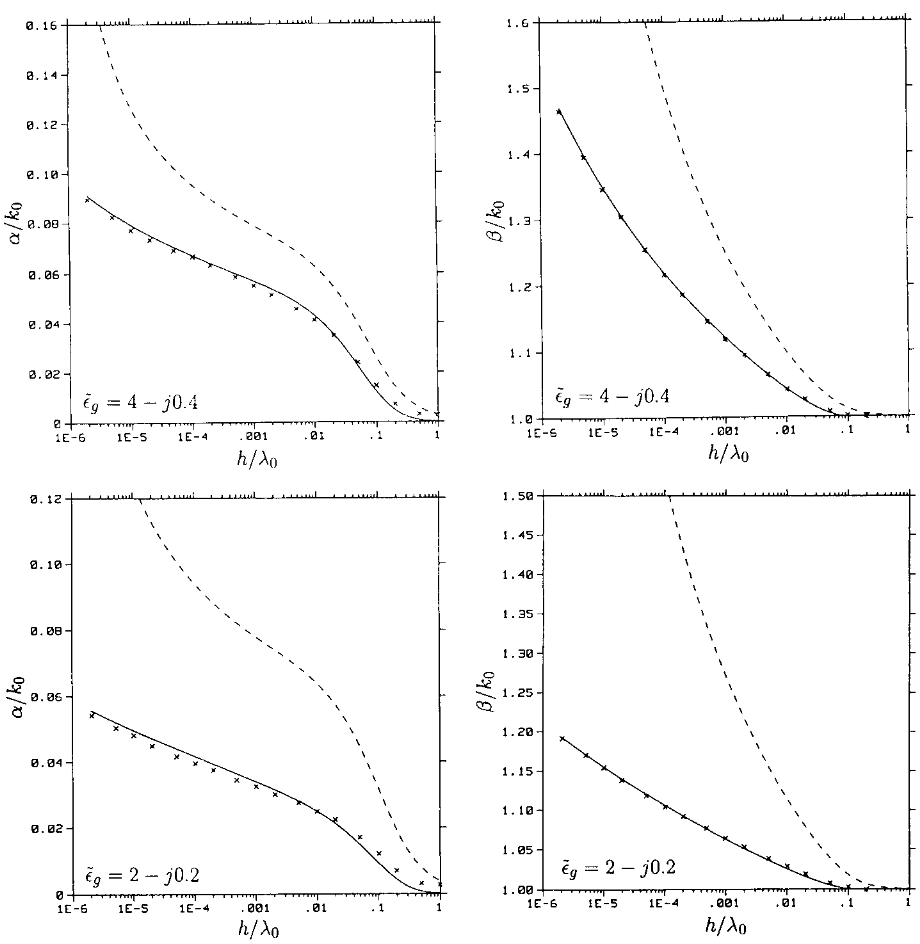

Fig. 2. Continued.

Plots of the relative error of the transmission line approximation from [5] are shown in Fig. 3 for varying $|\tilde{\epsilon}_g|$. The solution of (2) for the transmission line mode was used as a reference. The approximation is seen to be more accurate for β than for α.

The existence of multiple modes on a wire over ground can be seen in Fig. 4 for a wire $30\lambda_0$ long. For wires close to the ground, the transmission line mode decays away leaving a remainder that decreases as the inverse square of distance from the source. This remainder apparently results from the integral of the branch cut from k_1 in (1). The analysis in [6] indicates that the structure-attached mode would dominate far from the source for large h. However, observing it in the NEC solution would require longer wires than in Fig. 4 or signal processing.

Conclusion

Comparison with the results from [6] supports the accuracy of the NEC ground model over a wide range of wire heights and ground parameters.

References

[1] G. J. Burke and A. J. Poggio, *Numerical Electromagnetics Code (NEC) - Method of Moments*, Lawrence Livermore National Laboratory, Rept. UCID–18834, January 1981.

[2] G. J. Burke and E. K. Miller, "Modeling Antennas Near to and Penetrating a Lossy Interface," *IEEE Trans. Antennas and Propagation*, Vol. AP-32, No. 10, pp. 1040-1049, 1984.

[3] W. A. Johnson, "Analysis of a vertical, tubular cylinder which penetrates an air-dielectric interface and which is excited by an azimuthally symmetric source," *Radio Science*, Vol. 18, No. 6, pp. 1273-1281, 1983.

[4] G. J. Burke, "Validation of NEC for Antennas Near Ground," *Proceedings of AP-S EM Modeling Software Committee*, Workshop on Software Validation, San Jose, CA, June 30, 1989.

[5] R. W. P. King, T. T. Wu and L. C. Shen, "The horizontal wire antenna over a conducting or dielectric half space: current and admittance," *Radio Sci.*, Vol. 9, No. 7, pp. 701-709, 1974.

[6] D. C. Chang and R. G. Olsen, "Excitation of an Infinite Antenna Above a Dissipative Earth," *Radio Science*, Vol. 10, No. 8, 9, pp. 823-831, August-September 1975.

[7] E. F. Kuester, D. C. Chang and R. G. Olsen, "Modal Theory of Long Horizontal Wire Structures Above the Earth, 2, Properties of Discrete Modes," *Radio Science*, Vol./ 13, No. 4, pp. 615-623, July-August 1978.

[8] R. G. Olsen, E. F. Kuester and D. C. Chang, "Modal Theory of Long Horizontal Wire Structures Above the Earth, 1, Excitation," *Radio Science*, Vol./ 13, No. 4, pp. 605-613, July-August 1978.

[9] G. Haack, "Using the Numerical Electromagnetics Code (NEC) to Calculate the Magnetic Field Strength Close to a Sommerfeld Ground," *Proceedings of the 7th Annual Review of Progress in Applied Computational Electromagnetics*, March 18-22, 1991.

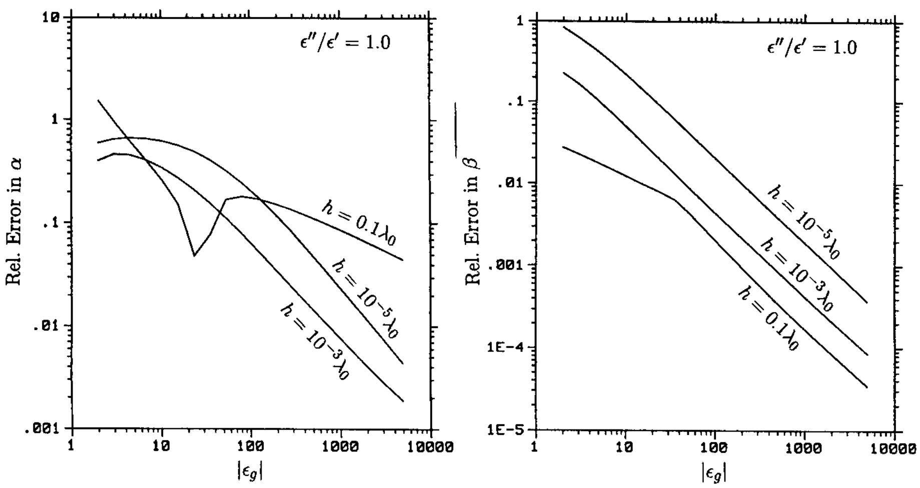

Fig. 3. Relative error in the transmission line approximation for the propagation constant on a wire over ground, for wire height h and radius $a = 10^{-6}\lambda_0$. The relative permittivity of the ground is $\tilde{\epsilon}_g = \epsilon'' - j\epsilon'$.

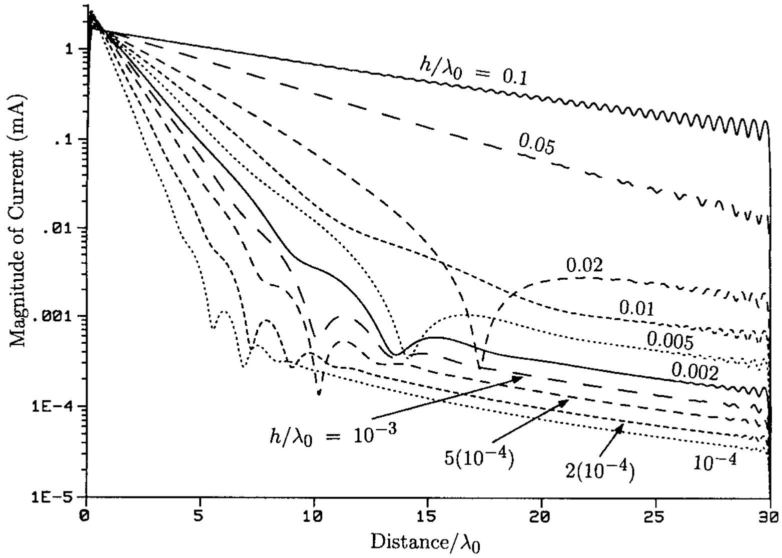

Fig. 4. Current on a $30\lambda_0$ long wire at height h over ground with $\tilde{\epsilon}_g = 15 - j15$.

Element Impedance Considerations in Array Design

Christopher J. McCormack and Randy L. Haupt

Deparment of Electrical Engineering
United States Air Force Academy, CO 80840

ABSTRACT

This paper examines the use of the NEC-2 program as a design tool for antenna arrays. In addition to optimizing the sidelobe level of an array, we consider the impedance mismatches caused by mutual coupling between elements. We want to design an antenna with low sidelobes and a simple feed structure. Our technique uses optimization routines to adjust the array parameters and calls NEC as a subroutine to evaluate the resulting system.

INTRODUCTION

Our research focused on the development of array antennas using simplified, lower cost feed networks. Arrays often use a single source connected to power dividers and transmission lines to connect each active element. In a tapered array, each element requires a different feed system, precluding the economy of mass production for parts in the feed network.

This paper follows our development of a realistic model for the array antenna. We started by looking only at the array factor for isotropic sources. With promising results, we expanded the model to include the effect of having dipoles as elements of the array. The next extension required the use of the Numerical Electromagnetics Code (NEC) to account for mutual coupling between the dipole elements. Our current model also considers the impedances mismatches resulting from mutual coupling and the effect it has on the power radiated by the array elements.

SOURCE MODELING

We modeled an antenna array of half-wave dipoles using the wire models in NEC. A voltage source, located at the center of the element, drives each element. When designing a partially tapered array, we start with several pairs of uniformly weighted elements in the center of the array, then place adjustable element pairs on the outer edges of the array. We adjust the voltage sources driving the outer elements to find the antenna exhibiting the minimum sidelobe level.

Figure 1 illustrates how NEC normally models an antenna. When we place voltage sources on the antenna, NEC uses ideal sources. The ideal voltage source connects directly to the array element which has an input impedance of Za ohms. The power each source provides in this

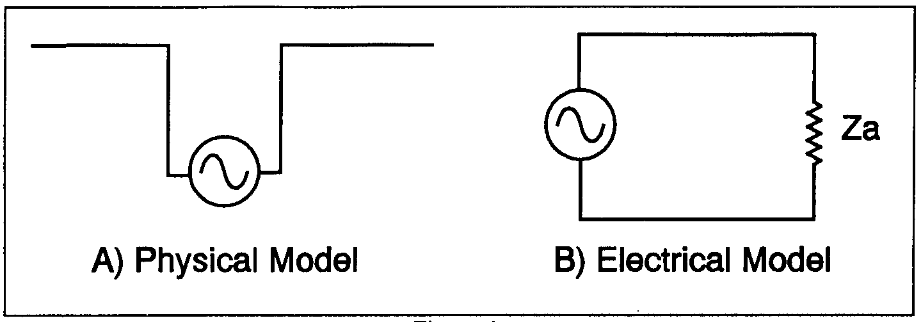

Figure 1

unloaded-source antenna can vary anywhere from zero to infinity depending on the element input impedance (Za) driven by that source. For our antenna arrays, mutual coupling effects change the impedance of the individual antenna elements. In an actual system, the resulting mismatches between sources and the radiating elements changes the array performance. We want a model sensitive to mismatches caused by changes of input impedance due to interactions throughout the array.

By placing a load on the same segment as the source, we place an impedance in series with

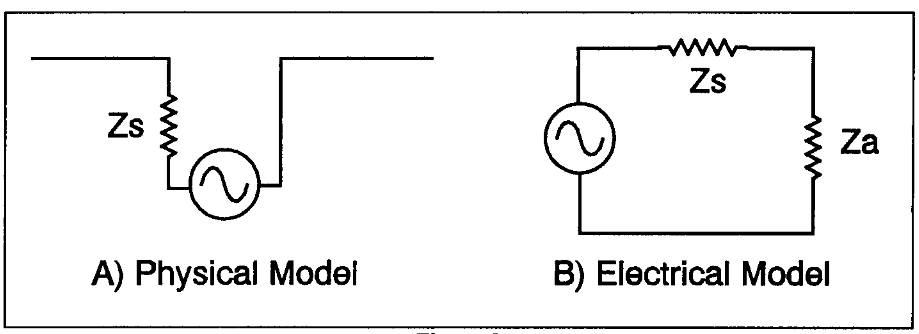

Figure 2

the source as shown in Figure 2. A single loaded-source dipole antenna behaves as expected, radiating the maximum power when the source impedance (the added load Zs) matches the input impedance of the antenna element (Za).

RESULTS

To examine the impact of this revised model, we looked at uniformly spaced dipole arrays

weighted both uniformly and with a binomial taper. The array consisted of 6 z-directed half wavelength dipoles placed along the y-axis (see Figure 3).

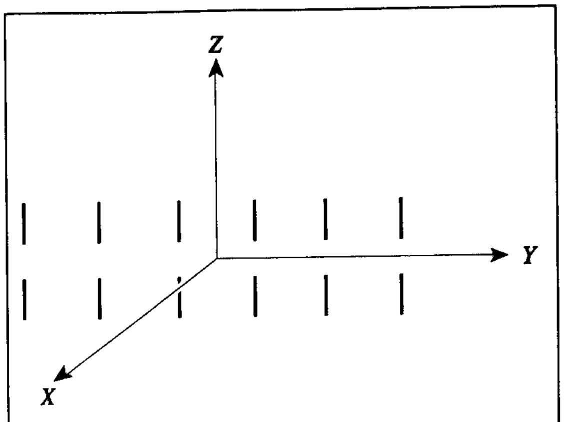

Figure 3

Figure 4 shows the normalized pattern based upon a uniform amplitude placed on each of the elements. We calculated the dotted trace by multiplying the array factor of 6 evenly spaced elements by the element pattern for a dipole in free space. We then used NEC to calculate the dashed trace for a six dipole unloaded-source array (ignoring the effects of impedance mismatches). The solid trace came from using NEC to evaluate a loaded-source array.

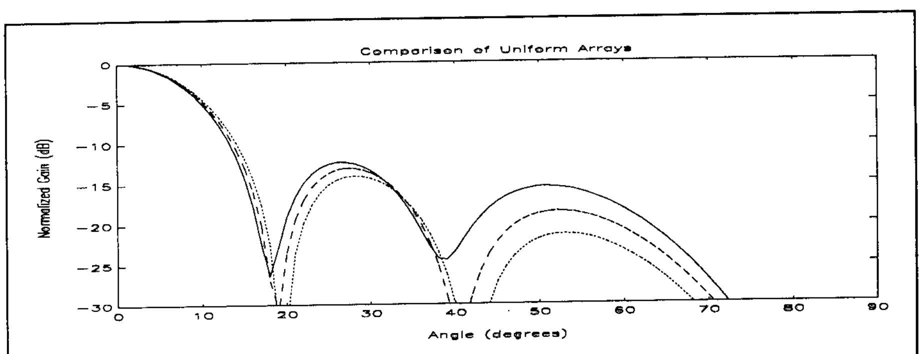

Figure 4

These three approaches to analyzing the array give almost identical results in the main beam. Noticable differences appear in the sidelobes. The array factor calculations give a first sidelobe level 1.5 dB lower than the unloaded-source NEC model. The unloaded-source model has a peak sidelobe level 1.5 dB lower than the loaded-source model. Considering impedance mismatches (unloaded-source model versus loaded-source model) has as much impact as the accounting for mutual coupling between elements (using NEC instead of array factor anlysis).

We also used these three approaches to find the far field pattern of a binomial array (Figure 5). Once again, all three analysis methods provide almost identical main beams. A binomial array should have no sidelobes, which corresponds to the array factor computation. The

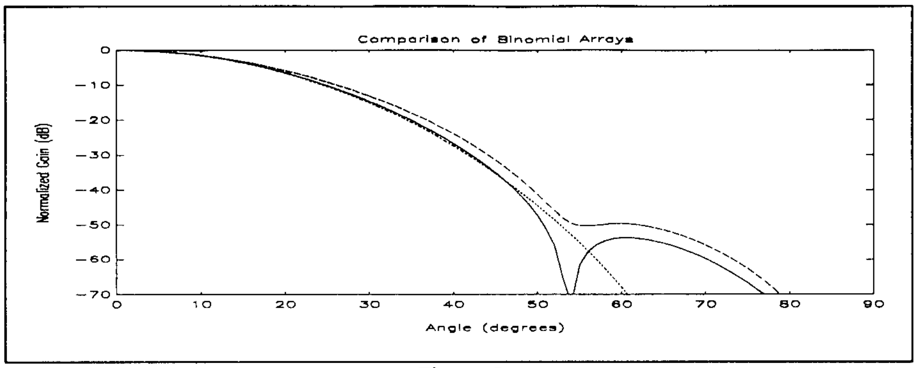

Figure 5

unloaded-source model (dashed line) in NEC shows a slightly wider pattern with no nulls but a slight shoulder. The loaded-source model (solid line) in NEC includes a null in the pattern along with a small sidelobe.

Our last example applies the extended NEC model to a computer optimization design program. The program adjusts the voltage sources placed on the outer elements of a linear dipole array for the lowest possible sidelobe level. Unlike traditional tapers, this approach uses a uniform amplitude over most of the array, and adjusts only a small number of sources.

The elements amplitudes chosen were 0.404558 volts for the original NEC model, and 0.424057 volts for the extended model. The resulting patterns (Figure 6) had a sidelobe level

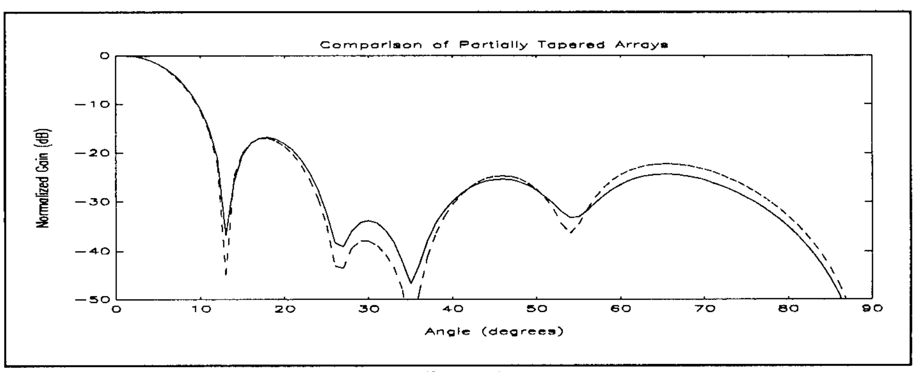

Figure 6

of -16.82dB for the unloaded-source (dashed line) and -17.09dB for the loaded-source (solid line) models.

CONCLUSION

Using the loaded source model in NEC does change the antenna performance reported by the program. Building feed structues to match each array is possible, but the complexity and fabrication costs make it unfeasible for some applications. NEC must account for the resulting impedance mismatches to provide an accurate picture of how the antenna will perform.

REFERENCES

[1] Haupt, McCormack, Brandow, "Optimizing Sidelobe Levels of an Array Using NEC," 7th Annual Review of Progress in Applied Computational Electromagnetics, 18-22 March 1991, Monterey, CA.

EXTENDING NEC TO MODEL WIRE OBJECTS IN INFINITE CHIRAL MEDIA

G. J. Burke, L-156
Lawrence Livermore National Laboratory
PO Box 5504, Livermore, CA 94550

E. K. Miller, MS J-580
Los Alamos National Laboratory
PO Box 1663, Los Alamos, NM 87545

A. K. Bhattacharyya
New Mexico State University, Physical Science Laboratory
PO Box 30002, Las Cruces, NM 88003

Abstract
The development of a moment-method model for wire objects in an infinite chiral medium is described. In this work, the Numerical Electromagnetics Code (NEC) was extended by including a new integral-equation kernel obtained from the dyadic Green's function for an infinite chiral medium. The NEC moment-method treatment using point matching and a three-term sinusoidal current expansion was adapted to the case of a chiral medium. Examples of current distributions and radiation patterns for simple antennas are presented, and the validation of the code is discussed.

Introduction
Interest has been growing recently in the uses and behavior of chiral media in electromagnetic applications. Chiral media can be thought of as ordinary media in which are distributed small helices of either right-hand or left-hand rotation. As a result, waves with linear polarization cannot propagate, and waves with right- or left-hand circular polarization propagate differently in the medium. The pertinent canonical problems were formulated sometime ago [Bassiri, Engheta and Papas (1986), Lakhtakia, Varadan and Varadan (1986)], e.g. point-source radiation, wave propagation and scattering. Interest is growing in more practical problems due to the advent of chiral composites and research is being conducted for chirality might be exploited in electromagnetic design. Research in chiral media has made continued progress in developing analytical tools for understanding fundamental electromagnetic behavior [e.g., Lakhtakia, Varadan and Varadan (1989), Lakhtakia (1990), Lakhtakia, Varadan and Varadan (1990), Uslenghi (1990), Lakhtakia, (1991), Engheta, Pelet and Li (1991)] but the results thereof remain of somewhat limited applicability. In order to analyze the behavior of complex radiators in chiral media it is necessary to resort to numerical techniques such as the integral-equation models (e.g., like NEC) that have become routine tools for many years in analyzing radiation and scattering in achiral media.

In this paper, extension of NEC [Burke and Poggio (1981)] to model arbitrary wire objects in chiral media is briefly summarized, continuing work described elsewhere [Bhattacharyya (1990), Bhattacharyya, Burke and Miller (1992a), (1992b)]. First, a new kernel is implemented in the Electric-Field Integral Equation (EFIE) for thin wires, starting from the dyadic Green's function for a chiral medium. Then the solution of this equation using point-matching and a three-term sinusoidal current expansion is developed. Finally, examples are shown of the solutions obtained for typical dipole and loop antennas operating in chiral media to demonstrate the effects of chirality on current distributions and impedance.

Formulation of the EFIE for Chiral Media
The EFIE for chiral media is conveniently formulated by starting with the dyadic Green's function

for an infinite chiral medium, one form of which is given by Bassiri (1990) (dyadic quantities are outlined and vectors are boldface)

$$\mathbb{\Gamma}_{\text{chiral}}(\mathbf{r},\mathbf{r}') = a_1\left(\mathbb{I} + \frac{1}{h_1}\mathbb{I}\times\nabla + \frac{1}{h_1^2}\nabla\nabla\right)\frac{e^{-jh_1R}}{4\pi R} + a_2\left(\mathbb{I} - \frac{1}{h_2}\mathbb{I}\times\nabla + \frac{1}{h_2^2}\nabla\nabla\right)\frac{e^{-jh_2R}}{4\pi R} \quad (1)$$

where

$$a_1 = \frac{h_1^2 - k^2}{h_1^2 - h_2^2},\; a_2 = -\frac{h_2^2 - k^2}{h_1^2 - h_2^2}$$

and h_1 and h_2 are the wavenumbers for right- and left-hand circularly-polarized waves in the medium as given by

$$h_{1,2} = \pm\omega\mu\gamma + \sqrt{(\omega\mu\gamma)^2 + k^2}.$$

The chirality constant γ determines the degree of chirality of the medium, and $k = \omega\sqrt{\mu\varepsilon}$ where μ and ε are the medium permeability and permittivity respectively.

The electric field at a point $\mathbf{r}$ due to a current distribution $\mathbf{J}(\mathbf{r})$ is given by

$$\mathbf{E}(\mathbf{r}) = j\omega\mu\int\mathbb{\Gamma}(\mathbf{r},\mathbf{r}')\cdot\mathbf{J}(\mathbf{r}')dV'$$

so that an integral equation for the current can be derived in the usual way using the thin-wire approximation. We thus obtain

$$j\omega\mu\int_{C(s)} I(s')\hat{s}\cdot\mathbb{\Gamma}(\mathbf{r},\mathbf{r}_a')\cdot\hat{s}'ds' = -\hat{s}\cdot\mathbf{E}^{inc}(\mathbf{r}),\; \mathbf{r}\in C(s) \quad (2)$$

where $\hat{s}$ and $\hat{s}'$ are unti vectors tangent to the wire axis at observation point s and source point s' respectively. By letting $\mathbf{r}$ represent a point on the wire axis at s while $\mathbf{r}_a'$ is a point on the wire surface at s', the problem of the singularity in the Green's function is avoided for the thin wire. The incident field, E^{inc}, may be an incident wave or a localized field due to a voltage source.

Numerical Solution of the EFIE for Chiral Media

NEC was used as a starting point for developing a code for wires in chiral media, since much of the present code can be used. For modeling wires, NEC employs point matching and a three-term sinusoidal current expansion, which on segment i has the form

$$I_i(s) = A_i + B_i\sin[k_s(s - s_i)] + C_i\cos[k_s(s - s_i)],\; |s - s_i| \le \Delta_i/2 \quad (3)$$

where Δ_i is the segment length. Continuity conditions are imposed on current and its derivative to obtain basis functions extending over three segments with the shape of a B-spline. For ordinary media, k_s is set equal to the wave number in the medium, but for the chiral medium a different choice is made as indicated below.

Extension of NEC to chiral media is simplified by noting that, expect for the $\omega\times\nabla$ terms, Eq. (1) has the form of the free-space Green's function for two separate wave numbers h_1 and h_2. Hence, much of the existing NEC can be used. However, the fields due to the $\sin(k_s s)$ and $\cos(k_s s)$ terms in Eq. (3) now involve addition integrals that must be evaluated numerically or by series approximation because closed-form expressions are not available. For wavenumber k_1 and using

$$I(s) = I_0\begin{pmatrix} \sin(k_s s) \\ \cos(k_s s) \end{pmatrix}$$

for the current on a segment extending from $-\delta$ to $+\delta$ on the z axis, the ρ and z components of the electric field are given by

$$E_\rho(\rho,z) = \frac{-j\eta I_0}{4\pi k_1 \rho}\left\{ \begin{pmatrix} \sin k_s z' \\ \cos k_s z' \end{pmatrix}\left[1 - (z-z')^2 \frac{a + jk_1 R}{R^2} \right.\right.$$

$$\left.\left. + k_s\begin{pmatrix} \cos k_s z' \\ -\sin k_s z' \end{pmatrix}(z-z')\frac{e^{-jk_1R}}{R}\right]_{-\delta}^{\delta} - (k_1^2 - k_s^2)\int_{-\delta}^{\delta}\begin{pmatrix} \sin k_s z' \\ \cos k_s z' \end{pmatrix}(z-z')\frac{e^{-jk_1R}}{R}dz' \right\} \qquad (4)$$

and

$$E_z(\rho,z) = \frac{-j\eta I_0}{4\pi k_1}\left\{ \begin{pmatrix} \sin k_s z' \\ \cos k_s z' \end{pmatrix}\left[(z-z')^2\frac{1 + jk_1R}{R^2} - k_s\begin{pmatrix} \cos k_s z' \\ -\sin k_s z' \end{pmatrix}\right]\frac{e^{-jk_1R}}{R}\right]_{-\delta}^{\delta}$$

$$\left. + (k_1^2 - k_s^2)\int_{-\delta}^{\delta}\begin{pmatrix} \sin k_s z' \\ \cos k_s z' \end{pmatrix}\frac{e^{-jk_1R}}{R}dz' \right\} \qquad (5)$$

where $R = \sqrt{[\rho^2 + (z - z')^2]}$. By successively using $k_1 = h_1$ and $k_1 = h_2$ in the above equations, the electric fields of a current source in a chiral medium are added to obtain the total field. The terms involving $\omega\times\nabla$ in Eq. (1) have the form of the magnetic field of a current filament in an achiral medium, so their evaluation also can use the existing code. These terms are not needed for wire objects lying in a plane, however. Note that for an ordinary medium, k_s is set equal to the medium wavenumber k, so that the integrals in Eqs. (4) and (5) drop out.

The optimum choice for k_s in Eq. (3) is not as clear as for a wire in a chiral medium as in the achiral case. Experience with modeling wires in chiral media has shown [Bhattacharyya, Burke and Miller (1992a), Bhattacharyya, Burke and Miller (1992a)] that the current travels along the wire with a propagation constant approximately $\sqrt{(h_1 h_2)}$, but with somewhat smaller phase constant and increased attenuation. Hence, k_s is usually set equal to $\sqrt{(h_1 h_2)}$. The alternate value $k_s = \max(h_1,h_2)$ has also been used, and gives results very close to the former choice as long as $|k_s\Delta_i| \ll 1$ for all segments on the wires. This result shows that the solution can converge to the correct result independent of the choice of k_s so long as the basis function is able to accurately enough represent the actual current. In fact, Eq. (3) becomes approximately a quadratic function of s when $|k_s\Delta_i| \ll 1$.

Results for Wire Antennas in Chiral Media

The chiral version of NEC (CHNEC), based on the analytical and numerical treatment discussed above, has been tested for problems involving an infinite chiral medium as well as for a vertical dipole located near a chiral half space, a problem discussed elsewhere [Bhattacharyya, Burke and Miller (1992b)]. Results obtained from CHNEC have been checked in various ways, some of which are reported here. The radiation resistance of a short dipole antenna in an infinite chiral medium was found to be in good agreement with the result **in taking** into account that a constant current is assumed in the latter while the CHNEC solution yields a natural triangular current distribution. The current on a $6\lambda_0$ dipole is shown in Fig. 1, and is close to that presented by Jaggard et. al. (1991) except for an unexplained difference in the current magnitude. As separate checks, for both the short dipole and the $6\lambda_0$ dipole, the total radiated power as obtained by integrating the radiated field from CHNEC was found agreed to within 1 percent of the computed input power. Note that reference here to object size in wavelengths is with respect to the achiral-medium situation, i.e., when $\gamma = 0$.

The current magnitude on a 30-wavelength long wire is plotted in Fig. 2 for chirality $\gamma = 0.01$ with the wire radius "a" a parameter. The wire is excited one-quarter wavelength from the left end and is resistively loaded at the right to reduce end reflections. As wire radius increases, we note an increased attenuation of the current. This behavior is observed in achiral media as an increase in the radiation resistance of a dipole with increasing radius. In this case, however, we observe two different attenuation regions. One begins at the feedpoint and is a region of higher attenuation the value of which seems to be dependent on wire radius. The other region is seen further out when the current has decayed adequately and where lower attenuation occurs, the value of which seems to be independent of wire radius. It is apparent that there is a change in the propagation characteristic of the current between these two regimes.

This is made more apparent in Fig. 3 by plotting both he magnitude and phase of the current for a $= 10^{-4}\lambda_0$. There we see that the wavelength associated with the high-attenuation rate is much shorter than that for the low-attenuation rate. In each region, the wavelength is longer than λ_0, indicating that both are what is called a "fastwave" region. Further evidence for the fastwave near-source current is provided in Fig. 4 where the attenuation ($-\alpha$) and phase ($\pm j\beta$) constants are plotted versus chirality for two different values of wire radius for the near-source current as obtained from estimating the wavenumber from the current on a $6\lambda_0$ wire. The CHNEC results are found to agree well with those obtained from evaluating the pole in the current spectrum of an infinite cylindrical antenna [Bhattacharyya, Burke and Miller (1992c)].

The input impedance of a center-fed dipole is shown as a function of chirality for a medium having $\varepsilon_r = 2.56$ and $\mu_r = 1.0$ for lengths of 0.5λ and 1.0λ in Fig. 5. The half-wave dipole is "tuned" through resonance, a phenomenon also produced for the full-wave dipole at a slightly greater value of chirality. These results seem to indicate the possibility of tuning antennas embedded in chiral media or possibly plated on chiral substrates if the chirality can be controlled.

Our concluding results in Fig. 6 are for the input impedance of a loop antenna in a medium having $\varepsilon_r = 2.56$ and $\mu_r = 1.0$ as a function of chirality for antenna circumferences of 0.5λ, 1.0λ, 1.6λ, and 5.03λ. In each case, the changing chirality produces oscillations in the input impedance, but which cannot be accurately described as resonances at least in the sense that the reactance does not always change sign. For the loop as well, it appears as though ,were the chirality of the medium in which the antenna is embedded to be controllable, that some degree of control could be produced over its input impedance.

Concluding Comments

We have demonstrated extension of NEC, implemented in a model called CHNEC, to the problem of modeling wire objects located in infinite, chiral media. Although attention here was limited to

simple dipoles and loops excited as antennas, CHNEC is now applicable to the same kinds of wire objects, e.g., non-planar wire configurations and wire-mesh approximations to solid surfaces, as is NEC itself. Furthermore, work is underway to extend the present interface treatment in CHNEC, presently limited to vertical wires over a chiral halfspace, to the same kinds of halfspace problems as NEC now handles for achiral media. Validation of CHNEC has been accomplished by using power-conservation checks, wavenumber comparison with infinite-antenna solutions, and comparison with other chiral results. Having the general kind of modeling capability represented by CHNEC means that we are now able to explore how chirality might modify the characteristics of antennas and scatterers located in or near chiral media for various design purposes.

References

Bassiri, S., N. Engheta and C. H. Papas (1986), "Dyadic Green's Function and Dipole Radiation in Chiral Medium," *Alta Frequenza*, **LV**, 2, pp. 83-88.

Bassiri, S. (1990), "Electromagnetic Waves in Chiral Medium," in *Recent Advances in Electromagnetic Theory*, H. N. Kritikos and D. L. Jaggard, Ed., Springer-Verlag.

Bhattacharyya, A. K. (1990),"Control of Radar Cross Section and Cross-Polarization Characteristics of an Isotropic Chiral Sphere," *Electronics Letters*, **26**, 14, pp. 1066-1067.

Bhattacharyya, A. K., G. J. Burke, and E. K. Miller (1992a), "Circular Loop antenna In Unbounded Chiral Medium: A Moment-Method Solution," Accepted for publication in *Journal of Electromagnetic Waves and Applications*.

Bhattacharyya, A. K., G. J. Burke, and E. K. Miller (1992b),"Modeling Wire Dipoles in An Infinite Chiral Medium and Vertically-Oriented Near a Chiral half space," *Microwave and Optical Technology Letters*, accepted for publication.

Bhattacharyya, A. K., G. J. Burke, and E. K. Miller (1992c), "Wavenumbers for Currents on Infinite- and Finite-Length Wires in a Chiral Medium," submitted to 1992 AP-S International Symposium, Chicago.

Burke, G. J. and A. J. Poggio (1981), "Numerical Electromagnetic Code (NEC)--Method of Moments," Lawrence Livermore Laboratory Rept. UCID-18834, January.

Engheta, N., P. Pelet and G. Li (1991), "Edge Diffraction in Chiral Medium and RCS Applications: Meixner Edge Condition and the Sommerfeld Half-Plane Problem in Chiral Medium," *IEEE/URSI Meeting*, Session 24, U. of Western Ontario, London, Ontario, Canada.

Jaggard, D. L, J. C. Lin, A. C. Grot and P. Pelet (1991), "Thin Wire Antennas in Chiral Medium," *Electronics Letters*, **27**, 3, pp. 243-244.

Lakhtakia, A., V. K. Varadan and V. V. Varadan (1986), "A Parametric Study of Microwave Reflection Characteristics of a Planar Achiral-Chiral Interface," *IEEE Trans. Electromag. Compat.*, **EMC-28**, 2, pp.

Lakhtakia, A., V. K. Varadan and V. V. Varadan (1989), "Time-Harmonic Fields in Chiral Medium," *Springer-Verlag*.

Lakhtakia, A. (1990), ed., *Selected Papers in Optical Activity,* SPIE Milestone Series, SPIE Optical Eng. Press.

Lakhtakia, A., V. K. Varadan and V. V. Varadan (1990), "Reflection of Plane Waves at Planar Achiral-Chiral Interface: Interdependence of the Reflected Polarization State," *J. Opt. Soc. Amer.*, **7**, 9, pp. 1654-1658.

Lakhtakia, A. (1991), "Recent Contribution to Classical Electromagnetic Theory of Chiral Materials: What Next?," *Speculat. Sci. Technol.*, **14**, 1, pp. 2-17.

Uslenghi, P. L. E. (1990), "Scattering by an Impedance Sphere Coated with a Chiral Layer," *Electromagnetics*, **10**, pp. 201-211.

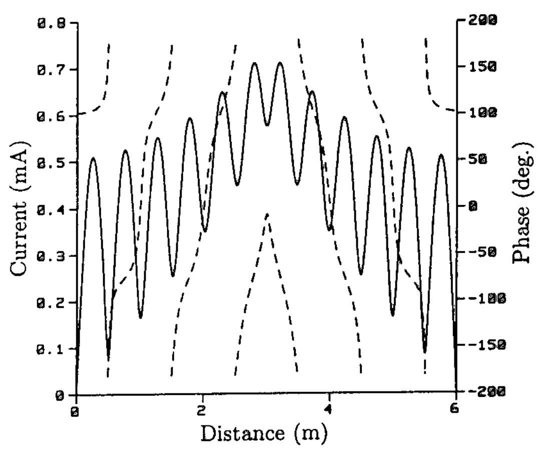

Fig. 1. Current on a dipole antenna of length $6\lambda_0$ and radius $10^{-6}\lambda_0$ in a chiral medium having $\varepsilon_r = \mu_r = 1.0$ and $\gamma\eta_0 = 1.0$, modeled using CHNEC and 121 segments. The current magnitude is shown as a solid line and the phase as a dashed line.

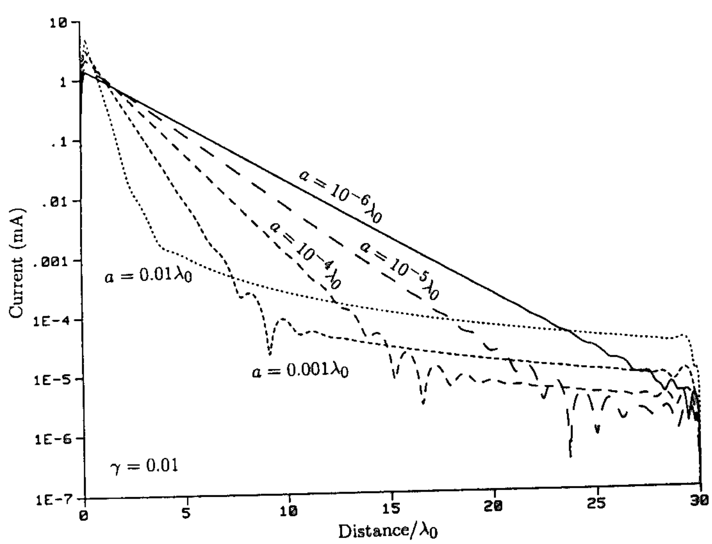

Fig. 2. Current magnitude on a $30\lambda_0$ wire with wire radius "a" a parameter for a chiality of $\gamma = 0.01$. The faster-decay slope that starts at the source may be seen to depend on wire radius, while the slower-decay region, when it is present, is apparently independent of radius.

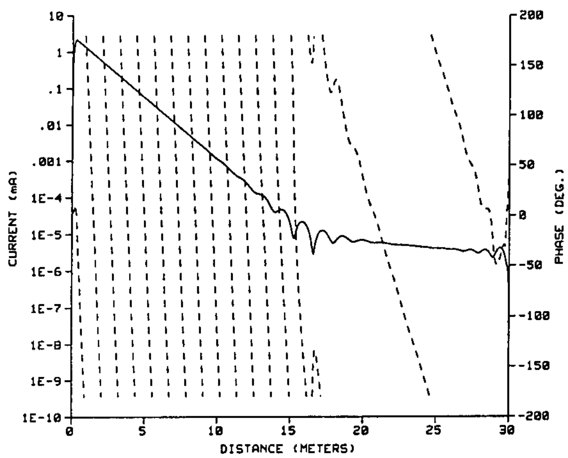

Fig. 3. The current magnitude (solid line) and phase (dashed line) on a $30\lambda_0$ wire for a chirality $\gamma = 0.01$ and a wire radius of $a = 10^{-4}\lambda_0$. The effective wavelength, as measured by the current phase progression with distance, can be seen to change from a value somewhat longer than λ_0 to one much longer than λ_0 at about the wire midpoint. The distance of this transition region depends on the wire radius, as seen in Fig. 2.

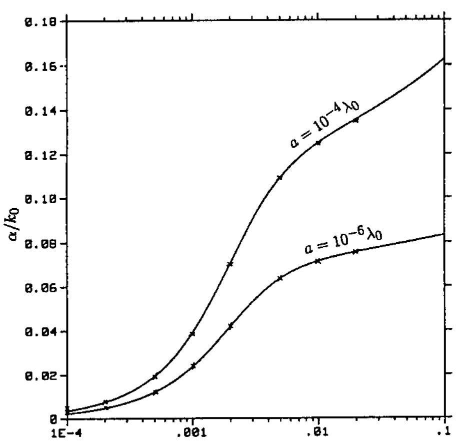

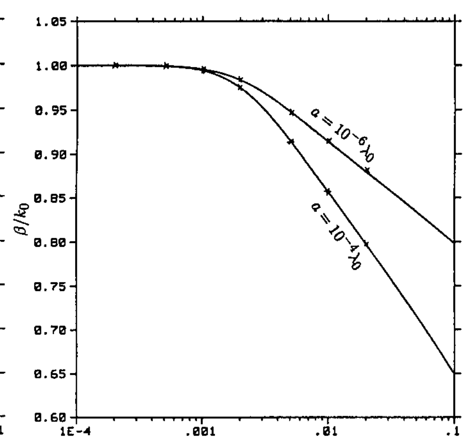

Fig. 4. The attenuation ($-\alpha$) and phase ($\pm j\beta$) constants on a wire as determined from the poles in the infinite antenna current spectrum (the solid line) and as estimated from CHNEC for a $6\lambda_0$ wire are shown as a function of chirality. The good agreement between these two results provides mutual validation for both. Note that these propagation constants apply to the near-source region of Figs. 2 and 3.

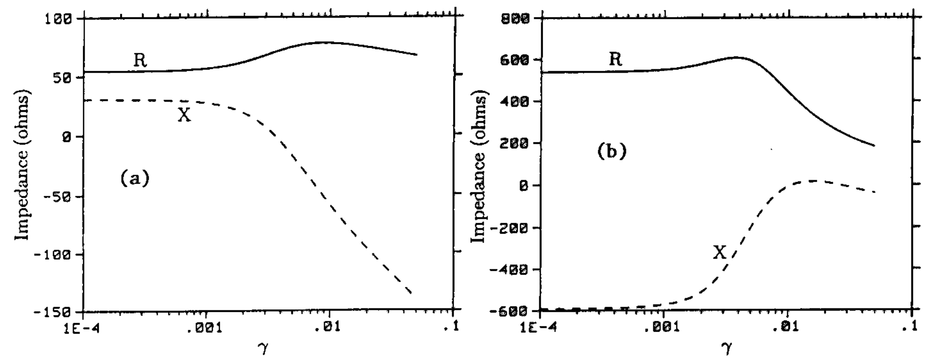

Fig. 5. The input impedance of a center-fed dipole $0.5\lambda_0$ (a) and $1.0\lambda_0$ (b) in length as a function of chirality. Chirality can evidently be used to "tune" a dipole through resonance.

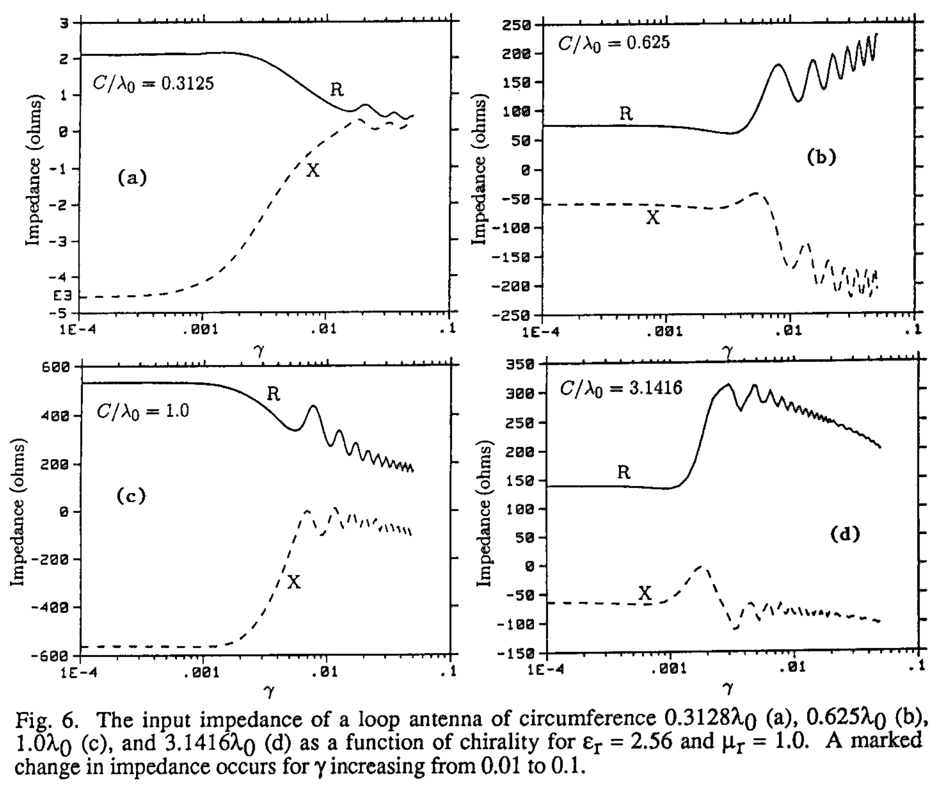

Fig. 6. The input impedance of a loop antenna of circumference $0.3128\lambda_0$ (a), $0.625\lambda_0$ (b), $1.0\lambda_0$ (c), and $3.1416\lambda_0$ (d) as a function of chirality for $\varepsilon_r = 2.56$ and $\mu_r = 1.0$. A marked change in impedance occurs for γ increasing from 0.01 to 0.1.

ELECTROMAGNETIC MODELLING OF A WARSHIP AT HF FREQUENCIES

by

J. McLachlan *
Canadian Armed Forces
Ottawa, Ont.

Y.M.M. Antar
Royal Military College
Kingston, Ont.

S.J. Kubina
Concordia University
Montreal, Que.

S. Kashyap
Defence Research Establishment
Ottawa, Ont.

ABSTRACT

This paper describes research work performed in the pursuit of a Masters of Engineering Degree at the Royal Military College of Canada, Kingston, Ontario that has centered around the very broad subject of computer modelling of complex structures for HF antenna analysis purposes. Specifically, a Canadian warship was modelled using the generic "Wire-Grid Modelling" technique. The electrical characteristics of the exterior of the ship are modelled as a grid of interconnected perfectly conducting thin wires. The HF antennas on the ship are likewise modelled as thin wires and excited by voltages at their feed region. The resulting currents on the segment elements of the model and the fields surrounding the warship are computed using the NEC(3) computer program. The computed radiation patterns and antenna input impedance were compared to measurements made on a 1/50th scale-model.

Since the segment mesh of the model serves only to approximate the electrical characteristics of the warship, the challenge in designing the model is to place the segments in locations where they will best represent the currents which would result on the surface of the ship from a similar excitation. Earlier work at Concordia University in Canada dealing with perfection of the software and techniques for modelling aircraft, has shown that with care, segment-grid modelling can produce accurate antenna impedance and radiation pattern results for aircraft. The work presented here is thus a logical extension of this earlier work. The antenna types modelled included whip, twin whip, and fan antennas. This paper will focus on the whip antenna results.

SUMMARY

With this technique, the number of wires or segments which can be used to define the structure of interest limits the size and amount of detail which can be incorporated into the model. In practice, this upper bound on the number of segments is determined not by the NEC software but by the available computer hardware and what is an acceptable solution time. With the NEC software the solution time is related both to computer memory and processing speed. With NEC the number of computations required to solve for the currents is proportional to the cube of the number of segments. In addition, if the number of segments is too great to allow the interaction matrix to fit into core memory then the processor becomes occupied with disk memory swaps. In the past, to achieve NEC execution times in the order of hours instead of days it has been necessary to minimize the number of segments of the model. The aircraft models were generally 500 segments or less.

To overcome this limitation, a modified version of the NEC(3) software, developed by Defence Research Establishment Ottawa (DREO) [1], was compiled and executed on a Hewlet Parkard DN 10000 R.I.S.C. machine with 16 Mb of RAM. This modified version practically eleminates page faults which occur when the interaction matrix is too large to fit into core memory. This combination of software and hardware permitted

the execution of models up to 1500 segments with solution times in the order of three to four hours for a single frequency.

A detailed account of the model design is contained in chapter 3 of ref [2]. It suffices to say here that in designing the segment model consideration must be given to both electrical and geometrical characteristics of the ship. From the electrical standpoint, segments should follow as closely as possible the paths of actual conductors. Where curves are to be modelled, piece-wise linear fits using short segments can be used. When modelling solid surfaces, such as a flat plate, it is important that the location of segments coincides with areas on the surface where current would be expected to show variation. When a voluminous object is modelled, such as a deckhouse, the surface is replaced with a rectangular grid of segments, their density and radii determined partially by the NEC modelling guidelines [3] and the requirement that the surface of the segments yields an equivalent surface area of the structure. From a geometrical standpoint, care must be taken to ensure that the various dimensions and angles of the original structure are preserved. The NEC modelling guidelines are just guidelines that if followed ensure compatibility of the model with the NEC software. They are not an exhaustive guide to segment-grid modelling. Here, in addition to the guidelines, past experience gained with the aircraft modelling was tapped. However, unlike an aircraft which is a relatively smooth and featureless structure, a warship is really a myriad of smaller complex structures - deckhouses, guns, radars, antennas, masts, etc. - which collectively form the structure.

Initially, three models of the ship of varying complexity were developed; one of 500 segment,s one of 1000 segments, and one of 1500 segments. The increase in the number of segments was a result of decreasing the segment length and adding increased complexity - in terms of features such as guns, antennas, etc. - to the model in the hope of increasing the model bandwidth. Using a .2 wavelength segment length as required by the NEC guidelines resulted in the 500 segment model having a theoretical bandwidth of approximately 2 to 10 Mhz while the 1000 segment model increased this to 20 Mhz and the 1500 segment model to 30 Mhz. Holding to the more stringent guideline of .1 wavelength segment length would have resulted in an unmanageable model size of some 2000 to 3000 segments at a frequency of 30 Mhz. Figure 1 shows the 1000 segment model of the ship. As is suggested in the literature, the radii of the model segments was such that the surface area of the segments in the vertical and horizontal planes were each set equal to the surface area of the warship. Thus the sum of the surface area of all of the segments is approximately twice that of the ship being modelled. Once designed, the model was converted from 1/100 scale drawings to a NEC input file format using the CAD software package DIDEC.DREO developed jointly by DREO and Concordia University [4]. This software allowed for design changes to the model from the computer keyboard.

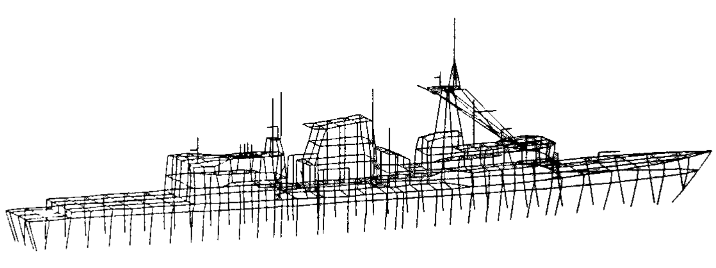

Figure 1 1000 segment wire-grid model of warship.

Finding the best method of exciting the antennas on the model required some thought. The NEC software allows for two methods of exciting a segment. The first method, referred to as the constant field source, specifies a voltage V between the ends of a segment. The alternate method, referred to as the current-slope-discontinuity source, is based on the discontinuity in the current derivative at the segment junctions. On the aircraft models the wire antennas were connected directly to the segments of the model via a segment which served as a feed segment . The other end of the antenna was not connected to the aircraft simulating the insulator which was found on the actual aircraft. The segments in the area of the feed segment were tapered in radius and segment length so that no NEC guideline errors would be produced. The feed segment was excited using the constant field source model.

In the design of the antenna feed area on the warship computer simulations were performed on a quarter wavelength monopole antenna over a perfectly conducting ground plane and compared to theoretical values. The two NEC source methods were simulated with the antenna alternately connected to ground, isolated from ground, and with a 50 ohm load on the bottom segment of each of the previous configurations. The closest agreement in both radiation pattern and input impedance was achieved with the constant field source method and the antenna connected directly to ground. Simulations with the warship model and the same feed arrangement confirmed these results.

In the design of the physical layout of the feed area various different schemes were tried, as shown in Figure 2. This antenna is a 35 foot whip antenna located on the rear left

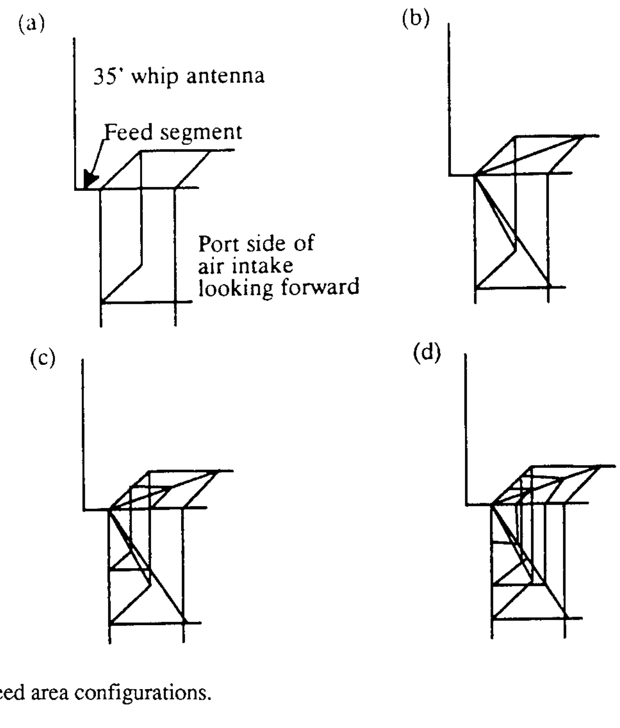

Figure 2 Antenna feed area configurations.

hand corner of an air intake. An air intake is essentially a rectangular metal box with a metallic mesh over one end to allow the passage of air. The mesh was treated as a flat metal plate for modelling purposes as the openings are small compared to a wavelength at HF frequencies. Figure 2(a) shows the simplest segment arrangement for the feed area. Here essentially the antenna feed segment has been attached directly to the air intake. A modification to this, not shown, has the segments leading to the feed segment tapered in both radii and length. In Fig 2(b) to (d) the number of segments in the feed area and their segmentation is increased.

A total of over 60 simulations were performed on the three warship models for the three whip antenna installations. The results were compared to the measured values obtained for input impedance and radiation patterns. The aim of these simulations was to optimise the segment-grid model of the warship to produce results in close agreement with those of the scale-model. The simulations tested the effects of:

a. varying the radii of all the segments of the model by some factor, varying the radii of select segments in the feed area, and varying the radius of the antenna;

b. increasing the number of segments in the antenna feed regions;

c. varying the lengths of segments on the model and antennas;

d. adding increased detail to the model - guns, antennas,etc.; and

e. varying the segment density in the antenna feed area.

A typical example of the the type of impedance and radiation pattern results which were obtained for the whip antennas are shown in Figures 3 and 4 respectively. An examination of the impedance results shows that there is good overall agreement between the measured and computed results, although the resistance values show considerable discrepancy above 10 Mhz. The general shape of the radiation patterns are in good agreement up to 10 Mhz. Generally, with few exceptions the positions of the nulls and lobes are in agreement. At 12 Mhz the measured patterns show more lobing than do the computed patterns, although there are still points of agreement between the two. There is, however, discrepancy between the absolute magnitudes of power gain between the two sets of plots. This discrepancy was present in all plots and varied anywhere from 5 dB to 20 dB. This can be partially accounted for by the manner in which the NEC program computes the isotropic power level used to reference the power gain. The isotropic power level is computed from the voltage and induced current at the feed segment. As has been documented, this value of voltage is not always accurate. A more reliable method is used by Larose [5] to compute the isotropic level. Here the power density is integrated over the surface of a sphere surrounding the antenna to determine the total radiated power. From this value the level is computed. Use of this revised isotropic level resulted in a reduction of the computed gain. The remainder of the difference could be a result of experimental error with the measured results.

Overall for all three whip antennas the results were very encouraging. The best agreement between the computed and measured radiation patterns was with the model of 1500 segments with the radius of each segment set to yield an equivalent surface area of the ship. This is logical as the increased number of segments would produce a better current resolution on the structure. Generally, the best pattern agreement was between the frequencies of 2 and 10 Mhz. Here there was consistently agreement on the location of lobes and nulls between the two sets of patterns. Between 10 and 20 Mhz the patterns were generally similar, although there were some points of disagreement on the locations of nulls and lobes between the two. Above 20 Mhz the patterns were generally dissimilar

(a)

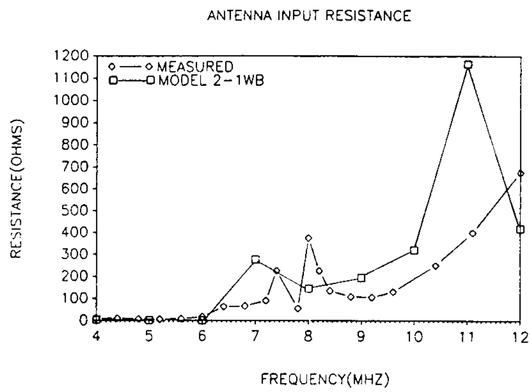

(b)

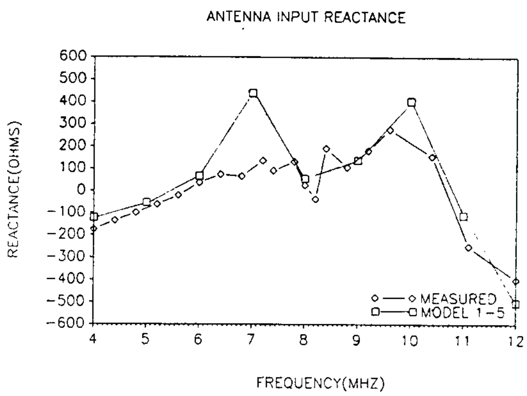

Figure 3 Antenna input (a) resistance and (b) reactance for whip antenna.

with the computed results showing much more lobing than the measured results. This is likely caused by the shorter wavelengths at the higher frequencies making smaller details on the model more important and might be rectified by increasing the number of segments. Increasing or decreasing the radius of the segments by some common factor did not provide any improvement. Increasing the number of segments in the feed region similarly had only very minor effect. Interestingly, when minor details on the ship such as guns, radars, masts, etc. were removed there was no apparent effect on the radiation patterns. It became evident that the general shape of the hull and superstructure of the ship were the greatest contributors to the shape of the radiation patterns below 20 Mhz. Above this frequency it is likely that some of the smaller details play an increasingly important role.

The accuracy of the computed impedance results varied from one antenna to another. In all cases there were points of agreement between the measured and computed results. However, there were usually some points of disagreement making it clear that further investigation of the modelling process is needed in order to properly simulate some aspect of the antenna at a particular frequency. Overall, the best impedance results with the

(a)

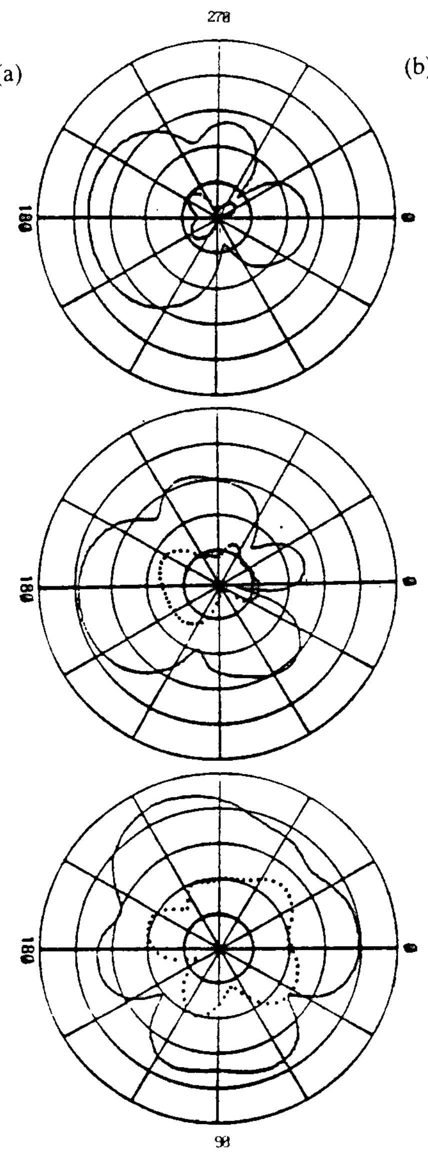

(b)

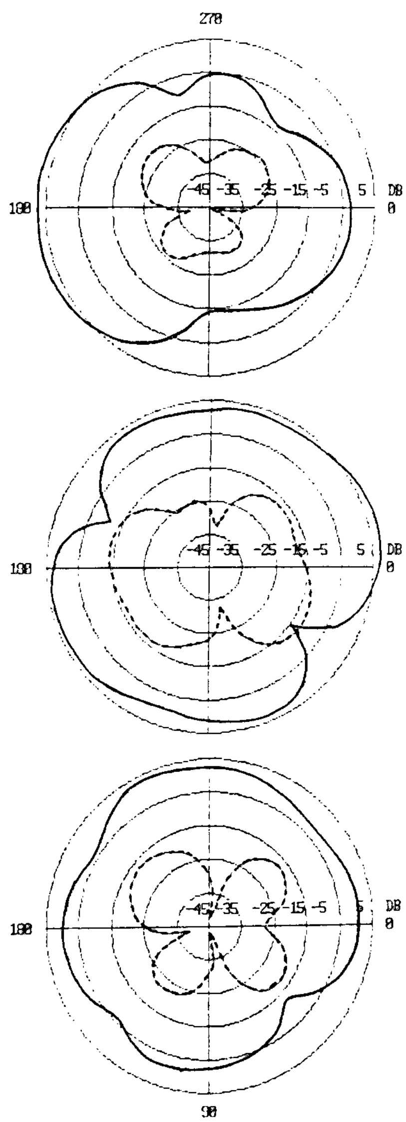

Figure 4(a) Azimuth Plane Pattern for $\Theta = 85°$ for (a) measured vs (b) computed results at 4, 5, 6, 8, 10, and 12 MHz–model 1–1ED. Outer scale is 5 DB and center point is –45 DB relative to a $\lambda/4$ monopole. Legend: ---- Horizontal power gain —— Vertical power gain

(a)

(b)

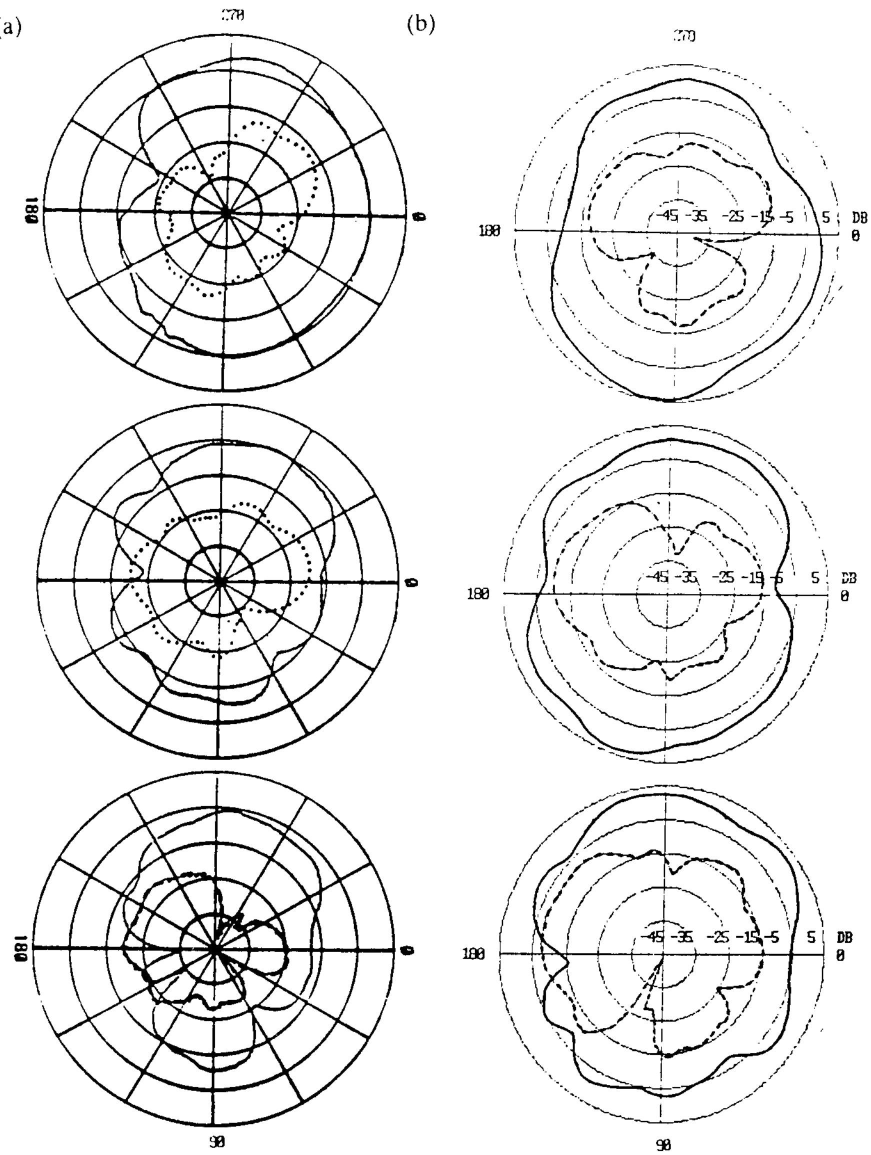

Figure 4(b) 8 (top), 10, 12 (bottom) MHz–Model 1–1ED.

whip antennas were achieved with the 500 segment model. The 1000 segment and 1500 segment models often showed inferior results. Agreement was equally good across the entire frequency band of 2 to 30 Mhz indicating that antenna input impedance was not affected by the theoretical bandwidth of 2-12 Mhz of the 500 segment model imposed by the NEC modelling guidelines. The feed arrangements of Fig 2(a) with the segments not tapered resulted in negative impedances. The best results were with the arrangements of Fig 2 (b), (c), and (d) which showed essentially the same results. Here the results were sensitive to the density of segments at the feed area and how they were segmented. This is logical as the impedance is computed from a computed value of current and voltage on the feed segment The accuracy of this computed value of voltage is sensitive to the segmentation of the wires at the feed area.

Modelling efforts with the twin whip and fan antennas were very encouraging. As with the whip antenna, the radiation pattens were best below 20 Mhz. The impedance results for the twin whip were encouraging as generally good agreement was seen below 20 Mhz. The impedance results for the fan antenna showed more disagreement and point to the requirement for more research into the best method of exciting this antenna.

CONCLUSION

All in all, these initial results were very encouraging. There are some areas of discrepancy that clearly require more research effort. Once perfected and validated, this technique will be a powerful design tool. At present, there is only one antenna range in Canada and it is not used for warship modelling. Thus traditionally, this work has been contracted out to other countries at great expense in time and money. In contrast, with the NEC and DIDEC software, a moderately powerful computer, and a technician to design and run the simulations in modest office space, interesting design and performance information on HF antennas can be readily produced to supplement any measurement results or to help diagnose specific operational scenarios.

REFERENCES

[1] M. Burton and S. Kashyap, "Using Software to Push Back the Limits of the Moment Method", Proceedings of IEEE AP-S International Symposium, June 1991, pp 1504-1507.

[2] J. McLachlan, "Electromagnetic Modelling of Complex Structures", M.Eng Thesis, Royal Military College, Kingston, Ontario, May 1991.

[3] G.J. Burke and A.J. Poggio, "Numerical Electromagnetic Code", Technical Document 116, Naval Electronic Systems Command, 18 July 1977.

[4] S.J. Kubina et al, "The DIDEC System: a new interactive Model Building Technique", Technical Note EMC-84-04, EMC Laboratory, Concordia University, Montreal, Quebec, April 1984.

[5] C.L. Larose, "Advances in Wire-Grid Modelling of Antennas and Auxiliary Computer Graphics Systems with the CP-140 Case Study", M.Eng Thesis, Concordia University, Montreal, Quebec, July 1986, 83-95.

* Presenter

BENCHMARK CALCULATIONS WITH CLASP

by

P. Kirby, D.W. Lizius, A.J. Marrison, J.G. Morgan, D.I. Shepherd and J.C. Wood

Radio Frequency Effects Department, Culham Laboratory,
Abingdon, Oxfordshire, OX14 3DB, United Kingdom

This paper presents the results for radar cross-sections that have been obtained from a new computer program, which is called *CLASP*. Seven different scattering bodies are discussed, namely: the wire, the sphere, the disk, the cube, the ACES 5:1 dipole, the dielectric sphere, and the coated sphere. Comparisons with analytical and experimental results show that *CLASP* is capable of considerable accuracy.

1. INTRODUCTION

This paper presents the numerical results that have been obtained for the radar cross-section of various objects from a new computer program, which is called *CLASP* (Culham Laboratory Advanced Scattering Program). A description of this program is given in a separate paper, *CLASP—A New General-Purpose Method of Moments Scattering Code*, in these proceedings. A further paper, *The Regular Tetrahedron—A Canonical Scattering Problem*, in these proceedings, presents various numerical and experimental results for the scattering from a conducting tetrahedron of edge 3λ, and proposes this as a new canonical problem for ACES.

Seven different scattering bodies are discussed in this paper, namely: the wire, the sphere, the disk, the cube, the ACES 5:1 dipole, the dielectric sphere, and the coated sphere. Comparisons of the results with those from analysis and experiment show that the program is capable of considerable accuracy.

2. THE SPHERE

The problem of electromagnetic scattering from a perfectly conducting sphere is useful because it provides a non-trivial calculation and yet has an analytical solution. Figure 1 shows the numerical model of the sphere that was used in the present calculations. It is constructed from 320 plane triangular patches that are obtained by a recursive refinement of the 20 faces of an icosahedron, in which each new vertex is raised to lie on the surface of the circumscribing sphere. The size of the icosahedron is chosen so that the mean spherical radius of the numerical model is exactly equal to the radius of the true sphere. This refinement, which constitutes a modelling rule for triangulated spheres, allows for the fact that a piece-wise plane model can represent a smoothly curved surface only by its average position.

The calculation was done on a SUN IPC workstation and took approximately 1500 CPU seconds to fill the impedance matrix, 250 seconds to factor the matrix, and 200 seconds to calculate the scattered fields.

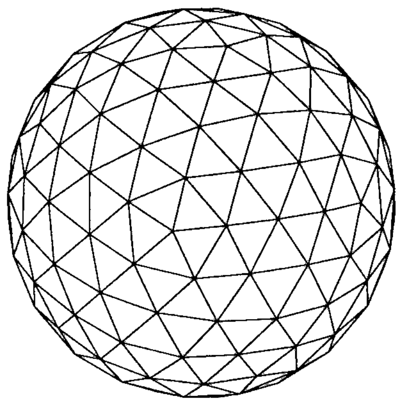

FIG.1 *The numerical model of the sphere.*

Figure 2 shows the results for the bistatic radar cross-section in the plane of the incident electric field. The radar cross-section in decibels relative to $1\,\mathrm{m}^2$ is plotted against the bistatic angle. The wave-length of the incident electromagnetic wave is 1 m, the wave-number k is $2\pi\,\mathrm{m}^{-1}$, and the radius a of the true sphere is given by $ka = 8$. The radius of the circumscribing sphere of the icosahedron is $1.0113a$, that is, about 1% larger than the true sphere. The solid line is the analytical result and the dashed line is the numerical result from *CLASP*. Comparison of the two curves shows that for angles less than 90° there are differences of about 0.4 dB, but at angles greater than 90° the results are almost coincident.

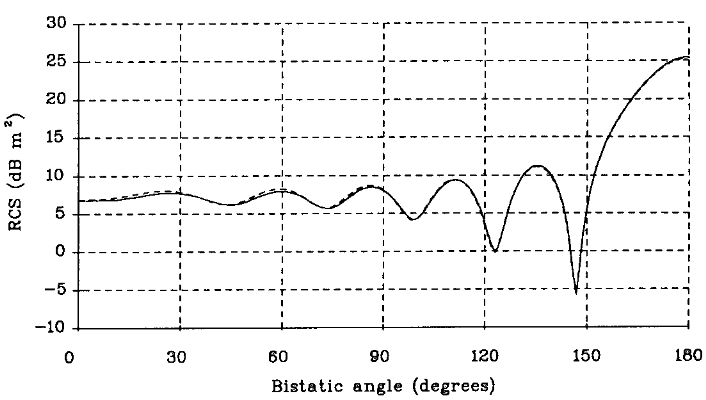

FIG.2 *The results for the bistatic RCS of a sphere, in the* **E***-plane. The dashed line is from CLASP. The solid line is the exact solution.*

A feature of this calculation is that the numerical model is rather coarse, for the condition $ka = 8$ corresponds to a patch size of $\lambda/2.6$, which is unusually large. When the size of

each patch is reduced, which is done here by reducing ka, the accuracy of the calculation increases; for $ka = 1$ the error is less than 0.01 dB.

3. THE WIRE

The radar cross-section of a straight, thin, perfectly conducting wire has been calculated using *CLASP* and the results have been compared with those from the approximate analytical theory of Shamansky et al. [1]. The frequency of the incident electromagnetic wave is 10 GHz, the length of the wire is 0.4953 m (equivalent to 16.5λ), and the radius of the wire is 2.9972×10^{-4} m (equivalent to 0.01λ). The calculation was done in two different ways, as described below.

First, the wire was modelled conventionally by a series of wire segments using the thin-wire approximation and reflection symmetry. The number of segments was 200 and the length of each segment was approximately $\lambda/12$. The calculation was done on a SUN IPC workstation and took approximately 100 CPU seconds to fill the impedance matrix, 4 seconds to factor the matrix, and 490 seconds to calculate the scattered fields.

Secondly, the wire was modelled unusually from plane triangular patches in the form of a very thin cylinder. The calculation used reflection symmetry and 5-fold rotational symmetry simultaneously. The numerical model contains 100 triangles along the length of the wire and 20 triangles around its circumference. The times to fill and factor the impedance matrix were approximately 7300 and 440 seconds respectively on a SUN IPC workstation, and the time to calculate the scattered fields was 4.4 hours.

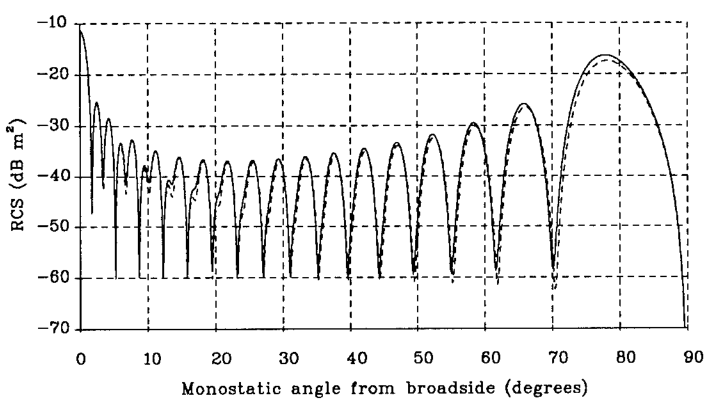

FIG.3 *The monostatic RCS of a wire of length* 16.5λ. *Both results are from CLASP. The dashed line is from the wire model. The solid line is from the patch model.*

Figure 3 shows the results for the monostatic radar cross-section that are obtained when the incident electric field and the wire are coplanar. The dashed line shows the results for the wire model, and the solid line shows the results for the patch model. The two sets of results are in good agreement. These results agree well with the figure in Ref. [1], but a comparison is not presented here because of difficulty with the analytical expressions in that paper.

4. THE DISK

The radar cross-section of a plane circular disk of zero thickness has been calculated with *CLASP* and the results have been compared with those from the experiment of Hey et al. [2].

The disk was modelled using plane triangular patches of approximate size $\lambda/8$ in a mesh with 6-fold rotational symmetry. The wave-length of the incident electromagnetic wave was 32.2 mm, which is that used in the experiment.

Figure 4 shows the results for the monostatic radar cross-section at normal incidence for a series of disks of different values of the radius a. The solid line shows the results of 64 runs of *CLASP*. The typical computing times were 1000 and 30 CPU seconds to fill and factor the impedance matrix respectively on a SUN IPC workstation. The circles show the experimental values. There is clearly very good agreement between the two sets of results.

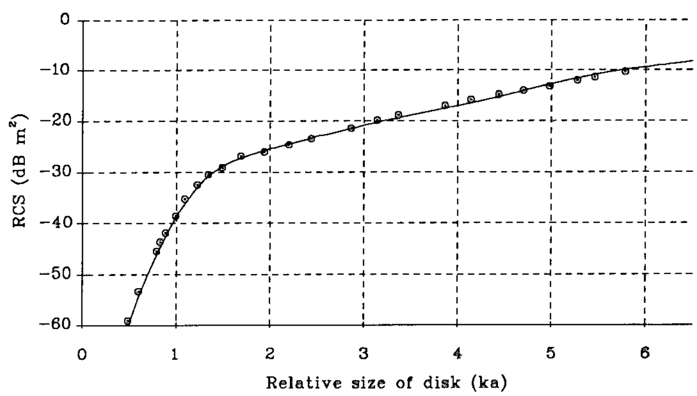

FIG.4 *The RCS of a disk for normal incidence as a function of ka. The solid line is from CLASP. The circles are from experiment.*

5. THE CUBE

The monostatic radar cross-section of a perfectly conducting cube has been calculated with *CLASP* and the results compared with those from the experiment of McGahan [3]. The cube was modelled using plane triangular patches in a mesh with 4-fold rotational symmetry and 2-fold reflection symmetry. Various calculations were done with patches in the range of size $\lambda/4$ to $\lambda/7$. The typical times to fill and factor the impedance matrix were 3600 and 150 seconds respectively on a SUN IPC workstation.

Figure 5 shows the results for the monostatic radar cross-section at normal incidence to a face for a series of cubes of different values of $4s/\lambda$, in which s is the length of a side of the cube. The solid line shows the results from 43 runs of the program, and the circles show the experimental values from Ref. [3]. (The values were taken from enlargements of the figures in that paper.) There is clearly good agreement between the computed and the experimental results.

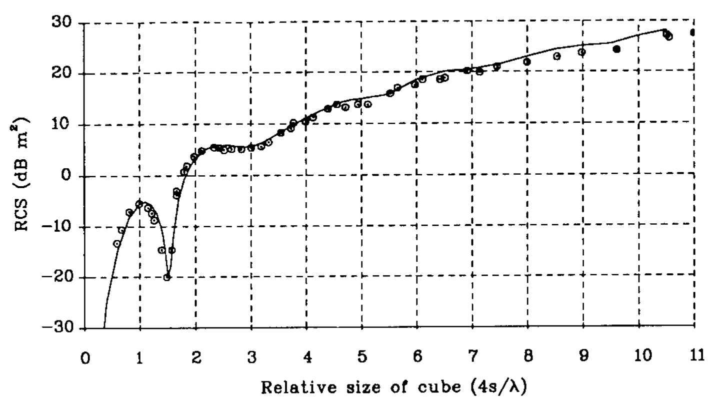

FIG.5 *The RCS of a cube for normal incidence as a function of* $4s/\lambda$. *The solid line is from CLASP. The circles are from experiment.*

6. THE ACES 5:1 DIPOLE

The ACES 5:1 dipole is a canonical problem in electromagnetic scattering [4]. The scattering body consists of a cylinder with hemispherical end-caps. The total length of the body is 0.5 m and its radius is 0.05 m. The incident electromagnetic wave has a wave-length of 1 m and is polarized with the electric field along the length of the body. The main quantity to be calculated is the monostatic radar cross-section for broadside incidence.

The dipole was modelled with *CLASP* using plane triangular patches. The numerical model used 5-fold rotational symmetry and 2-fold reflection symmetry. The end-caps were constructed from the refinements of an icosahedron (as described in section 2 for the sphere). Figure 6 shows the symmetry cell of the numerical model. Three meshes of different resolutions were used in order to demonstrate the convergence of the calculations. The three meshes were derived from the first three recursive refinements of the icosahedron and have the following properties:

Refinement	N_s	N_c	Resolution	f_s	f_c
1	40	280	$\lambda/33$	1.0450	1.0250
2	160	1200	$\lambda/65$	1.0113	1.0062
3	640	4640	$\lambda/129$	1.0028	1.0015

in which N_s is the number of triangles on each hemisphere, N_c is the number of triangles on the cylinder, and the resolution is the typical size of each triangular patch. The ratios f_s and f_c for the hemisphere and cylinder respectively are discussed below. The choice of such meshes, which are excessively fine for most practical calculations, was made in the pursuit of extreme accuracy.

These three meshes were each used in two different ways, so that in total six different calculations were done. The first three of these calculations used the standard inscribed geometry, in which the nodes of the numerical model lie exactly on the surface of the true object.

The second three calculations used a modified geometry, in which the *average* radii of the cylinder and end-cap in the numerical model are made equal to that in the true object,

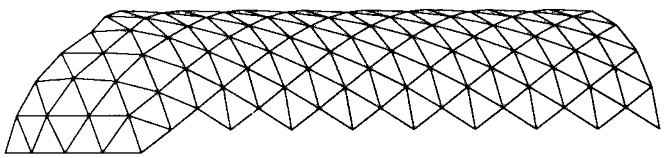

FIG.6 *The symmetry cell in the numerical model of the dipole. This represents one tenth of the complete object.*

but the total length is unchanged. This process allows for the fact that a piece-wise plane model can represent a smoothly curved surface only by its average position. The effect is to increase the circumscribing radii in the modified geometry over that in the inscribed geometry. The ratios of these circumscribing radii are given in the table above for the three different refinements; the ratio f_s applies to the hemisphere and the ratio f_c applies to the cylinder. The fact that these ratios are different means that the modified geometry spreads slightly where the cylinder joins the end-cap.

The results from *CLASP* for the monostatic radar cross-section for broadside incidence for the standard and modified meshes are given below in units of decibels relative to $1\,\mathrm{m}^2$.

Refinement	RCS (std)	RCS (mod)	Fill (s)	Factor (s)
1	−1.08	−1.12	257	2
2	−1.11	−1.12	4271	190
3	−1.12	−1.12	91100	15600

This table shows that the results from the modified mesh are independent of its refinement, and that the results from the standard mesh converge monotonically to that same value. This behaviour shows the importance of an accurate representation of the geometry of the scattering body. The results agree very well with those given in Ref. [4]. The table also shows the times required to fill and factor the impedance matrix on a SUN IPC workstation.

7. THE DIELECTRIC SPHERE

The bistatic radar cross-section of a homogeneous dielectric sphere has been calculated with *CLASP* and the results have been compared with those from analytical theory. The sphere was represented using tetrahedra in a numerical model that comprises a series of concentric layers. The layers start from an icosahedron at the centre, and each has four times the number of faces as the previous inner layer. The model that is used here contains three layers and 1120 tetrahedra. The typical size of the tetrahedra is $\lambda/38$. Five-fold rotational symmetry was exploited in the calculation.

Figure 7 shows the results for the case of **E**-plane scattering from a sphere of size $ka = 0.5$ with a relative permittivity of $2.0865 - 1.29 \times 10^{-2}i$. The times to fill and factor the impedance matrix were 20 hours and 1000 seconds respectively on a SUN IPC workstation. The dashed line shows the results from *CLASP*, and the solid line shows the analytical results. The typical difference between the two sets of results is only 0.04 dB, which means that they are largely indistinguishable on this graph.

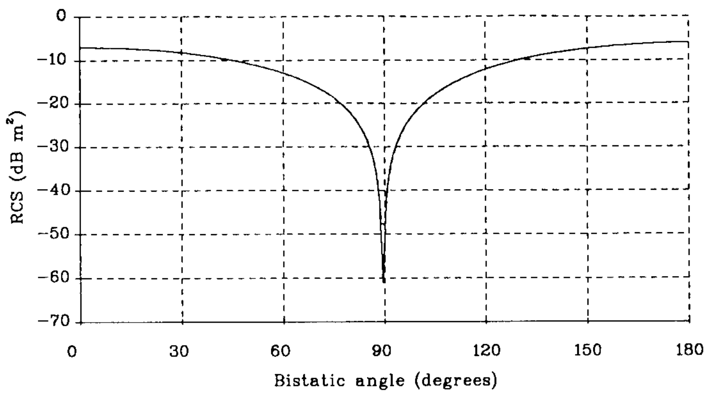

FIG.7 *The RCS of the dielectric sphere. The results from CLASP and the analytical solution are largely indistinguishable on this graph.*

8. THE COATED SPHERE

The bistatic radar cross-section of a coated sphere has been calculated with *CLASP* and the results have been compared with those from analytical theory. The coated sphere comprises an inner perfectly conducting sphere that is surrounded by a homogeneous dielectric shell. The inner sphere was modelled using 80 plane triangular patches on the surface of a refined icosahedron. The dielectric shell was modelled using 880 tetrahedra in one layer. The typical size of the tetrahedra was $\lambda/38$.

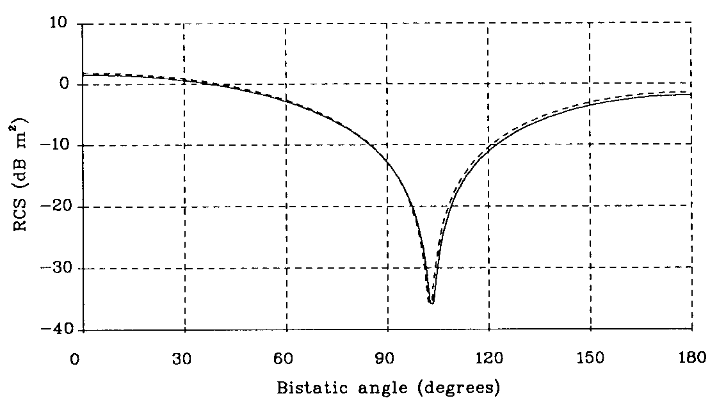

FIG.8 *The results for the bistatic RCS of a coated sphere, in the* **E**-*plane. The dashed line is from CLASP. The solid line is the exact solution.*

Figure 8 shows the results for the case of **E**-plane scattering from a coated sphere of overall size $ka = 0.5$. The radius of the inner conducting sphere is given by $ka = 1/3$ and the relative permittivity of the dielectric shell is $2.0865 - 1.29 \times 10^{-2}i$. The times to fill and factor the impedance matrix were 14 hours and 1300 seconds respectively on a SUN IPC

workstation. The dashed line shows the results from *CLASP*, and the solid line shows the analytical result. There is clearly very good agreement between the two.

Acknowledgement

This work was done partly under contract to the Electronics Division of the Defence Research Agency (RSRE Malvern), and partly under the Corporate Research Programme of AEA Technology (UK Atomic Energy Authority).

REFERENCES

1. H.T. Shamansky, A.K. Dominek and L. Peters Jr., *Electromagnetic Scattering by a Straight Thin Wire*, IEEE Trans. on Antennas and Propagat., Vol. AP-37, no. 8, pp. 1019–1025, 1989.
2. J.S. Hey, G.S. Stewart, J.T. Pinson and P.E.V. Prince, *The Scattering of Electromagnetic Waves by Conducting Spheres and Discs*, Proc. Phys. Soc. (London), Vol. 69, pp. 1038–1049, 1956.
3. R.V. McGahan, *Scattering Experiments at the Ipswich Electromagnetic Measurements Facility: Backscatter from Metal Cubes*, Rome Air Development Center, Griffiss Air Force Base, New York, USA, Report RADC-TR-85-24, 1985.
4. H.A. Sabbagh (Ed.), *The ACES Collection of Canonical Problems Set 1*, The Applied Computational Electromagnetics Society, 1990, pp. 34–59.

THE REGULAR TETRAHEDRON—A CANONICAL SCATTERING PROBLEM

by

A.J. Mackay

AD2 Division, DRA (RSRE) Malvern,
Great Malvern, Worcestershire, WR14 3PS, United Kingdom

and

P. Kirby and D.W. Lizius

Radio Frequency Effects Department, Culham Laboratory,
Abingdon, Oxfordshire, OX14 3DB, United Kingdom

This paper proposes a new canonical problem in electromagnetic scattering. The scattering body is a regular, perfectly conducting tetrahedron of several wave-lengths in size. In particular, this paper considers a tetrahedron with edges of length three wave-lengths. The results from three predictive codes, namely *FACETS*, *NEC* and *CLASP*, are presented. The results from an experiment are also presented and are compared with the predictions.

1. INTRODUCTION

The perfectly conducting regular tetrahedron is a simple three-dimensional object for which no analytical solution exists for the scattering problem. It exhibits scattering mechanisms that provide a challenge to approximate methods of calculation. Such mechanisms include the presence of creeping waves and multiple diffraction from the vertices and edges, which cannot be included properly in a treatment using Physical Optics (PO) or the Physical Theory of Diffraction (PTD), for instance. The tetrahedron is therefore a good canonical problem for the validation of computer codes for the prediction of radar cross-sections.

This paper considers a regular, conducting tetrahedron with edges of length three wave-lengths. Three computer codes have been used to model this object. The first code, *FACETS* [1], uses Physical Optics and the Physical Theory of Diffraction, and is intended for use at high frequencies. The second code, *NEC* [2], uses the Method of Moments and a wire-grid model. The third code, *CLASP* [3], is a new Method of Moments code and uses plane triangular patches.

In addition to these theoretical predictions, an experiment has been done on the scattering from a small gold-plated aluminium tetrahedron at a frequency of 10 GHz, and the results from this experiment have been compared with the predictions. Although the experimental results serve to confirm the essential correctness of the numerical calculations, they are not precise and should not be regarded as exact reference data.

2. DEFINITION OF THE PROBLEM

The tetrahedron has an edge length of three wave-lengths and is taken to be perfectly conducting. The tetrahedron is placed with one face on a horizontal support, as shown

in Fig. 1. This face defines the xy-plane. The vertical line through the opposite vertex defines the z-axis. The wave-vector $\mathbf{k}$ of the incident electromagnetic wave lies always in the xy-plane. The monostatic radar cross-section is calculated as a function of the azimuthal angle θ, which is the angle between $\mathbf{k}$ and the line that joins the centroid of the bottom face to a bottom corner.

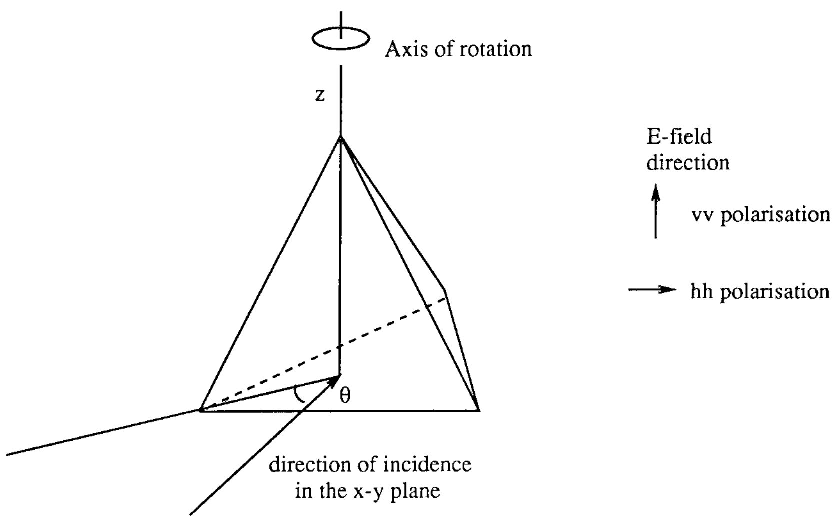

FIG.1 *The definition of the problem.*

The results should be periodic in θ, with period 120°, because of the three-fold rotational symmetry of the tetrahedron. The results should also be symmetric about $\theta = 60°$ because of the reflection symmetry about this position. The positions $\theta = 0°$ and $\theta = 60°$ represent edge-on and broadside incidence respectively.

Two types of polarization are considered. The first type, *HH*, has the electric vector horizontal (that is, in the xy-plane), for both the incident and the scattered wave. The second type, *VV*, has the electric vector vertical (that is, parallel to the z-axis), for both the incident and the scattered wave.

3. PREDICTIONS FROM FACETS

Calculations with version 5 of *FACETS* have been done using both Physical Optics and Physical Optics augmented by the Physical Theory of Diffraction. Such calculations are approximate; they are exact only in the limit of very high frequency. *FACETS* assumes that each face of the tetrahedron is a single facet and that the bottom face is always illuminated. This is achieved here by changing the angle of incidence by a small amount (0.01 degrees) out of the xy-plane, so that the bottom face is illuminated from below. The calculations were done for a tetrahedron of edge $10\sqrt{3}\,\mathrm{m}$, at a frequency of 51.9257 MHz. The radar cross-section was calculated for both polarizations in steps of 0.2°. The runs took about 60 seconds each on a SUN Sparcstation.

Figure 2 shows the results for the radar cross-section for *HH* polarization. The solid line shows the results from Physical Optics alone, and the dashed line shows the results from Physical Optics plus the Physical Theory of Diffraction. The contribution from the Physical Theory of Diffraction acts to increase the radar cross-section everywhere. The circles show the experimental results that are described in Section 6 below. The results from Physical Optics plus the Physical Theory of Diffraction agree well with the experimental results for the main lobe, which is at 60°, and the secondary lobes, which are near 30° and 90°. However, the numerical calculations fail near edge-on incidence, around 0° and 120°, as might be expected. Figure 3 shows the corresponding results for *VV* polarization.

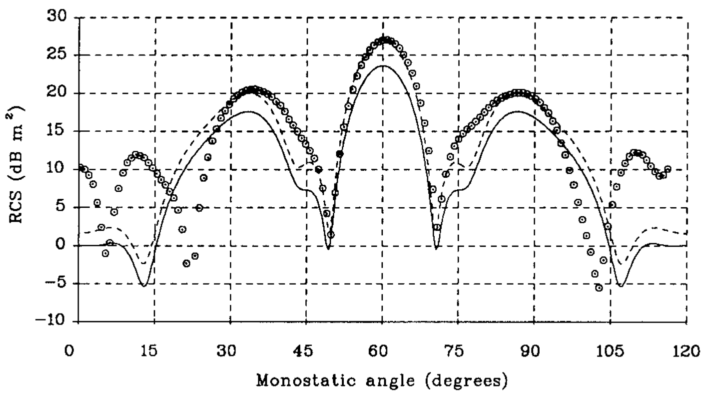

FIG.2 *The RCS results from FACETS for HH polarization; solid line: PO, dashed line: PO plus PTD. The circles are from the experiment.*

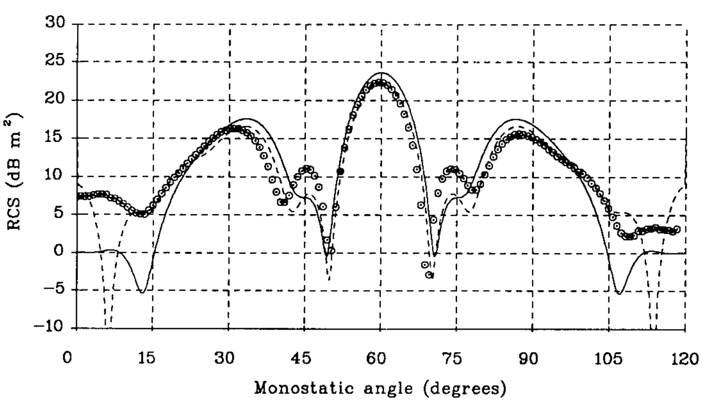

FIG.3 *The RCS results from FACETS for VV polarization; solid line: PO, dashed line: PO plus PTD. The circles are from the experiment.*

4. PREDICTIONS FROM NEC

Calculations with version 3 of *NEC* have been done with two wire meshes. The first mesh contains 26 divisions along each edge and contains a total of 2960 wire segments. This model gives a resolution of about $\lambda/9$. The second mesh contains 33 divisions along each edge and contains a total of 4699 wire segments. This model gives a resolution of $\lambda/11$. The calculations were done for a tetrahedron of edge $10\sqrt{3}\,\mathrm{m}$, at a frequency of 51.9257 MHz, and symmetry was not exploited. The code was run on a Meiko Computing Surface using four i860 processors in parallel [4]. The times to fill and factor the impedance matrix for the coarse mesh were 26 minutes and 28 minutes respectively. The corresponding times for the fine mesh were 65 minutes and 112 minutes respectively. The results for the two meshes are practically identical. Figure 4 shows the results for *HH* polarization. The solid line is from *NEC* and the dashed line is from the experiment. There is reasonably good agreement between the two sets of results, especially at the maxima of the cross-section. The lack of symmetry about 60° in the experimental results indicates the typical errors in those data.

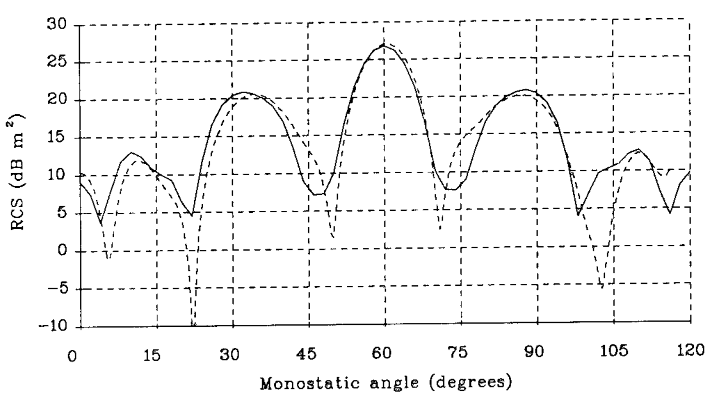

FIG.4 *The RCS results from NEC for HH polarization. The solid line is from NEC. The dashed line is from the experiment.*

5. PREDICTIONS FROM CLASP

Calculations with *CLASP* have been done using plane triangular patches in a numerical model with 3-fold rotational symmetry. The number of patches along an edge was taken to be a multiple of 3, so that the patches are identical equilateral triangles. Several different sizes of patch were used, from a resolution of $\lambda/3$, which is very coarse, to $\lambda/10$, which is the finest resolution that could be run conveniently. The mesh with a resolution of $\lambda/3$ contains 324 triangular patches. The times to fill and factor the impedance matrix were 400 seconds and 20 seconds respectively on Hitech-10 workstation, which is similar in speed to a SUN Sparcstation. The mesh with a resolution of $\lambda/10$ contains 3600 triangular patches. The times to fill and factor the impedance matrix were 12 hours and 9 hours respectively. Figure 5 shows the symmetry cell of the computational mesh for a resolution of $\lambda/3$.

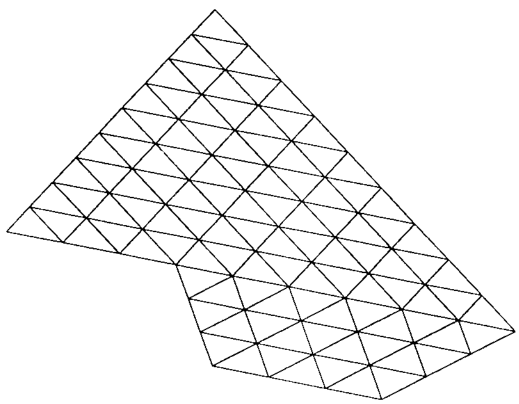

FIG.5 *The symmetry cell of the mesh for CLASP for a resolution of $\lambda/3$. This represents one third of the complete object.*

The calculations were done for a tetrahedron of 88.99 mm at a frequency of 10 GHz, which are the same values as those used in the experiment in Section 6. However, the results have been shifted by +45.78 dB in order to allow comparison with the results from the tetrahedron of size $10\sqrt{3}$ m in Sections 3 and 4. Figure 6 shows the results for *HH* polarization. The solid line shows the results for a resolution of $\lambda/10$ and the dashed line shows the results from the experiment. Again, there is reasonably good agreement between the numerical and the experimental results. As in Fig. 4, the lack of symmetry about 60° in the experimental results is apparent. Calculations with *CLASP* have also been done at resolutions of $\lambda/8$, $\lambda/5$, and $\lambda/3$, which is very coarse. The results for $\lambda/8$ are the same as those from $\lambda/10$. The results for $\lambda/5$ are barely different from those for $\lambda/8$. Remarkably, the results for $\lambda/3$ differ from those for $\lambda/10$ by about 1 dB only.

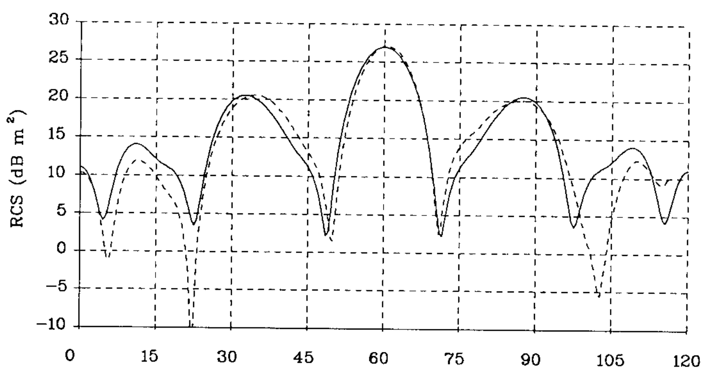

FIG.6 *The RCS results from CLASP for HH polarization. The solid line is from CLASP. The dashed line is from the experiment.*

Figure 7 shows the corresponding results for VV polarization. Again, the lack of symmetry about 60° in the experimental results is apparent. Of interest is the sensitivity of the numerical results to the resolution of the mesh at the edges and vertices of the tetrahedron. This point has not been addressed here because the mesh is uniform. It may be investigated in the future by performing calculations with a non-uniform mesh.

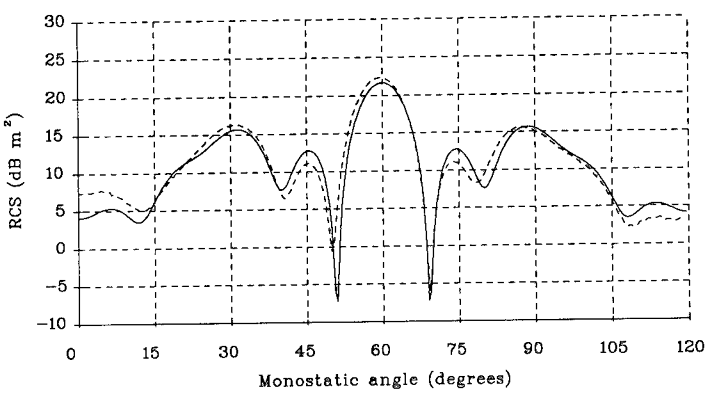

FIG.7 *The RCS results from CLASP for VV polarization. The solid line is from CLASP. The dashed line is from the experiment.*

6. EXPERIMENTAL MEASUREMENTS

Measurements at 10 GHz were made on a regular tetrahedron of edge approximately 90 mm. These measurements are not precise, but are able to give a good indication of the radar cross-section as a function of angle, and to serve to confirm the essential correctness of the numerical predictions.

The tetrahedron was made from a solid rod of aluminium alloy, with 4.5% Magnesium, by milling on three faces and parting-off on the fourth face. The machining was done to routine workshop tolerances. The faces were then finished by hand on abrasive paper and gold-plated so that the surface did not tarnish. The gold was applied by vacuum deposition and is about 500 nm thick. The dimensions of the tetrahedron were found using a travelling microscope and are as follows:

Edge	Length (mm)	Deviation from mean (mm)
1	89.00	+0.01
2	89.15	+0.16
3	88.87	−0.12
4	89.00	+0.01
5	88.94	−0.05
6	88.99	0.00

The mean length is 88.99 mm. The vertices of the tetrahedron are not perfect; there are distortions of ≤ 0.3 mm within 1 mm of the tips.

The tetrahedron was supported on an expanded polystyrene column within an anechoic chamber of approximate size 3 m × 3 m × 4 m. The incident electromagnetic field was a plane wave over the volume occupied by the tetrahedron to reasonable accuracy; the estimated power variation is ≤ 0.2 dB and the estimated phase variation is less than 2°. The distance from the target to the measurement horns was approximately 3 m. The measurement configuration was bistatic, with a bistatic angle of approximately 2° between the transmitting horn and the receiving horn, as shown in Fig. 8.

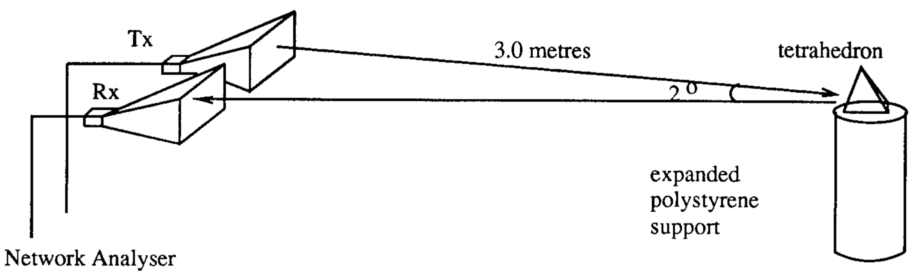

FIG.8 *The experimental arrangement (not to scale).*

The minimum value of radar cross-section that can be measured reliably is approximately $-50\,\mathrm{dB\,m^2}$. The accuracy of the experimental measurements is not known precisely. It is limited by two main factors. First, the mount for the radar target is not a precision element; the base of the tetrahedron may not be set horizontally to better than ±3°. This mis-alignment will change as the target is rotated. Secondly, no transformation is performed from near field to far field. Neither of these effects has been quantified. The results for *HH* polarization and *VV* polarization are those shown in the figures above.

Acknowledgements

The authors are grateful to Mr D.J. Brammer, DRA (RSRE) Malvern, for his help and the generation of the results from *NEC*. Part of this work was done under the Corporate Research Programme of AEA Technology (UK Atomic Energy Authority).

REFERENCES

1. G.N. Jepps, D. Bird and P.N. Short, *RCS Prediction Using the FACETS Computer Program*, Thorn EMI Electronics, Computer Systems Division, Wells, UK, Report DMP 20199.
2. G.J. Burke and A.J. Poggio, *Numerical Electromagnetics Code (NEC)—Method of Moments*, Lawrence Livermore National Laboratory, USA, Report UCID 18834, 1981.
3. P. Kirby, D.W. Lizius, A.J. Marrison, J.G. Morgan and J.C. Wood, *CLASP—A New General-Purpose Method of Moments Scattering Code*, in these proceedings.
4. A.D. Millis and D.J. Brammer, *Implementation of the Numerical Electromagnetics Code NEC3 on a Parallel Computer*, Proc. IEE Int. Conf. on Computation in Electromagnetics, London, November 1991, IEE Publication no. 350, pp. 47–50.

AN INTRODUCTION TO THE THREE-DIMENSIONAL FREQUENCY-INDEPENDENT PHASED-ARRAY (3D-FIPA)

J. K. Breakall
Department of Electrical and Computer Engineering
The Pennsylvania State University
University Park, PA 16802

A new and innovative antenna array, the Three-Dimensional Frequency-Independent Phased-Array (3D-FIPA), was developed by Penn State and is described in detail in this paper. This antenna has been entered into the patent process after much physical and computer modeling analysis. The 3D-FIPA can be designed to provide low grating lobes, low sidelobe levels, nearly constant gain, beamwidth, and impedance with a low Voltage Standing Wave Ratio over extremely large bandwidths. The full array maximizes use of physical volume required and can be built for HF through the microwave regions. The 3D-FIPA applies the log-periodic principle in a novel way to form multi-layer dipole arrays that maintain all electrical spacings and heights over a user-specified frequency range.

I. INTRODUCTION

Phased-array antennas have traditionally been composed of a group of similar, individual element antennas or radiators oriented along a line (a linear array) or in a two-dimensional plane (a planar array). The configurations have provided the ability to form, a single, directed, pencil-beam, fan beam or even multiple beams. The formation and characteristics of the beam or beams was controlled, entirely, by amplitude and phase excitations of individual element radiators in the antennas. The main beam was scanned in space by changing the phasing and excitation of individual radiating elements. The shape of the beam (its width and sidelobes) was controlled by amplitude, phasing and spacing of the radiating elements. Scanning of the beam was accomplished completely electronically.

Phased arrays have been used in many applications including electronically steered radar, shortwave broadcasting, curtain arrays, over-the-horizon radars, ionospheric modification antennas, satellite communications, broadcasting antennas, AM broadcast service antennas, etc.

Recent analysis at Penn State for the construction of a world-class Ionospheric Research Instrument to be constructed in Alaska has resulted in the development of a new and innovative antenna called the Three-Dimensional Frequency-Independent Phased-Array (3D-FIPA). This antenna has been proposed for the High Frequency Active Auroral Research Program (HAARP) of the Navy/Air Force for the unique design concept of a world-class high-power instrument for modification and research of the auroral ionosphere. Work has revealed that there are major difficulties with all current ionospheric modification arrays and phased arrays in general when characteristics are desired to be achieved over very wide bandwidths. Traditional phased arrays when operated over a wide bandwidth have the inherent properties of limited frequency range, disastrous grating lobes, inability to control sidelobes, limited scan elevation and azimuth angles, inability to add future modifications, and limited bandwidth for very fast slewing

of the beam. Rapid beam steering and frequency agility, which require large bandwidths, are characteristics which can be satisfied very easily with this new design.

The design presented in this paper incorporates an original phased-array antenna that has the following frequency-independent characteristics: low grating lobes, low sidelobe levels, nearly constant gain, beamwidth, and impedance, and low Voltage Standing Wave Ratio (VSWR) over any desired user chosen frequency bandwidth. This antenna for which the patent process has begun is believed to be the first solution ever proposed that will achieve all of the above characteristics. It applies the log-periodic principle in a novel way to form multi-layer dipole arrays that maintain all electrical spacings and heights over a user-specified frequency range.

II. BACKGROUND

A detailed examination of the most important and unique features that can only be obtained with the 3D-FIPA antenna follows:

Suppression of grating lobes is extremely important to insure a clean main beam pattern and prevent power from being wasted in unwanted directions. Any conventional array cannot achieve low grating lobes over a wide frequency range because the element spacings expressed in wavelengths increase with frequency, creating interferometer-like grating lobes. The only solution is to construct many narrowband phased arrays so that the spacing changes by only a small percentage with frequency. The range is so limited, however, that many arrays have to be built, and very complex switching systems must be employed. The 3D-FIPA antenna solves all of these problems by preserving all spacings and heights above ground (expressed in wavelengths) for active resonant elements as the frequency is varied. Every geometrical parameter of the antenna is therefore constant with frequency in a log-periodic sense.

Constant gain and beamwidth as a function of frequency is a very desirable characteristic of the 3D-FIPA antenna. Any array with constant physical distance between the elements, such as a conventional phased array, has gain versus angle characteristics that change greatly with frequency, even if the individual elements are inherently wideband. The 3D-FIPA antenna is designed to keep the electrical area constant with frequency. The decrease with frequency of the physical area covered by the active radiating elements causes this constant electrical performance. The gain and beamwidth remain extremely close to constant in a manner very similar to a single log-periodic element. Voltage Standing Wave Ratio, as well, is low throughout the complete frequency range because of the log-periodic concept utilized in the design.

The 3D-FIPA has a coincident location where all feedpoints intersect at a common location making excitation and phasing simpler than in a distributive system. Finally, the usage of physical volume and area is conserved by the judicious arrangement of nesting each subarray inside of other subarrays, all at different heights and specified non-intersecting locations.

Extensive code and experimental validation has established the superior performance of the 3D-FIPA. Measurements have been successful on several reduced-scale models of different versions of the 3D-FIPA. Gain, impedance, VSWR,

beam slewing, interaction with other wires and feedlines, and optimization of geometrical considerations have all been parametrically examined.

III. DESCRIPTION OF 3D-FIPA ANTENNA

Positioning of the various log-periodic antenna structures in the 3D-FIPA is such that each wire's height above a ground plane is some constant in wavelengths (ie. $.25\lambda$) at each wire's resonant frequency. At the prescribed height in wavelengths above the ground plane, each wire's center is also at a constant spacing distance in wavelengths (ie. $.60\lambda$) from adjacent like other wire's centers. Scaling of the antenna elements in a log-periodic sense causes physical wire lengths, heights, and inter-wire spacings to get progressively smaller as one moves towards the feed end of the element. The scaling factor is the same tau factor as used in classical log-periodic antenna design.

Figures 1, 2 and 3 show both overhead and side views of a 4x4 circularly polarized version of the 3D-FIPA. The dark highlighted antenna wires depict the planar nature of the array with excitation at a single frequency. Figure 1 shows the array excited at the lowest operating frequency. Figures 2 and 3 show the same array excited at a mid and highest frequency, respectively. These figures depict the constant above ground heights and constant spacings of the antenna wire elements, a point that was discussed earlier. A total of 32 feed points would provide beam slewing in all directions with switchable polarization.

IV. CONCLUSIONS

The 3D-FIPA concept can be thought of as having many separate N by N vertically stacked dipole planar subarrays of fixed spacings in wavelengths. Subarray dipole elements expand from the center of the array to maintain proper electrical spacings. The highest frequency planar subarray is at the lowest physical height. As frequency is lowered, the physical plane occupied by the planar subarray successively rises above the ground plane. The heights and horizontal spacings in wavelengths for the dipoles in the subarrays are constant with frequency.

To summarize, all presently known phased arrays have severe problems when large frequency ranges of operation are to be achieved. The 3D-FIPA antenna described here solves current phased-array design problems.

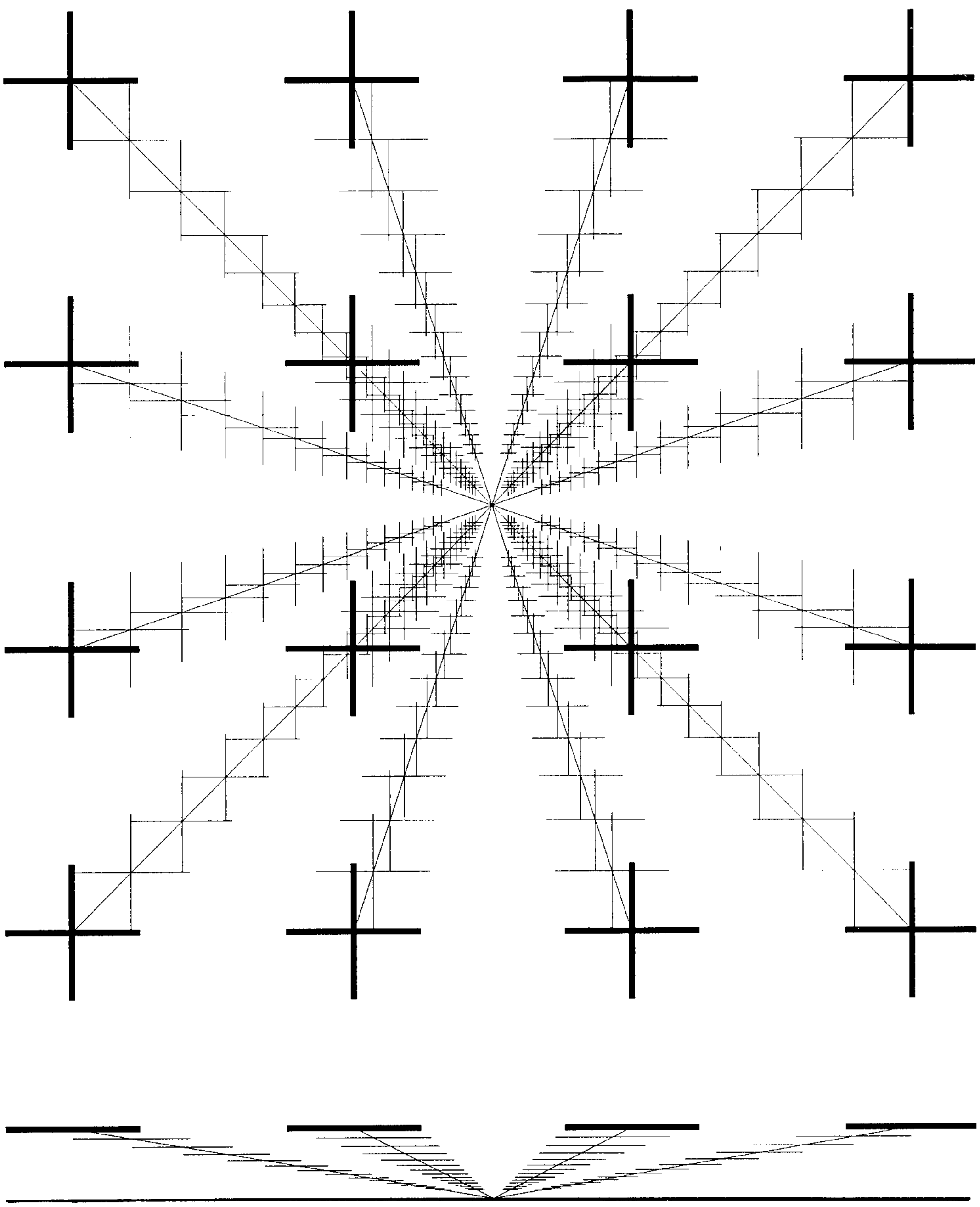

Figure 1. 4 By 4 3D-FIPA (Top And Side Views) Shown Excited At The Lowest Frequency.

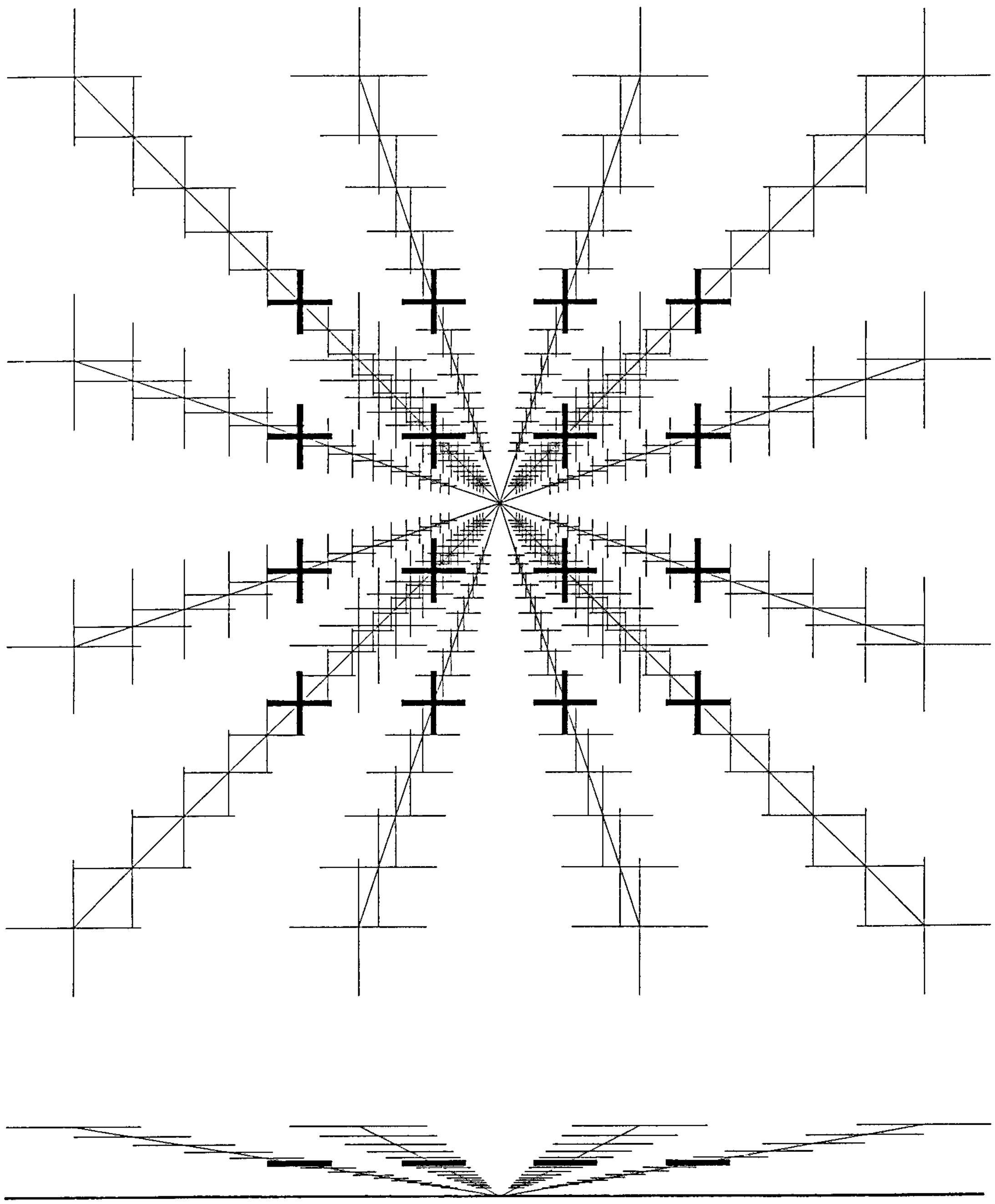

Figure 2. 4 By 4 3D-FIPA (Top And Side Views) Shown Excited At The Mid Frequency.

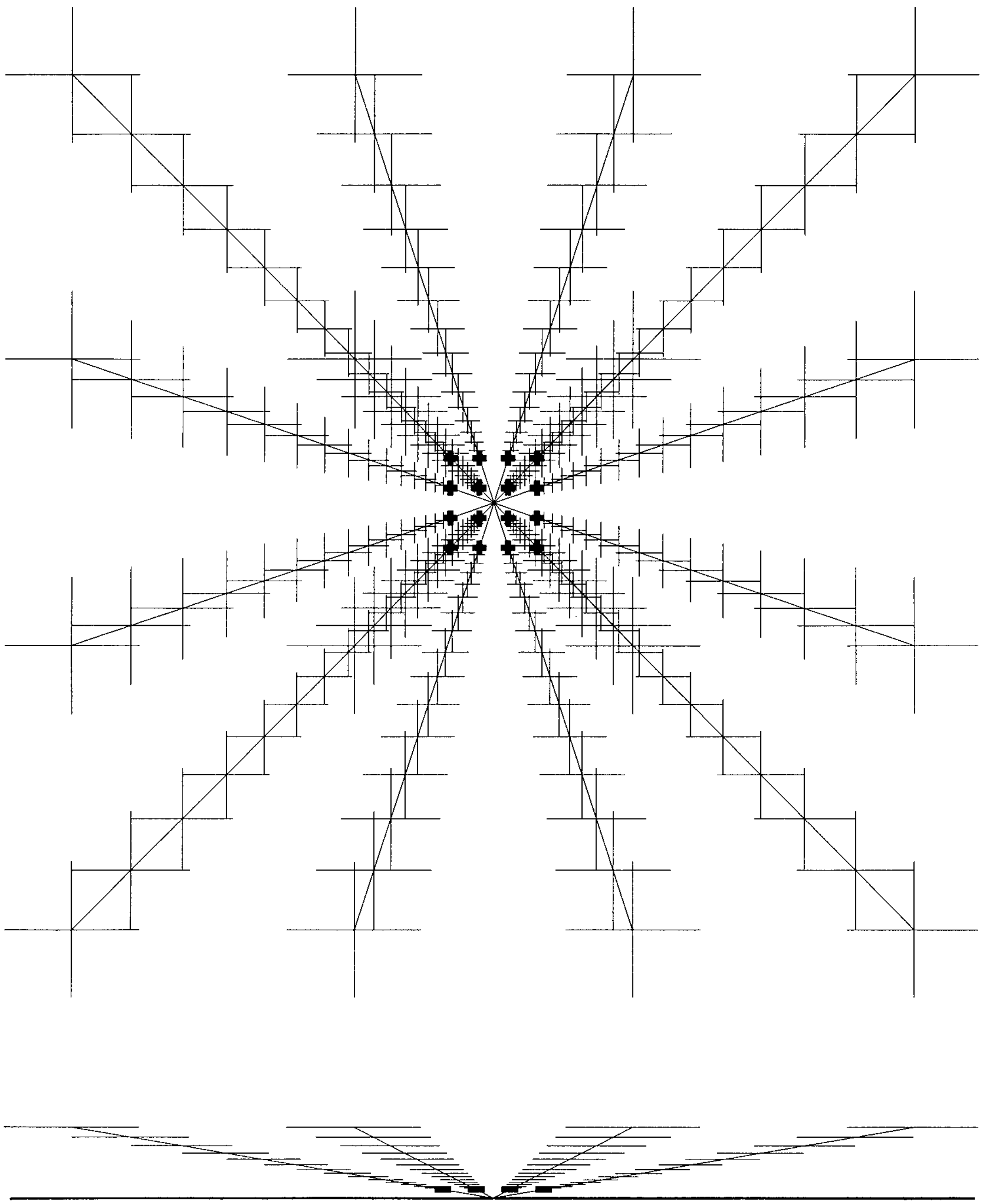

Figure 3. 4 By 4 3D-FIPA (Top And Side Views) Shown Excited At The Highest Frequency.

Time-Harmonic 2-D Electromagnetic Field Solutions using MATLAB

Dr. Jovan Lebaric Rose-Hulman Institute of Technology, Terre Haute, IN 47803
Dr. Darko Kajfez University of Mississippi, University, MS 38677

Abstract
The paper presents the Finite Integration Technique (FIT) formulation of interior and exterior electromagnetic eigenvalue problems. and its MATLAB implementation. Rotationally symmetric fields are considered, reducing the problem to an equivalent 2-D problem with TEϕ and TMϕ fields. Discretized Maxwell's equations are given for a sample problem and the matrix formulation deduced from the discretized equations. Using the concept of a diagonal localized impedance in this matrix formulation different boundaries can be implemented just by changing the matrix elements. Since this approach emphasizes the matrix nature of the discretized problem, MATLAB was used for the FIT implementation. Results of the MATLAB implementation are presented for TEϕ resonant modes of a PEC cavity, as well as a sample MATLAB program to illustrate the compactness of an electromagnetics code written in MATLAB.

Introduction
Finite Integration Technique (FIT) [1.] is a dual technique to the Finite Difference (FD) technique in the sense that FIT uses the integral forms of Maxwell's equations whereas FD uses the differential forms. The fundamentals of applying FIT to electromagnetic field problems involving rotationally symmetric domains have been presented in [2.]. This paper is an extension of the work presented in [2.]. A different matrix formulation is presented, suitable for implementing different boundary conditions on each of the three surfaces of the cylindrical domain. Furthermore, the program implementation has been done in MATLAB. The FIT has been applied to rotationally symmetric domains, with a uniform discretization grid for the rectangular cross-section in an r-z plane, as illustrated in Fig. 1 below.

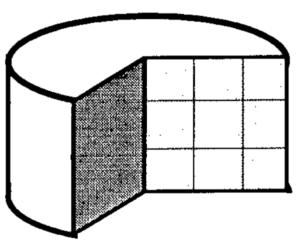

Fig. 1: Rotationally Symmetric Domain

FIT equations are written for the 3-by-3 cross-section of a rotationally symmetric domain shown in Fig. 2. The equations are for TE_{ϕ} fields, that is fields with the following three components in a cylindrical coordinate system: E_{ϕ}, H_r, and H_z. These sample equations illustrate how to form the matrices involved in the FIT formulation.

Sample FIT Equations

Consider a cross-section of a cylindrical domain shown in Fig. 2 below. The cross-section has been discretized using a 3-by-3 uniform grid of square cells: $\Delta r=\Delta z=\Delta l$. Three cells have been chosen in each coordinate direction because three is the minimum number of cells needed to show the matrix structure. The matrix structure observed for the 3-by-3 case is preserved for a uniform grid of any size, with the corresponding increase in the size of the matrices involved. Note that each of the cells can have different permittivity, as illustrated by the variable cell shading. In our application we are interested in solving for the eigenvalues and eigenvectors of the discretized electromagnetic field problem, and no sources are included. Electric field is in ϕ-direction (into the plane of the figure) and the magnetic field has radial (H_r) and axial (H_z) components.

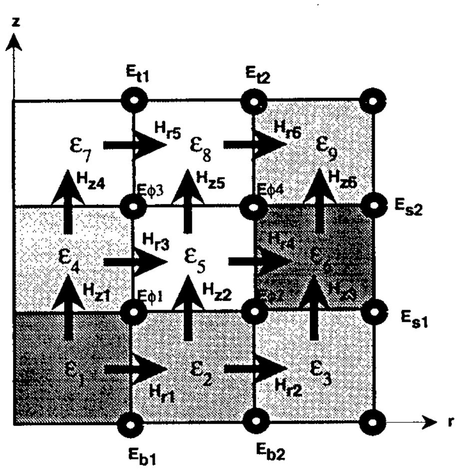

Fig. 2 : Cross-section of a Rotationally Symmetric Domain

The discretized equation are written by approximating the line and surface integrals in the curl equations of Maxwell for each of the cells. Again, the details of this are given in [2.]. Both curl equations (circulation of E and circulation of H) are used to write the discretized equations. Normalized complex frequency s_n is introduced as the product of the complex frequency $s=\alpha+j\omega$ and the ratio of the cell size Δl to the speed of light in free space c: $s_n= s\ \Delta l/c$. The impedance and the admittance of free space are denoted Z_0 and Y_0 , respectively. The number of cells in radial direction is denoted M, and the number of cells in the axial direction is denoted N.

Circulation of Electric Field (first curl equation)

$E_{b1} - E_{\phi 1} = -s_n Z_0 H_{r1}$

$E_{b2} - E_{\phi 2} = -s_n Z_0 H_{r2}$

$E_{\phi 1} - E_{\phi 3} = -s_n Z_0 H_{r3}$

$E_{\phi 2} - E_{\phi 4} = -s_n Z_0 H_{r4}$

$E_{\phi 3} - E_{t1} = -s_n Z_0 H_{r5}$

$E_{\phi 4} - E_{t2} = -s_n Z_0 H_{r6}$

$1E_{\phi 1} = -s_n Z_0 (1/2) H_{z1}$

$2E_{\phi 2} - 1E_{\phi 1} = -s_n Z_0 (3/2) H_{z2}$

$3E_{s1} - 2E_{\phi 2} = -s_n Z_0 (5/2) H_{z3}$

$1E_{\phi 3} = -s_n Z_0 (1/2) H_{z4}$

$2E_{\phi 4} - 1E_{\phi 3} = -s_n Z_0 (3/2) H_{z5}$

$3E_{s2} - 2E_{\phi 4} = -s_n Z_0 (5/2) H_{z6}$

Circulation of Magnetic Field (second curl equation)

$H_{r3} - H_{r1} + H_{z1} - H_{z2} = s_n Y_0 (\varepsilon_1 + \varepsilon_2 + \varepsilon_4 + \varepsilon_5)/4\, E_{\phi 1}$

$H_{r4} - H_{r2} + H_{z2} - H_{z3} = s_n Y_0 (\varepsilon_2 + \varepsilon_3 + \varepsilon_5 + \varepsilon_6)/4\, E_{\phi 2}$

$H_{r5} - H_{r3} + H_{z4} - H_{z5} = s_n Y_0 (\varepsilon_4 + \varepsilon_5 + \varepsilon_7 + \varepsilon_8)/4\, E_{\phi 3}$

$H_{r6} - H_{r4} + H_{z5} - H_{z6} = s_n Y_0 (\varepsilon_5 + \varepsilon_6 + \varepsilon_8 + \varepsilon_9)/4\, E_{\phi 4}$

It is convenient (simplifies the notation) to introduce the averaged permittivities:

$\varepsilon_{\phi 1} = (\varepsilon_1 + \varepsilon_2 + \varepsilon_4 + \varepsilon_5)/4 \qquad \varepsilon_{\phi 2} = (\varepsilon_2 + \varepsilon_3 + \varepsilon_5 + \varepsilon_6)/4$

$\varepsilon_{\phi 3} = (\varepsilon_4 + \varepsilon_5 + \varepsilon_7 + \varepsilon_8)/4 \qquad \varepsilon_{\phi 4} = (\varepsilon_5 + \varepsilon_6 + \varepsilon_8 + \varepsilon_9)/4.$

The matrix form of the above equations is:

$$\begin{vmatrix} -1 & 0 & 0 & 0 \\ 0 & -1 & 0 & 0 \\ 0 & 0 & 1 & 0 \\ 0 & 0 & 0 & 1 \\ 1 & 0 & -1 & 0 \\ 0 & 1 & 0 & -1 \end{vmatrix} \begin{vmatrix} E_{\phi 1} \\ E_{\phi 2} \\ E_{\phi 3} \\ E_{\phi 4} \end{vmatrix} = -s_n Z_0 \begin{vmatrix} H_{r1} \\ H_{r2} \\ H_{r5} \\ H_{r6} \\ H_{r3} \\ H_{r4} \end{vmatrix} - \begin{vmatrix} 1 & 0 & 0 & 0 \\ 0 & 1 & 0 & 0 \\ 0 & 0 & -1 & 0 \\ 0 & 0 & 0 & -1 \end{vmatrix} \begin{vmatrix} E_{b1} \\ E_{b2} \\ E_{t1} \\ E_{t2} \end{vmatrix} \qquad (1)$$

$$\begin{vmatrix} 0 & -1 & 0 & 0 \\ 0 & 0 & 0 & -1 \\ 1 & 0 & 0 & 0 \\ -1 & 1 & 0 & 0 \\ 0 & 0 & 1 & 0 \\ 0 & 0 & -1 & 1 \end{vmatrix} \begin{vmatrix} 1 & 0 & 0 & 0 \\ 0 & 2 & 0 & 0 \\ 0 & 0 & 1 & 0 \\ 0 & 0 & 0 & 2 \end{vmatrix} \begin{vmatrix} E_{\phi 1} \\ E_{\phi 2} \\ E_{\phi 3} \\ E_{\phi 4} \end{vmatrix} = -s_n Z_0 \begin{vmatrix} 5/2 & 0 & 0 & 0 & 0 & 0 \\ 0 & 5/2 & 0 & 0 & 0 & 0 \\ 0 & 0 & 1/2 & 0 & 0 & 0 \\ 0 & 0 & 0 & 3/2 & 0 & 0 \\ 0 & 0 & 0 & 0 & 1/2 & 0 \\ 0 & 0 & 0 & 0 & 0 & 3/2 \end{vmatrix} \begin{vmatrix} H_{z3} \\ H_{z6} \\ H_{z1} \\ H_{z2} \\ H_{z4} \\ H_{z5} \end{vmatrix} - \begin{vmatrix} 3 & 0 \\ 0 & 3 \end{vmatrix} \begin{vmatrix} E_{s1} \\ E_{s2} \end{vmatrix} \qquad (2)$$

$$\begin{vmatrix} -1 & 0 & 0 & 0 & 1 & 0 & 0 & 0 & 1 & -1 & 0 & 0 \\ 0 & -1 & 0 & 0 & 0 & 1 & -1 & 0 & 0 & 1 & 0 & 0 \\ 0 & 0 & 1 & 0 & -1 & 0 & 0 & 0 & 0 & 0 & 1 & -1 \\ 0 & 0 & 0 & 1 & 0 & -1 & 0 & -1 & 0 & 0 & 0 & 1 \end{vmatrix} \begin{vmatrix} H_{r1} \\ H_{r2} \\ H_{r5} \\ H_{r6} \\ H_{r3} \\ H_{r4} \\ H_{z3} \\ H_{z6} \\ H_{z1} \\ H_{z2} \\ H_{z4} \\ H_{z5} \end{vmatrix} = -s_n Y_0 \begin{vmatrix} \varepsilon_{\phi 1} & 0 & 0 & 0 \\ 0 & \varepsilon_{\phi 2} & 0 & 0 \\ 0 & 0 & \varepsilon_{\phi 3} & 0 \\ 0 & 0 & 0 & \varepsilon_{\phi 4} \end{vmatrix} \begin{vmatrix} E_{\phi 1} \\ E_{\phi 2} \\ E_{\phi 3} \\ E_{\phi 4} \end{vmatrix} \qquad (3)$$

Note that the equations have been re-ordered, such that the equations involving fields on the

boundaries are written first. The reason is the desired diagonal form of the matrices associated with the fields on the boundaries. The same can be accomplished by re-numbering the field components. The equations for the general case of an M by N cross-section can be written using the matrix notation as:

$$\mathbf{C}_{\phi r}\, \mathbf{e}_{\phi} = -s_n Z_0\, \mathbf{h}_r - \mathbf{D}_{bt}\, \mathbf{e}_{bt} \qquad (4)$$

$$\mathbf{C}_{\phi z}\mathbf{e}_{\phi} = -s_n Z_0\, \mathbf{h}_z - \mathbf{D}_s\, \mathbf{e}_s \qquad (5)$$

$$[\,(\mathbf{C}_{\phi r})^T\ (\mathbf{C}_{\phi z})^T\,]\, \mathbf{h}_{rz} = s_n Y_0\, \mathbf{D}_{\varepsilon}\, \mathbf{e}_{\phi} \qquad (6)$$

where:

$\mathbf{C}_{\phi r}$ and $\mathbf{C}_{\phi z}$ are "connection" matrices with elements 1 and -1 ("canonical" matrices) and sizes (M-1)N by (M-1)(N-1) and M(N-1) by (M-1)(N-1), respectively;

$\mathbf{e}_{\phi}$ denotes a column vector of ϕ–directed electric fields $E\phi$;

$(\ )^T$ denotes transpose of the matrix within parenthesis;

$\mathbf{h}_r$ denotes a column vector of r-directed magnetic fields H_r, length (M-1)N;

$\mathbf{h}_z$ denotes a column vector of z-directed magnetic fields H_z, length M(N-1);

$\mathbf{h}_{rz}$ denotes a column vector of all magnetic fields, that is a column vector consisting of the column vectors $\mathbf{h}_r$ and $\mathbf{h}_z$, length (M-1)N+M(N-1);

$\mathbf{D}_{bt}$ denotes a diagonal matrix of coefficients associated with electric fields at the bottom and the top of the rotationally symmetric domain, size (M-1) by (M-1);

$\mathbf{e}_{bt}$ denotes a column vector of ϕ–directed electric fields E_{ϕ} at the bottom and the top of the domain, length (M-1)

$\mathbf{D}_s$ denotes a diagonal matrix of coefficients associated with electric fields at the side of the rotationally symmetric domain, size (N-1) by (N-1);

$\mathbf{e}_s$ denotes a column vector of ϕ–directed electric fields E_{ϕ} at the domain side, length (N-1);

and $\mathbf{D}_{\varepsilon}$ denotes a diagonal matrix of averaged relative dielectric constants, size (M-1)(N-1) by (M-1)(N-1).

We implement impedance-type **local** boundary conditions by expressing the ϕ–directed electric fields on the boundaries in terms of the magnetic fields just inside the grid. For example, we may write: $E_{b1} = Z_{b1}\, H_{r1}$, $E_{t1} = Z_{t1}\, H_{r5}$, $E_{s1} = Z_{s1}\, H_{z3}$, and so on. Note that the local impedances Z_{xx} are, in principle, all different and can have both positive and negative values (such that the vector product of the electric and magnetic field gives a Poyinting vector in the direction of the outward normal to the boundary). The local impedance boundary conditions can be represented in a matrix form using diagonal impedance matrices, one for the bottom and the top boundary and one for the side boundary:

$$\mathbf{e}_{bt} = \mathbf{Z}_{bt}\, \mathbf{h}_r \qquad (7)$$

$$\mathbf{e}_s = \mathbf{Z}_s\, \mathbf{h}_z\,. \qquad (8)$$

Replacing the electric fields on the boundaries with the local impedance boundary conditions we

obtain the following matrix equations:

$$\mathbf{C}_{\phi r}\mathbf{e}_{\phi} = -s_n Z_0 \mathbf{h}_r - \mathbf{D}_{bt} \mathbf{z}_{bt} \mathbf{h}_r \qquad (9)$$

$$\mathbf{C}_{\phi z}\mathbf{e}_{\phi} = -s_n Z_0 \mathbf{h}_z - \mathbf{D}_s \mathbf{z}_s \mathbf{h}_z \qquad (10)$$

$$[\,(\mathbf{C}_{\phi r})^T \ \ (\mathbf{C}_{\phi z})^T\,]\,\mathbf{h}_{rz} = s_n Y_0 \mathbf{D}_{\varepsilon} \mathbf{e}_{\phi} \qquad (11)$$

From the last matrix equation we express the electric field as:

$$\mathbf{e}_{\phi} = (s_n)^{-1} Z_0 \mathbf{D}_{\varepsilon}^{-1} [\,(\mathbf{C}_{\phi r})^T \ \ (\mathbf{C}_{\phi z})^T\,]\,\mathbf{h}_{rz} \qquad (12)$$

and substitute into the first two equations:

$$(s_n)^{-1} Z_0 \mathbf{C}_{\phi r} \mathbf{D}_{\varepsilon}^{-1} [\,(\mathbf{C}_{\phi r})^T \ \ (\mathbf{C}_{\phi z})^T\,]\,\mathbf{h}_{rz} = -s_n Z_0 \mathbf{h}_r - \mathbf{D}_{bt} \mathbf{z}_{bt} \mathbf{h}_r \qquad (13)$$

$$(s_n)^{-1} Z_0 \mathbf{C}_{\phi z} \mathbf{D}_{\varepsilon}^{-1} [\,(\mathbf{C}_{\phi r})^T \ \ (\mathbf{C}_{\phi z})^T\,]\,\mathbf{h}_{rz} = -s_n Z_0 \mathbf{h}_z - \mathbf{D}_s \mathbf{z}_s \mathbf{h}_z \qquad (14)$$

which further gives:

$$\mathbf{C}_{\phi r} \mathbf{D}_{\varepsilon}^{-1} [\,(\mathbf{C}_{\phi r})^T \ \ (\mathbf{C}_{\phi z})^T\,]\,\mathbf{h}_{rz} = -s_n^2 \mathbf{h}_r - s_n Y_0 \mathbf{D}_{bt} \mathbf{z}_{bt} \mathbf{h}_r \qquad (15)$$

$$\mathbf{C}_{\phi z} \mathbf{D}_{\varepsilon}^{-1} [\,(\mathbf{C}_{\phi r})^T \ \ (\mathbf{C}_{\phi z})^T\,]\,\mathbf{h}_{rz} = -s_n^2 \mathbf{h}_z - s_n Y_0 \mathbf{D}_s \mathbf{z}_s \mathbf{h}_z \qquad (16).$$

The above can be written as a standard eigenvalue problem (at the expense of doubling its size) if the following transformation is introduced:

$$\mathbf{h}_r' = -s_n \mathbf{h}_r$$

$$\mathbf{h}_z' = -s_n \mathbf{h}_z, \qquad (17).$$

or, using the combined column vector:

$$\mathbf{h}_{rz}' = -s_n \mathbf{h}_{rz}. \qquad (18).$$

We now obtain a set of two matrix equations:

$$\mathbf{C}_{\phi r} \mathbf{D}_{\varepsilon}^{-1} [\,(\mathbf{C}_{\phi r})^T \ \ (\mathbf{C}_{\phi z})^T\,]\,\mathbf{h}_{rz} = s_n \mathbf{h}_r' - s_n Y_0 \mathbf{D}_{bt} \mathbf{z}_{bt} \mathbf{h}_r \qquad (19)$$

$$\mathbf{C}_{\phi z} \mathbf{D}_{\varepsilon}^{-1} [\,(\mathbf{C}_{\phi r})^T \ \ (\mathbf{C}_{\phi z})^T\,]\,\mathbf{h}_{rz} = s_n \mathbf{h}_z' - s_n Y_0 \mathbf{D}_s \mathbf{z}_s \mathbf{h}_z. \qquad (20)$$

Introducing the notation:

$$[\mathbf{A} \ \ \mathbf{B}\,] = \mathbf{C}_{\phi r} \mathbf{D}_{\varepsilon}^{-1} [\,(\mathbf{C}_{\phi r})^T \ \ (\mathbf{C}_{\phi z})^T\,] \qquad (21)$$

$$[\mathbf{C} \ \ \mathbf{D}\,] = \mathbf{C}_{\phi z} \mathbf{D}_{\varepsilon}^{-1} [\,(\mathbf{C}_{\phi r})^T \ \ (\mathbf{C}_{\phi z})^T\,] \qquad (22)$$

$$\mathbf{F} = -Y_0 \mathbf{D}_{bt} \mathbf{z}_{bt} \qquad (23)$$

$$\mathbf{G} = -Y_0 \mathbf{D}_s \mathbf{z}_s, \qquad (24)$$

and using **1** to denote a unit matrix, the eigenvalue problem can now written using two "supermatrices" **L** and **R**:

$$\begin{vmatrix} \mathbf{0} & \mathbf{0} & \mathbf{A} & \mathbf{B} \\ \mathbf{0} & \mathbf{0} & \mathbf{C} & \mathbf{D} \\ \mathbf{1} & \mathbf{0} & \mathbf{0} & \mathbf{0} \\ \mathbf{0} & \mathbf{1} & \mathbf{0} & \mathbf{0} \end{vmatrix} \begin{vmatrix} \mathbf{h}_r' \\ \mathbf{h}_z' \\ \mathbf{h}_r \\ \mathbf{h}_z \end{vmatrix} = s_n \begin{vmatrix} \mathbf{1} & \mathbf{0} & \mathbf{F} & \mathbf{0} \\ \mathbf{0} & \mathbf{1} & \mathbf{0} & \mathbf{G} \\ \mathbf{0} & \mathbf{0} & \mathbf{1} & \mathbf{0} \\ \mathbf{0} & \mathbf{0} & \mathbf{0} & \mathbf{1} \end{vmatrix} \begin{vmatrix} \mathbf{h}_r' \\ \mathbf{h}_z' \\ \mathbf{h}_r \\ \mathbf{h}_z \end{vmatrix} \qquad (25)$$

This is recognized as a generalized eigenvalue problem of the form:

/

$$\mathbf{L}\,\mathbf{x} = \lambda\,\mathbf{R}\,\mathbf{x}.$$

Note that, in this formulation, different local impedance-type boundary conditions on the "caps" (bottom and top) and the side of the cylindrical domain are simply imposed by altering the two diagonal matrices **F** and **G**. In the special case of PEC boundaries, matrices **F** and **G** are zero (local impedances on the boundaries are all zero) and the generalized eigenvalue problem reduces to the standard eigenvalue problem:

$$\mathbf{L}\,\mathbf{x} = \lambda\,\mathbf{x}.$$

MATLAB Implementation and Sample Results

MATLAB has been selected to implement the above for several reasons, some of which are mentioned here. MATLAB provides a good programming environment with plenty of built-in matrix functions and algorithms based on EISPACK and LINPACK algebra packages. Since MATLAB is available for a variety of platforms, from PC's to workstations to mainframes at a moderate cost ($495 for a PC-386 version), the programs are readily "ported" and exchanged. MATLAB also provides decent graphical output in the form of contour, vector and 3-D "mesh" plots. This allows one to concentrate on just the "electromagnetics" part of the code and typically results in fairly compact code that is easy to follow. Results are presented for the resonant frequencies of the first four TE_{ϕ} modes of a tubular dielectric resonator with the inner radius of 3mm, the outer radius of 6mm, and the height of 6mm. The relative permittivity of the resonator is 38. The resonator is mounted on a substrate whose thickness is 3mm and whose relative permittivity is 9. The PEC cavity radius is 12mm, and the cavity height is 12mm as well. The domain was modelled using a uniform grid of 12 by 12 cells (M=N=12). Cells are square 1mm by 1mm. Contour plots of E_{ϕ} and vector plots of H are shown for the first and the third resonant mode. Complete eigensolution took less than 30 seconds on a 25 MHz 386-class PC.

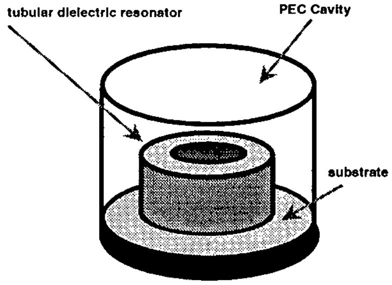

Fig. 3: Tubular Dielectric Resonator in a PEC Cavity

References:

[1.]M. Albani and P. Bernardi, 'A numerical method based on the discretization of Maxwell's equations in integral form', *IEEE Trans. Microwave Theory Tech.*,vol. MTT-24, pp 446-449, Apr. 1974.

[2.] J. Lebaric and D. Kajfez, 'Analysis of dielectric resonator cavities using the Finite Integration Technique', *IEEE Trans. Microwave Theory Tech.*,vol. MTT-37, pp 1740-1748, Nov. 1989.

E-FIELD CONTOUR PLOT

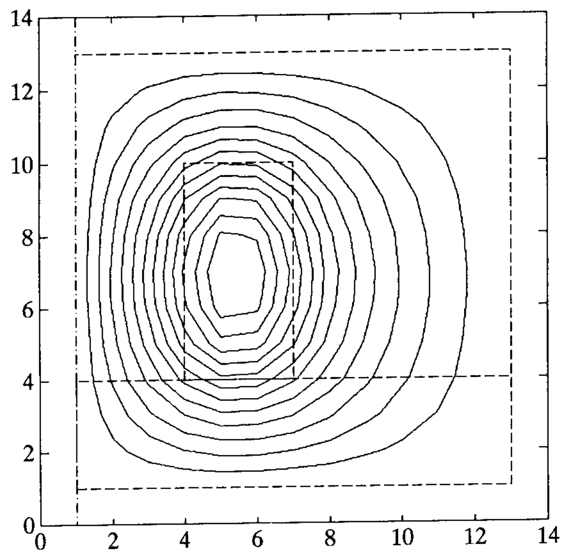

Countour plots of ϕ–directed electric field E_ϕ for the first two TE modes with resonant frequencies of 4.7545GHz and 7.3052GHz, respectively.

E-FIELD CONTOUR PLOT

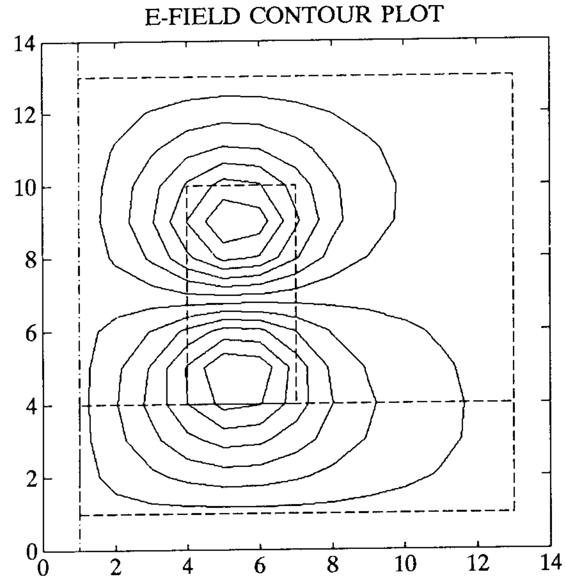

H-FIELD VECTOR PLOT

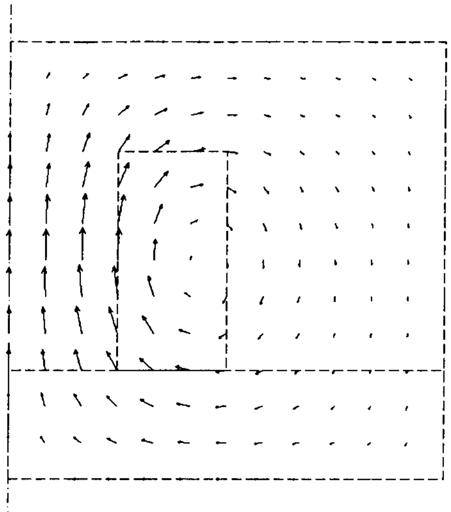

Vector plots of transverse magnetic field H for the first two TE modes with resonant frequencies of 4.7545GHz and 7.3052GHz, respectively.

H-FIELD VECTOR PLOT

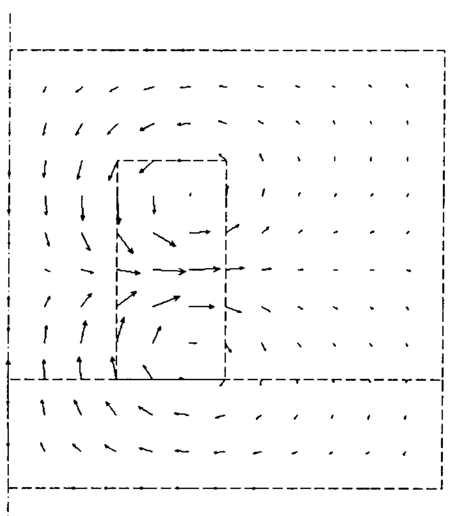

ELECTROSTATIC FIELD INSIDE A SPLIT CYLINDER -

A MATLAB APPROACH

Darko Kajfez and Yuliang Wu
Department of Electrical Engineering
University of Mississippi, University, MS 38677, USA

Abstract. The electrostatic vector field inside a conducting cylinder with a finite size gap is evaluated by rigorous numerical procedure. The conductor edge is modeled as a separate region, matched with other regions to insure the continuity of the field. The number of matching equations is larger than the number of expansion coefficients, and the matrix equation is solved by a least squares procedure. The development of the numerical code is greatly simplified by using the software package Matlab, but some difficulties have been encountered in generating the modified Bessel functions.

1. Introduction

The electrostatic boundary-value problem discussed here consists of a hollow metal cylinder, which is split in two halves as shown in Fig. 1. The upper half is held at potential V_0, and the lower half at potential $-V_0$. The gap continues into a parallel-plate region that extends to infinity.

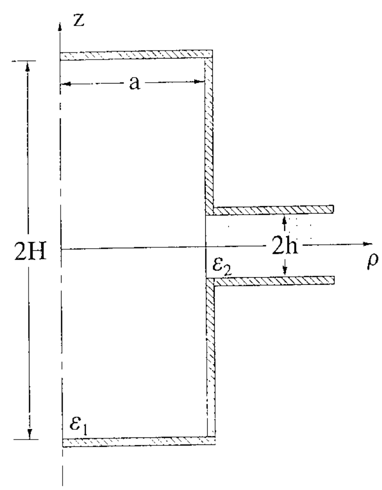

Fig. 1 Conducting cylinder with a finite gap

A rigorous solution of this canonical problem may be of practical interest in measurement of materials inside microwave cavities. Rotationally symmetric resonant cavities have often a tubular central portion, which contains the material to be measured. This tubular portion is coupled by a gap to the outside cavity. The radius of the tube is typically small enough that all the modes inside the tube are evanescent. Therefore, an electrostatic solution accurately describes the field inside the material sample. In practical applications, the gap will not extend to infinity as in Fig. 1, but it will open to the surrounding resonant cavity.

The mathematical expressions for the field inside the split cylinder will be obtained by dividing the cross section into several regions. The expansion coefficients will be determined by requiring the continuity of the tangential field at the region interfaces. The novelty of the approach used here is that a separate region is introduced to take care of the edge condition, that the number of the matching equations is larger than the number of the expansion coefficients, and that the problem has been solved on a personal computer, using Matlab software.

The reason for choosing Matlab, instead of the more common Fortran or Basic languages, has been to judge the suitability of Matlab in solving the real-life electromagnetic field problems. The conclusions are described in section 4.

2. Mathematical formulation

Because of symmetry, only the upper part $z > 0$ need to be considered, as shown in Fig. 2. The cross section is divided in three regions. Region 1 is the interior of the cylinder (radius a and height H), and region 2 is the gap region (height h, radius > a). We introduce a separate region 3 with radius Δ in order to consider the singularity of the electric field near the edge (located at $\rho = a$, $z = h$). All three regions are filled with the same dielectric.

The solution is assumed to have no azimuthal variation. The potential in region 1 is selected as

$$\Phi_1(\rho,\ z) = \frac{V_0}{H}z + \sum_{n=1}^{\infty} A_n' I_0(\frac{n\pi}{H}\rho)\sin(\frac{n\pi}{H}z) \tag{1}$$

The corresponding electric field components are

$$\begin{aligned} E_{z_1}(\rho,\ z) &= -\frac{V_0}{H} - \sum_{n=1}^{\infty} A_n I_0(\frac{n\pi}{H}\rho)\cos(\frac{n\pi}{H}z) \\ E_{\rho_1}(\rho,\ z) &= -\sum_{n=1}^{\infty} A_n I_1(\frac{n\pi}{H}\rho)\sin(\frac{n\pi}{H}z) \end{aligned} \tag{2}$$

where

where

$$A_n = \frac{n\pi}{H} A_n'$$

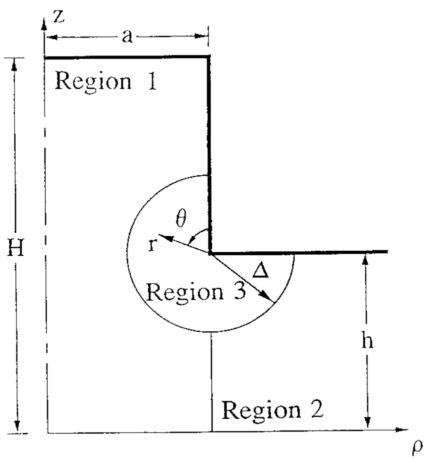

Fig. 2 Defining the three regions of interest

In a similar way, the potential in region 2 is

$$\Phi_2(\rho,\ z) = \frac{V_0}{h} z + \sum_{m=1}^{\infty} B_m' K_0(\frac{m\pi}{h}\rho)\sin(\frac{m\pi}{h}z) \tag{3}$$

The components of the electric field in region 2 are

$$E_{z_2}(\rho,\ z) = -\frac{V_0}{h} - \sum_{m=1}^{\infty} B_m K_0(\frac{m\pi}{h}\rho)\cos(\frac{m\pi}{h}z)$$

$$E_{\rho_2}(\rho,\ z) = \sum_{m=1}^{\infty} B_m K_1(\frac{m\pi}{h}\rho)\sin(\frac{m\pi}{h}z) \tag{4}$$

where

$$B_m = \frac{m\pi}{h} B_m'$$

In region 3, it is convenient to introduce local coordinates r and θ as shown in Fig. 2. The electric field in this region displays the edge singularity [1-3]. The appropriate choice of the potential in this region is

$$\Phi_3(\rho,\ z) = V_0 + \sum_{\ell=1}^{\infty} C_\ell' r^{\frac{\ell\pi}{\beta}} \sin(\frac{\ell\pi}{\beta}\theta) \tag{5}$$

The corresponding electric field components are

$$E_{z_3}(\rho,\ z) = -\sum_{\ell=1}^{\infty} C_\ell r^{\frac{\ell\pi}{\beta}-1} \sin[(\frac{\ell\pi}{\beta} - 1)\theta]$$

$$E_{\rho_3}(\rho,\ z) = \sum_{\ell=1}^{\infty} C_\ell r^{\frac{\ell\pi}{\beta}-1} \cos[(\frac{\ell\pi}{\beta} - 1)\theta] \tag{6}$$

where

$$r = [(\rho - a)^2 + (z - h)^2]^{\frac{1}{2}}$$

$$0 \leq \theta \leq \frac{3}{2}\pi$$

$$\beta = \frac{3}{2}\pi$$

$$C_\ell = C_\ell' \frac{\ell\pi}{\beta}$$

Therefore, the field is described in terms of three sets of coefficients, A_n, B_m, and C_ℓ. The total number of coefficients will be truncated to the following finite numbers:

N = total number of coefficients A_n (region 1)
M = total number of coefficients B_m (region 2)
L = total number of coefficients C_ℓ (region 3)

3. Enforcing the continuity

The following seven boundary and continuity conditions must be satisfied

$$\Phi_1 = V_0 \quad \text{at } \rho = a,\ h + \Delta \leq z \leq H \tag{7}$$

$$\left.\begin{aligned} E_{z_1} &= E_{z_2} \\ E_{\rho_1} &= E_{\rho_2} \end{aligned}\right\} \quad at\ \rho = a,\ 0 \le z \le h - \Delta \tag{8}$$

$$\left.\begin{aligned} E_{z_1} &= E_{z_3} \\ E_{\rho_1} &= E_{\rho_3} \end{aligned}\right\} \quad at\ r = \Delta,\ 0 \le \theta \le \pi \tag{9}$$

$$\left.\begin{aligned} E_{z_2} &= E_{z_3} \\ E_{\rho_2} &= E_{\rho_3} \end{aligned}\right\} \quad at\ r = \Delta,\ \pi \le \theta \le \frac{3}{2}\pi \tag{10}$$

To establish the system of linear equations for solving the expansion coefficients A_n, B_m, and C_ℓ, the matching and continuity conditions are enforced at a number of match points, as follows.

> On the conductor surface bordering region 1, the match points are specified by $\rho = a$, $h + \Delta \le z_i \le H$, $i = 1, 2, \ldots, Q$ (total number of match points is Q).
>
> On the interface between region 1 and region 2, the match points are specified by $\rho = a$, $0 \le z_j \le h - \Delta$, $j = 1, 2, \ldots, P$ (total number of match points is P).
>
> On the cylindrical interface between region 1 and region 3, the match points are specified by $r = \Delta$, $0 \le \theta_{k1} \le \pi$, $k_1 = 1, 2, \ldots, R_1$ (total number of match points is R_1).
>
> On the cylindrical interface between region 2 and region 3, the match points are specified by $r = \Delta$, $\pi \le \theta_{k2} \le 3\pi/2$, $k_2 = 1, 2, \ldots, R_2$ (total number of match points is R_2).

Enforcing the conditions (7) to (10) at all the match points, one obtains a linear system of equations, which is written in matrix form as follows

$$\underline{A}\ |X\rangle = |b\rangle \tag{11}$$

The matrix $\underline{A}$ consists of (M+N+L) columns and of ($Q+2P+2R_1+2R_2$) rows. The column vectors $|X\rangle$ and $|b\rangle$ have the compatible number of elements. The detailed expressions for partitioned matrix blocks can be found in [4].

4. Numerical Solution

The linear system of equations specified by (11) can be conveniently cast into a computer code with the help of the software package Matlab [5]. The Matlab language is well suited for building a large partitioned matrix from its elementary blocks. The user is never required to specify "dimension" and "common" statements, which are traditional sources of headache in Fortran and Basic languages. Furthermore, built-in subroutine exists in Matlab for solving an overdetermined system of equations in the least-squares sense. Thus, Matlab can save a great amount of time spent on the initial code development for an electromagnetic boundary value problem. The matrix inversion is also extremely fast.

However, we found the subroutine for computing the modified Bessel functions $I_n(x)$ and $K_n(x)$ to be erroneous. Argument $x > 10$ produces incorrect results, which even oscillate between positive and negative values for $x > 20$. For that reason, we had to replace the Matlab subroutine with our own subroutines for generating these functions, based on the polynomial approximations from [6]. Another problem with Matlab is its lack of portability. Namely, a Matlab program cannot be compiled in an .EXE file like Fortran or Basic programs.

First, we illustrate the improvement obtained by choosing more match points than the number of expansion coefficients. The results will be plotted for H/h=4, h/a=1, M=10, N=40, and L=16. Figure 3 shows the potential along the metal cylinder, computed for the case that the number of match points is Q=18, P=9, R_1=10, R_2=5, which means that the number of matching equations is the same as the number of expansion coefficients ($Q+2P+2R_1+2R_2$ = M+N+L = 66). The size of the region 3 is specified by Δ/a=0.4. At each match point, the value of the potential is correct, but in between these points the potential wildly oscillates. The largest discrepancy (up to 500 times the correct value) occurs close to the top of the cylinder ($z > 3a$).

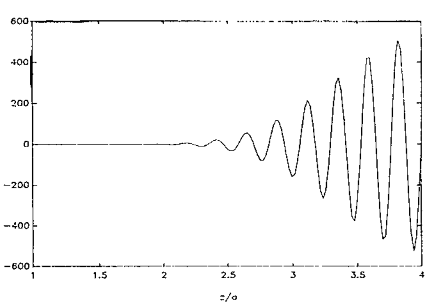

Fig. 3 Computed potential on cylindrical conductor, number of match points same as the number of expansion coefficients.

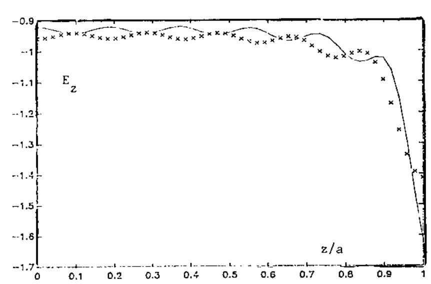

Fig. 4 Imperfect continuity of the electric field at the interface of regions 1 and 2, if region 3 is eliminated (Δ=0, no proper edge behavior). Solid line: E_{z1}, crosses: E_{z2}.

Next, the number of match points is increased to Q=33, P=11, R_1=12, and R_2=6. The resulting potential cannot be shown because of limited pages, but it is very close to the nominal value 1 Volt, with a relative error smaller than 10^{-3}. The figure will be shown at the poster session.

The second example shows what happens if the edge condition is not taken into account. This can be simulated by substituting $\Delta=0$ into the program. In this case the continuity of the tangential field over the gap clearly shows deficiency, as seen in Fig. 4. This diagram depicts the z-component of the electric field, computed for H/h=3, h/a=1, M=10, N=40. Obviously, there is a discrepancy between the fields on each side of the interface between regions 1 and 2. Furthermore, the field magnitude does not tend to infinity, for $z \rightarrow a$. When the region 3 is included, there is no noticeable difference between the fields on both sides of the gap, and the field magnitude tends to infinity as z/a approaches unity. The corresponding figure will be shown at the poster session.

5. Computed results

The electric field lines are shown in Fig. 5. They have been constructed in two steps. First, the field components have been computed at a number of equidistant points across the entire cross section (30×47 points). Then, the continuous field lines have been drawn using the software VMAP [7]. One can observe how the field becomes weaker when the observer moves from the interior of the gap toward the center of the cylinder.

Several dashed lines have been plotted with a different field intensity (about 50 times smaller flux between any two neighboring lines) for a better view of the field near the top of the cylinder. It is recalled from the previous discussion (Fig.3), that the field distribution in this area would appear erratic, if the solution was computed by choosing the number of matching equations equal to the number of expansion coefficients. It is reassuring to observe the dashed field lines being smooth and uniformly distributed.

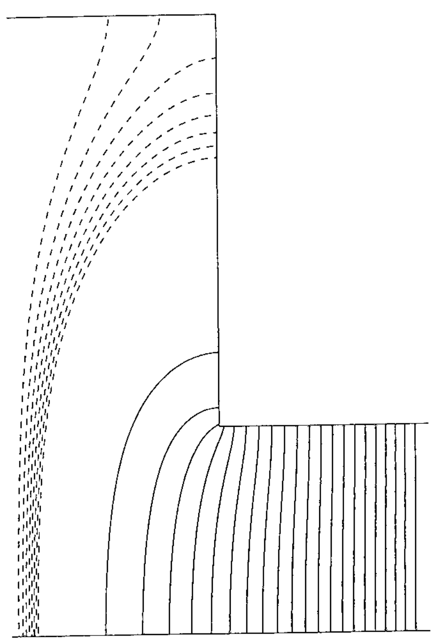

Fig. 5 Electric field lines

Information of interest for applications is the data on how much the field at the center of the cylinder is weaker than the field in the uniform gap. This value can be read from the diagram shown in Fig. 6. It displays the ratio of the electric field at the center of the cylinder to the field in the uniform gap (which is, in turn, equal to the potential difference divided by the gap height). Several curves are drawn for various relative cylinder heights H/h.

For the large values of h/a, all curves tend toward unity. In other words, if the gap is larger than radius, the field at the center of the cylinder is about the same as the field in the uniform gap. On the other hand, when the gap h is much smaller than the cylinder radius a, the field at the center of the cylinder tends to zero, providing the cylinder height remains larger than a.

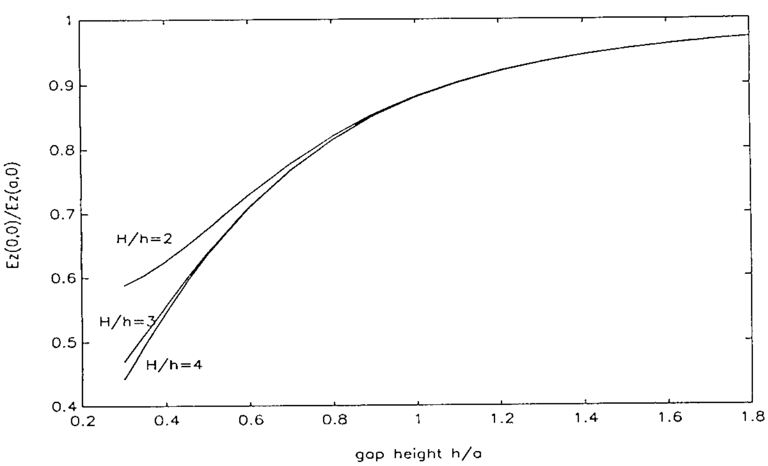

Fig. 6 Ratio of field intensity at the center of the cylinder to field intensity in the uniform gap.

6. References

[1] J. D. Jackson, *Classical Electrodynamics*. Second ed., New York: Wiley, 1975.

[2] J. Van Bladel, *Electromagnetic Fields*. New York: Hemisphere, 1985.

[3] R. Mittra and S. W. Lee, *Analytical Techniques in the Theory of Guided Waves*. New York: MacMillan, 1971.

[4] Y. Wu, "Electrostatic Field Inside a Split Cylinder - A Matlab Approach", M.S. Thesis, *Dept. of Electrical Engineering*, Univ. of Mississippi, December 1991.

[5] *PC-MATLAB User's Guide*. South Natick, MA: The Mathworks Inc., 1989.

[6] M. Abramowitz and I. A. Stegun (Eds.), *Handbook of Mathematical Functions*. Washington, DC: Nat. Bureau of Standards, pp. 378-379, 1964.

[7] D. Kajfez, K. Mahadevan, and J. A. Gerald, "PC Software Maps Electromagnetic Vector Fields", *Microwave Journal*, pp. 267-280, May 1989.

SYNTHESIS OF SUM AND DELTA BEAMS FOR CONTINUOUS CIRCULAR APERTURES FOR MONOPULSE PROCESSING

M.A. Hussain, K-B Yu and B. Noble
General Electric Research and Development Center
Schenectady, New York

1. ABSTRACT

In radar, monopulse or simultaneous lobe comparison is a well known technique for measuring direction of arrival of radiation either from an active or a passive source. Monopulse method is capable of producing measurements based on a single pulse and is not susceptible to echo fluctuation. Also the method is independent of pulse repetition frequency and mechanical vibrations. For a comprehensive account see references [1] and [2].

Monopulse technique for a planer array requires synthesis of sum beam, difference beam in elevation , difference beam in azimuth and a double difference beam. These beams are quite well understood for a rectangular array.

In this paper we give a synthesis method for obtaining these beams for a circular aperture. For the sum beam we obtain circular Taylor type solution with equal side-lobes for sigma beam. For difference beam we get Bayliss type solution with equal side lobes for delta in elevation and azimuth. For double difference we get circular aperture solution of 'Frequency Two' with equal side-lobes for delta-delta beam. In addition we also investigate synthesis for 'commutative property' sigma-delta and delta-delta beams, as an extension of a property satisfied by corresponding beams of recatangular planer arrays.

2. INTRODUCTION

The approach we have taken is based on the extension of Taylor synthesis procedure [4] as well as his theorem of synthesis. The procedure is numerical, requiring iteration and asymptotically gives a correct value as pedicted by the theory. It is well known in the literature that the model or idealized pattern obtained as the asymptotic Tchebycheff array is not realizable due to illumination functions singularities.

Taylor devised a method to shift the near-in zeros to avoid the singularity but the side lobes are no longer of equal heights. Our method satisfies the basic criteria asymptotically for non-singular behavior and at the same time gives us equal side lobes.

Above method can be generalized for the synthesis of Bayliss [3] as well as delta-delta beam required for monopulse processing. The model function can be derived from the asymptotic analysis of Dolph-Tchebycheff theory for the sum beam.

The model function for the difference beam (i.e Bayliss and delta-delta) can be derived approximately as derivative of the above model function.

3. TWO DIMENSIONAL INTEGRAL EQUATION

This section outlines the specific problem solved and provides basic formulas to construct all the beams for application to monopulse processing. Using the same notation as Taylor integral equation for the illumination function g for a specific array pattern F is given by:

$$F(u,\Phi) = \frac{1}{2\pi} \int_{\phi=\Phi}^{\phi=2\pi+\Phi} d\phi \int_{0}^{\pi} g(p,\phi) e^{(jpu\cos(\Phi-\phi))} \; pdp \tag{1}$$

where $u = \frac{2a\sin(\theta)}{\lambda}$ and a is aperture radius. If the illumination $g(p,\phi)$ (for integer m) is expanded in truncated form:

$$g(p,\phi) = \cos(m\phi) \sum_{l=0}^{l=\overline{n}-1} B_l J_m(\mu_l p) \tag{2}$$

After some manipulation it can be shown that eq(1) reduces to:

$$F_m(u,\phi) = i^m \cos(m\Phi) \sum_{l=0}^{l=\overline{n}-1} B_l \frac{\pi}{(\mu_l^2 - u^2)} [uJ_m(\mu_l \pi) J'_m(u\pi)] \tag{3}$$

(In equations (2) and (3) cos can be replaced by sine). Where the asymptotic zeros are selected to satisfy the finiteness of the illumination function and hence the requirement:

$$J'_m \; (\mu_l \pi) = 0. \tag{4}$$

The above eq(3) is central in our formulation and tables are provided for each coefficient and various parameters needed for a practical design application.

With m=0 and m=1,in eq(3), we easily obtain Taylor and Bayliss cases respectively.

4. NUMERICAL PROCEDURE

The numerical method followed here is similar to that given in [5]. Generally first we select $\overline{n}$-1 nulls either from the model function or from the streching parameter defined by Taylor together with side lobe ratio. First we iterate around parameter that depend upon sidelobe ratio to obtain a desired value for the first sidelobe. Then the iteration procedure is carried out to make the rest of the sidelobes equal to design value. Result are identical to those of Taylor and Bayliss for the first iteration, if it is started with their parameters. Compared to Taylor, additional complication arose due to lack of analytical form for the side-lobe ratios for difference beams.

Results are tabulated for easy generation of patterns from formulas given. Only few iterations are enough for error within a couple of percent. More iterations can be carried out for higher accuracy.

5. ILLUSTRATION OF THE METHOD FOR A CIRCULAR APERTURE

We can alsoobtain the solution of the sum-beam problem by a different approach. Consider the integral equation given in eq(1) with m=0 and axisymmetric illumination (with obvious change of notation):

$$F(u) = \int_{0}^{\pi} p\, g(p)\, J_0(p\, u)\, dp \tag{5}$$

where $u = \frac{2a\sin(\theta)}{\lambda}$ Using the method of Dossier we let

$$g(p) = \sum_{m=0}^{\overline{n}-1} D_m J_0(\mu_m p) \tag{6}$$

with $J_1(\pi\mu_m) = 0$. Substituting equation (6) into (5) we have:

$$F(u) = a_0(u) + \sum_{m=1}^{\overline{n}-1} F(\mu_m) a_m(u) \tag{7}$$

where

$$a_0(u) = \frac{2J_1(\pi u)}{\pi u} \tag{8}$$

$$a_m(u) = \frac{2u\, J_1(\pi u)}{\pi(u^2 - \mu_m{}^2) J_0(\pi\mu_m)} \tag{9}$$

With the usual method of Taylor we define the beam broadening factor for starting the iteration procedure and solve for the coefficient $F(\mu_m)$ by locating the central zeros of the space factor. This method can be modified to control the $\overline{n}$-1 sidelobes to be of equal magnitude. The results of such an iteration procedure are shown in figures (1).

Similar procedure carried out for the difference beam and delta-delta beam and results are shown in figures (2) and (3). Tables (1)-(6) provide all the coefficients needed for generating these patterns for design purposes.

For advance monopulse processing it is further required that the product of sum and delta-delta beam should be be equal (or should 'commute') with the product of difference beam in elevation and azimuth in the vicinity of the main beam. In our method, by controlling the zeros of each pattern and the same time controlling the asymptotic zeros we were able to obtain the commutative properties. The results are given in table (7).

6. CONCLUSION

We have given a simple method for obtaining beam for monopulse processing for circular array. For rectangular array the general method is essentially an extension of two one-dimensional product method however the circular synthesis cannot be found in the literature.

The method can be modified for matching of beams up to any reasonable extent without degradation of beam width. We have given a few tables given for rapid evaluation of different beams but can be easily generated by the method given.

7. REFERENCES

1. S.M. Sherman, Monopulse Principles and Techinques, Artech House , 1984.
2. A.I. Leonov and K.I. Fomichev, Monopulse Radar, Foreign Tecnology Division, Springfield, VA. FTD-MT-24-982-71. AD 742696 NTIS.
3. E.T.Bayliss, " Design of Monopulse Antenna Difference Patterns with Low Sidelobes". The Bell System Technical Journal May-June 1968. pp. 623-650.
4. Taylor, T. T.,"Design of Line-source Antennas for Narrow Beamwidth and Low Sidelobes", IRE Trans. on Antennas and Propagation Vol. Ap-3 pp 16-28 January 1955.
5. M.A Hussain,Ben Noble and W-T. Lin, "Numerical Solution of an Aperture Integral Equation " Transaction of the Seventh Army Conference on Applied Mathematics ans Computing. ARO Report 90-1. February 1990.

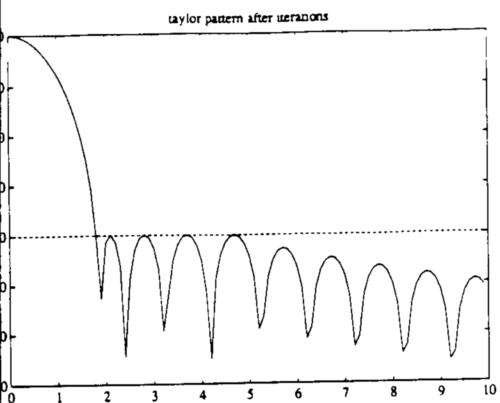

FIGURE 1a:
Sum-beam with equal side lobes.

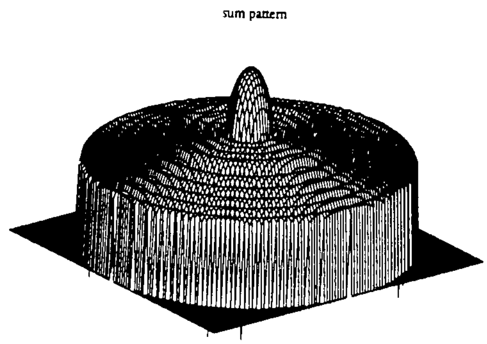

FIGURE 1b:
Sum-beam with equal side lobes.

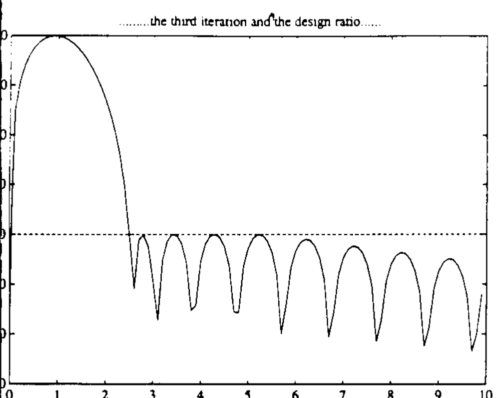

FIGURE 2a
The difference beam of Bayliss type with equal side lobes.

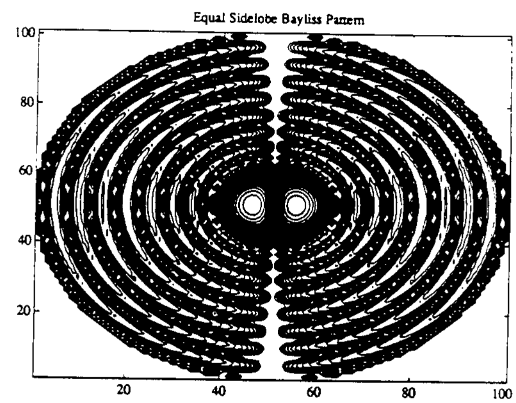

FIGURE 2b
The difference beam of Bayliss type with equal side lobes.

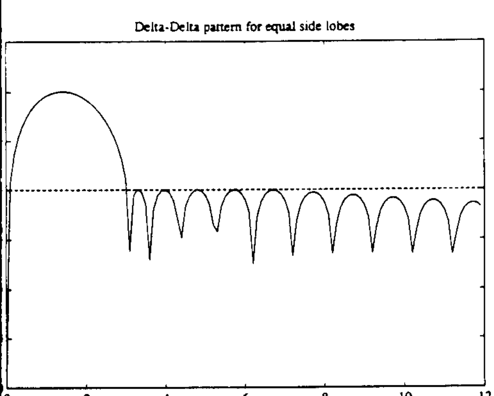

FIGURE 3a
The Delta-Delta Beam with equal side-lobes.

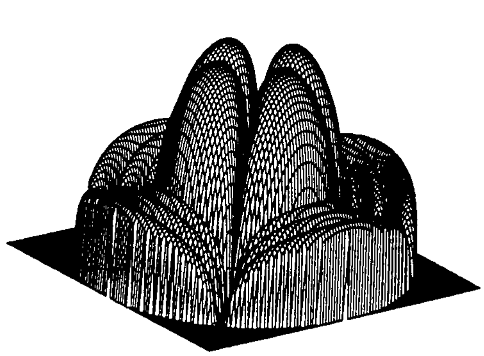

FIGURE 3b
The delta-delta Beam with equal side-lobes.

Set for circular Taylor						
N-bar.	Ratio Db	B0	Bl/B0=1	2	3	4
5	30	0.2026	-0.8510	-0.0893	0.2541	-0.2855
5	35	0.2026	-1.2142	0.0471	0.0821	-0.1181
5	40	0.2026	-1.5181	0.0838	0.0038	-0.0380
5	45	0.2026	-1.7737	0.0622	-0.0264	-0.0031

Table 1 for the sum beam for the circular aperture

Set for circular Taylor								
N-bar.	Ratio Db	B0	Bl/B0=1	2	3	4	5	6
7	30	0.2026	-0.7643	-0.1442	0.3506	-0.4722	0.5266	-0.4602
7	35	0.2026	-1.1385	0.0142	0.1365	-0.2154	0.2530	-0.2261
7	40	0.2026	-1.4582	0.0720	0.0301	-0.0844	0.1126	-0.1056
7	45	0.2026	-1.7331	0.0624	-0.0167	-0.0224	0.0434	-0.0454

Table 2 for the sum beam for the circular aperture nbar=7

Set for circular Bayliss						
N-bar.	Ratio Db	B0	Bl/B0=1	2	3	4
5	30	0.7608	0.7563	-0.0446	-0.0266	0.0479
5	35	0.7420	0.9652	-0.0575	0.0102	0.0109
5	40	0.7266	1.1466	-0.0354	0.0228	-0.0044
5	45	0.7143	1.3062	0.0098	0.0223	-0.0091

Table 3 for the Bayliss beam for the circular aperture

Set for circular Bayliss								
N-bar.	Ratio Db	B0	Bl/B0=1	2	3	4	5	6
7	30	0.7646	0.7074	-0.0281	-0.0537	0.0944	-0.1127	0.1010
7	35	0.7458	0.9275	-0.0532	-0.0012	0.0313	-0.0467	0.0453
7	40	0.7286	1.1248	-0.0367	0.0196	0.0026	-0.0147	0.0178
7	45	0.7146	1.3027	0.0087	0.0218	-0.0083	-0.0004	0.0048

Table 4 for the Bayliss beam for the circular aperture

Set for circular delta-delta.						
N-bar.	Ratio Db	B0	Bl/B0=1	2	3	4
5	30	1.258	0.7273	-0.0512	-0.0013	0.0203
5	35	1.2244	0.9143	-0.0483	0.0188	-0.0004
5	40	1.2000	1.0817	-0.0166	0.0224	-0.0082
5	45	1.1837	1.2319	0.0350	0.0182	-0.0095

Table 5 for the delta beam for the circular aperture

Set for circular delta-delta								
N-bar.	Ratio Db	B0	Bl/B0=1	2	3	4	5	6
7	30	1.2679	0.6892	-0.0422	-0.0166	0.0461	-0.0592	0.0539
7	35	1.2305	0.8899	-0.0471	0.0132	0.0092	-0.0209	0.02200
7	40	1.2020	1.0739	-0.0176	0.0216	-0.0065	-0.0029	0.0068
7	45	1.1813	1.2429	0.0381	0.0187	-0.0110	0.0042	0.000

Table 6 for delta-delta beam for the circular aperture

TABLES OF COEFFICIENTS FOR SUM AND DELTA BEAM FOR CONTINUOUS CIRCULAR APERTURES FOR MONOPULSE PROCESSING

Table for commutative sigma-delta and delta-delta beams: 7

Set for circular Taylor Bayliss and delta Type. Example 1.						
TYPE	B0	B1	B2	B3	B4	dB
SIGMA	0.2026	-2.6882	-0.3918	0.0079	0.0016	55.0447
BAYLISS	0.7065	1.3789	0.0026	0.0395	-0.0273	39.362
DELTA	1.2575	0.7282	-0.0509	-0.0013	0.0203	30.0161

Set for circular Taylor Bayliss and delta Type. Example 2.						
TYPE	B0	B1	B2	B3	B4	dB
SIGMA	0.2026	-2.8599	-0.5732	0.0186	-0.0005	57.9628
BAYLISS	0.6879	1.5742	0.1029	0.0058	-0.0130	41.6967
DELTA	1.2029	0.9599	-0.0715	0.0129	-0.0003	31.5461

SESSION 5 B- “CAEME (POSTERS)

AND

SOFTWARE DEMONSTRATIONS"

Moderator: Magdy Iskander

A Transmission-Line Laboratory Exercise Using Computer Simulations to Verify Measurements

by

Dr. Michael E. McKaughan
Department of Engineering
U. S. Coast Guard Academy
15 Mohegan Avenue
New London, CT. 06320-4195

ABSTRACT

An undergraduate laboratory exercise is described which uses actual measurements and computer simulations to help students gain greater understanding of the characteristics of transmission lines. Using the software program "TLS Transmission Line Simulator", written by Charles H. Roth of the University of Texas, Austin, students observe transmission line standing waves for various terminations. Using features of the program, voltage standing wave ratios are calculated. Complex impedances may be used. Next, the student observes the behavior of pulse waveforms on the line. Following the computer simulation session, the students make laboratory measurements which parallel the computer simulations. Terminations for the laboratory measurements match those loads used in the computer simulation. Again, voltage standing wave ratios are calculated. Finally, time domain reflectometry is introduced using pulsed signals and a laboratory oscilloscope. The results of these measurements are compared to the simulations. Agreement between the two methods is excellent, and the students believe that they have learned much about the characteristics of the transmission lines.

THE LABORATORY EXERCISE

Introduction

Part one of this experiment is a computer simulation of the behavior of transmission lines using transient and steady-state excitations. This part of the experiment is performed using a computer simulation software package called "TLS Transmission Line Simulator" by Charles H. Roth, Jr. (Roth, 1989). Part two of this experiment, involves investigating the transient behavior of transmission lines in the laboratory. Part three of the exercise deals with standing waves on transmission lines. We will use a simple method to probe the line and observe the voltage standing-wave patterns along a line.

Equipment:

Part One :	TLS Transmission Line Simulator, Version 2.41 software package	
	Macintosh computer system	
	User's Manual for TLS	
Part Two:	Time-Domain Reflectometry	
	1	coil of RG-213/U coaxial transmission line
	1	Hewlett Packard Digital Oscilloscope HP-54501A
	1	Hewlett Packard Thinkjet printer HP-2225A
	1	Hewlett Packard pulse generator HP-8002A
	1	Hewlett-Packard L-C-R Meter HP-4332A (one per room)
	5	transmission line terminations
		open circuit
		short circuit
		51-Ω
		two unknown resistive terminations
Part Three:	Slotted-Line Apparatus	
	1	slotted line section
	1	microwave signal source
		Miscellaneous waveguide terminations
	1	Voltage probe
	1	R. F. Voltmeter

Procedure:

Part One: Computer Simulation

This part of the experiment serves as an introduction to transmission line theory and practice. Each student completes this part of the experiment prior to visiting the laboratory to conduct the actual experimental parts of the exercise.

1. Read the instruction manual for the software package "TLS Transmission Line Simulator."
2. Work each of the examples in the instruction manual.
3. Solve the following problems using the TLS program.

a. Using a 50-Ω source impedance and a 50-Ω transmission line characteristic impedance, verify equation 1.33 in Schwarz (Schwarz, 1990) for both voltage and current using these load impedances:

1) 0 Ω, 2) 24 Ω, 3) 50 Ω 4) 75 Ω, 5) 100 Ω 6) 150 Ω. 7) ∞ Ω

Include the voltage reading observed on the TLS meter using a single pulse incident on the load. Assume no attenuation for this problem.

b. The transmission coefficient gives some idea of the power delivered to the load terminating a transmission line (equation 1.40 in Schwarz) (Schwarz, 1990). Compute the transmission coefficient for each of the loads in problem a above.

c. Using the sine wave source in the TLS, determine the standing wave ratio, SWR, for each load termination in problem a. above. Equation 2.6 in Schwarz (Schwarz, 1990) defines SWR. Compare the SWR measured in each case to the value computed using the reflection coefficient.

d. Now, to simulate the experiment to be performed in the Laboratory, add some attenuation to the transmission line. Use a value of attenuation that demonstrates dramatically the effect. Set the attenuation to 50%. Now measure the SWR for each load termination from problem a. above. Make measurements as near to the load and as near to the source as possible. Tabulate the observed results.

Part Two: Time-Domain Reflectometry

For this part of the laboratory exercise, a length of coaxial transmission line is assigned to each student. Using different measurements and methodologies, investigate the characteristics of the transmission line.

1. Observe the voltage waveform at the generator end of the transmission line for each load condition specified.
2. Compare the predicted and measured reflection coefficients for each case.
3. Measure the propagation velocity of the transmission line. Compare your results with published data.
4. Measure the capacitance and inductance of the transmission line with the L-C-R meter. Use these values to calculate the velocity of propagation of your transmission line. Compare your results here with the results you found in the previous step.
5. Measure the loss in the transmission line using the network analyzer. Obtain a plot of this attenuation versus frequency. Compare results with published data.
6. Observe the waveform for an open-, short-, and matched-circuit line using the commercial time-domain reflectometer. Comparison this method to the method used above.

Part Three: Slotted-Line Apparatus

1. Using the voltage probe and R. F. Voltmeter, determine the SWR and the locations of voltage minimums and maximums along the slotted line using a short circuit termination.
2. Repeat the procedure for an open circuit termination.
3. Repeat the procedure for a matched termination.

Report: Discuss the results and observations in a formal laboratory report.

COMPUTER SIMULATION OPERATION AND OUTPUT

The TLS program is simple to use. The transmission line circuit to be simulated is shown using computer graphics, and by conventional Macintosh© computer point-and-click technics, the student can easily modify circuit parameters to match the conditions required in the laboratory. A sample of the graphics is shown in Figure 1. Simulation is even more simple; just point-and-click on the SIMULATE button. The output display is graphic, and appears as the screen of an oscillograph. The picture drawn shows the voltage or current wave

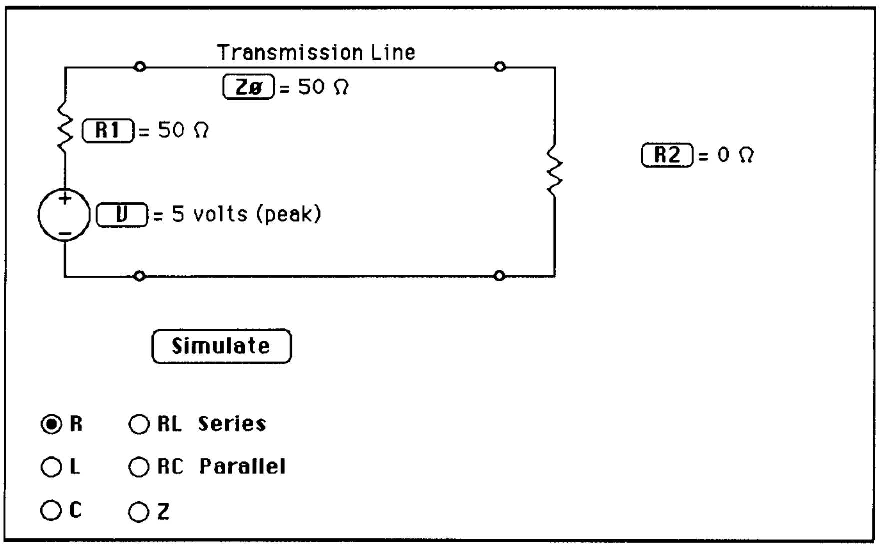

Figure 1. Graphics display of the circuit set-up for the TLS.

traveling down the transmission line to the load, and then the reflected wave traveling back toward the source. Standing wave patterns develop, just as they would on the actual transmission line. A sample output is shown in Figure 2 for an open circuit termination. A "meter" is provided that can be used to measure voltage or current at any point along the line. Both amplitude and position are displayed. By selecting a single pulse for the source, time-domain reflectometry is simulated. Using the "meter", incident and reflected amplitudes can be observed. An example is shown in Figure 3.

Once the student is familiar with the operation of the program, he/she can change the parameters of the simulation and study the behavior of signals on the transmission line. Detailed analysis is possible in the default mode 1 and the more powerful mode 2 where attenuation, line length, propagation velocity, and pulse parameters can be added.

The documentation is complete, including examples and sample outputs. In fact, it is so complete that the students were able to complete the simulation section of the laboratory without assistance from the instructor.

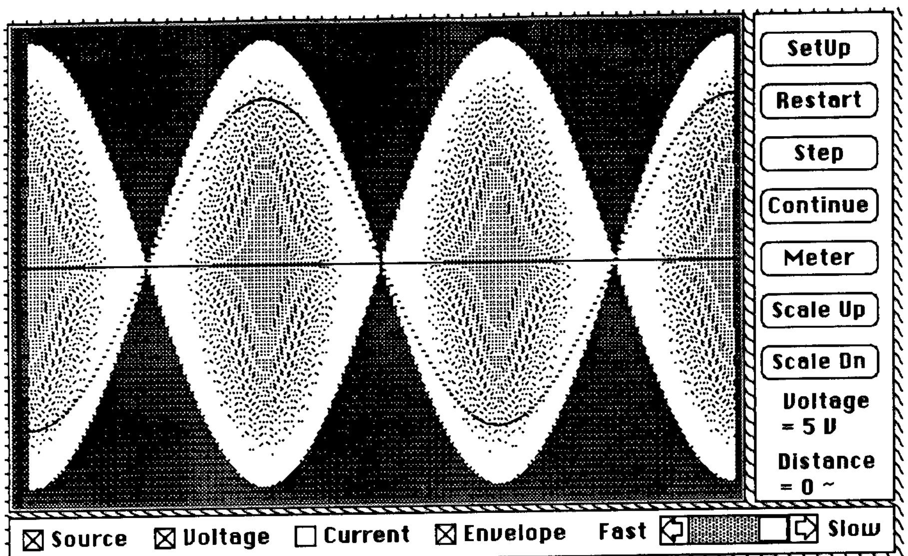

Figure 2. TLS display showing a standing wave pattern on an open-circuit terminated transmission line.

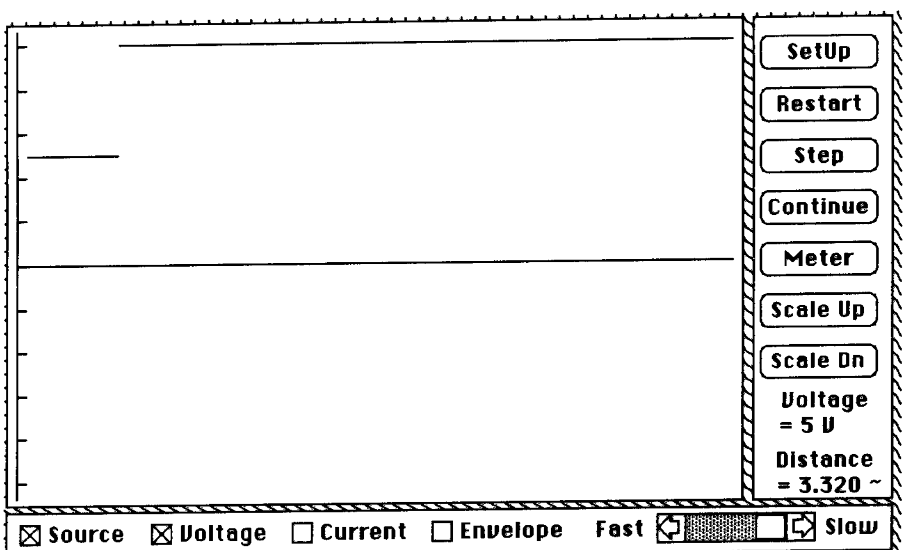

Figure 3. TLS Simulation display for an open-circuit termination with DC excitation to simulate time-domain reflectrometry.

LABORATORY MEASUREMENTS AND OUTPUT

The actual in-lab measurements are simple to make. The equipment setup is shown schematically in Figure 4. Students make measurements of pulse amplitude for the incident and reflected pulses. Propagation times are recorded, and terminations are tested to match the computer simulations and the physical transmission line tests. Figure 5 presents a typical oscilloscope display printout. Fortunately for us, digital oscilloscopes are available, and the students are familiar with their operation. Thus, results can be accurately compared to the computer simulations by using the time and voltage marker features on the oscilloscope. Adequate results are possible using analog oscilloscopes, but experience has shown that student results are less accurate in this case. The entire laboratory exercise seems to have been enhances with the addition of the digital oscilloscope. Students were able to precisely compare the two methods and obtain excellent agreement.

In the laboratory, the standing wave part of the experiment is more difficult to match to the computer simulation. Good agreement could be observed if a length of perforated transmission line was available. We were only able to use a slotted line at a frequency of approximately 8 GHz. Thus, we could view standing wave patterns, but various calibrated fixed loads were not practical with our apparatus.

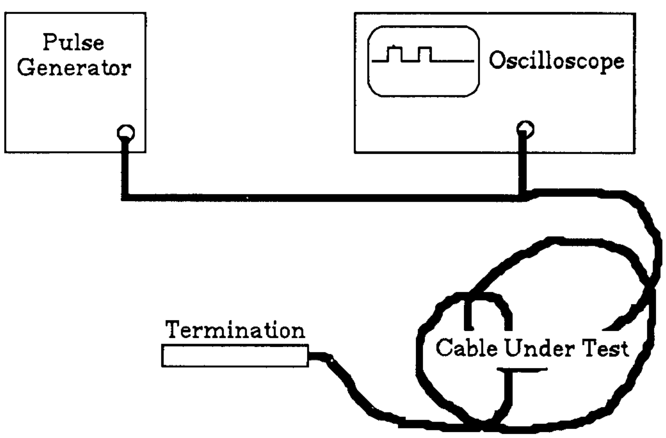

Figure 4. Equipment setup for Laboratory measurement of transmission line parameters

REPORT OF THE RESULTS

As expected, the students were pleased with the results of the experiment. Most had positive comments about the agreement of the simulation and experimental results. One student's comments are repeated here: "This laboratory was an excellent addition to the classroom material presented about transmission line characteristics. Several concepts were easily demonstrated, including propagation velocity, reflection coefficient, and loss due to attenuation. There was a relatively small amount of error in this lab, which makes everything taught in the classroom more believable, Overall, I believe this lab was a good addition to the course...."(Czerwonka, 1991)

The TLS program is simple to use, may be demonstrated in a classroom, and is well documented. Students can learn to use the software quickly without assistance. This make it an excellent program for the student to experiment with. If laboratory facilities are unavailable for an entire lab section experiment, a classroom demonstration of the physical measurements could be substituted. Hands-on experience is, however, far more enlightening for the student.

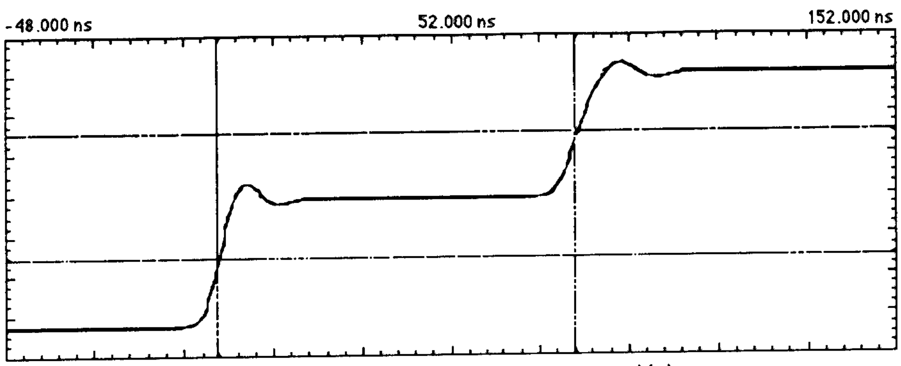

	Timebase	Delay / Pos	Reference	Mode	Markers
Main	20.0 ns/div	-48.000 ns	Left	Realtime (NORMAL)	Ymarker2(c1) = 2.39063 V
					Ymarker1(c1) = 843.750 mV
	Sensitivity	Offset	Probe	Coupling	delta Y (c1) = 1.54688 V
Channel 1	500 mV/div	1.62500 V	1.00 : 1	dc (1Mohm)	

Trigger mode : Edge

On Positive Edge of Chan 1
Trigger Level
Chan1 = 750.000 mV (noise reject OFF)
Holdoff = 7.70346 ms

stop = 80.000 ns
start = -800 ps
delta t = 80.800 ns
1/delta t = 12.3762 MHz

Figure 5. Typical Laboratory oscilloscope display for time-domain reflectometry using an open circuited transmission line.

CONCLUSIONS

A laboratory exercise has been discussed where computer simulations of transmission line behavior are used to help the student understand and verify laboratory measurements. Agreement between physical and computer results is extremely accurate. The experimental equipment is commonly available in most undergraduate electrical engineering departments, and the software is easily obtained and will run on a modest Macintosh© computer. The software package is well documented and students are able to operate the program and learn to perform simulations without instructor assistance. The combination of computer simulation and physical laboratory measurements enhances the student's understanding of the theory presented in the classroom.

REFERENCES:

1. Czerwonka, Gregory J., "Laboratory Reoprt, Transmission Line Characteristics," U. S. Coast Guard Academy Department of Engineering, unpublished report, 1991.

2. Roth, Charles H., Jr., "TLS Transmission Line Simulator, Version 2.41 USER'S MANUAL," Kinko's Academic Courseware Exchange, 225 West Stanley Avenue, P. O. Box 8000, Ventura, Ca., 93002-8000, (800) 235-6919 or in CA. (800) 292-6640, 1989

3. Schwarz, Steven E., <u>Electromagnetics for Engineering</u>, Sanders College Publishing, Holt, Rhinehart, and Winston, 1990.

Visualization of Radiation Effects from Simple Charged Particles

Rodney Cole & Curtis Brune
Physics Department
Learning Skills Center
University of California, Davis

Abstract

Electromagnetic radiation, involving non-local retarded solutions to Maxwell's equations, has long been difficult to teach and frustrating to learn. It often takes years of study to be able to conceptually understand a solution without using the powerful mathematics of Maxwell's theory. This steep learning curve is a major contribution to the decrease in the number of students choosing electromagnetics as a career. This state of affairs lead us to develop *SilverHammer* which is a program with a graphical user interface much like *MacDraw* and runs on a MacIntosh microcomputer. *SilverHammer* allows the user to arrange point-charges and assign velocities and accelerations by pointing and clicking. There is a tool palette for contour, pseudo-color, and false-height 3-D graphs that map out the time-domain fields and potentials. Animation is supported through Apple's *QuickTime* System Software. QuickTime allows the animations to be cut and pasted into professional animation programs, HyperCard or a movie player.

Radiation is often introduced in antennas; however, antennas are not the simplest radiating systems. Many advanced topics in antennas can be conceptually understood in terms of the motions of simple point charges. This approach leads to a better grasp of the fundamentals of antenna theory and design as well as those related to complicated electromagnetic environments. *SilverHammer* allows users to do "What if" analyses with arrangements of point-charges, and thereby, conceptually understand more complicated systems by modeling the motions of the charges in those systems.

Visualization of Radiation Effects from Simple Charged Particles

by

Rodney Cole[1], Curtis Brune

Physics Department

Learning Skills Center

University of California, Davis 95616

SilverHammer is a 2-D field mapping program for mapping the fields in the region of a set of point charges. The charges can be at rest so the maps are of static fields or accelerating so the maps provide information on the radiated fields. SilverHammer runs on the Apple Macintosh with at least 2MB of ram memory and system 6.0.4 or later; however, it is calculationally intensive and realistically needs a floating point processor. SilverHammer comes in two versions: a standard version that runs without a math coprocessor, and an FPU version that requires a math coprocessor. Electromagnetic radiation, involving non-local retarded solutions to Maxwell's equations, has long been difficult to teach and frustrating to learn. It often takes years of study to be able to conceptually understand a solution without using the powerful mathematics of Maxwell's theory. This steep learning curve is a major contribution to the decrease in the number of students choosing electromagnetics as a career. This state of affairs lead us to develop a program with a graphical user interface much like *MacDraw*. *SilverHammer* allows the user to arrange point-charges and assign velocities and accelerations by pointing and clicking. There is a tool palette for contour, pseudo-color, and false-height 3-D graphs that map out the time-domain fields and potentials. Animation will be supported through Apple's *QuickTime* System Software. QuickTime allows the animations to be cut and pasted into professional animation programs, HyperCard or a movie player. In Section 1 we motivate the teaching of electromagnetic radiation in terms of the motions of charged particles and the Lienard-Wiechert potentials from point charges. Next in Section 2 we show how various properties of the Lienard-Wiechert solutions can be

modeled using *SilverHammer*. In Section 3, we discuss how some of these properties relate to radiating antenna problems. The computational model for *SilverHammer* as well as a brief demonstration of its use is in the CAEME Software Volume 1.[2]

1. Motivation

If you could list the most important topics to be taught in an electricity and magnetism course, electromagnetic radiation would probably be at the top of the list. After all, how do we interact with the world around us? We see using light. TV and radio carry news and entertainment on electromagnetic waves. What are the characteristics of the systems that produce them? How are these waves produced? How can we teach a course in electricity and magnetism without giving our students a fundamental understanding of radiation. All too frequently, discussions of radiation begin and end with dipole radiation. We use circuit equivalents that work fine for discussing non-radiating systems, but are not the clearest models for discussing field theoretic processes. This is often compounded by spending the majority of the time discussing the radiation in the frequency domain. To an experienced researcher this abstract presentation of dipole radiation is quite eloquent, however, to a neophyte, it can be quite confusing. It would perhaps be better to spend some time discussing how the charges are actually moving on the antenna. Voltages, inductances, reactances are all very important, but intuition comes from understanding how the charge will move. Learning comes about by asking simple questions. For instance, how is it that the electric field lines rip off from a radiating dipole and form closed loops? A simple model can be constructed from the motion of point charges.

Maxwell's equations for a point charge can be solved exactly in all zones using the Lienard–Wiechertpotentials[3]

$$\boldsymbol{E}^{\pm}(\boldsymbol{x},t) = Q\left(\frac{(\hat{\boldsymbol{n}}-\boldsymbol{\beta})}{\gamma^2 K^3 R^2}\right)_{\pm} + \frac{Q}{c}\left(\frac{\hat{\boldsymbol{n}}\times(\hat{\boldsymbol{n}}\times\dot{\boldsymbol{\beta}} - \boldsymbol{\beta}\times\dot{\boldsymbol{\beta}})}{K^3 R}\right)_{\pm} \qquad (1)$$

$$\boldsymbol{B}^{\pm}(\boldsymbol{x},t) = \hat{\boldsymbol{n}}\times\boldsymbol{E}^{\pm}(\boldsymbol{x},t)$$

where c is the speed of light, $\beta = v/c$, $\gamma = (1-\beta^2)^{-1/2}$, $K = 1 - \hat{\mathbf{n}} \bullet \boldsymbol{\beta}$, $\hat{\mathbf{n}}$ is a unit vector pointing radially out from the charge towards the point in space where the field is being evaluated as shown in Figure 1. The first term for the electric field is the called the velocity field and is just the inverse r squared Coulomb term. The second term is called the acceleration field representing the radiated contribution and decreases as an inverse r. the simple closed form of the solution means that radiation from a single point charge is a more appropriate place to start a discussion of radiation. After discussing the salient features for a point charge, radiation from dipoles and more complicated structures can then be discussed in terms of the models developed for a point charge.

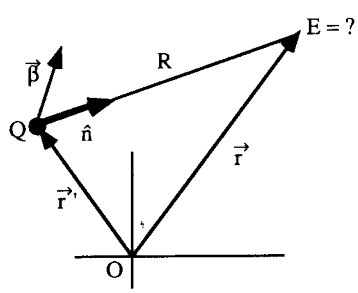

Figure 1

Unfortunately, the Lienard–Wiechert solution is not one that a student can sit down and play with. It is not a solution at all in the usual sense because of the retarded and advanced times at which all quantities in the above formula must be evaluated. That is, if we want the retarded solution, we must evaluate all the variables not according to where the charge is now but rather where the charge

was at the moment it emitted the radiation that is now reaching us. For anything beyond trivial motions of the charge, the retarded time cannot be solved exactly. Is it any wonder that an intuitive feel for radiation takes years to develop? What we need is a solution the student can play with -- do a "What if..." analysis. Herein, is where a computer can help.

2. Properties of Non-Radiating Systems

SilverHammer is a program designed to allow the student to graph the fields around a moving, accelerating charge. The data entry for such a program is usually prohibitively expensive in terms of time and typing. Machine calculations tend to be long, and thus a student becomes easily frustrated because it takes a long time to enter the data, then a longer time to wait for the solution to appear, only to realize that the result is fairly uninteresting and then have to go through the process again for a hopefully better result. We have tried to construct a program that fully conforms to the Macintosh graphical interface so that data entry occurs quickly and naturally in a Draw-like environment. In SilverHammer there are two views provided, and shown in Figure 2 for a static dipole.

Figure 2

One is the *Charge View*, Figure 2a, which is a map for placement of the particles and assigning values such as charge, velocity, and acceleration. These values are assigned not by typing or using a menu, but by choosing the appropriate tool from a palette and drawing. This technique allows the user to directly manipulate the objects. Since an object programming language is being used, this is manipulation of objects by the user closely follows the actual program code objects. For instance, the magnitude of the charge is assigned by drawing a circle, with the radius of the circle being the magnitude of the charge. When the mouse is held down with the charge tool, the coordinates are assigned to the position of the particle. If the circle is dragged to the right of center with the mouse

down, then the particle is assigned a positive charge value. If it is dragged to the left of center, it is assigned a negative charge value. Velocity and acceleration are represented by arrow tools. The length of the arrow represents the magnitude of the velocity or acceleration. The user can enter as many charges as memory allows. A scroll bar just below the tool palette advances the time (the time control) and the particles move in the view according to the initial assigned velocity and acceleration. With this release, the user can only assign initial values of velocity and acceleration.

The other view, Figure 2b, is a graph view. This window is a place to experiment with graphs. There are several graph tools available. A particular graph is generated by selecting the appropriate tool and dragging the graph to the size you wish. The size of the graph is automatically scaled to the charge view so the proportions remain true. The graph is a map of the fields in a plane containing the charges. Graph tools are provided for contour, pseudo-color (grey-scale or black and white patterns in monochrome systems), fieldline, and 3-D pseudo-height plots. Graphs may be overlaid, copied to the clipboard for export to professional drawing or animation programs or saved to a disk file.

One concept that the student needs to understand is the difference between the near fields and the far fields. In Figure 2b, we contrast the near fields for a simple static dipole with that of a dipole perturbed by the presence of another positive charge. The third graph is that of the far fields. The student can clearly see from the fieldline map that although the near fields are quite complex, the far fields look similar to that of a single positive charge because the effects of the dipole tend to cancel at large distances. The far field behavior of the static electric dipole falls off as an inverse cube with distance, but the field from the other charge falls off as the inverse square. Thus, at large distances the behavior is dominated by single non-paired charge. The far fields were constructed by simply moving the charges close together while preserving the geometry of the charge distribution.

Next consider what happens to the field from a charge when it is moving? Although Maxwell's theory and the Lienard-Wiechert potentials were derived before relativity, they are relativistically correct. The relativistic effects can be seen by plotting the fields from a point charge that has been given a constant velocity close to the speed of light as shown in Figure 3 where the contours for the electric field are plotted by shading the area between the contours with a pattern. The charge has been given a velocity straight down, and the relativistic length contraction of the field can be clearly seen.

Figure 3

These relativistic effects will be seen in the next section when we discuss radiation from a dipole.

The interface on SilverHammer is meant to allow the student's imagination to flow freely without being distracted by the mechanics of using the computer. Many aspects of the program work the same way as popular drawing programs. For instance, the map in Figure 3 was made by going to the charge view and selecting a charge tool. One charge with a radius of 15 was entered by dragging the charge tool to the right. Next, a velocity was given to the charge by selecting the velocity tool and dragging straight down. A velocity of 40 was used in this case. The speed of light is 50 so the charge has a velocity of 80% the speed of light. The numerical values can be viewed and altered by double-clicking on the charge. A dialog box appears with the relevant information in it as shown in Figure 4. After dismissing the dialog box, the density plot tool was chosen in the graph view palette. It was dragged to the appropriate size and released creating the plot shown in Figure 3. In this way, the student has to spend less time learning how to work the computer and is more easily able to concentrate on the motions of the charged particles and the fields they produce. A student can easily and quickly test an idea.

Figure 4

3. Radiation Effects

Radiation from a dipole can be understood by looking first at individual charges. The key point is understanding that radiation occurs whenever charge is accelerated. The charge shown in the field line plot in Figure 5 has been given a impulse. During the time it accelerated, its changing fields create the kinks in the field lines. These kinks travel outwards and represent the electromagnetic radiation.

Figure 5

There are HyperCard tutorials to help the student interpret what he is seeing. In the HyperCard Stack "Impulse Radiation" the student is lead to understand how the formation of a kink in the field line from an impulsively driven point charge follows from the basic laws namely Ampere's law and Faraday's law. The kink can be thought of as the superposition of the induced field and the Coulomb field. One of the cards from the HyperCard tutorial showing how to obtain the induced field from Ampere's law and Faraday's law is shown in Figure 6.

Figure 6.

Once the student understands the simplest radiation process, the next step in understanding dipole radiation is to look at the harmonic aspects. In radiation from a dipole, the fields oscillate back and forth. We can see how to create an oscillating field by taking a single charge and causing it to oscillate harmonically. The fields depicted in Figure 7 are from a HyperCard tutorial called "Harmonic Monopole". By driving a charge harmonically, you can see how the waves in the field lines build up as a natural extension of the impulsively excited charge. This oscillating case is still much simpler than dipole radiation because the geometry of the field lines is strongly influenced by the divergence created by the single charge. This divergence prevents the field lines from tearing away from the charge. Because of the divergence there is a polar as well as a transverse component to the field. In the dipole, the radiated field is purely transverse with no polar component, so we need to understand how to remove the divergence. We might accomplish this

by having no net charge, i.e., by using equal but opposite charges as in a dipole or quadrupole. The dipole is simplest to understand, so we will consider it next.

Figure 7

Using *SilverHammer*, we can gain a deeper understanding into why the field lines tear off from a dipole by considering a very simple scenario. Consider two equal but opposite point charges forming a dipole. What happens if we send the two charges towards one another with a constant velocity?. In the sequence shown in Figure 8, at the moment they pass, the fields virtually disappear because the fields from the opposite charges cancel each other, i.e., we have removed the divergence for that brief moment. Of course the charges are not accelerating so there is no radiation.

Figure 8

The simplest radiation we can create is from a constant acceleration of the charges, as shown in Figure 9. At the moment they pass each other, the divergence from the velocity fields disappears because the charges are opposite, but the acceleration fields are not opposite and do not cancel out. In fact, since the charges are accelerating in opposite directions, and are oppositely charged, the two effects cancel so the acceleration fields add, giving a very strong contribution at this moment. In Figure 9, at the moment the charges overlap, the fields do not cancel as they did in Figure 8. One see's that the velocity and acceleration fields are fundamentally very different. The velocity fields are radial diverging fields. On the other hand the acceleration fields are transverse to the direction of propagation, and are fields with pure circulation. At the moment the diverging field disappears, it leaves only the circulating field which has reached a maximum. This is the moment the field lines close and tear away from the dipole. In the last scene in Figure 9, the charges have become

relativistic and the length contraction of the fields can be seen as the field pattern flattens in the direction of propagation.

Figure 9

4. Conclusion

Although SilverHammer only reproduces radiation from point charges, it can be a very useful tool for building intuition and a fundamental understanding of more complex systems. The usual circuit analogies that have been developed are very powerful calculational tools, however, they are abstract and can leave the student able to perform calculations without a fundamental understanding of the physics behind the process. To understand the physics, you must know how the charge is distributed and how it is moving. SilverHammer allows the student to play with different charge distributions and develop a basic understanding of electromagnetics. Many useful exercises can be created by asking the student to simulate the field from a complex structure by distributing the charge appropriately. For instance, Figure 10 shows the electric fields about a uniform line of charge. The fields are often mapped from the charge distribution in statics because it helps build a solid command of the subject. So too, understanding how the fields and charge interact in a radiating system can also lead to an enhanced understanding of radiating systems.

Figure 10

SilverHammer is in a very formative stage. We plan to have the alpha release of SilverHammer for the second volume of the CAEME Software Book. Feedback is needed on what works, what doesn't, and how you would like to see the program change in the future. We have attempted to make SilverHammer as solid and bug-free as possible; however, we do not have the resources of a

major software house, and requests can be overwhelming. We will attempt to get back to you as quickly as possible on any request.

---

[1]presenter, Internet address: cole@ucdphy.ucdavis.edu

[2]Iskander, M., ed., CAEME Software Book, V. 1, Chapter 3, 1991.

[3]A. Lienard, L'Eclairage Elec., **16**, 5, 53, 106 (1898); E. Wiechert, Arch. Neerl., **5**, 549 (1900).

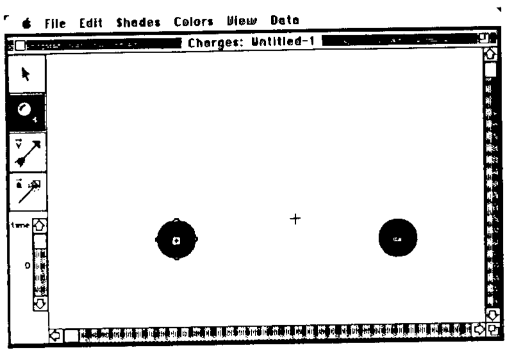

Figure 2a

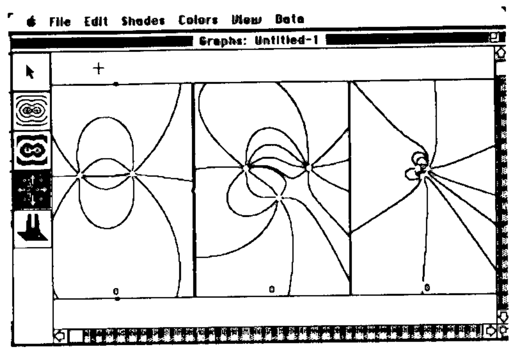

Figure 2b

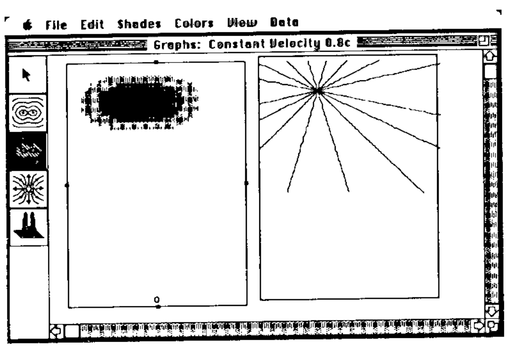

Figure 3

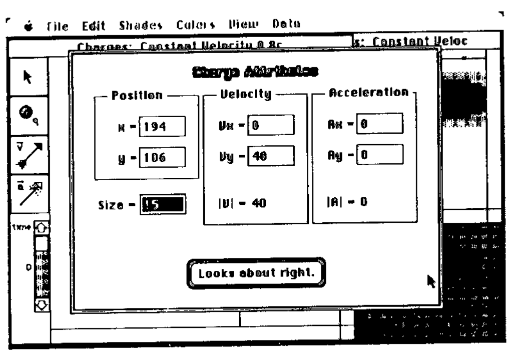

Figure 4

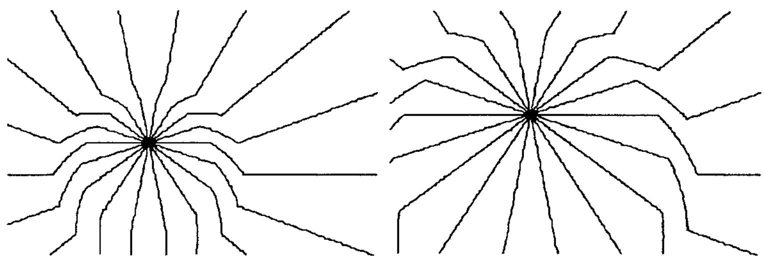

Figure 5

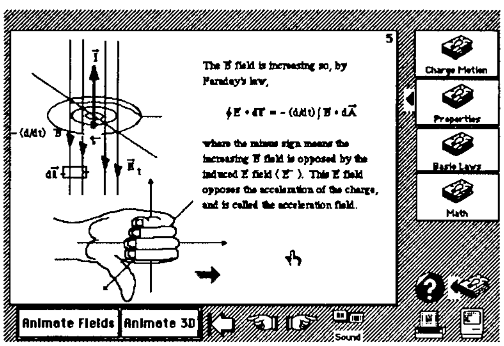

Figure 6

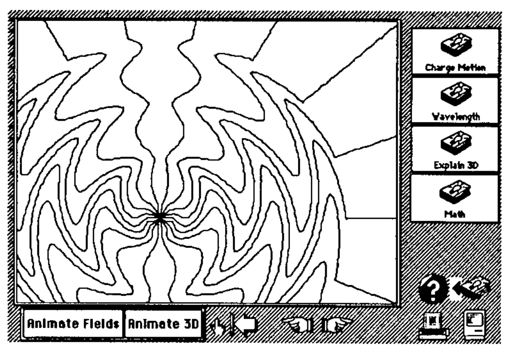

Figure 7

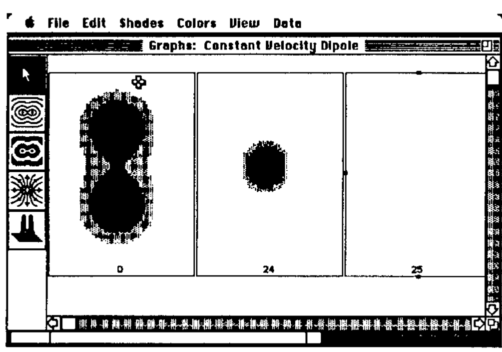

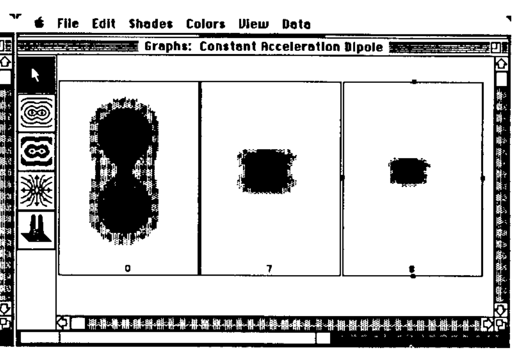

Figure 8

Figure 9

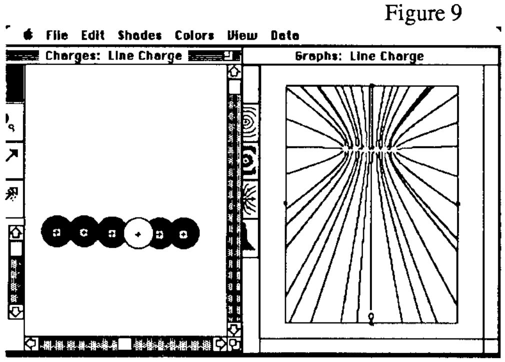

SESSION 6 - “MEETING ON CANONICAL PROBLEMS"

(No Papers)

Moderator: Hal Sabbagh

SESSION 7 - "ANTENNA AND MICROWAVE CIRCUITS"

Moderator: Darko Kajfez

CG-FFT ANALYSIS OF TWO DIMENSIONAL FRESNEL ZONE PLATE ANTENNAS

Y. J. Guo and S. K. Barton
Department of Electrical Engineering
University of Bradford, Bradford, UK

Abstract

The Conjugate gradient method together with the fast Fourier transform (CG-FFT) is applied to analyse the flat printed two dimensional Fresnel zone plate antennas. It is found that the antenna pattern is mainly determined by the F/D ratio. Decreasing F/D ratio yields lower first sidelobe, deeper first null but higher far-axis sidelobes. Reducing the edge illumination level can smear the first sidelobe but does not change the far-axis sidelobe level much.

1. Introduction

The Fresnel zone plate antenna is becoming a promising cheap and low-profile alternative to the conventional paraboloidal reflector [1]. Various versions of the zone plates have been proposed and a multi-layered zone plate reflector with 54.8% efficiency has been reported by the authors [2]. The commonly accepted approach for attacking zone plates is to employ the geometrical optics (GO) approximation, in which the aperture field is deduced through the transmission and reflection analysis and the focal or radiation field is obtained through the integration of the aperture field [3,4]. Due to the complexity of the zone plate structure, this approach has a few severe shortcomings. Firstly, since the full wave zone width decreases with the zone order number starting from the central zone, only the central aperture field can be well approximated with that of the geometrical optics. This is especially true for the phase correcting zone plates, in which each full wave zone is divided into several sub-zones. Secondly, complicated multiple reflection and refraction always occur in the zone plate structure and much effort has to be made in ray tracing when considering the radiation field. Thirdly, GO approximation does not yield reliable far-axis radiation patterns.

Among various versions of Fresnel zone plats, one of the most promising configurations is the so called flat printed zone plate reflector which consists of a conducting reflector, a dielectric substrate and a layer of circular or elliptical metallic rings [5,6]. Since there is no transmission loss through the plate, high efficiency can be realized by employing the phase correcting technique [2]. In this paper, the spectral domain method is introduced to accurately analyse the radiation characteristic of the flat printed zone plate antennas. For convenience, only the two dimensional version is considered, so rings are replaced by strips and the feed is assumed to radiate a directional TM or TE wave. The approach starts with representing the electromagnetic fields in and outside the substrate with travelling and evanescent plane waves. Enforcing boundary conditions yields a spectral domain integral equation of the electric current induced on the strips. Since the structure is electrically large, the conjugate gradient method together with the fast Fourier transformation algorithm (CG-FFT) is used to solve the integral equation [7]. Finally, the radiation field of the antenna is obtained through the FFT of the current. The radiation characteristic of the zone plate antennas and the influence of factors like F/D ratio, edge illumnation level, dielectric constant variation and edge impedance loading are investigated with the method.

2. Spectral Domain Formulation

Assume the radiation field of a two dimensional feed as

$$\vec{E^i}=E_0 f(\theta)/\sqrt{\rho}\ \hat{y} \qquad \text{for TM wave} \qquad (1.a)$$
$$=E_0 f(\theta)/\sqrt{\rho}\ \hat{\theta} \qquad \text{for TE wave} \qquad (1.b)$$

where E_0 is a constant, $\sqrt{\rho}$ accounts for the space attenuation of the cylindrical wave and the directional factor $f(\theta)$ is given by

$$f(\theta)=\cos^n\theta \qquad |\theta|<\pi/2$$
$$=0 \qquad \text{otherwise} \qquad (2)$$

with index 'n' used to control the beamwidth. At the zone plate surface, Eq. (1) yields the tangential component of the incident field

$$E^i{}_s(x)= \begin{vmatrix} 0 \\ E_0 f(\theta)/\sqrt{\rho} \end{vmatrix} \qquad \text{for TM wave}$$

$$= \begin{vmatrix} E_0 f(\theta)\cos\theta/\sqrt{\rho} \\ 0 \end{vmatrix} \qquad \text{for TE wave}$$

with θ determined by

$$\theta=tg^{-1}(x/F)$$

where F is the focal distance of the antenna (see Fig. 1). According to the spectral domain theory, the transverse component of the feed radiation field can be expressed as a superposition of elementary plane waves:

$$E^i{}_s(x,z)=1/(2\pi)\ \int E^i{}_s(\alpha)\exp(-j(\alpha x-k_{0z}(z-F)]d\alpha \qquad (0\leqslant z<F) \qquad (3)$$

where

$$E^i{}_s(\alpha)=\int E^i{}_s(x)\exp(j\alpha x)dx \qquad (4)$$

and k_{0z} is given by

$$k_{iz}=(k_i{}^2-\alpha^2)^{1/2} \qquad (5)$$

with i=0 and $k_i=\omega(\mu_i\epsilon_i)^{1/2}$ as the wavenumber in rigon i [8]. In Eq. (5), a root is chosen which has a nonnegative real part and a nonpositive imaginary part.

The feed field excites the scattering fields in and outside the substrate of the zone plate reflector. The toatal field in $z\geqslant 0$ region is the addition of the incident field (E^i,H^i) and the scattering field(E^s,H^s)

$$E^0{}_s(x,z)=E^i{}_s(x,z)+E^s{}_s(x,z) \qquad (6.a)$$
$$H^0{}_s(x,z)=H^i{}_s(x,z)+H^s{}_s(x,z) \qquad (6.b).$$

$H^i{}_s$ is deduced from $E^i{}_s$ as

$$H^i{}_s=-1/(2\pi)\int[K_0(\alpha)][X]E^i{}_s(\alpha)\exp[-j(\alpha x-k_{0z}(z-F)]d\alpha \qquad (0\leqslant z<F) \qquad (7)$$

where

$$[X]= \begin{vmatrix} 0 & 1 \\ -1 & 0 \end{vmatrix}$$

and $[K_0(\alpha)]$ is the following matrix with i=0:

$$[K_i(\alpha)]=-1/[k_{iz}\omega\mu_i] \begin{vmatrix} k_i^2-\alpha^2 & 0 \\ 0 & k_i^2 \end{vmatrix} \tag{8}$$

The scattering field in $z \geqslant 0$ region can be expressed as

$$E^s_s(x,z)=1/(2\pi)\int E^s_s(\alpha)\exp[-j(\alpha x+k_{0z}z)]d\alpha d \tag{9.a}$$
$$H^s_s(x,,z)=1/(2\pi)\int [K_0(\alpha)][X]E^s_s(\alpha)\exp[-j(\alpha x+k_{0z}z)]d\alpha \tag{9.b}$$

In the substrate ($-d \leqslant z \geqslant 0$) the field is the addition of the plane waves propagating in the positive and negative z direction

$$E^1_s(x,z)=E^+_s(x,z)+E^-_s(x,z) \tag{10.a}$$
$$H^1_s(x,z)=H^+_s(x,z)+H^-_s(x,z) \tag{10.b}$$

where

$$E^+_s(x,z)=1/(2\pi)\int E^+_s(\alpha)\exp[-j(\alpha x+k_{1z}z)]d\alpha \tag{11.a}$$
$$H^+_s(x,z)=1/(2\pi)\int [K_1(\alpha)][X]E^+_s(\alpha)\exp[-j(\alpha x+k_{1z}z)]d\alpha \tag{11.b}$$
$$E^-_s(x,z)=1/(2\pi)\int E^-_s(\alpha)\exp[-j(\alpha x-k_{1z}z)]d\alpha \tag{11.c}$$
$$H^-_s(x,z)=-1/(2\pi)\int [K_1(\alpha)][X]E^-_s(\alpha)\exp[-j(\alpha x-k_{1z}z]d\alpha \tag{11.d}$$

The boundary condition at z=-d (conducting) plane yields

$$E^-_s(\alpha)=-E^+_s(\alpha)e^{j2k_{1z}d} \tag{12}$$

At z=0 plane, E^1_s, H^1_s, E^0_s and H^0_s satisfy the following boundary conditions

$$E^0_s(x,0)=E^1_s(x,0) \tag{13.a}$$
$$H^0_s(x,0)-H^1_s(x,0)=[X]J(x) \tag{13.b}$$
$$E^0_s(x,0)=E^1_s(x,0)=Z_sJ(x) \qquad (x \epsilon D_m) \tag{13.c}$$

where Z_s is the surface impedance of the metal, D_m represents the area where metal exists and

$$J(x)= \begin{vmatrix} J_x(x) \\ J_y(x) \end{vmatrix}.$$

Substituting Eqs. (6-12) into Eq. (13) yields the spectral domain integral equation

$$\int [G_s(\alpha)]J(\alpha)\exp(-j\alpha x)d\alpha-Z_sJ(x)$$
$$=-\int [B_s(\alpha)]E^i_s(\alpha)\exp(-j\alpha x)d\alpha \qquad (x\epsilon D_m) \tag{14}$$

where $J(\alpha)$ is the Fourier trnsform of J(x) and

$$[G_s(\alpha,\beta)]=(1-\exp(-j2k_{1z}d))[M]^{-1}[X]$$
$$[B_s(\alpha,\beta)]=2(1-\exp(-j2k_{1z}d))[M]^{-1}[K_0][X]$$
$$[M]=(1+\exp(-j2k_{1z}d))[K_1][X]+(1-\exp(-j2k_{1z}d))[K_0][X]$$

Once $J(\alpha)$ is found, the transverse scattering field can be obtained through

$$E^s_s(x,z)=1/(2\pi)\int [G_s(\alpha)]J(\alpha)\exp[-j(\alpha x+k_{0z}z)]d\alpha+$$
$$+1/(2\pi)\int [C_s(\alpha)]E^i_s(\alpha)\exp[-j(\alpha x+k_{0z}z)]d\alpha \tag{15}$$

where

$$[C_s(\alpha)]=[B_s(\alpha)]-[I_2]$$

with $[I_2]$ as a two dimensional identity matrix. The z component of the scattering field is related with its transverse component through the divergence theorem $\mathrm{div}.\hat{E}=0$. Let

$$\xi=e^{-j2k_{1z}d}$$

we get the explicit expressions of the matrixes $[G_s(\alpha)]$, $[B_s(\alpha)]$ and $[C_s(\alpha)]$:

$$[G_s(\alpha)]=-\omega\mu(1-\xi)\begin{vmatrix} 1/[(1+\xi)k_1^2/k_{1z}+(1-\xi)k_0^2/k_{0z}] & 0 \\ 0 & 1/[(1+\xi)k_{1z}+(1-\xi)k_{0z}] \end{vmatrix}$$

$$[B_s(\alpha)]=2(1-\xi)\begin{vmatrix} k_{1z}/[(1+\xi)\epsilon_r k_{0z}+(1-\xi)k_{1z}] & 0 \\ 0 & k_{0z}/[(1+\xi)k_{1z}+(1-\xi)k_{0z}] \end{vmatrix}$$

$$[C_s(\alpha)]=2(1-\xi)\begin{vmatrix} k_{1z}/[(1+\xi)\epsilon_r k_{0z}+(1-\xi)k_{1z}]-1 & 0 \\ 0 & k_{0z}/[(1+\xi)k_{1z}+(1-\xi)k_{0z}]-1 \end{vmatrix}$$

TM wave excitation:

For TM-wave excitation, the electric current and electric field have y components only. Let

$$G_e(\alpha)=-\omega\mu(1-\xi)/[(1+\xi)k_{1z}+(1-\xi)k_{0z}]$$
$$B_e(\alpha)=2(1-\xi)k_{0z}/[(1+\xi)k_{1z}+(1-\xi)k_{0z}]$$
$$C_e(\alpha)=B_e(\alpha)-1$$

we get the spectral domain integral equation

$$\int G_e(\alpha)J_y(\alpha)e^{-j\alpha x}d\alpha-Z_sJ_y(x)=-\int B_e(\alpha)E^i{}_y(\alpha)e^{-j\alpha x}d\alpha \qquad (x\varepsilon D_m) \qquad (16)$$

The scattering field is given by

$$E^s{}_y=1/(2\pi)\{\int[G_e(\alpha)J_y(\alpha)+C_e(\alpha)E^i{}_y(\alpha)]e^{-j(\alpha x+k_{0z}z)}d\alpha\} \qquad (17)$$

Applying the steepest decent method to Eq.(17) yields the far field [9]

$$E^r{}_y=-1/\lambda(2\pi/(k\rho))^{1/2}e^{-j(k\rho-\pi/4)}\cos\theta\{J_y(2\pi\sin\theta/\lambda)G_e(2\pi\sin\theta/\lambda)+ +E^i{}_y(2\pi\sin\theta/\lambda)C_e(2\pi\sin\theta/\lambda)\} \qquad (18)$$

where θ is the angle between the observation direction and z axis.

TE wave excitation:

For TE wave excitation, the current has only x component and the magnetic field has only y component. We have

$$G_h(\alpha)=-\omega\mu(1-\xi)k_{1z}k_{0z}/[(1+\xi)k_1^2k_{0z}+(1-\xi)k_0^2k_{1z}]$$
$$B_h(\alpha)=2(1-\xi)k_{1z}/[(1+\xi)\epsilon_r k_{0z}+(1-\xi)k_{1z}]$$
$$C_h(\alpha)=B_h(\alpha)-1$$

The integral equation becomes

$$\int G_h(\alpha)J_x(\alpha)e^{-j\alpha x}d\alpha-Z_sJ_x(x)=-\int B_h(\alpha)E^i{}_x(\alpha)e^{-j\alpha x}d\alpha \quad (x\epsilon D_m) \qquad (19)$$

The scattering electric field has both x and z components

$$E^s{}_x(x,z)=1/(2\pi)\{\int[G_h(\alpha)J_x(\alpha)+C_h(\alpha)E^i{}_x(\alpha)]e^{-j(\alpha x+k_{0z}z)}d\alpha\} \quad (20.a)$$
$$E^s{}_z(x,z)=-1/(2\pi)\{\int\alpha/k_{0z}[G_h(\alpha)J_x(\alpha)+C_h(\alpha)E^i{}_x(\alpha)]e^{-j(\alpha x+k_{0z}z)}d\alpha\} \quad (20.b)$$

Applying the steepest decent method to Eq. (20) yields the far field

$$E_\theta=-/\lambda(2\pi/(k\rho))^{1/2}e^{-j(k\rho-\pi/4)}[G_h(2\pi\sin\theta/\lambda)J_x(2\pi\sin\theta/\lambda)+ +C_h(2\pi\sin\theta/\lambda)E^i{}_x(2\pi\sin\theta/\lambda)] \quad (21)$$

3. CG-FFT Algorithm

As reflector antennas, the Fresnel zone plates are always electrically large, so the integral equations derived above have to be solved by using the CG-FFT algorithm to save storage capacity and CPU time [7]. Following [10], we define a characteristic function X_D as

$$X_D(x)=\begin{cases} 1 & x\epsilon D_m \\ 0 & x\bar{\epsilon} D_m \end{cases} \quad (22)$$

and denote the Fourier transformation and inverse Fourier transformation as F and F^{-1}. Then, Eq. (14) becomes

$$X_DF^{-1}\{G_s(\alpha)F\{X_DJ(x)\}\}-X_DZ_sJ(x)=-X_DF^{-1}\{B_s(\alpha)F\{E^i{}_s(x)\}\} \quad (23)$$

To write Eq. (23) in operator form, we further introduce the operator A acting on a function f as

$$Af=X_DF^{-1}\{G_s(\alpha)F\{X_Df(x)\}\}-X_DZ_sf(x) \quad (24)$$

and let

$$Y=-X_DF^{-1}\{B_s(\alpha)F\{E^i{}_s(x)\}\} \quad (25)$$

Eq. (23) yields

$$AJ=Y \quad (26)$$

It can be easily proved that the adjoint opator of A is given by

$$A^+J=X_DF^{-1}\{G_s{}^*(\alpha)F\{X_DJ\}\}-X_DZ_s{}^*J \quad (27)$$

where '*' denotes the complex conjugate.

Implementing the Fourier transformation and inverse Fourier transformation involved in the operators A and A^+ by using the fast Fourier transformation (FFT), the operator equation (26) can be solved with the conjugate gradient method (CG). Define the error norm as

$$E(R_i)=||R_i||=<R_i,R_i>^{1/2}$$

where < > denotes the inner product and the residual R_i is given by

$$R_i=AJ_i-Y$$

The CG method stars with an initial guess J_0 and lets

$$R_0 = Y - AJ_0$$
$$P_0 = G_0 = A^+ R_0$$

At the ith iteration the CG method develops the following

$$a_i = \|G_i\|^2 / \|AP_i\|^2$$
$$J_{i+1} = J_i + a_i P_i$$
$$R_{i+1} = R_i - a_i AP_i$$
$$G_{i+1} = A^+ R_{i+1}$$
$$P_{i+1} = G_{i+1} + b_i P_i$$
$$b_i = \|G_{i+1}\|^2 / \|G_i\|^2$$

The interative operation yields a sequence of least square solutions to Eq. (26).

4. Numerical Results

Convergence:

Since the Green function $G_h(\alpha)$ has a much worse characteristic than $G_e(\alpha)$, the CG-FFT algorithm for the TM case converges much more rapidly than for the TE case. With the zone plate width D kept at at 30λ (λ=2.5cm) and 8192 samples, it always takes less than 25 iterations to obtain 0.01 relative accuracy for the TM wave excitation, but requires 200 iterations to achieve less than 0.05 relative accuracy for the TE excitation. Increasing the relative dielectric constant ϵ_r makes the converging speed slightly slower.

Influence of edge field taper:

It is well known that for a conventional aperture antenna, the radiation pattern is closely related with the aperture field taper. Decreasing the edge illumination level always lowers the sidelobe level and widens the beamwidth. However, it is found that for the zone plate antenna, only the near axis pattern is influenced by the edge illumination level, while the far-axis sidelobe level is almost fixed. Fig. 2 shows the radiation patterns of a zone plate with D=30λ (λ=2.5cm), the number of full wave zones composing the plate N=8, a conducting strip existing at the central wave zone and excited by a TE wave. It is observed that lowering the edge field taper from -8db to -14db blurs the first sidelobe and yields a wide main beam, but does not change the far-axis pattern much.

Influence of F/D:

It has been found using GO approximation that changing the F/D of a zone plate significantly affects its close-in pattern [4]. The spectral domain method analysis has confirmed this phenomenon. Fig. 3 shows the radiation patterns of a zone plate with the edge field taper fixed at -14db, D=30λ and excited by a TM wave. It is seen that when F/D is reduced from 1.2 to 0.42 (N increased from 3 to 7) the smeared first sidelobe appears with its level decreasing with F/D and the first null gets deeper. Unfortunately, the far-axis sidelobe increases with decreasing F/D, which makes the phenomenon less useful.

Other factors:

Other factors like substrate dielectric constant and edge impedance loading have also been investigated and no significant influence on the antenna pattern has been observed.

5. Conclusions

The CG-FFT algorithm has been applied in the spectral domain method analysis of flat printed two dimensional Fresnel zone plate antennas. The influence of edge

illumination level, F/D ratio, substrate dielectric constant, and edge impedance loading has been investigated. It is found that the antenna pattern is significantly affected by F/D. Decreasing F/D reduces the first sidelobes and yields deeper first nulls, but increases the far-axis sidelobe. Lowering the edge field illumination smears the fist sidelobe and leads to a wide main beam. However, the far-axis sidelobe level does not change much with the aperture field taper.

Acknowledgement: This work was sponsored by the UK Science and Engineering Research Council (SERC) and Mawzones Ltd.

References

[1] J. E. Garret and J. C. Wiltse, 'Fresnel Zone Plate Antennas at Millimeter Wavelength', Int. Journal of Infrared and Millimeter Waves, Vol. 12, No.3, pp.195-216, 1991.
[2] Y. J. Guo, S. K. Barton and T. M. B. Wright, 'Design of High Efficiency Fresnel Zone Plate Antennas', 1991 IEEE AP-S Symp. Digest, pp.182-185.
[3] Y. J. Guo, S. K. Barton and T. M. B. Wright, 'Focal Field Distribution of Fresnel Zone Plate Antennas', Proc. of the 7th Int. Conf. on Antennas and Propagation, York, UK, April 1991.
[4] Y. J. Guo and S. K. Barton, 'On the Sidelobe Performance of Fresnel Zone Plate Antennas', Submitted to 1992 IEEE AP-S Symp.
[5] L. F. Van Buskirk and C. E. Hendrix, 'The Zone Plate as a Radio Frequency Focusing Element', IRE Trans. Vol. AP-9, pp.319-320, 1961.
[6] B. Hunder and W. Menzei, 'Flat Printed Reflector for mm-wave Applications, Electronic Letters, Vol. 24, No. 3, pp.318-319, Mar. 1988.
[7] M. F. Catedra, 'Solution to Some Electromagnetic Problems Using Fast Fourier Transformation with Conjugate Gradient Method', Electronic Letters, Vol. 22, No. 20, pp.1049-1051, Sept. 1986.
[8] G. Scott, The Spectral Domain Method in Electromagnetics, Artech House, Inc., 1989.
[9] R. E. Collin, Antennas and Radiowave Propagation, McGrow-Hill, Inc., 1985.
[10] P. M. Van Den Berg and R. E. Kleinman, 'The Conjugate Gradient Spectral Iterative Technique for Planar Structures', IEEE Trans. Antennas Propagat., Vol. AP-36, No. 10, pp.1418-1424, Oct. 1988.

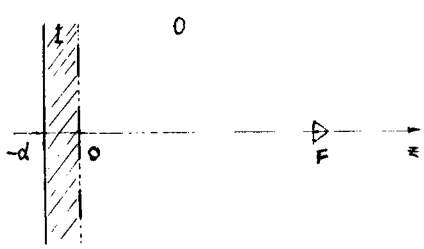

Fig.1 Illustration of the problem

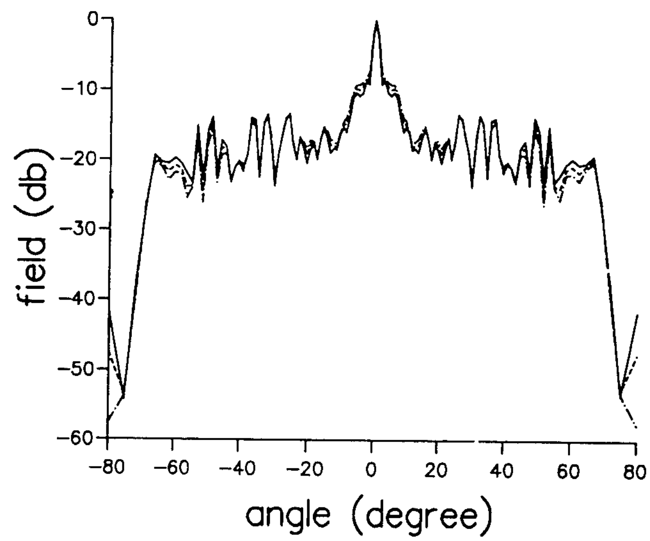

—— et=-8db, ---- et=-11db, -·-·- et=-14db
Fig. 2 Influence of edge field taper (with a conducting strip at central zone)

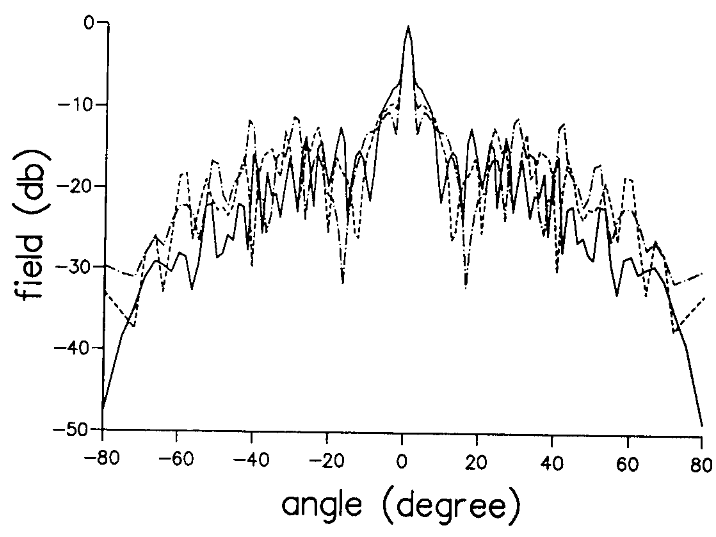

—— F/D=1.2, ---- F/D=0.67, -·-·- F/D=0.42 (N=3,5,7)
Fig. 3 Influence of F/D (with central zone clear)

SECTORED CYLINDRICAL CAVITY RESONATORS

Ross A. Speciale
General Dynamics, Air Defense Systems Division
P.O. Box 50-800, MZ 601-71, Ontario, CA 91761-1885

ABSTRACT

Cylindrical cavity resonators, with either four or six external ports symmetrically located around the cylinder axis, are analyzed as sectored ring-resonators. Circuit models are used, that include either four or six mutually identical cylindrical cavity-sectors, with either 90° or 60° azimuthal angular span, that are sequentially connected around the cylinder axis.

Each of the cylinder sectors is represented as a reciprocal, and symmetric three-port black-box network, and includes one of the resonator external ports on its radial reflection-symmetry plane.

A classical linear multiport network analysis treatment of the problem leads to: a) An independent confirmation of prior results, and b) A very extensive set of new mathematical expressions, that fully describe the propagation of guided electromagnetic waves through electrically-large, two-dimensional clusters of identical, directly-coupled, cylindrical cavity resonators, with either a square or an hexagonal cluster lattice.

1 – THE ANALYSIS METHOD.

Each of the four or six sectors of either a four-port or of a six-port cylindrical cavity resonator, one that exhibits both rotational and reflection-symmetries (Speciale[1,2]), is represented as a reciprocal, and symmetric (but not necessarily lossless) three-port black-box network (Fig. 1). The ports of all sectors are sequentially numbered, in cyclic order around the cylinder axis, with port 2 of each sectors representing one of the resonator external ports. The ports 1 and 3 of each resonator represent the internal, radial reference planes through the cylinder axis, that: a) Define the azimuthal location and angular span of each sector, b) Are azimuthally spaced by either 90° or 60°, halfway between external ports, and c) Are axial reflection-symmetry planes for the whole cylindrical resonator.

The assumed reciprocity and symmetry of the sectors implies a doubly-symmetric structure for the otherwise unknown 3 x 3 impedance matrix Z_S of each sector. This symmetry, with respect to both matrix diagonals, reduces the number of different matrix-entries from nine to only four, so that the structure of the sector impedance matrix is:

$$Z_S = \begin{vmatrix} \zeta_{11} & \zeta_{12} & \zeta_{13} \\ \zeta_{12} & \zeta_{22} & \zeta_{12} \\ \zeta_{13} & \zeta_{12} & \zeta_{11} \end{vmatrix} = \zeta_{22} \cdot \begin{vmatrix} u & v & w \\ v & 1 & v \\ w & v & u \end{vmatrix} = M_3 \cdot \Lambda_{ZS} \cdot M_3^* = M_3 \cdot DIAG(\lambda_{i\,ZS}) \cdot M_3^* \tag{1}$$

Similarly, the structure of the admittance matrix of a sector is:

$$Y_S = \begin{vmatrix} y_{11} & y_{12} & y_{13} \\ y_{12} & y_{22} & y_{12} \\ y_{13} & y_{12} & y_{11} \end{vmatrix} = y_{22} \cdot \begin{vmatrix} \varrho & \sigma & \tau \\ \sigma & 1 & \sigma \\ \tau & \sigma & \varrho \end{vmatrix} = M_3 \cdot \Lambda_{ZS}^{-1} \cdot M_3^* = M_3 \cdot DIAG(1/\lambda_{i\,ZS}) \cdot M_3^* \tag{2}$$

The three-port cylinder sectors are sequentially cascaded, around the cylinder axis, in a sectored ring-resonator configuration (Fig. 2 and 3), with port 3 of each sector connected to port 1 of the next, in a clockwise cyclic sequence. The resulting four-port or six-port cavity resonators exhibit rotational symmetry around the cylinder axis, reflection symmetry with respect to the axial planes that delimit the sectors, and constitute the 'unit-cells' of a new class of doubly-periodic, two-dimensional traveling-wave structures. These 'artificial delay surfaces' consist of clusters of mutually identical, directly-coupled, cylindrical cavity resonators, geometrically ordered in either a square of in an hexagonal cluster lattice (Fig. 4 and 5; Speciale[3,4]). Electrically-large, two-dimensional clusters of directly-coupled, cylindrical cavity resonators, spanning hundreds of wavelengths in physical length and width, propagate guided electromagnetic waves in any of the infinite azimuthal directions, parallel to the cluster surface, and have, therefore, many practical applications, either in the form of passive wave-guiding structures or, in combination with distributed electron devices, in the form of many different types of active and/or adaptive microwave and millimeter-wave system components (Andreasen[5]).

The guided-wave propagation process, on such cavity resonator clusters, is in general dispersive, azimuthally anisotropic, and characterized by multiple bandpass frequency responses, similar to those of coupled-cavity microwave filters and of the cold, slow-wave structures of coupled-cavity traveling-wave tubes. Very complex two-dimensional traveling-wave patterns may be, however, synthesized by propagating a large number of simultaneous wave-components (a 'complex wave-spectrum'), in many different azimuthal directions with different relative amplitudes and relative phases.

Each of the resonator axial reflection-symmetry planes cuts the ring- resonator into two anti-symmetric halves, including either two 90° or three 60° sectors, with a total azimuthal angular span of 180° for each half. The electrical interface between the two halves of the ring-resonator always includes two pairs of mutually connected No. 1 and No. 3 sector-ports. But, while the two halves of a four-port resonator also have four ports, those of a six-port resonator have five, three of the five being external ports. Formal expressions of the 4 x 4 and 6 x 6 impedance matrices Z_4 and Z_6 of the two circuit models are obtained, as functions of the Z-parameters ζ_{ij} of a single sector, by first interconnecting the two or three sectors of one-half resonator, and then interconnecting the two halves together. The formal network-analysis math is basically straightforward, and is greatly simplified by the reflection-symmetry of each half-resonator, with respect to its median radial plane, and by the mutual anti-symmetry of the two halves. The necessary analytical work is, nevertheless, substantially laborious.

Formal expressions of the 4 x 4 and 6 x 6 ABCD-matrices K_4 and K_6 of the four-port and the six-port resonators, respectively, have also been obtained, by using Z-to-ABCD matrix-conversion transforms. Further, formal expressions of the 2 x 2 and 3 x 3 image-impedance matrices Z_I, and of the 2 x 2 and 3 x 3 image-transfer-function matrices T_{IV} have been obtained and formally diagonalized, thus identifying the mutually-orthogonal, external-port modes of the four-, and six-port resonators, as functions of the Z-parameters ζ_{ij} of a single sector. The image-impedance matrix Z_I is here defined as the 2 x 2 or 3 x 3 impedance matrix of either a two- or three-port load-network that is transformed into itself through the resonator, from the output interface to the input interface (Fig. 2 and 3) and back. Further, the image-transfer-function matrix T_{IV} is here defined as the 2 x 2 or 3 x 3 matrix that maps any arbitrary input voltage-wave vector, to the corresponding output voltage-wave vector, while the cavity resonator is connected between a multi-phase (and multi-amplitude) generator and a multiport load-network with (internal) impedance matrices equal to the matrix Z_I.

2 – ANALYTICAL RESULTS.

The 4 x 4 and 6 x 6 impedance matrices Z_4 and Z_6 of the four-port and six-port, reciprocal, rotationally and reflection-symmetric, cylindrical cavity-resonators are doubly-symmetric and **'circulant'** (Davis[6]), as shown by the two matrix structures:

$$Z_4 = \begin{vmatrix} Z_{11} & Z_{12} & Z_{13} & Z_{12} \\ Z_{12} & Z_{11} & Z_{12} & Z_{13} \\ Z_{13} & Z_{12} & Z_{11} & Z_{12} \\ Z_{12} & Z_{13} & Z_{12} & Z_{11} \end{vmatrix} = \begin{vmatrix} a & b & c & b \\ b & a & b & c \\ c & b & a & b \\ b & c & b & a \end{vmatrix} \tag{3}$$

$$Z_6 = \begin{vmatrix} Z_{11} & Z_{12} & Z_{13} & Z_{14} & Z_{13} & Z_{12} \\ Z_{12} & Z_{11} & Z_{12} & Z_{13} & Z_{14} & Z_{13} \\ Z_{13} & Z_{12} & Z_{11} & Z_{12} & Z_{13} & Z_{14} \\ Z_{14} & Z_{13} & Z_{12} & Z_{11} & Z_{12} & Z_{13} \\ Z_{13} & Z_{14} & Z_{13} & Z_{12} & Z_{11} & Z_{12} \\ Z_{12} & Z_{13} & Z_{14} & Z_{13} & Z_{12} & Z_{11} \end{vmatrix} = \begin{vmatrix} a & b & c & d & c & b \\ b & a & b & c & d & c \\ c & b & a & b & c & d \\ d & c & b & a & b & c \\ c & d & c & b & a & b \\ b & c & d & c & b & a \end{vmatrix} \tag{4}$$

Further, the matrix Z_4 only has three different entries (out of 16):

$$Z_{11} = \zeta_{22} - \frac{\zeta_{12}^2 \left(2\, \zeta_{11} + \zeta_{13}\right)}{2\, \zeta_{11} \left(\zeta_{11} + \zeta_{13}\right)} = \zeta_{22} \cdot \left(1 - \frac{v^2}{2\, u}\, \frac{2 - w/u}{1 + w/u} \right) \tag{5}$$

$$Z_{12} = \frac{\zeta_{12}^2}{2 \left(\zeta_{11} + \zeta_{13}\right)} = \zeta_{22}\, \frac{v^2/u}{1 + w/u} \tag{6}$$

$$Z_{13} = \frac{\zeta_{12}^2\, \zeta_{13}}{2\, \zeta_{11} \left(\zeta_{11} + \zeta_{13}\right)} = \zeta_{22}\, \frac{v^2}{u}\, \frac{w/u}{1 + w/u} \tag{7}$$

and only three different eigenvalues (because of a single degeneracy):

$$\lambda_{1Z} = \lambda_{2Z} = \lambda_{12Z} = Z_{11} - Z_{13} = \zeta_{22} - \frac{\zeta_{12}^2}{\zeta_{11}} = \zeta_{22} \cdot \left(1 - \frac{v^2}{u} \right) \tag{8}$$

$$\lambda_{3Z} = Z_{11} + Z_{13} - 2 \cdot Z_{12} = \zeta_{22} - \frac{2\, \zeta_{12}^2}{\zeta_{11} + \zeta_{13}} = \zeta_{22} \cdot \left(1 - \frac{v^2}{u}\, \frac{1}{1 + w/u} \right) \tag{9}$$

$$\lambda_{4Z} = Z_{11} + Z_{13} + 2 \cdot Z_{12} = \zeta_{22} \tag{10}$$

The λ_{iZ} eigenvalues are associated to the orthogonal modal matrix M_4 of Z_4, which is the same modal matrix previously determined for the corresponding scattering matrix S_4 of the four-port resonator:

$$M_4 = \frac{1}{2} \begin{vmatrix} 1 & 1 & -1 & 1 \\ 1 & -1 & 1 & 1 \\ -1 & -1 & -1 & 1 \\ -1 & 1 & 1 & 1 \end{vmatrix} \tag{11}$$

Similarly, the matrix Z_6 only has four different entries (out of 36: Z_{11} through Z_{14}), and only four different eigenvalues (because of two degeneracies), associated to a 6 x 6 unitary **'Discrete Fourier Transform'** modal matrix M_6, also shared by the corresponding scattering matrix S_6 of the six-port resonator. The expressions of these quantities are similar to (5)-(10) above but their size exceeds the format constraints of this paper. As exemplified by the expressions (8)-(10), the different eigenvalues of all these matrices are linearly related to the different entries of the corresponding matrix.

The mutually-orthogonal external-port modes of the rotationally and reflection-symmetric cylindrical four-port resonator are identified by the eigenvectors of the 2 x 2 orthogonal modal matrix M_2 of the image-transfer-function matrix T_{IV}, and are an even and an odd mode:

$$M_2 = \frac{1}{\sqrt{2}} \begin{vmatrix} 1 & 1 \\ 1 & -1 \end{vmatrix} \tag{12}$$

The matrix M_2 is the modal matrix of both the image-impedance matrix Z_I and the image-transfer-function matrix T_{IV}. The matrices Z_I and T_{IV} are then fully defined by their eigenvalues, which represent the scalar even-, and odd-mode image-impedances:

$$Z_{IE} = \sqrt{\lambda_{12Z}\, \lambda_{4Z}} = \sqrt{\zeta_{22} \cdot \left(\zeta_{22} - \frac{\zeta_{12}^2}{\zeta_{11}} \right)} = \zeta_{22} \cdot \sqrt{1 - \frac{v^2}{u}} \tag{13}$$

$$Z_{IO} = \sqrt{\lambda_{12Z}\, \lambda_{3Z}} = \sqrt{\left(\zeta_{22} - \frac{\zeta_{12}^2}{\zeta_{11}} \right) \cdot \left(\zeta_{22} - \frac{2\, \zeta_{12}^2}{\zeta_{11} + \zeta_{13}} \right)} = \zeta_{22} \cdot \sqrt{\left(1 - \frac{v^2}{u} \right) \left(1 - \frac{v^2}{u}\, \frac{1}{1 + w/u} \right)} \tag{14}$$

and the corresponding scalar even-, and odd-mode image-transfer functions:

$$T_{IVE} = \frac{\lambda_{12Z} + \lambda_{4Z} - 2\sqrt{\lambda_{12Z} \cdot \lambda_{4Z}}}{\lambda_{4Z} - \lambda_{12Z}} = \tag{15}$$

$$= \frac{1}{\zeta_{12}^2} \left[\left(2\ \zeta_{11}\ \zeta_{22} - \zeta_{12}^2\right) - 2\ \sqrt{\zeta_{11}\ \zeta_{22} \cdot \left(\zeta_{11}\ \zeta_{22} - \zeta_{12}^2\right)}\ \right] = e^{\gamma_{IE}}$$

$$T_{IVO} = \frac{\lambda_{12Z} + \lambda_{3Z} - 2\sqrt{\lambda_{12Z} \cdot \lambda_{3Z}}}{\lambda_{3Z} - \lambda_{12Z}} = \tag{16}$$

$$= \frac{1}{DEN} \left[\left(NUM\ TERM\ 1\right) - 2 \cdot \sqrt{RADICAND}\ \right] = e^{\gamma_{IO}}$$

where:

$$NUM\ TERM\ 1 = 2\ \zeta_{11}\ \zeta_{22} \cdot \left(\zeta_{11} + \zeta_{13}\right) - \zeta_{12}^2 \cdot \left(3\ \zeta_{11} + \zeta_{13}\right) \tag{17}$$

$$RADICAND = \zeta_{11} \cdot \left(\zeta_{11} + \zeta_{13}\right) \left(\zeta_{11}\ \zeta_{22} - \zeta_{12}^2\right) \left[\zeta_{22} \left(\zeta_{11} + \zeta_{13}\right) - 2\ \zeta_{12}^2\right] \tag{18}$$

$$DEN = -\ \zeta_{12}^2 \cdot \left(\zeta_{11} - \zeta_{13}\right) \tag{19}$$

The exponential arguments γ_{IE} and γ_{IO} are the even-, and odd-mode propagation constants, that measure both the attenuation and the image-phase rotation of the two modes through a single resonator in a two-dimensional cluster. These quantities are, in general, complex unless: a) The resonators in the cluster are assumed to be lossless (with S_4 **unitary** and Z_4 **imaginary**), **and** b) The excitation frequency is within a mode-passband of the cluster, where Z_{IE} and/or Z_{IO} are **real** and T_{IE} and/or T_{IO} are **unimodular**.

The eigenvalues λ_{iZ} of the Z-matrices Z_4 and Z_6 are related to the eigenvalues λ_{iS} of the corresponding scattering matrices S_4 and S_6 by the relation:

$$\lambda_{iZ} = -\frac{Z_0}{\tanh\left(\frac{\gamma_{iS}}{2}\right)} \tag{20}$$

where Z_0 is the normalization impedance of the scattering matrix, and γ_{iS} is the exponential argument of the corresponding scattering-matrix eigenvalue: .

$$\lambda_{iS} = e^{\gamma_{iS}} \tag{21}$$

The internal resonances of the two sectored ring-resonators in Figure 1, with all the external ports either open or shorted, appear to correspond to cut-off frequencies that define the boundaries between passbands and stopbands of the image-transfer response, through a single resonator in a cluster, from input- to output-interface (Figures 2 and 3).

It appears from the expressions (5)-(7) that it is possible to extract the values of the port 2 sector-impedance ζ_{22} and of the ratios v^2/u and w/u from calibrated scattering parameter measurements, performed on physical models of rotationally and reflection-symmetric, cylindrical cavity resonators. Indeed, the values of Z_{11}, Z_{12}, and Z_{13} can be easily expressed as functions of S_{11}, S_{12}, and S_{13}, and the expressions (5)-(7) can be easily solved for ζ_{22}, v^2/u, and w/u.

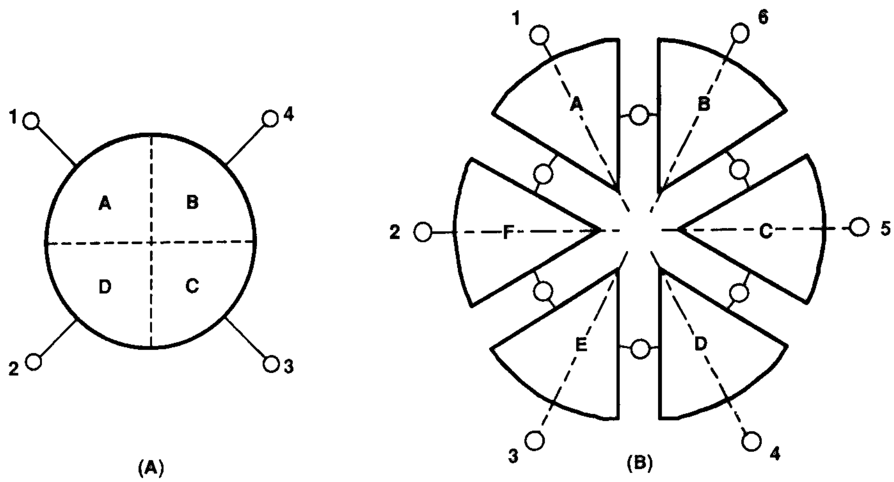

Figure 1 – Sectored, Reciprocal, Four-Port, C_{4V}-Symmetric, and Six-Port, C_{6V}-Symmetric Cavity Resonators.

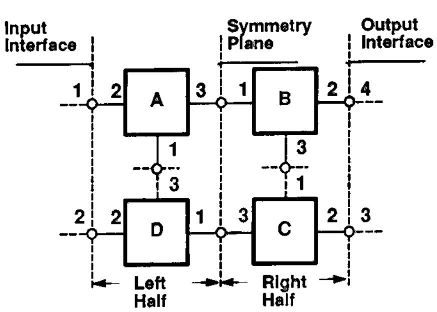

Figure 2 – Network Interconnection of the Four Sectors of a C_{4V}- Symmetric Cavity Resonator.

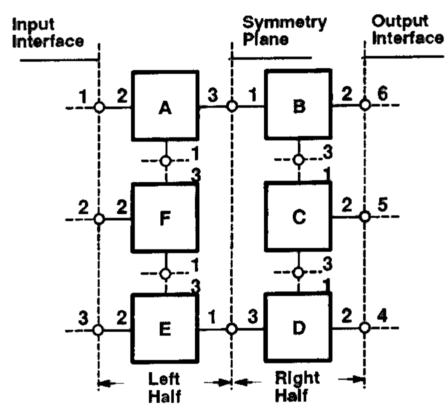

Figure 3 – Network Interconnection of the Six Sectors of a C_{6V}- Symmetric Cavity Resonator.

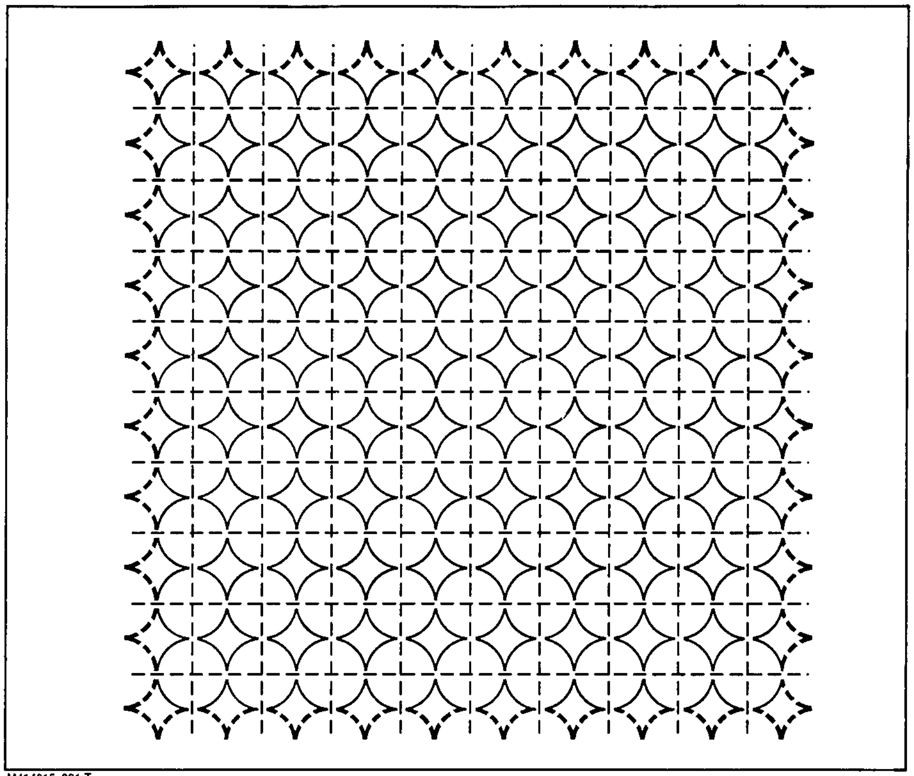

M414015 931 T

Figure 4 – A Two-Dimensional Cluster of Directly Coupled, Circular-Cylindrical Cavity Resonators, Ordered in a Square Lattice.

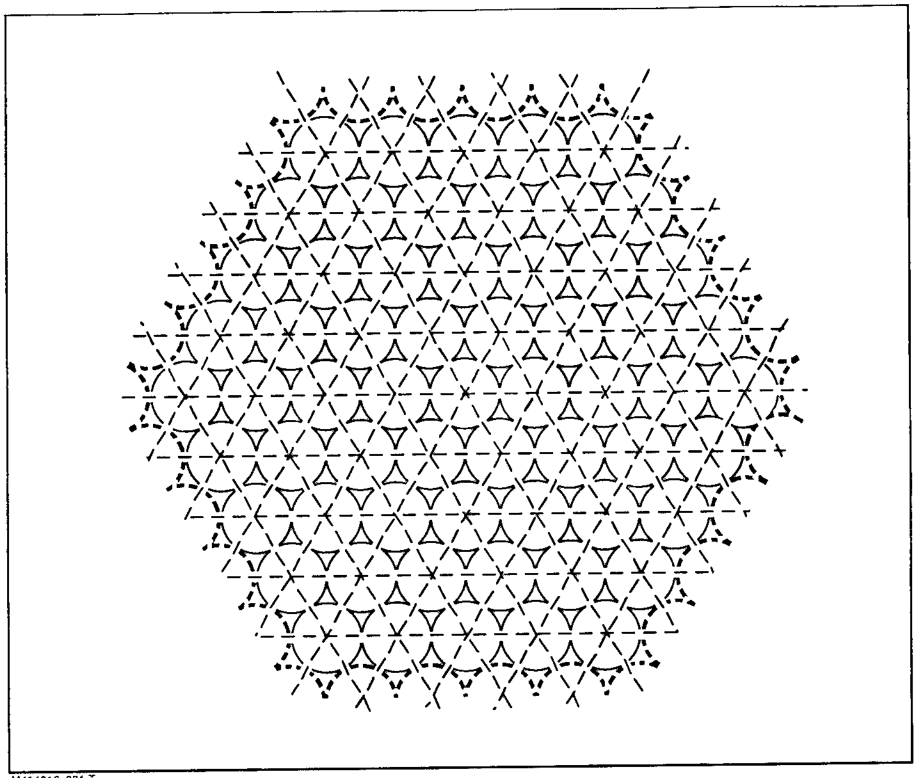

M414016 931 T

Figure 5 – A Two-Dimensional Cluster of Directly Coupled, Circular-Cylindrical Cavity Resonators, Ordered in a Hexagonal Lattice.

3 – REFERENCES.

[1] R. A. Speciale, "Wave Propagation on Infinite, Two-Dimensional Structures," 5th Annual Review of Progress in Applied Computational Electromagnetics, Naval Postgraduate School, Monterey, California, March 21-23, 1989, pp. 200-244.

[2] R. A. Speciale, "Guided Wave Propagation on Two-Dimensional Clusters of Directly-Coupled Cavity Resonators," 7th Annual Review of Progress in Applied Computational Electromagnetics, Naval Postgraduate School, Monterey, California, March 18-22, 1991, pp. 428-431.

[3] R. A. Speciale, "Projective Matrix Transformations in Microwave Network Theory," IEEE 1981 International Microwave Symposium Digest of Technical Papers (Los Angeles, CA), pp. 510-512.

[4] R. A. Speciale, "Projective Matrix Transformations in Microwave Network Theory," pp. 1-59, in the class notes of the short course "Unified Scattering Theory of Guided and Unguided Waves", Los Angeles, California, 1983.

[5] M. G. Andreasen and R. L. Tanner, "A Wire-Grid Lens Antenna of Wide Application – Part II: Wave-Propagation Properties of a Pair of Wire Grids with Square, Hexagonal or Triangular Mesh," IRE Trans. on Antennas and Propagation, July 1962, pp. 416-429.

[6] P. J. Davis, "Circulant Matrices," John Wiley & Sons, Inc., Pure and Applied Mathematics Series, New York, 1979.

A STUDY OF EDGE DIFFRACTION ON A GROUNDED DIELECTRIC SHEET BY A COMPUTATIONAL METHOD.

J.Watkins, Department of Electronic and Electrical Engineering King's College London.

Abstract.

A proprietary package called MAGIC, employing a finite difference time domain code has been used to study diffraction at a conducting edge situated on a grounded dielectric for different values of the relative permittivity and dielectric thickness. Three types of behaviour have been studied.

i) how energy radiates into free space and into the dielectric as surface waves, shown by the spatial variation of the electric fields.

ii) the division of energy radiated into free space and into surface waves, the results showing a favourable comparison with those obtained from a WIENER-HOPF analysis.

iii) the patterns of the surface wave shown by the electric fields, the results showing a favourable comparison with established analysis.

The experience gained in using this package shows it to be a valuable tool which is capable of providing solutions to a number of electromagnetic problems. The applications under the present study are of direct relevance to designers of patch antennas. A detailed study of surface wave effects is essential since their presence in array systems of patches can seriously degrade the performance by the production of 'blind' angles of transmission/reception. Using MAGIC it is possible that the designer can investigate particular geometries in order to suppress the surface waves.

Introduction.

The patch antenna with its attractive characteristic of a low profile is a radiating element which has found popular use. The patch is a shaped conducting sheet with a thickness much greater than a skin depth and is designed to resonate in such a manner that currents flowing in the conductor at the conductor-dielectric interface define the electromagnetic modes of an eigenvector-eigenvalue system. Although the nature of these currents is well understood for a variety of geometries their relation to the currents flowing on the upper surface is more complicated and has been described by CHANG and KUESTER [1]. The process of radiation into free space based on the upper surface currents is in turn more difficult to formulate and a more successful description can be obtained using aperture models such as that proposed by DERNERYD [2]. In these models the fringe fields at the edges of the conductors set up displacement currents in the dielectric which in turn can account for the observed nature of the far-field electric field.The action of the fringe fields at the 'aperture' may be more succinctly described as edge diffraction and mathematical descriptions of such processes exist in the literature. One example is the treatment of BATES and MITTRA [3] which in addition to describing radiation into free space also describes how energy is transferred into the dielectric in the form of surface waves.

It is the objective of this present work to demonstrate through computation and graphic display the following aspects of edge diffraction:-

i) how a wave is generated at the edge
ii) the balance between energy radiated into free space
and that appearing in the dielectric as surface waves
iii) the pattern of the surface waves

The computational model.

Fig 1 which is taken from the paper of DERNERYD [loc.cit] shows a practical example of a rectangular resonator from which radiation emanates from the edges ab and cd. In comparing it with the geometry used by BATES and MITTRA for their analysis in which current flowing in a conductor on a grounded dielectric substrate and at right angles to an infinite edge and is there diffracted, the analysis and conclusions provide considerable insight to the behaviour of the finite patch resonator. The results of the analysis given in Fig 2 show that although an increase in the substrate thickness and consequently an increase in the radiation aperture leads to an increase in the energy radiated into free space so also can increased energy be launched into the dielectric in the form of a surface wave. The BATES and MITTRA analysis is for the TM mode shown in Fig 3 which shows that the pattern in the xy-plane extends without variation in the z-direction. (Here k_0 in the independent variable $k_0 b$ is given by the relation

$$k_0 = \frac{2\pi}{\lambda_0}$$

where λ_0 is the free space wavelength.)

This type of variation can be conveniently investigated by a proprietary computer package called MAGIC [4]. MAGIC is a finite difference time domain code which although principally developed for the understanding and design of microwave vacuum tubes enables many electromagnetic problems to be studied through the use of its extensive range of options.

Wave generation.

MAGIC uses the convention that field components -x and -y are represented by 1 and 2 respectively. Thus E1 and E2 are the electric field time varying components E_x and E_y respectively and E1ST and E2ST are the static components. In the model proposed by DERNERYD and referring to the geometry of Fig 1 the E_x field component is the major contributor to the radiation process. We can gain insight into its variation with distance away from the edge of the conductor, by examining the variation of the static field component E_x and Fig 4 shows the variation of E1ST obtained in the MAGIC code by using the POISSON command. It can be seen that there is a region along the x-axis in which E1ST retains values comparable to that at the edge of the conductor. Using other features of MAGIC it is possible to create a generator of TM waves and Fig 5 shows results of E1 for a wave with frequency 10GHz at various time intervals up to $1.2x10^{-10}$sec. These show the diffraction process at the edge of the conductor and the growth of the E1 field both in the free space and the dielectric where the emergence of a structured pattern can be seen. (In MAGIC complete lines denote positive values and dashed lines negative ones.) Fig 6 shows the time variation of the other component E2 and again the formation of a pattern which can be interpreted as the presence of a surface wave. This wave is discussed in more detail below.

Energy balances.

Using another MAGIC option it is possible to compute , over a period of time, the energies delivered into free space and into the dielectric. Fig 7 shows results obtained for a permittivity of $\epsilon_r = 2.1$ and a number of substrate thicknesses to produce the variable k_0b. These results compare favourably with those of Fig 2, and the MAGIC variation of the free space electric energy shows a peak value which occurs at a value of k_0b similar to that of the BATES and MITTRA analysis. The variation of the surface wave energy at low values of k_0b is unexpected but better agreement might result if the distance increment used in the MAGIC simulation was made smaller. (An increase in computation time would result however.)

Similar results were obtained with a permittivity value of $\epsilon_r = 9.8$ representing alumina, a material commonly used for substrates in microstrip technology.

Surface wave patterns.

The generation of the wave described reveals the formation of distinct patterns of field variation within the dielectric. By defining regions of interest more closely, the exact nature of these patterns can be seen more clearly and Fig 8 shows the E1 variation and Fig 9 that of E2. The theoretical analysis of the electric field variation has been given by COLLIN [5] and the relevant equations are:-

$$E_x = \frac{-jh}{\epsilon_0\epsilon_r\omega}.A\sin(hy)e^{-j\beta x} \tag{1}$$

$$E_y = \frac{-\beta}{\epsilon_0\epsilon_r\omega}.A\cos(hy)e^{-j\beta x} \tag{2}$$

within the dielectric, and

$$E_x = \frac{-jh}{\epsilon_0\epsilon_r\omega}.Asin(hb)e^{-p(y-b)}e^{-j\beta x} \tag{3}$$

$$E_y = \frac{-\beta}{\epsilon_0\omega}A.\cos(hb)e^{-p(y-b)}e^{-j\beta x} \tag{4}$$

above the dielectric.

Here

$$\epsilon_r pb = hb\tan(hb) \tag{5}$$

$$(\epsilon_r - 1)(k_0b)^2 = (pb)^2 + (hb)^2 \tag{6}$$

$$\beta^2 = \epsilon_r k_0^2 - h^2 \tag{7}$$

so allowing h,p and β to be found by computational methods.
The graphical results of Figs 8 and 9 using a permittivity of $\epsilon_r = 9.8$, are in agreement with the above analysis. It is particularly interesting to note that whereas the field component E1 is continuous across the dielectric-free space interface, the E2 component is not and discontinuously increases by a factor of ϵ_r on going from the dielectric to the free space. This discontinuity is clearly demonstrated by MAGIC in Fig 10 although the indicated magnitude of the change, 7.3, is less than the expected value of 9.8. Again the influence of the coarseness of the grid used in the simulation is a subject for further study. The variation of the surface wave pattern along the x-axis was found to agree closely with that associated with the value of β computed from the given values of ϵ_r and b.

Conclusions.

The MAGIC code has successfully been used to study the behaviour of surface waves in a model of a dielectric patch resonator by producing graphical details of generation, energy balance and electric field patterns. As a powerful tool it offers help in the investigation of other geometries which are of interest to the antenna designer.

Acknowledgements.

This work is supported by the Ministry of Defence (UK) and the author would like to thank the M.O.D for permission to publish this paper. The author is also grateful for many helpful discussions with Dr Bruce Goplen of Mission Research Corporation.

References.

1. Chang,D.C. and Kuester,E.F.
   'Geometrical theory of one dimensional resonators:
   The effects of topside charges and currents.'
   Radio Science vol 20(4) pp819-826 July-August 1985.

2. Derneryd,A.G.
   'Linearly polarised microstrip antennas.'
   IEEE Trans AP-24,1976,pp 846-851.

3. Bates,C.P. and Mittra,R.
   'Waveguide excitation of dielectric and plasma slabs.'
   Radio Science vol 3 1968 pp 251-256.

4. The MAGIC code is a product of the
   MISSION RESEARCH CORPORATION
   8560 Cinderbed Road, Suite 700
   Newington, VA 22122.

5. Collin,R.E.
   'Field theory of guided waves.'
   2nd. Edition 1991 IEEE Press pp 712:716.

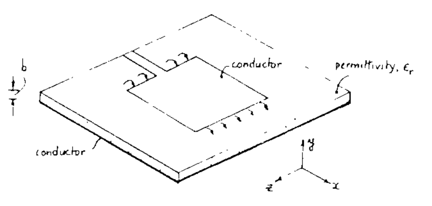

Fig 1

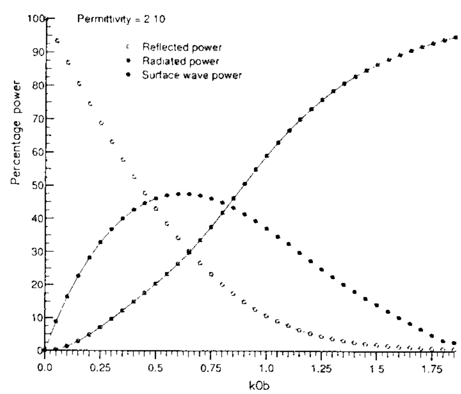

Fig 2

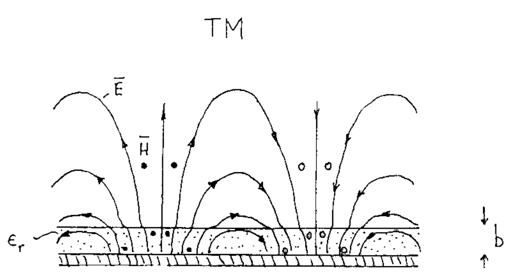

Fig 3

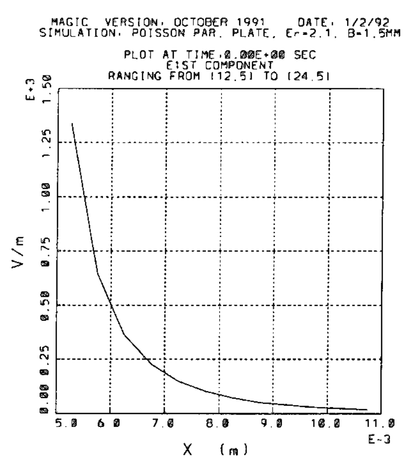

Fig 4

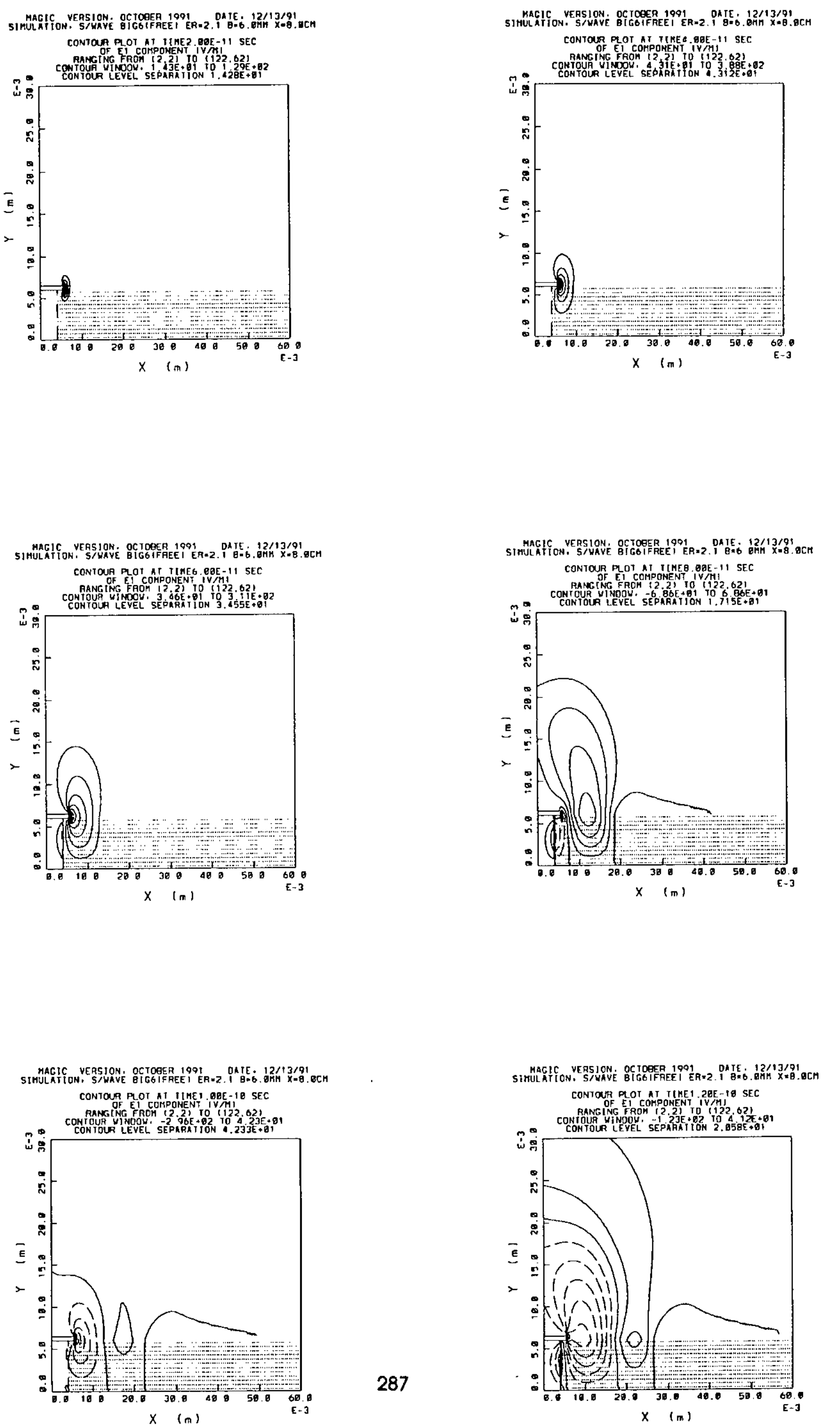
MAGIC VERSION: OCTOBER 1991 DATE: 12/13/91
SIMULATION: S/WAVE BIG6(FREE) ER=2.1 B=6.0MM X=8.0CM
CONTOUR PLOT AT TIME2.00E-11 SEC
OF E1 COMPONENT (V/M)
RANGING FROM (2,2) TO (122,62)
CONTOUR WINDOW: 1.43E+01 TO 1.29E+02
CONTOUR LEVEL SEPARATION 1.428E+01
MAGIC VERSION: OCTOBER 1991 DATE: 12/13/91
SIMULATION: S/WAVE BIG6(FREE) ER=2.1 B=6.0MM X=8.0CM
CONTOUR PLOT AT TIME4.00E-11 SEC
OF E1 COMPONENT (V/M)
RANGING FROM (2,2) TO (122,62)
CONTOUR WINDOW: 4.31E+01 TO 3.88E+02
CONTOUR LEVEL SEPARATION 4.312E+01
MAGIC VERSION: OCTOBER 1991 DATE: 12/13/91
SIMULATION: S/WAVE BIG6(FREE) ER=2.1 B=6.0MM X=8.0CM
CONTOUR PLOT AT TIME6.00E-11 SEC
OF E1 COMPONENT (V/M)
RANGING FROM (2,2) TO (122,62)
CONTOUR WINDOW: 3.46E+01 TO 3.11E+02
CONTOUR LEVEL SEPARATION 3.455E+01
MAGIC VERSION: OCTOBER 1991 DATE: 12/13/91
SIMULATION: S/WAVE BIG6(FREE) ER=2.1 B=6.0MM X=8.0CM
CONTOUR PLOT AT TIME8.00E-11 SEC
OF E1 COMPONENT (V/M)
RANGING FROM (2,2) TO (122,62)
CONTOUR WINDOW: -6.86E+01 TO 6.86E+01
CONTOUR LEVEL SEPARATION 1.715E+01
MAGIC VERSION: OCTOBER 1991 DATE: 12/13/91
SIMULATION: S/WAVE BIG6(FREE) ER=2.1 B=6.0MM X=8.0CM
CONTOUR PLOT AT TIME1.00E-10 SEC
OF E1 COMPONENT (V/M)
RANGING FROM (2,2) TO (122,62)
CONTOUR WINDOW: -2.96E+02 TO 4.23E+01
CONTOUR LEVEL SEPARATION 4.233E+01
MAGIC VERSION: OCTOBER 1991 DATE: 12/13/91
SIMULATION: S/WAVE BIG6(FREE) ER=2.1 B=6.0MM X=8.0CM
CONTOUR PLOT AT TIME1.20E-10 SEC
OF E1 COMPONENT (V/M)
RANGING FROM (2,2) TO (122,62)
CONTOUR WINDOW: -1.23E+02 TO 4.12E+01
CONTOUR LEVEL SEPARATION 2.058E+01
X (m)
Y (m)
E-3

Fiq 5

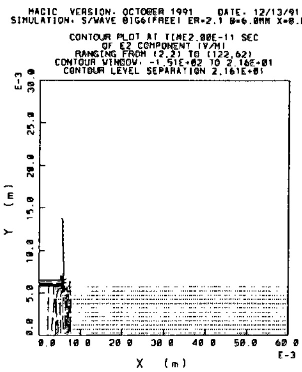
MAGIC VERSION, OCTOBER 1991 DATE, 12/13/91
SIMULATION, S/WAVE BIG6(FREE) ER=2.1 B=6.0MM X=8.0CM
CONTOUR PLOT AT TIME2.00E-11 SEC
OF E2 COMPONENT (V/M)
RANGING FROM (2,2) TO (122,62)
CONTOUR WINDOW, -1.51E+02 TO 2.16E+01
CONTOUR LEVEL SEPARATION 2.161E+01
E-3
Y (m)
X (m)
E-3

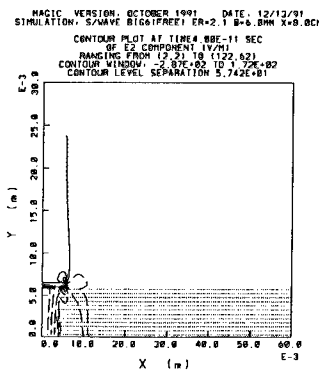
MAGIC VERSION, OCTOBER 1991 DATE, 12/13/91
SIMULATION, S/WAVE BIG6(FREE) ER=2.1 B=6.0MM X=8.0CM
CONTOUR PLOT AT TIME4.00E-11 SEC
OF E2 COMPONENT (V/M)
RANGING FROM (2,2) TO (122,62)
CONTOUR WINDOW, -2.87E+02 TO 1.72E+02
CONTOUR LEVEL SEPARATION 5.742E+01
E-3
Y (m)
X (m)
E-3

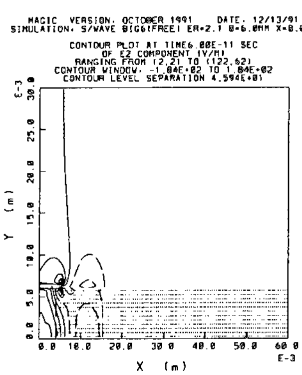
MAGIC VERSION, OCTOBER 1991 DATE, 12/13/91
SIMULATION, S/WAVE BIG6(FREE) ER=2.1 B=6.0MM X=8.0CM
CONTOUR PLOT AT TIME6.00E-11 SEC
OF E2 COMPONENT (V/M)
RANGING FROM (2,2) TO (122,62)
CONTOUR WINDOW, -1.84E+02 TO 1.84E+02
CONTOUR LEVEL SEPARATION 4.594E+01
E-3
Y (m)
X (m)
E-3

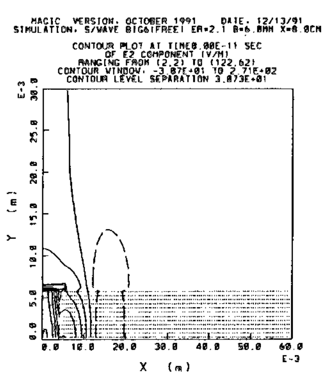
MAGIC VERSION, OCTOBER 1991 DATE, 12/13/91
SIMULATION, S/WAVE BIG6(FREE) ER=2.1 B=6.0MM X=8.0CM
CONTOUR PLOT AT TIME8.00E-11 SEC
OF E2 COMPONENT (V/M)
RANGING FROM (2,2) TO (122,62)
CONTOUR WINDOW, -3.07E+01 TO 2.71E+02
CONTOUR LEVEL SEPARATION 3.073E+01
E-3
Y (m)
X (m)
E-3

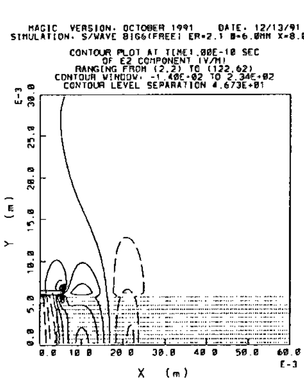
MAGIC VERSION, OCTOBER 1991 DATE, 12/13/91
SIMULATION, S/WAVE BIG6(FREE) ER=2.1 B=6.0MM X=8.0CM
CONTOUR PLOT AT TIME1.00E-10 SEC
OF E2 COMPONENT (V/M)
RANGING FROM (2,2) TO (122,62)
CONTOUR WINDOW, -1.40E+02 TO 2.34E+02
CONTOUR LEVEL SEPARATION 4.673E+01
E-3
Y (m)
X (m)
E-3

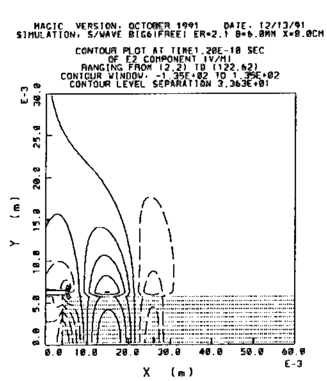
MAGIC VERSION, OCTOBER 1991 DATE, 12/13/91
SIMULATION, S/WAVE BIG6(FREE) ER=2.1 B=6.0MM X=8.0CM
CONTOUR PLOT AT TIME1.20E-10 SEC
OF E2 COMPONENT (V/M)
RANGING FROM (2,2) TO (122,62)
CONTOUR WINDOW, -1.35E+02 TO 1.35E+02
CONTOUR LEVEL SEPARATION 3.363E+01
E-3
Y (m)
X (m)
E-3

G-L

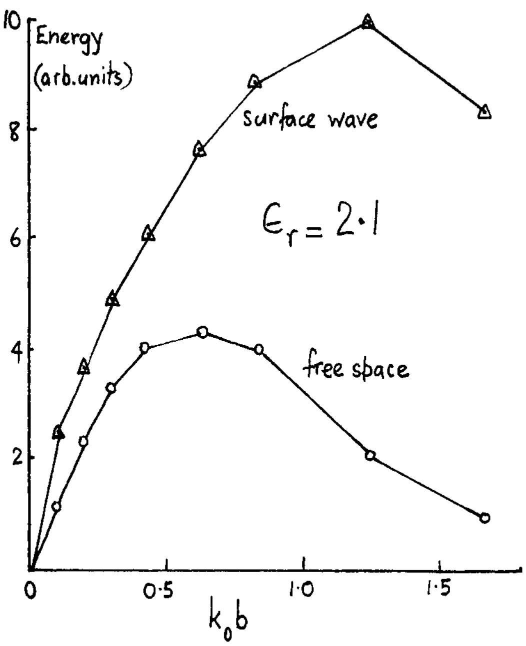

Fig 7

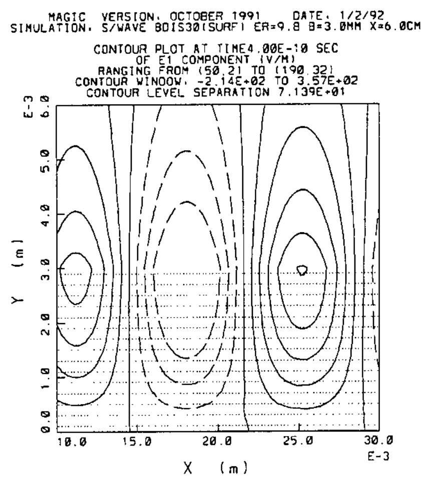

Fig 8

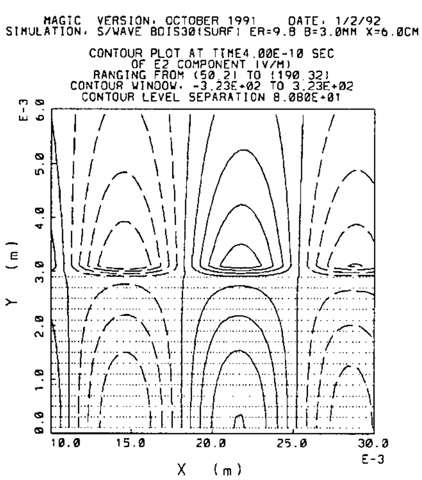

Fig 9

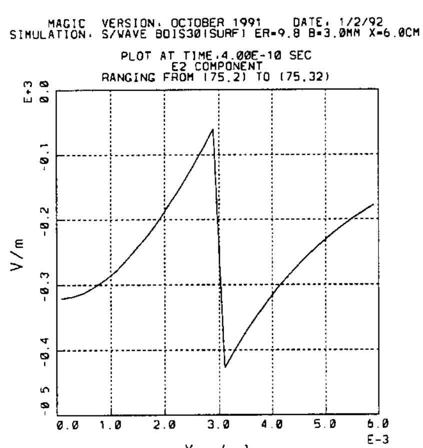

Fig 10

SPECTRAL DOMAIN ANALYSIS OF PRINTED TRANSMISSION LINES IN MULTILAYERED SUBSTRATE AND SUPERSTRATE CONFIGURATION

J. R. SOUZA
Center for Telecommunication Studies - CETUC
Pontifical Catholic University of Rio de Janeiro - PUC/Rio
Rua Marquês de São Vicente, 225
22453 Rio de Janeiro - RJ, Brazil

ABSTRACT

A formulation of the well-known Spectral Domain Approach (SDA) is presented for the analysis of printed transmission lines in multilayered substrate and superstrate configuration, including dielectric losses, with application to microwave monolithic integrated circuits (MMICs). It is assumed that conductors are placed at one of the dielectric interface, and the Green's dyadic in the spectral domain is determined using the boundary conditions at the other interfaces. The formulation is then used in the determination of the dispersion and attenuation characteristics of strip- and slot-like transmission lines, as well as their characteristic impedances.

1 - INTRODUCTION

The modern microwave monolithic integrated circuit (MMIC) technology uses transmission lines printed on Gallium Arsenide (GaAs) substrate. Frequently, auxiliary dielectric layers in addition to the semi-isolating GaAs substrate [1], whose dielectric constants differ considerably from that of the GaAs material, and which may have the function of passivation layers or may be due to the construction of over-lay capacitors. Due to the multi-dielectric layer configuration, such structures do not support TEM propagation, and are not amenable to analytical solution.

This paper presents a numerical solution for transmission lines in multilayered substrate and superstrate configuration, as shown in Figure 1. The solution is based on the Spectral Domain Approach (SDA), which has proved itself to be a powerful tool for the analysis of printed, non-TEM transmission lines [1], as it allows a high degree of spatial resolution. The present formulation has some advantages over those found in the literature for multilayered substrate, e.g. [2], as it does not require matrix multiplications, thus saving considerable computer memory and CPU time. In spite of being developed for shielded transmission lines, the resulting computer program allows the analysis of structures which are open along the Y- or X-axis, or both, as will be explained later on, thus providing the same flexibility of analysis as the general formulation of reference [3].

2 - FORMULATION

In Figure 1, it is assumed that perfect conductor strips are placed only at the $y=y_N$ interface. The electromagnetic field is represented in terms of hybrid TM- and TE-to-y fields through vector potentials $\bar{\psi}^e$ and $\bar{\psi}^h$, respectively, at each dielectric layer:

$$\bar{\psi}^{e,h}(x,y,z) = \bar{a}_y \, \phi^{e,h}(x,y)\cdot\exp(-j\beta z) \tag{1}$$

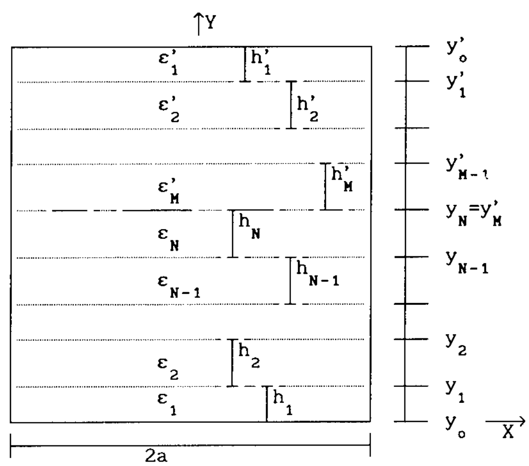

Figure 1: Multilayered substrate and superstrate transmission line.

where β is the propagation constant, $\bar{a}_y$ is the Y-axis unit vector, and a time dependence of the form $\exp(j\omega t)$ is implicit. The electromagnetic field in each layer i is written as

$$\bar{E}_i = -\nabla\times\bar{\psi}_i^h + \frac{1}{\hat{y}_i}\cdot\nabla\times\nabla\times\bar{\psi}_i^e$$
$$\bar{H}_i = \nabla\times\bar{\psi}_i^e + \frac{1}{\hat{z}_i}\cdot\nabla\times\nabla\times\bar{\psi}_i^h \tag{2}$$

with $\hat{y}_i=j\omega\hat{\varepsilon}_i$ and $\hat{z}_i=j\omega\mu_i$.

The permittivity $\hat{\varepsilon}_i$ of each layer i includes the dielectric loss, which is represented by a finite conductivity σ_i:

$$\hat{\varepsilon}_i = \varepsilon_o\cdot(\varepsilon_{ri} - j\sigma_i/\omega\varepsilon_o) = \varepsilon_o\hat{\varepsilon}_{ri} \tag{3}$$

where ε_o represents the permittivity of vacuum and ε_{ri}, the dielectric constant of the layer. ω is the angular frequency.

Following the initial steps of the SDA, all the potentials and field components are Fourier transformed. As shielded transmission lines are considered here, a discrete Fourier Transform is used. The transform and its inverse are defined, respectively, as:

$$\tilde{\varphi}(\alpha,y) = \int_{-a}^{a}\varphi(x,y)\cdot\exp(j\alpha x)\cdot dx \quad , \quad \varphi(x,y) = \frac{1}{2a}\cdot\sum_{n=-\infty}^{\infty}\tilde{\varphi}(\alpha,y)\cdot\exp(-j\alpha x) \tag{4}$$

where n represents the variation of the Fourier Transform parameter α.

Next, the following variable transformation is introduced [4]:

$$u = (\beta x - \alpha z)\cdot(\alpha^2 + \beta^2)^{-1/2} \quad , \quad v = (\alpha x + \beta z)\cdot(\alpha^2 + \beta^2)^{-1/2} \tag{5}$$

It can be shown [4] that in the (y,v,u) coordinate system the hybrid field can be written in terms of TM_y $(\tilde{E}_y,\tilde{E}_v,\tilde{H}_u)$ and TE_y $(\tilde{H}_y,\tilde{H}_v,\tilde{E}_u)$ components,

and so $\tilde{J}_v$ currents creates only the TM fields, while $\tilde{J}_u$ creates only the TE fields [4]. It is a simple task to show that if the (v,u) field components satisfy the boundary conditions at the dielectric interfaces, then the (x,z) components also do. These boundary conditions are then used to write the (v,u) electric field components in each layer in terms of their values at corresponding interfaces.

The Fourier transformed electric field components $\tilde{E}_u$ and $\tilde{E}_v$ are then written in terms of the transformed potentials $\tilde{\phi}^h$ and $\tilde{\phi}^e$, respectively, which are determined from the solution of the homogeneous Helmholtz equation in each layer. All the other field components are written in terms of $\tilde{E}_u$ and $\tilde{E}_v$, for each layer.

Let $\tilde{E}_{pi}$ represent $\tilde{E}_p$, p=u,v, in layer i ($y_i \le y \le y_{i-1}$), and let $\tilde{E}_{psi}$ be its value at the interface $y=y_i$. With a ground plane at $y=y_o$, $\tilde{E}_{pso}$ equals zero. At the intermediate interfaces $y_2 \le y_i \le y_{N-1}$ the boundary conditions for the tangential electric field yield:

$$\tilde{E}_{psi+1} = A_{pi}\,\tilde{E}_{psi} + B_{pi-1}\tilde{E}_{psi-1} \tag{6-a}$$

where:

$$A_{pi} = \cosh(\gamma_{i+1}h_{i+1}) + \frac{g_i\sinh(\gamma_{i+1}h_{i+1})}{g_{i+1}\,\mathrm{tgh}(\gamma_i h_i)}$$
$$= \frac{\sinh(\gamma_{i+1}h_{i+1})}{g_{i+1}}\cdot[g_{i+1}\mathrm{ctgh}(\gamma_{i+1}h_{i+1}) + g_i\mathrm{ctgh}(\gamma_i h_i)] \tag{6-b}$$

with $1 \le i \le N-1$, and

$$B_{pi-1} = -\frac{g_i\sinh(\gamma_{i+1}h_{i+1})}{g_{i+1}\sinh(\gamma_i h_i)} \quad , \; 2 \le i \le N-1 \tag{6-c}$$

In (6), for p=u, $g_i=-\gamma_i/\hat{z}_i$, and for p=v, $g_i=-\hat{y}_i/\gamma_i$, with the parameter γ_i being given by:

$$\gamma_i = (\alpha^2 + \beta^2 - k_o^2\cdot\hat{\varepsilon}_{ri})^{1/2} \tag{6-d}$$

Similar expressions are written for the superstrate layers:

$$\tilde{E}_{psj+1} = A'_{pj}\,\tilde{E}_{psj} + B'_{pj-1}\tilde{E}_{psj-1} \quad , \; 2 \le j \le M-1 \tag{7}$$

with A'_{pj} and B'_{pj-1} also given by (6-b) and (6-c).

At $y=y_1$: $\tilde{E}_{ps2} = A_{p1}\,\tilde{E}_{ps1}$, and at $y=y'_1$: $\tilde{E}_{psN+M-2} = A'_{p1}\tilde{E}_{psN+M-1}$ (8)

At $y=y_N$:

$$\frac{g_{N+1}}{\sinh(\gamma_{N+1}h_{N+1})}\cdot\left\{\frac{g_N/\sinh(\gamma_N h_N)}{g_{N+1}/\sinh(\gamma_{N+1}h_{N+1})}\cdot\tilde{E}_{psN-1} - \frac{\sinh(\gamma_{N+1}h_{N+1})}{g_{N+1}}\cdot\left[g_N\mathrm{ctgh}(\gamma_N h_N)+g_{N+1}\mathrm{ctgh}(\gamma_{N+1}h_{N+1})\right]\cdot\tilde{E}_{psN}+\tilde{E}_{psN+1}\right\} = \tilde{J}_{pN} \tag{9}$$

Now, $\tilde{E}_{psi}$ is written in terms of $\tilde{E}_{psN}$ using equations (6) to (8). The following relations are obtained for the substrate layers:

$$\tilde{E}_{psN-i} = \frac{1}{\Delta_{pN}}(T_{pN})_i\cdot\tilde{E}_{psN} \quad , \; 1 \le i \le N-1 \tag{10-a}$$

with: $(T_{pN})_N=0,\quad (T_{pN})_{N-1} = 1$

$$(T_{pN})_{N-(i+1)} = A_{pi}(T_{pN})_{N-i} + B_{p(i-1)}(T_{pN})_{N-(i-1)}\ ,\quad 1\le i\le N-2 \qquad (10\text{-b})$$

$$\Delta_{pN} = A_{pN-1}(T_{pN})_1 + B_{pN-2}(T_{pN})_2$$

Similar expressions are obtained for the superstrate layers. (10) yields:

$$\tilde{E}_{psN-1} = \frac{1}{\Delta_{pN}}(T_{pN})_1\cdot\tilde{E}_{psN}\ ,\qquad \tilde{E}_{psN+1} = \frac{1}{\Delta'_{pM}}(T'_{pM})_1\cdot\tilde{E}_{psN} \qquad (11)$$

Substitution of (11) into (9) results in:

$$Y_p\ \tilde{E}_{psN} = \tilde{J}_{pN} \qquad (12\text{-a})$$

$$\text{with: } Y_p = \frac{1}{S^2_{pN}}\cdot\frac{(T_{pN})_1/P_{pN-1}}{\Delta_{pN}/P_{pN}} - G_{pN} + \frac{1}{S'^2_{pM}}\cdot\frac{(T'_{pM})_1/P'_{pM-1}}{\Delta'_{pM}/P'_{pM}} - G'_{pM} \qquad (12\text{-b})$$

$$S_{ui} = \frac{\sinh(\gamma_i h_i)}{\gamma_i}\ ,\quad G_{ui} = \gamma_i \operatorname{ctgh}(\gamma_i h_i)\ ,\quad S_{vi} = \frac{\gamma_i}{\varepsilon_{ri}}\cdot\sinh(\gamma_i h_i) \qquad (12\text{-c})$$

$$G_{vi} = \frac{\varepsilon_{ri}}{\gamma_i}\cdot\operatorname{ctgh}(\gamma_i h_i)\ ,\quad P_{pi} = \begin{cases} \prod_{k=2}^{i} S_{pk}\ , & i\ge 2 \\ 1\ , & i<2 \end{cases} \qquad (12\text{-d})$$

$$\frac{(T_{pN})_{N-(i+1)}}{P_{p(i+1)}} = (G_{p(i+1)} + G_{pi})\cdot\frac{(T_{pN})_{(N-i)}}{P_{pi}} - \frac{1}{S^2_{pi}}\cdot\frac{(T_{pN})_{N-(i-1)}}{P_{p(i-1)}} \qquad (12\text{-e})$$

all for $1\le i\le N-2$, and

$$\frac{\Delta_{pN}}{P_{pN}} = (G_{pN} + G_{p(N-1)})\cdot\frac{(T_{pN})_1}{P_{p(N-1)}} - \frac{1}{S^2_{p(N-1)}}\cdot\frac{(T_{pN})_2}{P_{p(N-2)}} \qquad (12\text{-f})$$

The dashed terms in (12-b), which correspond to the superstrate layers, have similar expression as (12-c) to 12-f).

Equation (12-a), which describes the boundary conditions at the interface where the conducting strips are placed, is then transformed back to the (x,z) coordinate system:

$$\begin{bmatrix} \tilde{E}_z \\ \tilde{E}_x \end{bmatrix} = \begin{bmatrix} \tilde{Z}_{zz} & \tilde{Z}_{zx} \\ \tilde{Z}_{xz} & \tilde{Z}_{xx} \end{bmatrix}\cdot\begin{bmatrix} \tilde{J}_z \\ \tilde{J}_x \end{bmatrix} \qquad (13\text{-a})$$

with:

$$\tilde{Z}_{zz} = \frac{\beta^2}{\alpha^2+\beta^2}Z_v + \frac{\alpha^2}{\alpha^2+\beta^2}Z_u,\qquad \tilde{Z}_{zx} = \tilde{Z}_{xz} = \frac{\alpha\beta}{\alpha^2+\beta^2}(Z_v - Z_u)$$

$$\tilde{Z}_{xx} = \frac{\alpha^2}{\alpha^2+\beta^2}Z_v + \frac{\beta^2}{\alpha^2+\beta^2}Z_u \qquad (13\text{-b})$$

where $Z_p=1/Y_p$, p=u,v, with Y_p given by (12-b).

The usual steps of the SDA [1]-[4] are now followed in order to obtain

from (13-a) a homogeneous set of equations, from which the propagation constant β is calculated: the currents $\tilde{J}_z$ and $\tilde{J}_x$, or the field components $\tilde{E}_z$ and $\tilde{E}_x$, are written in terms of known basis functions. The choice between currents or field components is determined by the characteristics of the transmission line: if it is of the "strip" type, then the currents are used; for "slot-like" transmission lines, the electric field components are used, and the matrix equation (13-a) should be inverted.

The analysis process proceeds with the calculation of the transmission line characteristic impedance. However, as the wave propagation is of hybrid-mode type in the structures considered here, a precise definition of characteristic impedance is difficult. Following suggestions found in the literature [1]-[4], for strip-like transmission lines the characteristic impedance is calculated through the ratio between the average power and the total longitudinal current, while for slot-like transmission lines the ratio between the "voltage" across the slot and the average power is used. In all cases, the average power is calculated via the integral of the Poynting vector:

$$P_{av} = \frac{1}{2} \,\mathbb{R}\mathrm{e} \left\{ \int_{-a}^{a} \int_{y_o}^{y'_o} (E_x H_y^* - E_y H_x^*) dx dy \right\} \tag{14}$$

where $\mathbb{R}\mathrm{e}$ represents the real part of a complex number and the asterisk, the complex conjugate. With the present formulation, the equation (14) can be written in the spectral domain as:

$$P_{av} = \frac{1}{4a} \,\mathbb{R}\mathrm{e} \left\{ \sum_{n=-\infty}^{\infty} \left[\sum_{i=1}^{N} \tilde{f}_i(n) + \sum_{j=1}^{M} \tilde{f}'_j(n) \right] \right\} \tag{15-a}$$

with:

$$\begin{aligned} \tilde{f}_i(n) = \frac{1}{2\omega\mu_o} \cdot \Bigg\{ \Bigg(& U_{i-1}^* V_{i-1} \left[2j\alpha \mathbb{I}\mathrm{m}(B) Q_1 + \frac{2\alpha}{\gamma_i} \cdot B^* \mathrm{ctgh}(\Theta_i) \right] + U_{i-1}^* V_i \Big[2j\alpha \mathbb{I}\mathrm{m}(B) Q_2 \\ & - \frac{2\alpha}{\gamma_i \sinh(\Theta_i)} \cdot B^* \Big] + U_i^* V_{i-1} \left[2j\alpha \mathbb{I}\mathrm{m}(B) Q_2^* - \frac{2\alpha}{\gamma_i \sinh(\Theta_i)} \cdot B^* \right] + U_i^* V_i \Big[2j\alpha \mathbb{I}\mathrm{m}(B) Q_3 \\ & + \frac{2\alpha}{\gamma_i} \cdot B^* \mathrm{ctgh}(\Theta_i) \Big] \Bigg) \cdot \tilde{E}_{usN}^* \tilde{E}_{vsN} + \beta B \left[|U_{i-1}|^2 Q_1 + 2\mathbb{R}\mathrm{e}(U_i U_{i-1}^* Q_2) + |U_i|^2 Q_3 \right] \cdot |\tilde{E}_{usN}|^2 \\ & + \frac{k_o^2 \hat{\varepsilon}_{ri} \beta^*}{\gamma_i^{2*}} \cdot B^* \cdot \Bigg[|V_{i-1}|^2 \left(\frac{2\mathrm{ctgh}(\Theta_i)}{\gamma_i} - Q_1 \right) - V_{i-1}^* V_i \left(\frac{2}{\gamma_i \sinh(\Theta_i)} + Q_2 \right) \\ & - V_{i-1} V_i^* \left(\frac{2}{\gamma_i \sinh(\Theta_i)} + Q_2^* \right) + |V_i|^2 \left(\frac{2\mathrm{ctgh}(\Theta_i)}{\gamma_i} - Q_3 \right) \Bigg] \cdot |\tilde{E}_{vsN}|^2 \Bigg\} \end{aligned} \tag{15-b}$$

and:
$$B = \sqrt{\alpha^2 + \beta^2}^{\,*} \Big/ \sqrt{\alpha^2 + \beta^2} \tag{15-c}$$

$$\begin{aligned} Q_1 = & \frac{\sinh(\Theta_{ir})}{\gamma_{ir}} \cdot \left[\cosh(\Theta_{ir}) \cdot \left(1 + |\mathrm{ctgh}(\Theta_i)|^2 \right) - 2\mathbb{R}\mathrm{e}\left(\sinh(\Theta_{ir}) \mathrm{ctgh}(\Theta_i) \right) \right] \\ & + \frac{\sin(\Theta_{ii})}{\gamma_{ii}} \cdot \left[\cos(\Theta_{ii}) \cdot \left(1 - |\mathrm{ctgh}(\Theta_i)|^2 \right) + 2\mathbb{I}\mathrm{m}\left(\sin(\Theta_{ii}) \mathrm{ctgh}(\Theta_i) \right) \right] \end{aligned} \tag{15-d}$$

$$Q_2 = \frac{1}{\sinh(\Theta_i)} \cdot \left\{ \frac{\sinh(\Theta_{ir})}{\gamma_{ir}} \cdot \left[\sinh(\Theta_{ir}) - \mathrm{ctgh}^*(\Theta_i)\cosh(\Theta_{ir}) \right] + \frac{\sin(\Theta_{ii})}{\gamma_{ii}} \cdot \left[\mathrm{ctgh}^*(\Theta_i)\cos(\Theta_{ii}) + j\sin(\Theta_{ii}) \right] \right\} \tag{15-e}$$

$$Q_3 = \frac{1}{|\sinh(\Theta_i)|^2} \cdot \left\{ \frac{1}{\gamma_{ir}} \cdot \cosh(\Theta_{ir})\sinh(\Theta_{ir}) - \frac{1}{\gamma_{ii}} \cdot \cos(\Theta_{ii})\sin(\Theta_{ii}) \right\} \tag{15-f}$$

$$\Theta_i = \gamma_i h_i = \Theta_{ir} + j\Theta_{ii}, \qquad \gamma_i = \gamma_{ir} + j\gamma_{ii} \tag{15-g}$$

$$U_i = \frac{1}{\nabla_{uN}} \cdot (T_{uN})_{N-i}, \; U_N=1, \; U_o=0, \; V_i = \frac{1}{\nabla_{vN}} \cdot (T_{vN})_{N-i}, \; V_N=1, \; V_o=0 \tag{15-h}$$

with $1 \le i \le N-1$ in (15-h), ∇_{PN} and $(T_{PN})_{N-i}$, p = u, v, given by equations (12), and:

$$\tilde{E}_{usN} = \frac{Z_u}{(\alpha^2 + \beta^2)^{1/2}} \cdot (\beta\tilde{J}_x - \alpha\tilde{J}_z), \; \tilde{E}_{vsN} = \frac{Z_v}{(\alpha^2 + \beta^2)^{1/2}} \cdot (\alpha\tilde{J}_x + \beta\tilde{J}_z) \tag{15-i}$$

with Z_u and Z_v given by (16-b) ($Z_p = 1/Y_p$, p=u, v), and $\Im m$ representing the imaginary part of a complex number.

In equation (15-a), the functions $\tilde{f}_j$, which correspond to the superstrate layers ($1 \le j \le M$), are given by expressions similar to (15-b) to (15-i).

3 - RESULTS

Based on the formulation presented here, a computer program was developed to analyze several types of transmission lines, such as single and coupled microstrips, single and coupled slotlines, coplanar waveguides (CPW), and coplanar strips, all in multilayered substrate and superstrate configuration.

Initially, a microstrip line of the metal-isolator-semiconductor type was considered, as illustrated in Figure 2.

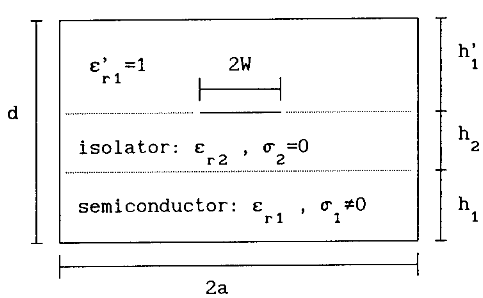

Figure 2: MIS microstrip line.

The line dimensions were taken as: $2W=160\mu m$, $h_1=250\mu m$, $h_2=1.0\mu m$, $d=1.50\mu m$, $2a=10\mu m$. The dielectric constants of semiconductor and isolator were respectively fixed as: $\varepsilon_{r1}=12.0$ and $\varepsilon_{r2}=4.0$. Three values were considered for semiconductor conductivity, $\sigma_1=5$, 1000, and 10000 Mho/m. Figure 3 shows the variation of the slow-wave factor S ($S=\lambda_g/\lambda_o$) with frequency. In this figure, theoretical results as read from references [5] and [6], and experimental results read from reference [7]

are also shown, and the agreement is good. It is seen that for frequencies up to about 4 GHz the phase velocity in the structure is smaller than in any of the two substrate layers, as in the semiconductor the value of S would be approximately 0.288 and in the isolator, 0.707, thus explaining the meaning of the term "slow-wave factor". Figure 4 shows the variation of the characteristic impedance of this microstrip line, calculated as twice the ratio between the average power and the total longitudinal current, with frequency, and also result as read from reference [7]. The discrepancy between the results may be due to the fact that in [7] a parallel plate transmission line model was used in the calculations, in which the edge boundary condition is not account for, while it is correctly incorporated in the present formulation.

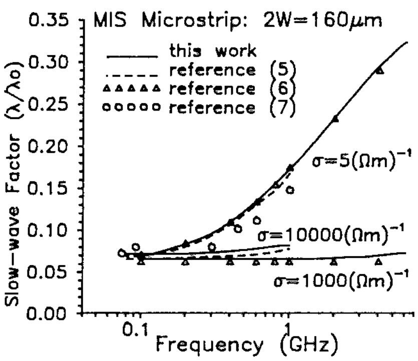

Figure 3: Variation of the slow wave factor with frequency for the microstrip line of Figure 2.

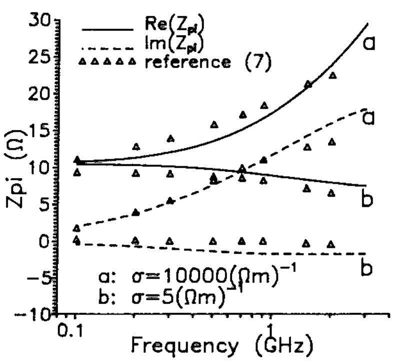

Figure 4: Characteristic impedance variation with frequency for the microstrip line of Figure 2.

Next, a unshielded coplanar waveguide was analyzed, in order to show that, although the formulation was developed for shielded structures, the resulting computer program can also be used in the analysis of open transmission lines. The CPW shown in Figure 5 was used to simulated the unshielded one, by fixing large values for the extreme layers and for the shielding width. The dimensions were chosen as: S=450μm, W=100μm, h_3=0.4μm, h_1=h'_1=10000μm, 2a=25000μm. The other parameters were taken as: $\varepsilon_{r1}=\varepsilon_{r2}$=13.1, ε_{r3}=8.5, and σ_2=18181.8181 Mho/m. Figure 6 shows the variation of the slow-wave and attenuation factors with frequency. The attenuation factor is given by the imaginary part of the propagation constant. Also shown in this figure are results as read from reference [6], and the agreement is seen to be very good, showing the flexibility provided by the computer program. It is worth mentioning that the formulation presented here also applies to open structures, provided the continuous Fourier Transform is used. But in the computer program, only the discrete Transform is employed, and so a larger number of terms is required in the summation in equation (4) to simulate open structures.

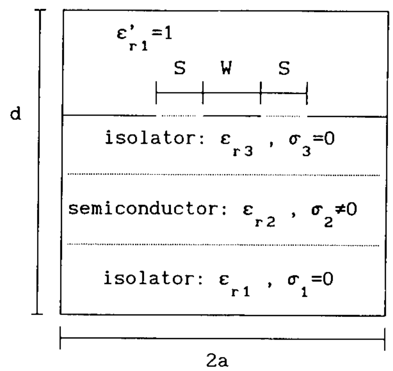

Figure 5: MIS coplanar waveguide.

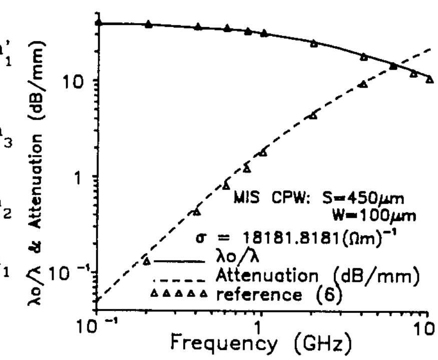

Figure 6: Frequency variation of slow-wave and attenuation factors for the MIS CPW of Figure 5.

4 - CONCLUSIONS

A formulation of the Spectral Domain Approach was developed for the analysis of printed transmission lines in multilayered substrate and superstrate configuration, in which the boundary conditions at the several interfaces are used in a recursive manner to reduce the problem to the interface were conductors are placed. Although results were presented only for microstrip lines and coplanar waveguides, many other types of transmission lines can be analyzed. It is worth mentioning that the formulation can be easily adapted to consider conducting strips placed at two neighboring interfaces, or to accommodate a magnetic wall at one of the extreme layers.

ACKNOWLEDGEMENT: This work was supported by TELEBRÁS through the contract PUC/TELEBRÁS 415/91.

REFERENCES

1 - R. H. Jansen, *IEEE MTT-Symposium Digest*, pp 711-714, 1985.
2 - J. B. Davies, and D. Mirshekar-Syahkal, *IEEE Trans. Microwave Theory Tech.*, vol. MTT-25, pp 143-146, 1977.
3 - S. Tedjini, D. Rauly, and P. Saguet, *Proc. 1986 European Microwave Conf.*, pp 483-489.
4 - T. Itoh, *IEEE Trans. Microwave Theory Tech.*, vol. MTT-28, pp 733-736, 1980.
5 - T. G. Livernoios, and P. B. Katehi, *IEEE Trans. Microwave Theory Tech.*, vol. MTT-37, pp 1761-1767, 1989.
6 - Y. Shin, and T. Itoh, *Microwave Report No. 84-2*, University of Texas, Austin, U.S.A., 1984.
7 - H. Hasegawa, M. Furukawa, and H. Yanai, *IEEE Trans. Microwave Theory Tech.*, vol. MTT-19, pp 869-881, 1971.

ON THE CALCULATION OF THE ELECTROMAGNETIC FIELD IN PLANAR STRUCTURES BY SPECTRAL DOMAIN TECHNIQUES

A. VILCOT - S. TEDJINI - P. CHAZAN
LEMO URA CNRS 833 - 23 Avenue des Martyrs BP 257
38 016 Grenoble Cedex FRANCE
Phone (33) 76 87 69 76 - Fax (33) 76 46 56 36

Abstract
The importance of the choice of the function basis in the Spectral Domain Techniques is studied in the case of a microstrip structure. The calculation of global values does not require a specific function basis. On the contrary, results on local values are very sensitive to the kind of function used in the calculation, particularly for values on the strip plane.

1. Introduction

The Spectral Domain Approach, first developped by Itoh and Mittra [1], and Denlinger [2], has been then extended to more general structures, including several layers of dielectrics or semiconductors, under and above the plane of metallisations. It is nowadays an attractive and very efficient method for the analysis of planar microwave and millimeter wave, hybrid and monolithic integrated circuits [3-4]. It is well-established that global values such as relative effective permittivity ε_{eff} or cut-off frequency f_c can be accurately computed with the SDA, with a small number and various types of basis functions, particularly trigonometric functions which do not respect individually boundary conditions on metallic edges [5]. As far as local values are concerned, only little work has been done. The aim of this paper is to compare the effect of the choice of the basis function on local values. A special attention will be given to the most used basis functions : trigonometric ones with or without the correction of the boundary conditions on metallic edges.

2. General principle of the Spectral Domain Approach.

In the SDA [1 - 3], the choice of the function basis occurs in the use of Galerkin's moment method. Using this method for a microstrip, tangential current densities (see fig. 1 for axes orientation) are expanded on a function basis as :

$$J_y(0,y) = \sum_{i=1}^{+\infty} a_i f_i(y)$$

$$J_z(0,y) = \sum_{j=0}^{+\infty} b_j g_j(y)$$

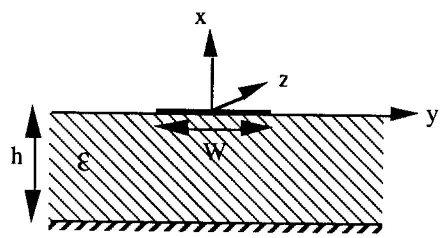

Fig.1 : Open microstrip line

The method leads then to a system of linear equations which requires, for practical calculations, truncations of the previous infinite sums [5] to a number Q of basis functions. It requires at the same time truncations to a finite value Umax of the infinite limits of Fourier transforms which occur in the analytical development. These truncations have to respect convergence criteria [3, 5], in order to give accurate results.

The propagation constant $\Gamma = \alpha + j\beta$ of the studied structure is obtained by setting the determinant of the system to zero. By putting the value of Γ into the system, we can calculate a_i and b_j as a function of b_0 for example. In the case of a microstrip structure, we obtain thus the values of the current densities $J_z(y)$ and $J_y(y)$ in the plane of metallisations ($x = 0$). We can then calculate the characteristic impedance, whose definition depends on the kind of studied structure. In the case of a microstrip line, the characteristic impedance is obtained by means of the power P and the current I :

$$Z_c = \frac{P}{2\,|I|^2}$$

The field is then calculated in Fourier domain, from the values of Γ, a_i and b_j , using Maxwell's equations and boundary conditions. Inverse Fourier transforms allow then the calculation of the field components in the space domain : $E_x(x,y)$, $E_y(x,y)$, $E_z(x,y)$, $H_x(x,y)$, $H_y(x,y)$, $H_z(x,y)$.

We have made this study on several bases, but we shall present results only for the first two bases. Indeed, the trigonometric basis (basis n°2) is one of the simplest to manipulate ; and the trigonometric basis corrected with the boundary conditions on metallic edges (basis n°1) seems to be the best suited to the calculation of local values.

1. $\cos\left(2p\pi\left(\frac{y}{W}+\frac{1}{2}\right)\right) \Big/ \sqrt{1-\left(\frac{2y}{W}\right)^2}\ ,\ \sin\left(2p\pi\left(\frac{y}{W}+\frac{1}{2}\right)\right) \Big/ \sqrt{1-\left(\frac{2y}{W}\right)^2}$

2. $\cos\left(2p\pi\left(\frac{y}{W}+\frac{1}{2}\right)\right),\ \sin\left(2p\pi\left(\frac{y}{W}+\frac{1}{2}\right)\right)$

3. $T_{2(n-1)}(2y/w) \,/\, \sqrt{-(2y/w)^2}$, $U_{2n}(2y/w)$ (T, U : Chebishev polynomials)

4. $1/\left(1+|2y/w|^3\right)$, $\sin\left(\Pi y/(0.7w)\right)$

3. Results on global parameters

Figure 2 shows that the relative effective permittivity does not depend much on the chosen basis. Indeed, the relative error between two points calculated at the same frequency with two different bases is within 1 %. In the case of the characteristic impedance Z_c, the relative error remains within 5 %. This confirms that the choice of the function basis is not much important in case of global parameters calculation. Moreover, the calculation of such parameters requires few basis functions : for a given basis, the relative error between parameters calculated with 2 and 5 functions is within 1 ‰.

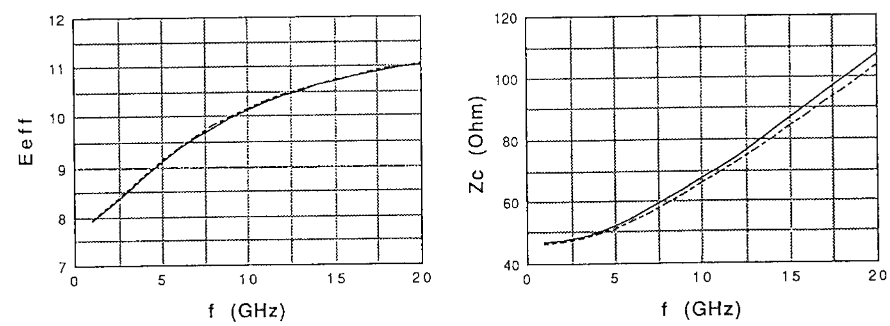

Fig.2 : Relative effective permittivity and characteristic impedance
for an open microstrip - Q = 2 - f = 1 GHz
- - - basis n°1 ___ basis n°2
W = 3.0432 mm, h = 3.17 mm, ε = 11.7

However, the first basis (trigonometric basis with the respect of the boundary conditions on metallic edges) requires a higher calculation time than the second, for two main reasons. First, each Fourier transform needs more time to be calculated in the case of the first basis, as it requires Bessel functions ; secondly, the first basis requires higher values of Umax in order to respect the convergence criterion [5]. This convergence criterion reads : Umax = K(Q) Q Π / W [5], where K(Q) is higher for the first basis than the second one (for instance : for Q = 2, K(2) = 5 and 2.6 respectively for the first and the second bases).

4. Results on local values

Figure 3 shows that the effect of the basis is particular noticeable for $J_z(y)$. Indeed, even for an important number of basis functions (Q = 5), the basis n°2 shows an horizontal tangent for y = W/2, which is opposite to the boundary conditions [6], which tell us that $J_z(y)$ should vary as $1/(y-W/2)^{1/2}$. Only an infinite superposition of the functions of the basis n°2 could respect this boundary condition on a metallic edge. This is not the case for the first basis, which needs few functions to give accurate results for local values.

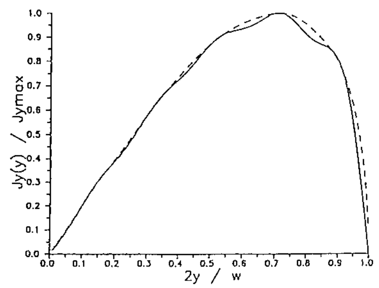

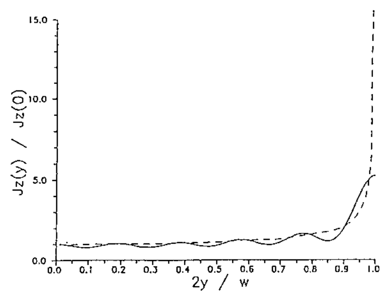

Fig. 3 : Tangential current densities $J_y(y)$ and $J_z(y)$
for an open microstrip
$Q = 5$ - $f = 1$ GHz - $W = 3.0432$ mm, $h = 3.17$ mm, $\varepsilon = 11.7$
--- basis n°1 ___ basis n°2

Kobayashi [7] extracted analytical formulae from results on tangential current densities obtained from the SDA with Chebyschev polynomials corrected by the term which respects the metallic edge condition (basis n°3). We compare on figure 4 the results obtained with these analytical formulae and our results with the first function basis. This shows a good agreement between local results as soon as the basis functions respect individually the boundary conditions on metallic edges, even for a small number of basis functions $Q = 2$. This indicates that the most important fact in the choice of the function basis is the respect of the boundary conditions on a metallic edge by each basis function.

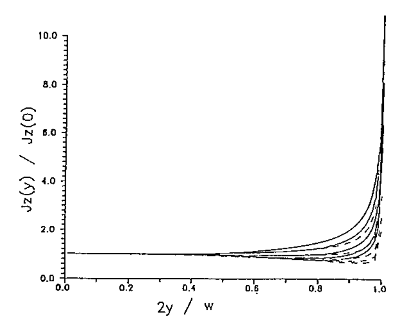

Fig. 4 : Tangential current densities J_z
for an open microstrip - $W = 6$ mm, $h = 3$ mm, $\varepsilon = 8.0$
$h/l_0 = 0.005, 0.1, 0.2, 0.3, 0.4$
___ our results basis n°1 --- Kobayashi's results

The SDA allows also the calculation of the electromagnetic field in the whole structure. As an example, results with the first basis (which respects the metallic edge conditions) are presented figure 5, for a microstrip structure.

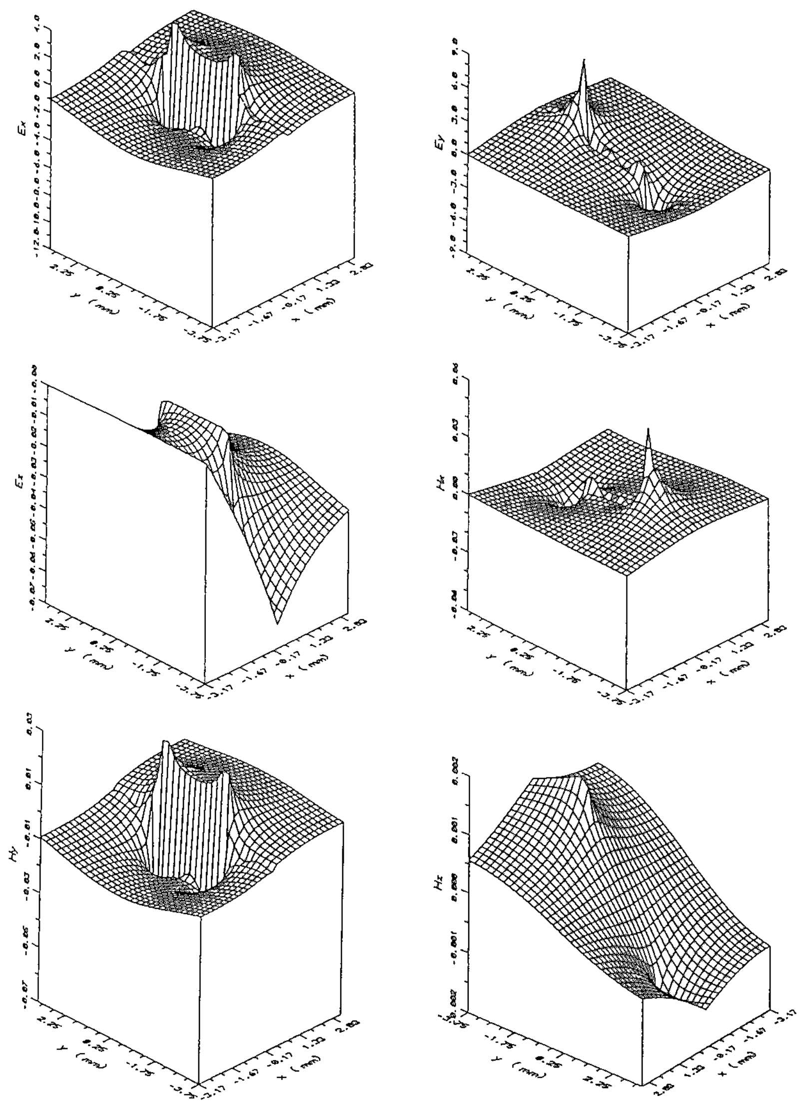

Fig.5 : Electromagnetic field in a microstrip structure
$f = 1$ GHz - $W = 3.0432$ mm, $h = 3.17$ mm, $\varepsilon_r = 11.7$
First basis

Comparing these results with those presented on figure 6, obtained with the second function basis, we can note that the results are similar, as well in their behavior as in the values of the fields, except on the strip plane where the second basis gives oscillations. The number of oscillations increases as we increase the number of basis functions, but at the same time their relative amplitude decreases : for an infinite number of functions, they would disappear.

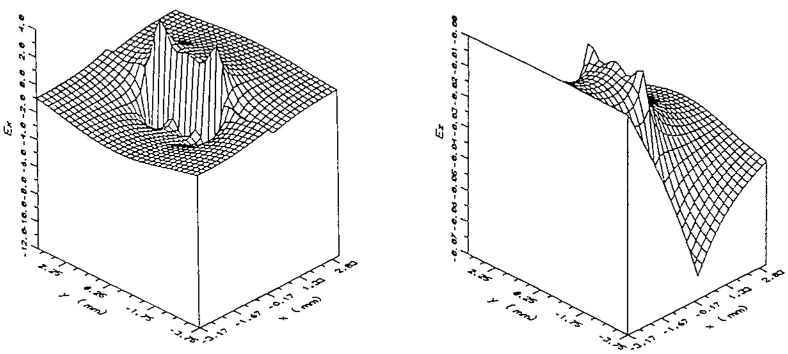

Fig.6 : Electromagnetic field in a microstrip structure
f = 1 GHz - W = 3.0432 mm, h = 3.17 mm, ε = 11.7
Second basis

These oscillations exist also in the case of the first basis but they have a weaker relative amplitude, which involves a more accurate result. Figure 7, which shows a cut of the electromagnetic field for the section x = 0, illustrates clearly this point (see for instance $E_x(y)$ and $E_z(y)$).

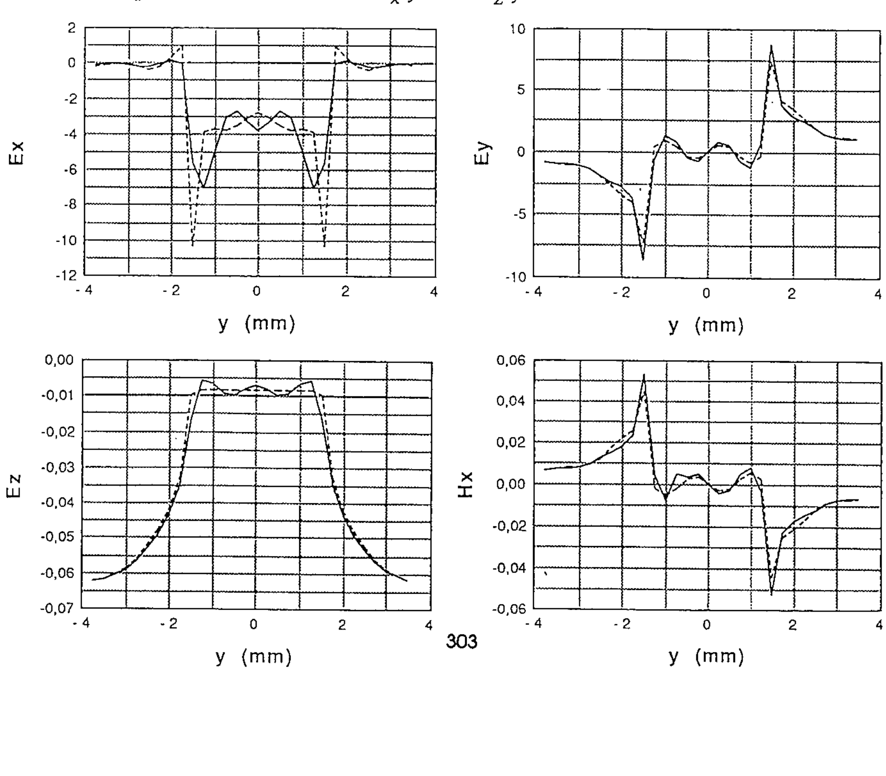

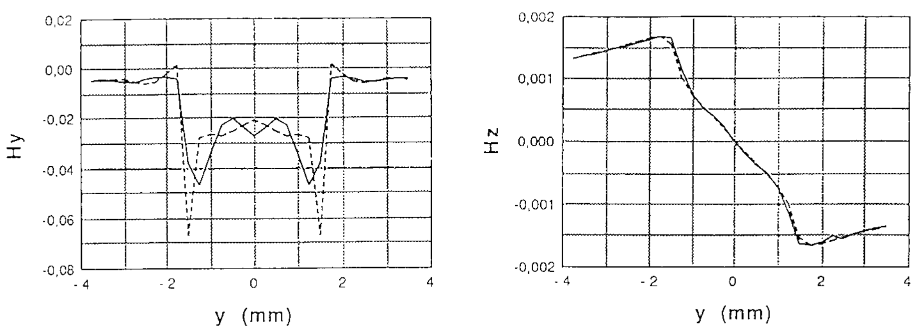

Fig.7 : Electromagnetic field in a microstrip structure
f = 1 GHz - W = 3.0432 mm, h = 3.17 mm, ε = 11.7
Cut in the section x = 0
- - - basis n°1 ___ basis n°2

On the other hand, the boundary conditions on the edge of the strip seem to be better respected in the case of the first basis, as an example see $E_x(y)$ and $H_y(y)$. If we make a cut in the section y = 1.5 mm, that is to say on the edge of the strip, we obtain the results presented on figure 8. This shows the discontinuity of $E_x(x)$ on the strip (x = 0). In the case of $E_z(x)$, it should be zero on the metallic planes (x = -3.17 mm and x = 0). This is respected on the ground plane since it is imposed in the calculations at the beginning of the calculations. However this is not the case, on the strip : in fact, $E_z(x, y)$ is calculated by means of direct and inverse Fourier transforms, which cannot give an exact zero on the strip. However, results nearer reality are obtained with the first basis and would be improved with an increase in the function number.

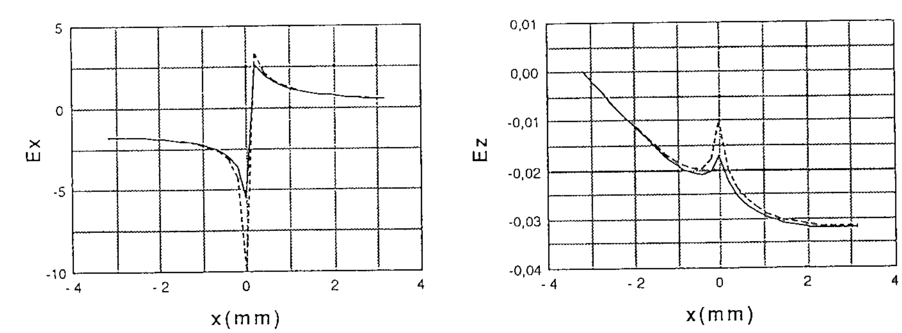

Fig.8 : Electromagnetic field in a microstrip structure
f = 1 GHz - W = 3.0432 mm, h = 3.17 mm, ε = 11.7
Cut in the section y = 1.5
- - - basis n°1 ___ basis n°2

The oscillations of fields on the strip and the respect of the boundary conditions on the strip edges lead to the conclusion that the first basis is more

suited for the calculations of the electromagnetic field. We can notice that the fields presented above are essentially transverse : E_z and H_z are weak compared to E_T and H_T . Looking at the structure and comparing with known results, these calculated results are logical : the electromagnetic field is quasi-TEM.

5. Conclusion

The Spectral Domain Approach is nowadays well-used for planar structures, but most results are given for global values in shielded structures. Little work is done on open structures, particularly on local values. That is why we centered our work on local values in open structures, and more precisely on the effect of the choice of the function basis.

We have confirmed, as well-established previously, that any kind of function basis can give correct and accurate results on global values. The only difference stays in the speed of the calculations, which mainly depends on the convergence criteria. As an example, on an Apollo DS 3500, to calculate the propagation constant Γ, it takes 30 seconds for the first basis and 20 seconds for the c basis. That is why, in case of global values calculation, the simpler basis can be used, for instance the trigonometric basis. On the contrary, the calculation of local values requires the respect of the metallic edge condition by each function of the basis, in order to give realistic results, in agreement with physical phenomena.

Comparison with litterature has been done on current densities on the strip and has shown good agreement with our results. But no published work on the electromagnetic field in the whole structure has been found yet.

The studied structure presented here has no loss, but the model we have developped can take the loss into consideration, in case of structures on semiconductors, for example. This work should be completed by a study on lines on semiconductor semi-insulator and on MIS structures.

Bibliography

[1] **T. Itoh and R. Mittra**, "A technique for computing dispersion characteristics of shielded microstrip lines". IEEE Trans. Microwave Theory Tech. vol. MTT-22, pp 896-898, Oct. 1974

[2] **E. J. Denlinger**, "A frequency dependant solution for microstrip transmission lines" IEEE Trans. Microwave Theory Tech. vol. MTT-19, pp 30-39, Jan. 1971

[3] **S. Tedjini, N. Daoud, D. Rauly, E. Pic**, "Analysis of MMIC's with finite strip thickness and conductivity", Electronics Letters, vàl 24 n°15, pp 965-966, July 1988

[4] **W . Wertgen, R.H. Jansen**, "Efficient direct and iterative electrodynamic analysis of geometrically complex MIC and MMIC structures", Int. journal of Numerical Modelling : electronic networks, devices and fields, vol 2, pp 153-186, 1989

[5] **A. Vilcot, S. Tedjini**, "Critère de convergence et choix de la base de fonctions dans les techniques de méthode spectrale". Journées Nationales Microondes, pp 185-186, mars 1991

[6] **J. Meixner**, "The behavior of electromagnetic fields at edges" IEEE Trans. Antenna Prop. vol. A.P.-20, pp 442-446, July 1972

[7] **M. Kobayashi and H. Sekine**, " Closed-form expressions for the current distributions on open microstrip lines". IEEE Trans. Microwave Theory Tech. vol. MTT-39, n°7, pp 1115-1118, July 1991

SESSION 8 - "LOW FREQUENCY APPLICATIONS"

Moderator: O. Mohamed

A Hybrid Method for the Computation of 2D Eddy Currents in Ferromagnetic Materials

A. Nicolet, A. Genon, P. Dular *, F. Delincé *, W. Legros

University of Liège, Dept of Electrical Engineering, Institut Montefiore

B28, Sart Tilman, B-4000, Liège, Belgium

Abstract

The paper presents a hybrid method coupling the finite elements and the boundary elements to solve 2D eddy current non linear problems. The non linearity of the problems prevents a pure boundary element treatment. Nevertheless, when the non linear part represents only a small part of the geometry, the use of the coupled method leads to an important reduction of the size of the problem. Some practical aspects of the implementation are examined. An induction furnace is chosen as an example.

Introduction

The boundary element method is very useful for the study of electromagnetic linear problems because of its accuracy and its ability to naturally take into account open boundary problems. On the other hand, when a problem involves a saturable ferromagnetic material, the boundary element method is not applicable and the finite element method must be used. Moreover, the non linearities prevent the use of the complex formalism and a time step analysis is required even for periodic time variations. If the non linear parts of the problem are only a small part of the geometry of the problem, it may be interesting to use a hybrid method coupling the boundary elements for the large (and may be infinite) linear parts and the finite elements for the small non linear parts.

Finite element - boundary element coupling

The equation for the two-dimensional magnetostatics is:

$$\mathrm{div}\, \nu\, \mathrm{grad}\, A = -J \qquad (1)$$

- A is the vector potential which has only one component;
- J is the current density;
- ν is the magnetic reluctivity.

In linear magnetic non-conducting media, the direct boundary element method (Brebbia 84) is based on the relation (2):

$$cA = \int_\Gamma A \frac{\partial G}{\partial n} d\Gamma - \int_\Gamma G \frac{\partial A}{\partial n} d\Gamma \qquad (2)$$

* These authors are Research Assistants with the Belgian National Fund for Scientific Research

where:

. G is the free space Green function of the two-dimensional Laplace operator;
. $c = 0.5$ on a smooth boundary;
. $\partial./\partial n$ is for the normal derivative.

Integrals are taken on the boundary Γ of the subdomains and the method involves only A and $\partial A/\partial n$ (tangential induction) on the boundaries.

The finite element formulation (Silvester 90) is based on the Galerkin method and we have for the domain Ω of boundary Γ:

$$\int_{\Omega} [\nu \text{ grad } A \text{ grad } w - J w] d\Omega - \int_{\Gamma} w \, \nu \partial A / \partial n \, d\Gamma = 0 \tag{3}$$

where ν is the magnetic reluctivity, J the current density and w the weighting function. The Galerkin method is obtained by choosing the same basic functions w_i for the weighting of the residue and the discretization of A given by $A = \Sigma A_i w_i$ where A_i are the model values. Here the w_i are chosen as piecewise linear functions on triangles.

The boundary term is usually used to apply a Neumann boundary condition. Here it is used at the interface between the finite element and the boundary element domains to couple the methods. This can be extended to the boundary between two finite element subdomains. The tangential field $\nu\partial A/\partial n = H_t$ is taken as an unknown on the boundary and the boundary term of (3) is introduced. It leads to the same solution for the vector potential A as the classical formulation but is also provides the value of the tangential field on the boundary.

As a demonstration, consider the boundary between two finite element domains (figure 1).

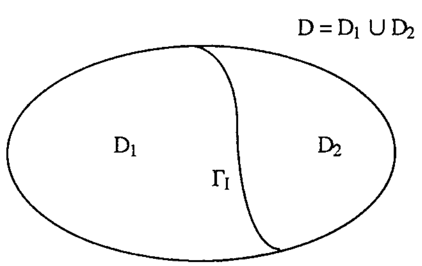

Figure 1: interface between two subdomains

In the classical finite element formulation the interface Γ_I does not exist and D_1 and D_2 form a single domain. In this case, the finite element equation for a node i on the interface is represented as follows:

$$\sum_{j \in D_1 \cup D_2} \alpha_{ij}^{D_1 \cup D_2} A_j = 0 \tag{4}$$

It involves only the nodal values A_j of the potential vector. In the subdomain method we have two equations and the tangential field is involved:

$$\sum_{j \in D_1} \alpha_{ij}^{D_1} A_j + \sum_{j \in \Gamma_I} \beta_{ij} H_{tj} = 0 \tag{5a}$$

$$\sum_{j \in D_2} \alpha_{ij}^{D_2} A_j - \sum_{j \in \Gamma_I} \beta_{ij} H_{tj} = 0 \tag{5b}$$

We know that $\alpha_{ij}^{D_1 \cup D_2} = \alpha_{ij}^{D1} + \alpha_{ij}^{D2}$. The superscripts D_1, D_2... indicate the domain of integration involved in the computation of the coefficients. The opposite signs of the $\beta_{ij} H_{tj}$ terms in equations (5a) and (5b) insure that their sum leads to equation (4). It implies that the subdomain method is equivalent to the classical method and gives the same value to the potential (if numerical errors are neglected). The particular value of the coefficients β_{ij} allows the physical interpretation of H_{ti} as the nodal value of the tangential field.

Eddy currents

Using Ohm's law, the case of eddy currents can be dealt with by introducing

$$J = \sigma E = \sigma\left(-\frac{\partial A}{\partial t} - U\right) \tag{6}$$

as the expression for the current density in equation (3). The conductor is characterized by its electrical conductivity σ. The time derivative of A expresses the inductive effects since U = grad V is due to an externally imposed electromotive force and can be interpreted as the terminal voltage of the conductor (per unit of length).

In this case (3) becomes:

$$\int_\Omega \left[\nu \text{ grad } A \text{ grad } w + \sigma\left(\frac{\partial A}{\partial t} + U\right) w \right] d\Omega - \int_\Gamma w\, \nu \frac{\partial A}{\partial n}\, d\Gamma = 0 \tag{7}$$

The presence of the dynamical terms does not change the method of coupling. The numerical method used to discretize this transient problem is a semi discrete Galerkin method. The first

step is a spatial discretization of the domains similar to the one used in the static case. This discretization uses the purely spatial weighting function w_i and leaves a continuous time variation of the degrees of freedom. It leads to a system of ordinary differential equations:

$$[S]\frac{\partial \underline{A}(t)}{\partial t} + [M]\,\underline{A}\,(t) = \underline{b} \qquad (8)$$

where $\underline{A}$ is the vector of the nodal values of A. [S] and [M] are the matrices of the system. The non linear nature of the problem is found in the dependence of [M] on $\underline{A}$.

The next step is a time discretization that gives an algebraic system. The backward method leads to:

$$\left(\frac{[S]}{\Delta t} + [M(\underline{A}_{n+1})]\right) \cdot \underline{A}_{n+1} = \underline{b} + \frac{[S]}{\Delta t}\underline{A}_n \qquad (9)$$

where $\underline{A}_n$ and $\underline{A}_{n+1}$ are the values of $\underline{A}$ at the times t_n and t_{n+1} with $t_{n+1} - t_n = \Delta t$
This leads to a time stepping method where each step requires the resolution of the non linear algebraic system (9).

If U is given for all the conductors of the problem, differential system can be solved. Unfortunately, in most cases, it is the total current I in a conductor which has to be imposed. As the finite element formulation involves the tangential field on the boundary, the total current I can be expressed as the line integral of the magnetic field (Ampere's law):

$$I = \int_\Gamma \nu\, \partial A/\partial n \, d\Gamma \qquad (10)$$

From a more general point of view we can systematically relate to every conductor an equation like (10) and two global degrees of freedom: the total current I and the terminal voltage U. To do so, a circuit equation is necessary for each conductor. The simplest cases correspond to imposing U or I for an individual conductor but any case of conductor interconnection and electric circuit coupling can be considered (Bourmanne 91).

Resolution algorithm

The backward Euler method leads to the resolution of non linear systems of equations for a sequence of time steps. The non linear system is solved with the Newton-Raphson method. This iterative method replaces the non linear problem by a sequence of linear problems. Thus the resolution algorithm consists of two nested loops: the outer loop for time stepping and the inner loop for Newton-Raphson. For each step, the main task is to construct and solve a linear system of algebraic equations. The construction of the system consists of writing the matrice [S], the matrice [M] and its associated jacobian. The finite element method leads to a sparse symmetric system while the boundary element method leads to a full non symmetric system. In the case of the coupled method it is difficult to take into account the characteristics of the subsystems coming from the finite elements and, globally, the system is

considered as full and non symmetric. For this reason, a direct resolution method is used that is based on the LU decomposition of matrices.

For a system $Ax = b$, the decomposition of the matrice A in a product LU of triangular matrices allows the resolution of the equivalent system $LUx = b$, by backward and forward substitution. The obtained solution x^* is not equal to the exact solution x because of the rounding errors.

The residue δx is expressed by:

$$\delta x = x^* - x \tag{11}$$

If this value is introduced in the original equation, the following identity is obtained

$$A\, x^* = A\, (x + \delta x) = b + \delta b \tag{12}$$

Thanks to the fact that x is the exact solution

$$A\, \delta x = \delta b \tag{13}$$

The error may be estimated by solving

$$A\, \delta x = A\, x^* - b \tag{14}$$

The computation of the right hand member of (14) is made in double precision but all the other computations are made in single precision. The value of δx is used to obtain a better approximation of the solution and the process may be repeated with this new approximation until the error δx is small enough. This procedure is called the iterative refinement (Press 89).

Some remarks must be done on this method.

- Almost all the computations are made in single precision and no double precision vector or array storage is required.

- This method is accurate and the convergence of the process gives a control of the quality of resolution

- The resolution of (14) is very easy because the LU decomposition of A is already known. The extra cost with respect to the simple direct method is negligible.

In the present context, this method has another advantage. The iteration refinement is supposed to correct inaccuracies in the LU decomposition due to the rounding errors. During the resolution process, a sequence of algebraic systems is solved for the successive time and Newton-Raphson steps. Under the hypothesis that successive systems do no differ too much, it may be hoped that the LU decomposition of the previous system is close enough to the actual LU decomposition to allow the convergence of the iterative refinement. Thus the following strategy is adopted: for each step, the new system is generated but the old LU decomposition is first tried in the iterative refinements. If the process does not converge, the LU decomposition is updated.

Another problem is the definition of the initial conditions. While a transient resolution method is used, we are interested in the periodic problem. The transient analysis may lead to a very large computation time because several time steps are needed to settle down the system (initially unexcited) to a periodic behaviour. The solution adopted here is to use a linear complex solution to load the system. The 'numerical settling down' from linear to non linear solution is much more faster.

Example: induction furnace

Figure 2 shows a steel plate induction furnace. It is composed of a five turn coil fed by a current of 1800 A at a frequency of 7400 Hz. The particular case of a half-entered plate is considered. This plate is magnetic (magnetic characteristic is given on figure 3) and conducting (σ=2.5 10^6 S/m). The length is 450 mm and the thickness is 1 mm (aspect ratio 1/450). The total current in the plate is forced to be zero.

Considering the linear part of the saturation curve ($\mu_r = 240$), a characteristic skin depth may be computed to be equal to 0.24 mm . This value must be taken into account in the finite element meshing of the plate. Figure 4 shows the meshing of the plate. On this figure, the thickness is magnified by a factor 100.

A point is considered which is just on the boundary of the plate under the turn 3.

Figure 5 shows the time evolution of the current density for this point. The appearance of higher harmonics due to non linearity is obvious.

Figure 6 shows the time evolution of the induction along the plate for this point; The flattening of the induction is due to the saturation phenomenon.

The computation has been made with an iterative refinement. The stopping criterium is that the maximum relative correction of a component of the solution vector is less than 10^{-5}. 15 iterative refinements where allowed before deciding the process does not converge. In the case of the furnace, for the given meshing and 250 time steps per period, the LU decomposition was to be recomputed about every 4 resolutions.

Conclusion

The coupling of boundary elements and finite elements is an attractive method in electromagnetism. The principal limitation of this method is the complexity of the resolution of the involved linear systems. In the particular case of non linear transient problems, the proposed algorithm allows a substantial saving of computation time.

References

Bourmanne, P., Delincé, F., Genon, A., Legros, W., Nicolet, A., Skin effect and proximity effect in multiconductor systems with applied currents and voltages, Journal of Applied Physics, 69(8), 15 April 1991, pp. 5035-5037

Brebbia, C.A., The boundary element method for engineers, Pentech Press, London, 1984.

Nicolet, A., Ph.D. Thesis, University of Liège, Liège, May 1991.

Press, W.H., Flannery, B.P., Teukolsky, S.A., Vetterling., W.T., Numerical recipes : the art of scientific computing, Cambridge University Press, Cambridge, 1989.

Silvester, P.P., Ferrari, R.L., Finite elements for electrical engineers, Cambridge University Press, Cambridge, 1990.

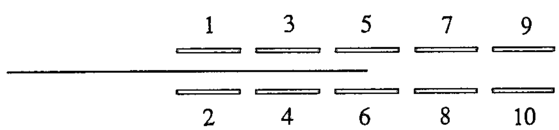

figure 2 : induction furnace

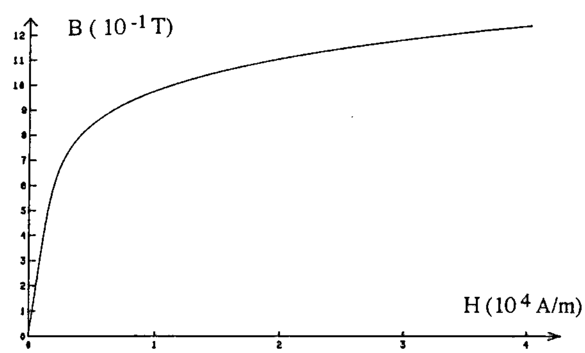

figure 3 : magnetic characteristic of the plate

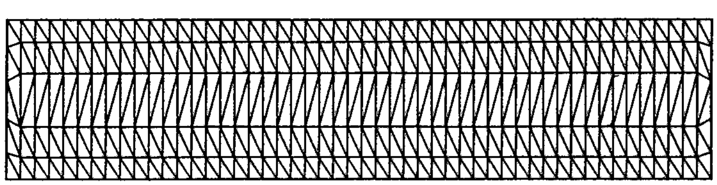

figure 4: meshing of the plate

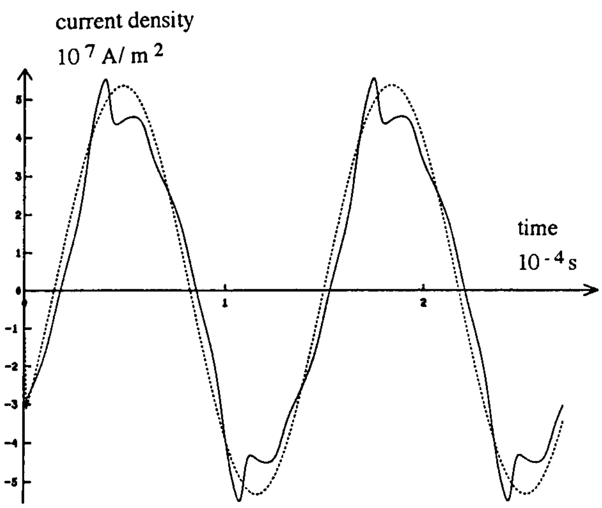

figure 5: time evolution of the current density
non linear: continuous line - linear : dashed line

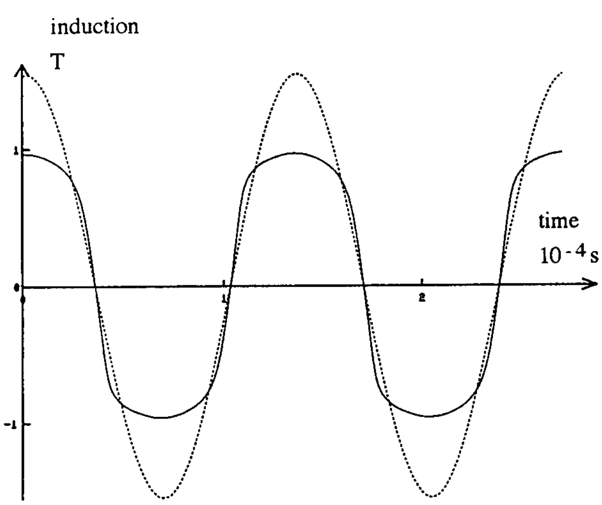

figure 6: time evolution of the induction
non linear: continuous line - linear : dashed line

ON THE DEVELOPMENT OF THE COMBINED EDDY CURRENT CODE

Z.Cheng, S.Gao, C.Ye, J.Wang, P.He

Baoding Transformer Works, Baoding 071056, China

Abstract

This paper develops a combined 3-D eddy current code based on the different sets of vector and scalar potentials, describes the large eddy current problems in electrical engineering, and proposes the numerical strategy of engineering electromagnetic field analysis.

1. INTRODUCTION

Nowadays, 3-D eddy current softwares have been large-scale produced [1,5-12] and compared each other in more detail. However, it seems that a single code is unsatisfactory to approach a large field problem, a combined code based on the $\mathbf{A}-V-\mathbf{A}-\psi$ and the $\mathbf{T}-\psi-\psi$ has been developed[13].

The major merits of the combined code is to make full use of the superiorities of each analysis methods, the number of unknown variables and the computing cost can be reduced, while the ability to deal with large eddy current problems including more type of connected regions can be enhanced, finally, the numerical implementation of the combined code is really simplified.

large eddy current problems are often encounted in electrical engineering, for example, the eddy currents (or circulating currents) are generated in big tank wall, or in steel construction parts, or in windings of large transformers. An impermissible and dangerous local overheating, in accident case, may occur there due to excessive eddy current losses, thus the development of the integrated and engineering-oriented computer aided analysis tools is of great significance.

For this reason, we made a combined 3-D eddy current code to strengthen the single analysis tool. Naturally, one can develop other kinds of combined codes to effectively solve relevant problems, it seems to be a promising way.

2. NUMERICAL STRATEGY OF LARGE EM FIELD ANALYSIS

2.1 Engineering EM field problem

It is hard to solve a large eddy current problem which can be briefly described as follows:

-Geometry: large size;
complicated shape and multi-subregions with quite different dimensions;
both the singly and the multiply connected regions;
-Material: Nonlinearity;
anisotropy;
hysterisis;
nonuniformity in the property which are time and/or space varying;
-Coupled field: electromagnetic, thermal, mechanical,and oil-fluid fields are coupled up and time dependent.

2.2 Engineering-oriented TEAM product

The TEAM workshops have played an important role in 3-D electromagnetic field analysis, many researchers pay special attention to TEAM work. We still more long to use the advanced electromagnetic analysis technique to effectively solve large engineering field problems[2], and to study some engineering-oriented TEAM products,perhaps, it can be refered to as "Engineering TEAM"[3]. A Comparison between Benchmark-TEAM and Engineering-TEAM is shown :

	Benchmark TEAM	Engineering TEAM
Problem	Benchmark prob. defined a more simple model	Engineering Prob. based on a large product
Goal	Testing [4]the effectiveness of analysis methods and their codes	Solving an engineering Prob. by both TEAMed codes and engineering dealing
Accuracy	Analysis and experiment results compared strictly	Having satisfactory engineering accuracy
Summary	To find out an effective tool	use the tools to solve engineering field prob.

2.3 "Field-Circuit" combined-type approach

A 'full-field' analysis of a large eddy current problem above mentioned is almost impossible due to the requiement of substantial computer resource, however, a "Field-Circuit" approach is a really practical method, namely, part circuit,part field, imaginatively, we can say that "ZOOM OUT" with the circuit methods and "ZOOM IN" with the field analysis. The key point is to set up a resolvable model which can be solved by TEAMed code or combined TEAMed code.

3. ON THE COMBINED EDDY CURRENT CODE

A typical large eddy current problem involving both singly and multiply connected regions is shown in Fig.1. In the combined code proposed here the $\vec{A}$-V-$\vec{A}$-ψ and the $\vec{T}$-ψ-ψ approaches[1] are used to deal with the multiply and singly connected regions, respectively. If the surface of the $\vec{A}$-V conductor is not regular then one can prescribe an 'artificial' regular boundary for easy interfacing, see Fig.1.

3.1 Formulation

The fundamental equations of the combined code are as follows:

1) $\vec{A}$-v-$\vec{A}$ subregion

$$\nabla \times \frac{1}{\mu} \nabla \times \vec{A} - \nabla \frac{1}{\mu_a} \nabla \cdot \vec{A} + \sigma \left(\frac{\partial \vec{A}}{\partial t} + \nabla V \right) = 0$$

$$\nabla \cdot \sigma \left(- \frac{\partial \vec{A}}{\partial t} - \nabla V \right) = 0$$

2) $\vec{T}$-ψ subregion

$$\nabla \times \frac{1}{\sigma} \nabla \times \vec{T} - \nabla \frac{1}{\sigma} \nabla \cdot \vec{T} + \mu \frac{\partial}{\partial t} (\vec{H}_s + \vec{T} - \nabla \psi) = 0$$

$$\nabla \cdot \mu (\vec{H}_s + \vec{T} - \nabla \psi) = 0$$

3) Common current-free region,

$$\nabla \cdot \mu_a (\vec{H}_s - \nabla \psi) = 0$$

4) Boundary conditions

on the interface between the $\vec{A}$ - V conductor or $\vec{A}$ subregions and the current-free subregions,

$$\vec{A} \cdot n = 0$$

if the $\vec{A}$ - V conductor has a symmetric plane, following conditions,

$$\vec{A} \times n = 0$$

and

$$V = 0$$

must be applied on the symmetric plane. Similarly, on the interface between the $T-\psi$ conductor and the current-free subregion,

$$\vec{T} \times n = 0$$

while on the symmetric plane of the $T-\psi$ conductor

$$\vec{T} \cdot n = 0$$

where n denoted the normal unit vector.
According to the actual situation of the magnetic field,

$$\psi = 0$$

or

$$\partial \psi / \partial n = 0$$

at the far field boundary.

3.2 Test example

A trend analysis of eddy currents including the distribution of eddy currents and the convegence behaviours of nonlinear solution is of the utmost importance for testing an analysis method and corresponding code.

First, the eddy current analysis has been done by a very simple combined-type test model in which the A-V and the T-ψ conductors are surrounded by the current-free space,the total number of elements is to 128,and 8 elements of 2 layers are for each conductor, it is named 'Micro-Benchmark' model as shown in Fig.2-a. The distribution of eddy currents in steel plates and the convergence trends using different relaxation factors are shown in Fig.2-b and 2-c , respectively.

Second, the reasonableness of the distribution of eddy currents has been further verified in a larger computing scale, the corresponding test model show in in Fig.3-a. In both test models the uniform and time varying magnetic fields normal to the steel plate are applied. The plots of eddy currents for second test model are shown in Fig.3-b.

We also made two engineering model, as shown in Fig.4-a and 5-a, to verify the combined code, the distributions of 2-D magnetic fields are shown in Fig.4 -b and 5-b, respectively.

4. SUMAARY

How to use the advanced TEAM products to successfully solve a large eddy

current problem is still a challenging and interested problem, engineers need some integrated engineering-oriented analysis tools. We have proposed and made a 3-D combined eddy current code, it has provided some reasonable results in test models, and we will further aim at the following subjects:

- the inherrent relationship between the solutions of flux (or eddy currents) by both $\mathbf{A}$-v and $\mathbf{T}$-ψ versions of TEAM products;
- the numerical stability of the combined code.

5. REFERENCES

[1] O.Biro,K.Preis,'Finite element analysis of 3-D eddy currents', IEEE Trans. Mag-26,2 (1990), pp. 418-423

[2] Z.Cheng,S.Gao,J.Wang,'Engineering solution of engineering field problems', 3-D electromagnetic field analysis (edited by T.Nakata),(1990),PP.151-154

[3] Z.Cheng,S.Gao,D.Zhang,J.Wang,C.Ye, 'Engineering resolvability of engineering eddy current problems', Proc. of 7th annual review of progress in applied computational electro-magnetics, (1990) pp.551-556

[4] TEAM Workshops: Test Problems, April 1988

[5] C.J.Carpenter,'Comparison of alternative formulations of 3-dimensional magnetic-field and eddy-current problem at power frequencies', Proc.IEE. Vol.124,Nov.1977,pp.1026-34

[6] C.W.Trowbridge,'Electromagnetic computing: the way ahead', IEEE Trans. Mag-24,2 (1988), pp. 8-13

[7] T.Nakata,N.Takahashi,K.Fujiwara,K.Muramatsu,' Investigation of effectiveness of various methods with different unknown variables for 3D eddy current analysis', IEEE Trans. Mag-26, (1990), pp.442-445

[8] W.Renhart,H.Stogner,K.Preis,'Calculation of 3D eddy current problems by finite element method using either an electric or a magnetic vector potential', IEEE Trans. Mag-24, (1987), pp.122-125

[9] A.Bossavite,J.C.Verite,'The Trifou code: Solving the 3-D eddy-currents problem by using h as state variable', IEEE Trans. Mag-19, (1983), pp.2465-70

[10] D.Rodger,J.F.Eastham, ' A formulation for low frequency eddy current solutions', IEEE Trans. Mag-19, (1983), pp.2443-46

[11] C.R.I.Emson,J.Simkin,'An optimal method for 3D eddy currents', IEEE Trans. Mag-19, (1983), pp.2450-2452

[12] P.J.Leonard, D.Rodger,R.J.Hill-Cottingham, ' Calulation of AC losses in current forced conductors using 3D finite elements and the $\mathbf{A}\psi$ V method', IEEE Trans. Mag-26, (1990), pp.490-492

[13] Z.Cheng,S.Gao,C.Ye,P.He, ' A 3-D combined code for solving large eddy current problems', Paper to ISEM-Nagoya, Jan.1992.

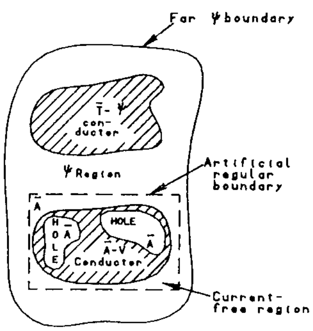

Fig.1 Model for a combined code

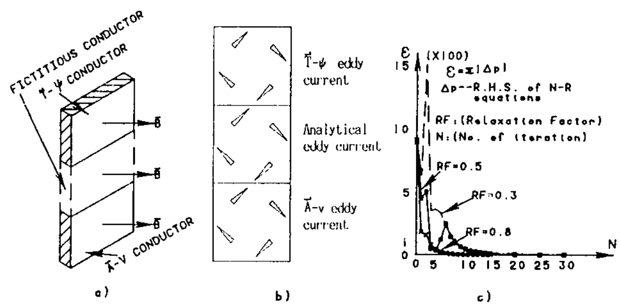

Fig.2 Test model 1 and trend analysis by combined code

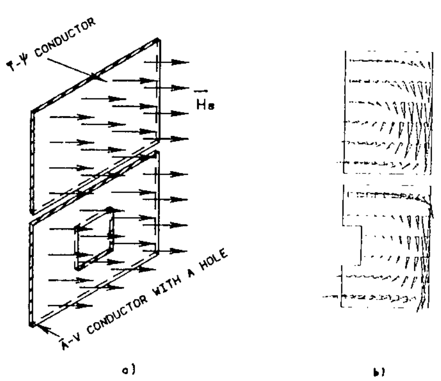

Fig.3 Test model 2 and distribution of eddy currents by combined code

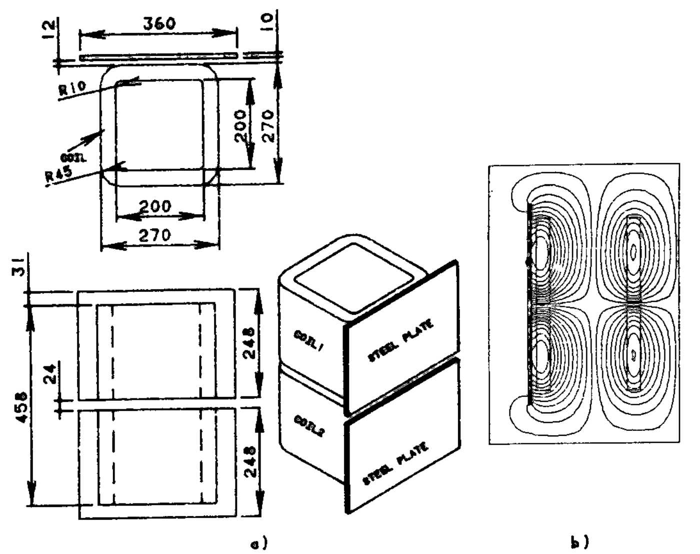

Fig.4 Engineering model 1 and 2D magnetic fied analysis

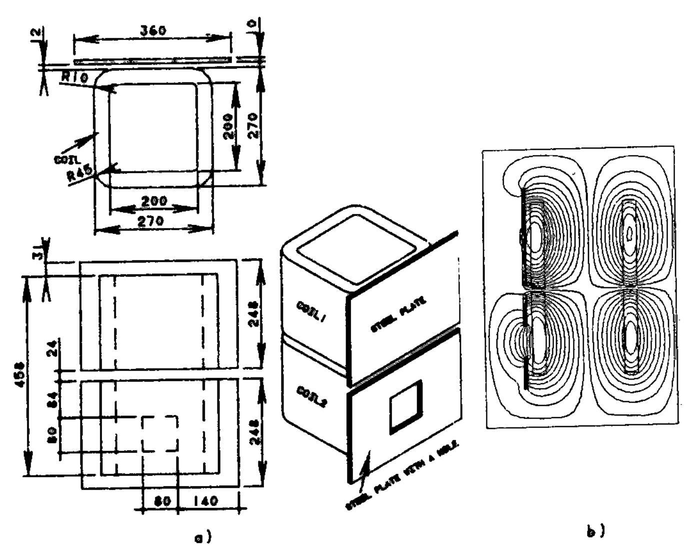

Fig.5 engineering model 2 and magnetic field analysis

Electrostatic Qualification of High and Very High Voltage Insulators.

Al.M.Morega[1], P.Minciunescu[2]

The most common insulating elements for high and very high voltage electrical power lines are the tempered-glass, "cape-rod" ones. The electrostatic qualification of such systems has as main goal the optimization of their design in terms of geometry, structure and dielectric properties. The present study is an integral method numerical approach to the Laplace problem with Dirichlet boundary conditions. The main difficulty of this problem is recognized to be its complicated, multi-structured geometry as well as its axial symmetry, which (in terms of the integral method) translates into elliptic integrals.

1. Introduction.

The cape-rode insulators made of tempered glass are the basic elements of the insulating chains used in the construction of high and very high as well as medium voltage electrical lines. An important role in their design optimization is played by the electrostatic modelling. The goal of this task is to study the influence of the shape of the electrodes as well as the specific insulation scheme (main insulating body, binding cement, etc.) on the overall dielectric properties.

The complicated, multi-structured geometry of the insulator and the fact that the associated eletrostatic field problem is of infinite domain type, determined us to use the boundary element method. This integral technique belongs to the group of numerical methods and is recognized [2,4] for its ability in addressing problems in this class.

2. Assumptions.

A set of restrictive assumptions is formulated in order to reduce the real, tri-dimensional problem to a bi-dimensional one, preserving however the main features of the real case:

- the cape-rod system is recognized to have axial symmetry;
- the effects of the armatures and clamps used to fasten the insulator to the pillars of the electric line and to the lines themselves are neglected;
- the presence of the other insulators of the chain is neglected;
- a constant voltage drop is assumed between the metalic armatures of the cape-rod system;
- the main insulating body (tempered glass) and the binding cement between the armatures are electrically linear, homogeneous and isotropic materials.

The cape-rod system can thus be considered in an electrostatic regime, governed by Laplace equation. Dirichlet boundary conditions (for the boundary at finite distance) as well as asympthotic conditions are specified as closure for the field problem.

For short, the system is a capacitor with multiple dielectric layers and the above assumptions observe some practical conditions in which it is tested in HVT laboratories.

[1] Dept.of Electrical Engineering, Poly.Institute of Bucharest, Romania
present address: Dept.of Mechanical Eng, Duke University, Durham, NC, 27706, USA

[2] The Institute for Research in Electrotechnics (ICPE), Bucharest, Romania

3. Numerical Model.

In local formulation the mathematical model is descriebed by the following equations:

$$\Delta V(\xi) = 0, \qquad \xi \in \Omega \tag{1}$$

$$V_{C_1} = V_1 \tag{2}$$

$$V_{C_2} = V_2 \tag{3}$$

where V is the electrostatic potential (for short, potential), Ω is the dielectric domain (outside the armatures), C_1, C_2 are the surfaces of the armatures (the boundary at finite distance), V_1, V_2 are the specified Dirichlet boundary conditions.

The integral formula which solves this problem is [1,2]:

$$\alpha(\xi)V(\xi) + \int_\Gamma V(x)\frac{\partial V^*}{\partial n}(\xi,x)\, d\Gamma(x) = \int_\Gamma \frac{\partial V}{\partial n}(x)V^*(\xi,x)d\Gamma(x) \tag{4}$$

where $\alpha(\xi)$ is the solid angle under which the Γ boundary is "seen" from the current point ξ; the quantities noted as $()^*$ represents a weighting function introduced by a biscalar field and identified with the fundamental solution of the problem (1)-(3).

As in this problem the boundary has no Neumann "portions", the equation (4) generates a second-order Fredholm type integral equation for the unknown function $\partial V/\partial n$ (normal derivative of V), when $\xi \in \Gamma$.

In order to solve (4) on Γ, the boundary is discretized in elements (segments, for a bi-dimensional problem); on each element the function and its normal derivative are supposed constant (collocation method). The curvilinear integrals generated by this discretization are evaluated using a four-point Gauss-Legendre quadrature rule and analytic formulas. Finaly, a linear system of algebraic equations is obtained.

Cylindrical coordinates (R,θ,z) are used for this axial-symmetric case. The area element, is $d\Gamma(x_1,x_2,x_3)=Rd\theta ds$, $ds=ds(R,z)$ and the integral equation (4) is written as:

$$\alpha(\xi)V(\xi) + \int_\Gamma V(x)\left(\int_0^{2\pi} \frac{\partial V^*}{\partial n}(\xi,x)d\theta(x)\right)R(x)ds = \int_\Gamma \frac{\partial V(x)}{\partial n}\left(\int_0^{2\pi} V^*(\xi,x)d\theta(x)\right)R(x)ds \tag{5}$$

where V^* is the fundamental solution for the 3-D problem:

$$V^*(\xi,x) = \frac{1}{4\pi}\frac{1}{r(\xi,x)} \tag{6}$$

After several transformations: (Appendix 1)

$$V^*(\xi,x) = \frac{1}{\pi\sqrt{(a-b)}}\,\mathrm{cel1}(K_c) \tag{7}$$

where cel1 is the complete elliptic integral of the first order [3]. Its normal derivative, on the boundary, (Appendix 2) is:

$$\frac{\partial \overline{V}^*}{\partial n}(\xi,x) = -\frac{1}{4\pi}\{n_R(x)\,R(x) - n_z(x)\left[Z(x) - Z(\xi)\right]\}\frac{4}{(a-b)^{\frac{3}{2}}}\,\mathrm{cel}(K_c,K_c^2,1,1) +$$
$$\frac{n_R(x)\,R(x)}{\pi b}\frac{1}{\sqrt{(a-b)}}\left[-\,\mathrm{cel1}(K_c) + \frac{a}{a-b}\,\mathrm{cel}\left(K_c,K_c^2,1,1\right)\right] \qquad (8)$$

With these expressions ($\overline{V}^*$ and $\partial\overline{V}^*/\partial n$), (5) is written on Γ as:

$$\alpha(\xi)\,V(\xi) + \int_\Gamma V(x)\frac{\partial \overline{V}^*}{\partial n}(\xi,x)\,R(x)\,ds = \int_\Gamma \frac{\partial V}{\partial n}(x)\,\overline{V}^*(\xi,x)\,R(x)\,ds \qquad (9)$$

After discretization ($\Gamma = \cup\, \Gamma_j$) and cosidering the equivalent sources on the boundary elements, an algebraic system of equations is obtained:

$$\frac{1}{2}V_i + \sum_{j=1}^{N}\left(\int_{\Gamma_j}\frac{\partial V^*}{\partial n}d\Gamma\right)V_j = \sum_{j=1}^{N}\left(\int_{\Gamma_j}V^* d\Gamma\right)\left(\frac{\partial V}{\partial n}\right)_j, \qquad i = 1,\dots,n \qquad (10)$$

$$H_{ij} = \int_{\Gamma_j}\frac{\partial V^*}{\partial n}d\Gamma, \qquad G_{ij} = \int_{\Gamma_j}V^* d\Gamma \qquad (11)$$

$$\mathbf{H}\,[V] = \mathbf{G}\,[\partial V/\partial n] \qquad (12)$$

The integrals H_{ij}, G_{ij}, ($i \neq j$) are evaluated using a Gauss-Legendre quadrature rule. H_{ii}, G_{ii}, singular integrals, the fundamental solution, $\overline{V}^*$, and the normal derivative $\partial\overline{V}^*/\partial n$ can be expressed in terms of Legendre functions of second kind [2] (Appendix 3).

When the insulating domain has a multi-dielectric structure, the interfaces are included in the boundary. The corresponding equations are:

$$\varepsilon_1\frac{\partial V_1}{\partial n}_{\Gamma_i} = -\,\varepsilon_2\frac{\partial V_2}{\partial n}_{\Gamma_i}, \quad V_{1\Gamma_i} = V_{2\Gamma_i} \qquad (13)$$

The above equations are added to the previousely descriebed system.

4. Calculations and Results.

A PASCAL code (for PC XT and AT systems), designed for integral methods in static and steady regimes - Laplace and Poisson bi-dimensional problems with Dirichlet and/or Neumann boundary conditions - has been used to implement numerically our electrostatic model. Its original input interface, addapted for a fast but accurate as well as interactive description of the problem, together with the built-in mesh generator (up to seven different grid generating systems) for the interior domains, enabled significant cut-offs in terms of time for solving a specific case.

The influence of the geometry, the structure as well as the materials properties have been investigated for a number of most common cape-rod systems designs. The outputs are field spectra (equipotential lines), fluxes through specified surfaces as well as numerical values for the electrostatic potential and/or its gradient at specified locations. We also report the tests of numerical (boundary) convergence carried out in order to validate the outputs.

A first module is designed to input the geometry of the domain and the electrical properties of the media. It performs also the discretization of the boundary. An ensamble of procedures for numerical grid generation (analytic: Laplace and Poisson elliptic systems, algebraic: linear, Lagrange, Hermite cubic and transfinite

interpolations) is available and enables the formulation of an adequate set of interior meshes, used to compute the potential inside the domain.

A second module generates the matrices and solves the algebraic system: LU (Crout) factorization/backward substitution with optimization of the solution as well as Gauss method are available.

A third module serves as postprocessor; it makes use of the interior meshes generated by the first module. These modules are linked and interactively called. A built-in full page text editor is provided as well.

In Figure 1. is depicted a typical discretized structure: D_1 domain - bounded by the cape and the insulating body ($\varepsilon_1=3$); D_2 domain - the insulating (glass) body ($\varepsilon_2=3$); D_3 domain - the binding cement between the rod and the insulating body ($\varepsilon_3=3$); D_1, D_2, D_3 and D_4 (the domain outside the system) surfaces represent the geometrical support of the integral equation which is the basis of the method. They have been discretized in 254 elements, the matrices assembled and the system solved. The electrical potential was computed at the interior nodes of the domain (defined by the meshes generated algebraically, Figure 2).

We have studied the influence of the finness of the boundary discretization utpon the convergence of the numerical solution. Typically, the quadratic quantity:

$$A = \sum_i \left(\frac{\partial V}{\partial n}\right)_i^2 l_i \tag{14}$$

was computed for different discretization modes (19, 21, 23 and 25 boundary elements) over the rod surface. The variation of this quantity, in relative units, is given in Figure 3 for $V_1=100V$, $V_2=0V$. It has a monotonic decaying behaviour, suggesting the convergence of the numerical scheme. The relative variation of this quantity is given in Figure 4, as $|A_{(k+1)}-A_{(k)}| \,/\, |A_{(k)}|$, where k denotes succesive grid refinements.

The influence of the permitivities of the dielectric parts for a specific cape-rod insulator (Figures 5-8; the domains D_1 and D_3 have the same ε_{cement}) was then analysed. Apparently, the equipotential lines are concentrated in the vicinity of the cape when $\varepsilon_{cement} > \varepsilon_{glass}$ (Figures 5,6 and 7,8). Figures 5,7,8 suggest the opposite effect when $\varepsilon_{glass} > \varepsilon_{cement}$.

The influence of different geometries has been investigated as well (Figures 9-12, all cases have the same ε_{glass} and ε_{cement}). We could note no important distinction from the spectrum point of view.

As a general, qualitative, remark the bottom face of the cape represents the zone with the greatest gradient of the potential. As a consequence, it is adequate to avoid small curvature radii in the design of this electrode. The inner face of the insulator does not influence significantly the distribution of the potential.

5. Conclusions.

The boundary element method has the advantage of a relative simple description for complicated geometrical structures making use of the boundary rather then the domain. The dimension of the geometrical support is thus one order lower. It allows also for a straightforward approach of infinite domain problems. The difficulties encountered in this axial symmetric case are generated mainly by the elliptic integrals which need a special treatment, and care has been taken to solve them accurately [3].

The collocation techinque used here is a satisfactory first-level approximation. If higher accuracy is needed, then it is advisable to use an orthogonal polynomial scheme, as the mesh further refinement is limited by the available PC resources.

The method of grid generation inside the domain (for postprocessing purposes) allows a higher level of adaptiveness of the interior mesh to the boundary

grid (used to actualy solve the problem) and provides for connecting the present code with finite differences or finite element codes, if needed.

6. Acknowledgements.

The theme of this study has been generated by the necessity of an electrostatical model for cape-rod insulators tested in the HVT laboratory (the Electro-Energetic Department, Poly.Inst.of Bucharest). We mention the special contribution of Professor S.Coatu for the discussions we had as well as the formulation of the theme which was a part of the MS disertation of P.Minciunescu. We gratefully acknowledge our debt to Professor A.Moraru for the fruitfull advises and suggestions he made during the project completion.

Appendix 1

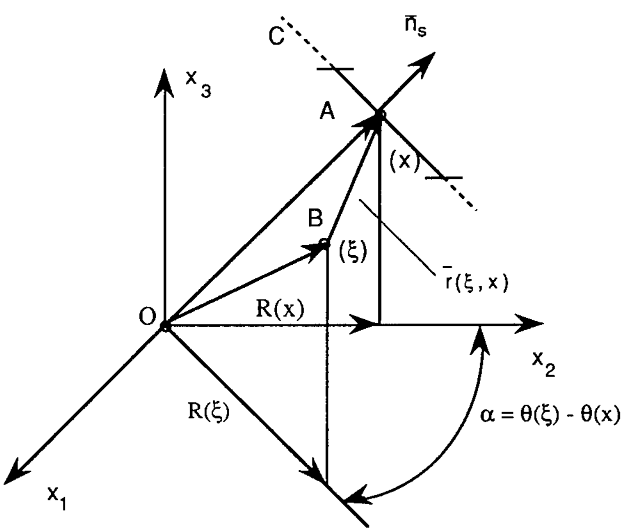

$$\overline{V}^*(\xi,x) = \int_0^{2\pi} V^*(\xi,x)\,d\theta(x); \quad \frac{\partial \overline{V}^*}{\partial n}(\xi,x) = \int_0^{2\pi} \frac{\partial V}{\partial n}(\xi,x)\,d\theta(x)$$

$$a = R^2(\xi) + R^2(x) + [Z(\xi) - Z(x)]^2; \quad b = 2\,R(\xi)\,R(x); \qquad m = \frac{2\,b}{a+b}$$

$$V^*(\xi,x) = \frac{1}{4\pi}\,\frac{1}{r(\xi,x)} = \frac{1}{4\pi\left\{R^2(\xi) + R^2(x) - 2\,R(x)R(\xi)\cos\left[\theta(\xi)-\theta(x)\right] + [Z(\xi) - Z(x)]^2\right\}^{\frac{1}{2}}}$$

$$V^*(\xi,x) = \frac{1}{4\pi}\int_0^{2\pi} \frac{d\theta}{r} = \frac{1}{2\pi}\int_0^{2\pi} \frac{d\theta}{(a-b\cos\theta)^{\frac{1}{2}}} = \frac{1}{\pi}\int_0^{\infty} \frac{dt}{\sqrt{1+t^2}\,\sqrt{(a-b)+t^2(a+b)}} =$$

$$= \frac{1}{\pi\sqrt{a-b}} \int_0^{\infty} \frac{dt}{\sqrt{(1+t^2)(1+K_c^2 t^2)}}; \qquad t = \tan\frac{\theta}{2}; \quad K_c = \sqrt{\frac{a+b}{a-b}}$$

$$\overline{V}^*(\xi,x) = \frac{1}{4\pi\sqrt{a-b}}\,\mathrm{cel1}(K_c); \qquad \mathrm{cel1}(K_c) = \int_0^{\infty} \frac{dt}{\sqrt{(1+t^2)(1+K_c^2 t^2)}}$$

Appendix 2

$$\frac{\partial \overline{V}^*}{\partial n}(\xi,x) = \frac{1}{4\pi}\frac{\partial}{\partial n}\left(\frac{1}{r(\xi,x)}\right) = \frac{1}{4\pi}\left(-\frac{1}{r^2(\xi,x)}\right)\frac{\overline{n}_s\,\overline{r}(\xi,x)}{r(\xi,x)} = -\frac{\overline{n}_s(x)\,\overline{r}(\xi,x)}{r^3(\xi,x)}$$

$$\overline{r}(\xi,x) = \overline{OA} - \overline{OB} = R(x)\overline{u}_2 + Z(x)\overline{u}_3 - \left[R(\xi)\cos\alpha\,\overline{u}_2 + R(\xi)\sin\alpha\,\overline{u}_1 + Z(\xi)\overline{u}_3\right]$$

$$\overline{n}_{s(x)} = n_R(x)\,\overline{u}_2 + n_z(x)\,\overline{u}_3$$

$$\frac{\partial \overline{V}^*}{\partial n}(\xi,x) = -\frac{1}{4\pi}\int_0^{2\pi} \frac{n_R(x)\left[R(x) - R(\xi)\cos\alpha\right] + n_z(x)\left[Z(x) - Z(\xi)\right]}{\left\{R^2(x) + R^2(\xi) - 2\,R(x)\,R(\xi)\cos\alpha + \left[Z(x) - Z(\xi)\right]^2\right\}^{\frac{3}{2}}}\,d\alpha =$$

$$= -\frac{1}{4\pi}\int_0^{2\pi} \frac{n_R(x)\,R(x) - n_z(x)\left[Z(x) - Z(\xi)\right]}{(a - b\cos\alpha)^{\frac{3}{2}}}\,d\alpha + \frac{1}{4\pi}\int_0^{2\pi} \frac{n_R(x)\,R(\xi)\cos\alpha}{(a - b\cos\alpha)^{\frac{3}{2}}}\,d\alpha =$$

$$= c_1\,I_1 + c_2\,I_2$$

$$I_1 = \int_0^{2\pi} \frac{d\alpha}{(a - b\cos\alpha)^{\frac{3}{2}}} = 4\int_0^{\infty} \frac{\sqrt{(1+t^2)}}{\left[(a-b) + t^2(a+b)\right]^{\frac{3}{2}}}\,dt = \frac{4}{(a-b)^{\frac{3}{2}}}\int_0^{\infty} \frac{\sqrt{1+t^2}}{\left[1 + b^2(a+b)/(a-b)\right]^{\frac{3}{2}}}\,dt =$$

$$= \frac{4}{(a-b)^{\frac{3}{2}}}\,\mathrm{cel}\left(K_c,\,K_c^2,\,1,\,1\right)$$

$$I_2 = \int_0^{2\pi} \frac{\cos\alpha}{(a - b\cos\alpha)^{\frac{3}{2}}} d\alpha = -\frac{1}{b}\int_0^{2\pi} \frac{d\alpha}{\sqrt{a - b\cos\alpha}} + \frac{a}{b}\int_0^{2\pi} \frac{d\alpha}{(a - b\cos\alpha)^{\frac{3}{2}}} =$$

$$= \frac{1}{b}\frac{4}{\sqrt{a-b}}\,\mathrm{cel1}\,(K_c) + \frac{a}{b}\frac{4}{(a-b)^{\frac{3}{2}}}\,\mathrm{cel}\left(K_c,\, K_c^2,\, 1,\, 1\right)$$

$$\mathrm{cel}\,(K_c,\, p,\, a,\, b) = \int_0^{\infty} \frac{a + b\xi^2}{\left(1 + p\xi^2\right)\sqrt{\left(1+\xi^2\right)\left(1 + K_c^2\xi^2\right)}} d\xi$$

Appendix 3

$$\overline{V}^*(\xi, x) = \frac{\sqrt{8}\, Q_{-\frac{1}{2}}(\gamma)}{b^{\frac{1}{2}}}$$

$$\frac{\partial \overline{V}^*}{\partial n}(\xi, x) = -\frac{\sqrt{8}}{R(x)\sqrt{b}} \left(\begin{array}{c} \left[\dfrac{Q_{-\frac{1}{2}}(\gamma)}{2} + \dfrac{R^2(\xi) - R^2(x) + \left[Z(\xi) - Z(x)\right]^2}{b} \cdot \dfrac{d\, Q_{-\frac{1}{2}}(\gamma)}{d\gamma}\right] n_R(x) + \\ \dfrac{Z(\xi) - Z(x)}{R(\xi)} \dfrac{dQ_{-\frac{1}{2}}(\gamma)}{d\gamma} n_Z(z) \end{array} \right)$$

$$\gamma = 1 + \frac{a - b}{b}$$

$$Q_{\frac{1}{2}}(\gamma) = -\frac{1}{2}\ln\left(\frac{\gamma - 1}{32}\right)$$

$$\frac{dQ_{\frac{1}{2}}(\gamma)}{d\gamma} = -\frac{1}{2\,(\gamma - 1)}$$

References.

[1] Mocanu,C.I.,-"Teoria cimpului electromagnetic", Editura Didactica si Pedagogica, Bucuresti, 1981.

[2] Brebbia,C.A., Tells,J.C.F., Wrobel,L.C.,-"Boundary Element Techniques - Theory and Applications in Engineering", Springer Verlag, Berlin, 1984.

[3] Bulirsch,R.,-"Numerical Calculation of Elliptic Integrals and Elliptic Functions", Numaerische Mathematik, 7, 78-90, Handbook Series, Special Functions, 1965.

[4] Brebbia,C.A.,-"The Boundary Element Method for Engineers", Pentech Press, London, Plymouth, 1984.

[5] Thompson,J.F, Warsi,Z.U.A, Mastin,W.C.,-"Numerical Grid Generation. Foundation and Applications.", North Holland, Elsevier Science Publising Co., 1985.

[6] Press,W.H., Flannery,B.P., Teukolsky,S.A., Vetterling,W.T.,-"Numerical Recipies in Pascal. The Art of Scientific Computing.", Cambridge University Press, 1989.

* Turbo PASCAL v5.5, 6.0 - Borland International.

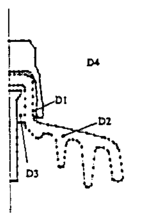

Figure 1

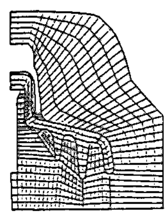

Figure 2

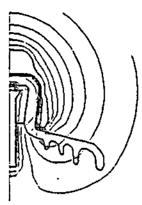

Figure 9

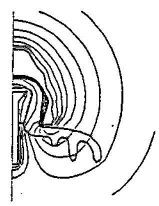

Figure 10

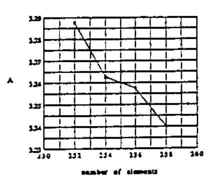

Figure 3

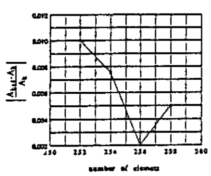

Figure 4

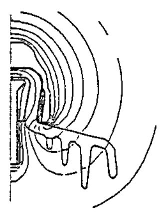

Figure 11

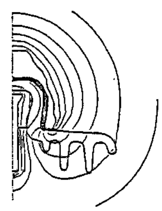

Figure 12

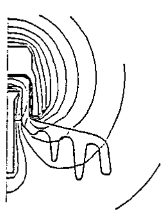

$\varepsilon_1=3;\ \varepsilon_2=3;\ \varepsilon_3=3;\ \varepsilon_4=1$

Figure 5

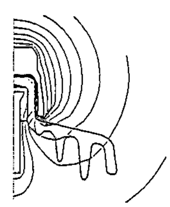

$\varepsilon_1=5;\ \varepsilon_2=3;\ \varepsilon_3=5;\ \varepsilon_4=1$

Figure 6

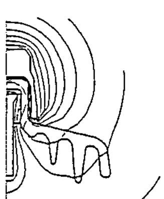

$\varepsilon_1=3;\ \varepsilon_2=5;\ \varepsilon_3=3;\ \varepsilon_4=1$

Figure 7

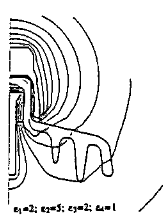

$\varepsilon_1=2;\ \varepsilon_2=5;\ \varepsilon_3=2;\ \varepsilon_4=1$

Figure 8

Hybrid Calculation of the Magnetic Vector Potential and Impedance for a Coil in Air

D. D. Derkacht, L. D. Philipp, D. J. Lynch, A. Mahmood
Washington State University at Tri-Cities, Richland WA 99352

Abstract

A well known triple integral expression for the magnetic vector potential of a circular coil with a rectangular cross section is used to create a hybrid method for calculating the magnetic vector potential. The technique combines two analytical integrations and one numerical integration to provide an efficient method for calculating the magnetic vector potential at any field point. Coil inductance is also calculated. While other methods calculate the inductance directly, this method differs in that it also provides quantitative information about the magnetic vector potential. Magnetic flux density and electric field intensity are also calculated from the magnetic vector potential.

Introduction

It is useful to know values of magnetic vector potential for a reference test case when working with eddy current programs that specify boundary values imposed along the edges of a finite element mesh. For a coil in air, the magnetic vector potential can be calculated at any field point without specifying boundary values other than those required by the Helmholtz theorem, that the field decrease to zero at infinity, assuming no sources there. This provides reference values of magnetic vector potential at nodes for eddy current programs and allows conclusions to be drawn about boundary values and mesh specifications which can be counter intuitive.

A circular coil with a rectangular cross section (see Figure (1)), driven by a sinusoidal current, generates a time-harmonic electromagnetic field. Ignoring coil resistance and assuming linear, isotropic and homogeneous material throughout space, a new expression for the magnetic vector potential, **A**, can be derived from a familiar triple integral and evaluated numerically at any field point.

While there exists in the literature analytical expressions for the magnetic vector potential that are valid for computer implementation, the expression derived in this paper was chosen because of its simplicity. Further, a literature search showed that this expression for vector potential is new, though others have derived different expressions in terms of one dimensional integrations [1].

Given numerical values of **A** in the coil cross-section, the coil inductance can then be calculated. Accurate calculation of coil inductance is computationally intensive. There are, however, formulas that provide estimates for coil inductance. For example, V. G. Welsby published the following formula [2]:

$$L = \frac{k(\pi N)^2(r_1 + r_2)^2}{l(10^9)}$$

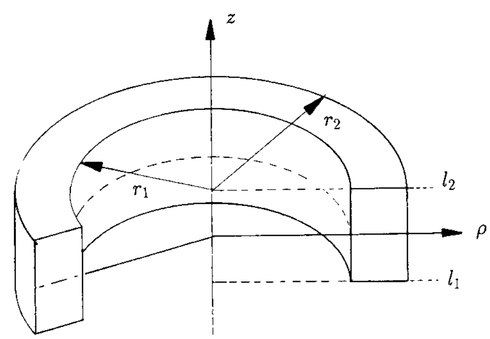

Figure 1: The Coil Cross Section for a Circular Coil.

where k, a constant, is

$$k = \left[1 + 0.45\left(\frac{r_1 + r_2}{l}\right) + 0.84\left(\frac{r_2 - r_1}{l}\right) + 0.64\left(\frac{r_2 - r_1}{r_2 + r_1}\right)\right]^{-1}.$$

In this result r_1 and r_2 are inner and outer coil radii respectively in inches, l is the coil length in inches and N is the turns density in turns per square inch. While this formula provides a value for the coil inductance, it offers no information about the magnetic vector potential. An analytical expression for the inductance of a coil in air given by Dodd et. al. [3] is

$$L = \frac{2\pi\mu n^2\bar{r}}{(l_2 - l_1)^2(r_2 - r_1)^2}\int_0^\infty \frac{1}{\alpha_o^3\alpha^3}J^2(r_2, r_1)\left\{\alpha_o(l_2 - l_1) + e^{-\alpha_o(l_2 - l_1)} - 1\right\}d\alpha \tag{1}$$

where $\bar{r} = (r_2 + r_1)/2$, the average of the inner and outer coil radii, l_1, l_2, r_1 and r_2 are as in Figure (1), n is the number of turns of wire in the coil's cross section, $\alpha_o = \sqrt{\alpha^2 - \bar{r}^2\omega^2\mu_o\epsilon_o}$ where ω is the angular frequency and $(1/\alpha^2)J(r_2, r_1) = (1/\alpha^2)\int_{\alpha r_1}^{\alpha r_2} xJ_1(x)\,dx$ where J_1 is a Bessel function of the first kind. SI units are used for all quantities. The computer implementation of this integral expression [4] provides accurate values for the coil inductance as verified by other investigators [5], [6]. However, just as with Welsby's formula, it does not provide any information about the magnetic vector potential.

This paper presents the technique and its implementation to calculate reference values for the magnetic vector potential, $\mathbf{A}$, and the inductance of a circular coil-in-air of rectangular cross section.

Calculation of the Magnetic Vector Potential for a Coil with a Rectangular Cross Section

One approach for analyzing a coil in air is to start with a δ-function coil carrying a sinusoidal current, obtain an integral expression for the magnetic vector potential and extend this result to model a circular coil with a rectangular cross section. Although there are many possible analytical forms for the solution for the magnetic vector potential, most are not easily amenable to numerical computation. The form chosen here has been most useful in that regard.

Consider a circular δ-function coil of radius a and a height l above the (ρ, θ) plane, with a current of $I(t) = I_o e^{j\omega t}$ flowing in the coil. The magnetic vector potential in terms of an elliptic integral is [7],[8]

$$A_\varphi(\rho, z) = \left(\frac{\mu_o I}{\pi}\right)\int_0^{\frac{\pi}{2}} \frac{a(2\sin^2(\theta') - 1)\,d\theta'}{\sqrt{(\rho + a)^2 + (z - l)^2 - 4\rho a\sin^2(\theta')}} \tag{2}$$

where ρ and z are the cylindrical coordinates of a field point at which the magnetic vector potential is calculated. The magnetic vector potential possesses an azimuthal component only, A_φ. The substitution $\varphi' = \pi + 2\theta'$ is used [8] to obtain equation (2), where φ' is the original azimuthal coordinate for source points. This equation is extendible to a coil with a rectangular cross section, by integrating the δ-function expression over the desired cross section.

Replacing the current I with a current density J_s in equation (2) for a coil with a rectangular cross section, results in

$$A_\varphi(\rho,z) = \frac{\mu_o J_s}{\pi}\int_0^{\frac{\pi}{2}}\int_{l_1}^{l_2}\int_{r_1}^{r_2}\frac{a(2\sin^2(\theta')-1)\,da\,dl\,d\theta'}{\sqrt{(\rho+a)^2+(z-l)^2-4\rho a\sin^2(\theta')}} \tag{3}$$

where r_1 and r_2 are the inner and outer coil radii respectively in meters and l_1 and l_2 are the z-coordinates of the top and bottom of the coil cross section in meters, as in Figure (1). (ρ, z) are the coordinates for the field point, assuming a constant φ, J_s is the current density in the coil and μ_o is the permittivity of free space (approximately air).

While integration over θ' is not possible in terms of elementary functions, integration over both a and l is possible. The following integrations were performed using *Mathematica* [9], an application program capable of symbolic integration. Integrating equation (3) with respect to a yields

$$A_\varphi(\rho,z) = \frac{\mu_o J_s}{\pi}\int_0^{\frac{\pi}{2}}\int_{l_1}^{l_2}\gamma(\rho,z,\theta',l)[2\sin^2(\theta')-1]\,dl\,d\theta' \tag{4}$$

where

$$\gamma(\rho,z,l,\theta') = \rho\left[2\sin^2(\theta')-1\right]e_1(\rho,z,a,l,\theta') + e_2(\rho,z,a,l,\theta')\Big|_{a=r_1}^{r_2} \tag{5}$$

and

$$\begin{aligned} e_1(\rho,z,a,l,\theta') &= \ln\left[\rho+a-2\rho\sin^2(\theta')+\sqrt{(l-z)^2+(\rho-a)^2-4\rho a\sin^2(\theta')}\right] \\ e_2(\rho,z,a,l,\theta') &= \sqrt{(l-z)^2+(\rho+a)^2-4\rho a\sin^2(\theta')} \end{aligned}$$

Integrating equation (4) with respect to l yields

$$A_\varphi(\rho,z) = \frac{\mu_o J_s}{\pi}\int_0^{\frac{\pi}{2}}\Gamma(\rho,z,\theta')[2\sin^2(\theta')-1]\,d\theta' \tag{6}$$

where

$$\begin{aligned} \Gamma(\rho,z,\theta') &= [2\sin^2(\theta')-1]\Big\{f_1(\rho,z,a,l,\theta')+f_2(\rho,z,a,l,\theta')+f_3(\rho,z,a,l,\theta')\Big\} \\ &\quad + f_4(\rho,z,a,l,\theta')+f_5(\rho,z,a,l,\theta')\Big|_{a=r_1}^{r_2}\Big|_{l=l_1}^{l_2} \end{aligned}$$

and

$$\begin{aligned} f_1(\rho,z,a,l,\theta') &= 4\rho^2\sin(\theta')\cos(\theta') \\ &\quad\cdot\arctan\left[\frac{\rho+a-2\rho\sin^2(\theta')+(l-z)+\sqrt{(\rho+a)^2-4\rho a\sin^2(\theta')+(l-z)^2}}{2\rho\sin(\theta')\cos(\theta')}\right] \end{aligned}$$

$$\begin{aligned} f_2(\rho,z,a,l,\theta') &= \rho(l-z)\ln\left[\rho+a-2\rho\sin^2(\theta')+\sqrt{(\rho+a)^2-4\rho a\sin^2(\theta')+(l-z)^2}\right] \\ f_3(\rho,z,a,l,\theta') &= \rho\left[\rho+a-2\rho\sin^2(\theta')\right]\ln\left[(l-z)+\sqrt{(\rho+a)^2-4\rho a\sin^2(\theta')+(l-z)^2}\right] \end{aligned}$$

$$f_4(\rho, z, a, l, \theta') = \frac{(l-z)\sqrt{(\rho+a)^2 - 4\rho a \sin^2(\theta') + (l-z)^2}}{2}$$

$$f_5(\rho, z, a, l, \theta') = \frac{\left[(\rho+a)^2 - 4\rho a \sin^2(\theta')\right] \ln\left[(l-z) + \sqrt{(\rho+a)^2 - 4\rho a \sin^2(\theta') + (l-z)^2}\right]}{2}$$

This integral requires careful analysis for field points at the corners of the coil's cross section, for field points on the cylindrical axis, and when θ' takes on either the value of 0 or $\pi/2$. Limits must be evaluated at these special points in order to obtain valid values for A_φ.

For f_1 the necessary limits can be broken into two categories: 1) those that applies when the denominator of the argument of the arctan function tends toward zero, and 2) when both the numerator and denominator of the argument tend toward zero. Thus, the following four limits are required for the first case:

1) $\lim_{\theta' \to 0} f_1 = 0$;

2) $\lim_{\theta' \to \frac{\pi}{2}} f_1 = 0$;

3) $\lim_{\rho \to 0} f_1 = 0$.

4) Lastly, of course, variables can tend toward limiting cases simultaneously; for example, $\rho \to 0$ and $\theta' \to \frac{\pi}{2}$.

For the second case, the numerator and denominator tend toward zero when $\rho = r_1$ or r_2, $z = l$ and $\theta' \to \frac{\pi}{2}$ and the following two limits are required:

5) $\lim_{\theta' \to \frac{\pi}{2}} f_1(\rho = r_1, z = l, a = r_1, l) = 0$;

6) $\lim_{\theta' \to \frac{\pi}{2}} f_1(\rho = r_2, z = l, a = r_2, l) = 0$.

Some of these limits are required during the process of numerical integration when $\theta' \to \frac{\pi}{2}$ or $\theta' \to 0$. Others are required when the field point is on the z-axis; namely, when $\rho \to 0$.

For f_2, the argument of the logarithm is never less than zero. However, it becomes zero when $z = l$; that is, when the field point chosen is on the top or bottom of the coil cross section. The following limit is required:

1) $\lim_{z \to l} f_2 = 0$, where $z = l_2$ or $z = l_1$.

For f_3 the following three limits are required:

1) $\lim_{\theta' \to \frac{\pi}{2}} f_3(a, l, a, l, \theta') = 0$;

2) $\lim_{\theta' \to \frac{\pi}{2}} f_3(a, l_2, a, l_1, \theta') = 0$;

3) $\lim_{\theta' \to \frac{\pi}{2}} f_3(a, z^\star, a, l^\star, \theta') = 0$, where $l^\star - z^\star < 0$.

The radicand of f_4 is always greater than or equal to zero for all values of the variables. No limits are needed for this function.

For f_5, the following three limits are required:

1) $\lim_{\theta' \to \frac{\pi}{2}} f_5(a, l, a, l, \theta') = 0$;

2) $\lim_{\theta' \to \frac{\pi}{2}} f_5(a, l_2, a, l_1, \theta') = 0$;

3) $\lim_{\theta' \to \frac{\pi}{2}} f_5(a, z^\star, a, l^\star, \theta') = 0$, where $l^\star - z^\star < 0$.

For all the above limits the only permissible values for a and l are $a = r_1$ or r_2 and $l = l_1$ or l_2. When the field point coordinates r and z take on the values of a or l respectively, the same condition applies. While this expression for the magnetic vector potential results from a known triple integral, the two analytic integrations result in a new expression, equation (6).

Combining analytic integration over the radial and axial coordinates with numerical integration

Steps	ρ *(meters)*	z *(meters)*	A_φ (Wb/m)
10	0.0000	0.0000	$6.029519332 \cdot 10^{-17}$
10	$3.0000 \cdot 10^{-3}$	0.0000	$3.769214913 \cdot 10^{-6}$
20	$3.0000 \cdot 10^{-3}$	0.0000	$3.769214967 \cdot 10^{-6}$
10	$7.9375 \cdot 10^{-3}$	0.0000	$1.253851277 \cdot 10^{-5}$
20	$7.9375 \cdot 10^{-3}$	0.0000	$1.252714222 \cdot 10^{-5}$
100	$7.9375 \cdot 10^{-3}$	0.0000	$1.252740190 \cdot 10^{-5}$
200	$7.9375 \cdot 10^{-3}$	0.0000	$1.252740242 \cdot 10^{-5}$
10	$9.5250 \cdot 10^{-3}$	$1.5875 \cdot 10^{-3}$	$8.394313817 \cdot 10^{-6}$
20	$9.5250 \cdot 10^{-3}$	$1.5875 \cdot 10^{-3}$	$8.388305142 \cdot 10^{-6}$
30	$9.5250 \cdot 10^{-3}$	$1.5875 \cdot 10^{-3}$	$8.387645117 \cdot 10^{-6}$
50	$9.5250 \cdot 10^{-3}$	$1.5875 \cdot 10^{-3}$	$8.387416996 \cdot 10^{-6}$
10	$1.00000 \cdot 10^{-2}$	$1.0000 \cdot 10^{-2}$	$1.740090826 \cdot 10^{-6}$
20	$1.00000 \cdot 10^{-2}$	$1.0000 \cdot 10^{-2}$	$1.740090830 \cdot 10^{-6}$

Table 1: Values of magnetic vector potential for some field points.
Coil dimensions: $r_1 = 0.00635$ m, $r_2 = 0.009525$ m, $l_1 = -0.0015875$ m and $l_2 = 0.0015875$ m, Current Density: $J_s = 3 \cdot 10^6$ Amperes/m^2.

over the azimuthal coordinate of the source results in the technique used here for evaluating the magnetic vector potential for a coil with a rectangular cross section.

The speed and accuracy of this method makes feasible the calculation of A_φ for large numbers of field points. Thus, it is possible to obtain a reference against which various computer codes, that use the finite element method for the calculation of A_φ, can be compared.

A partial output from the implementation of this expression for the vector potential using second order Newton-Cotes integration [10] is included in Table (1) for several field points. As expected, at field points on-axis the calculated magnetic vector potential for a coil in air is very close to the actual value of zero. The number of steps into which the domain of numerical integration is divided is indicated in the table. The table shows, depending upon the field point, that rapid convergence can be obtained when field points are not in the coil cross section. In the cross section more steps are needed to obtain an accurate result since the graph of the integrand becomes less amenable to second order numerical integration. Because of the symmetry of the coil in air, one need not calculate values of A_φ below the plane $z = 0$. However, AirCoil-1, the programmed implementation of equation (6), does this to check the algorithm.

Calculation of the Coil Impedance

With a hybrid method for calculating the magnetic vector potential developed, the value for coil inductance can also be evaluated. This formulation can use magnetic vector potential values at node points within the coil cross section to calculate coil impedance. The following formula for inductance results by considering the energy stored in the magnetic field [11] (all variables are r.m.s. quantities):

$$L = \frac{2\pi J_s}{I^2} \int_s \rho A_\varphi \, ds = \frac{2\pi N_s}{I} \int_s \rho A_\varphi \, ds \tag{7}$$

where $J_s = I \cdot N_s$ and N_s is the number of turns per square meter in the coil cross section. The s subscript on the current density and turns density simply refer to source and should not be confused with the s for the region of integration, which is over a triangular element.

Finally, coil impedance is calculated from the coil inductance using the following relationship between impedance and inductance for sinusoidal currents in an inductor with zero resistance

$$Z = j\omega L. \tag{8}$$

Thus, the inductance and impedance for the coil can be calculated from **A** by numerical integration over the coil cross section.

From equation (7), the inductance, L_Δ, for a single triangular element can be expressed in terms of second order natural coordinates as [10]

$$\begin{aligned}
L_\Delta &= \frac{2\pi N_s}{I}\int_s \rho A_\varphi \, ds \\
&= \frac{2\pi N_s}{I}\begin{bmatrix}\rho_1\\ \rho_3\\ \rho_5\end{bmatrix}^T \int_s \left\{\begin{bmatrix}L_1\\ L_2\\ L_3\end{bmatrix}\begin{bmatrix}L_1(2L_1-1)\\ 4L_1L_2\\ L_2(2L_2-1)\\ 4L_2L_3\\ L_3(2L_3-1)\\ 4L_1L_3\end{bmatrix}^T\right\} ds \begin{bmatrix}A_1\\ A_2\\ A_3\\ A_4\\ A_5\\ A_6\end{bmatrix} \\
&= \frac{2\pi N_s}{I}\begin{bmatrix}\rho_1\\ \rho_3\\ \rho_5\end{bmatrix}^T \int_s \begin{bmatrix} 2L_1^3 - L_1^2 & 2L_1^2 - L_2L_1 & 2L_1^2L_3 - L_1L_3 \\ 4L_1^2L_2 & 4L_1L_2^2 & 4L_1L_2L_3 \\ 2L_1L_2^2 - L_1L_2 & 2L_2^3 - L_2^2 & 2L_2^2L_3 - L_2L_3 \\ 4L_1L_2L_3 & 4L_2^2L_3 & 4L_2L_3^2 \\ 2L_1L_3^2 - L_1L_3 & 2L_2L_3^2 - L_2L_3 & 2L_3^3 - L_3^2 \\ 4L_1^2L_3 & 4L_1L_2L_3 & 4L_1L_3^2 \end{bmatrix}^T ds \begin{bmatrix}A_1\\ A_2\\ A_3\\ A_4\\ A_5\\ A_6\end{bmatrix}
\end{aligned} \tag{9}$$

In equation (9), the A_i where $i = 1, \ldots, 6$ are vector potential values calculated, using equation (6), at the vertices and midpoints between the vertices of a triangle. The integrations in equation (9) can be performed by using the following equation [10]:

$$\int_s L_1^\alpha L_2^\beta L_3^\gamma \, ds = \frac{2\Delta\alpha!\beta!\gamma!}{(\alpha+\beta+\gamma+2)!}, \tag{10}$$

where Δ is the area of a triangular element. After integration, equation (9), the inductance L_Δ due to a single triangular element, becomes

$$\begin{aligned}
L_\Delta &= \frac{\pi N_s \Delta}{30I}\begin{bmatrix}\rho_1\\ \rho_3\\ \rho_5\end{bmatrix}^T \begin{bmatrix} 2 & -1 & -1 \\ 8 & 8 & 4 \\ -1 & 2 & -1 \\ 4 & 8 & 8 \\ -1 & -1 & 2 \\ 8 & 4 & 8 \end{bmatrix}^T \begin{bmatrix}A_1\\ A_2\\ A_3\\ A_4\\ A_5\\ A_6\end{bmatrix} \\
&= \left(\frac{\pi N_s \Delta}{30I}\right)\{\rho_1[2A_1 + 8A_2 - A_3 + 4A_4 - A_5 + 8A_6] \\
&\qquad + \rho_3[-A_1 + 8A_2 + 2A_3 + 8A_4 - A_5 + 4A_6] \\
&\qquad + \rho_5[-A_1 + 4A_2 - A_3 + 8A_4 + 2A_5 + 8A_6]\}.
\end{aligned}$$

The total coil inductance is obtained by summing over all triangular elements within the coil cross section. Thus,

$$L = \sum_{\substack{all \\ elements}} L_\Delta. \tag{11}$$

Program	*Impedance (Ohms)*	*Δ's Used*
Welsby's Formula	5103.17	Not Applicable
Dodd's Method	5006.1907	Not Applicable
AirCoil-1	5006.099230	50
AirCoil-1	5006.240425	200
AirCoil-1	5006.251041	800
AirCoil-1	5006.251838	1800
AirCoil-1	5006.252187	3200

Table 2: Impedance values.
For AirCoil-1: the number of steps used to perform the integrations for A_φ was 300. The number of triangles used for the inductance integration is indicated in the third column. Coil dimensions: r_1 = 0.00635 m, r_2 = 0.009525 m, l_1 = -0.0015875 m, l_2 = 0.0015875 m. Turns density: $3.28 \cdot 10^7$ turns/m^2; Current Density: $J_s = 3 \cdot 10^6$ Amperes/m^2; Frequency: $\omega = 8\pi \cdot 10^5$ radians/s.

Once the integration for the inductance is complete, the impedance can be calculated immediately from coil inductance with equation (8).

Inductance can also be calculated by considering the energy stored in the magnetic field throughout all space [11]. If a mesh comprised of triangles is imposed on the cross section of the coil and a rectangular region of space surrounding the coil cross section, obviously it must be finite and yet sized large enough so that the values of magnetic vector potential in the region of space excluded have negligible affect on the calculation of coil inductance. This method has been programmed as part of this study, but it is numerically intensive due to the large number of elements needed to obtain a reasonably accurate result.

Calculation of the inductance from the values of magnetic vector potential in the coil cross section is more accurate, and fewer elements are needed. Table (2) shows the results of the computer implementation of this technique, (code name AirCoil-1). A comparison is made between AirCoil-1 and C. V. Dodd's integral method discussed earlier [3]. Dodd's method provides a value for inductance, from which impedance can easily be calculated. AirCoil-1 provides a value for the inductance and values of magnetic vector potential at all the node points of the mesh generated for a particular run.

From Table (2) it is clear that AirCoil-1 produces an impedance value lower than Dodd's integral, but with an increase in the number of triangles into which the coil cross section is divided, the impedance starts to converge to a value slightly above Dodd's result. The program used to calculate Dodd's result was never modified to achieve a better result.

Calculation of the Magnetic Flux Density and Electric Field Intensity

The magnetic flux density $\mathbf{B}$ can be calculated from the curl of $\mathbf{A}$. This result can then be expressed using natural coordinates so that numerical values of $\mathbf{B}$ can be calculated from the numerical values of the magnetic vector potential.

The electric field intensity, $\mathbf{E}$, is also easily calculated from the magnetic vector potential for a coil in air from $\mathbf{E} = -j\omega\mathbf{A}$.

Consistency can easily be shown by taking the expressions for $\mathbf{B}$ and $\mathbf{E}$ as a vector functions of $\mathbf{A}$ and recasting them into a form using natural coordinates, and demonstrating that $\nabla \times \mathbf{E} = -j\omega\mathbf{B}$. AirCoil-1 calculates $\mathbf{E}$ and $\mathbf{B}$ at the centroids of the triangles comprising the mesh used to calculate inductance. Of course, expressions for $\mathbf{E}$ and $\mathbf{B}$ could also be derived directly from equation (6), resulting in one dimensional integral expressions that could be integrated numerically with high accuracy.

Conclusions

The calculation of the magnetic vector potential **A** for a coil with a rectangular cross section can be performed using an integral expression derived for a δ-function coil and extended to model a coil with a rectangular cross section (resulting in a triple definite integral). This triple integral can be evaluated by using a hybrid approach combining two analytic integrations followed by one numerical integration. From the numerical values of the magnetic vector potential at the node points of a mesh imposed on the coil cross section, the coil impedance can be calculated. Also, the magnetic flux density **B** and the electric field intensity **E** are easily obtained from the magnetic vector potential **A** using a formulation in terms of natural coordinates. While values for **E** and **B** calculated with a rough mesh and are within an order of magnitude of the actual values, with a proper mesh containing a large number of triangles all the quantities approach ideal values within the limits of accuracy of the computing facilities available.

Acknowledgments

The Electric Power Research Institute (EPRI) funded this research.

References

[1] Laxmikant K. Urankar *Vector Potential and Magnetic Field of Current-Carrying Finite Arc Segment in Analytical Form, Part III: Exact Computation for Rectangular Cross Section*, IEEE Transactions of Magnetics, Vol. Mag-18, No. 6, November 1982.

[2] V. G. Welsby, *The Theory and Design of Inductance Coils*, John Wiley and Sons, 1960.

[3] C. V. Dodd, W. E. Deeds, J. W. Luquire, W. G. Spoeri, *Some Eddy-Current Problems and their Integral Solutions*, ORNL-4384, 1969.

[4] J. W. Luquire, W. E. Deeds, C. V. Dodd, W. G. Spoeri, *Computer Programs for Some Eddy Current Problems*, ORNL-TM-2501, 1969.

[5] W. Lord, *Development of a Finite Element Model for Eddy-Current NDT Phenomena*, Electric Power Research Institute Interim Report, NP-2026, September 1981.

[6] Lee D. Philipp , "Eddy-Current Testing", *Nondestructive Evaluation Research Progress in 1989; Proceedings from the Tenth Annual EPRI NDE Information Meeting*, Electric Power Research Institute NP-6609, June 1990.

[7] John David Jackson, *Classical Electrodynamics*, Second Edition, New York: John Wiley and Sons, 1975.

[8] William R. Smythe, *Static and Dynamic Electricity*, Hemisphere Publishing Corporation: 1989.

[9] Stephen Wolfram, *Mathematica, A System for Doing Mathematics by Computer*, Addison-Wesley Publishing Company, 1988.

[10] Kenneth H. Heubner and Earl A. Thornton, *The Finite Element Method for Engineers*, Second Edition, New York: John Wiley and Sons, 1982.

[11] Markus Zahn, *Electromagnetic Field Theory: A Problem Solving Approach*, Malabar, Florida, Robert E. Krieger Publishing Company, 1987.

THE FINITE ELEMENT ANALYSIS OF THE 50 CYCLES INDUCTION FURNACE

Qinke Zhang Yuanren Qiu Dazi Hou Shikun Chen
E. E. Dept. , Xi' an Jiaotong University, P. R. China

ABSTRACT

Based on the Maxwell' s equations and the Poynting' s theory, electromagnetic field analysis to predict the parameters of the induction furnace has been presented in this paper. Experimental results show that the electromagnetic field analysis in aid of the induction furnace design has higher accuracy than the conventional method.

INTRODUCTION

The application of the induction furnace in industry has been well developed in late decades, since it has a working enviroment of less noise, less dust and less air pollution.

Publications from investigators [1] — [3] show their successful analysis in induction heating devices. Papers on numerical calculation of skin effect and eddy current problems [4]—[6] are also helpful in guiding to the electromagnetic field analysis for induction furnace design.

In this paper, electromagnetic field analysis in aid of the induction furnace design aims to overcome the situation that conventional method with simplified formulae often fails to meet the desired results. A computer aided design program by means of finite element method has been completed. For practical applications, calculations have been performed to both the smelting and the thermal preservation coreless induction furnaces. Results show that the CAD program has higher accuracy than the conventional design method.

MODEL FOR NUMERICAL ANALYSIS

Assumptions:

The structure of the induction furnace is shown in Fig. 1 a). For simplifying the analysis, assumptions are made as follows:

a) Currentt density of the inductor has only the tangential component in the cylindrical coordinate system, $J = J_\theta 0$. Skin effect in the inductor coils are negligible during field analysis.

b) Mediums under consideration are isotropical. The effects of the hysteresis and saturation of the laminated yoke are negligible.

c) Smelting charge has been thoroughly melted. The resistivity of the smelting charge is

a constant and its permeability is approximately equal to the permeability of the vacuum, since the temperature of the ferromagnetic substance is higher than the Curie point.

d) Constant voltage of 50 cycles is supplied to the inductor. Field quantities are sinusoidal time variables.

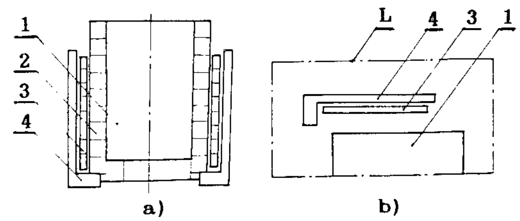

Fig. 1 a) Structure of the induction furnace
b) Model for finite element analysis
1. Smelting charge 2. Crucible 3. Inductor (Coils) 4. Yoke

Boundary Value Problem:

The Maxwell's equations in differential form are as follows:

$$\begin{aligned} \text{rot } H &= J \\ rot\ E &= -\frac{\partial B}{\partial t} \\ div\ B &= 0 \\ div\ D &= 0 \end{aligned} \tag{1}$$

where H, B, E, D and J are the magnetic field strength, flux density, electric field strength, electric displacement and current density respectively, while the charge density is assumed to be zero.

The relationships of the electromagnetic properties are:

$$D = \varepsilon E \qquad B = \mu H \qquad J = \sigma E \tag{2}$$

where ε, σ and μ are the specific inductive capacity, conductivity and the permeability respectively.

For magnetic vector potential (MVP) A, let

$$\begin{aligned} \text{rot } A &= B \\ \text{div } A &= 0 \end{aligned}$$

According to the symmetrical structure and the assumption a), the electromagnetic field of these induction furnaces may be considered axisymmetric. Then, the magnetic vector potential $A = A_\theta 0$ satisfies the diffusion equation:

$$\frac{\partial}{\partial r}\left[\frac{\nu}{r}\frac{\partial(rA_\theta)}{\partial r}\right] + \frac{\partial}{\partial z}\left[\frac{\nu}{r}\frac{\partial(rA_\theta)}{\partial z}\right] = -J_\theta + \sigma\frac{\partial A_\theta}{\partial t} \tag{4}$$

where v is the reluctivity of the medium. The values of v and σ vary with different kinds of media within the region.

The boundary of the solving region Ω is defined by the dot—dash line L, it partially coincides with the symmetrical axis as shown in Fig. 1 b). Imagine that this boundary line L is the most outer line of the flux diffusing into the air space. Since the flux distribution line can be drawn by the equipotential line of $U=rA_\theta$, the boundary condition can be expressed as:

$$U=rA_\theta=\text{const.}=0$$

For equation (4), take the phaser form and replace rA_θ by U, the boundary value problem is as follows:

$$\begin{cases} \dfrac{\partial}{\partial r}(\dfrac{v}{r}\dfrac{\partial\dot{U}}{\partial r})+\dfrac{\partial}{\partial z}(\dfrac{v}{r}\dfrac{\partial\dot{U}}{\partial z})=-\dot{J}_\theta+j\dfrac{\omega\sigma\dot{U}}{r} & \text{in the region } \Omega \\ \dot{U}|_L=0 & \text{along the boundary L} \end{cases} \tag{5}$$

The conditional variational problem corresponding to equ. 5 is:

$$\begin{cases} W_{(\dot{U})}=\iint_\Omega\{\dfrac{v}{2}\dfrac{1}{r}[(\dfrac{\partial\dot{U}}{\partial r})^2+(\dfrac{\partial\dot{U}}{\partial z})^2]-\dot{J}_\theta\dot{U}+\dfrac{1}{2}j\dfrac{\omega\sigma}{r}\dot{U}^2\}drdz=min \\ \dot{U}|_L=0 \end{cases} \tag{6}$$

It is known that the equivalence of equ. 5 and equ. 6 are verified.

The Finite Element Discretization Model:

The solving region Ω is subdivided into a set of triangular elements. For each element, the linear interpolating function is expressed as:

$$\dot{U}=N_i\dot{U}_i+N_j\dot{U}_j+N_m\dot{U}_m$$

where $\dot{U}_i$, $\dot{U}_j$, $\dot{U}_m$ are the value of $\dot{U}$ at each vertex of the triangle, and N_i, N_j, N_m are the shape function of the triangle. According to the Ritz formulation, a set of finite element equations will be formed:

$$[K]\{\dot{U}\}=\{P\} \tag{7}$$

the upper $[K]$ is the complex coefficient matrix, $\{\dot{U}\}$ is the column vector for solving, and $\{P\}$ is the right side column matrix. The values of each term in $\{P\}$ are effected by $\dot{J}_\theta$ —— the current density of the inductor.

SOLUTION OF THE FINITE ELEMENT EQUATIONS AND CALCULATION FOR THE PARAMETERS

Solution for the Finite Element Equations:

It should be noted that quantity J_θ is unknown in equ. 5 to equ. 7. Since the system under investigation is linear and the field quantities $\dot{B}$, $\dot{H}$ & $\dot{E}$ are calculated by the derivation of $\dot{U}$ with respect to the coordinates of r and z, therefore, $\dot{J}_\theta$ can be assumed

arbitrarilly at the first time to solve for $\dot{A}$. From $\dot{A}$, the field quantities $\dot{E}$ and $\dot{H}$ can be calculated, and the reluctance $Z=R+jX$ of the induction furnace can be calculated as well. (The calculation of Z will be discussed afterward.) As Z is linear, the current of the inductor varies directly with the applied voltage.

For normal voltage V, the rated current of the inductor is:

$$I = \frac{V}{Z}$$

The current density J_θ under rated situation can thus be obtained. Then the finite element equations should be solved for the seccnd time in order to get the rated field distribution, input power and power factor, etc.

Calculation for the Parameters:

The equivalent circuit of the coreless induction furnace is shown in Fig. 2. where R represents the ac resistance of the inductor, X is the reactance of the system, including inductor and the smelting charge. R is the equivalent resistance corresponding to the resistance losses of the eddy current induced in the smelting charge. Values of resistances R_1 and R, and the reactance X are unchanged for a certain induction furnace with its smelting charge under fixed frequency.

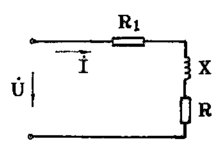

Fig. 2 Equivalent circuit

The power losses P of the eddy current induced in the smelting charge, and the reactance losses Q of the system are:

$$P = I^2R \qquad \text{and} \qquad Q = I^2X$$

On the other hand, according to Poynting's theory, the complex energy flowing directly through the unit surface per unit time is defined as:

$$\dot{S} = \dot{E} \times \dot{H}^*$$

where $\dot{S}$ is the Poynting vector, $\dot{H}^*$ is the conjugate of $\dot{H}$.

The total complex power flowing through the closed surface is:

$$\oint_s (\dot{E} \times \dot{H}^*) \cdot ds = \int_v \nabla(\dot{E} \times \dot{H}^*) dv = -\int_v [\dot{E} \cdot (\nabla \times \dot{H}^*) - \dot{H}^* (\nabla \times E)] dv \tag{8.a}$$

$$\int_v [\dot{E} \cdot (\nabla \times \dot{H}^*) - \dot{H}^* (\nabla \times E)] dv \tag{8.b}$$

Equ. 8. b represents the electric power which is flowing into the closed surface S from the supply, and V is the volumn surrounded by the closed surface S.

In axisymmetric system, substitute equ. 1 & 2 into equ. 8. b, and replace the volumn integration by surface integration, equ. 8. b can be rewritten as:

$$\int_{v}[\dot{E}\cdot\nabla\times\dot{H}^{*}-H^{*}\cdot\nabla\times E]dv=\int_{\Omega}(\sigma|\dot{E}|^{2}+j\omega\mu|\dot{H}|^{2})2\pi r drdz \qquad (9)$$

If the solving region Ω of Fig. 1 b) is assigned to be the region of the integration of equ. 9, the resistance losses P caused by the eddy current induced in the smelting charge can be calculated by:

$$P=\int_{\Omega}\sigma|\dot{E}|^{2}2\pi r drdz \qquad (10)$$

Resistance R corresponding to the eddy current losses of the smeling charge should be:

$$R=P/I^{2}=\int_{\Omega}\frac{\sigma|\dot{E}|^{2}}{I^{2}}2\pi r drdz \qquad (11)$$

Reactance X of the system can be calculated by:

$$X=Q/I^{2}=\frac{\omega}{I^{2}}\cdot\int_{\Omega}\mu|\dot{H}|^{2}\,2\pi r drdz$$

The resistance losses of the inductor can be calculated directly by:

$$Pcu=I^{2}R_{1}$$

where R_1 is the ac resistance of the inductor.

The power factor of the system is:

$$\cos\Phi_{1}=(R+R_{1})/\sqrt{(R+R_{1})^{2}+X^{2}} \qquad (12)$$

RESULTS AND ANALYSIS

For practical application, calculations have been performed to both the smelting and the thermal preservation coreless induction furnace. The rated capacities and the main properties of the materials are listed below:

Items	Smelting Furnace	Thermal preservation furnace
Rated Capacity (Ton)	1.5	3.0
Frequency (Hz)	50	50
Rated Voltage (V)	380	380
Turns of the Inductor	36	18
Resistivity ($\Omega\cdot$m) (copper)	2.0×10^{-8}	2.0×10^{-8}
Resistivity ($\Omega\cdot$m) (smelting charge)	1.36×10^{-6}	1.36×10^{-6}
Permeability (H/m) (smelting charge)	$4\pi\times10^{-7}$	$4\pi\times10^{-7}$

From fig. 3 a) & b), it is evident that the magnetic field distribution of the smelting charge along the height of the crucible is ununiform, magnetic field near by the inductor is much stronger than those at the other places, it becomes weaker as reaching the surface of the smelting charge. Therefore, the distribution of the induced eddy current density along the height could not be uniform. This result shows a great difference compared with the analytical model which assume that the eddy current density distributes uniformly along the height of the smelting charge.

The yoke is available in preventing the magnetic flux diffusing into the outer space. It can be seen that the shorter yoke may cause a greater flux diffusion than the longer one.

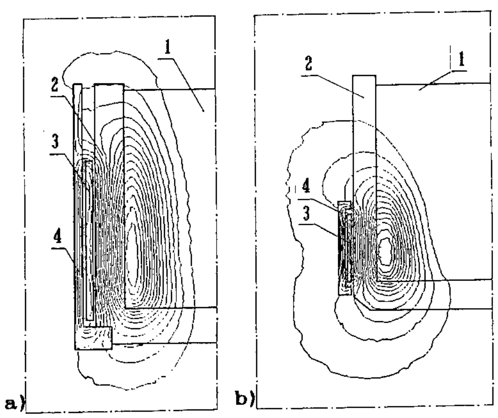

Fig. 3 Instantaneous distribution of the magnetic field at $\omega t = 0°$.
a) Field distribution of the smelting induction furnace
b) Field distribution of the thermal preservation furnace

The distributions of the induced eddy current density in different heights against radius r are shown in Fig. 4. The curves show that the skin effect of the smelting charge is rather strong.

Table 1 and table 2 show the calculational and experimental results of the inductor current, input power and power factor. The results from the finite element method coincide fairly with the experimental results.

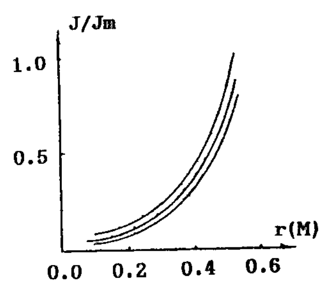

Fig. 4 Distribution of the induced eddy current densities

Table 1. Calculating & Experimental Resulgts of the Smelting Furnace

ITEMS		Supply Voltage (V)	Inductor Current (A)	Input Power (Kw)	Power Factor
Experimental Results		380	5810	442	0.2
Conventional Method	Abs. Value	380	6460	425	0.173
	Error		11×10^{-2}	-3.7×10^{-2}	-14×10^{-2}
FEM	Abs. Value	380	5604	445	0.209
	Error		-3.5×10^{-2}	0.81×10^{-2}	4.5×10^{-2}

Table 2. Calculating & Experimental Results of the Thermal Preservation Furnace

ITEMS		Supply Voltage (V)	Inductor Current (A)	Input Power (Kw)	Power Factor
Experimental Results		380	2472	210	0.216
Conventional Method	Abs. Value	380	2987	237	0.21
	Error		21×10^{-2}	13×10^{-2}	-2.6×10^{-2}
FEM	Abs. Value	380	2574	209	0.214
	Error		4.1×10^{-2}	0.19×10^{-2}	-0.83×10^{-2}

CONCLUSION

* Finite element analysis shows its advantage over the conventional method in calculating the parameters of the induction furnace as well as the distribution of the magnetic field and the induced eddy current.

* The CAD program completed is predicted to be suitable for the analysis and calculation of the induction furnace with similar structure at other power fuequency.

REFERENCES

[1] J. D. Lavers, "Using Commercial Finite Element Packages for Induction Heating Applications", IEEE Conference Recordings of IAS, 1984.

[2]Michal G. Reynolds, "Power Loss in Tubular Conductors of Induction Heating Coils", IEEE Conference Recordings of IAS, 1984

[3]R. F. Rudley and P. E. Burke,"The Prediction of Current Distribution in Induction Heating Installation",IEEE Trans. Ind. App., Vol. IA—8,1972.

[4]Q. S. Huang, L. Kraherbuhl, A. Nicolos, "Numerical Calculation of Steady—state Skin Effect Problems in Axisymmetry", IEEE. Trans. Mag, Vol. 24, No. 1, Jan. 1988

[5]M. V. K. Chari,"Finite Element Solutions of the Eddy Current Problem in Magnetic Structure", IEEE Trans., Vol. PAS—93, 1974.

[6]T. H. Fawzi, K. F. Ali, P. E. Burke, "Eddy Current Losses in Finite Length Conducting Cylinders", IEEE Trans. MAG, Vol—19, No. 5, Sept. 1983.

TIME DOMAIN ANALYSIS OF THE MAGNETIC FIELD PENETRATION INTO STRATIFIED CONDUCTIVE SHIELDS, USING F E M

Constantin V. Bala, Ovidiu C. Craiu, Mihaela I. Morega
Polytechnic Institute of Bucharest
Department of Electrical Engineering
Spl. Independentei 313, Bucharest, ROMANIA

ABSTRACT:

A FEM computational method for the specific magnetic field problems in shielded electromagnetic structures is presented. The transient magnetic field approach and the associated phenomena (eddy current density and losses) evaluation refers to domains with both cylindrical and plan-parallel symmetry.
The mathematical model gathers the finite difference Crank Nicolson technique equations, the field boundary restrictions and the specific eddy current conditions.
The method can be used as a general tool to simulate the magnetic flux penetration into stratified or homogeneous conductive shields and the numerical applications support its efficiency.

INTRODUCTION

The transient eddy current computation using FEM and a large variety of applications appear often in the specialized literature; the referenced works are significant examples. The eddy current problem in homogeneous ferromagnetic media with linear or nonlinear magnetic properties and constant electric conductivity (σ=const.) is one of the most important applications [1],[2],[3]. Paper [5] presents an efficient approach for the transient magnetic field problem in structures which include laminated ferromagnetic shields, with the assumption that the eddy current reaction is weak and therefore negligible.

The electromagnetic phenomena produced in anisotropic materials at the penetration of the transient magnetic field are governed by Maxwell's laws:

$$curl\frac{1}{\mu}curl\bar{A}=\bar{J}+\bar{J}_F$$

$$curl\frac{1}{\sigma}curl\bar{T}=-\frac{\partial\bar{B}}{\partial t} \tag{1}$$

$$curl\bar{A}=\bar{B};\,div\bar{A}=0$$

$$curl\bar{T}=\bar{J}_F;\,div\bar{T}=0$$

where: μ is the magnetic permeability, σ is the electric conductivity, $\bar{A}$ is the magnetic vector potential, $\bar{T}$ is the electric vector potential, $\bar{J}$ is the feed current density, $\bar{J}_F$ is the eddy current density and $\bar{B}$ is the magnetic flux density.

The system (1) is associated with the equations derived from the specific boundary conditions.

The solution of this partial differential equations system is a difficult process for anisotropic media and certain geometry.

This paper presents an adequate method to solving the electromagnetic field problems with plan-parallel or cylindrical symmetry, in anisotropic media, such as the geometrical domain of the lamellated shields.

The association between the standard FEM and the restriction that the eddy current must close their circuit within each sheet of the conductive shield, allows to formulate the field problem only in terms of the magnetic vector potential $\bar{A}$ and the eddy current density $\bar{J}_F$.

ADEQUATE FORMULATION FOR FEM

The characteristic geometrical domain includes a coil, fed by a current source, in the vicinity of an electromagnetic shield. The

domain shows either cylindrical or plan-parallel symmetry. The current through the winding is supposed to have a step like time shape, estimated as follows:

$$i=I(1-e^{-\frac{t}{T_i}}) \tag{2}$$

where $T_i=10^{-6}$s. The value is chosen so that the transient evolution of the current through the coil and the transient process of the magnetic field penetration into the shield, do not interfere.
They were considered both the geometries of the electromagnetic homogeneous shield (made of full material), as Fig.1a shows, and the lamellated shield (made of insulated sheets and placed perpendicularly on the plane of symmetry), as Fig.1b and Fig.1c show.

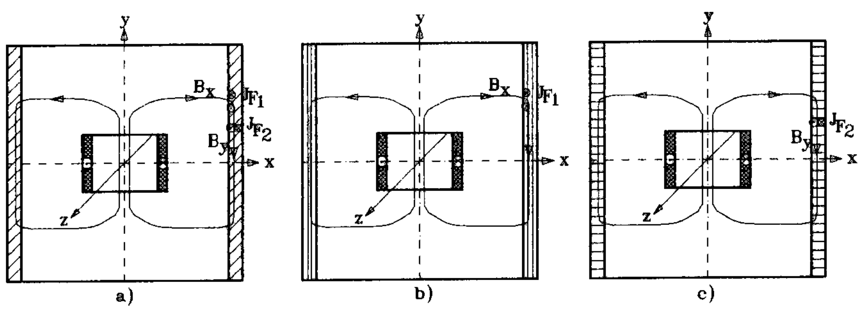

Fig.1 The domain

The electric conductivity in the lamellated shield is constant (and of a finite value) on the longitudinal direction (σ=const.) and is zero on the cross direction (σ=0), with regard to the shape of one sheet, so that the eddy current induced in the cross-section of each sheet is neglected.
Fig.1 shows, at the same time, the boundary conditions.
The system of differential equations is solved using the Crank Nicolson technique, familiar and available to the authors, although

the procedure presented in ref. [3] ensures a considerable shorten of the computing time. The standard FEM equations for the magnetic vector potential $A^{(k+1)}$ and the eddy current density $J_p^{(k+1)}$, considered at the (k+1)-th time step, are the following:

$$(GK)\{A\}^{(k+1)} = \{R\}J^{(k+1)} + \{R\}J_p^{(k+1)} \qquad (3)$$

$$\{R\}J_p^{(k+1)} = (C)\ [\{A\}^{(k+1)} - \{A\}^{(k)}] - \{R\}J_p^{(k+1)} \qquad (4)$$

where (GK) is the coefficient matrix, dependent on the geometrical coordinates of each node of the triangular FEM mesh and the magnetic reluctivity of the finite elements; {R} is a vector characteristic for the subdomains with conduction or eddy current densities ($J^{(k+1)}$, respectively $J_p^{(k+1)}$ at the specific time step (k+1)); $J_p^{(k+1)}$ is a particular constant for the (k+1)-th step, due to the integration process on each subdomain with eddy current. Details for the evaluation of matrices: (GK), (C) and vector {R} are given in ref.[6].To estimate the constant values of $J_p^{(k+1)}$ it is necessary to solve the integral equations:

$$I_p = \int_{S_p} \left(J_p^{(k+1)} - \frac{\sigma}{\Delta t}\left(A^{(k+1)} - A^{(k)}\right)\right) ds_p = 0,\ p=1,\ldots,NEE \qquad (5)$$

where NEE is the number of distinct subdomains related to the sheets of the electromagnetic shield; S_p is the cross-section surface of one sheet; σ is the electric conductivity of the shield (on the longitudinal direction); Δt is the time step.
The integral equations (5) state the restriction that the eddy current must close their circuit within each subdomain.
The numerical treatment of eq.(5) leads to:

$$\sum_{i=1}^{NEP} \left(J_p^{(k+1)} - \frac{\sigma_i}{\Delta t}\left(A_i^{(k+1)} - A_i^{(k)}\right)\right)\Delta_i = 0,\ p=1,\ldots,NEE \qquad (6)$$

where A_i is the magnetic vector potential in the central point of the finite element (for the triangular element: $A_i = (A_l + A_m + A_n)/3$; with A_l, A_m and A_n the nodal values of the magnetic vector potential), Δ_i is the geometrical surface of the (i)-th element and NEP is the number of elements in the subdomain "p".

Equation (6) allows to estimate the constant values:

$$J_p^{(k+1)} = \frac{1}{S_p} \sum_{i=1}^{NEP} \frac{\sigma_i}{\Delta t} \left(A_i^{(k+1)} - A_i^{(k)}\right) \Delta_i \tag{7}$$

where: $S_p = \sum_i \Delta_i$

Equations (3),(4) and (6) build up a system, whose solution contents the values of the magnetic vector potential A, and the eddy current density J_p.

That way become possible the estimate of the magnetic field lines spectrum and the eddy current losses within the electromagnetic shield.

NUMERICAL APPLICATION

Numerical results of the above method are related to the computational model of Fig.2, with plan-parallel symmetry. Two separate situations are compared: first, the shield of homogeneous material, second, the lamellated electromagnetic shield.

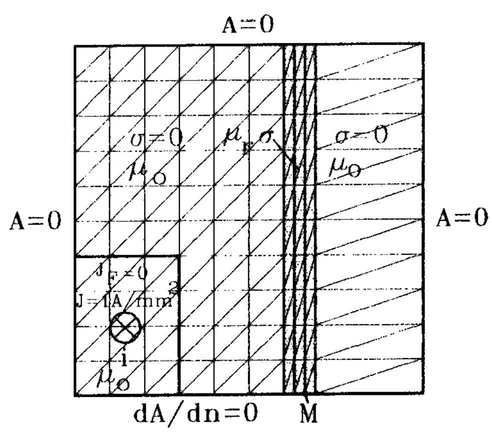

Fig.2 Computational model

Fig.3 shows the magnetic field lines at several time steps and Fig.4 presents the time evolution of the magnetic vector potential at a certain point M (see Fig.2) dependent on the evolution of the source of this transient process: the current i(t).

It is possible to estimate the eddy current losses with the following expression:

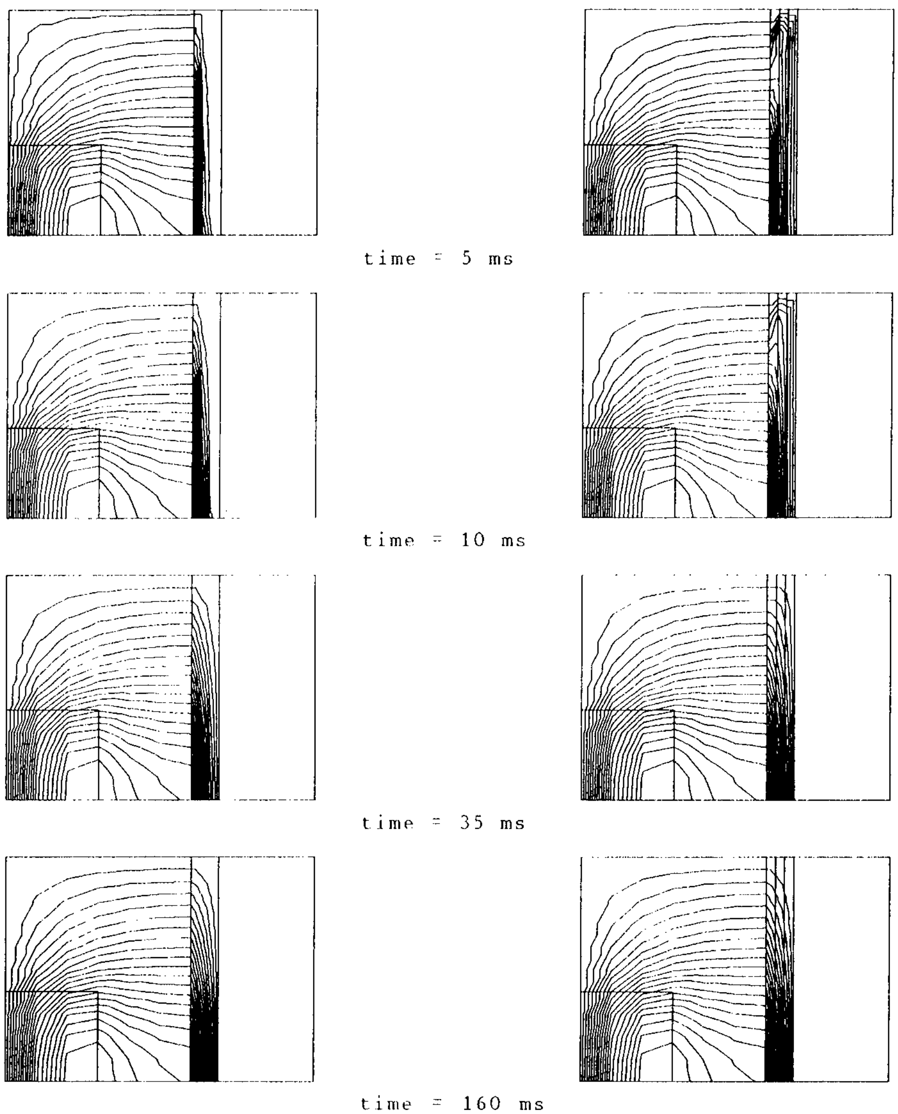

Homogeneous shield

Lamellated shield

Fig.3 Magnetic field lines for the two types of shields

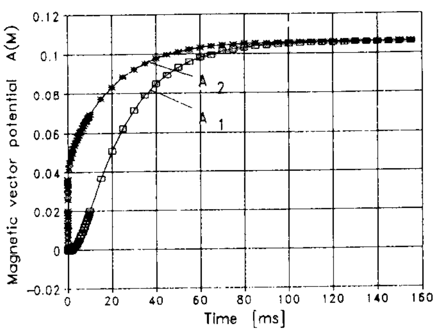

Fig.4 Time evolution of the magnetic vector potential at point M:
- A_1 homogeneous shield:
- A_2 lamellated shield.

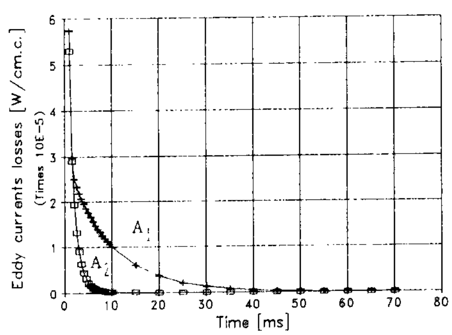

Fig.5 Time evolution of eddy current losses:
- A_1 homogeneous shield;
- A_2 lamellated shield.

$$p_F = \frac{\sum_{k=1}^{NET} \frac{1}{\sigma_k} J_{F,k}^2 \Delta_{ek}}{\sum_{k=1}^{NET} \Delta_{ek}} \qquad (8)$$

with NET = NEP*NEE, the whole number of elements in the shield and Δ_{ek} the geometrical surface of each element.
The time evolution of eddy current losses is displayed in Fig.5 for

the two geometrical structures: homogeneous and lamellated.
As one can see, the above method offers the possibility for a wide-range study of the transient phenomena which accompany the magnetic field penetration in conductive materials.

CONCLUSIONS

FEM allows to solve the problem of transient magnetic field penetration into electromagnetic shields, taking into account the eddy current influence. The method discussed here avoids the intricate way of solving systems with simultaneous partial differential equations in A and T.
The main advantage of the above method is the possibility to solve together the standard FEM equation and the integration constants conditions, both type of equations expressed in terms of the magnetic vector potential.
The application exposed here is not only an adequate numerical example for the method, but opens the way to the optimum design of proper electromagnetic shielding for electrical devices.

REFERENCES

[1].Konrad,A.,Chari,M.V.K.,Csendes,Z.J. "New finite element technique for skin effect problems" IEEE Trans. on Magnetics, vol.MAG-18, 1982, pp.450-455

[2].Tarasiewicz,E.,Dableh,J.,Findaly,R. "Accurate computation of axisymmetric vector potential with FEM" IEEE Trans. on Energ.Conv., vol.EC-2, 1987, pp.321-328

[3].Mohamed,O.A.,Uler,F.G. "A State Space Approach and Formulation for the Solution of Nonlinear 3-D Transient Fields and Eddy-Current Problems" COMPUMAG Sorrento 1991, pp.3-5

[4].Bala,C.V.,Badea,E.A.,Teodorescu,R.M. "The 3-D FEM to estimate the transient parameters of coils with nonferromagnetic core" COMPEL, vol.9 (1989), Supplement A, pp.91-96

[5].Bala,C.V.,Craiu,O.C.,Morega,M.I. "Finite element analysis of magnetic field distribution in ferromagnetic shields" Conference Proceedings ACES, Monterey CA, 1991, pp.534-539

[6].Rao,S.S. "The finite element method in engineering" Pergamon Press, Oxford, 1991 (2-nd edition)

SESSION 9 - "HF APPLICATIONS"

Moderator: C.E. Ryan

RCS Prediction Validation of the *Simulated Radar Image* Code[1]

Dale A. Stanley, Andrew J. Terzuoli, Jr.
School of Engineering
Air Force Institute of Technology
Wright-Patterson AFB, Ohio 45433

Abstract

The monostatic radar cross section (RCS) prediction capability of the Simulated Radar Image (SRIM) Code[2] Version 4.0 was verified and validated for perfectly-conducting, smooth canonical shapes. SRIM uses the theory of Physical Optics (PO) to predict backscatter for a user specified aspect angle and takes into account target obscuration and multiple reflections by sampling the target with rays. The software verification and validation technique followed in this study entailed comparing the code predictions to closed form PO equations and measured test data. The targets analyzed were a sphere, rectangular flat plate, circular flat plate, solid right circular cylinder, dihedral and trihedral corner reflectors, top hat, and generic missile. SRIM RCS predictions are shown for each of the targets as a function of frequency, aspect angle, and ray density. The results show that the accuracy of the SRIM predictions improve as the ray density increases. Except for the top hat, there is close agreement between the SRIM predictions and PO equations when the targets are sampled with fine ray spacing. There is also good agreement between the SRIM predictions and measured data near the specular region.

Introduction

The success of the stealth fighter during Desert Storm proved the value of employing low observable technology on weapon systems. One of the many parameters that must be considered in the design of such systems is the radar cross section. When confined to the high frequency regime in which the target electrical length is large, one of the first steps in minimizing the system RCS is identifying the major scattering centers. One way to accomplish this is through high resolution Synthetic Aperture Radar (SAR) imaging [1]. However, it would be cost prohibitive to construct a prototype model of a proposed weapon system for each design iteration for the sole purpose of determining its RCS by imaging. A better approach is to simulate the SAR image with software. This prompted the Environmental Research Institute of Michigan (ERIM) to develop the Simulated Radar Image (SRIM) software package. Using the high frequency technique of Physical Optics (PO), SRIM provides monostatic RCS predictions and the data required to generate simulated synthetic aperture radar images. SRIM supports a set of 25 primitives and uses Constructive Solid Geometry (CSG) to model complex targets. The primitives include solid geometry shapes such as boxes, cylinders, and spheres.

Problem Statement

As in every software program, SRIM cannot be used with confidence until it is thoroughly verified and validated (V&V). Prior to this study, a thoroughly documented SRIM V&V had not been completed for either the RCS predictions or image generation files. Within the realm of Physical

---

[1]This work was sponsored by the U.S. Air Force Wright Laboratory, Avionics Directorate, Mission Avionics Division, Target Recognition Branch.

[2]developed by the Environmental Research Institute of Michigan (ERIM)

Optics applicability, the objective of this study was to verify and validate the SRIM Version 4.0 RCS predictions for simple primitives that have a closed form PO solution. In this study, verification and validation are defined as the processes of ensuring the code correctly implements Physical Optics theory and ensuring the code gives results to within an acceptable accuracy over its region of applicability, respectively.

Methodology

The Electromagnetic Code Consortium [2] has undertaken efforts to address the issue of code validation. Two of their goals are to establish validation/measurement procedures which will be imposed on all future code developments and to benchmark industry/university-developed computational codes. Unfortunately, these procedures and benchmarks for RCS software validation have not yet been established. Therefore, the approach used in this study follows an approach proposed by Sargent [3] that applies to software in general. Specifically, verification is completed by using internal validity and fixed value tests. After verification, measured data is then used to validate the software. In the measured data comparison, the code's region of applicability (limitations due to assumptions in Physical Optics theory) has to be taken into consideration.

Internal validity tests verify the software gives consistent results from run to run. Fixed value tests verify the code gives the same results obtained by "hand calculation." To establish a baseline that served as the hand calculated values, equations that predict RCS using the theory of Physical Optics were encoded in FORTRAN. SRIM predictions were compared to this baseline.

SRIM RCS Calculations

SRIM samples the target by sequentially firing rays that are uniformly distributed in a view plane rectangle which is located in the "emanation plane" perpendicular to the radar line of sight (LOS). As each ray is cast from the view plane rectangle, it is traced through each specular reflection until no more reflections are encountered or until a user-specified maximum number of reflections is reached. When a ray strikes the target, the location of the hit is recorded and the surface normal and curvature for the reflection point are calculated. At each subsequent reflection, shadowing is taken into account by firing a ray towards the emanation plane to determine if the reflection is within the radar LOS. At each reflection point, a surface scattering patch is established by using the projected area of the ray tube associated with each ray. The SAR reflectivity density is calculated for each surface patch by using PO approximations. If the surface is flat, the integration is performed exactly. If the surface is curved, the method of stationary phase is used by approximating a singly curved surface with a parabolic cylinder and a doubly curved surface with an elliptic paraboloid. Multiple reflections are accounted for in the same way, but geometrical optics is used to define the area illuminated (surface patch) by subsequent reflections of the ray tube. The SAR reflectivity density is used to calculate the RCS of the target by coherently summing the contribution from each surface patch [4,5].

Verification Results

Internal Validity Tests. This phase of the testing was done to ensure the SRIM RCS predictions were repeatable. It served a two-fold purpose. First, it was essential to establish that when identical targets and radar parameters are used, SRIM gives identical results. Second, because SRIM samples the geometry with rays, the effect on RCS predictions due to the distance between rays (i.e. ray spacing) had to be established.

Repeatability. SRIM repeatability for identical target and radar parameters was established by analyzing a 10 x 15 cm rectangular flat plate. Three runs were completed using a ray spacing (RS) of .5 cm and frequency of 10 GHz. For each run, the plate was oriented in the XZ plane (the long dimension was in the Z direction) but was defined differently with respect to the origin. In each case, the results were identical.

Ray Spacing. The parameter that has the greatest effect on the SRIM predictions is ray spacing. Due to this dependency on ray spacing, SRIM runs with different ray spacing values were completed for each target. As an example, Figure 1 shows the SRIM predictions for a 5 cm radius sphere as a function of ray spacing. As noted in the figure, ray spacing is specified as a percentage of a distance L, where L is the shortest length of the target that is perpendicular to the radar LOS when the target is normal to the radar. This method was selected to provide for consistency between targets of different sizes. That is, targets of different sizes that have the same ray spacing percentage are sampled with the same number of rays.

Fixed Value Tests. In this phase of the testing, SRIM RCS predictions were compared to RCS predictions generated with established Physical Optic equations.

Sphere Results. Figure 2 shows the comparison between SRIM predictions and the PO equation [6] for a 5 cm radius sphere centered at the origin. As already noted, ray spacing plays a major role as demonstrated by the fluctuations prevalent in the .05L trace. As the ray density increases, the fluctuations decrease. Aside from the oscillations, the PO and SRIM predictions agree quite well with less than a .6 dBsm difference.

Rectangular Flat Plate Results. Figure 3 shows the effect of ray spacing on SRIM predictions for a 10 x 15 cm plate in the XZ plane viewed at 0° elevation (measured from XY plane). As seen in the figure, the match between SRIM and the PO equation [7] improves as the ray spacing decreases. There are significant differences in the depths of the nulls.

Circular Disk Results. Figure 4 shows the comparison between SRIM and PO equation [8] predictions for a 5 cm radius circular flat plate oriented in the XZ plane at 0° elevation. Again, it is quite evident that the agreement is better as the distance between rays decreases. Comparing Figures 3 and 4 show the RCS differences for the circular plate are greater than for the rectangular plate near grazing incidence.

Corner Reflector Results. PO predictions are generally polarization insensitive. However, this is not true when the signal undergoes an even number of reflections before returning to the observer. Thus, the dihedral response is polarization sensitive because the return consists not only of the single bounce response from each plate, but also a double bounce response due to the interaction between the plates. The trihedral has single, double, and triple bounce responses. Thus, its response is also polarization sensitive. Therefore, results are shown for horizontal and vertical polarizations. The nomenclature HH and VV imply the transmitter and receiver are both either horizontally or vertically polarized, respectively.

Figure 5 compares SRIM and PO equation [9] RCS predictions for a 10 x 15 cm right dihedral at 0° elevation for HH polarization. The dihedral crease (15 cm) is aligned along the Z axis. The vertical plates are in the XZ and YZ planes. As shown, there is excellent agreement between the PO and SRIM predictions.

Figure 6 shows the comparisons between SRIM and PO equation [10,11] RCS predictions for a 10 cm right trihedral at 0° elevation with VV polarization. The vertical crease is aligned along the Z axis. The plates are oriented in the XZ, YZ, and XY planes. There are large disagreements in the null depths. But generally, the differences are less than 1 dBsm in the region of interest.

Top Hat Results. Physically, a top hat is constructed of a solid right circular cylinder which is axially positioned perpendicular to a circular disk. In this study, the disk radius was 20.32 cm, the cylinder radius was 10.16 cm, and the cylinder length was 20.32 cm.

A top hat is polarization sensitive because of the double bounce response between the cylinder and circular base. Figures 7 and 8 show the SRIM and PO equation [12] RCS predictions for a top hat with the cylinder axially positioned along the X axis at 0° elevation. As shown, the only exact agreement occurs when broadside to the cylinder (90°). Large differences between the predictions are prevalent in the 70° to 85° region (HH case) and the 7° to 12° region (VV case). Other than the null point differences, the disagreement is approximately 4 dBsm across the entire scan.

Validation

The data used for this study was collected in the Air Force Institute of Technology anechoic test chamber. Since PO theory does not take into account surface waves and incorrectly accounts for edge diffractions, SRIM is only expected to match predictions in the specular region of the target.

Square Plate Results. Figure 9 shows the results for the square flat plate with thickness .159 cm. SRIM sampled the target with rays 1.52 mm apart (1% of target length). The null depths do not match, but the magnitude of the peaks agree remarkably well (less than 2 dBsm difference) out to 45° from the target normal. The largest difference occurs at 22° from edge-on because this is where the effect of the traveling wave is seen in the measured data.

Circular Disk Results. Figure 10 shows the comparison for the circular disk with thickness .159 cm. The target was sampled with a ray spacing of 3 mm (1% of diameter). As in the case of the square plate, the depth of the nulls do not match, but the differences at the peaks are less than 1.5 dBsm out to 45° from the target normal. There is a larger difference at the specular point (90°) than expected. This indicates that the target may have been leaning slightly. Between 0° and 45° SRIM does not accurately predict the lobe positions. In this region, the return is dominated by edge diffractions which are not accurately modeled by PO. The lobing structure is more complicated for the disk than for the square plate because of the phase variations caused by the disk curvature.

Solid Right Circular Cylinder Results. Figure 11 shows the comparison for the solid right circular cylinder. SRIM sampled the target with .76 mm (1% of cylinder diameter) ray spacing. Broadside to the cylinder is at 0°. Generally, there is good agreement between the predictions and measured data at the peak points between 0° and 30° (less than a 3 dBsm difference). Between 30° and 60° the lobe positions are in slight disagreement. This is probably due to diffractions off both ends of the cylinder. Between 60° and 90° there is fairly good agreement. The differences at 73° and 90° are attributed to the traveling wave and measurement errors, respectively.

Generic Missile Results. A generic missile was used for the final comparisons. The primitives used for modeling the target were two right circular cylinders (RCC), an ellipsoid of revolution (ELL), and four arbitrary wedges (ARW). The target was sampled with .76 mm (1% of cylinder diameter) ray spacing. Figure 12 shows the RCS comparisons. As shown, the SRIM predictions follow the same trend as the measured data, but there are significant differences in the lobing structures. However, at all the major return locations there is good agreement.

Verification Conclusions

The differences between the SRIM predictions and other sources of data were in good agreement at the maximum point of return for all the targets except the top hat. However, there were major differences in the depth of the nulls. There is a 4-7 dBsm disagreement between the SRIM and PO equation predictions for the top hat.

With the exception of the top hat results, this comparison study shows that SRIM correctly implements PO theory. Furthermore, since the predictions are accurate for dihedrals and trihedrals, the code correctly accounts for double and triple bounces between flat plates. The error in the top hat predictions indicate there may be a problem with SRIM's treatment of multiple bounces between a curved object and flat plate.

Validation Conclusions

The SRIM predictions agreed remarkably well with the measured data near the specular region of the target. In the off-specular region there are differences in the lobing structures. There is good agreement between the SRIM predictions and measured data for the generic missile at all aspect angles (only analyzed 0° elevation plane). This validation study shows that SRIM is a good predictor of RCS when restricted to the specular region of the target. Furthermore, as evidenced by the generic missile results, the restriction to the specular region can be relaxed as the number of specular regions in the target increase.

References

1. Mensa, Dean. *High Resolution Radar Cross Section Imaging.* Four tutorial VCR tapes, not dated.

2. Faison, Joseph C. "The Electromagnetic Code Consortium," *IEEE Antennas and Propagation Society Magazine,* 19-23 (February 1990).

3. Sargent, Robert G. "A Tutorial on Validation and Verification of Simulation Models," *Proceedings of the 1988 Winter Simulation Conference.* 33-38. San Diego, December 1988.

4. Arnold, Charles L. Jr. and Mervyn Walsh. *SRIM User Reference Manual, Release 4.0.* Wright Research and Development Center Contract F33615-88-C-1749 with Environmental Research Institute of Michigan. Wright-Patterson AFB OH, January 1991.

5. Herrick D. F. and I. J. LaHaie. *SRIM Polarimetric Signature Modeling,* Internal Research and Development Final Report, October 1987-September 1988. Environmental Research Institute of Michigan Report No. 675805-1-F, 13 December 1988.

6. Knott, Eugene F. and others. *Radar Cross Section.* Norwood MA: Artech House, Inc., 1985.

7. Young, Capt Dennis John. *Primitive Target Validation for the Signature Prediction Tools Software Package.* MS thesis, AFIT/GE/ENG/90D-68. School of Engineering, Air Force Institute of Technology (AU), Wright-Patterson AFB OH, December 1990.

8. Ruck, George T. *Radar Cross Section Handbook,* Volume 2. New York: Plenum Press, 1970.

9. Blejer, Dennis J. *Physical Optics Polarization Scattering Matrix and Impulse Response of a Right Dihedral Corner Reflector.* Unpublished report No. 47PM-ADT-0052. Massachusetts Institute of Technology (MIT), Lincoln Laboratory, Lexington MA, 22 December 1986.

10. Blejer, Dennis J. *Scattering Matrix Transformations for Polarimetric Target Modeling.* Unpublished report No. 47PM-ADT-0057. MIT, Lincoln Laboratory, Lexington MA, 20 May 1987.

11. Blejer, Dennis J. *Physical Optics Polarization Scattering Matrix of a Square Trihedral Corner Reflector.* Unpublished report No. 47PM-ADT-0059. MIT, Lincoln Laboratory, Lexington MA, 30 June 1987.

12. Blejer, Dennis J. "Physical Optics Polarization Scattering Matrix for a Top Hat Reflector," *IEEE Transactions on Antennas and Propagation, 39*: 857-859 (June 1991).

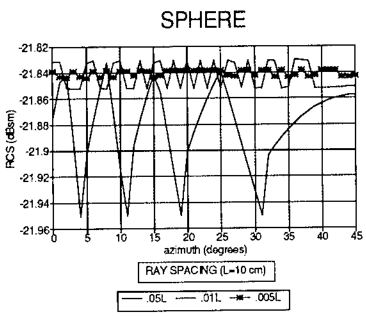

Figure 1. Sphere - SRIM RCS Prediction as a Function of Ray Spacing, Radius=5 cm, F=10 GHz, Elev=0°

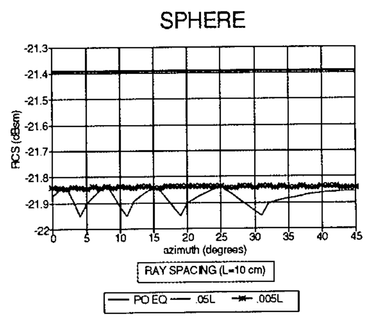

Figure 2. Sphere - SRIM & PO RCS Predictions, Radius=5 cm, F=10 GHz, Elev=0°

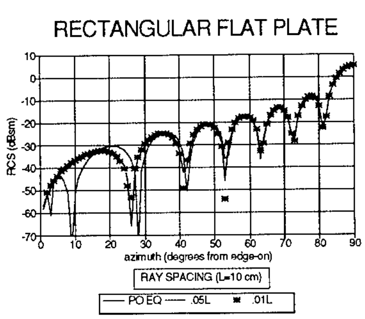

Figure 3. Plate in XZ Plane - SRIM & PO RCS Predictions, X=10 cm, Z=15 cm, F=10 GHz, Elev=0°

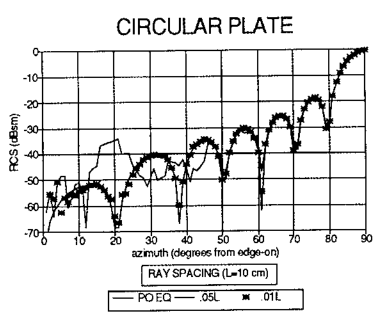

Figure 4. Disk in XZ Plane - SRIM & PO RCS Predictions, Radius=5 cm, F=10 GHz, Elev=0°

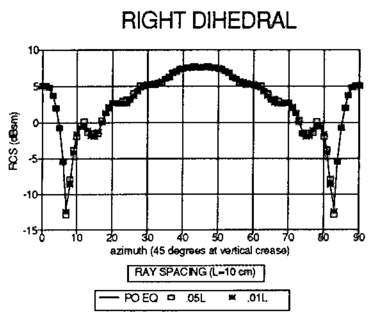

Figure 5. Right Dihedral - SRIM & PO RCS Predictions, X=Y=10 cm, Z=15 cm, F=10 GHz, P=HH, Elev=0°

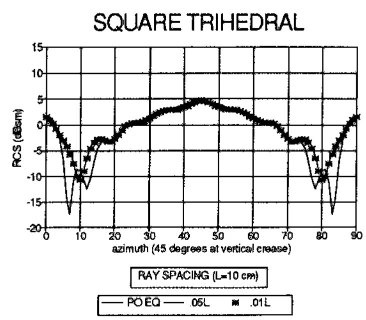

Figure 6. Square Trihedral - SRIM & PO RCS Predictions, X=Y=Z=10 cm, F=10 GHz, P=VV, Elev=0°

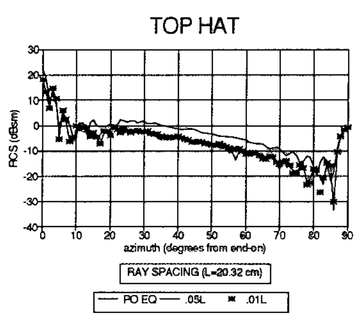

Figure 7. Top Hat - SRIM & PO RCS Predictions, Disk Radius=20.32 cm, Cyl Radius=10.16 cm, Cyl Length=20.32 cm, F=10 GHz, P=HH, Elev=0°

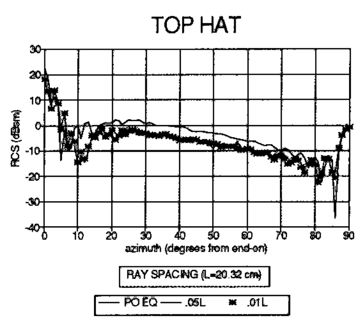

Figure 8. Top Hat - SRIM & PO RCS Predictions, Disk Radius=20.32 cm, Cyl Radius=10.16 cm, Cyl Length=20.32 cm, F=10 GHz, P=VV, Elev=0°

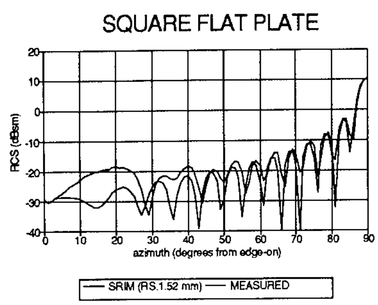

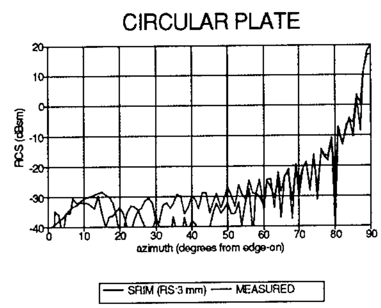

Figure 9. Square Plate in XZ Plane - SRIM RCS Prediction & Measured Data, X=Z=15.24 cm, Y=.159 cm, F=12 GHz, P=HH, Elev=0°

Figure 10. Circular Disk in XZ Plane - SRIM RCS Prediction & Measured Data, Radius=15.24 cm, Y=.159 cm, F=12 GHz, P=HH, Elev=0°

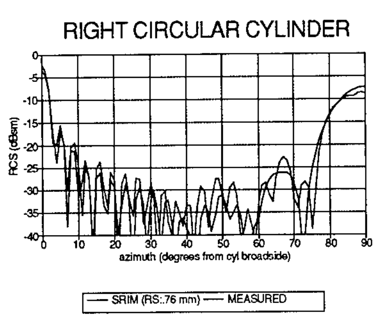

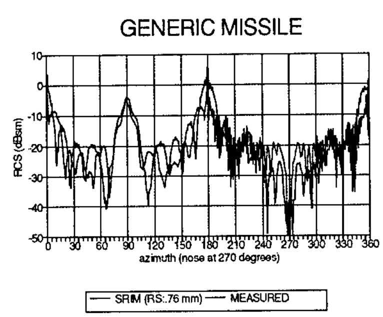

Figure 11. Circular Cylinder Along Y Axis - SRIM RCS Prediction & Measured Data, Radius=3.8 cm, Length=31.27 cm, F=8 GHz, P=HH, Elev=0°

Figure 12. Generic Missile - SRIM RCS Prediction & Measured Data, Length=53.3 cm, Radius=3.81 cm, F=8.5 GHz, P=HH, Elev=0°

Far Zone Scattering by a Flat Plate with Higher Order Effects

Ronald J. Marhefka
The Ohio State University
ElectroScience Laboratory
1320 Kinnear Road
Columbus, Ohio 43212-1191
Phone: (614)292-5752
Fax: (614)292-7297
E-mail: rjm@tiger.eng.ohio-state.edu

Abstract

The far zone scattering from perfectly conducting flat plates will be discussed. An overview of a high frequency solution derived from exact and asymptotic currents cast in the form of rays based on the Uniform Geometrical Theory of Diffraction (UTD) will be presented. Corner diffraction is the primary scattering mechanism with additional contributions from multiple diffracted fields across the plate. The corner term is composed of physical optics, isolated and coupled edge current components, along with a newly derived vertex component. The relationship of this modern UTD solution with modern PTD concepts will be discussed. This method has advantages for computational purposes, since the analysis can be performed on large plates without an increase in computer time.

Triangular and rectangular plate results are validated by comparing with moment methods and measurements. High resolution measurements are also employed to isolate and validate the local UTD diffraction coefficients.

I Introduction

The study of the high frequency far zone scattering from flat plates has been of interest for many years. The two most widely used methods are based on asymptotic currents and rays. The current method is referred to as physical optics (PO) and physical theory of diffraction (PTD). The ray method is referred to as geometrical

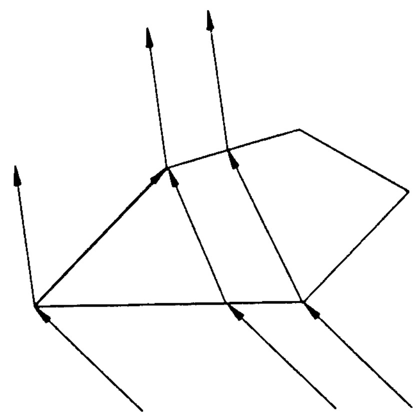

Figure 1: Ray contributions for far zone scattering from a polygonal plate.

optics (GO) and uniform geometrical theory of diffraction (UTD). Historically these methods have accurately produced the scattering in the higher levels of the patterns. In the lower level regions, especially near grazing angles, the first order techniques are inadequate. Plates with narrow angled corners are particularly challenging.

This paper will discuss some recent advances in the understanding of the phenomenology associated with the monostatic and bistatic scattering from flat perfectly conducting polygonal plates. High resolution measurements have allowed us to pin point how well various analytic technique work, thereby showing where to concentrate efforts for improvement.

The present work attempts to show how asymptotic rays relate to asymptotic currents. Three dimensional canonical problems are difficult to obtain and even more difficult to use for practical problems when known. However, approximations obtained to the various mechanisms are efficient to compute and correlate to what the high resolution images suggest. The mechanisms include the scattering from the corners along with higher order terms associated with the corners themselves and interactions of corners with edges, edges with corners, and corners with corners. Typical ray paths are illustrated in Figure 1.

The ray formulation, favored here, has a computation time independent of the size of the plate. The techniques employed here also have been implemented directly from the current integration approach. The results are identical as long as equivalent terms are included.

II Corner Diffraction

A far zone, first order, corner diffraction solution [1] has been derived based on the modern PTD and cast in the form of the (method of equivalent currents) (MEC) [2] and then into a UTD diffraction coefficient. The PO is first used to approximate the currents resulting in a double integral over the surface. Either Stoke's theorem or an asymptotic evaluation is applied to reduce the equation to a line integral. The Michaeli currents are added to produce a total first order MEC result. This integral is then evaluated using the method of stationary phase to obtain the contribution from each corner.

This solution produces an equivalent result to the modern PTD integration of the currents. However, only the corners of the polygonal plate need to be added. This results in a solution whose computer time is independent of the size of the plate.

III Double Diffraction

The first order corner solution neglects the effect of the truncation of the fringe currents from the first edge onto a second edge. This effect automatically gets included if the exact diffraction currents are integrated, but not if the MEC currents are used. A UTD solution [3, 4] has been developed by asymptotically evaluating the truncation of the exact currents on the three dimensional plate. Edge to corner and corner to edge type diffraction coefficients result for the interaction between corner - edge combinations that are not adjacent. For adjacent edge end points, an addition to the corner diffraction coefficient results from the evaluation of the limit form of the current's truncation at the corner. These terms are most important near grazing incidence of knife-edged plates for vertical polarization. It pairs with the first order terms to help produce the expected null in the plane of the plate.

The solution, however, is still not complete. The currents will diffract from the second edge causing a secondary current. This current can be derived using spectral theory or by assumptions of how the MEC currents diffract from the second edge [3, 4]. The ray paths for the asymptotically derived diffraction coefficient will be the same as the primary double effect mentioned above. The addition of this term will improve the results for some parts of the pattern but will actually make the null levels in the plane of knife edged plate worst for vertical polarization. This is because it is best to include UTD solutions in pairs. A triple diffraction is then needed to complete this solution if the null region is accurately desired. At some point, however, efficiency versus accuracy becomes an issue.

IV Edge Waves

A corner to corner diffraction term can be formulated based on the assumption that the fields that propagate along the accompanying edge is trapped, similar to a transmission line. This is sometimes referred to as an edge wave. A solution [3] has been derived based on the result for a dipole near an edge [5] interacting with an adjoining edge. This solution can be shown to significantly contribute to the solution over a limited range. However, most of the time it appears to be small.

V Higher Order Vertex Diffraction

The mechanisms above provide a useful means of calculating the scattering from a plate. It has been known for some time, however, that these mechanism do not account for all situations. The two best known cases are the missing lobing that occurs in the plane of the plate for horizontal polarization and the missing lobe looking back at a narrow angled vertex of a triangular plate for vertical polarization. High resolution measurements of triangular plates has been accomplished and compared with analysis. It became clear that the scattering from a simple corner of a plate was incomplete using the methods defined above.

The exact solution for a vertex [6] is very difficult to compute for large distances from the tip. The convergence of the solution is very slow because the coefficient are not definable in closed form. It has been discovered [7, 8], however, that the solution for the currents within two wavelengths or so of the tip can be calculated using a CRAY computer. Once the PO and exact edge currents for the two individual edges making up the vertex are subtracted off, it is found that the currents have a monotonic decreasing functionality radially away from the tip. The transverse (ϕ) behavior is less easily defined.

An asymptotic evaluation [7, 9] in the radial direction can be performed and matched to the exact solution about 0.2λ from the tip. A bounded one dimensional numerical integration in the ϕ direction can then be easily obtained. The coefficients of the exact solution are still found on the CRAY and tabulated, but then the field calculations can be done on a regular computer. The present process takes about a factor of four longer than the previous corner diffraction coefficient, however, it provides the heretofore missing physics.

VI Results

The backscatter from a triangular plate is used to illustrate the validity of the solution discussed here. The geometry, sometimes referred to as Sikta's triangle, is illustrated

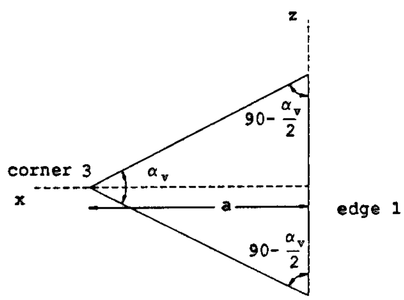

Figure 2: Geometry of triangular plate.

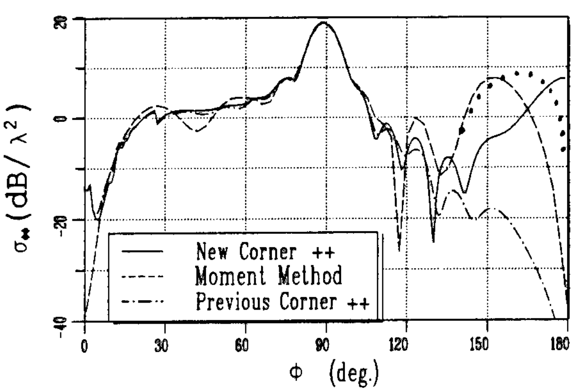

Figure 3: Backscatter ($\sigma_{\phi\phi}$) from a triangle with $a = 3\lambda$ and $\alpha_v = 30°$ for a $\theta = 90°$ pattern cut. (Dots are from the current integration method.)

in Figure 2. The triangle is 3λ long with a tip angle of 30°. Calculations made with the new corner solution which includes all of the mechanisms discussed here is compare with moment methods [10, 11] and the corner solution which does not include the new vertex component. The $\sigma_{\phi\phi}$ pattern in the $x - y$ plane is shown in Figure 3. Note that the new component contributes the missing lobe in the 135° - 180° region. The dots represent the current integration method which picks up the truncation of the vertex current (vertex to edge double effect) at the opposite end of the plate. Asymptotic analysis to put this in ray form hopefully will be completed in the future. In any event, the agreement is very encouraging.

The backscatter in the plane of a plate is illustrated next. The plate is 11.875" on a side as shown in Figure 4. Calculations are made using the new corner and

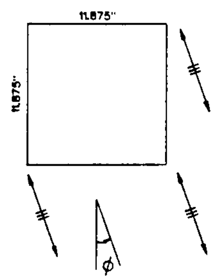

Figure 4: 11.875" square plate in the $x - y$ plane.

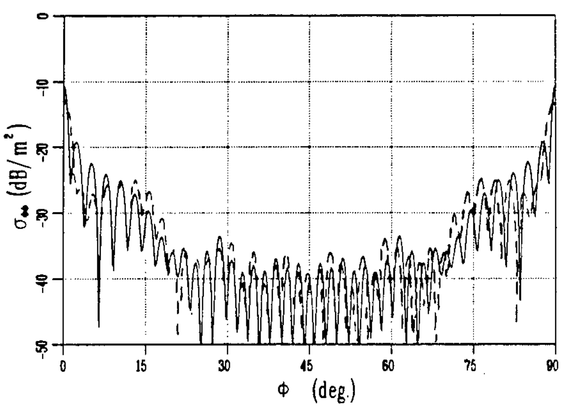

Figure 5: Backscatter ($\sigma_{\phi\phi}$) in the plane of the 11.875" square plate at 10 GHz using the new corner and higher order terms. (Calculated is solid and measured is dashed).

additional higher order terms. The results are compared with measurements [12] at 10 GHz for the $\sigma_{\phi\phi}$ polarization in Figure 5. The results differ in the region of $\theta = 0°$ and $\theta = 90°$ due to an edge caustic not presently accounted for in the analysis. Otherwise, the agreement is very good and provides a significant improvement over other asymptotic methods.

VII Conclusions

This paper discusses a method for calculating the far zone monostatic or bistatic scattering from a perfectly conducting polygonal plate. The solution is formulated

in the from of UTD asymptotic rays based on physical optics, MEC, exact edge, and exact eigen function vertex currents. The solution is efficient when based upon rays since it is independent of the size of the plate.

In addition, the physics is clearly tied to high resolution images of the scattering. This has allowed the validation of individual scattering mechanisms. It also leads to a better understanding of the phenomenology, which can be exploited for design or target ID purposes.

Even with this new information, the job is not complete. The algorithms for the new vertex component can be made more efficient as more cases provide insight into how to best tabulate some the coefficient. In addition, it may be possible to get rid of the last one dimensional integration. The special cases, such as edge waves, that are difficult to resolve using present imaging techniques may be better understood with further validation experiments. The extension to dielectric coated plates also will be a challenge for the future.

Acknowledgement

The hard work and dedication of T. J. Brinkley and L. P. Ivrissimtzis are acknowledged. Some of the numerical results presented in this work were made possible by a grant from the Ohio Supercomputing Center, Columbus, Ohio.

References

[1] T. J. Brinkley and R. J. Marhefka, "Comparison of methods for far zone scattering from a flat plate and cube," *Applied Computational Electromagnetics Society*, vol. 3, pp. 57–78, Fall 1988.

[2] A. Michaeli, "Elimination of infinities in equivalent edge currents, Part I: Fringe current components," *IEEE Trans. Antennas Propagat.*, vol. AP-34, pp. 912–918, July 1986.

[3] L. P. Ivrissimtzis and R. J. Marhefka, "High frequency electromagnetic scattering by polyhedral structures," Technical Report 721198-4, The Ohio State University ElectroScience Laboratory, Department of Electrical Engineering, Mar. 1991.

[4] L. P. Ivrissimtzis and R. J. Marhefka, "A uniform ray approximation of the scattering by polyhedral structures including higher order terms." Accepted for publication, *IEEE Trans. Antennas Propagat.*

[5] L. P. Ivrissimtzis and R. J. Marhefka, "Edge wave vertex and edge diffraction," *Radio Sci.*, vol. 24, pp. 771–784, Nov.-Dec. 1989.

[6] R. Satterwhite, "Diffraction by a quarter plane, the exact solution, and some numerical results," *IEEE Trans. Antennas Propagat.*, vol. AP-22, pp. 500–503, May 1974.

[7] T. J. Brinkley and R. J. Marhefka, "Current near the vertex of a perfectly conducting angular sector," Technical Report 721198-5, The Ohio State University ElectroScience Laboratory, Department of Electrical Engineering, July 1991.

[8] T. J. Brinkley and R. J. Marhefka, "Current near the vertex of a perfectly conducting angular sector." Submitted for publication July 1991 to *IEEE Trans. Antennas Propagat.*

[9] T. J. Brinkley and R. J. Marhefka, "Far zone field scattered by a perfectly conducting angular sector." Submitted for publication July 1991 to *IEEE Trans. Antennas Propagat.*

[10] E. H. Newman, "A user's manual for the electromagnetic surface patch code: ESP version IV," Technical Report 716199-11, The Ohio State University ElectroScience Laboratory, Department of Electrical Engineering, Aug. 1988.

[11] E. H. Newman and R. J. Marhefka, "An overview of MM and UTD methods at The Ohio State University," *Proc. IEEE*, vol. 77, pp. 700–708, May 1989. also IEEE Press book, *Radar Cross Sections of Complex Objects.*

[12] T. Nguyen and A. K. Dominek, "An edge wave reflection coefficient," Technical Report 721929-22, The Ohio State University ElectroScience Laboratory, Department of Electrical Engineering, Mar. 1990.

ELECTROMAGNETIC SCATTERING BY TWO DIMENSIONAL PERIODIC BODIES

K. J. Harker
Systems Techniques Laboratory
SRI International, Menlo Park, CA 94025

ABSTRACT

An electromagnetic code - PERIODIC - has been developed for calculating the scattering from periodic two-dimensional (2D) bodies. The uniqueness of PERIODIC is its applicability to periodic 2D bodies of arbitrary cross section and composition, dielectric and/or magnetic, homogeneous or inhomogeneous, and isotropic or anisotropic. The mathematical basis for the inclusion of periodicity in the code is Floquet's Theorem. Using this principle, the governing integral equation can be reduced to a one-period domain. As a result of this simplification, the original Green's function, a Hankel function, is replaced by an infinite series of Hankel functions with arguments successively incremented in the periodic direction. The resulting periodic Green's function was summed using the Kummer series and Poisson sum formula. There are two different output regimes for the scattered field in PERIODIC. In both, the observation distance is large compared to the period. In the first regime, the observation distance is small compared to the body size and the scattered field consists of a finite number of plane waves. In the second output regime, the observation distance is assumed to be much larger than the physical dimensions of the body.

INTRODUCTION

A computer program, PERIODIC, has been developed for calculating the scattering from two dimensional (2D) periodic bodies. By two-dimensional we mean that the body is periodic in one direction (the x-direction), of arbitrary variation in the y-direction, and unbounded in the z-direction. There are basically two polarization versions of the program: the E field polarization version where the E field is parallel to z and the two H field components are in the x-y plane, and the H field polarization version with the roles of E and H reversed.

PERIODIC was developed by means of a modification of the GAS (General Anisotropic Scattering) code of Damaskos, Inc. [1987]. Because the general capabilities of the GAS code have been translated over to PERIODIC, PERIODIC possesses the same generality, in particular applicability to isotropic or anisotropic media, homogeneous or inhomogeneous media, and dielectric materials with both dielectric constant and permeability complex and different from unity.

There are two basic regimes in which the code operates. In the first regime the observation distance is greater than the period and small compared to the length. This is referred to as the plane wave regime, since the scattered energy is distributed amongst a set of plane waves. The second regime, called the cylindrical wave regime, corresponds to observation distances large compared to the body length. In this regime the scattered energy consists of a sum of the cylindrical waves generated by each current rod in the body. In this regime it is assumed that

the radiating currents in the body are the same as those of the body with infinite length, and therefore is based on the approximation that end effects can be ignored.

THE PERIODIC INTEGRAL EQUATION

We assume a body with period h and the (x,y,z) rectangular coordinate system described above. There is incident upon the body a plane wave with an electric field of the form

$$E_i(x,y)=E_{io}e^{-j(k_x x+k_y y)} \tag{1}$$

The integral equation for such a body can be written in the form

$$E(x,y)-E_{i0}e^{-j(k_x x+k_y y)}=\int_S dx'dy'G(x-x',y-y')\ J(x',y') \tag{2}$$

where the integral is over the two dimensional cross section, S, of the body. The symbol **J** in this equation represents either the electric or magnetic current. Also there are additional equations in which **H** and $\mathbf{H}_i$ appear on the on the left hand side of this equation in place of **E** and $\mathbf{E}_i$.

We now invoke Floquet's Theorem, which states that in a periodic configuration we can write all variables as

$$e^{-jk_x x}\ F(x,y) \tag{3}$$

where F(x,y) is periodic in x. We can therefore write the currents and fields as

$$J(x,y)=J_0(x,y)e^{-jk_x x} \qquad E(x,y)=E_0(x,y)e^{-jk_x x} \tag{4}$$

where $\mathbf{J}_0$ and $\mathbf{E}_0$ are periodic in x. Substituting (1) and (4) into (2) gives

$$E_0-E_{i0}e^{-jk_y y}=\sum_{j=1}^{3} I_j \tag{5}$$

where

$$I_j = d_j e^{jk_x x} \int_S dx' dy' O_j H_0^{(2)}(kr) J_0(x',y') e^{-jk_x x'} \tag{6}$$

and $H_0^{(2)}$ is the zero-order Hankel function, I_j are the three basic integrals that appear in the electromagnetic field integral equations, O_j are the three integral operators which are associated with each integral, d_j are constants, $r=[(x-x')^2+(y-y')^2]^{1/2}$, and $k=[k_x^2+k_y^2]^{1/2}$.

We will now consider the three specific types of integrals. The first type is simply given by

$$I_1 = d_1 \int_S dx' dy' J_0(x',y') e^{jk_x(x-x')} H_0^{(2)}(kr) \tag{7}$$

We now break up the integration region into periodic cells S_n, each of which is displaced from the central cell, C, by nh. Since J_0 is periodic, we can rewrite (7) as

$$I_1 = d_1 \int_C dx' dy' J_0(x',y') G_1(x-x',y-y') \tag{8}$$

where

$$G_1 = \sum_{n=-\infty}^{\infty} H_0^{(2)}(kr_n) e^{jk_x(x-x'-nh)} \tag{9}$$

and $r_n=[(x-x'-nh)^2+(y-y')^2]^{1/2}$. We have now performed the important step of reducing the integration area to a single cell, C, albeit at the expense of the more complicated kernel in (9).

The second type of integral has the form

$$I_2 = d_2 e^{jk_x x} \int_S dx' dy' \nabla \times H_0^{(2)}(kr)\ J_0(x',y')\ e^{-jk_x x'} \tag{10}$$

Carrying out the curl operation and rearranging gives

$$I_2 = d_2 \int_S dx' dy'\ J_0(x',y') \times e^{jk_x(x-x')}\ \nabla' H_0^{(2)}(kr) \tag{11}$$

where the prime on the grad operator denotes differentiation of the primed variables. Breaking up the integration region into periodic cells again reduces the integration region to a single cell C, and we obtain thereby the expression

$$I_2=d_2\int_C dx'dy'\; J_0(x',y')\times G_2(x-x',y-y') \tag{12}$$

where

$$G_2=\sum_{n=-\infty}^{\infty} e^{jk_x(x-x'-nh)}\; \nabla'\; H_0^{(2)}(kr_n) \tag{13}$$

The third type of integral has the form

$$I_3=d_3 e^{jk_x x}\nabla\int_S dx'dy' H_o^{(2)}(x-x',y-y')\;\; \nabla'\cdot J_0(x',y')e^{-jk_x x'} \tag{14}$$

We can use the Lorentz gauge condition to show that

$$\int dx'dy' H_0^{(2)}\,(\nabla'\cdot J_0 e^{-jk_x x'})=-\int dx'dy'\,(J_0 e^{-jk_x x'}\cdot\nabla')\,H_0^{(2)} \tag{15}$$

We also know that

$$e^{-jk_x x'}\nabla'=(\nabla'+jk_x)e^{-jk_x x'} \tag{16}$$

Substituting (15) and (16) into (14) and again breaking the integration region into periodic zones yields the result

$$I_3=d_3\int_C dx'dy'[(J_0\cdot\nabla')\nabla'+j(J_0\cdot\nabla')k_x+j(J_0\cdot k_x)\nabla'-(J_0\cdot k_x)k_x]G_1 \tag{17}$$

where G_1 is given by (9).

It is important to note that these equations have been structured so that all differentiations act on the Green's function and never on **J**. This considerably simplifies the code, since it eliminates the half-displaced cells required when differentiations must be performed on the unknown varible of the integral equation.

FORMULAS FOR THE PERIODIC GREEN'S FUNCTION

We will now show how these periodic Green's functions are calculated using the Poisson addition formula [Morse and Feshbach, 1953] in conjunction with the Kummer series [Abramowitz and Stegun, 1964; Richards et al., 1987; Jorgenson and Mittra, 1990].

Using the Poisson sum formula in the same manner as outlined in Morse and Feshbach [1953], it can be shown that

$$G_1 = \frac{2}{h} \sum_{\nu=-\infty}^{\infty} e^{-2\pi j \nu (x-x')/h - jk_{y\nu}|y-y'|} \, k_{y\nu}^{-1} \tag{18}$$

where $k_{y\nu} = [k^2 - (k_x + 2\pi\nu/h)^2]^{1/2}$. For sufficiently large values of ν, $k_{y\nu}$ becomes negative imaginary and the second term in the argument of e in (18) gives rise to a decaying exponential with argument $|k_{y\nu}|\,|y-y'|$. The series can then be terminated at that value of ν which causes the decaying exponential to fall below the precision of the calculation.

Likewise, we can show that

$$G_2 = \frac{2j}{kh} \sum_{\nu=-\infty}^{\infty} e^{-2\pi j \nu (x-x')/h - jk_{y\nu}|y-y'|} \left[\mathbf{x} \, \frac{k_x + 2\pi\nu/h}{k_{y\nu}} + \mathbf{y} \; sn(y-y') \right] \tag{19}$$

x and **y** are the x and y unit vectors and the sn function denotes the sign of its argument.

If $|y-y'|$ is small, or worse yet, zero, then the exponential decay in (18) and (19) referred to above only becomes significant for very large values of ν, and the series converges much too slowly or not at all. This problem is solved by using the Kummer series, where we add and subtract two equal series to the original series, and then rearrange the resultant into two separate series which converge rapidly. For example, we write G_1 as

$$G_1 = \left\{ \sum_n H_0^{(2)}(kr_n) e^{jk_x(x-x'-nh)} - \sum_n H_0^{(2)}(kr_{nc}) e^{jk_x(x-x'-nh)} \right\} + \frac{2}{h} \sum_n e^{-2\pi jn(x-x')/h - jk_{yn}(|y-y'|+ch)} k_{yn}^{-1} \tag{20}$$

where

$$r_{nc} = \sqrt{(x-x'-nh)^2 + (|y-y'|+ch)^2} \tag{21}$$

and c is a convergence constant. The first series converges much more rapidly than (9) alone, while the second series converges because $|y-y'|$ has been incremented by ch. Furthermore, the first series in (20) converges more rapidly as c goes to zero, while the second series converges more rapidly as c increases. There is, therefore, an optimum value of c for the fastest overall convergence. This value of c was found as follows: In practice both series must be truncated at a finite number of terms, and the error of the truncation is roughly the magnitude of the last term in the truncated series. We then choose c so that both the error and the number of terms in each series is equal. This process led to values of c equal to to 0.02, max[.02, $0.0003(h/(y-y'))^2$], and 0.0 for $|y-y'|=0$, $0<|y-y'|<0.15h$, and $|y-y'|>0.15h$, respectively.

For non-self terms, the kernels in (17) were calculated by finite difference formulas, using the values of G_1 generated with (20) in the formulas. For self terms this process must be modified for the first term in (17). If s is the unit vector in the direction of **J**, then this term has the form

$$(s\cdot\nabla')\ (s\cdot\nabla')G_1 \tag{22}$$

The finite difference form of the term contains a value of G_1 at the singular point $x=x'$ and $y=y'$. It was found that any attempt to include such a term in a finite difference formula led to great inaccuracies. This problem was resolved by writing this term in the form

$$\frac{\dfrac{dG_1}{ds}(r_o+ls) - \dfrac{dG_1}{ds}(r_o-ls)}{2l} \tag{23}$$

where s is the distance along the direction **J**, $\mathbf{r}_o$ is a point near the cell center, 2l is the cell size along the direction of **J**, and dG_1/ds is evaluated analytically.

FAR FIELDS

Once the kernels in (6) are determined, this equation can be solved by the method of moments to determine the body currents. Eq. (5) can then be used to determine the exterior fields by evaluating $\mathbf{E}_0$ at the observation point (x,y).

The distance of observation point from the body determines the type of approximation to be used for the Green's function in (5). For the plane wave regime the Poisson sum expansions in (18) and (19) are used, but only those terms corresponding to propagating waves for the Green's function are included. The absense of evanescent waves is guaranteed by the plane wave asssumption that the observation distance is large compared to the period. In the cylindrical wave regime the cylindrical wave far field function, $e^{-jkr}/r^{1/2}$, is used for the Green's function.

COMPARISON WITH LAYERED THEORY

Comparisons were made with results from other theories. Figure 1 compares the results from PERIODIC with theoretical results from theory for a planar dielectric sheet using H polarization in an angular sweep. Since a planar sheet can be considered a periodic structure with arbitrary period, the results should agree for any choice of period. The results agree within 0.5dB over the full angular range.

SUMMARY

A computer program for calculating the scattering by 2D periodic bodies has been developed. This program is completely general, being capable of modeling a body of arbitrary complexity, including inhomogeneity, anisotropy, and loss. Comparison with other theories, including planar theory, shows close agreement.

REFERENCES

1. M. Abramowitz and I.A. Stegun, "Handbook of Mathematical Functions," p. 16, U.S. Government Printing Office, Washington, D.C., 1964.
2. R.E. Jorgenson and R. Mittra, "Efficient Computation of Free-Space Periodic Green's Functions," IEEE Trans. Ant. Prop. 38, 633-642, 1990.
3. P.M. Morse and H. Feshbach, "Methods of Theoretical Physics, Part I," p. 817-818, Mc Graw Hill Book Co., New York, 1953.
4. W.F. Richards, K. McInturff, and P.S. Simon, "An Efficient Technique for Computing the Potential Green's Function for a Thin, Periodically Excited Parallel-Plate Waveguide Bounded by Electric and Magnetic Walls," IEEE Trans. on Microwave Theory and Techniques, MTT-35, pp. 276-281, 1987.
5. "Two Dimensional Electromagnetic Scattering By an Anisotropic Body of General Shape," Vols. I-III, Damaskos, Inc., P.O. Box 469, Concordville, PA, 1987.

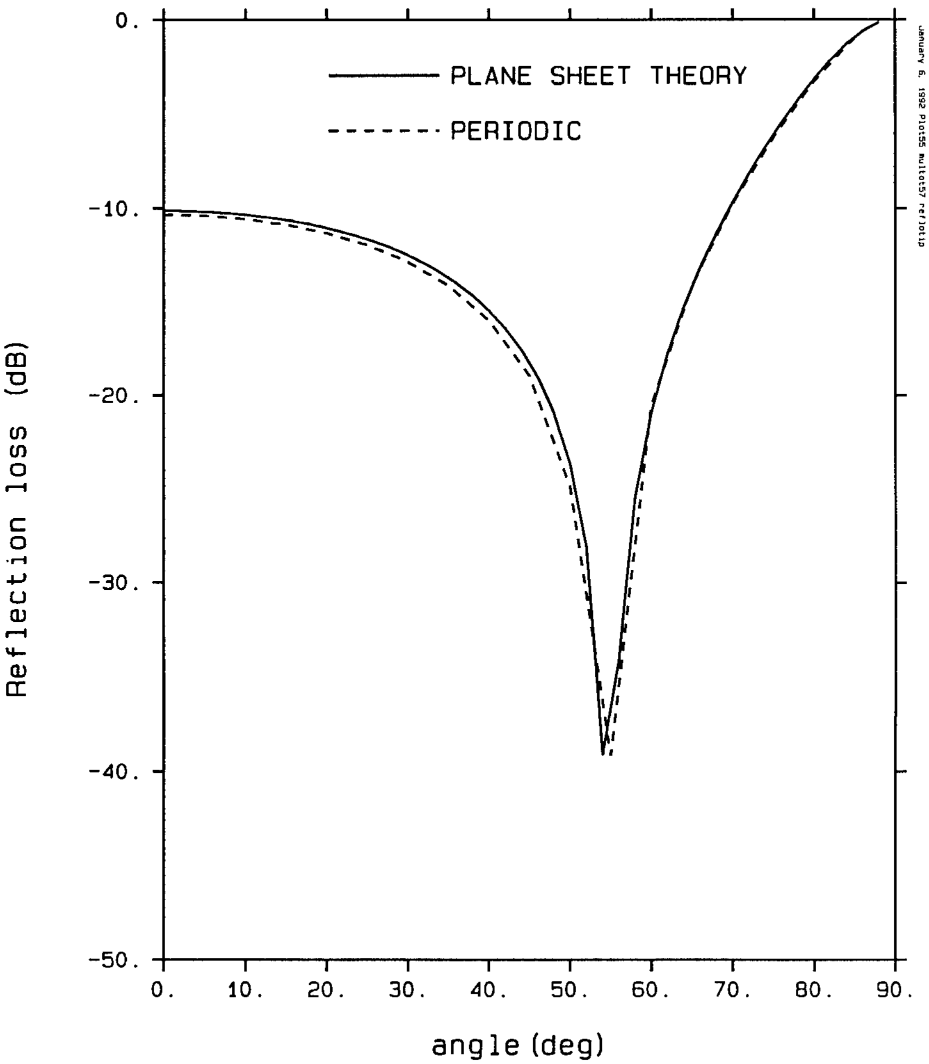

Figure 1. Reflection loss vs. angle of deviation from normal incidence for a dielectric layer 0.04mm thick with a dielectric constant of 2.0. Incident wave had a frequency of 10 GHz and H-polarization. The period was 0.15mm.

Screening Properties of the Inclined Strip Grating

EMMANOUIL E. KRIEZIS and DIMITRIS P. CHRISSOULIDIS

Division of Telecommunications, Department of Electrical Engineering,
Faculty of Technology, Aristotle University of Thessaloniki,
P.O. Box 1562, GR-54006 Thessaloniki, Greece

Abstract - The spectral response of an inclined strip grating, either free standing or embedded in a dielecric slab, is quite sensitive to variations of the cant angle. It is an attractive frequency-selective surface which allows for considerable desigh flexibility through the cant angle or the refractive index of the host dielectric. Such gratings can be used in radar antenna systems as filters in front of radomes and even as polarizers or dichroic antenna subreflectors. The inclined strip grating is analyzed through an indirect mode-matching technique based on Green's second theorem. The analytical approach is simple and numerically efficient. Reflection and transmission coefficients as well as far-field radiation patterns on both sides of the structure are determined with special attention to the effect of the cant angle.

I. Mathematical Formulation

The inclined strip grating (fig. 1) is a periodic screen composed of metallic canted strips which are infinitely long in the y dimension. Furthermore, strips are assumed to be infinitesimally thin and perfectly conducting. The metallic structure may be enclosed in a dielectric slab.

A free-standing inclined strip grating has previously been analyzed by a formidable but involved approach based on the Wiener-Hopf and modified residue calculus techniques *(Kobayashi and Inoue, 1988)*. Other free-standing strip gratings of finite thickness have been analyzed through the electric field integral equation (EFIE) which is discretized by the spectral-Galerkin technique *(Hall et. al., 1988)*. The above mentioned papers have not investigated the scattering behaviour of the grating in the Fraunhofer zone as well as the effect of the refractive index of the dielectric slab.

The incident electromagnetic wave is linearly polarized along the y direction, having a wavenumber vector $\vec{k}_i$ that lies in the x0z plane (TE polarization). The nature of the incident radiation and the fact that the scattering surface is uniform in the y direction justify a scalar treatment of the problem. The 2-D Helmholtz equation should be satisfied in the x0z plane.

Due to the periodicity of the structure along the x axis, the fields in the half-spaces I and III can be expanded in Floquet series*(Scott, 1989)*

$$\psi^{I}(x,z) = e^{-j(\alpha_0 x-\beta_0 z)} + \sum_{m=-\infty}^{\infty} A_m e^{-j(\alpha_m x+\beta_m z)} \tag{1}$$

$$\psi^{III}(x,z) = \sum_{m=-\infty}^{\infty} D_m e^{-j(\alpha_m x-\beta_m z)} \tag{2}$$

$$\alpha_m = \alpha_0 + 2\pi\frac{m}{L} \quad ; \quad \alpha_0 = \pm k_0 \sin\theta_{inc}$$

$$\beta_m = \begin{cases} \sqrt{k_0^2 - \alpha_m^2} \\ -j\sqrt{\alpha_m^2 - k_0^2} \end{cases} \quad \text{if} \quad \begin{cases} k_0^2 \geq \alpha_m^2 \\ k_0^2 < \alpha_m^2 \end{cases}$$

where ψ stands for the field component E_y. The coefficient A_0 is the reflection coefficient of the surface and D_0 is the transmission coefficient *(Hall et al., 1988)*.

The electric field intensity in region II is expanded in terms of TE_n-modes accomodated by a parallel plate waveguide:

$$\psi^{II}(\eta,\xi) = \sum_{m=1}^{\infty} B_m \sin\left(\frac{m\pi\xi}{L\sin\gamma}\right)\left\{ e^{-jk_m\eta} + C_m e^{jk_m\eta} \right\} \tag{3}$$

$$k_m = \left\{k^2 - \left(\frac{m\pi}{L\sin\gamma}\right)^2\right\}^{1/2} \quad ; \quad k = k_0\sqrt{\varepsilon_r} = k_0 n$$

It is clear that the expression of (3) is not valid in the triangular areas ABC and DEF. Hence the field expressions (1), (2) and (3) cannot be matched directly on the interfaces of the three regions. This difficulty is

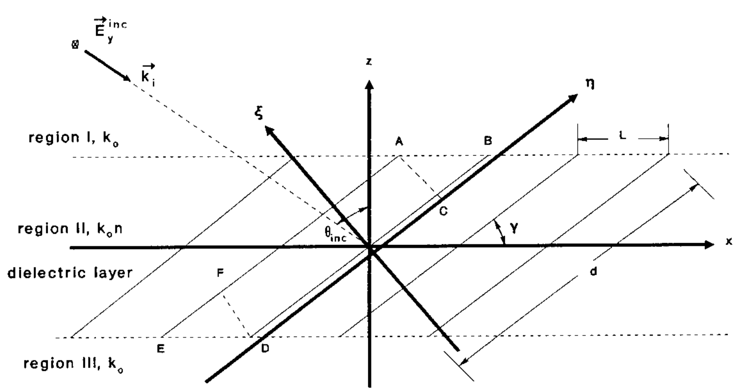

Fig. 1 Inclined strip grating geometry

circumvented by applying Green's second theorem *(Mittra, 1973)*, which is writ ten is scalar form as follows

$$\oint_C \left(\phi\frac{\partial\psi}{\partial N} - \psi\frac{\partial\phi}{\partial N}\right) dl = \iint_S \left(\phi\nabla^2\psi - \psi\nabla^2\phi\right) ds \tag{4}$$

and $\partial/\partial N$ denotes the derivative along the direction normal to the integration path. Selecting an appropriate function ϕ that obeys the 2-D Helmholtz equation, the right-hand side of (4) vanishes. A simple, but wise choise (for the following calculations) for ϕ is:

$$\phi_n^{\pm} = \sin\left(\frac{n\pi\xi}{L\sin\gamma}\right) e^{\pm jk_n\eta} \quad ; \quad n = 1,2,... \tag{5}$$

Enforcing (4) along the closed triangular paths ABC and DEF, yields four families of linear equations involving the unknown coefficients A_m, B_m, C_m, D_m for successive values of the index n:

$$\int_{AB} \left(\phi_n^{\pm}\frac{\partial\psi^{I}}{\partial z} - \psi^{I}\frac{\partial\phi_n^{\pm}}{\partial z}\right) dx - \int_{CA} \left(\phi_n^{\pm}\frac{\partial\psi^{II}}{\partial\eta} - \psi^{II}\frac{\partial\phi_n^{\pm}}{\partial\eta}\right) d\xi = 0 \tag{6a}$$

$$-\int_{DE} \left(\phi_n^{\pm}\frac{\partial\psi^{III}}{\partial z} - \psi^{III}\frac{\partial\phi_n^{\pm}}{\partial z}\right) dx + \int_{FD} \left(\phi_n^{\pm}\frac{\partial\psi^{II}}{\partial\eta} - \psi^{II}\frac{\partial\phi_n^{\pm}}{\partial\eta}\right) d\xi = 0 \tag{6b}$$

It should be clear that $\phi_n^{\pm}$ and ψ - which represents tangential electric field with respect to the strips - are equal to zero along BC and EF.

The orthogonality properties that exhibit the functions $\phi_n^{\pm}$ allow for a significant simplification in the linear system (6a) and (6b). The coefficients B_m and C_m can be eliminated and the system acquires its final form:

$$\sum_{m=-\infty}^{\infty} A_m(\beta_m-\alpha_m\cot\gamma\pm k_n\csc\gamma)\frac{e^{-j(\alpha_m\cos\gamma+\beta_m\sin\gamma)d/2}}{(\pm k_n\cos\gamma-\alpha_m)^2-(n\pi/L)^2}$$

$$- e^{\mp jk_n d}\sum_{m=-\infty}^{\infty} D_m(-\beta_m-\alpha_m\cot\gamma\pm k_n\csc\gamma)\frac{e^{-j(-\alpha_m\cos\gamma+\beta_m\sin\gamma)d/2}}{(\pm k_n\cos\gamma-\alpha_m)^2-(n\pi/L)^2}$$

$$= (\beta_0+\alpha_0\cot\gamma\mp k_n\csc\gamma)\frac{e^{-j(\alpha_0\cos\gamma-\beta_0\sin\gamma)d/2}}{(\pm k_n\cos\gamma-\alpha_0)^2-(n\pi/L)^2} \quad ; \quad n = 1,2,... \tag{7}$$

The infinite summation with respect to m is truncated in the interval $-M\leq m\leq M$, while n is allowed to vary in the interval $1\leq n\leq 2M+1$. Thus, the number of unknowns is equal to $2(2M+1)$ which is the same as the number of the resulting

equations.

When the distribution of the electric field intensity along the interfaces of the regions I/II and II/III has been determined, one can proceed to the construction of far field radiation patterns. We shall focus our interest on scattering directions within the plane of incidence (x0z), wherein $\phi_s = 0$ or $\phi_s = \pi$ (fig. 2). The only non vanishing component of the electric field intensity in the Fraunhofer zone, with regard to a system of spherical coordinates is the E_ϕ which is given by the following expression *(Ishimaru, 1978)*:

$$E^r_\phi = \frac{(-jk_0)\, e^{-jk_0R}}{4\pi R} \iint_{S'} \left(-E^s_y(\vec{r}\,')\cos\phi_s\cos\theta_s + Z_0 H^s_x(\vec{r}\,')\cos\phi_s\right) e^{jk_0\vec{r}\,'\cdot\hat{r}_s}\, ds' \quad (8)$$

$$\hat{r}_s = \sin\theta_s\cos\phi_s\hat{x} + \cos\theta_s\hat{z} \quad ; \quad \phi_s = 0 \text{ or } \pi$$

$$\vec{r}\,' = x'\hat{x} + y'\hat{y}$$

In order to describe how this surface radiates, the scattering coefficient

$$p = \frac{E^r}{E^{ro}} \quad (9)$$

is introduced *(Beckmann and Spizzichino, 1963)* where E^{ro} is the electric field intensity radiated by a perfectly conducting sheet of the same dimensions, at distance R, in the specular direction, under the same illumination conditions (i.e., angle of incidence and polarization). That fictitious metal sheet is considered to be placed at $z = (d/2)\sin\gamma$ (fig. 2).

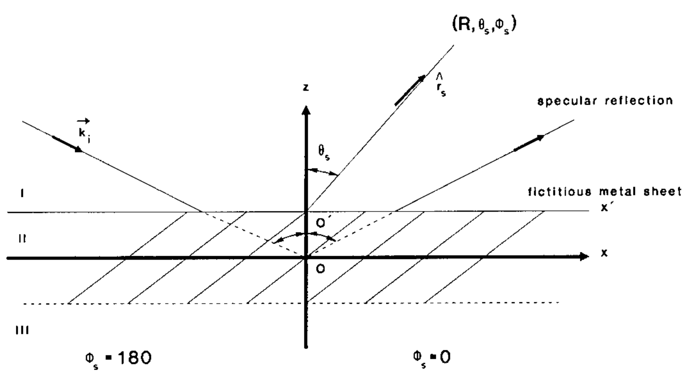

Fig. 2 Radiation in the Fraunhofer zone from the inclined strip grating

Substituting (8) into (9), carrying out the integrations over $2N_s$ periods

of the structure ($2N_sL \gg \lambda$), which are of unit length along the y direction, the squared magnitude of p, which represents the normalized radiated power, is written as:

$$\text{PRC} = \frac{\left| \sum_m A_m(\cos\theta_s + \beta_m/k_0)\frac{\sin(u_0 N_s L)}{u_m} \; e^{-j(\beta_m \sin\gamma - u_m\cos\gamma)d/2} \right|^2}{4\cos^2\theta_{inc} N_s^2 L^2} \tag{10}$$

$$0 \le \theta_s \le \pi/2 \quad ; \quad \phi_s = 0 \text{ or } \pi$$

$$u_m = k_0\sin\theta_s\cos\phi_s - \alpha_m$$

It is evident that the power reflection coefficient (PRC) is generally dependent on all Floquet modes. If the scattering derection $\vec{r}_s$ coincides with the propagation direction of a Floquet mode, then PRC depends only upon that mode.

By analogy to (10), an expression for the power transmission coefficient (PTC) can be developed for the region III:

$$\text{PTC} = \frac{\left| \sum_m D_m(\cos\theta_s - \beta_m/k_0)\frac{\sin(u_0 N_s L)}{u_m} \; e^{-j(\beta_m \sin\gamma - u_m\cos\gamma)d/2} \right|^2}{4\cos^2\theta_{inc} N_s^2 L^2} \tag{11}$$

$$\pi/2 \le \theta_s \le \pi \quad ; \quad \phi_s = 0 \text{ or } \pi$$

II. Numerical Applications

In this section, numerical results are presented for the inclined strip grating. The reflection (A_0) and transmission (D_0) coefficients of the structure are plotted versus frequency. Furthermore, polar patterns of the power coefficients (PRC & PTC) are presented.

The diagrams of fig. 3 provide a general view to the behaviour of the structure in the frequency band 5 to 40 GHz. The strip width d = 1.5 cm and the spacing L = 1.5 cm. A dielectric material of relative dielectric constant $\varepsilon_r = 1.5$ is assumed to fill region II. The cant angle - measured with respect to the x axis - is $\gamma = 60^0$. Incidence from the side $\phi_{inc} = 180^0$ has been considered, while $\theta_{inc} = 0^0, 15^0, 30^0$. The total number of Floquet modes encountered is equal to 21 ($-10 \le m \le 10$). Moreover, the scattering surface is extended over 20 periods ($N_s = 10$). The diagrams verify the frequency selective nature of the surface. The surface acts as a frequency filter with passbands seperated by stopbands. In addition, when the wavelength of the incident radiation is large compared to the strip spacing L, total reflection occurs.

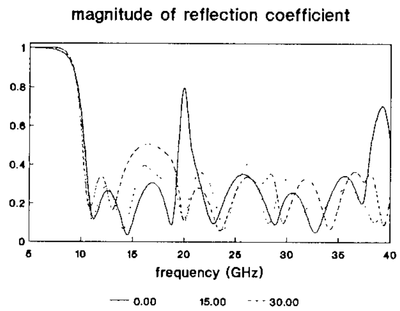

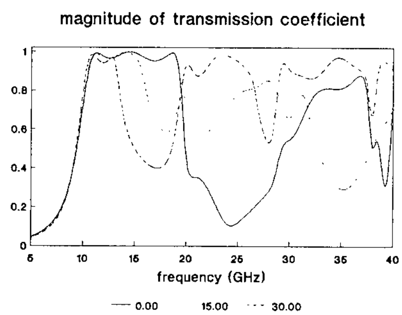

Fig.3 Reflection and Transmission coefficients versus frequency

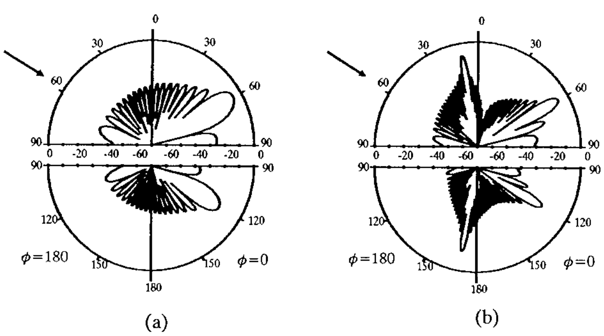

Fig.4 Scattering diagrams

The diagrams of fig. 3 further exhibit resonances predicted by the *Wood's anomaly* and the waveguide resonance.

Polar patterns of the squared magnitude of the scattering coefficient p are presented in fig. 4. For that case, the parameters were set to the following values $d = L = 1.2$ cm, $\varepsilon_r = 1.0$, $\gamma = 75^0$, $\theta_{inc} = 60^0$, $\phi_{inc} = 180^0$, $2N_s = 20$. In fig. 4a the frequency is held at f = 12 GHz while in fig. 4b f = 24 GHz. The upper semi-circle corresponds to the PRC while the lower semi-circle to the PTC. The arrow shows the direction of incidence. It is apparent that power is mainly radiated in the direcions of propagating Floquet modes and that the number of minor lobes is proportional to frequency.

III. Conclusions

The potentials of an inclined strip grating as an FSS or radome have been investigated through an indirect mode-matching technique based on Green's second theorem. The analysis is simple and efficient, the end result being an infinite matrix equation which is easily handled by the computer. The numerical results, especially the far-field radiation patterns, lucidly demonstrate that the scattering behavior of the structure can be drastically altered through the variation of the cant angle. The principal physical mechanism is waveguide resonance: energy is transferred from the incident to the scattered wave on both sides of the grating through coupling with a mode of the parallel plate waveguide formed by the successive strips.

IV. References

[1] Beckmann P. and Spizzichino A., *The Scattering of Electromagnetic Waves From Rough Surfaces*. Oxford: Pergamon Press, 1963.

[2] Hall R.C., Mittra R., and Mitzner K.M., "Scattering from finite thickness resistive strip gratings," *IEEE Trans. Antennas Propagat.*, vol. AP-36, pp. 504-510, Apr. 1988.

[3] Ishimaru A., *Wave Propagation and Scattering in Random Media* (vol. II). New York: Academic Press, 1978.

[4] Kobayashi K. and Inoue T., "Diffraction of a plane wave by an inclined parallel plate grating," *IEEE Trans. Antennas Propagat.*, vol. AP-36, pp. 1424-1434, Oct. 1988.

[5] Mittra R. (Ed.), *Computer Techniques for Electromagnetics*. Oxford: Pergamon Press, 1973.

[6] Scott G., *The Spectral Domain Method in Electromagnetics*. Boston: Artech House, 1989.

COMPARISON OF NUMERICAL INTEGRATION OF RING SURFACE FIELDS, AND 1ST ORDER PHYSICAL OPTICS FOR THE SKYWAVE FIELD OF HF ANTENNAS IN THE VICINITY OF THE UTAH TEST SITE AND AN ELECTRICALLY LARGE GAUSSIAN RIDGE.

R.H. Ott
GRCI, Inc.
Albuquerque, NM 87106

G.J. Burke
LLNL/ERD
Livermore, CA 94550

I INTRODUCTION

Berry [1] demonstrated the effects of terrain features on the skywave elevation patterns of HF antennas when he calculated the fields on and above the surface of a Gaussian shaped ridge 5 km from the source, 1 km high at its highest point at 1 and 10 MHz. Berry [2] reported possible numerical uncertainties in the 10 MHz results. The convergence of the surfaces fields at 10 MHz was difficult to verify numerically due to the lack of computational speed. These results were obtained on a CDC 3600 using double precision word length (120 bits on CDC architecture). Berry's initial calculations provided motivation to create an alternative integral equation for propagation over realistic terrain profiles at frequencies well into the VHF band. CRPL and NRL [3] provided the financial support to begin the research for finding an alternative integral equation. In a series of two papers, Ott [4], [5], derived an alternative integral equation using a Green's function related to the Sommerfeld flat earth attenuation function. The associated computer algorithm, named WAGNER, was used to compute the fields on irregular terrain profiles and the results were compared with the integral equation used by Berry and "4-Ray Theory" (Geometrical Optics plus knife-edge diffraction) for the 1 km Gaussian ridge, at 1 MHz. Berry used Hufford's integral equation which uses the free-space Green's function. A comparison of these three methods for the Gaussian ridge indicated some slight differences in the surface field. This example, together with many additional ones such as an island in the middle of the sea, an antenna radiating near a cliff overlooking the sea and a vertical monopole with associated ground screen in the presence of a sloping beach at low and high tides gave confidence in the accuracy of PROGRAM WAGNER to treat realistic, smoothly varying inhomogeneous terrain when compared with actual measurement [6].

As PROGRAM WAGNER became excepted as the most accurate model for predicting the effects of terrain on propagation, its use at higher frequencies was tested [7]. These numerical experiments indicated that when the combination of slope and frequency became sufficiently large, that the results for the attenuation function became unstable and began to oscillate. A possible source of this instability was suggested by Bevensee [8], and Vogler [9].

LLNL and NPGS [10] recently provided support for R.H. Ott to examine the source of instabilities in PROGRAM WAGNER and he has derived a modified integral equation (called RING) for the field on the surface of an irregular terrain profile based on the Sommerfeld flat earth attenuation function for the Green's function and the proper choice of sign in the integral part of the Sommerfeld attenuation function depending on whether the profile is concave-up or concave-down.

The mathematical development is beyond the scope of this paper and has been submitted for publication. The results indicate the new algorithm, RING, is extremely fast and accurate for terrain profiles having large slopes; e.g., the Gaussian ridge example, at frequencies as high as 100 MHz. The computation time required for RING to solve the Gaussian hill example at 30 MHz using a 80386 PC with an 80387 math co-processor, was about 10 minutes.

II Two Examples Comparing Elevation Patterns Using RING and PO.

Measurements have been made by NPGS for the purpose of validating numerical models. The terrain profile (Cedar Valley test site in Utah) is shown in Figure 1. The source is located near the origin in Figure 1. Figure 2 shows a plot of the magnitude of the attenuation function, $|f(x)|$, normalized to twice the free-space field, versus distance, x, for an observation point on the surface of the profile in Figure 1, at 27.7415 MHz. The terrain in Figure 1 was fit with a cubic spline to provide continuous derivatives as a function of x. There were 351 field points used to solve for the field on the surface in Figure 2. WAGNER yields large peaks at $x = 104$ m and 162 m, while the largest peak from RING occurs at $x = 430$ m. The RING surface fields are better correlated with the maxima and minima in the derivative of the terrain profile than the WAGNER surface fields, and are more accurate than the WAGNER results.

In order to calculate the elevation pattern in the vicinity of a terrain feature like the one in Figure 1, it is necessary to substitute the surface fields, $f(x)$, in Figure 2 back into the integral equation and

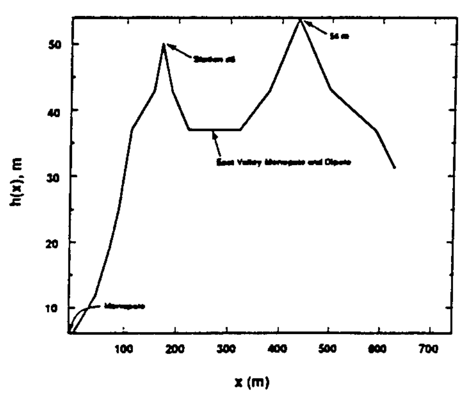

Figure 1. Terrain Profile at the Cedar Valley Test Site in Utah.

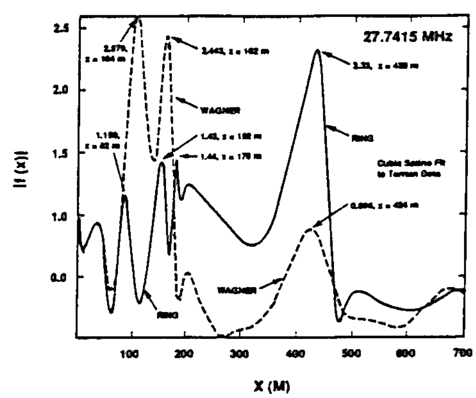

Figure 2. Field on Surface of profile in Figure 1 computed using RING, and WAGNER versus distance x in km. Freq = 27.7415 MHz, $\sigma = 0.0161$ s/m, $\epsilon_r = 9.5$. There are 351 field points, for both RING and WAGNER.

perform the integration. From Green's Theorem in 2-D, the scattered field is given by

$$\psi^s(P) = \int_c [\, \psi(Q) \frac{\partial G}{\partial n} - G \frac{\partial \psi}{\partial n} \,] \, d\, l \tag{1}$$

where the field at the integration point, Q, is, in 2-D

$$\psi(Q) = \frac{2f(x)e^{-i\pi/4 + ikr_1}}{\sqrt{8\pi k r_1}} \qquad (e^{-i\omega t}) \tag{2}$$

and $f(x)$ is the field on the surface obtained from the solution of the integral equation using the algorithm RING. The normal derivative of the field on the surface at the integration point is

$$\frac{\partial \psi(Q)}{\partial n} = -i\, k\, \delta\, \psi(Q) \Big/ \sqrt{1 + (dh/dx)^2} \tag{3}$$

with δ the normalized impedance

$$\delta \cong \begin{cases} \dfrac{1}{\sqrt{\eta}}, & \text{vertical polarization} \\ \sqrt{\eta}, & \text{horizontal polarization} \end{cases} \tag{4}$$

and

$$\eta = \epsilon_r + \frac{i\sigma}{w\epsilon_o} \tag{5}$$

The Green's function, and its normal derivative for an observer above the surface are

$$G = \frac{e^{i\pi/4 + ikr_2}}{\sqrt{8\pi k r_2}} \tag{6}$$

and

$$\frac{\partial G}{\partial n} = i\, k\, G\, \frac{\partial r_2}{\partial n} \tag{7}$$

with r_1 and r_2 the distance from O to Q and Q to P respectively. The total field is obtained by adding the scattered field in (1) to the incident field

$$\psi^i(P) = \frac{e^{-i\pi/4 + ikr_o}}{\sqrt{8\pi k r_o}} \tag{8}$$

giving

$$\psi^T(P) = \psi^i(P) + \psi^s(P) \tag{9}$$

Substituting (1) through (8) into (9) gives

$$\psi^T(P) = \frac{e^{-i\pi/4 + ikr_o}}{\sqrt{8\pi k r_o}} \left\{ 1 - \sqrt{\frac{-ik}{2\pi}} \int_o^{\zeta_m} f(\zeta) e^{ik(r_1 + r_2 - r_o)} \cdot \right.$$

$$\left. \cdot \sqrt{\frac{r_o}{r_1 r_2}} \left(\delta + \frac{\partial r_2}{\partial n} \right) d\,\zeta \right\} \tag{10}$$

Figure 3 shows a plot of the elevation pattern, 20 log_{10} $[\psi^T(P)]$ from equation (10) versus the elevation angle in degrees.

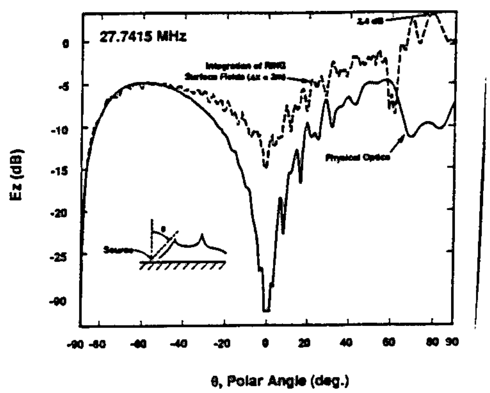

Figure 3. Elevation pattern corresponding to the RING surface fields in Figure 2. Freq = 27.7415 MHz monopole in front of hill). Also shown is the elevation pattern computed using Physical Optics.

We next compute the normalized field strength using Physical Optics, or, since a scalar formulation for this 2-D problem is sufficient, Kirchhoff theory. From Kirchhoff theory, the field and its normal derivative on the surface are given approximately in terms of the incident field at the integration point as

$$\psi\,(Q) \;=\; (1+\Gamma)\,\psi^{i}\,(Q) \tag{11a}$$

$$\frac{\partial\psi(Q)}{\partial n} \;=\; (1-\Gamma)\,\frac{\partial\psi^{i}}{\partial n}\,(Q) \tag{11b}$$

where the Fresnel reflection coefficient, is

$$\Gamma \;=\; \frac{cos\theta_s - \delta}{cos\theta_s + \delta} \tag{12}$$

and

$$\frac{\partial\psi^{i}(Q)}{\partial n} \;=\; i\,k\,\psi^{i}\,(Q)\,(\mathbf{e}_{r_1}\cdot\mathbf{e}_n) \tag{13}$$

with θ_s the angle between the local normal at Q and the line OQ. At that point,

$$\mathbf{e}_{r_1} \;=\; -\,\mathbf{e}_x\,sin\theta_s \,+\, \mathbf{e}_y\,cos\theta_s \tag{14a}$$

since the origin is taken at the local integration point. Also, the angle θ_o between the local normal at Q and the line QP, we have

$$\mathbf{e}_{r_2} = \mathbf{e}_x \sin\theta_o + \mathbf{e}_y \cos\theta_o \tag{14b}$$

Then, using

$$\mathbf{e}_n \cong [-\mathbf{e}_x (dh/dx) + \mathbf{e}_y] 1 + \sqrt{1 + h_x'^2} \tag{15}$$

we find, for the integrand in (1), using Kirchhoff theory

$$\psi \frac{\partial G}{\partial n} - G \frac{\partial \psi}{\partial n} = i\,k\,G\,\psi^i(Q)\ [\,(1+\Gamma)\,(-\frac{dh}{dx}\sin\theta_o + \cos\theta_o)$$

$$-(1-\Gamma)\,(\frac{dh}{dx}\sin\theta_s + \cos\theta_s)\,] \tag{16}$$

From (16) the total field for Physical Optics is

$$\psi^T(P) = \frac{e^{-i\pi/4 + ikr_o}}{\sqrt{8\pi k r_o}} \left\{ 1 + \sqrt{\frac{-ik}{8\pi}} \int_{\sqrt{\lambda h_T}}^{\zeta_m} e^{ik(r_1 + r_2 - r_o)} \sqrt{\frac{r_o}{r_1 r_2}} \left[(1-\Gamma) \right.\right.$$

$$\left.\left. \left(-\frac{dh}{dx}\sin\theta_o + \cos\theta_2 \right) - \left(1+\Gamma \right) \left(-\frac{dh}{dx}\sin\theta_s + \cos\theta_s \right) \right] dx \right\}, \tag{17}$$

where h_T is the transmitter height and $\sqrt{\lambda h_T}$ is the 1st Fresnel zone radius.

Figure 3 shows a plot of 20 $log_{10}\,[\psi_T(p)]$ in equation (17) versus the elevation angle in degrees. The results from Kirchhoff theory in Figure 3 agree best with the results from RING in Figure 3 in the region near backscatter; i.e., $160^\circ \leq \theta \leq 180^\circ$. Backscatter is the region where Physical Optics is most accurate; being least accurate in the forward scatter region. However, the maximum values for the two results agree reasonably well; i.e., 2.82 dB for PO vs 2.11 for integration of RING surface field.

Figure 4 shows a plot of the measured elevation pattern versus elevation angle in degrees together with the elevation pattern computed from the RING surface fields in Figure 2.

Figure 5 shows a comparison of the elevation pattern as computed using RING and PO for a Gaussian ridge 1 km high and 5 km from the source at 30 MHz. In Figure 5, PO and RING compare

...

reasonably well, except in the region near grazing ($0 \cong 78.7$) and in the shaded portion of the hill where PO predicts zero surface fields.

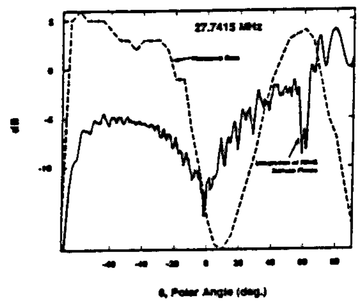

Figure 4. Measured elevation pattern for 27.7415 MHz and elevation pattern computed using RING surface fields. Monopole in front of hill).

III CONCLUDING REMARKS

The surface fields and elevation patterns from a path in Utah are compared using a new integral equation formulation for propagation over irregular terrain, and its associated computer algorithm RING at 27.7415 MHz. The results are compared with PO and measurements. The new integral equation and algorithm RING provides a numerically efficient method for frequencies as high as 100 MHz for terrain profiles having slopes near unity. The comparison of integrating the RING surface fields with the measured data in Figure 4 shows significant differences which could be caused by uncertainties in the experiment or what is important in the model. These questions will be looked at in the future.

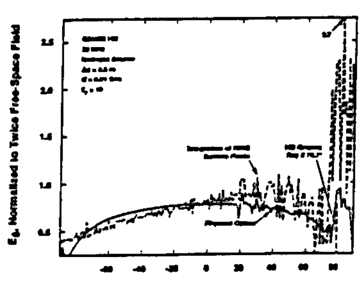

Figure 5. Elevation pattern computed using RING surface fields and Physical Optics for a Gaussian ridge 1 km high and 5 km from the source at 30 MHz.

IV REFERENCES

1) Berry, L.A., Radio Propagation over a Gaussian-Shaped Ridge, IEEE Transactions on Antennas and Propagation, Sept., 1967, pp. 701-702.

2) Berry, L.A., Private Communication, Aug., 1991.

3) Gordon Little, What on Earth Happened to CRPL, Antennas and Propagation Magazine, Aug., 1991, p. 24 and E.K. Smith, Propagation Corner, p. 45.

4) R.H. Ott, and L.A. Barry (1970), An Alternative Integral Equation for Propagation over Irregular Terrain, Radio Science, Vol. 5, No. 5, pages 767-771, May.

5) R. H. Ott (1971), An Alternative Integral Equation for Propagation over Irregular Terrain, Part 2, Radio Science, Vol. 6, No. 4, April, 1971.

6) R. H. Ott, L.E. Vogler, and G.A. Hufford, Ground Wave Propagation over Irregular, Inhomogeneous Terrain: Comparisons of Calculations and Measurements, NTIA-Report-79-20, May, 1979, U.S. Department of Commerce.

7) L.J. Lipa and D.E. Barrick, Improved Numerical Solution of Ott's Integral Equation for HF Ground Wave Attenuation, IEEE Transactions on Antennas and Propagation, Vol. 37, No. 2, Feb., 1989, pp. 260-261.

8) R.M. Bevensee, Compensation-Theorem Analyses of Ground Wave Propagation over Irregular, Inhomogeneous Terrains, Journal of Atmospheric and Terrestrial Physics, Vol. 51, No. 9/10, pp. 797-810, 1989.

9) Vogler, L., Private Communication, Aug., 1991.

10) Lawrence Livermore National Labs (LLNL) under the direction of G.J. Burke and Naval Post Graduate School under the direction of D.R. Adler.

Statistics of Radar Cross Sections Calculated from Geometrical Optics

William B. Gordon
Radar Division
Naval Research Laboratory
Code 5311
Washington, D.C. 20375-5000

ABSTRACT

The radar cross section (RCS) σ for backscatter from a smooth closed convex surface reflector, as calculated from Geometrical Optics (GO), has a mean value equal to 1/4 the surface area of the reflector, where the mean is obtained by averaging over all aspects. More generally, considering σ as a function of aspect, we show how the problem of calculating the statistical moments and probability density for σ can be reduced to a quadrature on the reflecting surface. The details are worked out for spheroids, and the statistical properties of scatter from prolate and oblate spheroids are found to have some qualitatively different features. We then discuss some possible generalizations of these results to more general surfaces and to RCS as calculated according to theories more rigorous than GO.

§ 1. STATEMENT OF THE MAIN RESULTS:

We consider the backscatter from a smooth closed surface reflector, *i.e.*, a surface $\mathbf{S}$ which has a continuously turning unit normal vector ξ, and which is not terminated by one or more boundary edges. In addition, it is assumed that the Gaussian curvature K of $\mathbf{S}$ is everywhere positive, and that the radar cross section σ is calculated according to the Geometrical Optics formula

$$\sigma = \pi / K(p) \quad ,$$

where $K(p)$ is the curvature evaluated at the specular point p [Born & Wolf, Maffett, Skolnik]. Let s be the *scatter vector*, the unit vector that points from **S** to the radar, and let Σ be the *aspect sphere*, the unit sphere identified with all possible positions for the vector s. The surface **S** is convex since $K > 0$, and therefore for each value of s the specular point is the unique point p where $\xi(p) = s$. Hence σ can be expressed either as a function on **S** or as a function on Σ: *viz.*, $\sigma = \sigma(p)$, where p is the specular point, or $\sigma = \sigma(s)$ where s is the scatter vector. We endow **S** and Σ with the uniform probability measures, and we let $\overline{\sigma_S}$ and $\overline{\sigma_\Sigma}$ denote the mean values of σ averaged over **S** and Σ, respectively. Hence $\overline{\sigma_\Sigma}$ is the mean value of σ averaged over all aspects, and it turns out that

$$\overline{\sigma_\Sigma} \quad = \quad A/4 \quad , \tag{1}$$

where A is the total area of **S** . Letting $Var_\Sigma(\sigma)$ denote the variance of σ over all aspects, it turns out that

$$Var_\Sigma(\sigma) \quad = \quad \overline{\sigma_\Sigma} \;\; \overline{\sigma_S} \; - \; (\; \overline{\sigma_\Sigma} \;)^2 \quad . \tag{2}$$

The quantity $\overline{\sigma_S}$ is calculable by straight forward numerical quadrature since

$$\overline{\sigma_S} \quad = \quad (1/A) \int_{\mathbf{S}} \sigma(p)\; dA \; .$$

Hence (1) and (2) provide a method for the calculation of $Var_\Sigma(\sigma)$ by quadrature on **S**.

Let P_Σ and P_S denote the probability density functions of

σ on Σ and $\mathbf{S}$, respectively. Then

$$P_\Sigma(\sigma) \quad = \quad \frac{A}{4\sigma} \quad P_S(\sigma) \qquad . \tag{3}$$

Since $P_S(\sigma)$ can be calculated directly from first principles by quadrature on $\mathbf{S}$, it follows that eq.(3) provides a means of calculating $P_\Sigma(\sigma)$ by quadrature on $\mathbf{S}$. More specifically, the distribution function $F_S = F_S(x)$ for $\sigma = \sigma(p)$ is given by

$$F_S(x) \quad = \quad (1/A) \; \textit{measure}\{ \; p \in \mathbf{S} \; : \sigma(p) \le x \; \} \; ,$$

and

$$P_S(\sigma) \quad = \quad F_S'(\sigma) \qquad .$$

The results (1)-(3) are all consequences of the following theorem.

Theorem. Let $\mathcal{E}_\Sigma$ *and* $\mathcal{E}_S$ *be the expected value operators on* Σ *and* $\mathbf{S}$, *respectively. Then for every real number* n , *we have*

$$\mathcal{E}_\Sigma (\sigma^n) \quad = \quad \frac{A}{4} \; \mathcal{E}_S (\; \sigma^{n-1} \;) \qquad . \tag{4}$$

The proof of (4) is given in [Gordon]. It is based on the classical result of Gauss,

$$K(p) \quad = \quad \frac{d\Omega}{dA} \quad ,$$

where $d\Omega$ is the area swept out by the head of the normal ξ as the foot of ξ varies over an infinitesimal neighborhood dA of the point p.

§ 2. APPLICATION TO SPHEROIDS:

Suppose now that **S** is the spheroid

$$\frac{x^2 + y^2}{a^2} + \frac{z^2}{c^2} = 1 \quad .$$

For the prolate case, $a < c$, $\pi a^4/c^2 \leq \sigma \leq \pi c^2$, and

$$P_\Sigma(\sigma) = \frac{a c^2}{\sqrt{c^2 - a^2}} \frac{1}{4 \sigma \left(\frac{c^2 \sigma}{\pi} \right)^{1/4}} \frac{1}{\left(c^2 - \left(\frac{c^2 \sigma}{\pi} \right)^{1/2} \right)^{1/2}} \quad . \tag{5}$$

For the oblate case, $a > c$, $\pi c^2 \leq \sigma \leq \pi a^4/c^2$, and

$$P_\Sigma(\sigma) = \frac{a c^2}{\sqrt{a^2 - c^2}} \frac{1}{4 \sigma \left(\frac{c^2 \sigma}{\pi} \right)^{1/4}} \frac{1}{\left(\left(\frac{c^2 \sigma}{\pi} \right)^{1/2} - c^2 \right)^{1/2}} \quad . \tag{6}$$

Hence $P_\Sigma = P_\Sigma(\sigma)$ has a singularity at the right-hand end-point of its range in the prolate case, and at the left-hand end point in the oblate case.

Let ρ be the ratio of the largest to the smallest semi-axis of the spheroid. Then $\rho > 1$, and for large ρ we have the approximations

$$\frac{Var_\Sigma(\sigma)}{\overline{\sigma_\Sigma}^2} \sim \frac{5}{2\pi} \rho - 1 \qquad (\textit{Prolate Case}) , \tag{7}$$

and

$$\frac{Var_\Sigma(\sigma)}{\overline{\sigma_\Sigma}^2} \sim \frac{2}{3} \rho^2 - 1 \qquad (\textit{Oblate Case}) . \tag{8}$$

Actually, these approximations are very good when $\rho \geq 1.5$.

From the results (5)-(8) we see that the statistical properties of the backscatter from prolate and oblate spheroids, *as calculated by Geometrical Optics,* have qualitatively different features, and we expect that the same is probably true for the physically real backscatter.

§ 3. DISCUSSION:

There is a folk theorem (or conjecture) which asserts that the use of shaping to reduce the RCS of an object in a given direction always has the effect of increasing the RCS at other directions. Eq.(1) is a result which points in this direction, and for this reason we would like to generalize our results to more general types of reflectors and to theories which are more rigorous than GO. Another possible application of such generalized results might be their use as a check on numerical calculations and theoretically derived estimates.

The existence of such results for edged reflectors appears to be extremely problematical. For one thing, there is a conceptual problem in defining a density function P_S because there is no natural way of associating the scatter in a given direction s with a unique point $p \in \mathbf{S}$; for edged reflectors, the backscatter involves specular points as well as bright points on the edge, *i.e.,* points on the edge at which the radar line-of-sight is perpendicular to the edge. Another problem with edged reflectors involves dynamic range: although edge effects may dominate the scatter in certain directions, they are often orders of magnitude less than the largest specular effect. Hence it would not appear likely to obtain a generalization to (1) which could provide useful information about edge effects.

Confining the remainder of our discussion to closed

surface reflectors without boundary edges, it might happen that generalizations to (1) might take the form of inequalities. For example, from the standard Physical Optics (PO) scattering integral (based on the tangent plane approximation), the PO predicted value σ_{po} of RCS in a given direction s is easily shown to satisfy the inequality

$$\sigma_{po} \quad \leq \quad 4\pi \frac{A_0^2}{\lambda^2} \quad ,$$

where λ is the radar wavelength and A_0 is the projected area of **S** onto a plane perpendicular to s. Also, for any direction s we have $A_0 \leq (1/2)\ A$, and therefore

$$\sigma_{po} \quad \leq \quad \pi \frac{A^2}{\lambda^2} \quad .$$

However, what we seek are equalities which are valid for PO and more physically rigorous theories, or inequalities of the type

$$\sigma \quad \geq \quad ? \quad .$$

4. REFERENCES:

(1) *[M. Born and E. Wolf, 1980] Principles of Optics, 6'th ed., Pergamon Press, Oxford.*

(2) *[W.B. Gordon] Statistical properties of backscatter from convex bodies, to appear.*

(3) *[A.L. Maffett, 1989] Topics for a Statistical Description of Radar Cross Section, Wiley, New York.*

(4) *[M.I. Skolnik, 1980] Introduction to Radar Systems, 2'nd ed., McGraw-Hill, New York.*

SPACE STATION ASSEMBLY/CONTINGENCY SUBSYSTEM (ACS) ANTENNA PATTERN ANALYSIS

Shian U. Hwu, Ba P. Lu, Larry A. Johnson, Jon S. Fournet
Lockheed Engineering & Sciences Company
Houston, Texas

Robert J. Panneton, Donald S. Eggers, G. Dickey Arndt
NASA/Lyndon B. Johnson Space Center
Houston, Texas

Abstract

The purpose of this study is to characterize the scattering effects of the Space Station structural elements on the Assembly/Contingency Subsystem (ACS) high gain antenna patterns and to verify the accuracy of the Geometrical Theory of Diffraction (GTD) modeling technique, which has been identified as a computer modeling tool for the Space Station antenna pattern prediction and interference studies. The predicted antenna patterns were computed using the GTD technique in which the multipath interference from Space Station structures was included. In order to check the numerical results obtained, a series of measurements have been carried out in the Radio Frequency (RF) Anechoic Chamber of the NASA Johnson Space Center. Based on the results accomplished in this study, good agreement on experimental and computed results was obtained. Worst case interference situations, in which there is diffraction from the nearest edge of the major structures, were considered. If a $\pm$ 15 degree cone is used to protect the ACS high gain antenna boresight pattern, up to 1 dB of link budget may be required to compensate for the gain degradation in the ± 4 degree boresight region due to multipath interference from Space Station structure.

I. Introduction

It is important to be able to predict antenna performance in the Space Station environment since the timely recognition of interference problems, and subsequent modification of the design and position of the antenna, or the surrounding structures, can minimize performance degradations.

The Space Station ACS antennas are designed to provide an S-Band communications link. This is a bi-directional Radio Frequency link utilizing the Tracking and Data Relay Satellite System (TDRSS) S-Band single access service to receive audio, software uploads, and commands from the earth and to transmit audio and core telemetry to earth.

The ACS antenna pattern will be distorted due to electromagnetic reflection and diffraction by space station obstructions. To ensure the ACS can meet design requirements, the system design must take into account such antenna pattern distortion. The system should be able to compensate for the distortion of the antenna patterns, but the antennas must provide reasonable gain throughout their assigned areas of coverage for the ACS to function effectively.

Formerly, conventional pattern prediction was based on full-scale mockup measurements. In addition to the full-scale mockup test technique, one approach to help in solving the measurement problem is using the scale-model mockup technique. This approach has a number of advantages over the full-model measurement technique since it can be performed in the indoor anechoic chamber where the effects of weather are eliminated. It usually gives reasonably accurate data, but still requires a great deal of engineering time and expense.

Another approach in solving the measurement problem is using an electromagnetic modeling technique capable of computing both near-field and far-field patterns. A reliable analytical tool provides for the early detection of problems and helps to find the best solutions.

Two general theoretical radiation pattern computation methods have been developed: the method of moments and the geometrical theory of diffraction. Which method should be used will depend on the size of the vehicle compared to the wavelength of the antenna under consideration.

Considering the complicated geometry and the large electrical size of the Space Station, the Geometrical Theory of Diffraction (GTD) is the best candidate for the task. The GTD modeling technique has been identified and selected as the modeling tools for the Space Station antenna pattern prediction and interference studies [1]. The purpose of this study is to characterize the scattering effects of the Space Station structural elements on the Assembly/Contingency Subsystem (ACS) high gain antenna patterns and to verify the accuracy of the Geometrical Theory of Diffraction (GTD) modeling technique.

To simulate the Space Station environment, a frequency of 2.175 GHz was used in this study. The actual operating frequencies of the Space Station S-Band ACS antenna system are 2.265 GHz for transmitting and 2.086 GHz for receiving.

II. Pattern Prediction and Verification

II.a. Flat Metal Plate Interference

The setup for the flat metal plate interference measurements is illustrated in Fig. 1. The dimension of the metal plate is 14-foot by 11-foot. A Narda standard gain horn was used to simulate the ACS high gain antenna. This antenna exhibits similar gain and beamwidth characteristics as the Space Station ACS high gain antenna - 16 dBi peak gain and a 30° 3-dB beamwidth.

The predicted and measured antenna interference patterns for an 11-foot by 14-foot aluminum plate, located 3 feet away from the antenna, at a frequency of 2.175 GHz are shown in Figs. 2 and 3 for the soft and hard polarization cases, respectively.

For the similar case, the 11-foot by 14-foot aluminum plate was located 5 feet away from the antenna. The predicted and measured antenna interference patterns are shown in Figs. 4 and 5, for the soft and hard polarization cases, respectively.

As shown in the measured and computed patterns, at the shadow side of the interference metal plate (which is in the negative angle region) the pattern shows a sharp decrease in signal power level due to the plate blockage. The blockage effect of the plate decreases the field in the shadowed region by about 10 to 15 dB.

In the antenna boresight region between the reflection and the incident shadow boundaries, where no reflected fields exist, the field is composed by interference between the direct field from the antenna and the edge diffracted field from the top edge of the plate. Thus, the ripples on the boresight region of the antenna patterns were caused by the diffraction fields from the top edge of the plate.

Also, it is observed that the plate when closer to the antenna gives stronger interference on the antenna patterns. This is obvious because the direct field causes stronger edge diffraction when the plate is located closer to the antenna.

The agreement between predicted and measured results is excellent around the antenna boresight region, which is of primary interest. Small discrepancies between computed and measured results were found around $-45°$ for the soft polarization pattern, which is in the shadow region of the metal plate and where the signal strength is 30 dB below the antenna boresight. Also found are differences around the 90° region for the hard polarization patterns where the signal level is about 20 dB below the peak boresight level. The reason for such low level signal discrepancies is not known and is hard to identify. For most applications, such noise level signals are not important and usually can be ignored.

II.b. Dish Antenna Interference

The setup for the dish antenna interference measurements is illustrated in Fig. 6. The dish antenna mockup simulates a dish with a 6.4 foot diameter on a 15 foot pole with 21 inche diameter.

The predicted and measured antenna interference patterns for a 6.4 foot dish antenna, located 6 feet away from the antenna, at a frequency of 2.175 GHz are shown in Fig. 7 for the soft polarization cases.

Similarly, the 6.4 foot dish antenna was located 7 feet away from the antenna. The predicted and measured antenna interference patterns are shown in Fig. 8 for the soft polarization cases.

In general, reasonable agreement between measured and computed patterns was obtained for the ACS antenna with dish interference. But, the agreement is not as close as for the plate interference cases. This is because the dish interference cases involve a cylindrical structure which exhibits a more complicated diffraction mechanism than for the rectangular flat plate. Since the dish antenna structure includes curved surfaces, the antenna pattern is more sensitive to the mockup alignment in the dish interference cases than for the plate interference cases.

Based on the results presented in this chapter, it is shown that the GTD modeling technique is capable of predicting the ACS antenna patterns with interference structure at S-Band frequencies with reasonable accuracy. In general, good agreement is obtained for the antenna boresight region. Since low level signals are difficult to measure and predict, the pattern far from the antenna boresight, for both the experimental and theoretical results, is not reliable.

III. Antenna Interference Analysis

In this section, Space Station ACS high gain antenna patterns with multipath interference from space station major obscuration structures are computed using the GTD modeling technique.

The locations of the ACS antennas used in this analysis are shown in Fig. 9. The ACS inboard antenna is located at (-0.2, 20.72, -3.99) meters and the outboard antenna is located at (0.38, 22.68, -3.99) meters referenced to the origin of the Space Station coordinate system. These are the latest locations available that were obtained from the ongoing contractor location study effort. The antenna locations have been changed from the Delta Preliminary Design Review (DPDR) baseline locations due to significant blockage and interference caused by the propulsion modules and SGS antenna mast.

The major structure elements causing interference to the ACS high gain antenna patterns were identified as the RCS module, the starboard side thermal radiator and the starboard side solar panel.

There are four different flight orientation modes that have been considered for Space Station operation. These are the Local Vertical Local Horizontal (LVLH), Arrow, Gravity Gradient (GG), and Inverted Gravity Gradient (IGG) flight modes.

Since the ACS high gain antenna has a directive pattern, it is not necessary to include all structural elements of the Space Station in the model. Instead, only major components such as solar panels, RCS modules, and thermal radiators are modeled in this analysis. It is further assumed that the electromagnetic properties of the Space Station structure are such that the surfaces are highly reflective at S-Band. Thus, the Space Station structure elements are modeled as perfect electrical conductors.

The ACS antenna patterns with various antenna orientations for each major structure interference are computed using the GTD technique. For the worst case consideration, the interference from the nearest edge of each major structure was analyzed.

Fig. 10 shows a summary of the maximum antenna gain degradation in the $\pm 4°$ antenna boresight region due to each major interference structure. Also, shown in Table 1, is maximum antenna gain degradation in the antenna $\pm 4°$ boresight region with various size cone protection.

Based on the GTD predicted results, the following summary is offered. If the center line of the antenna beam is tangential to the major obscuration structure, more than 10 dB of gain loss may be suffered. If a $\pm$ 10 degree cone is used to protect the ACS high gain antenna boresight pattern, more than 1 dB gain loss will be expected. If a $\pm$ 15 degree cone is used to protect the ACS high gain antenna boresight pattern, less than 1 dB gain degradation is expected. If no more than 0.5 dB gain degradation is desired, a $\pm$ 20 degree cone is required to protect the ACS high gain antenna boresight pattern.

The results of this study indicate that, if significant interference (more than 1 dB antenna gain loss) with ACS antenna patterns is to be avoided, the ACS steerable antenna 3 dB beamwidth must be kept clear of Space Station structural blockage. This means that the ACS high gain antennas should not be pointed within 15 degrees of obstructions.

IV. Conclusions

In this study, the ACS antenna patterns were computed using the GTD technique in which the multipath interference from the Space Station structures was included. In order to check the numerical results obtained, a series of measurements have been carried out in the RF Anechoic Chamber of the NASA Johnson Space Center. Based on the results accomplished in this study, good agreement on experimental and computed results was obtained. The validity of the GTD modeling technique for ACS high gain antenna pattern predictions has been verified.

The ACS antenna patterns with each major structure interference were computed using the GTD technique. For the worst interference cases, the diffraction from the nearest edge of the major structures was considered. The maximum ACS high gain antenna gain degradation, in the $\pm 4^\circ$ antenna boresight region, due to each major interference structure was given.

The following conclusions, supported by measured and GTD computed results presented in this report, are offered.

- The GTD modeling technique is capable of predicting the ACS antenna pattern, including multipath effects from Space Station structure, with reasonable accuracy.
- In general, good agreement between measured and computed results is obtained in the antenna boresight region which is of primary interest.
- The edge diffracted field is the primary source causing the interference around the antenna boresight direction, and in other directions, the interference is mainly due to reflection from structure surfaces.
- If a $\pm$ 10 degree cone is used to protect the ACS high gain antenna boresight pattern, more than 1 dB gain loss may be expected.
- If a $\pm$ 15 degree cone is used to protect the ACS high gain antenna boresight pattern, less than 1 dB gain degradation is expected.
- If no more than 0.5 dB gain degradation is desired, a $\pm$ 20 degree cone is required to protect the ACS high gain antenna boresight pattern.

References

[1] R. J. Marhefka, and J. W. Silvestro,"Near Zone - Basic Scattering Code User's Manual with Space Station Applications", NASA Contractor Report 181944, ElectroScience Laboratory, Ohio State University, December 1989.

[2] R. G. Kouyoumjian, and P. H. Pathak, "A Uniform Geometrical Theory of Diffraction for an Edge in a Perfectly Conducting Surface," *Proceedings of the IEEE,* Vol. 62, No. 11, pp. 1448–1461, November 1974.

Table 1: Maximum gain degradation in the antenna ±4° boresight region with various size cone protection.

Cone	RCS Module	Thermal Radiator	Solar Panel
±0°	13.9 dB	10.1 dB	15.3 dB
±5°	4.11 dB	4.3 dB	3.31 dB
±10°	1.13 dB	1.13 dB	0.58 dB
±15°	0.73 dB	0.81 dB	0.36 dB
±20°	0.33 dB	0.35 dB	0.26 dB
±25°	0.11 dB	0.21 dB	0.06 dB
±30°	0.07 dB	0.09 dB	0.06 dB

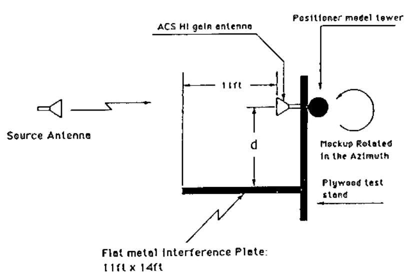

Figure 1: The setup for the ACS antenna interference measurement using a 14-foot by 11-foot aluminum plate.

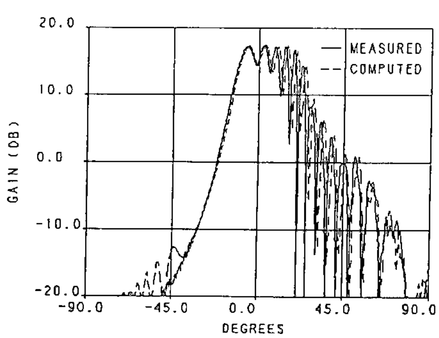

Figure 2: Predicted and measured patterns with a metal plate located 3 feet away from the antenna for the soft polarization case.

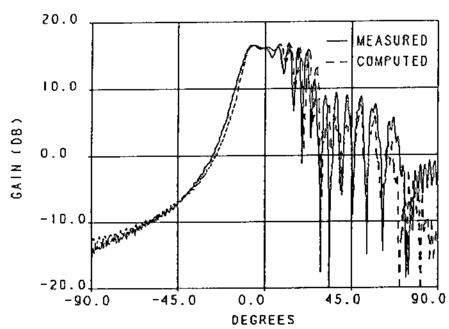

Figure 3: Predicted and measured patterns with a metal plate located 3 feet away from the antenna for the hard polarization case.

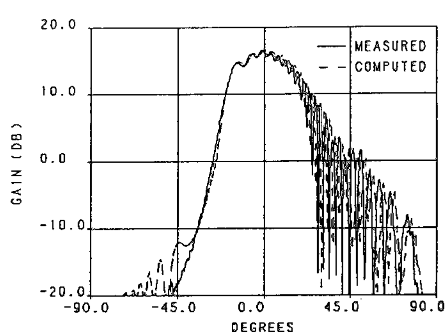

Figure 4: Predicted and measured patterns with a metal plate located 5 feet away from the antenna for the soft polarization case.

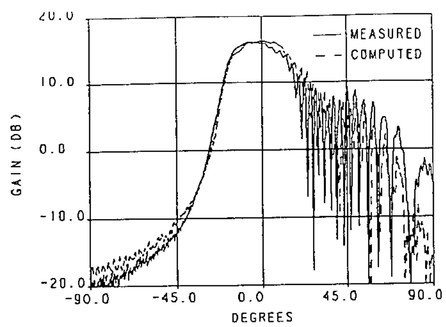

Figure 5: Predicted and measured patterns with a metal plate located 5 feet away from the antenna for the hard polarization case.

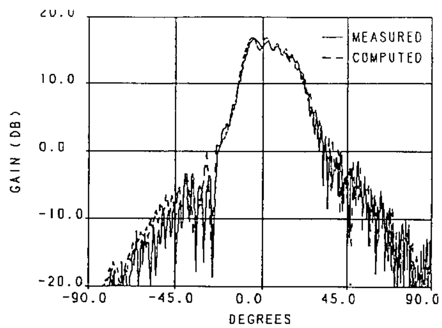

Figure 8: Predicted and measured patterns with a dish antenna mockup located 7 feet away from the antenna for the soft polarization case.

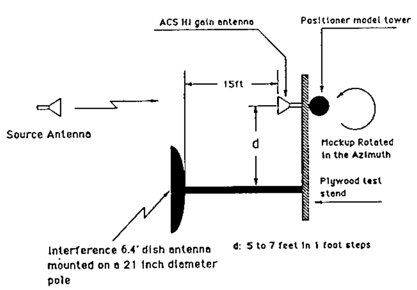

Figure 6: The setup for the ACS antenna interference measurement using a 6.4 foot dish antenna mockup.

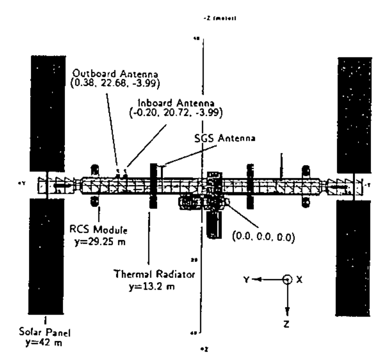

Figure 9: The new proposed ACS antenna locations.

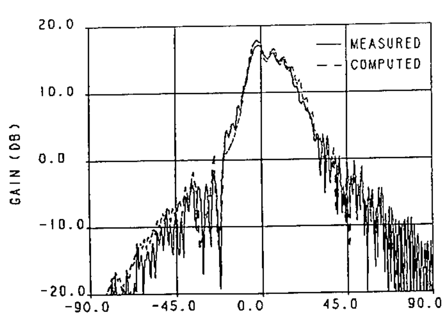

Figure 7: Predicted and measured patterns with a dish antenna mockup located 6 feet away from the antenna for the soft polarization case.

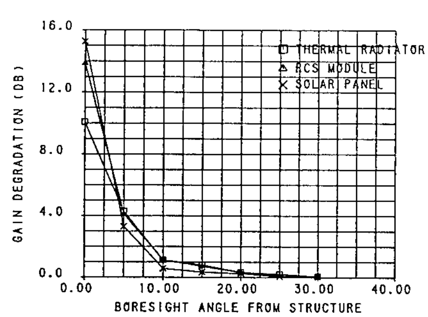

Figure 10: Maximum antenna gain degradation in the $\pm 4^{\circ}$ antenna boresight region due to each major interference structure.

GEODESICS ON CONVEX SURFACES FOR A GTD/UTD PROGRAM

P R Foster

Microwave and Antenna Systems, UK

ABSTRACT

The radiation from a source in the presence of a convex surface can be found using GTD/UTD methods when the dimensions of the object are more than one or two wavelengths. The major problem is finding the geodesics on the surface along which the rays travel in the shadow and transition regions. The method adopted is based on the Runge-Kutta integration method and has high accuracy.

1 Introduction

The theory of diffraction from a smooth curved surface in a conducting material is well developed [1] and has been verified for many cases such as cylinders and composite ellipsoids. The problem in implementing such theory in a computer code is not the diffraction theory but the geometry of the geodesics. According to Fermat's principle, the ray path of a creeping ray on a surface is a geodesic and this geodesic must be found before the appropriate diffraction terms can be applied. The problem may be subdivided into several different classes as follows

- both source and observation points on the curved surface
- source off the surface and observation point on the surface
- source on the surface and observation point off the surface
- source and observation points off the surface

The treatment in this paper deals with the last two cases, that is, the cases where the observation point is not on the surface.

When the observation point is off the surface, the output ray from the surface which is at the end point of the geodesic must be tangential to the surface and be directed towards the observation point. Geodesics on cylinders and cones of elliptical cross-section can be found exactly by recourse to developable surfaces but difficulties arise with non-developable surfaces because general theories of geodesics do not include such boundary conditions. The inclusion of non-developable surfaces in a UTD program is essential if aircraft are to be modelled with accuracy. In particular, an aircraft fuselage can be modelled by use of a general ellipsoid.

Various methods have been devised to find geodesics on non-developable surfaces. One method used by Burnside [2] involved applying the calculus of variations to the geodesic differential equations. Because of the approximations involved, this does introduce increasing errors as the length

of the geodesic path is increased. Kim [3] subsequently developed a perturbation method which was checked against an exact solution. Further work at Ohio State University has been reported by Choi and Marhefka [4] in connection with bistatic scattering. Jha [5, 6] has dealt with the problem of geodesics when the source and observation points are on the surface. The solution is exact but involves the computation of elliptic integrals of the third kind which leads to very long runtimes.

Initially, the inclusion of non-developable surfaces into ALDAS [7] was attempted by solving the problem in Cartesian coordinates [8] for a general ellipsoid described as

$$(\frac{x}{A})^2 + (\frac{y}{B})^2 + (\frac{z}{C})^2 = 1.0 \tag{1}$$

with A, B, and C as the semiaxes of the ellipsoid. The results were clearly inaccurate and a more ambitious project of writing a general set of routines for dealing with concave surfaces was undertaken. The method assumes that the surface can be described in terms of a parametric coordinate system and that geodesics terminate on a curve which can be determined from the geometry and the output ray direction. A 5th order Runge-Kutta solution is employed to find the geodesics starting from a point and terminating on the specified terminating curve. Since the initial directions of the geodesics are not known a priori, a preliminary search over all initial directions is carried out and all geodesics are found approximately. The true geodesics are then found by a second iterative search using the approximate initial geodesics. The use of the Runge-Kutta method allows the integration of all the required UTD parameters to be incorporated in the second step. It can be applied to sources on and off the surface as well as to near and farfield output points. Although the example of the general ellipsoid is used through this paper, the method can be applied to any surface where the equations can be set up in parametric form.

2 Boundary Conditions for Geodesics

To find any geodesic on a curved surface, initial and terminating conditions must be defined.

2.1 Initial Condition

When the source is on the surface, the source position, P (Figure 1), is the start point for the geodesic and the geodesic may leave the source in any tangential direction. The initial tangent can take any direction through 360.0 degrees in the plane of the local surface.

When the source is off the surface, the geodesic starts at a point, Q_1, on the shadow boundary illuminated by the source. Given the initial point, Q_1, the initial tangential direction of the geodesic is defined as the unit vector from P to Q_1.

2.2 Terminating Condition

An important part of finding the geodesics when the observation point, Q, is not on the surface is to determine the end point, Q_2. If the observation point is treated as an illuminating point, the shadow boundary on the curved surface will define the points in space from which the ray may leave the surface tangentially towards the observation point. For the case of a general ellipsoid and a far-field output direction, this surface is a plane through the centre of the ellipsoid and with a normal direction to the plane defined by the output direction and semiaxes of the ellipsoid (Figure 2). For a composite ellipsoid which has different values of the semiaxis A for $x < 0.0$ and $x > 0.0$, two such planes must be defined. For a nearfield observation point, the shadow boundary can be found by a search based on the method described below for the geodesics. For 'distant' nearfield points and an ellipsoid, the shadow boundary is still a plane but, for more complex

surfaces and observation points near to the surface, the shadow boundary has to be defined as a set of points and fitted with a spline to find intermediate points.

3 Finding the Geodesics

It can be seen from Section 2 that some decisions as to method of finding the final geodesic have to be taken. Since the required geodesics cannot be found analytically but a search must be carried out, a method was evolved in which 36 rays at 10.0 degrees intervals round a circle centred on the source are examined and the characteristics of each geodesic found. Thus, there are 36 start directions from the source. When the source is on the surface, 36 tangential directions are used. When the source is off the surface, 36 tangential rays to the surface are found and the 36 tangential points, Q_1, are found (Figure 1). All parameters are expressed as arrays of 36 variables related to the initial tangential directions.

The geodesics which are defined as the shortest distance between two points on the surface, are found using a Runge-Kutta method based on tensor calculus [9]. The geodesic starts at a specified point with a specified tangential direction. A ray moves along this tangential direction to a new position where the distance is a minimum. The choice of parametric description of the path length, s, on the surface is important and it is essential that there is only one point on the surface for each parametric point. For an ellipsoid, suitable parameters are (θ, ϕ) which are related to the Cartesian coordinates by

$$X = Asin\theta cos\phi : Y = Bsin\theta sin\phi : Z = Ccos\theta \tag{2}$$

The differentials, $\frac{ds}{d\theta}, \frac{ds}{d\phi}, \frac{d^2s}{d\theta^2}, \frac{d^2s}{d\phi^2}$ and $\frac{d^2s}{d\theta d\phi}$ can be calculated using Christoffel symbols. They become extremely complicated and, for ease of handling, were generated for a general ellipsoid using a specially written Mathematica package [10] which output FORTRAN code. A fifth order Runge-Kutta solution with adaptive stepsize [11] is arranged to call up a subroutine to calculate the differentials at each new point. The adaptive control is within the Runge-Kutta operation but, in addition, each new point is checked for proximity to the output shadow boundary and the step size adjusted, if necessary.

When each of the 36 trial geodesics reaches a point on the shadow boundary, the local vector tangent to the geodesic, $\hat{T}$, is found and compared with the wanted output direction, $\hat{R}$. The unit normal, $\hat{U}$, and binormal, $\hat{B}$, at the output point are found (Figure 3). The vector dot product, $\gamma = \hat{R}.\hat{B}$, will pass through zero when $\hat{R}$ and $\hat{T}$ are parallel. When the observation point is the nearfield, the output vector is variable according to the coordinates of the end point of the geodesic, Q_2, and must be recalculated as the unit vector from Q_2 to Q for each geodesic. The wanted geodesics are those which result in a zero value for the quantity $\gamma(\alpha)$. The values of α corresponding to the wanted geodesics are those which correspond to a zero-crossing. Originally these values were determined by taking the nearest value of initial angle which might be 5.0 degrees away and a secondary search carried out using a sliding window which might take the computation of another 4 or 5 geodesics. A more (computationally) effective method is to spline fit $\gamma(\alpha)$ and determine the initial angles of the geodesics immediately. It is rarely necessary to compute each true geodesic more than once using this method although a search is in place should the value of γ not be sufficiently near zero.

The true geodesics are then recalculated with the addition of the determination of two extra parameters, the length of the geodesic and ζ, the parameter required by the diffraction terms. The divergence for a particular geodesic is calculated by shifting the angle of the input tangent by 0.5 degree and computing the change in the direction of the output tangent.

4 Results

The technique has been applied extensively to general composite ellipsoids. Figure 4 shows all the geodesics from a point on the surface to a direction in the shadow region. The variation of the vector dot product, $\hat{R}.\hat{B}$, with input angle (Figure 5) provides the angular directions in which the wanted geodesics set off from the source point, P. Usually, there will be four geodesics but there are special geometries where up to eight geodesics may be present. Figure 5 contains six possible geodesics. Whether these all make a large contribution to the final radiation pattern depends on the length of the geodesic path and the radius of curvature along the path. A short path over the tip of an ellipsoid may be just as lossy as a long path over a section of large radius of curvature.

The radiation patterns from a monopole on an ellipsoid (Figure 6) show a 'focussing' effect as the semi-axis, A, is increased so that the surface moves from a sphere to an elongated ellipsoid.

Although the method has high accuracy, the runtime is longer than for an elliptical cylinder which is solved using a developable surface (Table 1). One reason for this is the need to operate in double precision for the computation of the geodesics.

5 Conclusions

A set of subroutines has been developed which will find the geodesics on a concave curved surface using a fifth order Runge-Kutta integration. In order to be sure that all relevant geodesics are found, an initial search is performed. Runtimes are increased substantially over modelling the structure as an elliptical cylinder but the accuracy is much higher. The method can be applied to sources on or off the surface and the observation point off the surface. A change of a single subroutine will enable other surfaces which can be parametrically described to be modelled.

Table 1: Run times for monopole on ellipsoid. Times are for 720 angles on a 80386 machine (25 MHz with co-processor)

Modelled as Elliptical Cylinder	10.4 seconds
Ellipsoid with one (shortest) geodesic	1870.0 seconds
Ellipsoid with all geodesics	2760.0 seconds

References

[1] Pathak P H, 'Techniques for high Frequency Problems', Chapter 4 of Antenna Handbook, ed Lo Y T and Lee S W, Van Nostrand Reinhold, New York 1988

[2] Burnside W, 'Analysis on On-aircraft antenna patterns', PhD Thesis, Ohio State University, 1972

[3] Kim J J ,'Simulation and Analysis of Airborne Antenna radiation patterns', PhD Thesis, Ohio State University, 1984.

[4] Choi J and Marhefka R J, 'Numerical techniques to determine the UTD bistatic creeping wave paths and parameters for an ellipsoid', ACES Journal, Vol 6, No 1, 1991,pp140-158.

[5] Jha R M and Edwards D J, 'A novel method for surface-ray tracing on non-developable surfaces', IEE Conf No 350, CEM-91, London, 1991, pp181-184

[6] Jha R M and Edwards D J, 'Computation of elliptic integrals of the third kind in high-frequency EM scattering problems', IEE Conf No 350, CEM-91, London, 1991, pp178-180

[7] Foster P R, 'Analysis of Low Directivity Antennas on Structures', ACES 1990, p362-369

[8] Albertsen N C and Jensen Fl, 'Pattern prediction for S-band antennas on aircraft', TICRA Report S-77-03 on ESTEC Contract 3157/77, 1977

[9] Spain B, 'Tensor Calculus', Published by Oliver and Boyd, London, 1953

[10] Wolfram S,'Mathematica: A System for Doing Mathematics by Computer', Addison-Wesley Publishing Co, 1988

[11] Press W H et al, 'Numerical Recipes: The Art of Scientific Computing', Cambridge University Press, 1986

Figure 1:

Geometry of rays from a source point, P, on and off the surface. Q is the observation point. Q_1 is the initial point of the geodesic and Q_2 is the final point.

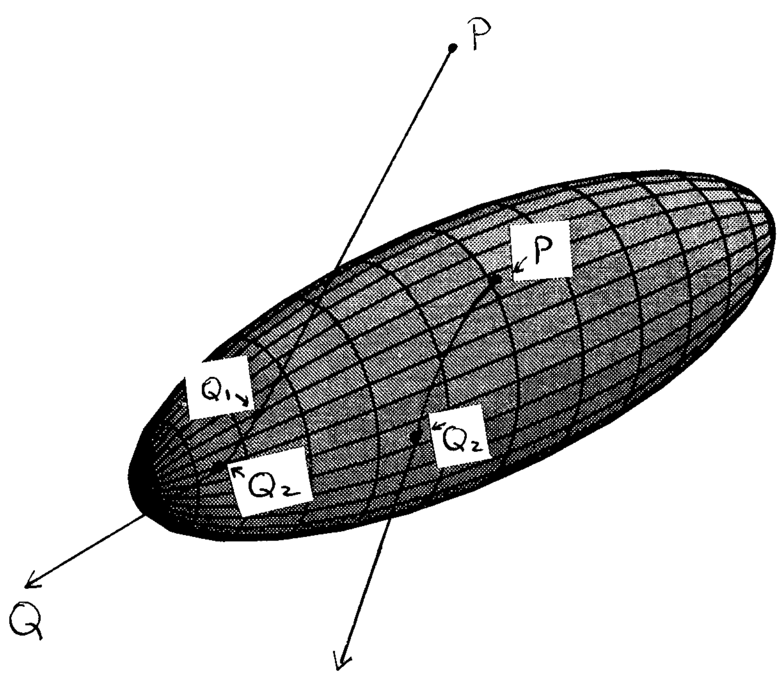

Figure 2:

The shadow plane on an ellipsoid for an output point, Q which is in the farfield.

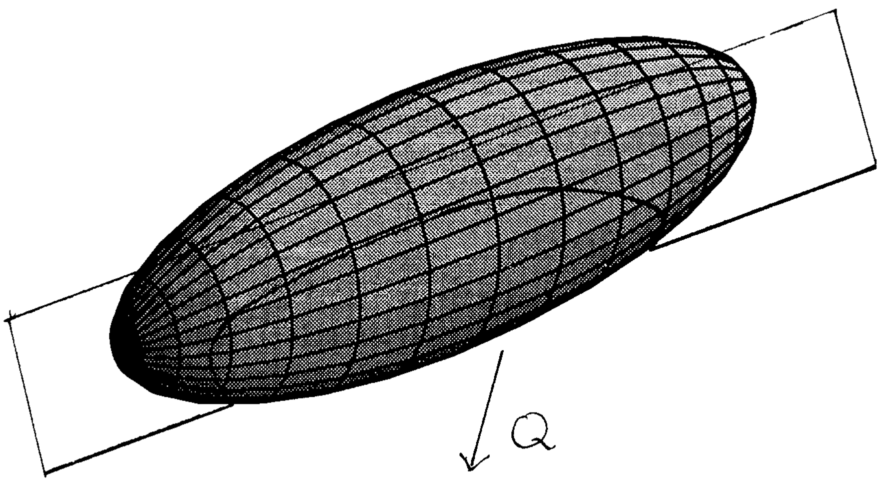

Figure 3:

Vectors at output point, Q_2, of geodesic from a source at P. $\hat{T}$ is the output tangent, $\hat{N}$ is the normal to the surface at Q_2, $\hat{B}$ is the local binormal. $\hat{R}$ is the output direction.

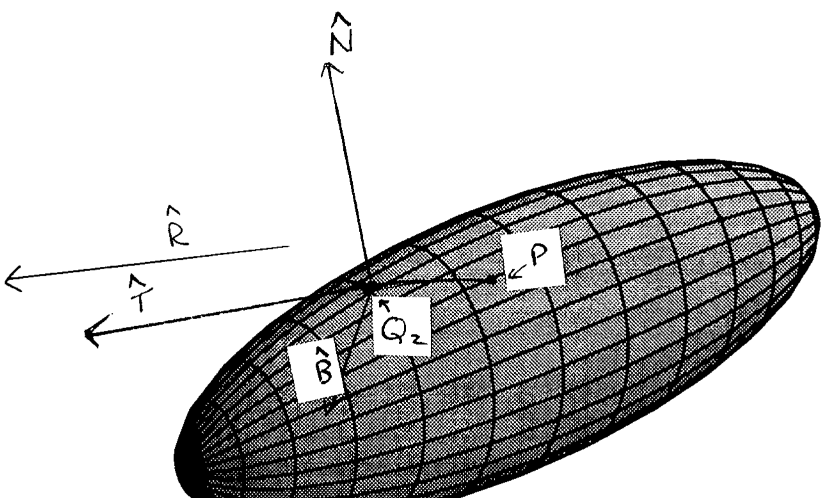

Figure 4:

Geodesics from a point, P, on an ellipsoid with semiaxes 7.5, 2.0, 2.5 metres. The output ray is in direction θ = -60.0 degrees, ϕ = -45.0 degrees. Rays 1 and 2 are the largest contributors.

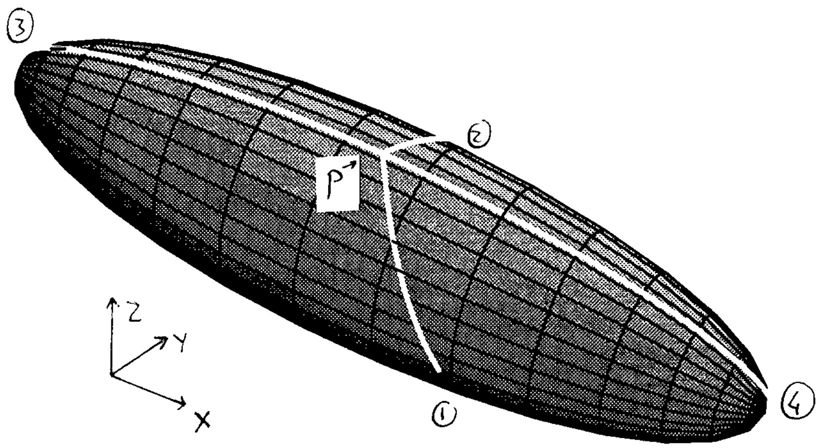

Figure 5:

Variation of vector product, $\hat{R}$. $\hat{B}$ with initial tangent angle, showing that six geodesics are possible. Output direction is θ = -40.0 degrees, ϕ = 0.0 degrees.

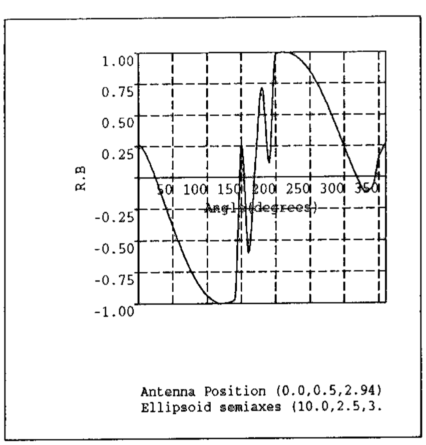

Figure 6:

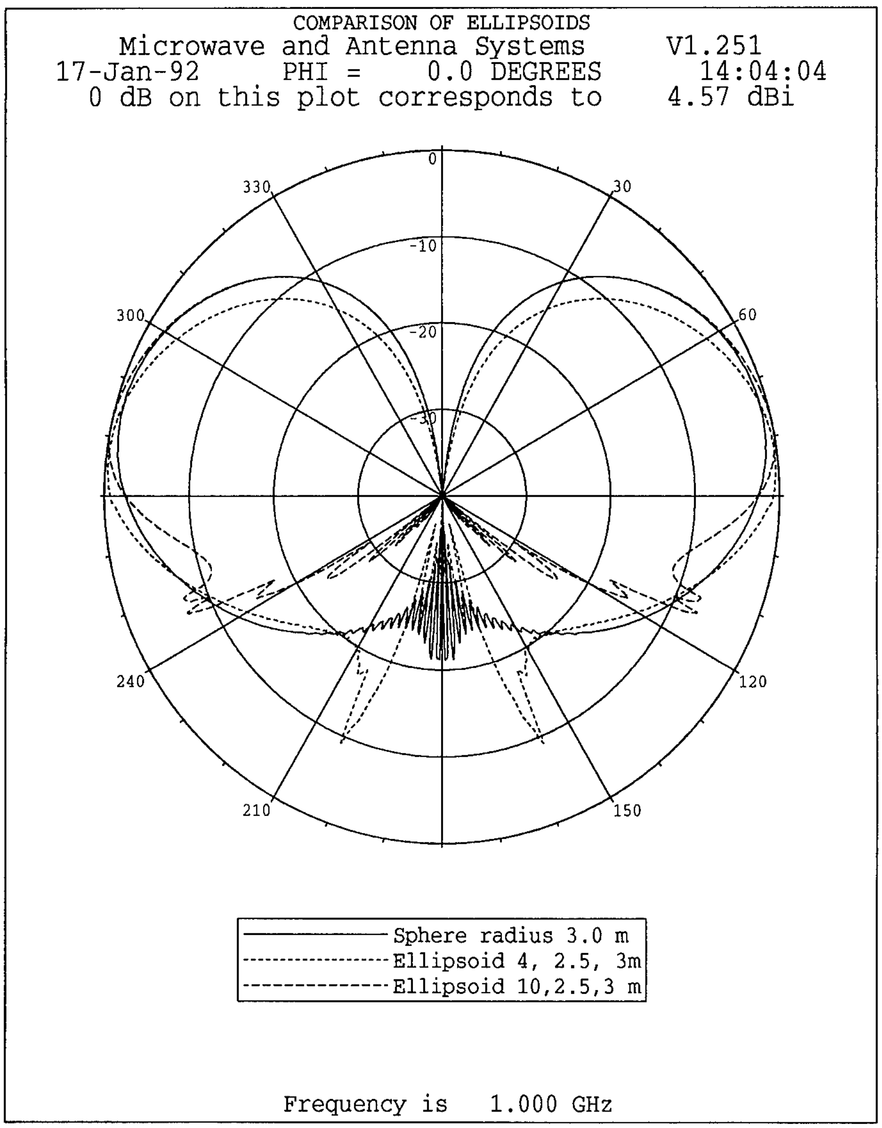
COMPARISON OF ELLIPSOIDS
Microwave and Antenna Systems V1.251
17-Jan-92 PHI = 0.0 DEGREES 14:04:04
0 dB on this plot corresponds to 4.57 dBi
0
-10
-20
-30
330
30
300
60
240
120
210
150
Sphere radius 3.0 m
Ellipsoid 4, 2.5, 3m
Ellipsoid 10,2.5,3 m
Frequency is 1.000 GHz

SESSION 10 - "ELECTROMAGNETIC COMPATIBILITY"

Moderator: Frank Walker

Abstract

Kevin Slattery
CKC Laboratories
5473A Clouds Rest
Mariposa, CA 95338

Investigating Electromagnetic Interference Using Symbolic Mathematical Software

During the 1980's symbolic mathematics software has emerged from the laboratories and become readily available, not just on large mainframe systems, but at the desktop level. It is the applicability of these software packages for the practising EMC engineer that we wish to briefly investigate.

Using a commercial package such as Mathematica, Macsyma, Derive, Maple, or Theorist, completely symbolic representations of EMI problems can be developed and investigated. By looking into the logical structure of the equations that describe EMI geometries, the EMC engineer should be able to develop an intimate knowledge of EMI, it's causes, effects, and possible solutions.

These general symbolic software packages also give the EMC engineer access to functionalities that more specific and directed software cannot. Typically, the commercially available packages allow both numerical and symbolic manipulation of equations. They allow importation of data gathered from experiment, giving the EMC engineer the ability to visualize the data from many different viewpoints. As an example, we here at CKC have been measuring the induced currents in ground planes illuminated by signals in the frequency range 30-1000 MHz. The software that we use has allowed us to perceive current structures that were not intuitively apparent. We have also used the software to investigate the near field effects of thin wire antennas in close proximity. Lastly, the software has been extensively used to develop EMI predictive methods for radiated emissions, radiated susceptibility, coupling through apertures, and crosstalk.

Numerical Techniques for EMI Source Modeling: A Review of Progress

Todd H. Hubing
University of Missouri-Rolla
Rolla, Missouri 65401

Abstract - This paper presents a review of recent progress towards using numerical modeling techniques to analyze sources of electromagnetic interference.

Electromagnetic compatibility engineers have witnessed the revolutionary impact that numerical electromagnetic modeling techniques have had in the fields of antenna engineering, microwave engineering, and magnetics. There is a great deal of interest in applying these same techniques to model sources of electromagnetic interference (EMI). Full-wave electromagnetic modeling of circuits and electronic systems could help to prevent unforeseen radiation and susceptibility problems, decrease product development time, and reduce the cost of meeting electromagnetic compatibility requirements.

Unfortunately, even relatively simple sources of EMI can be very difficult to analyze using a numerical technique. For example, analyzing a simple printed circuit board configuration requires a numerical technique capable of modeling,

- complex source geometries
- dielectrics
- thin metal surfaces
- tightly coupled, electrically small conductors
- thin, electrically long or resonant wires
- unbounded geometries.

In general, surface integral techniques such as the boundary element method have difficulty meeting the first three or four requirements. Finite methods such as the finite element method, FDTD, and TLM do not efficiently model large unbounded geometries or long wires.

In a paper presented at the 7th Annual Review of Progress in Applied Computational Electromagnetics [1], a very simple EMI source model was described. It consisted of a simple printed circuit board configuration with a partial metal enclosure and an attached cable. The EMI source model was a slightly modified version of the second canonical problem in *The ACES Collection of Canonical Problems, Set 1* [2]. At that time neither the EMI source model nor the canonical problem could be analyzed using any existing numerical technique. Apparently, this is still true today. However significant progress has been made in a number of areas. Major developments have

occurred relating to each of the five techniques described below. Numerical codes based on each of these techniques may play a significant role in EMI source modeling in the coming years.

The Finite Element Method

The finite element method is well-suited for modeling complex source geometries. Nevertheless, the complexity of most EMI source configurations can be overwhelming even for a finite element model. Researchers at the University of Ottawa [3], the Naval Underwater Systems Center [4], and others have been working on the problem of matching the capabilities of finite element methods to the complexity of EMI source models.

Two weaknesses of the finite element method have been vector parasites and problems modeling three-dimensional radiation problems. Perhaps the most significant development in the past year for finite element modelers was the publication of two papers by Paulsen and Lynch [5,6] that help code developers to understand and eliminate vector parasites. Thanks to this work, vector parasites can no longer be considered a major problem with the finite element method. One solution to the three-dimensional radiation modeling problem is the development of adequate three-dimensional *infinite elements*. This is an area of research that has received a lot of attention recently. Infinite elements were the subject of at least 7 papers at the 1991 IEEE Antennas and Propagation Society symposium.

Method of Moments

Three-dimensional moment method techniques have no trouble with far field radiation calculations and they can usually model thin wires very effectively. In the past, they have not been effective for modeling complex source geometries with inhomogeneous dielectrics. Researchers at the T. J. Watson Research Center however, have overcome this limitation and are using a modified boundary element method to model EMI source configurations with volume dielectrics [7-9]. Their approach makes it possible to model a number of source configurations that previously defied numerical modeling.

Finite Difference Time Domain

Researchers at a number of institutions including Pennsylvania State University, MIT, and Digital Equipment Corporation [10] are applying FDTD to printed circuit card geometries. FDTD is a relatively young technique and a number of researchers are working on its development. An enhancement to FDTD known as the finite-volume time-domain method [11] eliminates the requirement of maintaining a uniform grid spacing. FDTD and FVTD are sure to play an important role in future attempts to model EMI source configurations.

Generalized Multipole Technique

The Generalized Multipole Technique (GMT) is essentially a moment method with expansion functions that are analytic solutions of the fields generated by sources located some distance away from the surface where the boundary condition is being enforced. The expansion functions are spherical wave field solutions corresponding to multipole sources. By locating these sources away from the boundary, singularities on the boundary are avoided. There is little difference in the way dielectric and conducting boundaries are treated. Configurations with multiple dielectrics and conductors are more readily modeled by GMT than with other general purpose moment-method techniques.

Researchers at the Swiss Federal Institute of Technology and other institutions have been making steady progress with this relatively new technique [12-14]. As new expansion functions are developed and introduced, the number of configurations that can be analyzed by this technique is growing rapidly.

Hybrid Techniques

A number of hybrid techniques that combine the features of two existing methods have been introduced in the past two years [15-24]. So far, none of them have been developed specifically for EMI source modeling and none of them are capable of modeling basic EMI source configurations like the canonical problem [2]. However, work is continuing. Hybrid techniques are certain to play a major role in future attempts to model sources of EMI.

Summary

Although many simple EMI source configurations still defy analysis by existing numerical codes, a lot of progress has been made just in the past year. New or enhanced finite element methods, moment methods, and FDTD techniques have been applied to basic printed circuit card geometries with some degree of success. The progress that has been made in the development of each of the techniques described above indicates that codes based on these techniques will ultimately be used to analyze a variety of EMI source configurations.

Given the current rate of progress, it is very possible that by next year there will be one or more codes that are able to model the second canonical problem in the *ACES Collection of Canonical Problems, Set 1.* Any code with this capability will be a valuable tool for electromagnetic compatibility engineers and is likely to have a tremendous impact in this field.

References

[1] T. H. Hubing, "A Survey of Numerical Techniques for Modeling Sources of Electromagnetic Interference," Proceedings of the 7th Annual Review of Progress in Applied Computational Electromagnetics, Monterey, CA, March, 1991, pp. 516-519.

[2] T. H. Hubing, "Calculating the Currents Induced on Wires Attached to Opposite Sides of a Thin Plate," ACES Collection of Canonical Problems, Set 1, published by The Applied Computational Electromagnetics Society, Spring 1990, pp.9-13.

[3] G. Costache and M. Radojicic, "A Model to Predict Radiated Emissions from Electric Circuits," Proceedings of the 1991 IEEE EMC Symposium, Cherry Hill, NJ, August 1991.

[4] D. S. Dixon, "Development of an Electromagnetic Compatibility (EMC) Analysis and Prediction Capability using Finite Element Analysis Techniques," 8th Annual Review of Progress in Applied Computational Electromagnetics, Monterey, CA, March 1992.

[5] D. R. Lynch and K. D. Paulsen, "Origin of Vector Parasites in Numerical Maxwell Solutions," IEEE Trans. Microwave Theory and Tech., vol. 39, March 1991, pp.383-394.

[6] K. D. Paulsen and D. R. Lynch, "Elimination of Vector Parasites in Finite Element Maxwell Solutions," IEEE Trans. Microwave Theory and Tech., vol. 39, March 1991, pp.395-404.

[7] B. J. Rubin, "An Electromagnetic Approach for Modeling High-Performance Computer Packages," IBM Journal of Research and Development, vol. 34, July 1990, pp. 585-600.

[8] B. J. Rubin and S. Daijavad, "Radiation and Scattering from Structures Involving Finite-Size Dielectric Regions," IEEE Transactions on Antennas and Propagation, vol. 38, November 1990, pp. 1863-1873.

[9] B. J. Rubin, "Full-Wave Modeling of Signal Propagation and Radiation in Electronic Packages," presented at the 1991 IEEE APS symposium and URSI Radio Science Meeting, London, Ontario, Canada, June 1991.

[10] C. F. Lee et al., "Electromagnetic Radiation from a VLSI Package and Heatsink Configuration," Proceedings of the 1991 IEEE EMC Symposium, Cherry Hill, NJ, August 1991.

[11] R. Holland, V. P. Cable, and L. Wilson, "Finite-Volume Time-Domain (FVTD) Techniques for EM Scattering," IEEE Transactions on EMC, vol. 33, November, 1991, pp. 281-294.

[12] P. Leuchtmann and L. Bomholt, "Thin Wire Features for the MMP-Code," Proc. 6th Annual Rev. of Progress in Applied Computational Electromagnetics, March 1990, pp.233-240.

[13] P. Leuchtmann, "New Expansion Functions for Long Structures in the MMP-Code," Proceedings of the 7th Annual Review of Progress in Applied Computational Electromagnetics, March 1991, pp.198-202.

[14] J. Zheng, "A New Expansion Function of GMT: The Ringpole,", Proceedings of the 7th Annual Review of Progress in Applied Computational Electromagnetics, March 1991, pp.170-173.

[15] J. Sroka, H. Baggenstos, and R. Ballisti, "On the Coupling of the Generalized Multipole Technique with the Finite Element Method," IEEE Trans. on Magnetics, vol. 26, March 1990, pp. 658-661.

[16] X. C. Yuan, D. R. Lynch, and J. W. Strohbehn, "Coupling of Finite Element and Moment Methods for Electromagnetic Scattering from Inhomogeneous Objects," IEEE Trans. Antennas and Propagation, vol. 38, March 1990, pp. 386-393.

[17] X. C. Yuan, "Three-Dimensional Electromagnetic Scattering from Inhomogeneous Objects by the Hybrid Moment and Finite Element Method," IEEE Trans. Microwave Theory and Tech., vol. 38, August 1990, pp. 1053-1058.

[18] J. M. Jin and J. L. Volakis, "A Finite Element-Boundary Integral Formulation for Scattering by Three-Dimensional Cavity-Backed Apertures," IEEE Trans. Antennas and Propagation, vol. 39, January 1991, pp.97-104.

[19] W. E. Boyse and A. A. Seidl, "A Hybrid Finite Element and Moment Method for Electromagnetic Scattering from inhomogeneous Objects," Proceedings of the 7th Annual Review of Progress in Applied Computational Electromagnetics, March 1991,pp.160-169.

[20] R. P. Jedlicka and S. P. Castillo, "A Hybrid Finite Element/Boundary Element Method for solving Three-Dimensional Electromagnetic Coupling Problems, 1991 URSI Radio Science Meeting, London, Ontario, Canada, June, 1991.

[21] E. W. Lucas and T. P. Fontana, "A 3-D Vector Variational Hybrid Finite-Element/Boundary-Element Formulation for the Scattering Analysis of Arbitrary Infinite Doubly Periodic Arrays," 1991 IEEE Antennas and Propagation Symposium, London, Ontario, Canada, June, 1991.

[22] D. S. Wang et al., "Efficient Coupling of Finite Methods and Method of Moments in Electromagnetic Modeling," 1991 URSI Radio Science Meeting, London, Ontario, Canada, June, 1991.

[23] J. M. Jin and J. L. Volakis, A Hybrid Finite Element Method for Scattering and Radiation by Microstrip Patch Antennas and Arrays Residing in a Cavity," IEEE Trans. on Antennas and Propagation, vol. 39, November, 1991, pp. 1598-1604.

[24] S. D. Gedney and R. Mittra, "Analysis of the Electromagnetic Scattering by Thick Gratings using a Combined FEM/MM Solution," IEEE Trans. on Antennas and Propagation, vol. 39, November, 1991, pp. 1605-1614.

E^3 MODELING AND SIMULATION TOOL

David P. Millard, Jimmy A. Woody and Ralph M. Herkert
Georgia Tech Research Institute
Georgia Institute of Technology
Atlanta, Georgia 30332
(404) 894-8234
dmillard@gtri01.gatech.edu

BACKGROUND

Due to the changing world and military environment, weapon system platforms are in a constant state of transition. Modern military platforms are designed to employ complex systems and electronic devices (i.e., communications-electronics (C-E), radars, jammers, etc.) which utilize much of the electromagnetic (EM) spectrum. The electromagnetic environment (EME) to which these platforms will be subjected is very complex and can contain emitters (both friendly and hostile) which generate field strengths capable of causing adverse electromagnetic environmental effects (E^3). In addition, use of the platform's electronics can create E^3 problems for other friendly platforms attempting to use the EM spectrum. Thus a sophisticated weapon systems may be of little value if its capability is degraded by adverse E^3.

DISCUSSION

To mitigate adverse E^3 DoD Directive 3222.3, "Electromagnetic Compatibility (EMC) Program," states

> "adherence by all DoD components to all EMC standards and specifications shall be mandatory for the applicable operational C-E equipments, subsystems, and systems unless duly waived."; and

MIL-E-6051, "Electromagnetic Compatibility Requirements, Systems," states

> "Program Managers shall ensure electromagnetic compatibility (EMC) of their airborne systems and subsystems."

To ensure platform EMC a program manager and design engineers must have the tools and resources to _model_, _simulate_, _analyze_ and _control_ E^3. To reduce cost and increase reliability and maintainability (R&M), E^3 modeling and simulation (M&S) should be performed during each phase of the platform's life cycle from concept to deployment. Also, as the E^3 simulation is exercised it will provide feedback to the engineer to improve the overall E^3 design thereby improving the overall outcome of the simulation (war fighting capability).

Computer-based M&S offers the only cost effective way to improve weapons platform E^3 in a complex joint or special mission scenario. The E^3 M&S databases then become a source of data for the E^3 history (similar to that maintained by an EMC Advisor Board (EMCAB)) of the platform and will be a source of high fidelity component and platform E^3 data for larger simulations. An E^3 M&S tool which meets these requirements has been designed and specified by the Georgia Tech Research Institute (GTRI) and is called the Georgia Tech Configuration Analysis Program (GTCAP) [1-4]. GTCAP is a modular E^3 M&S tool which utilizes relational databases (Oracle) in a framework implementation. It is menu and list directed, has a graphical user interface (GUI), and contains default input values based on specifications. GTCAP is designed to operate on PC-based machines under several operating systems.

METHODOLOGY

An E^3 problem can be classified in several categories based on the MIL-STD-461 types of tests. These classifications are radiated emissions (RE), radiated susceptibility (RS), conducted emissions (CE) and conducted susceptibilities (CS). E^3 problems arise in systems when an unwanted interaction takes place between an emission (defined here as a source EM field) and a susceptible system. To analyze and solve the problems created by these unwanted interactions, knowledge and data of a system's emissions and susceptibilities (E&S) and a valid computational technique are required. Typically system level E^3 problems are analyzed (approached) in the order given in Table 1.

Table 1. E^3 Problems and Solution Methods.

PROBLEM TYPE	SOLUTION METHOD	OUTPUT
	(Front Door)	
Tx - Rx	AACIM, IEMCAP computer solutions to EFIE	EMI margin, frequency management (offsets,etc.), antenna patterns
	(Back Door)	
box to box via cable	specification, table look-up, measured data	EMI margin
field to wire, apertures	heuristic, neural network	EMI margin
wire or aperture to field	heuristic, neural network	EMI margin

The front-door coupling (RE/RS) problem is the classical EMI problem for communications and radar systems where the spectrum use by several systems must be de-conflicted. This problem involves computing the transmitter emission spectrum (fundamental and harmonics) and the receiver tuning spectrum (fundamental and spurious responses). The computation which determines how much of the transmitter's energy is input to the receiver's detector circuits must account for the transmit and receive antenna factors and the attenuation over the coupling path. This computation must include in-band and out-of-band frequencies. Usually the data for in-band frequency calculations is known; however, the out-of-band frequency data is usually not available and assumptions will have to be made. Several system level EM codes are available for solving this problem: they include AACIM, IEMCAP and AAPG.

The conducted interference problem (CE/CS - box-to-box via cable) is another classical EMI problem which is usually addressed while designing the interfaces between equipment in the system. The straightforward method of analyzing this type of problem is to use the actual measured data for each system or, in leu of test data, to use the military standard specifications as the CE and CS limits. Using this approach the system interfaces can be designed/hardened (filters, etc.) to mitigate any unwanted interference. Typically internal circuit data and descriptions are not available to the E^3 analyst and therefore SPICE type analyses cannot be performed to produce CE and CS data to solve this problem.

The field-to-wire or field-to-apertures and the wire- or aperture-to-field radiation problems are hard to solve algorithmically and therefore lend themselves to heuristic solutions. A method is needed that can solve the configuration E^3 problem based on past experience and knowledge of the technology of the systems on the platform. Neural-networks using back propagation techniques have been used to solve problems with many parameters that would be computationally very intensive if an exact numerical algorithm was used to solve the problem. If "good" and "bad" configurations (from an E^3 sense) were used to "teach" a neural network, it may be possible for the network to learn [5] to "solve" an problem. The combination of analytical and heurisitic algorithms could be utilized in a CAE program to rapidly analyze configurations to determine whether they are electromagnetically compatible.

CONFIGURATION ANALYSIS PROGRAM

The general structure of the GTCAP CAE software is shown in Figure 1. A modular software structure is used which includes all required inputs and outputs for module-to-module communication, and the software is programmed to DOD-STD-2167 [6]. The major modules include the User Interface Module (UIM), the Platform Evaluation Module (PEM), and the various measures of performance (MOP) modules.

The UIM is the program "executive" which provides the interface between the GTCAP operator and the PEM. The logic for the UIM and GTCAP analysis process is shown in Figure 2. The UIM allows the operator to (1) select the platform and the work order (WO) being implemented; (2) position the equipment on the platform; (3) compute and store the equipment position and orientation in a database; and (4) set-up the evaluation scenario by selecting the mode (baseline without interference, intersystem, or platform with external EME), the equipment and the platform operation/mission. After the E^3 evaluation is complete, the UIM generates the analysis reports. It then permits the operator to reiterate the configuration/analysis process. A typical GUI screen for the UIM is shown in Figure 3.

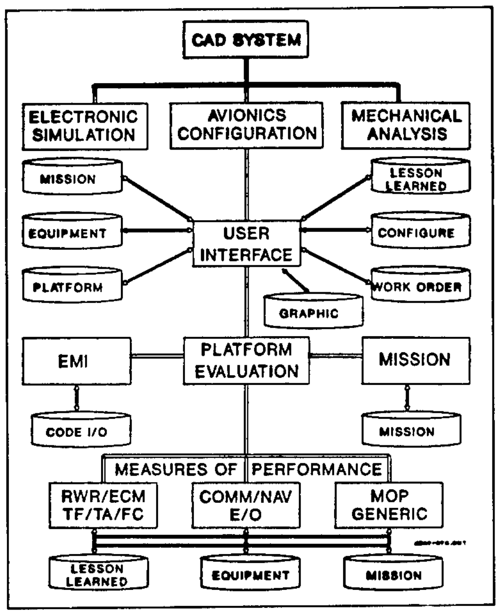

Figure 1 GTCAP Software Structure.

The PEM is called by the UIM to perform the E^3 evaluation of the platform configuration defined in the platform configuration database. The PEM uses the electromagnetic interference (EMI) module to compute the intra-platform coupling and perform E^3 analyses of the configuration. The PEM also uses the mission module to compute the coupling of external emitters to on-board antennas and perform electromagnetic vulnerability (EMV) predictions.

The MOP evaluation modules utilize intersystem and inter-platform E^3 analysis results from the PEM to determine the degradation in the MOP's on the platform. Each system (Flight Control, Communications, Navigation, Electronic Warfare, Radar, Electro/Optic) has its own MOP evaluation module, EMI database and MOP database.

GTCAP utilizes large databases generated off-line. These databases include: the platform structure descriptors, the electromagnetic MOP, platform graphics based on NASTRAN finite element models (FEM), equipment EMI parameters, and platform operations/mission descriptors. The equipment EMI and MOP databases, which are critical to the E^3 evaluation of the platform, must be constructed from EMI and EMV test results or generated through analyses. The MOP databases are generated by the various system specialists in collaboration with E^3 engineers. Where actual EMI test data or analysis results are not available, MIL-STD-461 [7] emission and susceptibility limits are assumed to apply

and are used as default data. All database entry and update screens are designed to accommodate off-line database management.

PLATFORM EVALUATION MODULE

The PEM is the E^3 engineering core of GTCAP. Its purpose is to direct the E^3 evaluation of the electronics for various platform configurations in a defined EME. The PEM saves the E^3 results for each evaluated equipment and provides a matrix of intersystem EMI interaction between equipment.

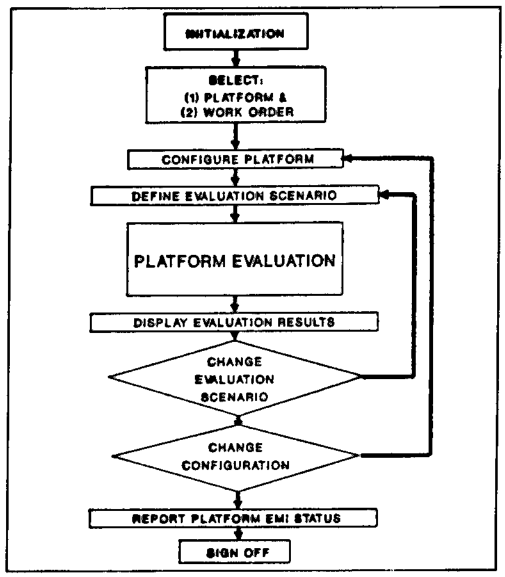

Figure 2 GTCAP Analysis Process Flow Diagram.

The PEM obtains, from the appropriate databases: (1) the platform configuration, (2) the selected analysis mode, and (3) the created equipment list. The PEM uses the EMI module to perform the EMI analysis and uses the mission module to define the EME produced by external emitters and to determine the active equipment list for specific mission segments. The PEM relies on each of the equipment MOP modules to determine the amount of degradation (adverse E^3) caused by on-board and external emitters.

EMI MODULE

The EMI Module is used to compute the intersystem coupling, "quick look" EMI margins, and the EM susceptibility assessment for the platform. The on-board, intersystem EME is defined by the radiated and conducted emissions of the equipment on the platform. The external inter-platform EME is defined by emitters external to the platform. The primary EMI assessment codes utilized in the EMI module include:

AACIM - Antenna-to-Antenna Coupling Interference Model (GTRI Intrasystem EMI Analysis Program)
GEMACS - Generalized Electromagnetic Model for the Analysis of Complex Systems
IEMCAP - Intrasystem Electromagnetic Compatibility Analysis Program
BSC - Basic Scattering Code
AAPG - Aircraft inter-Antenna Propagation with Graphics

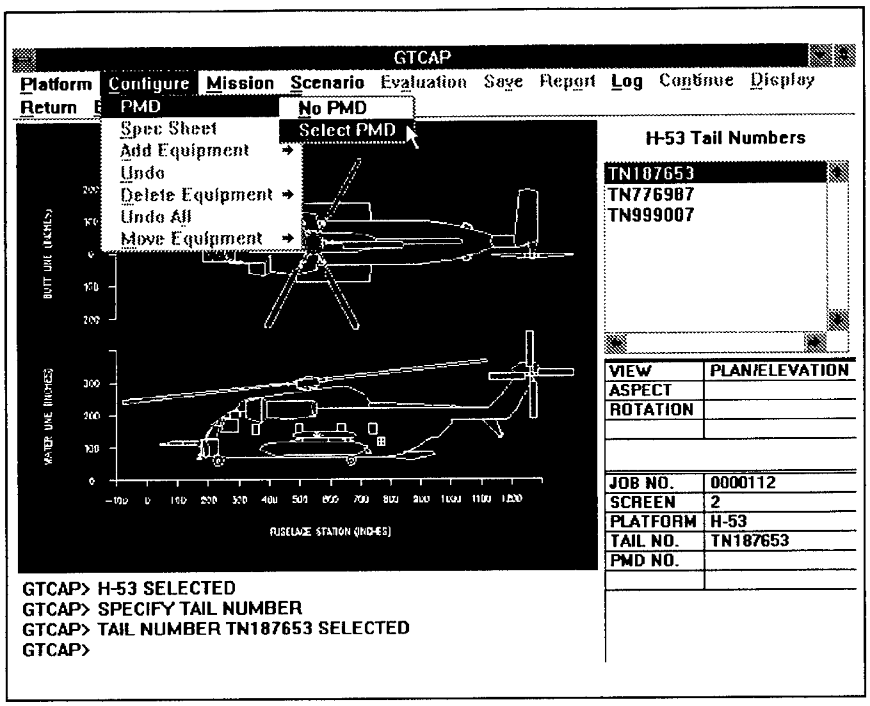

Figure 3 Typical GUI Screen.

GTCAP uses these codes, unmodified, to compute antenna-to-antenna coupling, antenna patterns of on-board antennas, and box-to-box, box-to-cable and cable-to-cable coupling internal to the platform. In addition GTCAP utilizes AACIM for quick look antenna-to-antenna coupling analyses and frequency culls.

ANALYSIS APPROACH

Equipment/system EMI parameters and MOP data together with EM coupling data form the basis for E^3 analyses and EMI margin calculations. The EMI Module accesses the EMI and MOP databases and calculates the EM coupling. First-order approximations of the effects of frequency, pulse width, and pulse repetition frequency (PRF) are assumed.

EM energy can couple to a system through one or more system ports of entry (POE's) [8]. POE's are grouped into two separate categories: front-door and back-door. From an analysis perspective, front-door paths are better characterized in terms of coupling to the POE. Front-door coupling is further subdivided into in-band and out-of-band cases. In-band coupling tends to be more straightforward to analyze than out-of-band coupling both

in terms of the interaction of the incident EM radiation with the antenna or sensor and the propagation of the coupled energy to a potentially susceptible component.

Solving EM coupling problems and performing an EMI analysis using computer codes can be an overwhelming task. To compute the coupling from a source (transmitter) to a receptor (receiver) the output level of the transmitter must be known. Then the cable loss between the transmitter and its antenna; the antenna gain; the coupling path loss; the receive antenna gain; and the cable loss to the receiver must be calculated. These factors must then be appropriately combined to calculate the EM coupling. Both in-band and out-of-band effects must be included.

The back-door coupling problem analysis will require that the EMI module compare specification, table look-up or measured data, or apply a heuristic algorithm. The EMI module will use the "lessons learned" database and the equipment database as the source of information and knowledge with which to define the parameters of the algorithms.

The EMI module also permits frequency and/or amplitude culls such that baseline "quick look" E^3 analyses may be initially performed. It also has the ability to perform trade-off analyses by comparing the EMI margins of the current configuration with that of a previously evaluated system. Finally, the EMI module permits tailoring of EMI limits to increase or decrease MIL-STD-461 limits to reflect the expected operational EME.

EMI CODE SELECTION

The various EM codes utilized in the EMI module can calculate various parts of the E^3 analysis problem. Since there are multiple codes to choose from, selection criteria must be established so that the correct EMI code for the particular problem is used. This selection criteria must reflect the input data available depending on the life-cycle phase, the transmit and receive frequencies of the equipment, the relative size of the platform in wave lengths, and whether the coupling is internal or external to the platform. Also the required input data to each of these codes is different and the amount of data is large. The data must provide an EM platform structural description, the equipment configuration, and the equipment EMI parameters. GTCAP utilizes an expert system process to select the appropriate EMI code and structures the input data in a proper format to accurately execute the code. The logic of the code selection process is based on the parametrics of each EM code and information contained in the "lessons learned" database. GTCAP's EM Codes Parameter Matrix contains a complete set of parameters for each of the EM codes in GTCAP and input data vectors are mapped into the GTCAP database.

HEURISTIC E^3 ANALYSIS

Heuristic E^3 analysis based on back-propagation neural-network (BPNN) algorithms is not a new concept [9]. However, unlike the previous work which used artificial intelligence (AI) knowledge techniques the BPNN knowledge lies in its inter-connections

and their associated weights [5] and not in the "rules" of an expert system. Thus a BPNN E^3 analysis would be driven by the "activation" that passes from the input of the BPNN to the output of the BPNN. An E^3 BPNN is shown in Figure 4. The inputs to the algorithm would be the configurations (databases) of the system under analysis and the outputs of the algorithm would be the expected EMI margins. Using existing databases and "lessons learned" from knowledge of experts, ongoing analysis and measurements, it may be possible to construct an E^3 BPNN and have it learn to predict EMI.

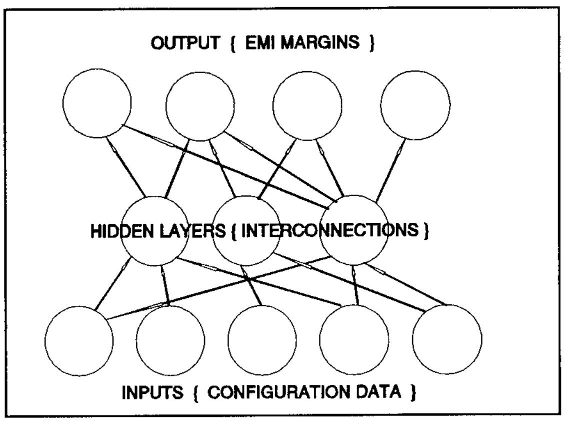

Figure 4 E^3 BPNN.

CONCLUSIONS

GTCAP, an E^3 Modeling and Simulation tool, provides the integration of existing E^3 models and databases into a cost effective means of evaluating the E^3 design of an electronics platform throughout the life cycle of that platform. This tool can be used to evaluate new technologies, tactics and systems, and it will generate high fidelity inputs for more complex simulations. GTCAP utilizes existing EM codes to minimize the development effort, thereby, resulting in a standard product which utilizes EM codes already developed. Experience has shown that "designing in" EMC from the start is significantly more cost effective than fixing E^3 problems in implemented plans or in deployed systems.

ACKNOWLEDGEMENTS

The authors wishes to thank the following people for their contributions to this work: T.A. Torres for the initial concept and funding, H.W. Denny, R.J. Levin, D.W. Acree, G.E. Beebe, M.L. Wheeler and Dr. J.A. Mahaffey for their enlightened discussions, assistance with the EM code evaluations, and providing the EM code input vectors and ideas on the user interfaces.

REFERENCES

1. Millard, D.P., Daher, J.K., Herkert, R.M. and Woody, J.A., "Computer Aided Electromagnetic Compatibility Analysis," 7th Review of Progress in Applied Computational Electromagnetic, Naval Post Graduate School, 19-22 March 1991, Monterey, CA..
2. Millard, David P. and Torres, T.A., "Helicopter and Avionics Systems Electromagnetic Environmental Effects," Digital Avionics Systems Conference, 16-18 October 1990, Virginia Beach, Virginia.
3. Millard, David P. and Woody, Jimmy A., "System E3 Platform Evaluation," IEEE 1990 International Symposium on Electromagnetic Compatibility - Symposium Record, Washington, D.C., pp. 607-611, 21-23 August 1990.
4. Millard, David P., "System E^3 Analysis and Prediction Program," EMC EXPO 89, Washington, D.C.
5. Jones, William P. and Hoskins J., "Back-Propagation," Byte, October 1987, pp. 155-162.
6. DOD-STD-2167A, "Defensive System Software Development," 27 October 1987.
7. MIL-STD-461C, "Electromagnetic Emission and Susceptibility Requirements for Control of Electromagnetic Interference," 4 August 1986.
8. Denny, H.W., Daher, J.K. and Beebe, G.E., "E^3 Analysis Guidelines,"Technical Report No. 2, GTRI Project No. A-4892 for Rome Laboratory, Air Force System Command, Griffiss AFB, New York, Contract No. F30602-87-C-0134, December 1990.
9. Surekha, M., Patki, A.B., Sudha, A.V., Sekhar, G.S., and Radha, G., "Knowledge based system applications on EMC," IEEE International Symposium on Electromagnetic Compatibility, 1989, pp. 101-104.

FINITE ELEMENT ANALYSIS FOR EMC APPLICATIONS: LESSONS LEARNED

By

David S. Dixon, IEEE Senior Member,

Michael Obara,

Nicholas Schade

Naval Undersea Warfare Center (NUWC), New London, CT, USA
[formerly the Naval Underwater Systems Center (NUSC)]

ABSTRACT

As electronic system complexity increases, the design and analysis tools must keep pace. In the mechanics, structures, and fluids worlds, design software such as finite element analysis (FEA) have become common place in the designers tool kit. In electronic circuit design, programs such as SPICE* are mature tools used in everything from filter construction to VLSI† modelling. In the world of electromagnetics (EM) such analysis tools are still in their infancy. Electromagnetic Compatibility (EMC) analysis is primarily limited to the analysis of simple circuits or measurements of a completed design. Few reliable methods exist to predict the EMC of a complex system or or group of systems, such as a shipboard compartment, before it leaves the designers' desk. Powerful electromagnetic software is now becoming available. Programs such as ElectroMagnetic Analysis System (EMAS) and Numerical Electromagnetic Code (NEC) are potentially capable of analyzing the complex electromagnetic environment surrounding modern shipboard electronic systems and/or antennas. This paper discusses the use of EMAS and NEC programs as below deck/compartmental EMC predictive tools.

BACKGROUND

At the Naval Undersea Warfare Center (NUWC), the EMC Branch of the Submarine Electromagnetics Systems Department is continually seeking new methods to maintain and improve the EMC posture of electronic and electrical equipment installed aboard submarines and surface ships. This EMC effort involves everything from the actual on-board improvement of existing systems to assisting in the development of new combat and communications systems. The majority of the below deck electromagnetic interference (EMI) problems found in the fleet today are caused by low frequency magnetic fields which typically are harmonics of the 60 and 400 Hz shipboard powerline. These EMI sources can have a significant effect on the performance of sonar, combat, control, and communication (particularly VLF) systems. The powerline related harmonics show up as structure currents that are flowing on cables and as well as the ship's ground plane, and magnetic fields that are radiated within all equipment spaces. Past EMC Technology Base efforts developed an EMC program to predict the compatibility of below-decks equipment spaces. This program was useful to predict coupling between various EMI sources and shipboard susceptors. However, this program could not analyze the complex EM interactions that occur between the EMI sources and the surrounding physical structure. The ability to consider the EM characteristics, physical location and the material properties of EMI sources and susceptors is inherent in programs such as NEC and EMAS.

INTRODUCTION

Present Technology

Most EMC analysis accomplished today is performed on an individual source-to-victim (radiator-to-susceptor) basis, where the EMC engineer analyzes the interaction between one device and another. EMI sources are typically modelled using simple discrete models, such as a wire over a ground plane or a powerline transformer. At NUWC, the EMC Branch's present capability uses such models to predict inter-component EMC within any group of equipments. By using various analytical and/or empirical models the program predicts the effect that the radiation of one equipment and will have on the susceptibility of another equipment. It then develops an "EMC

* SPICE: Simulation Program with Integrated Circuit Emphasis

† VLSI: Very Large Scale Integration

protective margin" value, as a function of frequency, indicating the probability that EMI will exist. If an EMC problem is predicted, the user may then employ traditional EMI reduction techniques, such as separating the source and/or the susceptors or adding shielding materials over the source or the susceptor. The analysis can then be re-run to evaluate the success of the changes.

This (existing) VAX based EMC analysis and predictive capability will not predict the effect of correlated noise (i.e., multiple sources) or the effect of transient EMI sources. Nor will it account for the inter-active presence of magnetic or conductive materials within the vicinity of the EMC model area (e.g.,within the compartment or within the equipment).

Benefits of Finite Element Analysis

The limitations cited above for the VAX based predictive program can be eliminated by using finite element methods. The power of the finite element method is in its ability to consider the EM presence of all material properties (linear and non-linear), and their specific physical locations in a precise model of the EM environment. For example, a wire over a ground plane, are typically represented by "free space" models. Introducing an instrument to measure the radiation from such a wire slightly changes the radiation, introducing a small error into the measurement. A finite element model can include the measuring device in the model, thus providing a more accurate prediction. In a very real sense, this describes an EMC model where the EMI source corresponds to the wire over the ground plane, and the measuring device is the susceptible equipment.

METHOD OF ANALYSIS

The primary thrust of this the NUWC effort was to evaluate the feasibility of using sophisticated FEA methods to predict compartmental EMC. The path to this goal included a research study of available technologies, as well as performing several "text book" analyses. The method of moments (MOM) technique used in Numerical Electromagnetic Code (NEC) is popular in the Navy for analyzing antenna systems. NEC was chosen as the alternate technology to be investigated. EMAS, by McNeal-Schwendler Corp., was determined to be one of the more capable finite element code available at this time. EMAS is a generalized FEA program which is not limited to specific applications. The user can specify the elements and grids to possess any material characteristic, load, constraint, boundary condition, etc.

Using these two codes, EMAS and NEC, several basic EMC problems were analyzed. This included the magnetic radiation from a wire over a ground plane, and from a simple coaxial cable. In general, when the predicted results of these simple sources agrees with the "text book" solutions, the complexity of the model can then be increased. For example, if the modeled field within a coax matches the text book prediction it is time to try a wire in a rectangular box, then one could proceed to model a wire suspended in an infinitely long room, etc. By increasing the complexity of the model, while continuously checking the prediction with the theoretical expected results, the user can begin to understand the limitations of the analysis capability.

NEC

NEC was developed by the Lawrence Livermore Laboratories, et.al., and performs it's EM analysis using the Method of Moments technique to solve the integral equations for the currents induced by sources or incident fields. NEC is best suited to "unbounded" systems such as antennas in open sites. NEC allows structures such as ground planes to be added. However, it is not intended to resolve "bounded" problems such as below-deck equipment spaces which have metallic walls. Its general use is for far field and near field radiation patterns for antennas.

EMAS

EMAS solves Maxwell's equations using a kernel based on the popular NASTRAN code. As a finite element code the boundaries of the model must be defined. This makes EMAS well suited to analyzing enclosed systems such as shipboard equipment spaces which are bounded by metallic walls.

RESULTS

Because most below decks EMC problems tend to be "bounded" in some form by either the metallic sides of an equipment cabinet or the metallic walls of a shipboard equipment space, finite element methods were determined to be more suitable for analyzing these type of EMC problems. Therefore, EMAS was determined to be a better choice than NEC for the particular conditions described.

The simple test cases started with a basic coax cable (a single conductor in a circular shield), and a single wire within a square shield. When these were verified to agree with the text book theoretical values, several complexities were then introduced to the models, such as parallel wires and a wire over a ground plane. When the results of these two predictions matched the theoretical values it was believed a simple "EMC" situation could then be tested.

For our detailed compartmental EMC analysis a rectangular shielded room with two equipment cabinets was modeled. The EMI source was a single current carrying conductor suspended below the ceiling similar to a common mode current flowing in a cableway. One of the cabinets was modeled as a dual CRT display console, made from aluminum, that has its two CRT openings shielded with high permeability materials. Such display consoles are common in Navy sonar and combat systems. The other cabinet is a typical data processing cabinet made of aluminum with no penetrations or apertures. To illustrate the location of model components, figure (1) was developed as a simple 2D mesh of the equipment space showing the common mode current source with an outline of the two cabinets. The figure (2) magnetic field contours are the results obtained after FEA analysis and processing of this problem. Figure (2) shows high magnitude magnetic fields in front of the video display opening and also near the high permeability CRT shields. The other cabinet shows magnetic field contour lines that do not have smooth transitions between adjacent elements. In both cases there is a high falloff across one element. This falloff occurs at the boundary between the air and the metal. Intuitively, this leads to the conclusion that the mesh is too course at the boundary. Figure (3) shows the results after the same equipment space was re-meshed to improve the detail in special areas. This produced "better" results without the large falloff across single elements. The difference between figures (2) and (3) is that figure (3) has a finer mesh. The two CRT's in figure (3) are meshed differently. The lower CRT shield has an intermediate mesh. Figure (4) is a close up of a similar mesh showing high level fields remaining near the CRT shield. Figure (5) is a close up of the optimized mesh around the upper CRT. This mesh includes a narrow element of air surrounding all the metallic elements making up the upper CRT shield. This one millimeter wide element permits all the falloff to occur at the surface of the metal. Figure (6) illustrates the results of the optimized mesh of figure (5).

The meshing, and re-meshing iterations show how difficult and complex the problem can become to accurately predict the magnetic field levels in a given region. The complexity of the problem is further compounded with a 3D model.

The following EMC related observations are noted for this room configuration and problem:

a. Although the data processing aluminum cabinet does not have a high permeability, it electromagnetically shades the area to the left and behind the cabinet. This produces an EM quiet area that may be useful to route sensitive cables or to locate sensitive equipment.

b. As expected, the area around the hi-permeability CRT shields concentrate the magnetic flux. At a compartmental level it may be possible to produce low flux areas within a compartment by routing hi-permeability materials away from the desired "quiet areas". This flux collection concept could also help within any specific equipment.

LESSONS LEARNED

The above models demonstrated the vast potential of utilizing FEA techniques to assist in EMC design. However, what was learned about the technology is of more interest. The lessons learned should be incorporated to make future versions of FEA a truly usable tool for the EMC engineer. The technology is at the point where the user must be an expert in creating the FEA model as well as an expert in EMC. The man-machine interface will have to be simplified before FEA can become a tool for non-EMC designers.

Geometry And Material Concerns

The detail of the geometric configuration and description of the material characteristics are critical in any finite element analysis. The geometry is the physical layout of the design to be analyzed. In an equipment this is the location of components and case materials, in an equipment space it is the location of equipments, cables, and surrounding structure. All passive and active elements that may effect the electromagnetic environment must be represented with their appropriate conductivities, permeabilities and permittivities.

Problems Relating To Geometry And Materials

EMI problems are a complex interaction between current flowing through wires and radiation in the air. These interactions happen over three dimensions. Even in a sparse equipment space, defining the geometry in 3D can be very complex. Cables running between cabinets typically follow a convoluted path. At present, the software interface for FEA graphics generation is rudimentary. Although it is acceptable for creating 2D models, it is barely usable for anything but the simplest 3D geometries. Also inherent in applying FEA to EMC design, is being able to test and then modify a model. If an initial design is unacceptable, redefining the geometry of the model must not be a major undertaking, otherwise FEA will not be used as a tool.

Solutions Relating To Geometry And Materials

In some situations, the quickest and easiest method of analyzing a design for EMC is to simplify it to a two dimensional model. When possible a 2D model can provide the required data far quicker than a 3D model. Candidate designs for 2D modeling possess a high degree of axial symmetry, or infinitely long and straight geometry. For example, a Helmholtz coil, or shipboard cableways have inherent 2D geometry.

Obviously most system designs are not symmetrical or inherently 2D over their length complete length or volume. The more complex 3D designs will require a system such as a solids modeler to efficiently create and modify the geometry of their model. A solids modeler manipulates volumes of material in a fully 3D environment. More investigation of the presently available technology is required to determine its' suitability to the FEA/EMC design problem.

Mesh Concerns

The actual FEA model is a "mesh" of "elements." The elements contain the definitions of material properties within the model. The mesh provides the inter-connections with the grid points where the FEA results are calculated. The accuracy of the FEA model analysis is dependant on the spacing of the grid points, as well as the interpolation and shape functions of the elements.

Problems Relating To Meshing

The easiest means to high accuracy is to create a very fine mesh, however, this is rarely practical. More points means more calculation time. With 3D models, the calculation time can quickly grow beyond reasonable computer resources. Core memory size, CPU speed, and computation time are all limiting values to the size and complexity of the model. Care must be taken to optimize the mesh such that the number of grid points is kept to the minimum value which does not reduce the desired accuracy. This is not necessarily as simple as it sounds. For example, the EM field is changed by the presence of different materials. The boundary between two materials exhibit discontinuities in electrical properties, which produce discontinuities of the field vectors and can produce sharp changes in field levels. A poorly meshed model will at best produce highly deceiving results and at worst produce results that are just plain wrong. Proper meshing requires some prior knowledge of what the results are expected to be.

A popular FEA term is "automatic meshing." Automatic meshing is somewhat of a misnomer. It does not mean that once a geometry is defined one need only sit back and wait for it to be meshed. Automatic meshing will create a mesh for a given region, but the user must indicate the region and specify the number of grid points on the boundaries of that region required for a given accuracy. Furthermore, the user must assure that the grid boundaries of any two contiguous regions match perfectly. Unlike the FEA model for structural analysis, an EM model must include the air between various components. With a complex geometry, the air is often the most complex region to mesh. Because the EMC designer is often interested in the EM field produced by an equipment, it is essential that the air is properly meshed.

Solutions Relating To Meshing

Like the problem with geometry, meshing is much easier when a 2D analysis can be implemented. When a 3D model is required there are not many alternatives. There has been some development of automatic mesh refinement. If EMAS detects too great a fall-off over an element, automatic mesh refinement will subdivide the offending element until an acceptable accuracy has been achieved. This ability should assist in the meshing process however, if the model starts with a poor initial mesh, the refinement may produce a unacceptably large number of new elements, making the analysis run time extremely long.

Often, a design has components that are used several times or that are used repeatedly in other designs. CAD programs typically offer a means to define symbols or macros so that these repeated elements need only be defined once. FEA may offer a similar capability with "super-elements". Super-elements are a group of predefined elements with their solution matrix already solved. When incorporated in a model, all that remains is the residual, or the interface with the super-element. It is important to note that the mesh of the model must match perfectly with that of the super-element. Super-elements may provide a means to simplify the development of models with repeated components, however, some standardized mesh interface would have to be developed to make their use practical.

One possible technique would be to incorporate an expert system front end on an automatic mesher. Such a front end would know when a fine mesh is required around a high permeability material and or when a coarser mesh will suffice. The analysis would then be done and the mesh would be evaluated. The expert system would automatically optimize the regions it suspects as being in error, and re-run the analysis until reasonable results are achieved. This system which could accept any geometry and would ideally return an optimized mesh.

Complexity of the Model

Even if the above geometry and meshing problems become trivial, analysis of a complex model may still not be practical when using a VAX or equivalent. In fact, if a 3D compartmental problem included all of the EMI sources and susceptors within a typical shipboard room, even a super computer may not be able to process the data. Most FEA programs permit an unlimited number of elements. But if the model has many elements, the time to perform the analysis maybe impractical and costly, and may exceed the resources of any state of the art computing system. Therefore, there are potentially practical limitations on the FEA/EMC analysis.

Problems Relating To Model Complexity

Many problems can not be simplified to a 2D case. No research has been done to determine how much detail is required to accurately analyze typical EMI problems. What level of detail is necessary to describe a model of a magnetic field produced by a structure current? When a source such as a current is introduced to an element, such as a copper wire in an FEA model, the copper is constrained to carry that level of current. If more current is coupled on to the wire, the source forces the current to maintain the original source level. Therefore, a wire that is defined as a source cannot be used as both a susceptor and an emitter. A more complex model is required. The source must be constrained at a point were there is no chance it would also act as a significant receiver. A twisted pair cable may require hundreds or thousands of elements per foot to accurately model it. A simple means of modeling a twisted pair so that it can be both a common mode and differential mode source and receiver is required.

Solutions Relating To Model Complexity

Some means of simplifying typical EMI sources and receivers must be developed. Super-elements may provide one simplification, however super-elements do not significantly reduce the complexity of the model. The amount of work required to create and solve the problem is reduced, but all the complexity is still there and must be solved at some point.

One possible solution would require the development of a new source type. This source should not constrain the element but would describe an initial condition that is subject to change by the surrounding elements. A twisted pair could then be defined to carry a given differential mode current and still be able to have a common mode current coupled onto it. A library of various EMI sources would be ideal for the EMC designer.

APPLICABILITY OF FEA TO EMC

There is great potential for FEA to assist in the EMC design of complex systems. Presently FEA should be able to assist a designer understand the EMC character of systems that can be modeled in 2D. Theoretically, FEA can solve virtually any problem involving Maxwell's equations. However, to make analysis of complex 3D systems practical will require further refinement in the tools available to the EMC specialist. The capability of the present FEA technology encourages its use where no other EMC tool can hope to provide an answer. Presently no other EMC tool is available that can take into account surrounding structure as readily as FEA.

SUMMARY

Without a doubt, EMC designers of the future will use FEA methods to predict EMI. How soon it becomes a practical tool depends to a large extent on the input the FEA industry receives from the EMC community. The limitations of FEA to EMC are not unique to EMC. A solution that helps the EMC designer running EMAS would certainly assist (in some form) the structural designer running NASTRAN. The only way to assure that these solutions are developed is by continued dialog between the EMC and FEA communities. The Navy systems of the future are going to be more sensitive, packaged closer together, and are expected to be more susceptible to a variety of new EMI sources. The tools to ensure EMC in the complex systems of the future must be developed today. FEA can be one of those tools.

ADMINISTRATIVE INFORMATION

This feasibility effort was supported by a NUWC Bid & Proposal special initiative. Dr. Donald Miller, Submarine EM Department Technology Manager, was the Program Manager, Mr. David S. Dixon, EMC Technology Manager, was the Principal Investigator.

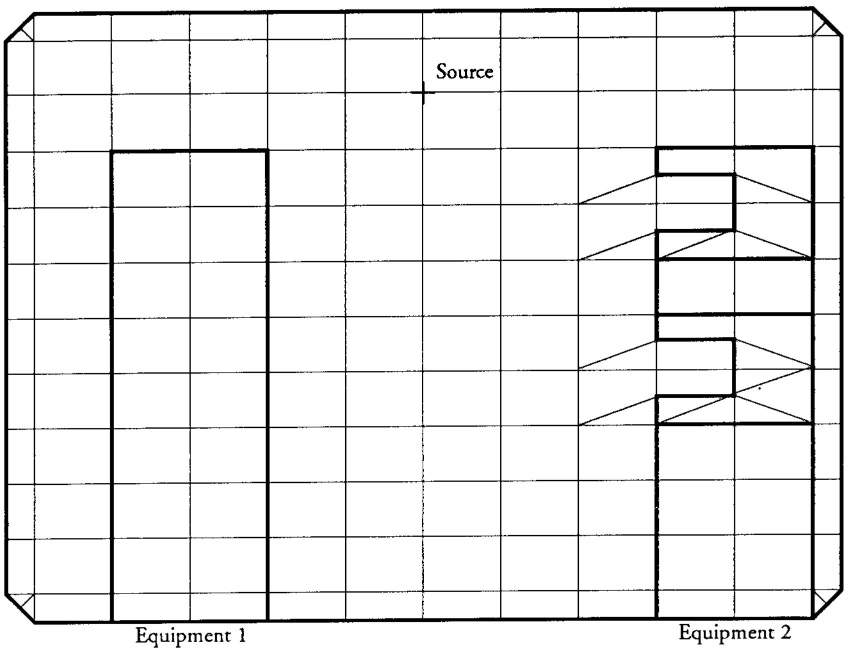

Figure 1: Initial coarse 2D mesh of a multi-cabinet compartment with a common-mode EMI source

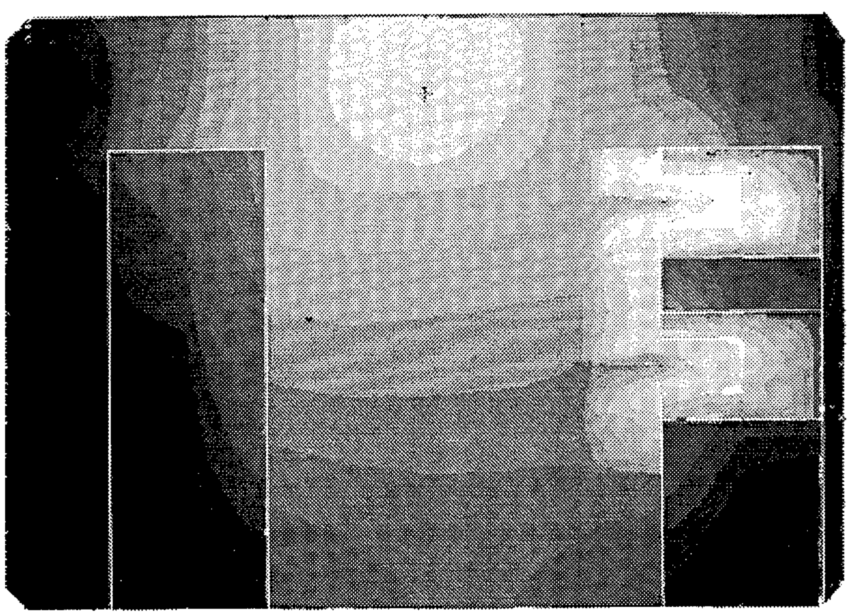

Figure 2: Low frequency magnetic field contours for a bounded metallic compartmental analyis using the above coarse 2D mesh. higher fields are lighter shades

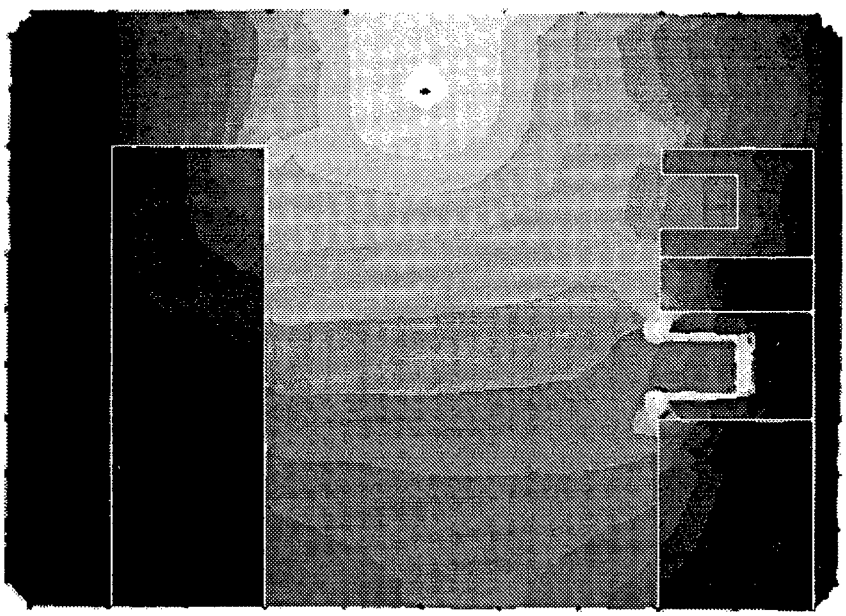

Figure 3: The same room as figures (1) and (2) but, using a fine mesh on both Equipment 1 and the upper CRT, and an intermediate mesh on the lower CRT

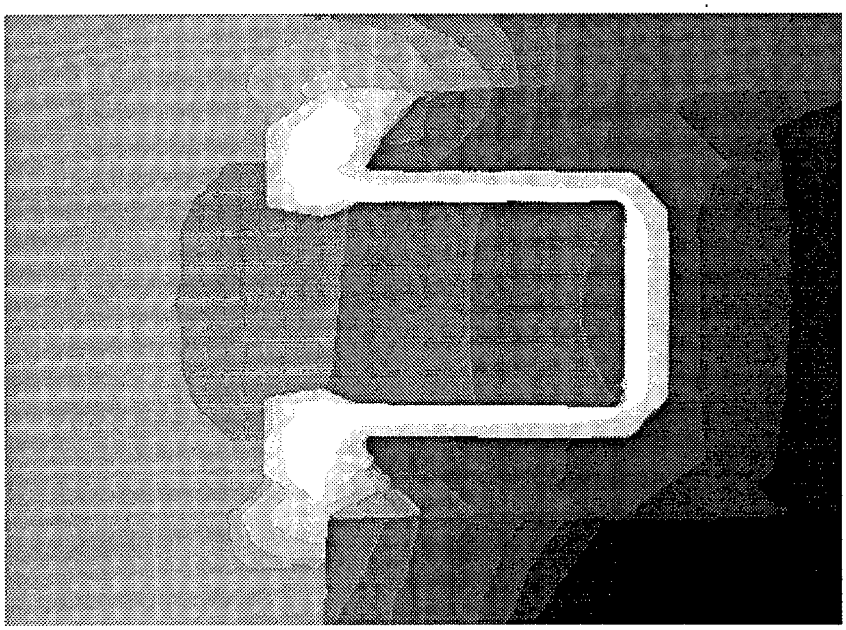

Figure 4: Close up intermediate mesh on the lower CRT, Note the high field around the CRT shield due to a large falloff across a single element.

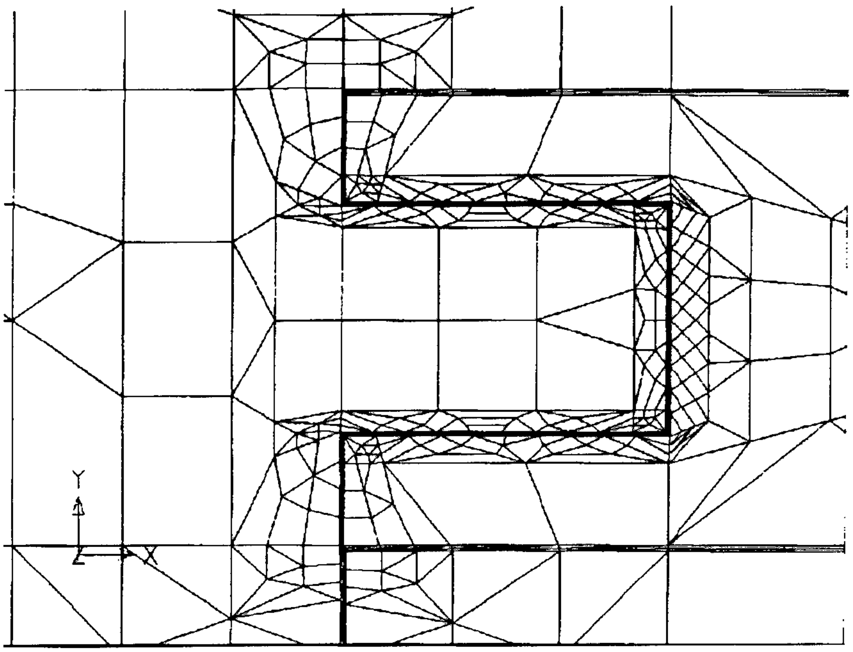

Figure 5: The final optimized mesh (fine) around the CRT shield.

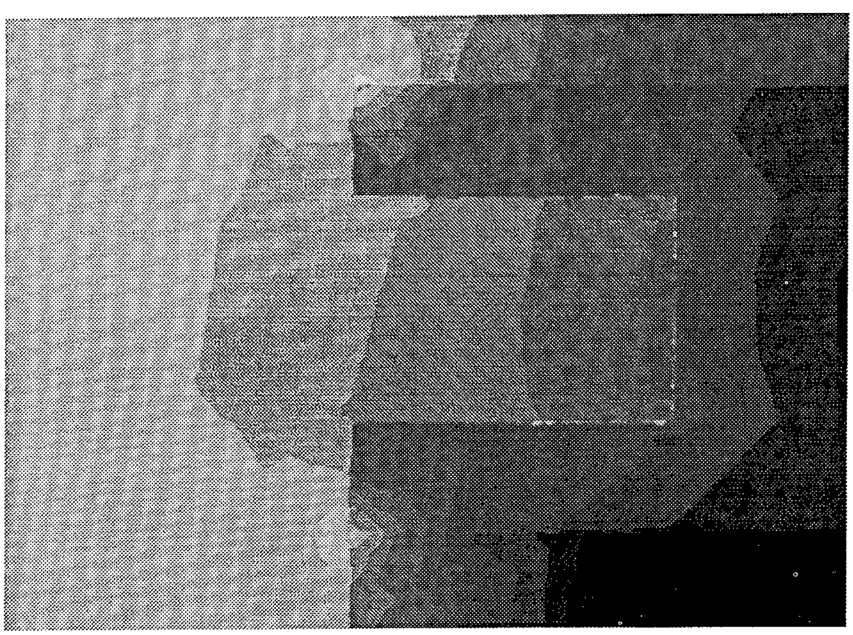

Figure 6: Close up of the results of the final optimized (fine) mesh of figure (5)

Optimizing EMI Shield Design with Numerical Techniques

Colin E. Brench
Digital Equipment Corp.
146 Main Street, Maynard MA 01754

Abstract

To meet the critical time to market goals for commercial computer systems it is essential that there are few if any surprises during compliance testing to the various EMC regulations. With CPU clock frequencies that can be in the uhf region it is crucial that some degree of initial modeling is performed early in the product development cycle. This paper discusses one possible approach which combines numerical and analytic methods to provide the information needed to produce a cost efficient shield design.

Introduction

Today's high performance computers and workstations use vhf and uhf clock frequencies. The most common enclosures are sheet metal and so behave as relatively thin emi shields. These require very small apertures to obtain the needed levels of shielding, which can cause both thermal and acoustics problems.

A second part of the problem is the very dense packaging of a computer system which can cause the electrically active components (both E and H field sources) to be in close proximity to apertures in the shield. The presence of a conductor, be it mounting bracket or cable, adjacent to the other side of the shield can provide an additional path for energy to couple out of the enclosure.

One solution is to use a thicker shield material with larger apertures, often implemented as honeycomb panels. The high level of attenuation available in off-the-shelf honeycomb panels is not needed to meet commercial standards. In addition, the high piece part cost of these panels is prohibitive.

The relatively large apertures and the proximity of a source and a susceptor provide the design challenge. Modeling makes it possible to optimize the shield geometry for maximum aperture size while retaining adequate shielding integrity. This greatly reduces the thermal and acoustics problems that would be caused by small apertures.

Method of Analysis

The complete solution to the problem of how much energy radiates from a source located in close proximity to an aperture in an emi shield is very complex. It depends upon the type of source, hardware configuration, and upon the presence of external conductors. In practical terms this problem needs to be solved for a number of different cases to determine the sensitivity to different parameters. These calculations need to be done quickly in response to

configuration changes that frequently occur during the concept and early design phases of a new product.

In this paper the problem is simplified from a full electromagnetics problem to four separate, though related, shielding functions which can be more easily modeled. The four key shielding functions are:

- shielding effectiveness
- surface impedance
- E field attenuation
- H field attenuation

Shielding effectiveness has largely been used as the sole guide to performance, even though it is strictly only relevant to a planewave source. The overall shield performance can be limited by any one of these functions depending upon the type and location of the source, the presence of adjacent conductors, and the geometry of the shield.

A further advantage of treating each of these functions separately is that an initial evaluation can be made to determine which one(s) will be the limiting case(s). This eliminates wasted time and effort solving irrelevent problems.

An analytic approach was used to evaluate shielding effectiveness. However, due to the complex three dimensional nature of the surface impedance, electric field and magnetic field functions, numerical techniques were most appropriate for the evaluation of these three. Two Digital internal software packages EISOP [1] and RAMAP/SITAP [2] were used for this work. These packages use the method of moments to solve three dimensional inductance and capacitance problems respectively. In this way the physical geometry is converted into a circuit analysis problem. The outputs from these are the capacitance and inductance matrices suitable for inclusion in a SPICE simulation. For the purposes of this work, the matrices are used directly to determine the degree of suppression expected.

Shielding Effectiveness

The use of analytic shielding effectiveness equation is a useful method of estimating the shield performance for sources located well away from any apertures. The equation shown includes correction terms for the number of apertures and shield thickness [3].

$$SE = 20*\log(2L/\lambda) - 10*\log(n) + 27.3*L/t$$

Where :

SE	expected shielding effectiveness
L	maximum opening dimension
λ	wavelength of noise source
n	number of apertures
t	thickness of shield

To correct for proximity to the aperture the result above is scaled by d/L where d is the distance from the source to the aperture. However, this does not take into account the type of source and whether it is physically large or small.

With the inclusion of the correction terms for the number of openings and shield thickness it is necessary for all openings to be equally illuminated with a planewave source. The inclusion of the proximity correction helps in correcting for a non-planewave source.

Surface Impedance

A shield works by keeping rf currents that are flowing on the inside of the shield from coupling to the outside. To achieve this, the internal surface impedance of the shield must be low compared to the impedance between the inside and outside. The shield surface was broken into an open grid (Figure 1) and EISOP was used to model the surface. This provided a matrix of inductors which in turn were used to generate the surface impedance (Figure 2).

The surface impedance may not be equal in all directions due to the shape and orientation of the apertures. This impedance information in conjunction with the expected current paths can provide vital design data.

Electric Field Attenuation

This aspect of the shield performance is important when an electric field source is close to an aperture. Of particular interest is a case where the opening size has been increased to permit greater airflow by increasing the shield thickness to maintain the shielding effectiveness. As relatively low shielding levels are required for commercial applications the use of honeycomb panels that have aspect ratios of 4:1 are not required; 1:1 or even 0.5:1 may be adequate. In these latter cases the possibility for direct coupling through the opening from the source to a close by conductor is much higher and so careful evaluation is needed.

To model this case three elements are needed: source, susceptor and shield. The source and susceptor were both simple square plates while the shield comprised a number of elements to realistically represent the shield geometry around a single aperture (Figure 3). RAMAP/SITAP was then utilized to model this geometry. The resulting capacitance matrix provided the direct coupling from source to susceptor and their coupling to the shield (Figure 4). The ratio of capacitance between source and susceptor to that between susceptor and shield was used as the measure of possible E field attenuation.

Various geometries were analyzed to evaluate a number of different variables, including the effects of source to shield separation, thickness to opening size ratio, web size between openings and the geometry of the aperture (circular vs square). The data obtained indicated the sensitivity to each of these variables and so provided key data to the design process.

Magnetic Field Attenuation

The need to suppress magnetic field coupling is not common at high frequencies as control is achieved with relative ease at the PC board. However, this does not mean that problems cannot arise. Therefore this case was included to complete the analysis.

For this analysis EISOP was utilized. The source and susceptor were modeled as simple straight conductors and the shield was modeled in a variety of ways: a full grid system of thick conductors, a few parallel conductors, and a single parallel conductor. This breakdown provided data on the effects of slot orientation with respect to the source and how the shield might be optimized. The difference between the mutual coupling with and without

the intervening shielding conductors was used as the measure of possible H field attenuation. Figures 5 and 6 show an example and the equivalent circuit.

Experimental Verification

To verify the models, a series of simple experiments were devised to duplicate the geometry evaluated with the computer model. An exception to this was the shielding effectiveness case which is well understood and it was felt that no further work would be beneficial at this stage.

Swept measurements were made from 500MHz to 1GHz using a spectrum analyzer with tracking generator. There were three shield samples for each of the measurements made: a solid copper surface, and two shield surfaces with different size hole patterns. Measurements were also made with no shield present. It should be noted that considerable care was needed to minimize stray coupling from clouding the results. This was done by carefully selecting the local rf ground point and by using ferite cores over the coaxial cables close to the test area to eliminate unwanted shield current. Also by making swept measurements, the presence of resonances could be clearly seen and avoided.

For the surface impedance measurement a current was fed into the shield via a 50 ohm resistor across an aperture located in the middle of the shield (to minimize edge effects). The voltage developed across the aperture was then measured. This was the hardest measurement to make cleanly as the source and probe were very close together and no doubt some error was introduced by direct E and H coupling between the source and measurement probes.

The electric field attenuation was measured by using small conductive pads for the source and susceptor with foam spacers to adjust and maintain the distance between them. The geometry of the experimental set up was the same as shown in Figure 3.

The magnetic field attenuation was measured by using small loops for the source and susceptor, and again foam spacers were used to keep the distances fixed. The geometry used was the same as shown in Figure 5, but the single conductor was replaced by a small loop.

Correlation between EMC theory and practice is seldom highly accurate and any prediction closer than 10dB would be useful; closer than 6dB would be ideal. The results obtained showed correlation within 10dB of the predicted figures for the surface impedance and within 8dB for the E and H field cases. The error was one sided, showing greater coupling and a higher surface impedance than predicted. This can be easily accounted for by an inadequate test set up. However it is unclear at this time whether prediction or experiment is most accurate. Even so, the data is very useful and provides good input to the EMC design engineer.

Conclusions

This paper outlines a method of analyzing the performance of an emi shield by examining four key characteristics, each related to a particular type of noise source. This method enables the EMC engineer to bridge the gap between the circuit model and physical implementation and begin to understand where the main design constraints will be.

The information obtained from shield modeling provides a higher level of understanding

shield behavior. This makes it easier to avoid over-design which can be very costly both directly in terms of component costs and indirectly in terms of additional cooling and/or acoustic controls.

The results of this work were given the most rigorous test. They have been used to design two new enclosures. While it is impossible to correlate actual regulatory measurements with the shield design it possible to say that no surprises have yet been found and that the shields are working as predicted for the application. It should be noted that for these designs the use of the shielding effectiveness equation alone would have resulted in a shield design with openings 30% to 50% larger than acceptable for the level of performance required.

There are many simplifications inherent in this approach which limit the ultimate accuracy and further work is needed to produce a complete electromagnetic solution to the more general problem.

Acknowledgements

I would like to thank my colleagues, Bruce Archambeault of Digital Equipment Corporation and Bronwyn Brench for their valuable inputs during this work and the preparation of this paper.

References

[1] Colin Gordon, "EISOP Users Guide", Digital Equipment Corporation, January 1986.

[2] Colin Gordon, "RAMAP/SITAP Users Guide", Digital Equipment Corporation, February 1, 1984.

[3] "EMI Shielding Design Guide", Tecknit EMI Shielding Products. 1982, pp 3.3 - 3.6

[4] Todd R. Hubing,"A Survey of Numerical Techniques for Modeling Sources of Electromagnetic Interference", Proc. 7th Annual Review of Progress in Applied Computational Electromagnetics, Monterey, CA, March 1991, pp 516-519.

[5] Colin E. Brench, "Electromagnetic Modeling for Commercial EMI Design and Analysis", Proc. 6th. Annual Review of Progress in Applied Computational Electromagnetics, Monterey, CA, March 1990, pp 228-232.

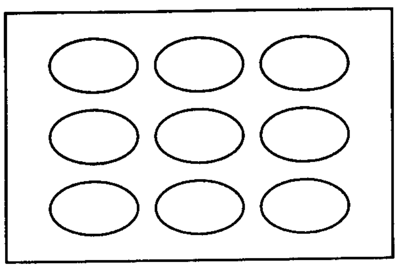

Figure 1. Shield Surface.

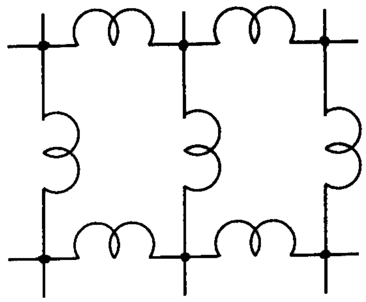

Figure 2. Surface Impedance Model.
(Two Apertures only)

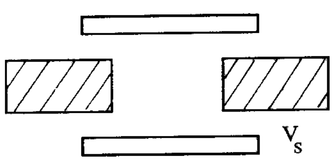

Figure 3. Electric Field Source to Susceptor Configuration.

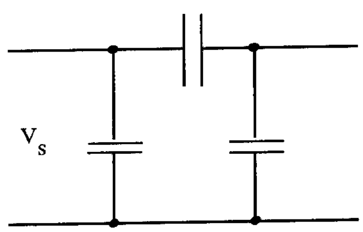

Figure 4. Electric Field Coupling Model.

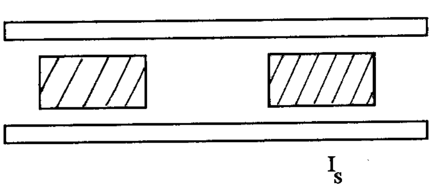

Figure 5. Magnetic Field Source to Susceptor Configuration.

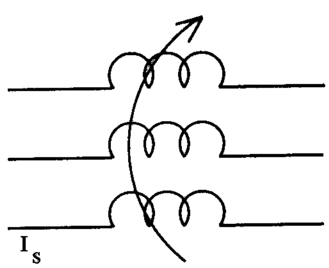

Figure 6. Magnetic Field Coupling Model.

The Use of Finite Element Methods and Closed Form Solutions for Electromagnetic Shielding Employing Conductive Composites

James V. Masi
Western New England College
Department of Electrical Engineering
Springfield, MA 01119
(413) 782-1344

Abstract

The use of electrically conductive composites for electromagnetic shielding is increasing with the need for better control of reflection, transmission, and absorption characteristics.[1,2] Measurements on these materials have been debated, due to lack of agreement upon standards and models which accurately measure and predict behavior of combinations of resins and fillers. Using computational methods which are hybrids of finite element and closed form solution methods, models have been developed and tested by accepted means.[3] Results to date are encouraging.

In this paper, models of composites will be explained, and finite element applications using ALGOR will be shown. Closed form subroutines will be explained and justified in the light of complex permittivity and permeability measurement verification. Shielding effectiveness will, in turn, be derived on the basis of these complex parameters and the appropriate model for the composite material.

Introduction

This work was part of a study which was a continuation of the effort to develop composite materials composed of conducting particles, fibers, or flakes in a matrix of polymeric material for use in connector and box shielding applications. This material was designed to satisfy a full range of electro-magnetic, chemical, and mechanical properties, including corrosion resistance to hostile environments and electrochemical compatibility with connecting enclosures and devices made from aluminum. Oxide and polymeric semiconductor materials and compatible conductive fillers provide a basis for a new class of stable current- and voltage-controlled negative resistance materials, the conductivities of which increase as the field and/or the voltage increases. The ability of the oxides to vary the oxide stoichiometry in the presence of other electro-chemical species make these materials of great interest to the designer.

The unique properties of certain oxides and catalytic-behaving materials to "self-adjust" their electrochemical EMF's (either by oxygen manipulation or other charge transfer) make them extremely attractive in minimizing corrosion due to the dissimilar galvanic potentials. In addition, some of these oxides are semiconductive, allowing for overall improvement of shielding effectiveness. Additionally, the incorporation into the polymeric matrix of polymeric semiconductors, such as polypyrolle, further

increased the shielding effectiveness of the composite. It was also expected that these materials would improve in electrical conductivity with applied voltage/current (due to field dependent charge carrier transport properties), thereby making them perform better during high level electromagnetic field exposure. Indium oxide (In_2O_3)/10 atomic % tin oxide SnO_2 (ITO) was chosen due to its availability and minimum of resistivity for the range of solid solutions for its components.

Early tests were run on polyester castings in order to see if certain fillers behaved in composite formulation as expected. The most promising of these were then injection molded in PEEK and polycarbonate matrices. This is the subject of previous work.[1,2] The tasks which seemed formidable were those of properties prediction, modeling, and computations based on this complex parameter model.

Prediction of Properties

The properties of a composite depend on relative proportions of resin and filler, size, shape, state of aggregation or agglomeration, relative dispersion, and orientation of filler. Finally, the level of interphase adhesion affects ultimate strength and elongation and is a measure of the unwanted condition of "pullaway". For example, for fibers with circular or square cross-section, one of the simplified methods of predicting the composite modulus, tensile or transverse, (the Halpin-Tsai equation) is:

Tensile:

$$E_c = V_f E_f + V_m E_m, \qquad (1)$$

and Transverse:

$$E_c = [(1+2nV_f)/(1-nV_f)]E_m \qquad (2)$$

where $n=\{[(E_f/E_m)-1]/[(E_f/E_m)+2]\}$, E_c is the modulus of the composite, E_f and E_m are the moduli of the filler and the matrix, respectively, and V_f and V_m are the volume fractions of the filler and matrix, respectively. These are the approximate bases on which the mechanical properties of the ideal composite were predicted. The measured mechanical properties are in good agreement with those predicted by the theory (in the absence of filler pullaway).

There are a number of theoretical models which conditionally predict the electrical properties of composites based upon a hopping model[4], percolation theory[5], critical loading[6], and simple RC networks[7]. A baseline effort has been made to establish, not only a verifiable model, but one which established the electromagnetic properties of the composite when given a set of specific component material parameters.

Using the model which relates the resistivity of the filler material to that of the composite via the volume fraction of the filler, the resistivity of the combination can be calculated, supposedly, for these small interparticle dimensions.

$$\rho_c = (V_f/3)[1/(1-(V_f)^{0.5}/3)]\rho_o. \qquad (3)$$

Using form factors for the particle, flake, or fiber, and combining this with a three-dimensional matrix, can lead to a solvable set of equations involving resistors, capacitors, and inductors at various frequencies and fields. The model needs inputs with respect to electric field and frequency dependence of the resistive and reactive elements, i.e. R(E,w) and X(E,w). This model is satisfactory for the cases where the geometries are planar. The actual working cases need an electromagnetic wave model for both the properties and finite element analyses.

A composite sample under an applied field has its potential distribution curves bent more drastically over the conducting filler contacts due to space charge. For purposes of simplicity, the particle/flake/fiber is assumed to have smooth contours and the polymer matrix is electrically homogeneous and isotropic. A model for the possible tunnelling phenomenon[2] is shown in Figure 1. Extensive work is presently being performed on this model and results will be forthcoming at a later date.

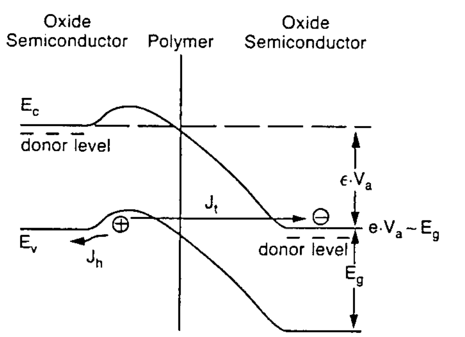

V_a - applied voltage	E_c - conduction band energy
E_v - valence band energy	E_g - energy gap
J_h - hole current density	J_t - tunnell current density

Figure 1
Tunnelling Model for Semiconductive Composite

A number of researchers have noted that current controlled negative resistance is observed (voltage dependent threshold initiation)[8]. Local heating of the matrix/conductive filler is deemed to be the cause, the result being quasi-filamentary conduction. This implies that, as the voltage (field) increases across a composite element, its conductivity and, as a result its shielding effectiveness, increases. This effect is enhanced by certain fillers, such as semiconductive oxides which themselves exhibit C.C.N.R. or V.C.N.R. This implies that the composite with semiconducting particles, flakes, or fibers (or combinations

thereof) should be an improved shield, not only for EMI, but also for EMP applications. Because of the complexity of the model and the level of impinging electromagnetic fields, the negative resistance effects were not considered in this work. They are, however, the subject of a patent pending.

Applying the effective medium theory[8] to the conductivity and the and the complex dielectric constant of the composite material, one can obtain a relationship between the properties of the matrix and those of its components by

$$V_f(\varepsilon_f^*-\varepsilon_c^*)/(\varepsilon_f^*+2\varepsilon_c^*) = -(1-V_f)(\varepsilon_m^*-\varepsilon_c^*)/(\varepsilon_m^*+2\varepsilon_c^*) \qquad (4)$$

where ε_f^*, ε_m^*, and ε_c^* are the complex dielectric constants of the filler, matrix, and composite, respectively, and V_f is the volume fraction of the filler.

In general,

$$\varepsilon^* = \varepsilon_r - j\sigma/\omega\varepsilon_o \quad , \qquad (5)$$

where σ is the conductivity (at the desired frequency) in S/m, ε_o is the permittivity of free space (approximately 8.85×10^{-12} F/m), ω is the angular frequency in rad./s, and ε_r is the real, relative dielectric constant. A similar relationship exists for the complex permittivity. So, the equivalent system now becomes a matter of defining a loss tangent of the medium polymer matrix and conductive polymer), the dielectric constant of the medium, the conductivity (loss tangent) and dielectric constant of the flake/fiber/particle, the complex dielectric constant of the filler, the effective morphology of the filler, and the fraction of filler participating in the process.

Using Maxwell's equations as a basis for the calculation of complex propagation parameters at various frequencies, based upon physical characterization of complex permittivity and permeability using network analysis with coaxial beaded line methods[3], a closed form solution was imbedded in a program which yielded an ASCII file for the key propagation parameters and shielding effectiveness over the range of frequencies of interest. With the knowledge that the complex propagation constant is given by

$$\mathbf{k} = \omega[\mu\varepsilon(1-j\sigma/\omega\varepsilon)]^{0.5} \quad , \text{ and} \qquad (6)$$

the penetration depth

$$\mathbf{d} = 1/\mathbf{k} \qquad (7)$$

A sample of the output is shown, for the sake of illustration, in Figure 2. Outputs similar to these are fed into the finite element/finite difference section of the program for the purpose of describing a variety of geometries of composites with properties which may vary due to processing, function, or material specification.

```
ENTER VALUES OF MATERIAL PARAMETERS:

CONDUCTIVITY IN SIEMENS/m = 10000
RELATIVE PERMEABILITY =1
RELATIVE PERMITTIVITY =11
FREQUENCY IN MHz =100

COMPUTED VALUES:

ATTENUATION CONSTANT = 1986.912 Np/m
ATTENUATION CONSTANT (LOG)= 17254.99 dB/m
PHASE CONSTANT = 1986.924 RAD/m
WAVELENGTH = 3.162268E-03 m
PHASE VELOCITY = 316226.8 m/s
INTRINSIC IMPEDANCE:
        MAGNITUDE = .2809926 OHMS
      PHASE ANGLE = 44.99982 DEGREES
IF THIS IS A SHIELDING MATERIAL,
INPUT THICKNESS OF THE MATERIAL IN METERS
? 0.005
THE SHIELDING EFFECTIVENESS IS 86.27492 dB.

PRESS ANY KEY TO CONTINUE
```

Sample Output of Properties Program

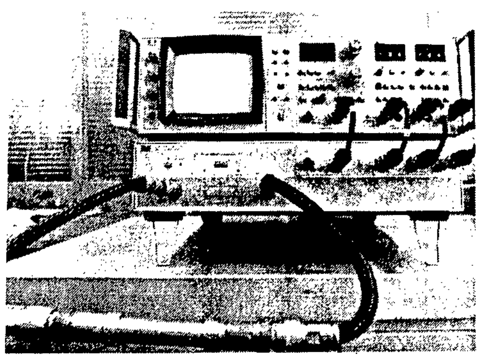

Network Analyzer/Beaded Line

Figure 2

Finite Element/Finite Difference Approximation

Using ALGOR Finite Element Electrostat and Heat Transfer software (ALGOR, Inc., Pittsburgh, PA) combined with finite difference methods developed by Ferrari, et al.[9], Webb, et al.[10], Mur[11], and DePourcq[12], the data from the program described previously are used as property bases for the FE/FD analysis of complex geometries and flow patterns of injection molded samples used as electromagnetic shields.

Once the proper boundary conditions are set for the geometry, field, and materials parameters, the pre-process proceeds with the location and magnitude of fields, boundary conditions, and dithering. Since all of the electromagnetic field modules are not in place at the time of the writing of this paper, many of the routines were escapes to finite difference field approaches previously mentioned (shown in Figures 3 & 4).

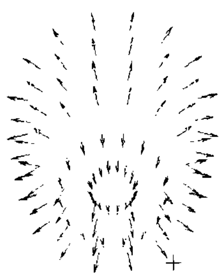

Figure 3: Simple Finite Element Analysis of Connector Backshell

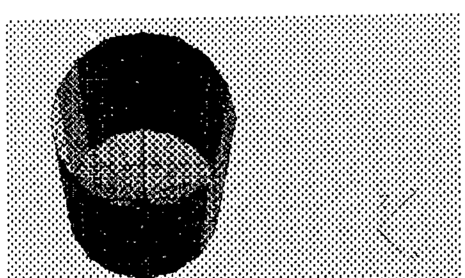

Figure 4: Shaded View of Backshell

In order to take the next step of viewing actual field profiles on composite slabs (the easiest geometry to analyze) and to attempt to begin a formalism for describing flow inhomogeneities in injection molded composite panels, a polycarbonate Ni Flake/ITO/polypyrolle composite was placed into a 750 watt microwave oven (2.45 GHz) and photographed with a full-field, broad-band infrared video camera. It was decided that the heating pattern would form a basis for describing the flow lines (conductivity/complex dielectric constant). These flow lines would lead to wide variations in shielding effectiveness already observed in experimental backshell connector housings made of conductive polymeric composites. The results of the heating and shielding effectiveness of samples are shown in Figure 5.

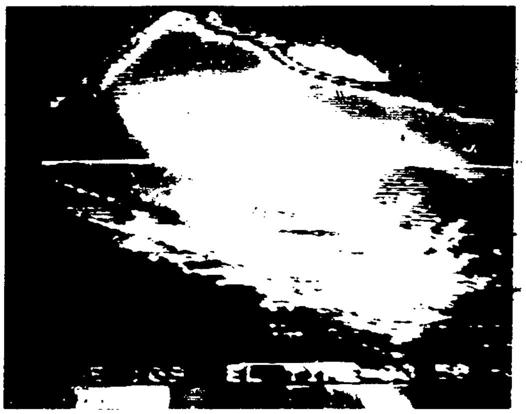

Microwave Heating of Inhomogeneous Composite Slab Shield

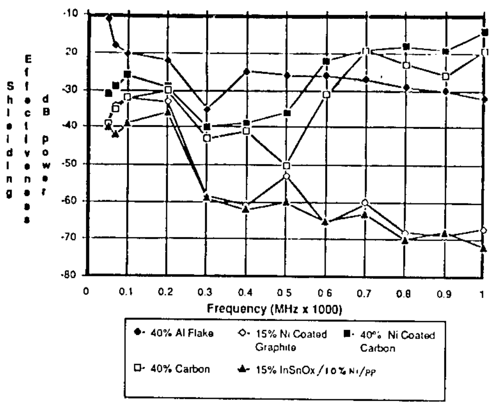

Shielding Effectiveness of Different Composites

Figure 5

Results/Conclusions

The mechanical properties of the polymeric/polypyrolle samples are adequate and can be predicted from the model.

The results shown in the previous studies indicate that there is a strong dependence of the real part and the imaginary parts of the impedance (resistive and reactive) on both electric field and frequency. Dependence of shielding effectiveness on frequency and electric field appears to have a constant value superimposed on a reciprocal dependence with respect to both frequency and electric field. The degree of dependence decreases with metallic loading.

The semiconductive oxide/polypyrrole composite samples behave in a manner which does not fit established empirical theories.[4,6,7,8,14,15,16] Using property prediction, proper modeling, and suitable finite element/finite difference routines, useful tools for complex shielding geometries can result.

The electromagnetic properties can be predicted and agree well with measured values. The program written to develop property information for the finite element/finite difference routines serves its purpose well. The difficulties associated with the finite element analyses are threefold:

1. The boundary conditions must be relatively simple;
2. The material property variation with spatial position makes the present approach suited only to ideal and homogeneous cases; and
3. The adaptation of modules within the ALGOR system falls short of performance of specialized FEA programs, in spite of the ease of use and ergonomic menus.

Work will proceed to refine and verify mechanisms responsible

for the semiconductive and metallic composite electrical behavior. The modeling and numerical methods attempted had reasonable success, though much work needs to be done to determine the level of accuracy of the computations. The results, though still in early stages of investigation, indicate a promising area for future study and open new areas and methods for investigation conductive composites for EMI and EMP applications.

ACKNOWLEDGEMENTS

Support for this project was provided in part by the Office of The Chief of Naval Research/Office of Naval Technology; Submarine Technology Program Element; Program element Manager is Mr. Gene Remmers, Code 233. Block Program Manager for the Submarine Technology Block Program is Mr. Lincoln Cathers, Code 012.4, of the David Taylor Naval Ship Research & Development Center. Principle Investigator of "The Ships Below-Decks EMC Program" is Mr. David S. Dixon, of the Naval Underwater Systems Center, Code 3431.

REFERENCES

1. Avoux, M., Dixon, D.S., Masi, J.V., I.E.E.E. Int. Symp. on Electromagnetic Compatibility, Atlanta, GA, (1987). pp. B1-5.
2. Dixon, D.S. and Masi, J.V., "Development of a Composite Material with Long-Term EMI Shielding Properties", 3rd Int. SAMPE Electronic Conference, Los Angeles, CA, June, 1989 Vol. 3, pp 456-467.
3. Weir, W.B., "Automatic Measurement of Complex Dielectric Constant and Permeability at Microwave Frequencies", Proceedings of the I.E.E.E., 62:1, January, 1974.
4. Mott, N.F., Adv. Phys. (Philos. Mag. Suppl.), 16:49 (1967).
5. McCullough, R.L., Composites Science and Technology, 22:3 (1985).
6. Bhattacharya, S.K., "Metal Filled Polymers: Properties and Applications", Marcel Dekker, N.Y., 1986. pp. 170, ff.
7. Sichel, E.K., "Carbon Black - Polymer Composites", Marcel Dekker, N.Y., 1982. pp. 152, ff.
8. Sichel, E.K., et al., J. Electron. Mater. 22:3, 77 (1982).
9. Ferrari, R.L. and Maile, G.L., Electron. Letters, 14:15, (1978).pp. 467-468.
10. Webb, J.P., Maile, G.L., and Ferrari, R.L., IEE Proc H, Microwaves, Opt. and Antennas, 130:2, (1983).pp. 153-159.
12. Mur, G., IEEE Transactions, EMC-23:4, (1981).pp. 377-382.
13. DePourcq, M., IEE Proceedings, 132:6, Pt. H, (1985).
14. Miyazaki, Y., Tominaga, S., and Tanka, M., "Electromagnetic Shield Properties of Plastics and Ceramics with Resistance and Conductance Particles", Tech. Rept. of IECE. Japan EMC J81-80 (1980).
15. Showalter, R.E. and Snyder, C.H., IEEE Trans. on Circuits and Systems, CAS-33:7, 707-710 (1986).
16. Pike, J.N., Private Communication, UCRI 618 (1970).

APPLICATION OF THE INTRASYSTEM EMC ANALYSIS PROGRAM (IEMCAP) FOR COMPLEX SYSTEM MODELING AND ANALYSIS

Andrew L. S. Drozd
Kaman Sciences Corporation
258 Genesee Street, Suite 103
Utica, NY 13502-4627

Gary L. Brock
Kaman Sciences Corporation
1500 Garden of the Gods Road
Colorado Springs, CO 80933-7463

ABSTRACT

This paper discusses a methodology employed in the EMC modeling and analysis of a complex space platform using the Intrasystem Electromagnetic Compatibility Analysis Program (IEMCAP). The purpose of this discussion is to illustrate the utility of IEMCAP in performing such analyses and to highlight several of its inherent capabilities that make it stand out as one of the most powerful EMC assessment tools in use today.

INTRODUCTION

This paper first presents a background discussion which establishes a foundation for an overall EMC assessment methodology. This is followed by a brief overview of IEMCAP including a summary of recent program enhancements. Also summarized are the IEMCAP system model input data parameters and the key EMC figures of merit computed by the program. Also briefly discussed are the implementation of a pre- and post-processing graphics user interface; program enhancements that address menu-driven/tutorial modeling techniques; the development of new engineering models; and techniques to "unify" existing codes like IEMCAP within an artificial intelligence/expert system framework.

BACKGROUND

Intrasystem EMC is primarily concerned with ensuring compatibility among various electrical and electronic equipments within a system. The increasing complexity and density of electronic subsystems and equipments, which in turn, may have associated with them a large number of electromagnetic transceiving elements (ports), have placed special demands upon the engineer to assure that total EMC is achieved within a system. Achieving total EMC for a complex system can be a difficult task in view of the potentially large number of undesired electromagnetic interactions that may occur. True EMC is achieved when this set of interactions is reduced to zero or some small subset of non-offending cases [1].

In the course of the past 20 years or so, significant strides have been made towards the development and use of computer-aided EMC analysis tools to address such concerns. The judicious use of computer-aided EMC analysis techniques in conjunction with an intelligent EMC test/repair methodology and wise application of EMC specifications has led to the implementation of a significant EMC assurance procedure. In this regard, one can use computer-aided analysis techniques to establish a matrix of various electromagnetic interactions for a complex system [1].

Conceptually, one can view the numerous interactions as representing an Interference Interaction Sample Space (IISS). The IISS can be organized as a matrix of all possible interactions (transfer functions) which relate the various receptors and emitters that may couple to each other. For example, the effect of the jth emitter on the ith receptor can be denoted by the T_{ij} term as shown in Figure 1. Figure 1 also depicts a rather straightforward approach that has been used as part of the US Air Force Intrasystem Analysis Program (IAP) [1]. A major objective of this strategy is to isolate those elements of a matrix which can result in incompatibility. These can be ranked by degree of severity using appropriate EMC engineering criteria. Having done this, remedial measures can then be considered to remove the incompatibilities. Also, there is much that can be done to reduce the initial

matrix size by way of engineering culls. Essentially, this involves culling out those interactions which have a high probability of being least troublesome. What remains are those cases which require further and more precise investigation. One method of establishing such a matrix of interactions and achieving the goals of the EMC analyst is through the use of IEMCAP.

IEMCAP CHARACTERISTICS

IEMCAP is a system-level EMC computer program written in ANSI Standard FORTRAN IV. It was developed by the US Air Force Rome Laboratory and is used extensively for the analysis of intrasystem EMC [2, 3]. It is typically used in analyzing EMC for spacecraft, missiles, aircraft, or ground stations. It is used to perform baseline EMC surveys and can assess the impact of waivers, as well as determine the effects of postulated design tradeoffs. The results of the IEMCAP analysis are furthermore used to influence the EMC test program.

The program incorporates frequency-domain math models to calculate spectra and to analyze coupling among all emitter and receptor ports within a system. As in the traditional EMC approach, the IEMCAP user describes all ports that have the potential for undesired signal coupling. It provides port-port EMI figures of merit for individual frequencies and calculates the cumulative effects for the entire emission environment for each receptor across a frequency range to provide a measure of system EMC. These figures of merit are denoted as the Point and Integrated EMI Margins, respectively.

IEMCAP evaluates the EMC of intentional ports such as antennas and connector pins which conduct desired power and signal waveforms. It also evaluates coupling to unintentional ports such as equipment enclosures. For unintentional port energy effects, IEMCAP makes use of MIL-STD-461 and spurious harmonic limits. IEMCAP is capable of evaluating the overall electromagnetic coupling for antenna-antenna, antenna-wire, wire-wire, case-case, and environmental field-to-port.

The IEMCAP program is structured as two separate software modules. The basic flow through these modules is shown in Figure 2. These modules are executed independently using a series of intermediate, working, and permanent disk storage files. The essential information needed to perform an intrasystem EMC analysis using IEMCAP is described below. In general, this information consists of a comprehensive list of all emitters and receptors for the system of interest, including: their baseband or RF spectral and time-domain characteristics; spatial locations; orientations with respect to system configuration; and their mutual electromagnetic characteristics.

It is useful to point out that emitter/receptor interactions can be categorized at different levels of system complexity (e.g., intrasystem, intersystem, and external field to system). Intrasystem interactions involve only the emitters/receptors on a single platform as illustrated in Figure 3. Such intrasystem interactions are focused upon herein.

<u>IEMCAP Data Parameters</u>. The IEMCAP input data structure is shown in Figure 4. This structure can be further broken down as follows:

- System Geometry (Common-Model/Global Data)
  - Structure parameters/dimensions and layouts
  - Antenna, wire, and filter table characteristics
  - Dielectric aperture parameters/dimensions
  - Environmental field specifications
- Subsystem/Equipment Data
  - Equipment EMC specs and location coordinates
  - Frequency tables and limits
- Port (Case, Wire, Antenna) Characteristics
  - Relative locations and wire bundle terminations

- Spectrum displacements
- Termination impedance
- Antenna look angles
- References to antenna, filter, wire, and aperture tables
- Filtering, shielding, grounding, and signal referencing constraints

- Source/Receptor Characteristics (RF, Signal/Control, Power, EED, and Case)
  - Functional signal waveform parameters
  - Applicable EMC specs
  - User data (in-band and/or out-of-band)
- Cable Bundle Routing Data
  - Bundle point coordinates and wire segment geometries
  - Aperture exposure
  - Height above ground

Other information is required in the form of Executive Control and Identification data which involves the selection of analysis options within IEMCAP [2, 3].

IEMCAP Coupling Models. The three components involved in any coupling problem consist of emitters, receptors, and coupling transfer functions. In IEMCAP, these components are characterized in the frequency domain. In summary, the coupling models available in IEMCAP include wire-wire, antenna-antenna, case-case, field-to-wire, field-to-case, and field-to-antenna. The reader is encouraged to consult the IEMCAP technical literature to obtain details on the various EMC models [2, 3].

IEMCAP Upgrades. Recent enhancements have been formally incorporated into IEMCAP [4, 5, 6]. These enhancements consist of: a more accurate spectrum modeling technique achieved through the removal of port spectrum quantization distortion processes formerly resident within IEMCAP; a capability of inputting measured data (for in-band and/or out-of-band frequencies) more readily to the program; an extended frequency range (DC to 50 GHz); automated frequency table generation; and, improved accuracy with regard to computing Integrated EMI margins. Also, non-average power susceptibility models were developed for future incorporation into the program for energy, risetime, and peak amplitude sensitive receptors. Additional enhancements to improve the accuracy of the field-to-wire model for the SHF/EHF range were also incorporated. The reader is encouraged to consult the appropriate reference on these enhancements.

IEMCAP I/O DATA MANAGEMENT AND GRAPHICS

Supplemental programs have been developed to interface with IEMCAP to operate on calculated values for summary and graphics purposes [7]. These programs permit the EMC engineer to readily scan the IEMCAP output and pinpoint potential interference situations at a glance. These interactions can be singled out and detailed information on them can be produced. The programs provide output matrices, extraction of data, antenna position graphics which also show geodesic coupling paths, and line plots based upon IEMCAP inputs and computed values. Examples of the matrices, line plots, and graphics are described next.

EMI Matrices. Supplemental programs generate a summary file containing various matrices to be used in interpreting the data and defining the extent of the potential problem areas, without printing out the massive IEMCAP output tables. The various port-port matrices include: Integrated EMI Margin Summary, EMI Margin for all Bands/Total Region, NB EMI Margin - Required Region, BB EMI Margin - Required Region, and BB EMI Margin - Non-Required Region.

Table 1 shows an example of Integrated EMI Margin Summary matrix. The number placed in each emitter-receptor entry is the integrated EMI margin computed for that pair. Only the results of using the Integrated EMI Margin Summary option are shown here to illustrate the general form and

content of this output. The outputs for the remaining options are similar in form and content and can be used to extract specific port-pair data for in-band or out-of-band regions, as well as focus on narrowband (NB) or broadband (BB) results.

Geometry Graphics and Line Plots. Another supplemental program provides graphical information for any selected antenna interaction. For example, geometry information, antenna-type descriptions, antenna port locations, and antenna orientation information can be used to produce plots for positions of the antennas on the structure, antenna gain patterns, and the coupling paths between antennas. Figure 5 shows an aircraft structure with two antennas for three different views. The information for such plots is taken from the IEMCAP input and output data files. This supplemental program can also produce line plots of port-pair EMI margins, port-pair received signal/signal susceptibility curves, total EMI margins, and total received signal/signal susceptibility curves. Figure 6 is a plot of an emitter-receptor received signal line plot. Corresponding emitter-receptor EMI line plots can also be generated exhibiting similar content and format.

IEMCAP MODELING/ANALYSIS METHODOLOGY: AN OVERVIEW

A typical aircraft, spacecraft, or ground system can contain thousands of ports. If every emitter port had to be analyzed in conjunction with every receptor port, the run time, core memory size, and file storage would be extremely demanding. Therefore, the maximum system size shown in Table 2 was established. For each equipment, the 15 ports include the case leakage and, therefore, 14 intentional ports are allowed.

Analysis Order. A general purpose approach for assessing the EMC of a large system using IEMCAP is worth presenting as an overview of what is further discussed later in this paper. One approach that is reasonable for a complex aerospace platform is to partition computer runs based on the coupling modes that IEMCAP considers. This approach was partially used in the assessment of IEMCAP on aircraft systems (e.g., the F-15) [8, 9]. The approach can be described as a series of steps starting with IEMCAP's baseline EMC survey procedure:

- Step (1) - Since the highest potential cause of EMI is probably via the RF ports within a system, then the structure should be described and all RF antenna-to-antenna coupling modes should be analyzed along with the external field-to-antenna coupling mode.
- Step (2) - All apertures within the system should be studied to determine those wires that pass near these apertures. Those wires that are connected to potentially susceptible ports near each aperture should be partitioned into like categories and a wire-per-category should be modeled for each aperture. The antenna and external field-to-wire run should then be made. For this step, only the emitter antenna ports need to be described. If the system is small, then this and Step 1 may be performed in one execution.
- Step (3) - For systems not yet built, the following may be a feasible approach. The total wiring of the system should be partitioned into subsets based on critical ports, susceptibility, signal type, wire lengths, loads, and wire types. Those signal-carrying wires that are unique within each subset should be grouped together into a "fictitious" bundle and terminated to "fictitious" equipments, then the wire-wire coupling mode can be exercised along with the internal field-to-wire coupling model. This will provide data to help design wire bundling, by designating which signal-carrying wires are likely to interfere with each other and which are compatible. If the system is already built, then the above partitioning can be applied to existing bundles. This will provide data for making decisions concerning filtering, shielding, wire rerouting, etc. These changes can then be further analyzed with IEMCAP.
- Step (4) - Box-to-box coupling can be assessed by clustering boxes of 40 or less to evaluate the potential of EMI among them.
- Step (5) - The results of Steps 1 through 4 should be studied and all those ports which show a high probability of EMI should be reassessed by using the Tradeoff Analysis mode.

- Step (6) - Those ports which still have a marginal chance of being degraded through one coupling mode should be assessed over all coupling modes using IEMCAP's EMI margins, including the total integrated EMI margin.

ILLUSTRATIVE EXAMPLE

Many of the modeling and analysis techniques described above were used to perform an intrasystem EMC analysis of a complex space payload system. This system and the IEMCAP modeling/analysis approach are discussed next in somewhat generic terms. This is done to illustrate the modeling approaches and "rules of thumb" which were used, and that are applicable to assessing virtually any complex aerospace system. However, the approach described herein should not be considered as the only method to analyze a system using IEMCAP. The various analysis procedures, options, and coupling modes used in IEMCAP should be chosen to "best fit" the problem.

Complex System Characteristics. IEMCAP has been used to model a large number of complex military and commercial systems. A partial list of systems is given in Table 3. The experimental system hardware in this discussion is assumed to comprise a space shuttle payload experiment. The intrasystem EMC concerns focus upon wire-wire, box-box, antenna-wire, antenna-box, and environmental field effects on the payload cargo.

A general conceptual layout of the system configuration is illustrated in Figure 8. The design of this payload system consists of sophisticated computer signal/data processing, as well as state-of-the-art adaptive optics hardware. For the purposes of this discussion, the mission and details of the system are immaterial. In any event, there was a need to assure intrasystem EMC as well as address overall payload system and shuttle EMC concerns. Thus, an IEMCAP analysis was undertaken. Described next are the EMC requirements and specification limits that were considered in the IEMCAP analysis.

EMC Requirements. The EMC assurance program for the payload system was established to satisfy the requirements of NASA Marshall Space Flight Center Specification MSFC-SPEC-521A and its supplementary EMC and safety documentation [10, 11]. The overall intent of MSFC-SPEC-521A is to assure that payload equipment will not generate levels of EMI which could degrade system performance or cause major shuttle system (e.g., orbiter, payload systems, etc.) malfunction. Both conducted emissions from power busses and radiated electromagnetic emissions produced by payload system equipments and interconnects were of concern. Furthermore, MSFC-SPEC-521A addresses the susceptibility of payload equipments to externally-produced shuttle electromagnetic emissions. These EMC limits and recommended test procedures are generally consistent with the requirements of MIL-STD-461A and MIL-STD-462. It was necessary to consider the relevant MSFC-SPEC-521A including any exceptions or deviations during the IEMCAP analysis effort. The results of the IEMCAP and supplementary EMC analyses were used to influence the test effort so as to focus on the more likely EMI situations that might arise during measurements.

Port Modeling. This assessment was primarily concerned with wire coupling effects. With regard to this concern, IEMCAP assumes that an equipment is compatible with itself, e.g., all signal/control lines entering a box are compatible with each other. However, wires that have a common run length and are located within the same bundle, and are perhaps part of another subsystem are of concern. Thus, a potential for cable crosstalk exists between any two wires in the same cable configuration. Therefore, those wires which run in bundle segments with wires conducting signals from other subsystems were assessed in this situation. The wires chosen were those that were potentially the most susceptible and those which were the most degrading. When the number of wires exceeded 14, than iterative computer runs or partitioning of the wires into subsets was performed as described previously. Also, one can perform iterative runs if interested in analyzing all the wires in the bundle entering an equipment, or one can prioritize the wires in the bundle according to susceptibility levels. Another approach that is appropriate in some situations is to partition the wires into like subsets of susceptibility levels, emission signal spectra, types of wires and loads, etc. This may partition the large

number of ports into 14 or less unique wires, which in this case, were analyzed in a single computer run.

Equipment Modeling. The equipment-per-run limitation usually can be solved by multiple runs based on a system's port types and coupling modes. The runs can be assessed based on box-to-box coupling i.e., analyzing those boxes which are near to each other first. Analysis up to forty boxes per run should in most systems, not be a problem as far as dividing the system up into compartments with 40 or less equipments per run. This did not arise as a limitation for the present case.

Antenna Modeling. The coupling mode that may present some concern by the user when limited to 40 equipments per run is antenna-antenna coupling. Some complex systems have more than 40 equipments and/or 40 individual antennas. There are ways to overcome this limitation. The first is to partition computer runs into smaller sizes based upon the time that the equipment will be operating. Depending upon the scenarios that the system must operate through, it is possible that fewer than 40 equipments will operate at any one time. If more than 40 equipments must operate at the same time, then a suggested approach might be to partition computer runs based upon frequency. First, one would model and assess those RF emitting equipments in the lower portion of the frequency bands against all those receiving equipments starting at the low end of the frequency spectrum until the number of equipments is equal to 40. Then one would perform the next computer run with those RF emitting equipments operating in the middle portion of the band and the receiving equipments starting near the lowest emitter tuned frequency of concern. Receiving equipments are added until the number of equipments equals 40 or until all equipments have been analyzed and so on. Exactly how one implements this or any other procedure is problem dependent. For the present case, concerns were restricted to accurately modeling S and Ku band communications and radar antennas exterior to the shuttle payload, therefore, the limitations described above did not arise in the present analysis.

Wire Modeling. In addition to the port modeling concerns cited above, a limitation encountered during the modeling effort for this system was associated with the number of wires per bundle, segments per bundle, and wire bundles that could be modeled. It was understood that there were many bundles of wires in this system that could not be physically modeled because of one or more of the size limitations in IEMCAP. However, it was felt that since one purpose of IEMCAP is to predict potential EMI problems, then what becomes of interest is whether one can model potential EMI situations concerning wire-wire coupling and field- or antenna-wire coupling modes. Therefore, it was considered that bundles with large numbers of wires could be partitioned such that they fit within these constraints. That is, a large number of wires in a bundle can be partitioned as suggested earlier. Partitioning by susceptibility levels, signal types, types of wires, etc., will most likely not exceed 280 different subsets. It should be noted that the analysis performed by IEMCAP with a fewer number of wires in a bundle will be more conservative for wire-wire coupling than using the total number of wires in the actual bundles. This will occur because the distance between the wires used in the coupling model is normally calculated at 1/4 the bundle diameter, which is calculated from the number and the total cross-section of wires in the bundle.

FUTURE DIRECTIONS

The lessons learned from this and similar complex system modeling efforts have helped to identify ways that IEMCAP and its practical utilization could be further enhanced. Several enhancements that have been investigated and are being considered include:

- Installation of IEMCAP for personal computer applications (a PC version of IEMCAP has already been approved for release).
- Implementing the non-average power receptor and coupling models.
- Incorporating more accurate models for complex aperture and antenna coupling for UHF frequencies and above.

- Incorporating scaling and bounding models for total energy penetration including the implementation of out-of-band antenna and aperture models.
- Developing and incorporating nonlinear effects/response models to account for transmitter intermods and associated spurious effects, receiver intermods, cross mods, desensitization, gain compression, and saturation.
- Development and implementation of a user graphical interface which consists of a menu-driven front end, a tutoring capability for inputting data and in-depth system modeling, and standardized (built-in) graphics pre- and post-processing features.
- Implementing IEMCAP within an artificial intelligence/expert system shell which could adapt the results of an IEMCAP analysis for the purposes of additional detailed modeling and analysis of embedded circuit responses and/or to facilitate automated communications with other tools (e.g., SPICE, CAD tools, etc.) or databases. Investigations on the use of certain expert system packages have already begun for this purpose [12].

The benefits to be obtained with regard to such enhancements include: increased modeling power, versatility, and solution accuracy; reduced manpower requirements for systems modeling; fewer modeling errors and error-related showstoppers; increased willingness on the part of users to apply IEMCAP as part of an EMC assurance program; overall reduced costs; and, more readily achievable systems EMC. Although such enhancements will lead to definite benefits, the problems associated with the up-front gathering of the potentially large amount of data for an IEMCAP modeling and analysis effort still persists. The latter may be alleviated by establishing an accessible, "common" IEMCAP database library on systems, subsystems/equipments, and their associated EMC characteristics. Once accessed, pertinent data can be tailored or modified quickly without having to rebuild an entire system or component from scratch.

CONCLUSION

Several important aspects related to the EMC assessment of a complex system using the IEMCAP program have been presented here. The assessment involved the design and implementation of an analysis methodology that can generally be applied to any complex system for which an IEMCAP intrasystem analysis must be performed. It is hoped that the EMC assurance program and IEMCAP analysis methodology outlined in this paper will assist other complex system developers in establishing and maintaining EMC throughout the system procurement life cycle.

REFERENCES

1. J. F. Spina, "The EMC Concept for Weapon Systems," AGARD Lecture Series No. 116 on EMC, AGARD-LS-116, pp. 1-1 to 1-9, September 1981.
2. G. T. Capraro, A. L. Drozd, and G. L. Brock, "Intrasystem Electromagnetic Compatibility Analysis Program - Version 6.0 User's Manual Engineering Section," Technical Report, RL-TR-91-217, Vol. I, Rome Laboratory, Griffiss AFB, NY, September 1991.
3. G. T. Capraro, A. L. Drozd, and G. L. Brock, "Intrasystem Electromagnetic Compatibility Analysis Program - Version 6.0 User's Manual Usage Section," Technical Report, RL-TR-91-217, Vol. II, Rome Laboratory, Griffiss AFB, NY, September 1991.
4. A. L. Drozd, S. Macris, G. Brock, and A. Pesta, "A New Port Spectrum Modeling Approach and the Design of Non-Average Power Receptor Models for IEMCAP", Proceedings of the 1988 International Symposium on Electromagnetic Compatibility, Vol. 88CH2623-7, p. 469, August 1988.
5. P. Griffin, et. al., "SHF/EHF Field-to-Wire Coupling Model", Proceedings of the 1988 International Symposium on Electromagnetic Compatibility, Vol. 88CH2623-7, p. 50, August 1988.
6. G. Brock, et. al., "Implementation of an SHF/EHF Field-to-Wire Coupling Model into IEMCAP", Proceedings of the 1988 International Symposium on Electromagnetic Compatibility, Vol. 88CH2623-7, p. 470, August 1988.

7. G. Brock, T. L. Bedford, and G. M. Grange, "An Overview of the Intrasystem EMC Analysis Program with Graphics", Proceedings of the 1985 International Symposium on Electromagnetic Compatibility, Vol. 85CH2116-2, p. 469, August 1985.
8. R. A. Pearlman, "Intrasystem Electromagnetic Compatibility Analysis Program (IEMCAP) F-15 Validation," Technical Report, RADC-TR-77-290, Part I, Rome Air Development Center, Griffiss AFB, NY, September 1977.
9. G. T. Capraro, "The Intrasystem EMC Analysis Program," AGARD Lecture Series No. 116 on EMC, AGARD-LS-116, pp. 4-1 to 4-22, September 1981.
10. R. W. Evans, "Electromagnetic Compatibility Requirements on Spacelab Payload Equipment", MSFC-SPEC-521, Rev. A, 16 March 1983, Section 3.1, pp. 3-1 to 3-4.
11. A. L. Drozd and P. J. Griffin, "An EMC Assurance Program for the Space Shuttle Advanced Adaptive Optics/Beam Stabilization Experiment Electronics", EMC Expo '88 Symposium Record published by EMC Technology Magazine, Gainesville, VA, p. T22.1, May 1988.
12. A. L. Drozd, V. Choo, A. Rich, et. al., "Analysis of EMI for Shuttle/Space Station Communications Links: An Expert System Approach," EMC Expo '91 Symposium Record published by EMC Technology Magazine, Gainesville, VA, p. A.3.24, June 1991.

Table 1. EMTR-RCPT Integrated EMI Margin Summary Matrix

	SUSBSYTEM EQUIPMENT PORT			RECEIVER PORT ECMPD TACAN TACLO	ECMPD TACH1 TACHI	ECMPD UHFC2 UHFCT	ECMPD UHFC2 UHFCB	ECMPD RADAR RANT1	ECMPD CURT1 CHRD
E	SBSYS	EQPT	PORT						
M									
I	ECMPD	ECMXM	OUTRR	2.7	11.7	43.1	41.9	53.5	-12.6
T	ECMPD	ECMXM	MIDOR	2.7	11.7	43.8	45.6	54.1	-12.3
T	ECMPD	ECMXM	MIDMR	2.7	11.7	44.4	45.7	54.6	-11.9
E	ECMPD	ECMXM	MIDIR	3.0	12.8	44.9	45.6	55.1	-11.4
R	ECMPD	ECMXM	INERR	-24.1	-24.0	4.9	6.4	-2.9	-35.7
	ECMPD	ECMXM	INERL	-24.0	-24.1	4.7	6.6	-2.9	-36.6
P	ECMPD	ECMXM	MIDIL	-23.9	-24.0	4.8	6.8	-3.5	-36.3
O	ECMPD	ECMXM	MIDML	-24.2	-24.4	4.4	6.9	-4.1	-37.3
R	ECMPD	ECMXM	MIDOL	-24.2	-24.4	3.9	6.9	-4.6	-38.3
T	ECMPD	ECMXM	OUTRL	-24.2	-24.3	3.3	3.1	-5.1	-39.2
	ECMPD	UHFC	UHFT	49.9	29.5		100.7	66.1	25.0
	ECMPD	UHFC	UHFB	*35.1	18.6	100.7		83.4	10.0
	ECMPD	UHFC1	UHFXT	32.0	32.9		100.6	35.1	30.2
	ECMPD	UHFC1	UHFXB	17.1	19.0	97.5		52.5	11.0
	ECMPD	CURT1	CHRD1	31.6	103.9	91.7	82.0	81.4	
	ECMPD	CURT2	CHRD2	22.2	28.4	101.7	98.3	43.8	6.5

Table 2. Maximum System Size

DATA CATEGORY	UPPER LIMIT
Equipments	40
Ports Per Equipment	15
Total Ports (40 x 15)	600
Apertures	10
Antennas	50
Filters	20
Wire Bundles	140
Bundle Segments	140
Total Number of Wires	280

Table 3. Systems Modeled With IAP

S-3A	B-52
F-15	EC-135
DSCS-111	SCATHA
F-18	IUS
F-14	SEEK IGLOO
F-16	BLACKHAWK HELICOPTER
A-10	PLSS
A-7D	DEB II
F-111	MX
F-105	P-3C
RF-4C	A-10, OV-10, AN/TRC-87
F-4	AN/SQS-53C SONAR SYSTEM
AN/ALQ-131	AN/ALR-74

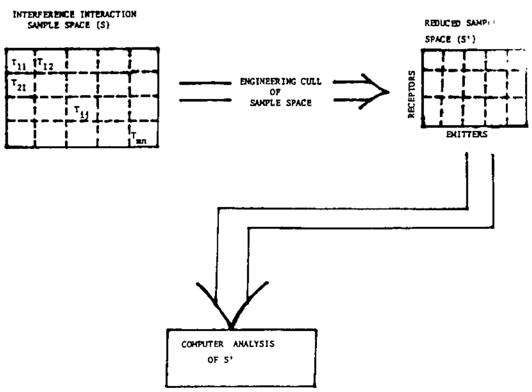

Figure 1. Interference Interaction Reduction

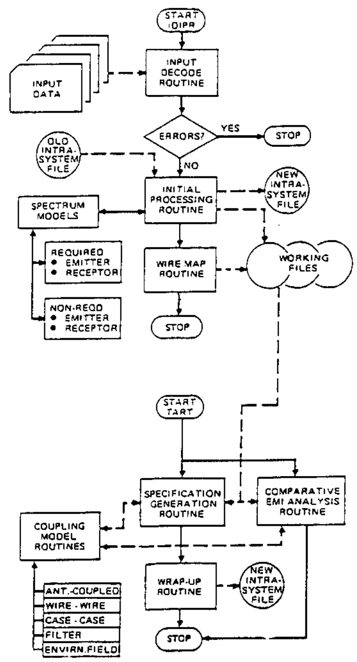

Figure 2. IEMCAP Functional Flow

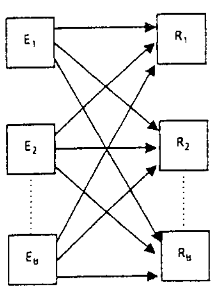

Figure 3. Intraplatform Electromagnetic Effects

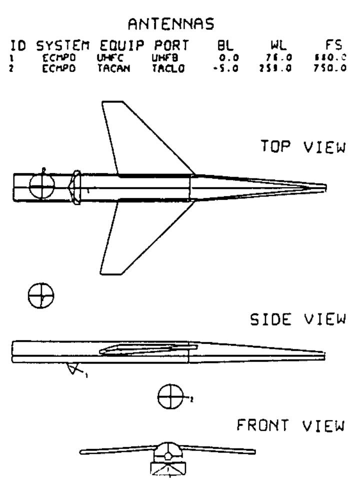

Figure 5. Antenna Positions and Gain Patterns

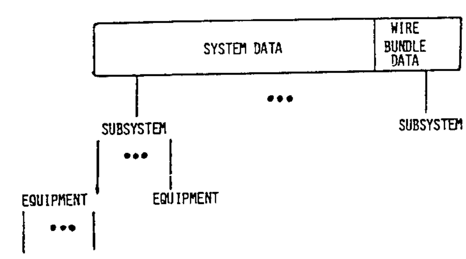

Figure 4. IEMCAP Intrasystem File

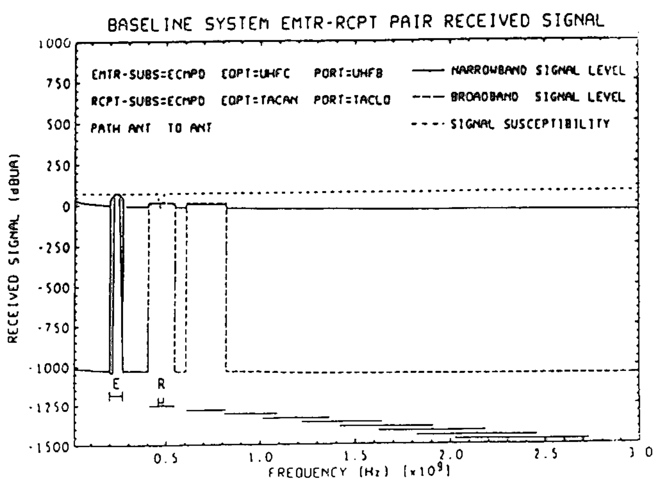

Figure 6. Emitter-Receptor Received Signal Line Plot

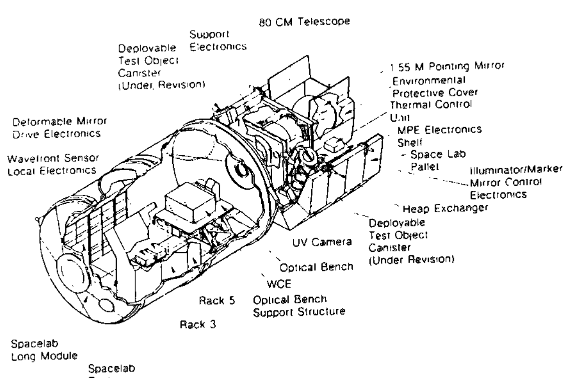

Figure 7. Electronics Configuration

Full-Wave Calculation of Emissions from Radiating Structures

Shahrokh Daijavad and Barry J. Rubin
IBM T.J. Watson Research Center
Yorktown Heights, NY 10598

Abstract

A general purpose electromagnetics code developed by the authors is used to determine the field radiated by a number of structures that appear in electromagnetic compatibility (EMC) studies for personal computers and workstations. The code involves a highly optimized moment method solution that employs rooftop basis functions to represent both conduction and polarization currents; its accuracy has been verified through extensive convergence studies and comparisons with measurements.

1 Introduction

Personal computers and workstations must meet strict specifications for emission set by government agencies such as the FCC in the United States. The study of electromagnetic interference (EMI), both at the printed circuit board (PCB) level and at the box (computer enclosure) level, is becoming more significant as the clock frequencies for computers increase and the signal rise-times decrease. The EMI study of PCBs involves microstrip and stripline structures with finite ground planes, vias between different signal and ground/power planes and other possible discontinuities in the ground plane. EMI study at the box level requires electromagnetic analysis of truly 3D structures. A general purpose electromagnetic code for calculating both near- and far-field quantities in arbitrary 3D inhomogeneous structures is needed. Recently, the authors have described the details of an algorithm, based on the use of rooftop functions [1], for such a code [2]. Some applications and comparisons with measurements have also been reported [3, 4]. In this paper, the basic ideas of the approach are first reviewed. A number of different structures encountered in our research on EMI constraints in the design of PCBs are then analyzed.

2 Modeling Approach

In this section, we summarize the approach presented in [2] for analyzing arbitrarily shaped 3D conductor-dielectric composite structures. In the so-called volume formulations [5] , the effect of all dielectrics are accounted for by the polarization currents in a free-space medium. The polarization charge is found through application of the continuity equation,

$$-j\omega\rho = \nabla \cdot \mathbf{J}\,, \tag{1}$$

where ω is the angular frequency, ρ is the total volume charge density, and $\mathbf{J}$ is the volume current density. Chan and Mittra [6] have also used rooftop functions, though with a different formulation, to model structures involving dielectrics. However, their technique can handle only infinite sheets and not finite-sized dielectrics.

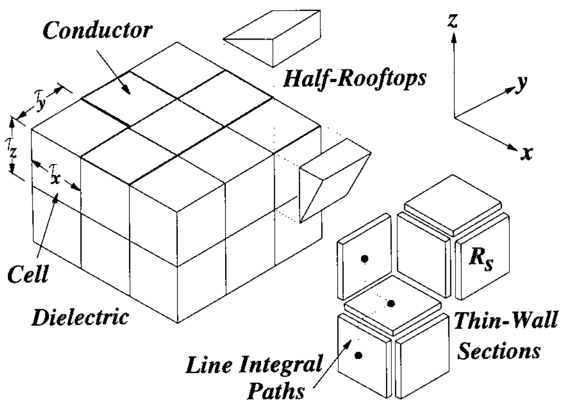

Figure 1: *Diagram indicating the use of thin-wall sections and rooftop functions to model the current density in a conductor-dielectric structure.*

To represent the volume polarization with surface currents, the dielectric region is first replaced by a thin-wall equivalent structure, a procedure which may be viewed as an extension of of the thin-sheet approximation used in [7]. As shown in Fig. 1, the dielectric is subdivided into sections along the Cartesian coordinates, so that the region is now composed of 3D cells having dimensions τ_x, τ_y and τ_z. If we push the dielectric material out from the center of each cell until it is compressed to zero thickness on the cell walls, a new structure is formed that is composed only of these zero-thickness cell walls. During compression, as the wall thickness δ goes to zero, the dielectric constant of the material in the wall goes to infinity as $1/\delta$. Provided the grid is sufficiently fine with respect to wavelength and to feature size, and provided the walls are properly modeled, this thin-wall structure is essentially equivalent to the solid dielectric.

We choose a sheet impedance such that the impedance is the same between two planes that sandwich a cell of either the solid dielectric or the thin-wall structure. From Fig. 1, the total impedance R_x along the x direction for a single cell of solid dielectric is

$$R_x = \frac{\tau_x}{j\omega\epsilon_0(\epsilon_r - 1)\tau_y\tau_z}, \tag{2}$$

where $e^{j\omega t}$ is the time dependence. For the thin-wall structure, the surface impedance must be such that when multiplied by length τ_x and divided by perimeter $2(\tau_y + \tau_z)$, the result is again R_x. Thus, the surface impedance along x, R_{sx}, is given by

$$R_{sx} = \frac{2(\frac{1}{\tau_y} + \frac{1}{\tau_z})}{j\omega\epsilon_0(\epsilon_r - 1)}. \tag{3}$$

For walls common to two cells, which may or may not have the same dielectric constant, R_{sx} would be the parallel combination of the two individual impedances. Through permutation of x, y and z, (3) also gives the surface impedances along y and z, namely R_{sy} and R_{sz}. Lossy dielectrics can be handled through appropriate choice of a complex permittivity.

The electric field boundary condition, applied over each dielectric cell wall and conductor surface, is

$$\mathbf{E}_t^s - \mathbf{J}_s R_s = -\mathbf{E}_t^i, \tag{4}$$

where $\mathbf{E}_t^s$ is the tangential scattered electric field, $\mathbf{E}_t^i$ is the tangential incident electric field, $\mathbf{J}_s$ is the surface current density, and R_s is the appropriate surface impedance. For dielectric volumes, R_s is either R_{sx}, R_{sy} or R_{sz}; for perfect conductors, R_s is zero, but for imperfect conductors it may be determined through skin-effect considerations.

We now focus on the formulation of the matrix equation. A 3D rectangular region that encloses the structure is defined, and subdivided into S_x, S_y and S_z sections along the coordinate axes. The volume current density $\mathbf{J}$ may be compactly expressed as

$$\mathbf{J} = \sum_{\alpha=1}^{P} R_\alpha(x, y, z) I_\alpha \mathbf{e}_\alpha \,, \tag{5}$$

where $R_\alpha(x, y, z)$ is the rooftop function centered at $x = x_\alpha$, $y = y_\alpha$, $z = z_\alpha$, I_α is the corresponding current coefficient, $\mathbf{e}_\alpha$ is the unit vector in the direction of current flow, and P is the total number of rooftop functions. The electric field produced by the current distribution (5) is calculated using scalar and vector potentials, and may be expressed as

$$\mathbf{E}^s = -j\omega\mathbf{A} - \nabla\Phi \,, \tag{6}$$

where $\mathbf{A}$ is the vector potential, given by

$$\mathbf{A} = \frac{\mu_0}{4\pi} \int\int\int \frac{\mathbf{J} e^{-jkr(x-x', y-y', z-z')}}{r(x - x', y - y', z - z')} dx'\, dy'\, dz' \tag{7}$$

and Φ is the scalar potential, given by

$$\Phi = \frac{1}{4\pi\epsilon_0} \int\int\int \frac{\rho e^{-jkr(x-x', y-y', z-z')}}{r(x - x', y - y', z - z')} dx'\, dy'\, dz' \,. \tag{8}$$

In the above equations,

$$r(x, y, z) = \sqrt{x^2 + y^2 + z^2} \,, \tag{9}$$

$$k = \omega\sqrt{\mu_0\epsilon_0} \,, \tag{10}$$

where μ_0 is the permeability of free space, x, y, and z are the field coordinates and x', y' and z' are the source coordinates. The charge density ρ is expressed in terms of the current density through the continuity equation (1). Line function testing of the electric field yields a matrix equation of the form

$$\mathbf{ZI} = \mathbf{V} \,. \tag{11}$$

For a current representation involving P currents, $\mathbf{Z}$ is an impedance matrix of order P, $\mathbf{I}$ is a current column vector of length P, and $\mathbf{V}$ is a column vector of length P that is obtained from the incident field.

For a source-driven problem, an impulse electric field is impressed across a delta-gap located within the conductor region associated with the source, as is conventionally done in moment methods involving wire antennas. The current density is found through equation (11) using standard Gauss elimination and back-substitution. Once the current coefficients I_α have been found, the near- or far-field electric field may be calculated. Complete details of the above are given in [2].

In our previous works, we have employed a computer code implementation that is limited to grids which are uniform along each of the Cartesian axes. Because table look-up facilities were included which are well-suited to such uniform grids, the matrix set-up time was relatively small. In this paper, we employ a computer code implementation that handles a certain class of nonuniform grids. Though the run time is generally far greater for a given matrix size, the code is much better suited for many of the

card geometries that appear in our EMI studies. For instance, structures that involve very thin signal lines with bends, or thin crossing signal lines, or conductors of widely differing sizes can be more easily accommodated.

For such nonuniform cases, however, more effort is needed in selecting the actual grid break-up. While we have observed that even the coarsest grid that accommodates a given uniform structure usually yields results of reasonable accuracy (provided, of course, that there are a sufficient number of sections per wavelength), this is not true for nonuniform cases. For instance, the signal return current is more confined in stripline structures than in microstrip structures; if the grid is not properly chosen in the ground planes of the stripline near the signal line, the radiated fields may not be correct. Thus, it is often necessary to perform at least a few sensitivity runs with different grid break-ups to make sure that the results are valid.

3 Examples

In a recent paper [4], the microstrip-shielding box structure shown in Fig. 2 was analyzed to study the contribution of common-mode radiation. The clock signal generation circuitry driving the microstrip is effectively shielded by a copper partition inside the box. For a 10 MHz oscillator, excellent agreement between measured and calculated results were observed over the few frequencies and angles considered. Here, we present new results for a 33 MHz oscillator driver showing excellent correlation between measured and modeled values across a broad frequency range. Electric field is measured from 30 to 1000 MHz in a semianechoic chamber that is regularly used for EMC qualification testing. Assuming that the device is at the origin of the axes shown in Fig. 2, the antenna measuring the field is at r = 3m, $\theta = 90°$ and $\phi = 90°$, i.e., on the y-axis at y = 3m. Measured and modeled values of $|E_x|$ are shown in Fig. 3. There is also good agreement between measured and modeled values for $|E_z|$ and for other relative orientations of device and antenna. Details of the shielding box structure can be found in [4].

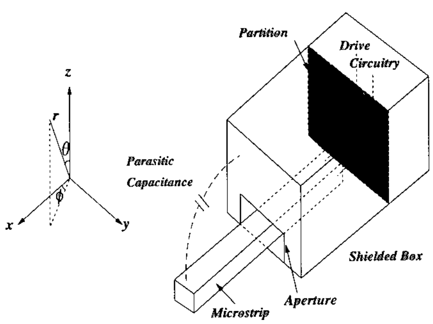

Figure 2: *The test structure consisting of a microstrip, drive circuitry and a shielding box.*

In the EMI studies of PCBs, microstrip and stripline structures with finite ground planes, as illustrated in Fig. 4, are frequently encountered. Of many signal traces on a typical board, the focus is usually on a few nets with significant harmonic content such as clock nets. Various studies on the effect of burying traces between ground/power planes (as opposed to having them on the board surfaces), of having discontinuities in the ground plane, and of having ground traces adjacent to signal traces can be performed using our code. These studies lead to definition of guidelines for good EMI practices in routing wires (nets) on a board. In this context, here we present two examples.

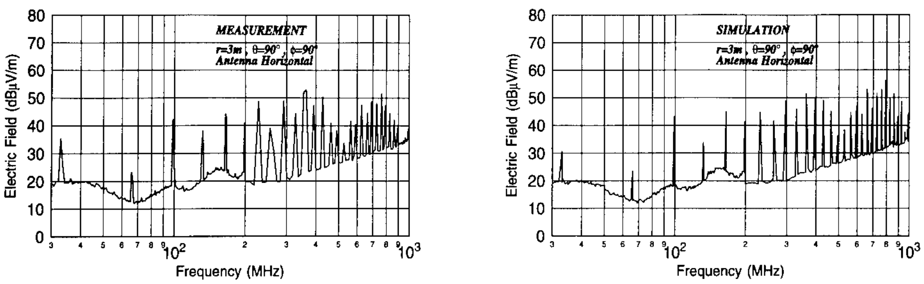

Figure 3: *Measured and modeled $|E_x|$ for the microstrip-shielding box structure with a 33 MHz oscillator.*

Consider a signal trace buried between two ground planes with the following parameters (see Fig. 4): $l_n = 12.7$ cm, $w_n = 0.0152$ cm, $l_b = 28.16$ cm, $w_b = 7.1$ cm and $h_1 = h_2 = 0.0218$ cm. The trace is 2.54 cm away from the board edge parallel to it. It is excited by a 1 V delta gap source in a small via conductor between signal line and ground plane. At the other end, the trace is terminated by a resistor having roughly the characteristic impedance of the signal line. In Fig. 5, the magnitude of maximum electric field on a hypothetical sphere, 3 meters from the structure, is plotted against frequency for three values of dielectric constant ϵ_r. The source voltage is 1 V for all frequencies. For $\epsilon_r = 1$, there is a resonance at around 550 MHz, i.e., at the frequency at which l_b is half a wavelength. For $\epsilon_r = 4.4$, this resonance shifts to about $550/\sqrt{4.4} = 260$ MHz and multiples of this frequency. To confirm both accuracy and continuity of the results from our code, ϵ_r is shifted from 4.4 to 4. As expected, the resonant peaks shift slightly and predictably toward the higher frequencies. The interesting result here is that the resonance frequencies are related to the board length and not to the trace length.

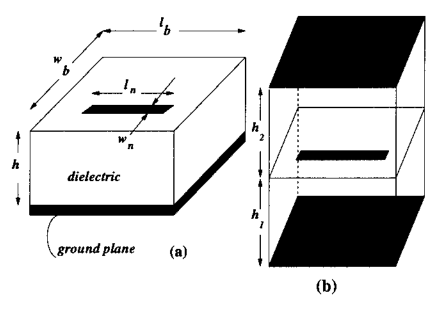

Figure 4: *Typical microstrip(a) and stripline(b) structures in PCBs.*

The second example on PCB traces is a study on the effect of ground plane discontinuity and ground traces. Consider a signal trace in the microstrip structure of Fig. 6(a). All trace and board dimensions are the same as in the previous example with $\epsilon_r = 1$. For a solid ground plane, the solid curve in Fig. 7 shows the maximum electric field, again 3 meters from the structure (notice that compared to the stripline structure, the sharp board resonance has disappeared). If there is an opening in the ground plane, as shown in Fig. 6 (the opening dimensions are: 0.02 cm parallel to the signal trace and 1.0152 cm perpendicular to the trace), the radiation goes up by an average of 6-7 dB across the entire frequency range (see Fig. 7). This is due to the disturbance in the return current path. To remedy the adverse

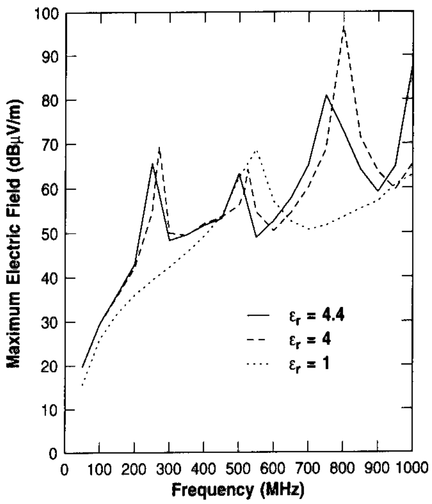

Figure 5: *Maximum electric field at a distance of 3 meters for the stripline example.*

effect of sometimes unavoidable discontinuities in the ground plane, the signal trace is accompanied by two adjacent ground traces (see the bottom right diagram in Fig. 6). These traces are connected to the ground plane via small conductors at the ends and also near the discontinuity. A desirable reduction in the electric field is achieved, as plotted in Fig. 7, due to the presence of ground traces.

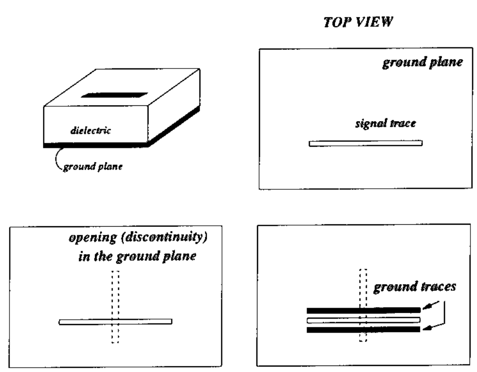

Figure 6: *Microstrip example to study the effect of ground plane discontinuity and ground traces.*

4 Conclusions

A highly versatile and robust algorithm for determining the radiation from general 3D conductor-dielectric composite structures was reviewed. A computer code based on this algorithm was then used

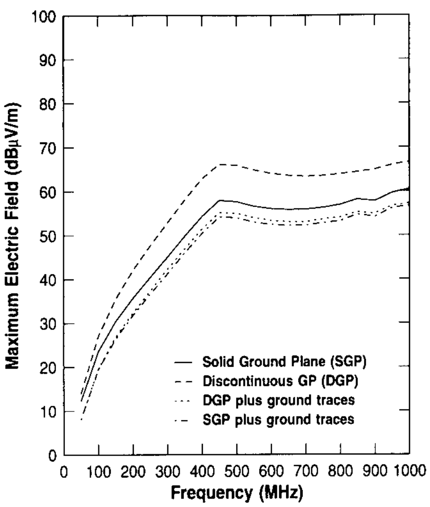

Figure 7: *Maximum electric field plots for the microstrip example with ground plane discontinuity and ground traces.*

to analyze several examples encountered in the EMC studies of PCBs. Physical insight into the results were given, and comparisons with EMC chamber measurements were also presented.

References

[1] A. W. Glisson and D. R. Wilton, "Simple and efficient numerical methods for problems of electromagnetic radiation and scattering from surfaces," *IEEE Trans. Antennas Propagat.*, vol. AP-25, pp. 593-603, Sept. 1980.

[2] B. J. Rubin and S. Daijavad, "Radiation and scattering from structures involving finite-size dielectric regions", *IEEE Trans. Antennas Propagat.*, vol. AP-38, pp. 1863-1873, Nov. 1990.

[3] R. A. York, R. C. Compton and B. J. Rubin, "Experimental verification of the 2-D rooftop approach for modeling microstrip patch antennas", *IEEE Trans. Antennas Propagat.*, vol. AP-39, pp. 690-694, May 1991.

[4] S. Daijavad and B. J. Rubin, "Modeling common-mode radiation of 3D structures", *IEEE Trans. Electromagn. Compat.*, vol. EMC-34, Feb. 1992.

[5] D. E. Livesay and K. M. Chen, "Electromagnetic fields induced inside arbitrarily shaped biological bodies," *IEEE Trans. Microwave Theory Tech.*, vol. MTT-22, pp. 1273-1280, Dec. 1974.

[6] C. H. Chan and R. Mittra, "The propagation characteristics of signal lines embedded in a multilayered structure in the presence of a periodically perforated ground plane," *IEEE Trans. Microwave Theory Tech.*, vol. MTT-36, pp. 968-975, June 1988.

[7] R. F. Harrington and J. R. Mautz, "An impedance sheet approximation for thin dielectric shells," *IEEE Trans. Antennas Propagat.*, vol. AP-23, pp. 531-534, July 1975.

SESSION 11 - "FINITE DIFFERENCE TIME DOMAIN"

(Part 1)

Moderator: Karl Kunz

FINITE AND INFINITE ELEMENTS APPLIED TO ELECTROMAGNETIC SCATTERING

M. S. Towers, J. A. R. Macnab and A. McCowen
Department of Electrical and Electronic Engineering,
University of Wales, Swansea,
Singleton Park,
SWANSEA SA2 8PP
UK

Abstract: *The use of finite elements to solve electromagnetic scattering problems in the resonance region is receiving increasing interest. In solving the relevant differential equations each node is only coupled to local nodes and thus the matrix obtained by applying finite elements is highly sparce. Storage requirements are low in relation to the number of unknowns and recent developments in efficient sparce linear algebra techniques can be exploited.*

A new code, SEMS (Swansea Electromagnetic Solver), has been developed for modelling 2D scattering problems. It has mesh generation, solution and post-processing facilities to allow full and useful validation of the techniques embodied. These include the use of infinite elements to model fields in the open domain of the problem and RCS predictions from either current distributions in the scattering body or from the infinite elements themselves. The work has been successfully validated for circular cylindrical bodies with known analytic solutions in both TM and TE modes. The cases tried include conductors, homogeneous dielectric/magnetic material and coated conductors with excellent results providing the mesh is adequately refined and the infinite elements are positioned sufficiently far from the body.

1. Introduction

Electromagnetic scattering problems have been traditionally solved using method of moments (MM) techniques which give rise to densely populated matrix equations in a relatively small number of unknown current parameters on the scattering body. The finite element method offers an alternative approach where the unknown near and far fields are solved for subject to Maxwell's equations. This results in more unknowns but in compensation the linear equations produced have a very sparce coefficient matrix. This allows great economies of storage to be made and the use of iterative linear algebra techniques to solve the equations. Also, in that the fields are solved for in the mesh surrounding the scatterer near field patterns are immediately available by interpolation of nodal values. If current distributions are solved for, as in the case of MM, each desired near field value requires an integration over the whole current distribution on the body. In addition, using finite elements allow great flexibility on where selective refinement may be placed. Also complicated geometries can be meshed without difficulty in principle.

A new code called SEMS (Swansea Electromagnetic Solver) has been developed at Swansea for 2D modelling of scatter using mixed finite and infinite elements. Triangular elements are used to mesh the body and the surrounding space close to it. Triangles are highly versatile for handling complex shapes and for allowing variable grading of the element sizes. Basically nodes are generated by the pre-processor on the boundaries and interiors of the regions defining the problem according to specified variable spacing requirements throughout. These are then connected into a Delaunay triangular mesh and infinite elements are attached to its outer boundary, which must be convex.

The formulation and finite elements used are described in Section 2 and the features of the infinite elements are dealt with in Section 3. The remaining sections present some results and conclusions.

2. Formulation

The time-independent form of Maxwell's equations in 2D for sinusoidal time variation of fields is

$$\nabla.\left(\frac{1}{\mu}\nabla E\right)+k^2 \in E=0 \qquad \text{(TM mode)} \tag{1}$$

$$\nabla.\left(\frac{1}{\in}\nabla H\right)+k^2\mu H=0 \qquad \text{(TE mode)} \tag{2}$$

where E and H are the components of electric and magnetic field perpendicular to the plane of the problem, ε and μ the local relative complex permittivity and permeability, respectively and k is the free space wavenumber. Referring to figure 1 the open problem domain is divided into inner and outer regions Ω_1 and Ω_2 by an artificial boundary Σ_2. Region Ω_1 contains the scatterer, and if this contains a perfectly conducting surface this is represented by a boundary Σ_1. Linear 3-noded triangular finite elements are used to mesh Ω_1 between Σ_1, if present, and Σ_2. The outer region is meshed by 4-noded infinite elements attached to the outer boundary of the finite element mesh. The boundary conditions on Σ_1 are for (1) and (2)

$E = 0$ (in (1)) and $\nabla H \cdot n = 0$ (in(2))

respectively, where n is the normal unit vector to Σ_1.

Equations (1) and (2) are discretised using the Petrov-Galerkin method with shape functions N_i and weight functions W_i. In the case of the finite elements Ni are bilinear functions of the Cartesian coordinates and each W_i is set to equal N_i. This results in an absolutely standard finite element with a `Laplace matrix' contribution from the div-grad term and a `mass matrix' contribution from the other term in Helmholtz's equation.

The discretised model is excited by a line integral of the incident wave along the Σ_2 boundary in a similar manner to that in reference (1). The unknowns inside Ω_1 correspond to total field whereas in Ω_2 only the scattered field is solved for, allowing an assumed decay law to be modelled here. The line integral on Σ_2 accommodates the transition between the choice of unknowns and provides part of the R.H.S. of the linear equations to be solved. More details of the formulation used in SEMS may be found in reference (2).

3. Infinite Elements

The open region of Ω_2 is modelled by infinite elements as shown in Figure 2. Each one is bounded on its inner edge by an attached member of the finite element mesh and on two sides by adjacent infinite elements. These last two are formed by semi-infinite straight lines radiating outwards. If produced backwards all the lines would be concurrent in a common centre O placed somewhere within the scattering body. Measuring distance r from O the shape function used for the infinite elements take the form

$$N_i=\sqrt{r}M_i(\xi,\eta)\exp\left(-jk\left(\frac{r}{R}-1\right)\right) \tag{3}$$

where $M(\xi,\eta)$ is a standard Lagrange shape function with quadratic variation with ξ in the radial direction and linear variation with η in the circumferential direction. Radial distance r is related to the local variable ξ through,

$$r = 2R\,(1 - \xi)^{-1} \tag{4}$$

and R is a decay length which varies as a linear function of local variable η.

Notice that due to the reciprocal mapping in equation (4) the term M_i is polynomial in r^{-1} with a leading term r^{-1}. The first term $\sqrt{r}$ in (3) then ensures that N_i decays as $r^{-1/2}$ as required in 2D. The exponential term in 3) models the wave behaviour where it is assumed that wavefronts are approximately cylindrical about an axis through O. Weight functions, used in the Petrov-Galerkin procedure are set such that

$$W_i = N_i^* \tag{5}$$

where * means complex conjugate. This results in cancellation of the exponential term allowing simple Gauss-Legendre integration to be used in generating the infinite element matrices.[3]

Far fields can be calculated directly and very cheaply from nodal solution values on the infinite elements through extrapolation using the shape functions [4]. SEMS does this, in fact, as well as using the more standard procedure based on convolution of Green's function with current distributions on the body. Comparison of the results provides a useful check on the validity of the mesh.

4. Results

Initial tests of this FEM technique have been made using plane wave scattering from circular cylindrical bodies with known analytical results. A typical comparison of far field results is shown in Figures 3 and 4. The first case is a TM dielectric problem with diameter $2\lambda_0/3$ and relative permittivity $4 + j0$. The infinite elements have been placed at a distance of $\lambda_0/6$ from the surface and the finite element density is approximately 18 per λ_0 (i.e. 9 per electric wavelength inside the body). The second case is a TE perfectly conducting problem with diameter $2\lambda_0/3$. The infinite elements are positioned $\lambda_0/6$ from the surface and the mesh density is approximately 18 per λ_0.

5. Conclusions

A mixed finite-infinite element technique has been discussed for modelling EM scattering in 2D for TE and TM modes. Far fields calculated from solution values on the infinite elements and from current distributions on the body have been shown in comparison with analytic predictions. The good agreement seen gives encouragement to the on-going validation work with composite bodies such as dielectric coated cylinders. Results of further tests will be presented at the conference session.

References

1. Bettess, P. and Zienkiewicz, O.C., "Diffraction and refraction of surface waves using finite and infinite elements", Int. J. for Num. Meths in Engineering, Vol. 11, pp 1271-1290, 1977

2. Towers, M.S., McCowen, A. and Macnab, J.A.R., "Electromagnetic scattering from an arbitrary inhomogeneous 2D object - a finite and infinite element solution", submitted for publication, IEEE Trans AP

3. Bettess, P., "A simple wave envelope element example", Comms in Appl. Num. Meths., Vol. 3, pp 77-80, 1987

4. Macnab, J.A.R., Towers, M.S. and McCowen, A., "Finite and infinite elements applied to electromagnetic scattering from arbitrary objects in 2D", IEE Proc. Int. Conf. on Comp. in EM, Conf. Publ. No. 350, pp 164-166, 1991

Acknowledgement

This work has been carried out with the support of the Procurement Executive of the Ministry of Defence.

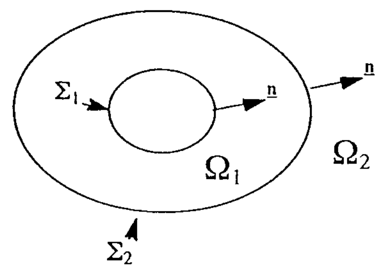

Figure 1 Definition of domain and boundaries

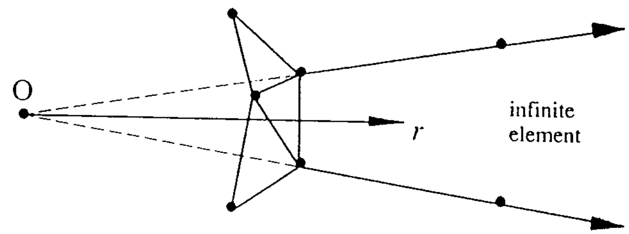

Figure 2 Construction of an infinite element

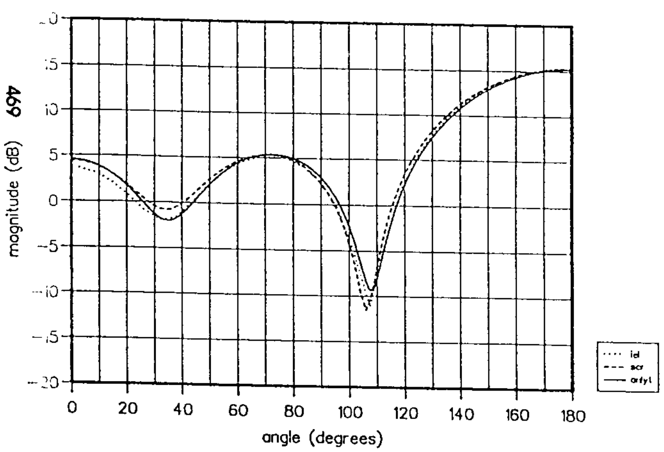

Figure 3 Far field results for a dielectric cylinder in TM mode

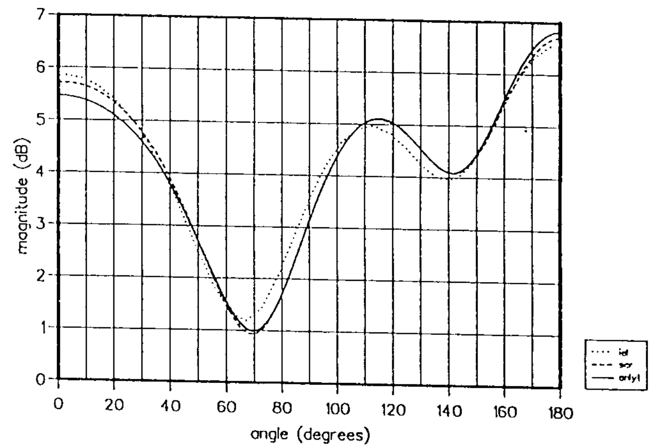

Figure 4 Far field results for a perfectly conducting cylinder in TE mode

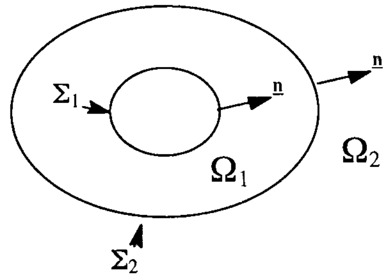

Figure 1 Definition of domain and boundaries

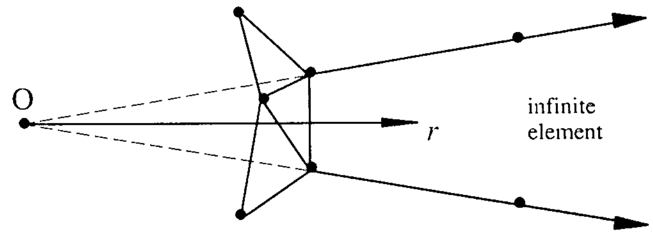

Figure 2 Construction of an infinite element

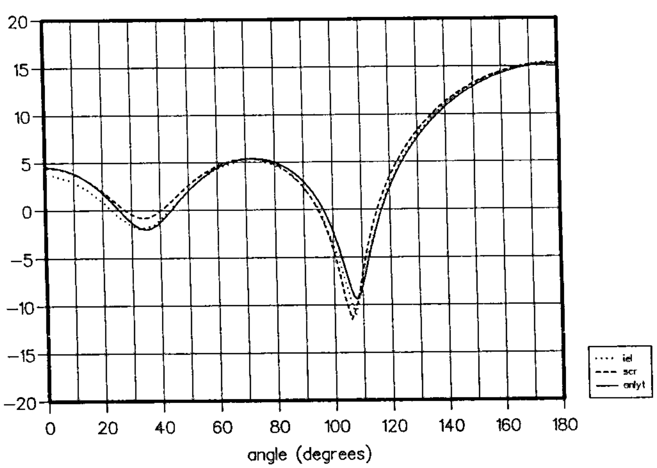

Figure 3 Far field results for a dielectric cylinder in TM mode

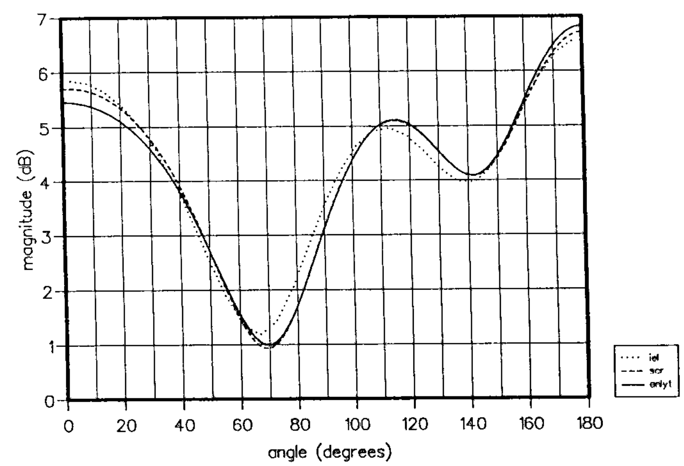

Figure 4 Far field results for a perfectly conducting cylinder in TE mode

TRANSIENT SCATTERING FROM ARBITRARY BODIES

D. A. Vechinski and S. M. Rao
200 Broun Hall
Department of Electrical Engineering
Auburn University, Auburn, AL 36849

Abstract

In this work, a solution procedure is presented to obtain the transient scattering by arbitrarily shaped three dimensional objects directly in the time-domain using the marching-on-in-time method. These objects may be perfectly conducting or a homogeneous dielectric. The late-time oscillations are eliminated by a simple stabilization procedure which involves a negligible amount of extra computation. Numerical results for surface current density and far-scattered fields are given for various structures and compared with other methods.

1 Introduction

In this work, we present the solution of the transient scattering by a arbitrarily shaped conducting or homogeneous dielectric body illuminated by a Gaussian plane wave. The numerical solution procedure is based on the well known method of moments, and we derive an iterative equation to calculate the current at a certain time instant as a function of past instants and the incident field. This technique is popularly known as the marching-on-in-time (MOT) method. An electric field integral equation (EFIE) is used for the conducting bodies while a PMCHW formulation is used for the dielectric structures. Further, it is also well known that these time-stepping algorithms exhibit late-time oscillations, and in this work, we adopt a simple averaging scheme to overcome this problem.

2 Integral Equation Formulation

Let S denote the surface of a closed or open perfectly conducting body illuminated by a transient electromagnetic pulse. This pulse induces a surface current, $\mathcal{J}(\boldsymbol{r},t)$, on S which then re-radiates a scattered field. If S is open, $\mathcal{J}(\boldsymbol{r},t)$ is regarded as the sum of the currents on opposite sides of the surface. By enforcing the boundary conditions of the tangential electric field on the PEC surface, the following integro-differential equation may be derived [1],

$$\left[\frac{\partial^2 \boldsymbol{\mathcal{A}}}{\partial t^2} + \nabla\Psi\right]_{\tan} = \left[\frac{\partial \boldsymbol{\mathcal{E}}^{\rm inc}}{\partial t}\right]_{\tan} \qquad \boldsymbol{r} \in S, \tag{1}$$

where

$$\boldsymbol{\mathcal{A}}(\boldsymbol{r},t) = \frac{\mu}{4\pi}\int_S \frac{\mathcal{J}(\boldsymbol{r}',t-\frac{R}{c})}{R}\, dS' , \tag{2}$$

$$\Psi(\boldsymbol{r},t) = \frac{-1}{4\pi\varepsilon}\int_S \frac{\nabla'_s \cdot \mathcal{J}(\boldsymbol{r}',t-\frac{R}{c})}{R}\, dS' , \tag{3}$$

$$R = |\boldsymbol{r}-\boldsymbol{r}'|. \tag{4}$$

In Eqs. (1)–(4), μ and ε are the permeability and permittivity of the surrounding medium, c is the velocity of propagation of the electromagnetic wave, $\boldsymbol{r}$, $\boldsymbol{r}'$, and $\boldsymbol{\mathcal{E}}^{\rm inc}$, are the arbitrarily located observation point, source point, and incident electric field, respectively, on the scatterer.

3 Numerical Solution Procedure

We assume that the surface of the given conducting body is approximated by planar triangular patches. Let triangles T_m^+ and T_m^- be associated with the m^{th} edge of the triangulated model. The position vector $\boldsymbol{\rho}_m^+$ locates points in T_m^+ relative to the free vertex of T_m^+; the position vector $\boldsymbol{\rho}_m^-$ similarly locates points in T_m^- except that it is directed toward the free vertex of T_m^-. In terms of these quantities, the basis functions associated with the m^{th} edge is

$$\boldsymbol{f}_m(\boldsymbol{r}) = \begin{cases} \dfrac{\ell_m}{2A_m^+}\boldsymbol{\rho}_m^+ & \text{for } \boldsymbol{r} \in T_m^+ \\ \dfrac{\ell_m}{2A_m^-}\boldsymbol{\rho}_m^- & \text{for } \boldsymbol{r} \in T_m^- \\ 0 & \text{otherwise.} \end{cases} \tag{5}$$

where ℓ_m is the length of the edge and $A_m^\pm$ is the area of the triangle $T_m^\pm$. The electric current density $\boldsymbol{\mathcal{J}}(\boldsymbol{r}, t_n)$ is approximated as

$$\boldsymbol{\mathcal{J}}(\boldsymbol{r}, t_n) = \sum_{k=1}^{N_e} \mathcal{I}_k(t_n)\boldsymbol{f}_k(\boldsymbol{r}), \tag{6}$$

where N_e is the number of non-boundary edges in the triangulated model. The unknown coefficient $\mathcal{I}_k(t_n)$ represents the value of the component of the surface current normal to the k^{th} edge at the time instant $t_n = n\Delta t$ where Δt is the increment in time. By using the basis functions also as testing functions and using finite differences to approximate the time derivatives we obtain

$$\langle \boldsymbol{f}_m, \boldsymbol{L}[\boldsymbol{\mathcal{J}}]\rangle = \left\langle \boldsymbol{f}_m, \frac{\partial \boldsymbol{\mathcal{E}}^{\mathrm{inc}}}{\partial t} \right\rangle \tag{7}$$

where

$$\boldsymbol{L}[\boldsymbol{\mathcal{J}}] = \frac{\boldsymbol{\mathcal{A}}(\boldsymbol{r}, t_{n+1}) - 2\boldsymbol{\mathcal{A}}(\boldsymbol{r}, t_n) + \boldsymbol{\mathcal{A}}(\boldsymbol{r}, t_{n-1})}{\Delta t^2} + \nabla\Psi(\boldsymbol{r}, t_n). \tag{8}$$

By using Eqs. (2)-(4), (5), and (6), replacing n with $n-1$, and following the mathematical steps in [1], the integro-differential equation (7) may be re-written as a recursive equation given by

$$\boldsymbol{\kappa}_{mm} \cdot \frac{\ell_m}{2}(\boldsymbol{\rho}_m^{c+} + \boldsymbol{\rho}_m^{c-})\frac{\mu}{4\pi\Delta t^2}\mathcal{I}_m(t_n) = \langle \boldsymbol{f}_m, \boldsymbol{Y}\rangle \tag{9}$$

where

$$\begin{aligned} \langle \boldsymbol{f}_m, \boldsymbol{Y}\rangle &= \frac{\ell_m}{2}(\boldsymbol{\rho}_m^{c+} + \boldsymbol{\rho}_m^{c-}) \cdot \frac{\partial \boldsymbol{\mathcal{E}}^{\mathrm{inc}}}{\partial t}(\boldsymbol{r}_m, t_{n-1}) \\ &\quad - \frac{\ell_m}{2}(\boldsymbol{\rho}_m^{c+} + \boldsymbol{\rho}_m^{c-}) \cdot \left[\frac{\boldsymbol{\mathcal{A}}(\boldsymbol{r}_m, t_n) - 2\boldsymbol{\mathcal{A}}(\boldsymbol{r}_m, t_{n-1}) + \boldsymbol{\mathcal{A}}(\boldsymbol{r}_m, t_{n-2})}{\Delta t^2}\right] \\ &\quad + \ell_m[\Psi(\boldsymbol{r}_m^{c+}, t_{n-1}) - \Psi(\boldsymbol{r}_m^{c-}, t_{n-1})], \end{aligned} \tag{10}$$

$$\boldsymbol{\mathcal{A}}(\boldsymbol{r}, t_n) = \frac{\mu}{4\pi}\sum_{k=1}^{N_e} \mathcal{I}_k(t_n - \frac{R_{mk}}{c})\boldsymbol{\kappa}_{mk}, \tag{11}$$

$$\Psi(\boldsymbol{r}, t_n) = \frac{-1}{4\pi\varepsilon}\sum_{k=1}^{N_e}\left[\mathcal{I}_k(t_n - \frac{R_{mk}^+}{c})\psi_{mk}^+ + \mathcal{I}_k(t_n - \frac{R_{mk}^-}{c})\psi_{mk}^-\right], \tag{12}$$

$$\begin{aligned}
\kappa_{mk} &= \int_{T_k^+ + T_k^-} \frac{\boldsymbol{f}_k}{R_m}\, dS', && (13)\\
\psi_{mk}^{\pm} &= \frac{\ell_k}{A_k^{\pm}} \int_{T_k^{\pm}} \frac{dS'}{R_m^{\pm}}, && (14)\\
R_{mk} &= |\boldsymbol{r}_m - \boldsymbol{r}_k|, && (15)\\
R_m &= |\boldsymbol{r}_m - \boldsymbol{r}'|, && (16)\\
R_{mk}^{\pm} &= |\boldsymbol{r} - \boldsymbol{r}_k^{c\pm}|, && (17)\\
R_m^{\pm} &= |\boldsymbol{r} - \boldsymbol{r}'|. && (18)
\end{aligned}$$

$\not{\mathcal{A}}(\boldsymbol{r}_m, t_n)$ represents $\boldsymbol{\mathcal{A}}(\boldsymbol{r}_m, t_n)$ with the $k = m$ term removed. In Eqs. (15)–(18), $\boldsymbol{r}_m$ and $\boldsymbol{r}_m^{c\pm}$ represent the position vectors to the center of the edge and centroids of triangles $T_m^{\pm}$, respectively, while $\boldsymbol{\rho}_m^{\pm}$ are the vectors between the centroid and free vertex of $T_m^{\pm}$. Similar definitions apply to edge k also.

An important factor to be noted in deriving Eq. (9) is that the choice of the time step, Δt, should be less than $R_{\min}/c$ where $R_{\min}$ is the minimum distance between the edge centers.

The numerical solution procedure discussed so far has the tendency to become unstable at late times. This phenomenon is common to most of the time-marching methods and a number of different causes were attributed such as insufficient sampling, possibility of internal resonances, and/or round-off errors caused while evaluating various intermediate quantities. Although several different techniques have been suggested to overcome these instabilities [2, 3, 4, 5], the problem still persists and requires further research.

In this work, a new averaging scheme is proposed which is simple, accurate, and involves a negligible amount of extra computation. This method is also easy to implement into any existing marching-in-time programs. Let $\mathcal{I}_{m,n}$ be the current coefficient at the m^{th} edge at a time instant $n\Delta t$. In the present stabilization scheme, we calculate $\mathcal{I}_{m,n+1}$ using Eq. (9) and simply approximate the averaged value $\tilde{\mathcal{I}}_{m,n}$ as

$$\tilde{\mathcal{I}}_{m,n} = \frac{1}{4}(\tilde{\mathcal{I}}_{m,n-1} + 2\mathcal{I}_{m,n} + \mathcal{I}_{m,n+1}). \tag{19}$$

Thus, in the present method, we need to add an extra step to the normal marching-on-in-time algorithm, and obviously, this step involves very little processing time. Moreover, it should be noted that this averaging scheme would be the same as the one presented in [5] if we recompute $\mathcal{I}_{m,n+1}$ after computing $\tilde{\mathcal{I}}_{m,n}$ with Eq. (19). However, we observe that the recomputation of $\mathcal{I}_{m,n+1}$ is not necessary and in some instances led to unstable results.

4 Dielectric Bodies

Consider an arbitrarily shaped dielectric body described by a surface S. The scatterer has material parameters of μ_d and ε_d while exterior to the body is a homogeneous medium with parameters μ_e and ε_e. Exterior to the body, the total fields are designated by $\boldsymbol{\mathcal{E}}_e$ and $\boldsymbol{\mathcal{H}}_e$, while interior to the object, the fields are given by $\boldsymbol{\mathcal{E}}_d$ and $\boldsymbol{\mathcal{H}}_d$. The structure is illuminated by an arbitrary electromagnetic, plane-wave pulse. Employing the equivalence principle, the body may be replaced by two sets of electric ($\boldsymbol{\mathcal{J}}_e$ and $\boldsymbol{\mathcal{J}}_d$) and magnetic ($\boldsymbol{\mathcal{M}}_e$ and $\boldsymbol{\mathcal{M}}_d$) currents. Each set radiates in an infinite homogeneous medium having constitutive parameters associated with medium "e" or "d". It can be easily proved that the continuity of the tangential fields requires that

$$\boldsymbol{\mathcal{J}}_e = -\boldsymbol{\mathcal{J}}_d \equiv \boldsymbol{\mathcal{J}} \qquad \boldsymbol{\mathcal{M}}_e = -\boldsymbol{\mathcal{M}}_d \equiv \boldsymbol{\mathcal{M}}. \tag{20}$$

The scattered fields radiated by the equivalent electric and magnetic currents may be written in terms of potential functions as

$$\mathcal{E}^s_\nu[\mathcal{J},\mathcal{M}] = \mp\frac{\partial \mathcal{A}_\nu}{\partial t} \mp \nabla\Phi^e_\nu \mp \frac{1}{\varepsilon_\nu}\nabla\times\mathcal{F}_\nu, \tag{21}$$

$$\mathcal{H}^s_\nu[\mathcal{J},\mathcal{M}] = \mp\frac{\partial \mathcal{F}_\nu}{\partial t} \mp \nabla\Phi^m_\nu \mp \frac{(-1)}{\mu_\nu}\nabla\times\mathcal{A}_\nu, \tag{22}$$

where

$$\mathcal{A}(r,t) = \frac{\mu_\nu}{4\pi}\int_S \frac{\mathcal{J}(r',t-\frac{R}{c_\nu})}{R}\,dS' , \qquad \mathcal{F}_\nu(r,t) = \frac{\varepsilon_\nu}{4\pi}\int_S \frac{\mathcal{M}(r',t-\frac{R}{c_\nu})}{R}\,dS' , \tag{23}$$

$$\Phi^e_\nu(r,t) = \frac{1}{4\pi\varepsilon_\nu}\int_S \frac{\rho^e_s(r',t-\frac{R}{c_\nu})}{R}\,dS' , \qquad \Phi^m_\nu(r,t) = \frac{1}{4\pi\mu_\nu}\int_S \frac{\rho^m_s(r',t-\frac{R}{c_\nu})}{R}\,dS' , \tag{24}$$

for $\nu = e$ or $\nu = d$, and the "$-$" sign is for $\nu = e$, and the "$+$" is for $\nu = d$. In Eqs. (23)–(24), $R = |r - r'|$, the distance from the field point, r, to the source point, r'. The electric and magnetic surface charge density, ρ^e_s and ρ^m_s, respectively, may be related to the electric and magnetic surface current density by the continuity equations

$$\nabla_s\cdot\mathcal{J} = -\frac{\partial\rho^e_s}{\partial t} \qquad \nabla_s\cdot\mathcal{M} = -\frac{\partial\rho^m_s}{\partial t}, \tag{25}$$

respectively. By enforcing the continuity of the tangential electric and magnetic fields at the dielectric interface and taking an extra derivative with respect to time, we derive the following integral equations:

$$\frac{\partial}{\partial t}\left[\mathcal{E}^s_e - \mathcal{E}^s_d\right]_{\tan} = -\frac{\partial}{\partial t}\left[\mathcal{E}^{\rm inc}\right]_{\tan} \qquad \frac{\partial}{\partial t}\left[\mathcal{H}^s_e - \mathcal{H}^s_d\right]_{\tan} = -\frac{\partial}{\partial t}\left[\mathcal{H}^{\rm inc}\right]_{\tan} \qquad r\in S. \tag{26}$$

The formulation described so far is popularly known as the PMCHW formulation [6]. Similar steps may be applied as in the conducting case to obtain a pair of recursive equations for the unknown currents $\mathcal{J}(r,t)$ and $\mathcal{M}(r,t)$.

5 Numerical Results

In this section, time-domain computational results of the currents and scattered fields for two geometries, *viz.* a sphere and cube, are shown. The structures are excited by a Gaussian plane wave of the form given by

$$\mathcal{E}^{\rm inc}(r,t) = \boldsymbol{E}_o\frac{4}{T\sqrt{\pi}}\mathrm{e}^{-\gamma^2} \tag{27}$$

with

$$\gamma = \frac{4}{T}(ct - ct_o - r\cdot\widehat{\mathbf{k}}), \tag{28}$$

where $\widehat{\mathbf{k}}$ is the unit vector in the direction of propagation of the incident wave, T is the pulse width of the Gaussian impulse, $\boldsymbol{E}_o\cdot\widehat{\mathbf{k}} = 0$, r is a position vector relative to the origin, c is the velocity of propagation in the external medium, and t_o is a time delay which represents the time at which the pulse peaks at the origin. The time delay is introduced to ensure a smooth rise of the incident field from zero a value. The pulse width T is defined such that for

$ct - ct_o - \boldsymbol{r} \cdot \widehat{\mathrm{k}} = \pm\frac{T}{2}$, the exponential has fallen to about 2% of its peak value. The specific field is Eq. (27) with $\boldsymbol{E}_o = \pm\widehat{\mathbf{a}}_x$, $\boldsymbol{k} = -\widehat{\mathbf{a}}_z$, $T = 4.0lm$, and $ct_o = 6.0lm$. Comparisons are made with frequency domain data which were inverse Fourier transformed. For all the data presented, the range of frequencies considered was $0 \le f \le 0.5$ GHz, with 128 sample points unless noted differently. The averaging process discussed earlier is used in calculating the currents for these geometries.

Conducting bodies are considered first, and we begin with a sphere of radius $1.0m$ centered about the origin. There were 6 divisions made in the θ direction and each "ring" had (starting from top) 13, 27, 29, 29, 27, and 13 patches, respectively, for a total of 138 patches and 207 unknowns. This scheme was chosen so that the triangles would be closer to being equilateral. With the present patch scheme, an edge lies along the equator and centered about $\phi = 0°$ where the dominant $\mathcal{J}_\theta$ may be obtained. Figure 1 shows the $\mathcal{J}_\theta$ and $\mathcal{J}_\phi$ currents at $\theta = 90°$, $\phi = 0°$, and $\theta = 90°$, $\phi = 90°$, respectively, obtained with a time step of $c\Delta t = 0.07777lm$ which is 50% of the allowed maximum. The currents are in good agreement with the frequency domain results which were obtained by using the Mie series solution. There is a small oscillating envelope present in the late time which does eventually become unstable. However, if averaging were not used, the solution breaks down during the main pulse. It was noted that when the time step was set to 95% of the maximum, which implies $c\Delta t = 0.14776lm$, a better late-time stable result was obtained. The transient response from a cube, $1.0m$ on a side, centered about the origin is shown next. The x, y, and z directions were divided into 4, 5, and 5 uniform segments. By connecting the diagonals of the resulting rectangular patches, a total of 260 triangular patches with 390 unknowns is obtained. Here the resulting time step that was used was $0.04714lm$. The backscattered and "side-scattered" ($\theta = 90°$, $\phi = 90°$) far electric fields are shown in Figure 2. The agreement with the frequency domain data is very good.

Next, homogeneous dielectric solids are considered. We first consider a dielectric sphere $1.0m$ in radius and $\varepsilon_r = 2.0$. The sphere is triangulated in the same manner as described before and has 207 edges. The time step was set to $0.14776lm$ or 95% of the allowed maximum time increment. Figure 3 depicts the equivalent electric and magnetic currents $\mathcal{J}_\theta$ and $\mathcal{M}_\phi$, respectively, at $\theta = 90°, \phi = 0°$. The results are in good agreement with the frequency domain result which was obtained by using 128 frequency samples of the Mie series solution. The equivalent $\mathcal{J}_\phi$ and $\mathcal{M}_\theta$ currents at $\theta = 90°$, $\phi = 90°$ are shown in Figure 4. It may be noted that both $\mathcal{J}_\theta$ and $\mathcal{M}_\theta$ agree very well while the the time-domain peaks are a little bit larger than the frequency-domain peaks for $\mathcal{J}_\phi$ and $\mathcal{M}_\phi$. Finally, a dielectric cube of side length $1.0m$ is considered. The cube is discretized in the same manner as the conducting cube and has a relative permittivity of 2.0. The time step was chosen to be 95% of the maximum allowable and was set to $c\Delta t = 0.08957lm$. The frequency domain result was obtained from a lossy dielectric cube which had a conductivity of 1.0 mS and 128 sample points between 0 and 250 MHz. This conductivity was included to develop a smooth frequency response. Figure 5 compares the backscattered and side-scattered electric fields with the frequency domain results. The two results are in close agreement with each other and show the same trends.

References

[1] S. M. Rao and D. R. Wilton. "Transient Scattering by Conducting Surfaces of Arbitrary Shape". *IEEE Transactions Antennas & Propagation*, AP-39:56–61, January 1991.

[2] B. P. Rynne and P. D. Smith. "Stability of Time Marching Algorithms for the Electric Field Integral Equation". *Journal of Electromagnetic Waves and Applications*, 4:1181–1205, December 1990.

[3] A. G. Tijhuis. "Toward a Stable Marching-on-in-Time Method for Two-Dimensional Transient Electromagnetic Scattering Problems". *Radio Science*, 19:1311–1317, Sept.–Oct. 1984.

[4] P. D. Smith. "Instabilities in Time Marching Methods for Scattering: Cause and Rectification". *Electromagnetics*, 10:439–451, 1990.

[5] B. P. Rynne. "Time Domain Scattering from Arbitrary Surfaces Using the Electric Field Integral Equation". *Journal of Electromagnetic Waves and Applications*, 5:93–112, January 1991.

[6] R. Mittra. *Computer Techniques for Electromagnetics.* Oxford:Pergamon, 1973.

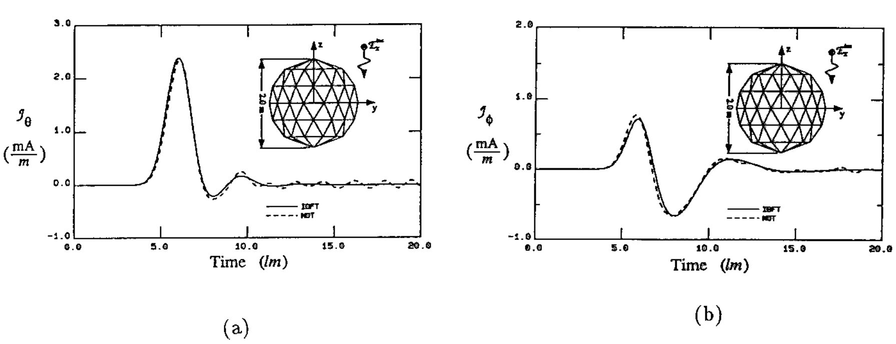

Figure 1: Transient current on a conducting sphere of radius $1.0m$ (a) $\mathcal{J}_\theta$ at $\theta = 90°, \phi = 0°$ and (b) $\mathcal{J}_\phi$ at $\theta = 90°$, $\phi = 90°$ illuminated by a Gaussian plane wave. Number of unknowns = 207.

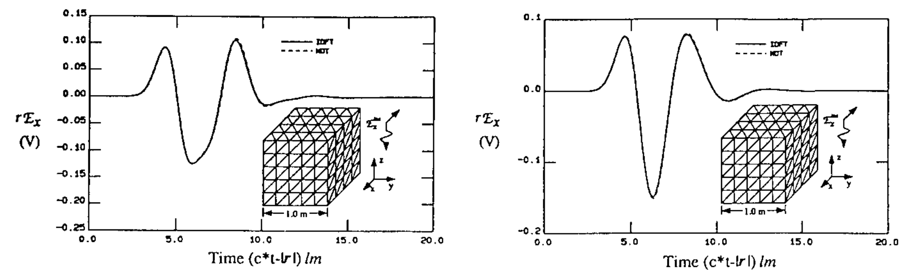

(a) (b)

Figure 2: Normalized (a) backscattered ($\theta = 0°$, $\phi = 0°$), (b) side-scattered ($\theta = 90°$, $\phi = 90°$) far-field response of a conducting cube $1.0m$ on a side illuminated by a Gaussian plane wave. Number of unknowns = 390.

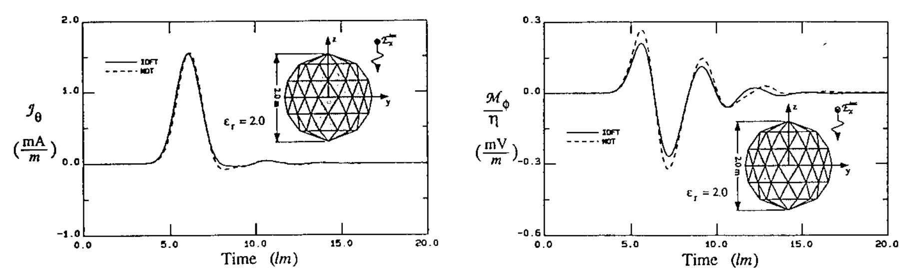

(a) (b)

Figure 3: Equivalent currents (a) $\mathcal{J}_\theta$ and (b) $\mathcal{M}_\phi$ on a dielectric ($\varepsilon_r = 2.0$) sphere of radius $1.0m$ at $\theta = 90°, \phi = 0°$ illuminated by a Gaussian plane wave. Number of edges = 207.

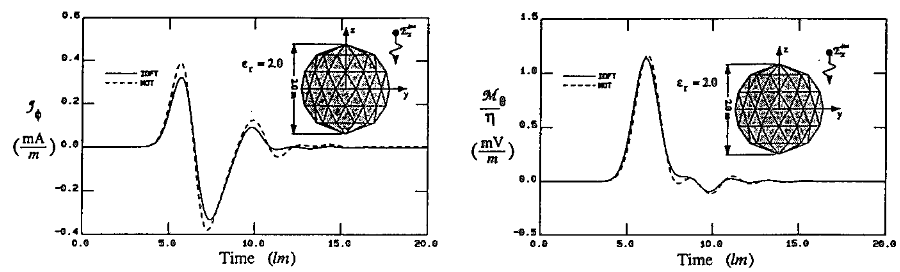

(a)

(b)

Figure 4: Equivalent currents (a) $\mathcal{J}_\phi$ and (b) $\mathcal{M}_\theta$ on a dielectric ($\varepsilon_r = 2.0$) sphere of radius $1.0m$ at $\theta = 90°$, $\phi = 90°$ illuminated by a Gaussian plane wave. Number of edges = 207.

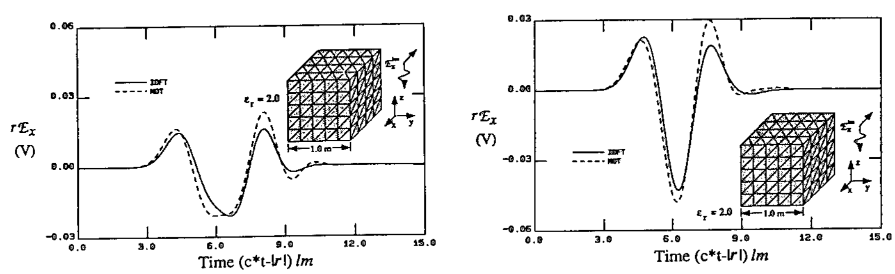

(a)

(b)

Figure 5: Normalized (a) backscattered ($\theta = 0°$, $\phi = 0°$), (b) side-scattered ($\theta = 90°$, $\phi = 90°$) far-field response of a dielectric ($\varepsilon_r = 2.0$) cube $1.0m$ on a side illuminated by a Gaussian plane wave. Number of edges = 390.

FINITE ELEMENT SOLVERS FOR RADAR CROSS-SECTION (RCS) CALCULATIONS

Benoît PETITJEAN, Rainald LÖHNER
CMEE, SEAS, The George Washington University
Washington, D.C. 20052

and

C. Richard DEVORE
LCP&FD, Naval Research Laboratory
Washington, D.C. 20375

Abstract

Two Finite Element solvers for Maxwell's equations in the time-domain are presented. FERCS is a node-centered code based on the Finite Element Flux Corrected Transport method, and RCSUP is a cell-centered code using second-order upwind fluxes. Both allow 2-D calculations of the electromagnetic fields scattered by targets made up of several linear, isotropic materials. The results in terms of bistatic RCS for various configurations are shown and include conducting cylinder, dielectric cylinder, conducting airfoil. Those Finite Element techniques use unstructured meshes and hence allow rapid mesh generation for complex geometries as well as mesh adaptation.

Introduction

The development of efficient numerical methods for the solution to Maxwell's equations is a prerequisite for the effective and rapid design of new products in many areas of electrical and mechanical engineering.

The problem of determining the RCS of typical aerodynamic (i.e. streamlined) objects in 2-D is no longer considered as difficult. For these applications, frequency-domain solvers based on boundary element methods (e.g. methods of moments) are standard tools throughout industry [1,3]. The situation is somewhat different for 3-D problems. For these the very favorable operation count achieved by singularity methods in 2-D deteriorates significantly and becomes rapidly overwhelming. As an alternative, time-domain solvers have been proposed [4,5]. The operation count for these is $N^3 \cdot N_t$, where N is the number of degrees of freedom and N_t the number of timesteps required to achieve the periodic state (monochromatic incident wave) or for the fields to die out (pulse wave). We also notice in passing that multimaterial applications pose only a linear increase in the operation count for time-domain solvers.

The main features of the time-domain Maxwell solvers we are developing are the following:

- Use of unstructured grids, in order to handle both geometrical and physical complexity, and also to allow mesh adaptation.
- Use of proven technology and experience from the Computational Fluid Dynamics (CFD) disciplines, modifying and improving them for the RCS applications.
- Developments in two directions : space-centered scheme with a node-based approximation, upwind scheme with a cell-centered interpolation.

In what follows, we recall the basic Maxwell's equations in the first section. Then the second and third sections are devoted to the presentation of the node-centered and cell-centered codes, respectively. In the fourth and final section we discuss the results.

1. Maxwell's Equations in the Time Domain

The general scattering problem requires the solution to the time-dependent Maxwell's equations. If we assume that the materials are homogeneous, isotropic, linear and that no current density is to be accounted for, they may be written as:

$$\nabla \times \mathbf{E} = -\mu \, \mathbf{H}_{,t} \qquad \nabla \times \mathbf{H} = \varepsilon \, \mathbf{E}_{,t}. \tag{1}$$

$\mathbf{H}$ denotes the magnetic field, $\mathbf{E}$ the electric field, ε and μ the permittivity and the permeability of the material.
If one breaks up the fields into an incident and a scattered field ($\mathbf{E} = \mathbf{E}^S + \mathbf{E}^I$), these equations may be rewritten in the following way:

$$\begin{aligned} \nabla \times \mathbf{E}^S + \mu \, \mathbf{H}^S_{,t} &= -\nabla \times \mathbf{E}^I - \mu \, \mathbf{H}^I_{,t} \\ \nabla \times \mathbf{H}^S - \varepsilon \, \mathbf{E}^S_{,t} &= -\nabla \times \mathbf{H}^I + \varepsilon \, \mathbf{E}^I_{,t} \, . \end{aligned} \tag{2}$$

We always compute the scattered fields only. When dealing with perfectly conducting bodies, the right-hand side of (2) vanishes, and we drive the solution by using the boundary conditions on the bodies.
In the presence of dielectric materials, the solution is driven by the incident terms of the right-hand side. These can be interpreted either as fluxes or as 'regular' source terms, depending upon whether they are expressed as space derivatives or time derivatives.

2. Node Centered Code : FEM-FCT

2. a. General Presentation

As the basic algorithm to advance the solution in time, we employ Finite Element Flux-Corrected Transport (FEM-FCT). This is a non-linear algorithm that blends a high-order and a low-order scheme in an appropriate manner in order to avoid non-physical ripples or oscillations. In regions where the variables under consideration vary smoothly the high-order scheme is employed, whereas in those regions where the variables vary abruptly the high- and low-order schemes are combined, in a conservative manner, in an attempt to ensure a monotonic solution.

Recasting Eqns.(2) in the conservation form that is more usual in Computational Fluid Dynamics (CFD) (with the conservative variables U, the fluxes $\mathbf{F}$ and the source terms S),

$$\frac{\partial U}{\partial t} + \nabla \cdot \mathbf{F} = S, \tag{3}$$

we advance the solution in time as follows:

$$U^{n+1} = U^l + c_a \cdot \left(\Delta U^h - \Delta U^l \right) \, , \tag{4}$$

where ΔU^h and ΔU^l denote the increments obtained by some high- and low-order scheme respectively, and U^l the monotone, ripple-free solution at time $t = t^{n+1}$ of the low-order scheme. c_a is a scalar varying between 0 and 1, calculated on a local basis in such a way that no new over/undershoots are created. FEM-FCT has been widely used in CFD [6,7]. However, there exist important differences between the Maxwell equations and the Euler or Navier-Stokes equations that govern the motion of fluids:

- The system of PDEs is linear, i.e. due care has to be taken not to damp out physically relevant modes. Most of the commonly used limitors in CFD would do this.
- In the scattering problem, the solution is oscillatory. This implies that one has to avoid clipping limitors.
- Except at material interfaces, the solution is C^0 continuous, i.e. does not contain sharp, shock-like discontinuities.

As high-order scheme, we employ a two-step Taylor-Galerkin method, whereas a lumped-mass Taylor-Galerkin scheme with diffusion is used as low-order scheme.
Further details can be found in references [6] and [7].

2. b. Material Interfaces

Let us consider the particular case of a TE wave in two dimensions (unknowns E_x, E_y, and H_z). On a material interface, the regular unknown $\mathbf{E}$ is not uniquely defined. We compute on these particular points the unknowns D_n and E_t instead, and use them in the elements surrounding the interface when necessary.

Besides, the basic equations have to be written in a slightly different way for the first and second half timestep in order to handle the discontinuity:

first half step : second half step :

$$\begin{cases} E_{x,t} = \dfrac{1}{\varepsilon} H_{z,y} \\ E_{y,t} = -\dfrac{1}{\varepsilon} H_{z,x} \\ H_{z,t} = \dfrac{1}{\mu} (E_{x,y} - E_{y,x}) \end{cases} \qquad \begin{cases} \varepsilon\, E_{x,t} = H_{z,y} \\ \varepsilon\, E_{y,t} = -H_{z,x} \\ \mu\, H_{z,t} = E_{x,y} - E_{y,x} \end{cases} \tag{5}$$

2. c. Limitor Options

In the elements surrounding the material interfaces, the low-order scheme is employed. This is the region where discontinuities occur. In addition, the updating of the 'regular' unknowns has to match that of the unknowns D_n and E_t.

Away from this critical region, the fields are generally smooth, as opposed to what happens for compressible flow fields. Therefore, the best solution is achieved with the highest order scheme.

As an illustration, the RCS of a conducting cylinder (TE wave, ka = 5.) is plotted on Figure 1 with various limitor options. When the code has to determine where to use the low- and high-order schemes, it chooses to use the high-order scheme in the whole domain. (The second and fifth curves are identical).

3. Cell-Centered Code : Upwind Scheme

An upwind code, based on approximate Riemann solvers, is also under development. This family of solvers has been used in the CFD area and has proven especially useful when dealing with sharp discontinuities in the fields. It has also been employed successfully for CEM problems, and is meant to be our 'reference code', on which we can base further developments.

We use a cell-centered approximation and a second-order scheme in the framework of a finite volume approach. To this end, we rewrite the weak formulation of (3) in the following form:

$$u^e(t+\Delta t) = u^e(t) - \frac{\Delta t}{|\Omega^e|} \int_{\partial\Omega^e} \mathbf{F}\cdot\mathbf{n}\, d\Gamma + \Delta t\, S^e \tag{6}$$

where Ω^e denotes the element e, $|\Omega^e|$ its volume, $\partial\Omega^e$ its boundary and $\mathbf{n}$ the outer unit normal on this boundary. The fluxes are evaluated by using any first-order upwind formulation. For the time being, we employ fluxes derived from Lax jump conditions on an interface between two adjacent cells ([12], [13]). To achieve second-order accuracy in both time and space, we employ a two step method and a MUSCL variable interpolation, respectively.

With this cell-centered method, there is no need to treat the material interfaces in any particular way. The fluxes account for the jump in the material properties.

4. Numerical Results

4. a. Cylinder

The RCS calculation for infinite circular cylinders is chosen as a test case. In this case, analytical results in the form of Bessel-functions exist [11], so that an accurate comparison is possible. The incident wave employed can be either a single frequency wave or a Gaussian pulse, allowing broadband response with a single transient calculation.

→ Conducting Cylinder

On Figure 2, both codes are compared, and the results show very good agreement with the exact solution.

→ Dielectric Cylinder

The case of a monochromatic wave (ka = 1.) impinging on a cylinder of permittivity 2. surrounded by the vacuum is chosen. Figures 3a and 3b show partial meshes used by the two codes and in particular the paths used for the RCS calculation: for the node-centered FCT code, we come up with a path connecting element sides, whereas an element-centered path is employed in order to process the results of the upwind code. The results of both codes are plotted on Figure 3c.

4. b. Airfoil

The RCS for a perfectly conducting airfoil has also been computed. This 'real-life' example shows in particular that a good accuracy can be obtained even with a rather coarse mesh: the mesh nr. 1 plotted on Figure 4a has only 10 points per wavelength in the areas close to the conducting boundary, and the results obtained with the further refined meshes (nr. 2

and 3) are not very different (Figure 4b). Thus, a good approximation of the RCS diagram can be obtained in less than 5 mn on a Cray YMP computer.

Conclusions and Outlook

Two Finite Element Solvers for the solution to Maxwell equations in the time domain have been presented. They allow the simulation of arbitrary geometries in 2-D and 3-D for multimaterial problems. By analyzing the response to a pulse, the RCS profile for a whole range of frequencies may be obtained in a single run. We have found this a very economical way to identify narrow regions of the spectrum where resonances may be present. The h-refinement capabilities of the FCT code allow optimal CPU requirements, since a fine grid is used only where necessary.

Work is currently in progress to extend the present capabilities to include more various material properties and 3-D problems. We are also working on advanced data-structures to minimize both CPU times and indirect addressing for these unstructured-grid solvers.

Acknowledgements

We would like to acknowledge the many insightful discussions that we had with Drs. John Ambrosiano and Scott Brandon from Lawrence Livermore National Laboratory. They led to many of the developments reported here.

The first author was partially supported by SAIC during part of this work, with Dr. Joseph Baum as the technical monitor. He is working at the George Washington University under the sponsorship of ONERA (Office National d'Études et de Recherches Aérospatiales), Châtillon, FRANCE.

References

[1] Special Issue on Radar Cross Sections of Complex Objects (W.R. Stone ed); *Proc. of the IEEE*, Vol. 77,5 (1989).

[2] Special Issue on Radar Cross Sections of Complex Objects; *IEEE Trans. Antennas and Propagation*, Vol. 37,5 (1989).

[3] Proceedings of the 7th Annual Review in Applied Computational Electromagnetics (Naval Postgraduate School, Monterey, March 18–22, 1991)

[4] A. Taflove, K. R. Umashankar - Review of FD-TD Numerical Modeling of Electromagnetic Wave Scattering and Radar Cross Section. *Proc. of the IEEE*, Vol. 77,5 682–699 (1989).

[5] V. Shankar, W. F. Hall. A. H. Mohammadian - Time-Domain Differential Solver for Electromagnetic Scattering Problems. *Proc. of the IEEE*, Vol. 77,5 709–721 (1989).

[6] R. Löhner, K. Morgan, J. Peraire and M. Vahdati - Finite Element Flux-Corrected Transport (FEM-FCT) for the Euler and Navier-Stokes Equations; *Int. J. Num. Meth. Fluids* 7, 1093–1109 (1987).

[7] R. Löhner, K. Morgan, M. Vahdati, J.P. Boris and D.L. Book - FEM-FCT: Combining Unstructured Grids with High Resolution; *Comm. Appl. Num. Meth.* 4, 717–730 (1988).

[8] R. Löhner, K. Morgan, J. Peraire and O.C. Zienkiewicz - Finite Element Methods for High Speed Flows; AIAA-85-1531-CP (1985).

[9] O. C. Zienkiewicz, K. Morgan - *Finite Elements and Approximation*, John Wiley & Sons (1983).

[10] R. Löhner and J. Ambrosiano - A Finite Element Solver for the Maxwell Equations; Paper presented at the GAMNI-SMAI Conf. on Numerical Methods for the Solution of Maxwell Equations, Paris, December 1989.

[11] J.D. Jackson - *Classical Electrodynamics*; John Wiley & Sons (1975).

[12] P. Lax - *Hyperbolic Systems of Conservation Laws and the Mathematical Theory of Shock Waves*, SIAM, Philadelphia, 1973.

[13] V. Shankar, W. Hall, A.H. Mohammadian - *A CFD-based Finite-Volume Procedure for CEM – Interdisciplinarity Applications of CFD Methods*, in AIAA 9th CFD Conference, 1989.

Results

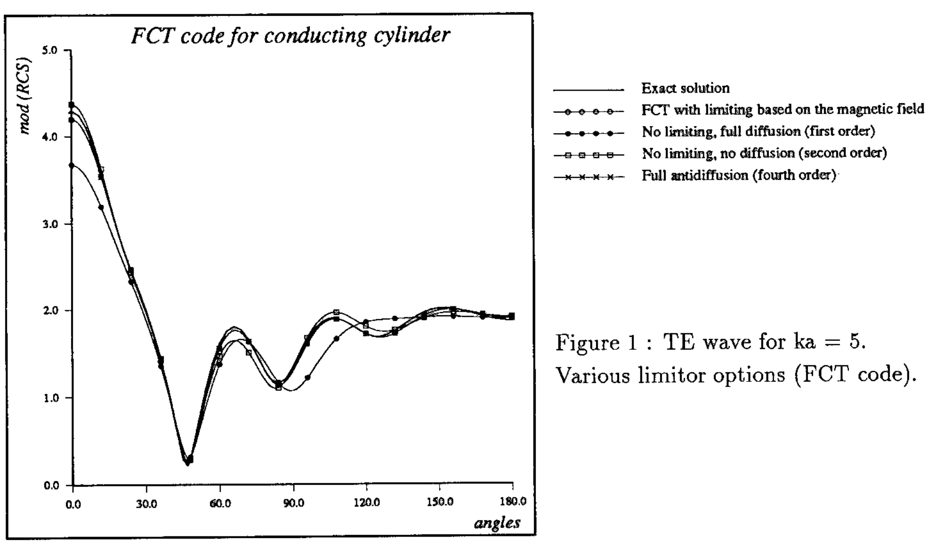

Figure 1 : TE wave for ka = 5. Various limitor options (FCT code).

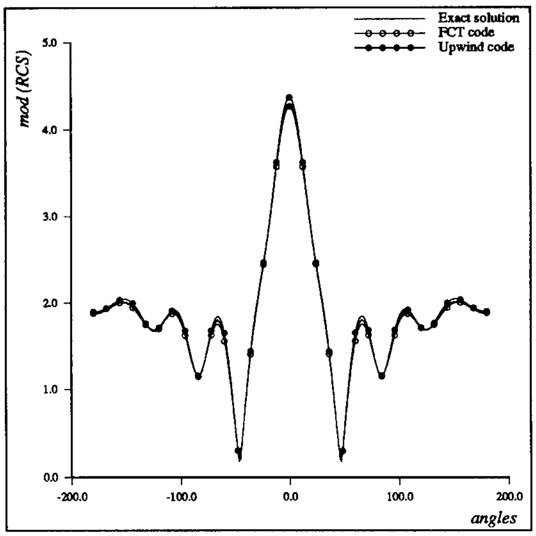

Figure 2 : TE wave on conducting cylinder (ka = 5.)

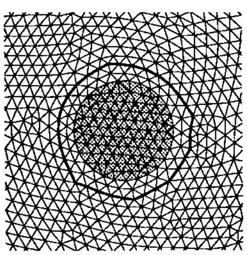

Figure 3a : node-centered path

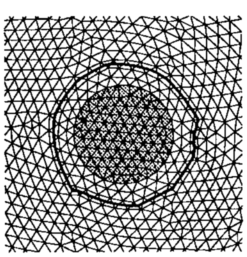

Figure 3b : element-centered path

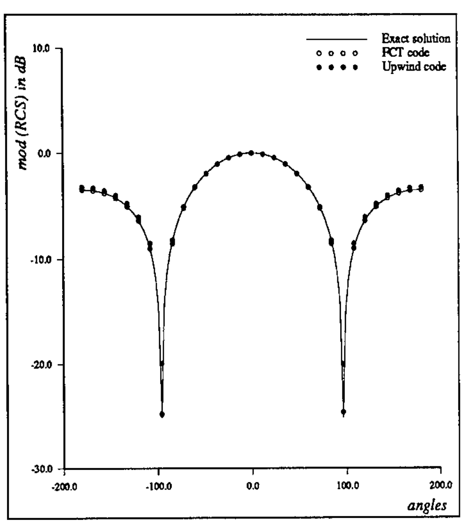

Figure 3c : RCS for ka = 1., $\varepsilon = 2$.

Dielectric cylinder

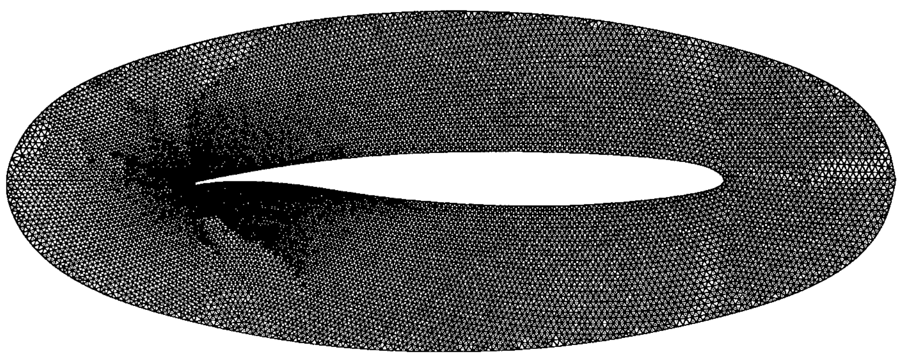

Figure 4a : Mesh nr. 1 (coarsest one) for the conducting airfoil.

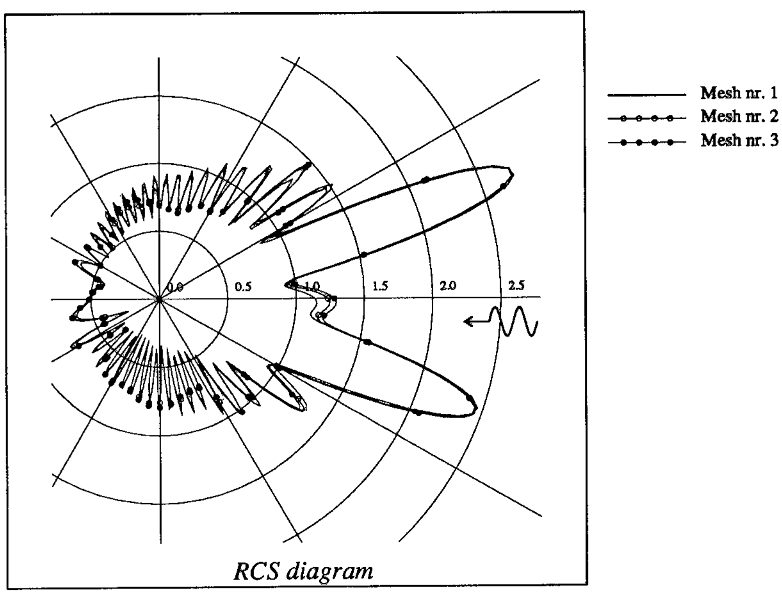

Figure 4b : RCS on airfoil (FCT code).
TE wave, $\lambda = 0.03$ m = L/10, normal incidence.

RCS of Cubes, Strips, Rods and Cylinders by FDTD

by

C.W. Trueman	R.J. Luebbers	S.R. Mishra
S.J. Kubina	K.S. Kunz	C. Larose
Concordia University,	The Pennsylvania	David Florida Laboratory,
Montreal, Quebec,	State University,	Canadian Space Agency,
Canada	University Park,	Ottawa, Ontario,
	Pennsylvania	Canada.

Abstract-This paper compares the radar cross-section(RCS) of perfectly-conducting targets calculated by the FDTD method with measured data. For a cube, excellent agreement is obtained over a 30 to 1 frequency range. The rod, strip and cylinder scatterers are used to explore the limitations of the FDTD model. It is demonstrated that the high-frequency scattered field is quite sensitive to the thickness of the free-space layer separating the scatterer surfaces from the Mur absorbing boundary. The measured RCS of the strip and cylinder, available to lengths of 4λ, agrees excellently with the FDTD computation. The measured data for the rod extends up to a length of 10λ, and agrees very well with the FDTD RCS.

Introduction

The "finite-difference time-domain" method solves Maxwell's Equations in the time domain[1], by replacing the partial derivatives with central-difference formulas, thus introducing a time step Δt, and introducing the sub-division of space into cells of size Δx by Δy by Δz. A finite volume of space consisting of N_x, N_y, N_z cells must contain both the scattering object and a sufficiently thick layer of free-space or "whitespace" separating the boundaries of the object on all sides from boundaries of the cell space. The total field is split into the incident field plus the scattered field[2]. The incident field is a plane wave of the Gaussian pulse waveshape shown in Fig. 1 and is analytically specified at each point at each time step, as if it were propagating in free space. The scattered field is computed by the Yee algorithm: E at the center of each cell face is determined from its previous value and from H on the edges of the face; time is stepped forward, then H on each edge is found from its previous value and E at the cell face centers; time is stepped, E found from H; time is stepped, H found from E; and the computation proceeds in leapfrog fashion.

As time is stepped forward, the plane wave induces conduction and polarization currents in the scattering object, which in turn produce both "near fields" and "far fields" in the whitespace between the scattering object and the outer boundary. The near fields store energy in the whitespace, whereas the far fields carry energy away into the far field. The outer boundary of the cell space is designed to absorb any energy incident upon it, by imposing the Mur second-order boundary condition on the electric field[3]. Since the scattered field is computed directly, there is no need to divide the FDTD cell space into scattered field and total field regions.

The Yee algorithm determines the vector field components in each cell at each time step. To find the far-zone scattered field, the near-zone to far-zone transformation of Ref. [4] is used. A convenient closed "integration surface" is selected, usually 4 cells from the absorbing boundary. Knowledge of the fields on the integration surface at each time step allows the computation of the electric and magnetic surface-current "equivalent sources" on the surface at each time step, and then, by integration, the far-zone scattered field at each time step. To compute the frequency-domain radar cross-section(RCS), the Fourier Transform of the time domain far zone electric field is computed and divided by the Fourier transform of the incident pulsed plane wave at each frequency. This is considerably more efficient than making a separate computation for each frequency of interest, especially when broadband results such as presented in this paper are required. Ref. [4] demonstrates excellent agreement between the RCS computed by FDTD in this way with moment-method computations for a square-plate scatterer. This paper compares FDTD RCS calculations with the measured RCS of a cube, a rod, a strip, and a cylinder.

This paper presents an impartial test of the FDTD method because the code development, the measurements, and the actual computations and comparisons were done by different people at different institutions. The code was developed by R.J. Luebbers and K.S. Kunz[4]. The measurements were done by S.R. Mishra and C. Larose in a cooperative effort with C.W. Trueman and S.J. Kubina aimed at obtaining excellent agreement with moment-method computations for simple targets smaller than 4λ[5,6]. The FDTD method allowed comparisons with measurements for targets as large as 20λ. Thus the FDTD validation presented in this paper is perhaps a more impartial test of FDTD performance than results obtained in situations where the same research group is developing an FDTD code, making the measurements and providing the comparisons.

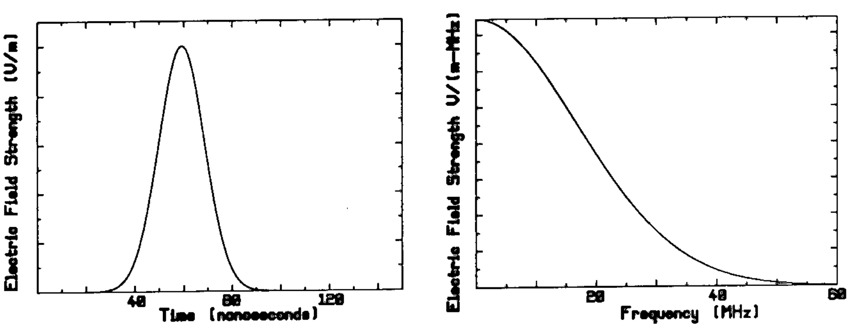

Fig. 1 The Gaussian pulse excitation and its spectrum, for cells of size 0.5 m.

FDTD Parameters

This paper examines FDTD modelling from the user's vantage point. The user must choose the cell size, Δx, Δy, and Δz, and the thickness of the whitespace, N_w cells. The size of the scattering object and the thickness of the whitespace determine the required extent of the FDTD cell space, N_x by N_y by N_z cells. Finally the user must choose a time-step Δt, and the total number of time-steps N_t for which the calculation will be done. These choices are fundamentally determined by the frequency range over which the RCS is required, as discussed in the following.

For stability of the Yee FDTD algorithm, the time step must be less than or equal to[7]

$$\Delta t_{max} = \frac{1}{c\sqrt{(1/\Delta x)^2 + (1/\Delta y)^2 + (1/\Delta z)^2}}$$

Though Ref. [4] demonstrates good agreement between FDTD and a moment method calculation with the maximum allowable time step, the time step in this paper will be set to $\Delta t = (\sqrt{3}/2)\Delta t_{max} = 0.866\Delta t_{max}$ for an "ample safety margin"[7]. The velocity of propagation of waves in the FDTD cell space depends upon the direction of propagation through the grid. Waves travelling parallel to the grid axes propagate faster than waves travelling diagonally. With time step $\Delta t = (\sqrt{3}/2)\Delta t_{max}$, the error in the speed of propagation is 0.31% for $\lambda/20$ cell size; 1.3% for $\lambda/10$ cells; and 5.7% for $\lambda/5$ cells[7]. The frequency range of the calculation is usually limited to cells smaller than $\lambda/10$ to keep the propagation velocity error within acceptable bounds. Indeed, cells smaller than $\lambda/20$ are often used[7].

The total number of time steps is estimated in terms of the number of end-to-end trips along the scatterer. In RCS computations using the FDTD algorithm with a sinusoidal time dependence of the plane wave, Ref. [7] allows sufficient time for two "front-to-back-to-front" interactions hence four end-to-end trips, for low-Q scatterers.

The wave shape of the plane wave excitation is designed to limit the spectrum to frequencies where the cells are smaller than $\lambda/10$. A Gaussian pulse is used here, given by

$$f(t) \quad = \quad A\,e^{-\alpha(t - d/c - \beta\Delta t)^2}$$

where, for PEC targets in free space, and for PEC targets in free-space, $\beta = 64$ is a time delay such that the pulse starts at $A\,e^{-16}$ at $t = 0, d = 0$, d/c is the time-delay as the pulse travels to the FDTD cell, $\alpha = 1/(16\Delta t)^2$ is chosen to limit the frequency bandwidth to frequencies where the cell size Δx is less than $\lambda/10$. Fig. 1(a) shows the Gaussian pulse for cells of size $\Delta x = 0.5$ m, with $\Delta t = (\sqrt{3}/2)\Delta t_{max} = 0.833$ ns, hence $\alpha = (75)^2\,(\mathrm{MHz})^2$. Fig. 1(b) shows that the spectrum of the pulse is limited to frequencies less than about $0.8\sqrt{\alpha} = 60$ MHz, at which frequency the 0.5 m cell size is $\lambda/10$.

The required thickness of the whitespace is a thorny problem. Ref. [5] uses 8 to 12 cells of free space between the scattering object's boundaries and the absorbing boundary. The plane wave induces surface current flow on the scatterer, with its associated "near" field in the white-space cells between the scatterer surface and the absorbing boundary. If the whitespace is too thin, then the near-field "runs into" the absorbing boundary, which may absorb some of its energy, and the imperfect absorbing boundary may reflect some near-zone energy back to re-illuminate the target. Certainly the near field would not be realistically represented, and poor results would be expected. This paper explores the effect of making the whitespace too thin.

The computation time for the FDTD calculation is directly proportional to the total number of time steps, and to the total number of cells that must be updated at each time step. Hence there is a desire to keep the whitespace thin. The following establishes agreement with measurements for the cube, then explores the consequences of a thin whitespace for the rod, strip and cylinder scatterers.

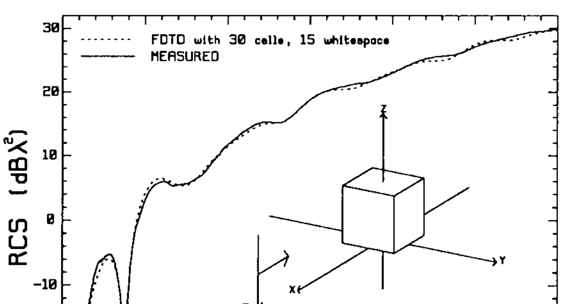

Fig. 2 The measured and computed RCS of a PEC cube.

Cube RCS

Fig. 2 compares the measured and computed RCS of a perfectly-conducting(PEC) cube with the plane wave incident normal to the face of the cube, and the electric field parallel to an edge. The scattered field was measured in a 6 m cubical anechoic chamber. For 6.35 cm targets, the target was mounted on a styrofoam support column 1.2 m from a pair of horn antennas, which measure the scattered field with a bistatic angle of about 8.2 degrees. Longer targets were measured at a range of 4.7 m. An HP8510 or a Wiltron 360 network analyzer is used to determine the scattered field

amplitude and phase at 801 frequencies from 2 to 18 GHz. Time-gating is used with a gate width of 7.5 nanoseconds to remove the direct coupling between the horn antennas, and also residual reflections arriving from the walls and floor after the response of the target has subsided. The scattered field of the target is measured as the difference at each frequency between the response of the target, column and chamber and the response of the column and chamber alone. The scattered field of a reference sphere is measured in the same way. Then the exact Mie series for the backscattered field of the sphere[8], evaluated with the 8.2 degree bistatic angle, is used to find a calibration factor for the system at each frequency. The measured cube curve in Fig. 2 is a composite of measured curves on four different sizes of cubes, and was verified against other measurements of cube RCS[9] and against a wire-grid model calculation for cube size less than 1.5λ[5].

To model the cube with FDTD, its side length was arbitrarily set to $a = 15$ m. The cell size Δx was chosen such that $\Delta x = \lambda/10$ at cube size $a/\lambda = 3$, hence $\Delta x = a/30$, for a 30x30x30 cell model. The whitespace thickness was set to $w = \lambda/20$ at the lowest frequency of the measured data, $a/\lambda = 0.1$, hence $w = 15\Delta x$. The number of time steps was set at 2048, allowing 34 trips along a cube edge, or about 8 trips around the periphery of the cube. Plotting the scattered field as a function of time shows that there is little response after the time required for about 4 peripheral trips. Fig. 2 shows excellent agreement between the RCS computed with this FDTD model and our measurement, over a 30 to 1 frequency range.

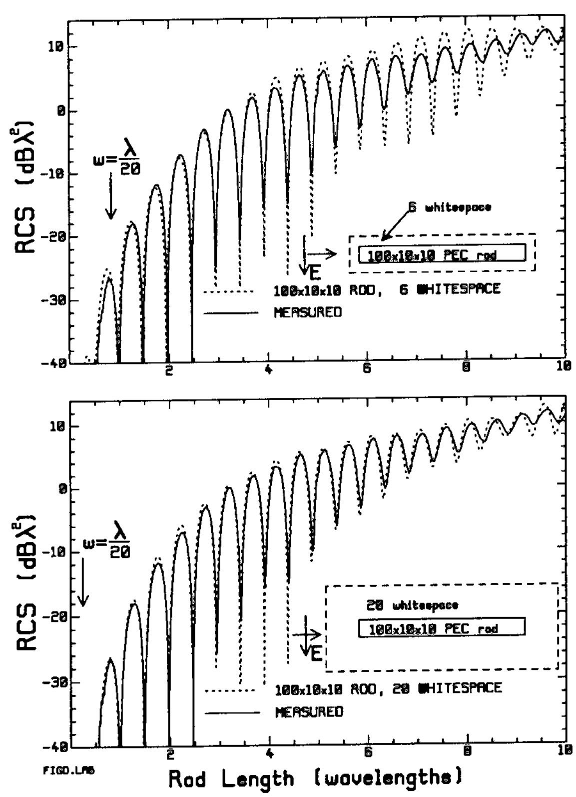

Fig. 3 The measured and computed RCS of a PEC rod, using 100 cells for the rod length.

Rod RCS

The PEC rod target has a square cross-section, and its length is ten times its cross-sectional side length. The rod is illuminated by the plane wave "end-on", with the plane wave travelling along the length of the rod, and the electric field parallel to one side of the cross-section. The measured RCS in Fig. 3 is in excellent agreement with a moment-method wire-grid calculation shown in Ref. [6] up to the limiting frequency of the wire-grid, at $L/\lambda = 4$. The FDTD model of the rod uses 100 cells along its length, and 10x10 cells for the cross-section, making the cell size $\lambda/10$ at $L/\lambda = 10$, where L is the rod length. Fig. 3(a) shows the rod RCS computed with a

whitespace of only 6 cells. It is remarkable that the computed RCS agrees as well as it does with the measurement between $L/\lambda = 1$ and 4. Below $L/\lambda = 1$, the peak in the computation is larger than that in the measurement, and the whitespace is thinner than $\lambda/20$. Above $L/\lambda = 4$, the peaks are generally too large and the minima too deep in the computation compared to the measurement, and the agreement is poor. When the whitespace is increased to a generous 20 cells, the agreement is enormously improved over the whole frequency range. At low frequencies, the whitespace is thicker than $\lambda/20$, and the peak near $L/\lambda = 0.75$ aligns nicely with the measurement. Above $L/\lambda = 1$, the computed peaks are 1 or 2 dB too large and the minima too deep, but the agreement is generally quite good up to $L/\lambda \approx 7.5$. For longer rods the location of the peaks and minima in the computation become shifted compared to those in the measurement, as the cell size approaches $\lambda/10$.

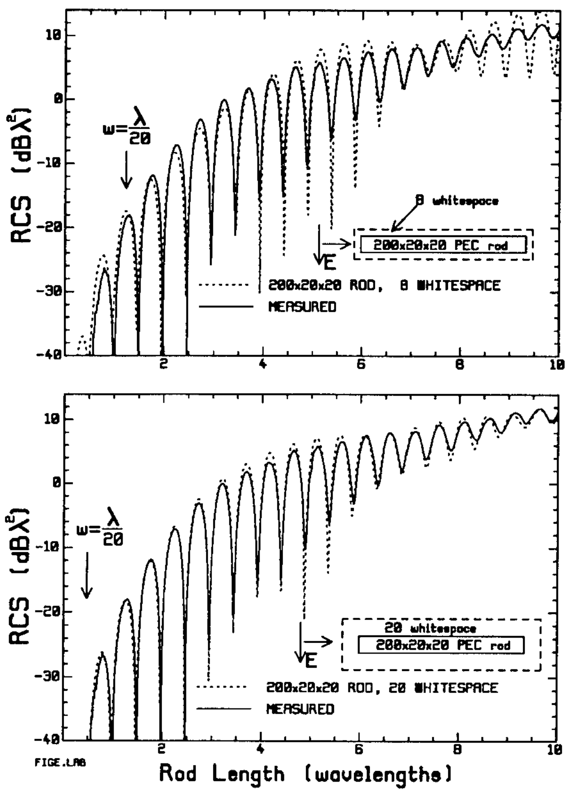

Fig. 4 The RCS of the PEC rod using 200 cells for the rod length.

Fig. 4 compares the measurement with an FDTD computation using 200 cells for the length of the rod, and 20x20 cells for the cross-section, and seeks to improve the agreement at the high end of the frequency range. Fig. 4(a) uses a thin whitespace of only 8 cells. The RCS is poor at the low frequency end where the whitespace is thinner than $\lambda/20$. Near L/λ=5 and again near L/λ=9 the computed peaks are too large. When the whitespace is increased to 20 cells, the agreement is again greatly improved, with quite good agreement across the whole frequency range. Now the cells are only $\lambda/20$ in size for rods 10λ in length. Note that the peaks near L/λ=4 agree less well than we would like. The 20 cell whitespace in Fig. 4(b) is physically only half as thick as that in Fig. 3(b).

The far-zone scattered field of the rod as a function of time was examined to determine whether the number of time steps was adequate. The 100 cell model with 2048 time-steps allows about 10 end-to-end trips. The time response shows an initial return from the front end, then after a delay of two end-to-end trip times, a large return from back end, then after a further two trip time delay a small third return. Time for five end-to-end trips would have been adequate. The 200 cell rod, with 2048 steps allows time for 5 end-to-end trips, just sufficient to pick up the third return. The 200 cell calculation was extended to 4096 steps, but no fourth return was found.

Figs. 3 and 4 show that, for the rod scatterer, if the whitespace is too thin then the high frequency behavior of the RCS and the scattered field is poorly predicted.

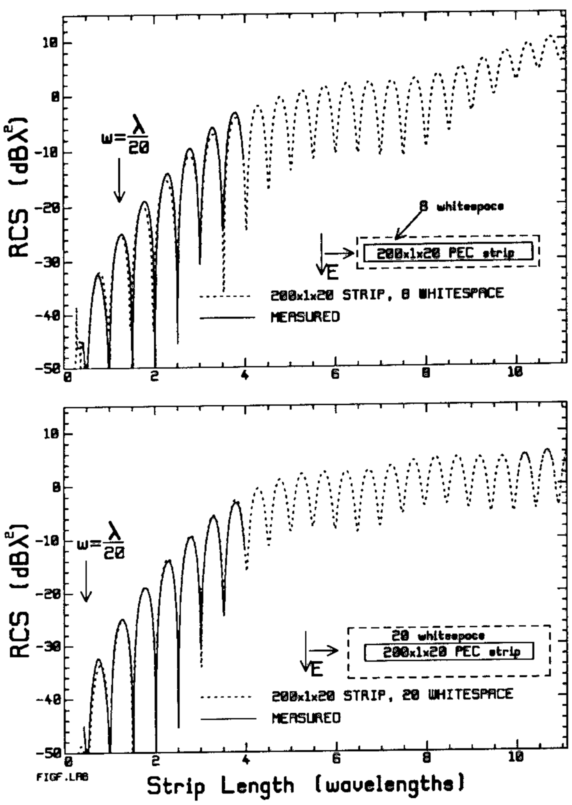

Fig. 5 The measured and computed RCS of a PEC strip, using 200 cells for the strip length.

Strip RCS

The strip target has its length equal to ten times its height, and the thickness of the strip equal to about 2/41 of the height. The RCS was measured for end-on incidence of the plane wave, with the electric field parallel to the height dimension, and the measurement agrees excellently with a wire-grid model calculation[6]. The measurement has not as yet been completed for strips longer than $L/\lambda = 4$. To model the strip by FDTD, 200 cells were used along the length, 20 for the height and one for the thickness, making the thickness 2/40 of the height. The precise thickness could be modelled by making the Δy cell dimension different from Δx or Δz, but this was not done. The strip RCS was computed with a whitespace thickness of 8 cells, Fig. 5(a), and of 20 cells, Fig. 5(b). The low frequency RCS for the strip is not sensitive to the whitespace thickness, showing equally good agreement with the measurement in both cases. With the thicker whitespace, the peaks in the size range from $L/\lambda \approx 1.25$ up to $L/\lambda \approx 4.25$ are in better agreement with the measurement than those computed with the thinner whitespace. Fig. 5 shows the high frequency scattered field changes with increased whitespace thickness. Thus for $L/\lambda > 8$, with 8 cells of whitespace the curve shows a strong upward trend, whereas with the 20 cell whitespace the level of the peaks is fairly constant.

The time dependence of the strip backscattered field was examined to see if enough time steps were used. The strip shows an initial return, then two end-to-end trip times later, a second return. No third return was seen, even when 4096 time steps were used for the 200 cell strip, enough time for 10 end-to-end trips. These observations are consistent with the time domain impulse response measured using the network analyzer.

Cylinder RCS

Fig. 6 compares the measured and computed RCS of a PEC circular cylinder of length 10 times its diameter, for end-on incidence of the plane wave. The FDTD cylinder model uses 110 cells for the length of the cylinder, and "builds" the cylinder out of blocks 3x1, 7x1, 9x2, 11x3, 9x2, 7x1 and 3x1 cells in size. Fig. 6(a) shows that with 8 cells of whitespace, the peak at 0.75λ is too large, whereas with 22 cells of whitespace, this peak agrees nicely with the computation.

The agreement between $L/\lambda = 1$ and $L/\lambda = 4$ with 8 cells of whitespace is quite good, and surprisingly is poorer with the thicker whitespace. Comparing parts (a) and (b) of Fig. 6 between $L/\lambda = 5$ and 8 shows higher peaks and deeper minima with 8 cells of whitespace than with 22 cells.

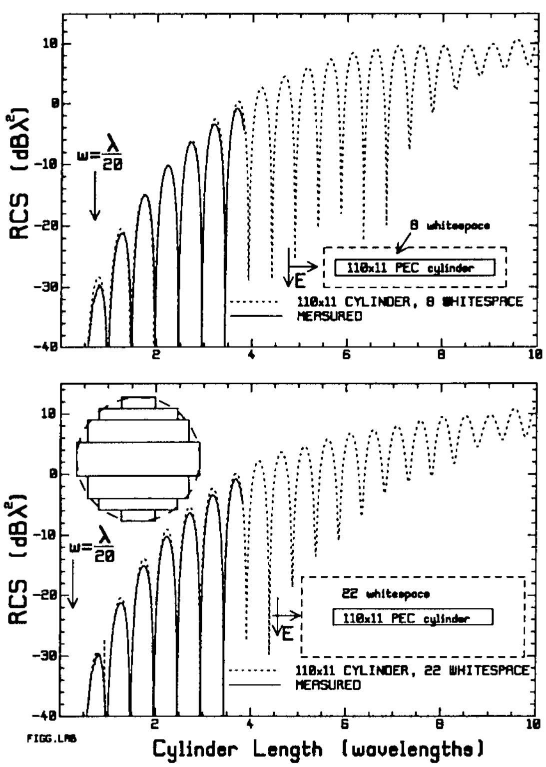

Fig. 6 The RCS of the PEC cylinder using 110 cells for the length.

Conclusions

This paper has shown excellent agreement between the measured RCS and that computed by FDTD for a cube scatterer over a 30 to 1 frequency range, and a rod scatterer over a $10/0.6 \approx 17$ to 1 frequency interval. Excellent agreement for a strip and a cylinder has been shown over the $4/0.6 \approx 7$ to 1 frequency range for which measured data are available.

This paper has explored the effect of the thickness of the free-space layer or "whitespace" separating the scattering object from the absorbing boundary. It has been demonstrated that the high-frequency RCS computed by FDTD is compromised by a too-thin whitespace layer. Good agreement with the measured RCS for the cube was found as the cell size approaches $\lambda/10$ with a whitespace of 15 cells. Poor agreement was found for the 100 cell rod as the cell size approaches $\lambda/10$ for 6 cells of whitespace, but good agreement was found for 20 cells of whitespace. Poor agreement was found for the 200 cell rod as the cell size approaches $\lambda/20$ for 8 cells of whitespace, and good agreement for 20 cells of whitespace. A whitespace 20 cells thick is two wavelengths in thickness at the top end of the bandwidth of the FDTD model, where the cell size is $\lambda/10$.

The rod and cylinder results, Figs. 3, 4 and 6, suggest that a minimum whitespace of $\lambda/20$ is required at the lowest frequency for which the RCS is to be relied upon. However, the strip RCS of Fig. 5 is not sensitive to whitespace thickness at the low frequency end.

Figs. 3 to 7 show that if the whitespace is too thin then the high frequency RCS is poorly predicted. The graphs presented here suggest that 20 cells of whitespace is "safe", but this may be too conservative a choice, leading to excessive computation time. Thus for the cube of Fig. 2, 15 cells is enough. Ref. [7] recommends 8 to 12 cells-but Figs. 4 to 6 show that 8 cells is not enough for the rod, strip and cylinder scatterers. The 100 cell rod computation was repeated with 10 and 12 cells of whitespace, showing that 10 cells is not adequate, but that the RCS with 12 cells is little different from the RCS with 20 cells of whitespace. The 200 cell rod calculation was repeated with 12 and 16 cells of whitespace. With 12 cells, the large deviation from the

measurement above $L/\lambda = 8$ in Fig. 4(a) is corrected, but there are large differences between the measurement and the computation between $L/\lambda = 4$ and 8, and so 12 cells is clearly insufficient. With 16 cells of whitespace, the agreement between $L/\lambda = 4$ and 8 is considerably improved, but the peaks are still too large. Fig. 4(b) shows that with 20 cells of whitespace, the agreement above $L/\lambda = 6$ is good, but there is room for improvement between $L/\lambda = 4$ and 6. One is tempted to "run" the FDTD code with 24 or 28 cells of whitespace.

The results presented in this paper are all for end-on incidence. Equally good agreement with measurements has been obtained for broadside incidence. For oblique incidence, the optimum whitespace size might be different. The computation time required for an FDTD "run" is heavily dependent upon the whitespace size: for a 200x20x20 cell rod with 20 cells of whitespace, less than 10% of the cells model the rod itself. Thus with an improved absorbing boundary condition, it may be possible to substantially reduce running times.

The cube and rod models presented here are "conformal" in the sense that they are precisely represented by the cubical cells of Yee's method. Thus if a "conformal" FDTD code were available such as that proposed in [10], no change in the results would be expected. The cylinder result might be improved with a conformal code.

The FDTD computation of the RCS for the targets presented here has been shown to agree very well with measurements over a wide frequency range, and is a promising method for evaluating the RCS of targets too large for moment-method analysis on modest workstation computers.

Acknowledgement

The measurements were supported by the Defence Research Establishment, Ottawa as a Research Task at DFL, with Dr. Tim Coyne as Scientific Authority. The computations were supported by the National Sciences and Engineering Research Council of Canada.

References

1. K.S. Yee, "Numerical Solution of Initial Boundary Value Problems Involving Maxwell's Equations in Isotropic Media", IEEE Trans. on Antennas and Propagation, Vol. AP-14, No. 3, pp. 302-307, May, 1966.
2. R. Holland, L. Simpson and K.S. Kunz, "Finite-Difference Analysis of EMP Coupling to Lossy Dielectric Structures", IEEE Trans. on Electromagnetic Compatibility, Vol. EMC-22, No. 3, pp. 203-209, August, 1980.
3. G. Mur, "Absorbing Boundary Condition for the Finite-Difference Approximation of the Time-Domain Electromagnetic Field Equations", IEEE Trans. on Electromagnetic Compatibility, Vol. EMC-23, No. 4, pp. 377-382, November 1981.
4. R.J. Luebbers, K.S. Kunz, M. Schneider and F. Hunsberger, "A Finite-Difference Time-Domain Near Zone to Far Zone Transformation", IEEE Trans. on Antennas and Propagation, Vol. 39, No. 4, pp. 429-434, April, 1991.
5. S.R. Mishra, C. Larose, and C.W. Trueman, "Radar Cross-Section Measurements for Computer Code Validation", Antenna Measurement Techniques Association 1991 Symposium Digest, Boulder, Colorado, Oct. 7-11, 1991.
6. C.W. Trueman, S.J. Kubina, S.R. Mishra and C. Larose, "RCS of Four Fuselage-Like Scatterers at HF Frequencies," to be published in the IEEE Trans. on Antennas and Propagation.
7. A. Taflove and K.A. Umashankar, "The Finite-Difference Time-Domain Method for Numerical Modeling of Electromagnetic Wave Interactions", Electromagnetics, Vol. 10., Nos. 1-2, January-June, 1991.
8. C.A. Balanis, "Advanced Engineering Electromagnetics", Wiley, New York, 1989.
9. M.C. Cote, M.B. Woodworth and A.D. Yaghjian, "Scattering from the Perfectly Conducting Cube", IEEE Trans. on Antennas and Propagation, Vol. 36, No. 9, pp. 1321-1329, Sept., 1988.
10. R. Holland, V.P. Cable, and L.C. Wilson, "Finite-Volume Time-Domain(FVTD) Techniques for EM Scattering", IEEE Trans. on Electromagnetic Compatibility, Vol. 33, No. 4, pp. 281-294, Nov., 1991.

THE ANALYSIS OF PULSE PROPAGATION IN LINEAR DISPERSIVE MEDIA WITH ABSORPTION BY THE FINITE-DIFFERENCE TIME-DOMAIN METHOD

Fred J. German and Griffin K. Gothard
Department of Electrical Engineering
Auburn University, AL 36830
(205) 844-1864

ABSTRACT

The finite-difference time-domain (FDTD) method is used to solve the Maxwell equations in media which exhibit frequency dependant complex permittivity using two conceptually different approaches. The first approach uses a convolution integral to relate the electric field (**E**) to the electric flux density (**D**) while the second approach relates the two via an ordinary differential equation. It has been observed that the differential equation method is the more accurate technique. Several examples illustrating pulse propagation in both Debye and Lorentz dispersive media are presented and the results obtained with the FDTD method are in good agreement with other available data. While the present work addresses only the one dimensional problem of a dispersive half-space, the method itself is applicable to general two and three dimensional problems as well.

INTRODUCTION

The calculation of electromagnetic pulse propagation in dispersive media is of fundamental importance when investigating the effects of radiation on biological tissue. The existence of field precursors can lead to unexpected field levels in the material. The classic works of Sommerfeld [1] and Brillioun [2] address the problem using asymptotic

analyses. More recently Oughstun and Sherman [3] have made improvements on the original asymptotic analyses of Sommerfeld and Brillioun. Albanese, Penn and Medina [4] and Durney, Moten and Stockham [5] have applied a Fourier series analysis to investigate the formation of transients in media exhibiting Debye dispersion. In [6] Wyns, Foty and Oughstun used a Laplace transform analysis to calculate the Sommerfeld precursor. In all of these analyses the problems investigated have been one dimensional in nature. Due to the techniques used, the extension of these methods to the analysis of arbitrary three dimensional structures is not an easy task.

More recently techniques have been proposed to analyze dispersive media in the time domain via direct discretization of the Maxwell equations. The well known finite-difference time-domain (FDTD) method developed by Yee [7] has been modified to account for dispersive media in the time domain [8,9]. The advantage of applying the FDTD method to this class of problems lies in its ability to handle complex three dimensional geometries.

The purpose of the research being reported here has been to investigate the accuracy of using the FDTD method to model pulse propagation in linear dispersive media. Two different approaches to the problem have been investigated and the accuracy of each approach assessed. It has been found that accurate results in both Debye and Lorentz dispersive media can be obtained with the FDTD method.

In this paper the formulation of the FDTD method in dispersive media is briefly outlined and the results for pulse propagation in a dispersive half-space are presented. The data obtained with the FDTD

method is found to be in good agreement with data obtained from other techniques.

While the present work addresses only the problem of one dimensional wave propagation, the FDTD method is a general three dimensional technique. The next logical step of this research is, of course, the development of two and three dimensional FDTD models for dispersive media.

FORMULATION

Two different approaches have been investigated. The first was developed by Leubbers et. al. [8] and uses a convolution integral to relate **E** to **D**. In [8], only a Debye material was investigated. Extension of this convolution integral technique to Lorentz media has been met with some difficulties. The second technique which was developed by Joseph, Hagness and Taflove [9] relates **E** to **D** using an ordinary differential equation. The latter approach has been applied to both Debye and Lorentz media and in the Debye case has been found to be more accurate than the convolution integral approach.

In this section the formulation of the two approaches is briefly discussed and the pertinent time-stepping relations are presented.

Convolution Integral Technique: We wish to find solutions to the Maxwell curl equations

$$\nabla \times \mathbf{E} = \frac{\partial \mathbf{D}}{\partial t} \tag{1a}$$

$$\nabla \times \mathbf{H} = -\frac{\partial \mathbf{B}}{\partial t} \tag{1b}$$

If we assume that there exists only a y-directed component of electric

field (E_y) and a z-directed component of magnetic field (H_z), and assuming field variation only in the x-direction, then (1) becomes

$$\frac{\partial H_z}{\partial x} = -\frac{\partial D_y}{\partial t} \tag{2a}$$

$$\frac{\partial E_y}{\partial x} = -\frac{\partial B_z}{\partial t} \tag{2b}$$

We further assume that the media of interest is non-magnetic (i.e., μ_r = 1.0) so that

$$B_z = \mu_o H_z \tag{3}$$

The relation between **D** and **E** is given in the time domain by

$$D_y(t) = \varepsilon_\infty E_y + \varepsilon_o \int_0^t \chi(\tau) E_y(t-\tau)\, d\tau \tag{4}$$

where

ε_o = permittivity of free space

ε_∞ = infinite frequency permittivity

$\chi(\tau)$ = time domain susceptibility function

using central difference approximations for the derivatives in (2), and with (3), we obtain the following finite-difference equations:

$$\frac{D_y^{n+1}(i) - D_y^{n}(i)}{\Delta t} = -\frac{H_z^{n+1/2}(i+1/2) - H_z^{n+1/2}(i-1/2)}{\Delta x} \tag{5a}$$

$$\frac{H_z^{n+1/2}(i+1/2) - H_z^{n-1/2}(i+1/2)}{\Delta t} = -\frac{E_y^{n}(i+1) - E_y^{n}(i)}{\Delta x} \tag{5b}$$

where the index n is for time and i is for space (see reference 6).

By assuming all field components to be constant over each time step we can approximate (4) as

$$D_y^{n}(i) = \varepsilon_\infty E_y^{n}(i) + \varepsilon_o \sum_{m=0}^{n} E_y^{n-m}(i) \int_{m\Delta t}^{(m+1)\Delta t} \chi(\tau)\, d\tau \tag{6}$$

Using (6) in (5a) and solving for $E_y^{n+1}(i)$ yields a time-stepping relation for the electric field given by

$$E_y^{n+1}(i) = \frac{1}{\varepsilon_\infty + \chi_o}\Big[\varepsilon_\infty E_y^{n}(i) + \sum_{m=1}^{n-1} E_y^{n-m}(i)\Delta\chi_m - \frac{\Delta t}{\varepsilon_o \Delta x}\Big(H_z^{n+1/2}(i+1/2) - H_z^{n+1/2}(i-1/2)\Big)\Big] \tag{7}$$

where

$$\Delta\chi_m = \chi_m - \chi_{m+1}$$

with

$$\chi_m = \int_{m\Delta t}^{(m+1)\Delta t} \chi(\tau)\, d\tau$$

From 5(b) we obtain the following time-stepping relation for H_z:

$$H_z^{n+1/2}(i+1/2) = H_z^{n-1/2}(i+1/2) - \frac{\Delta t}{\mu_o \Delta x}\Big(E_y^{n}(i+1) - E_y^{n}(i)\Big) \tag{8}$$

The FDTD algorithm is thus comprised of the repeated operation of equations (7) and (8).

For a Debye media the frequency domain permittivity is given by

$$\varepsilon(\omega) = \varepsilon_\infty + \frac{\varepsilon_s - \varepsilon_\infty}{1 + j\omega t_o} \tag{9}$$

where

ε_s = DC permittivity

t_o = relaxation time of media

ω = radian frequency

Using the inverse Fourier transform it is easy to show that the time domain susceptibility function is

$$\chi(\tau) = \frac{\varepsilon_s - \varepsilon_\infty}{\varepsilon_o} \; e^{-(\tau/t_o)} u(\tau) \tag{10}$$

where $u(\tau)$ is the unit step function.

For the Debye media the summation term appearing in (7) can be performed recursively. This eliminates the need to store all but one of the previous electric field values at each spatial point. The derivation of the recursion relation is given in detail in [8] and will not be repeated here.

In a Lorentz media the permittivity is given by

$$\varepsilon(\omega) = \varepsilon_\infty - \frac{\omega_o^2 \, (\varepsilon_s - \varepsilon_\infty)}{\omega^2 + 2j\omega\delta - \omega_o^2} \tag{11}$$

where

ω_o = resonant frequency of the media

δ = damping coefficient

Attempts to implement the above FDTD formulation for the Lorentz media have presented problems due to difficulties with the recursive evaluation of the convolution integral.

<u>Differential Equation Technique</u>: The differential equation technique developed by Joseph, Hagness and Taflove [9] relies on being able to obtain an ordinary differential equation that relates **E** to **D**. For both Debye and Lorentz media this relation is relatively simple to derive.

Consider first the Debye media with

$$\varepsilon(\omega) = \frac{D(\omega)}{E(\omega)} = \varepsilon_\infty + \frac{(\varepsilon_s - \varepsilon_\infty)}{1 + j\omega t_o} \tag{12}$$

Cross multiplying and taking the inverse Fourier transform of (12) yields the differential equation

$$D_y + t_o \frac{dD_y}{dt} = \varepsilon_s E_y + t_o \varepsilon_\infty \frac{dE_y}{dt} \tag{13}$$

applying a central difference to (13) we obtain the following which relates E_y at the current time step to D_y at the current and previous time steps and E_y at only previous time steps:

$$E_y^{n+1}(i) = \frac{\Delta t+2\tau}{2\tau\varepsilon_\infty + \varepsilon_s\Delta t} D_y^{n+1}(i) + \frac{\Delta t-2\tau}{2\tau\varepsilon_\infty + \varepsilon_s\Delta t} D_y^{n}(i) + \frac{2\tau\varepsilon_\infty-\varepsilon_s\Delta t}{2\tau\varepsilon_\infty+\varepsilon_s\Delta t} E_y^{n}(i) \tag{14}$$

Thus, the new FDTD algorithm consists of finding the magnetic field from equation (8), calculating the electric flux density using

$$D_y^{n+1}(i) = D_y^{n}(i) - \frac{\Delta t}{\Delta x}\left(H_z^{n+1/2}(i+1/2) - H_z^{n+1/2}(i-1/2)\right) \tag{15}$$

and determining the electric field from (14).

The procedure for the Lorentz media is very similar. Inverse Fourier transforming (11) as before and applying differencing yields

$$\begin{aligned} E_y^{n+1}(i) = \frac{1}{(\varepsilon_s\omega_o^2\Delta t^2+ 4\delta\varepsilon_\infty\Delta t + 2\varepsilon_\infty)} \Big[&(\omega_o^2\Delta t^2 + 4\delta\Delta t + 2)D_y^{n+1}(i) \\ &+ (\omega_o^2\Delta t^2 - 4\delta\Delta t - 4)D_y^{n}(i) + 2D_y^{n-1}(i) \\ &- (\omega_o^2\Delta t^2\varepsilon_s - 4\delta\Delta t\varepsilon_\infty - 4\varepsilon_\infty)E_y^{n}(i)\ 2\varepsilon_\infty E_y^{n-1}(i)\Big] \end{aligned} \tag{16}$$

The algorithm is the same as for the Debye media except that (16) is used in place of (14) for calculating the electric field from the electric flux density at each time and space point.

It should be pointed out that other types of dispersive media can be modeled using this technique provided the inverse Fourier transform of the permittivity function yields an ordinary differential equation relating D and E.

In the next section numerical results will be presented and compared to other available data in order to validate and assess the accuracy of the above dispersive FDTD formulations.

NUMERICAL RESULTS

Here results are presented for pulse propagation in dispersive media as calculated with the FDTD algorithms described above. For the Debye media it has been found that the differential equation approach is more accurate than the convolution integral approach under the same simulation conditions. Results from these algorithms will be compared to each other as well as results from a Fourier series analysis. Results obtained for the Lorentz media are presented and compared to data available in the literature.

Debye Media Results: For a Debye media the frequency dependant permittivity is given by (9). In the following examples the material parameters are the same as those used in [4] for modeling water, namely

$$\varepsilon_s = 78.2\varepsilon_o \qquad \varepsilon_\infty = 5.5\varepsilon_o \qquad t_o = 8.1\text{x}10^{-12} \text{ sec}$$

The geometry is an infinite half-space.

For the first example a Gaussian pulse of width 13.33 ps between -60dB points is taken to be normally incident on the half-space from free space. Using the FDTD algorithms, the complex reflection coefficient at the interface has been calculated by discrete Fourier transforming the reflected electric field and dividing by the spectrum of the incident Gaussian pulse.

The results obtained using the convolution integral approach are shown in Figure 1 along with the theoretical values. Figure 2 shows the

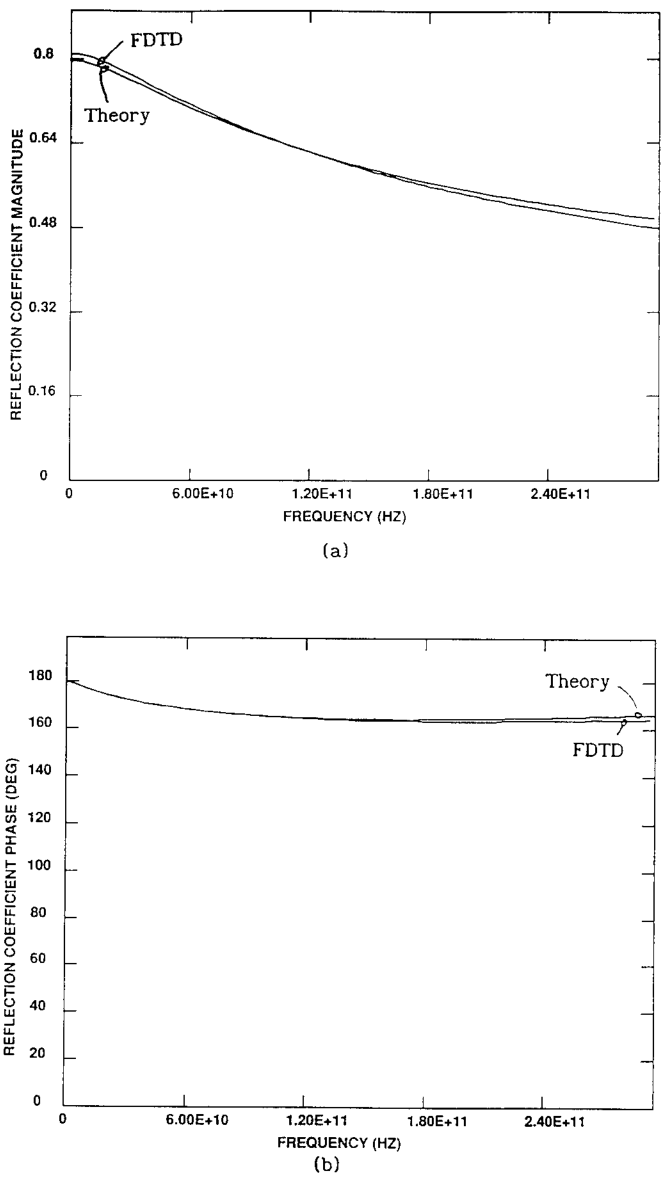

Figure 1. Reflection coefficient of Debye dispersive half-space using the convolution integral FDTD technique. (a) Magnitude and (b) phase.

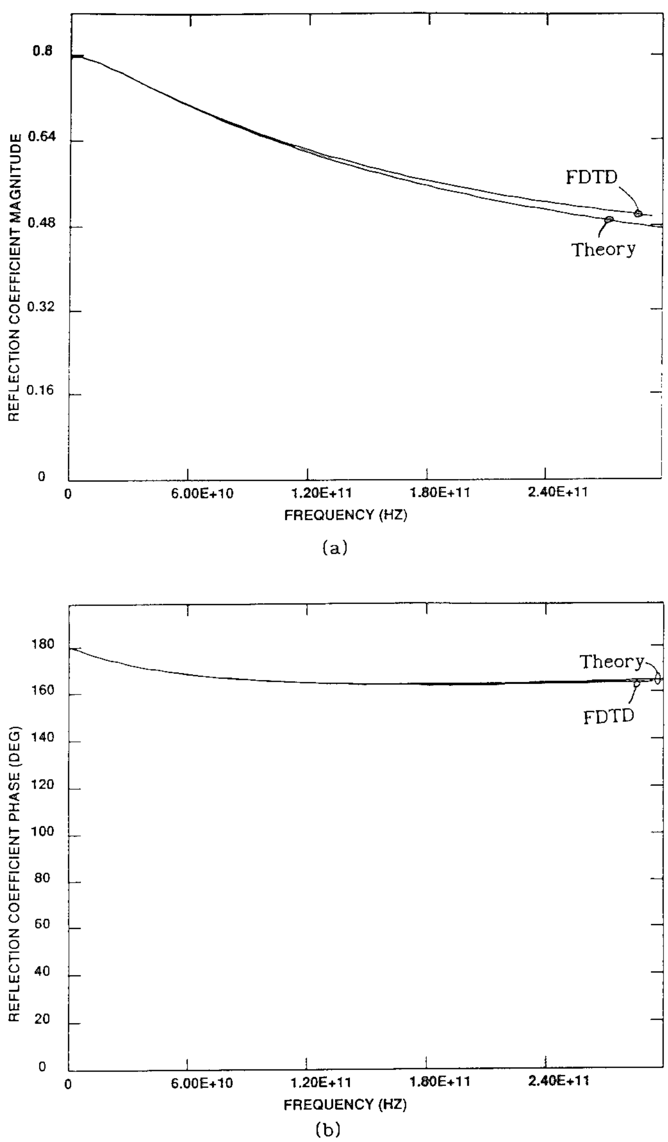

(a)

(b)

Figure 2. Reflection coefficient of Debye dispersive half-space using the differential equation FDTD technique. (a) Magnitude and (b) phase.

results of the same problem obtained using the differential equation approach.

We see that the accuracy for both methods is fairly good. It is interesting to observe that the convolution integral approach is less accurate than the differential equation approach at low frequencies for the parameters used in this test case, while both methods exhibit the same level of accuracy at the upper end of the frequency band. For both of these simulations the space and time increments were identical; Δx = 40 μm and Δt = 133.33 fs.

The next example demonstrates the propagation properties of the dispersive FDTD schemes. The same half-space as before is used with a normally incident plane wave with the incident electric field in the free space region being given by

$$E_y^i(t) = \begin{cases} \sin(20\pi \times 10^9 t) \ \ \text{V/m} & 0 \le t \le 1\text{ns} \\ 0 & t > 1\text{ns} \end{cases}$$

The temporal variation of the electric field at various points within the dispersive media was observed. An example waveform is shown in Figure 3. As reported in [4], leading and trailing edge transients corresponding to the Brillioun precursor are observed and have magnitudes exceeding that of the carrier frequency component.

In order to more quantitatively assess the accuracy of the two dispersive FDTD formulations, the maximum magnitude of the transient and the magnitude of the carrier frequency component are tabulated for observation points within the material at various distances from the material interface and compared to the results obtained from the graphs

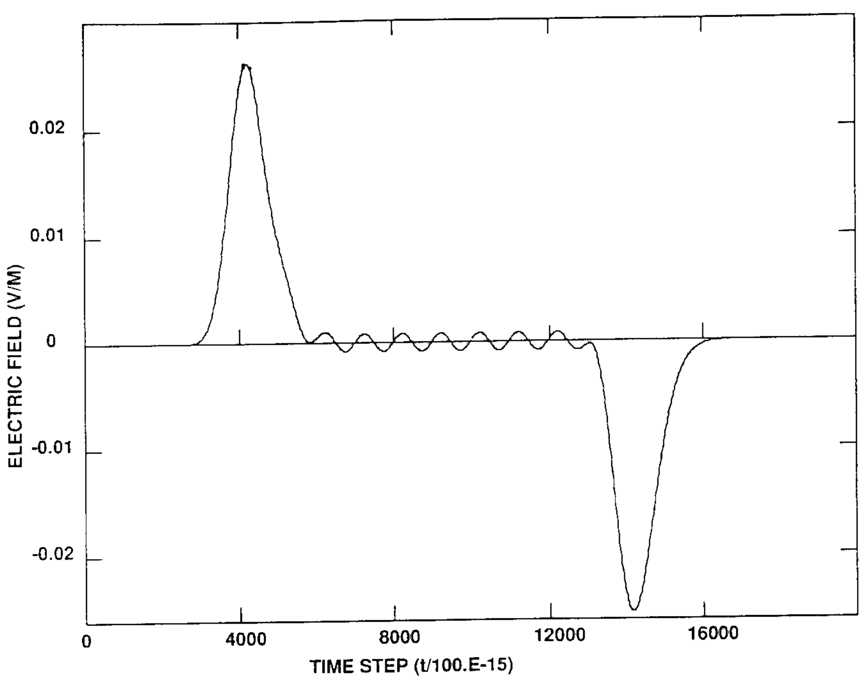

Figure 3. Temporal electric field behavior in Debye dispersive half-space at a distance of 14.7mm from the interface.

given in reference 4 which were calculated using a Fourier series technique. The results tabulated in Table 1 are for a mesh spacing of $\Delta x = 30\ \mu m$ and time step $\Delta t = 100$ fs.

From the data in Table 1 we see that the differential equation FDTD approach agrees with the Fourier series approach much better than the values obtained using the convolution integral approach.

TABLE 1

Electric field values in Debye dispersive material. D.E. is the differential equation approach and C.I. is the convolution integral approach.

Distance from Interface	Maximum Transient Amp (V/m)			Maximum Carrier Frequency Amp. (V/m)		
(mm)	D.E.	C.I.	Ref. 4	D.E.	C.I.	Theory
1.2	0.1456	0.1343	0.14	0.1364	0.1241	0.136
2.7	0.1005	0.0902	0.10	0.0774	0.0662	0.077
7.2	0.0483	0.0419	0.05	0.0141	0.0100	0.014
10.2	0.0355	0.0307	0.038	0.0045	0.0029	0.0046
14.7	0.0262	0.0209	0.033	0.0008	0.0004	0.0008

In order to determine the reason for the differing accuracy between the two methods a propagation analysis of the two techniques must be performed. This task has been begun but more work is needed before definitive results can be presented. Numerical experimentation has demonstrated that both methods approach the Fourier series and theoretical results for successively finer grid resolutions. In view of the better convergence of the differential equation method it was decided to concentrate efforts on this approach rather than the convolution integral method. The differential equation approach also has the advantage of being easily adapted for the Lorentz media.

Now, some results from a convergence study of the differential equation FDTD method will be presented. The same problem as above was solved using several different mesh sizes. Table 2 summarizes the results of this convergence study.

TABLE 2

Electric field values in Debye media for several mesh resolutions. Tran is the maximum amplitude of the transient and fc represents the amplitude of the carrier frequency component.

Δx (μm)	Distance from Interface (mm)									
	1.2		2.7		7.2		10.2		14.7	
	Tran	fc	Tran	fc	Tran	fc	Tran	fc	Tran	fc
30	.1456	.1364	.1005	.0774	.0483	.0141	.0355	.0045	.0262	.0008
60	.1456	.1364	.1005	.0774	.0483	.0141	.0355	.0045	.0262	.0008
150	.1459	.1368	.1459	.0773	.0481	.0148	.0354	.0045	.0261	.0008
250	.1437	.1350	.1437	.0756	.0474	.0141	.0350	.0042	.0260	.0007
500	.1553	.1536	.1536	.0822	.0470	.0130	.0348	.0036	.0261	.0006

We see from this data that reasonably accurate field values can be obtained using a mesh that is substantially coarser than the original 30 μm mesh. Thus, since coarser meshes can yield accurate results, larger problems can be solved with reasonable computer resource requirements, suggesting that extending the technique to solve two and three dimensional problems involving penetration into and scattering from dispersive bodies in the microwave frequency range can be accomplished without requiring unrealistic run time and memory requirements.

Lorentz Media Results: To test the differential equation FDTD approach for the case of Lorentz media the material parameters originally used by Brillouin [2] have been used. These parameters are as follows:

$$\varepsilon_s = 2.25\varepsilon_o\ , \quad \varepsilon_\infty = \varepsilon_o, \quad \omega_o = 4\text{x}10^{16}, \quad \delta = 0.28\text{x}10^{16}$$

As before, the reflection coefficient for a plane wave normally incident on the interface has been computed. For this simulation Δx is taken to be 60×10^{-12} m resulting in a Δt of 200×10^{-21} s. A Gaussian pulse narrow enough to provide data from DC up to 3×10^{16} Hz was used as the incident signal. Figure 4 plots the magnitude and phase of the reflection coefficient from the FDTD simulation along with the theoretical answer. Excellent agreement is observed.

Next, the observation point was moved to $1\mu m$ from the interface and the incident plane wave was changed from the Gaussian pulse to a unit step modulated sinusoid of frequency 1×10^{16} Hz. The purpose of this test case was to try and observe the formation of the first, or Sommerfeld, precursor in the dispersive media.

Figure 5 plots the temporal variation of the electric field $1\mu m$ from the interface. For this simulation the modeling parameters were $\Delta x = 20\times10^{-12}$m and $\Delta t = 66.67\times10^{-21}$s. Clearly this data displays the same behavior as associated with the Sommerfeld precursor as reported in [1], [3] and [6]. Before giving a more quantitative comparison to other data the convergence of the FDTD model for this problem will be addressed.

To test the convergence of the FDTD algorithm three different cases were run. The spatial increment (Δx) for these cases was 20×10^{-12}m, 30×10^{-12}m and 60×10^{-12}m with corresponding time steps of 66.67×10^{-21}s, 100×10^{-21}s and 200×10^{-21}s, respectively. Figure 6 shows the early development of the Sommerfeld precursor for all of these cases. It has been found that the zero crossing points converge faster than the amplitude. Also, notice that the high frequency ripple on these

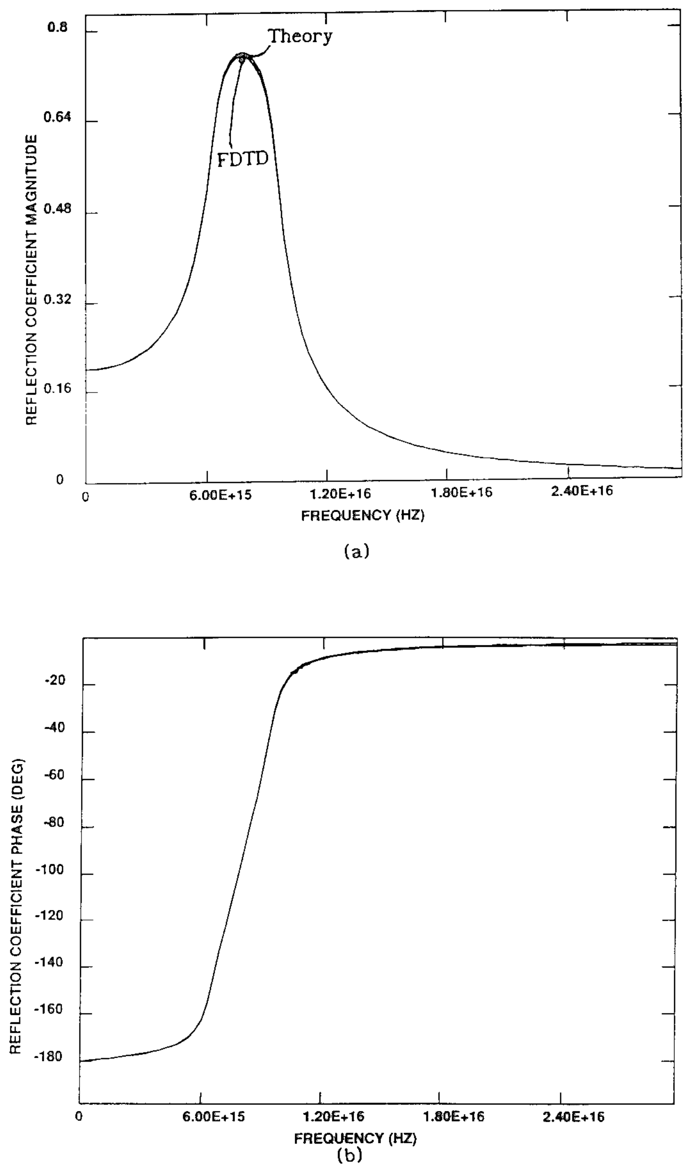

Figure 4. Reflection coefficient for Lorentz dispersive half-space. (a) Magnitude and (b) phase.

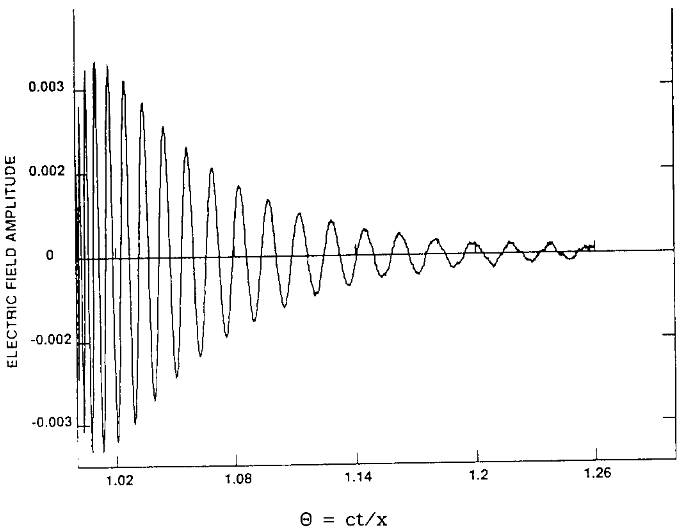

Figure 5. FDTD computed Sommerfeld precursor in the Lorentz half-space at a distance of 1μm from the interface.

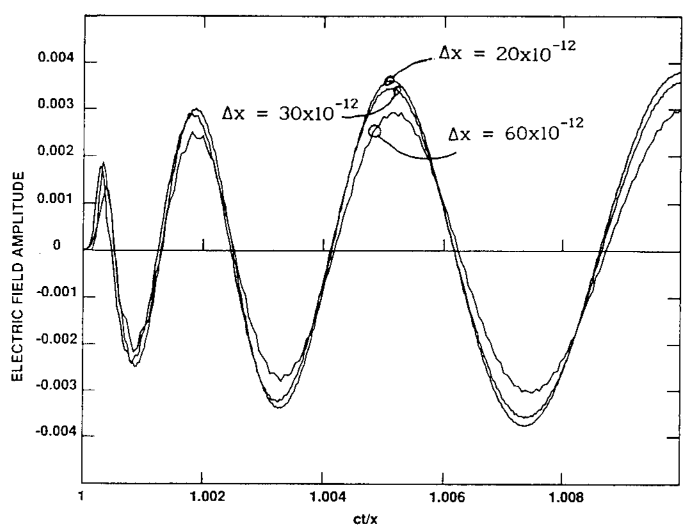

Figure 6. FDTD computed Sommerfeld precursor in Lorentz half-space at a distance of 1μm from the interface, for $\Delta x = 20\times10^{-12}$, 30×10^{-12}, and 60×10^{-12} m.

waveforms, which is due to the discrete sampling associated with the FDTD method, is reduced, as would be expected, for successively smaller mesh spacings.

Due to the computational requirements of simulating the infinite half-space with such a fine mesh, no cases with Δx smaller than 20×10^{-12}m were run. For more realistic problems such as a finite slab of material, it will be possible to use a finer mesh (thus obtaining better convergence) and still maintain reasonable computer run times.

For comparison purposes Figure 7, taken from reference 6 shows the Sommerfeld precursor as calculated from a Laplace transform analysis. The trends certainly agree with the FDTD data. In Figure 8 the FDTD data for the early development of the precursor is plotted with data points taken from a graph in [6]. We observe agreement to be fairly good. We note again that the amplitude discrepancy can more than likely be decreased by using a finer mesh at the expense of increased computer resources.

CONCLUSIONS

In this paper the results of research aimed at applying the FDTD method to the analysis of electromagnetic penetration into dispersive materials has been reported. It has been found that the FDTD method is capable of predicting transients that are associated with propagation in dispersive media and whose prediction is very important when analyzing penetration into and propagation in biological tissues. The data obtained using the FDTD algorithms has compared favorably to theoretical solutions when available and to data obtained by other researchers using different analysis techniques. The results obtained in this research

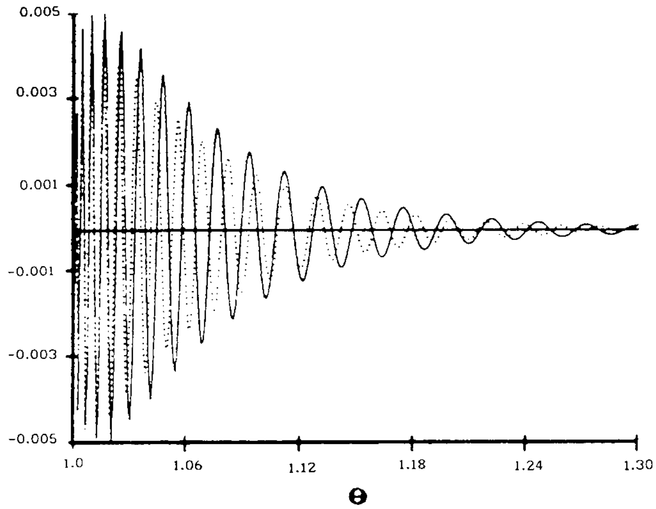

Figure 7. Sommerfeld precursor from reference 6 for comparison to Figure 5. (... - Laplace analysis, ——— - asymptotic analysis)

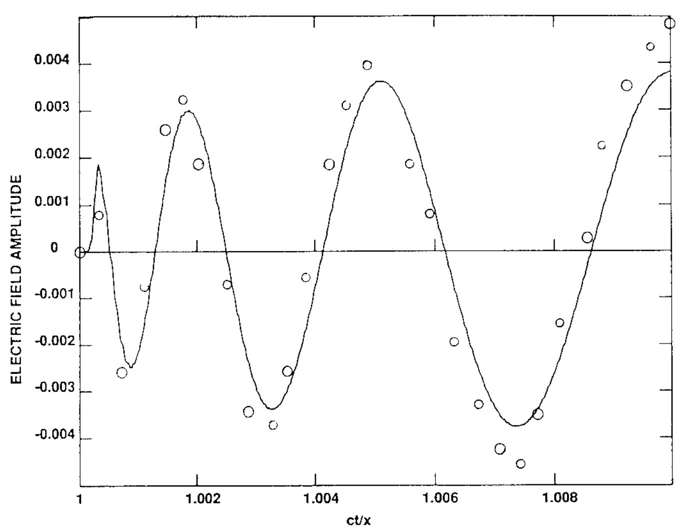

Figure 8. FDTD computed Sommerfeld precursor in early time with Laplace analysis values from [6] shown for comparison. (——— - FDTD, o o o - from [6])

demonstrate the feasibility of using the FDTD method for the solution of electromagnetic scattering and penetration problems involving Debye and Lorentz dispersive media. The next logical step in this research is the development of two and three dimensional computer programs that will allow the simulation of more realistic problems.

ACKNOWLEDGEMENT

This work was supported in part by the Air Force Office of Scientific Research.

REFERENCES

[1] A. Sommerfeld, "Uber die fortpflanzung des lichtes in disperdierenden medien," Ann. Phys., vol. 44, 177-202 (1914)

[2] L. Brillioun, *Wave Propagation and Group Velocity*, Academic, New York, 1960

[3] K.E. Oughstun and G.C. Sherman, "Propagation of electromagnetic pulses in linear dispersive medium with absorption (the Lorentz medium)," J. Opt. Soc. Am. A, vol. 5, 817-849 (1988)

[4] R. Albanese, J. Penn and R. Medina, "Short-rise-time microwave pulse propagation through dispersive biological media," J. Opt. Soc. Am. A, vol. 6, 1441-1446 (1989)

[5] K. Moten, C.H. Durney and T.G. Stockham, "Electromagnetic pulse propagation in dispersive planar dielectrics," Bioelectromagnetics, vol. 10, 35-49 (1989)

[6] P. Wyns, D.P. Foty and K.E. Oughstun, "Numerical analysis of the precursor fields in linear dispersive pulse propagation," J. Opt. Soc. Am. A, vol. 6, 1421-1429 (1989)

[7] K.S. Yee, "Numerical solution of initial boundary value problems involving Maxwell's equations in isotropic media," IEEE Trans. Ant. Prop., vol. 14, 302-307 (1966)

[8] R. Leubbers et. al., "A frequency-dependant finite-difference time-domain formulation for dispersive materials," IEEE Trans. Electromag. Comp., vol. 32, 222-227 (1990)

[9] R.M. Joseph, S.C. Hagness and A. Taflove, "Direct time integration of Maxwell's equations in linear dispersive media with absorption for scattering and propagation of femtosecond electromagnetic pulses," submitted to Optics Letters

Finite Difference - Time Domain Solution of the Maxwell Equations for the Dispersive Ionosphere

L. J. Nickisch
Mission Research Corporation
2300 Garden Road, Suite 2
Monterey, California 93940-5326
and
P. M. Franke
University of Illinois
Everitt Lab, Rm. 60H
1406 W. Green Street
Urbana, IL 61801-2991

Abstract

The Finite Difference - Time Domain (FDTD) technique is a conceptually simple, yet powerful method for obtaining numerical solutions to electromagnetic propagation problems. The application of FDTD methods to problems in ionospheric radiowave propagation is, however, complicated by the dispersive nature of the ionospheric plasma. In the time domain, the electric displacement is the convolution of the dielectric tensor with the electric field, and this convolution is untractable in the nearest neighbor FDTD approach. This difficulty can be avoided by returning to the constitutive relations from which the dielectric tensor is derived. By integrating these differential equations simultaneously with the Maxwell equations, dispersion (and absorption) is fully incorporated. The method is shown to be accurate by comparing to a known analytic solution for a special case.

Introduction

The accurate characterization of ionospherically modified received signals is of paramount importance in the performance assessment of communication and radar systems. During propagation, the RF signal is subject to dispersion (due to the frequency dependent ionospheric index of refraction), absorption, refraction and associated focusing/defocusing. In the disturbed ionosphere, these typical ionospheric propagation effects are augmented by scatter from geomagnetically aligned, small scale ionization structure. The RF signal can be diffracted broadly in angle, spreading the signal in delay and reducing its frequency and spatial coherence. Temporal variations in the structured medium or motion of the propagation path through the structure (moving transmitter or receiver) induce signal doppler spreading and loss of temporal signal coherence. Such structured ionization is typical of the natural polar and equatorial ionospheres, and the RF propagation problems associated with it are well known to, particularly, the HF community (e.g., OTH spread doppler clutter and HF communications fading).

Much effort over the past two decades has been devoted to the detailed understanding and prediction of these effects. These studies have been quite fruitful, and a good understanding of the important mechanisms now exists for many important propagation regimes. This progress has been made, in each case, by making use of a sequence of suitable approximations for each problem of interest which render the propagation calculations tractable, at least numerically. However, regimes of interest exist for which the approximation methods fail and suitable extensions cannot be found. An example is provided by the case of HF propagation through highly structured ionization. In this case the stochastic signal component is usually studied using the parabolic wave equation, an approximation to the scalar wave equation (in itself an approximation to the true vector wave equation) which is tractably soluble but which neglects terms which can be significant when the signal correlation length (ℓ_o) approaches or gets smaller than the signal wavelength. Yet measurements which imply $\ell_o \leq \lambda$ are typical of high latitude propagation.

With the advent of high speed supercomputers and parallel architectures (the Connection Machine or transputer networks), there now exists the potential to evaluate ionospheric propagation effects for a great many problems of interest without resorting to the usual approximations. The approach is to solve directly (by temporal integration) the Maxwell curl equations for the vector electric and magnetic fields using the Finite-Difference Time-Domain (FDTD) method. In this approach the propagation space is gridded to a resolution of several cells per wavelength (typically eight or sixteen) and the curl operator is applied in a finite difference sense and multiplied by the temporal step size. The procedure is repeated sequentially between the electric and magnetic field equations until the signal has propagated to the desired final state.

With the FDTD method, no approximations need be made other than that implicitly inherent in the finite differencing. The accuracy of the resulting vector EM fields is limited only by the grid resolution employed. The scope of problems which can be treated is limited only by the speed and memory capability of the computing device and the total amount of cpu-time available for the calculation. The full vector field can be calculated, including the polarization coupling effects which are neglected in the typical scalar wave equation approach. Magneto-ionic wave splitting is retained. Arbitrary pulse shapes and electron density distributions can be used.

FDTD application to the dispersive ionosphere

With the exception of one important element, the FDTD methodology is well established (see the review article by Taflove and Umashankar [1988]). The important missing element is the treatment of dispersive media. This has not previously been a concern to those involved in FDTD calculations owing to the nature of their problems of interest. The considered problems have primarily dealt with determining the scattered field from dielectric bodies or field penetration through narrow slots, etc. Thus the propagation medium has always been treated as free space or, at best, non-dispersive. This is expressly

not the case in ionospheric propagation, where the dispersive nature of the medium is of paramount importance.

The difficulty in treating dispersive media in the time domain stems from the relation of the electric displacement $\vec{D}$ to the electric field $\vec{E}$. It is in the frequency domain that the relation $\vec{D}(\omega) = \bar{\bar{\epsilon}}(\omega) \cdot \vec{E}(\omega)$ holds. The corresponding expression in the time domain involves a convolution of the dielectric tensor with the field, and is numerically untractable in the nearest neighbor FDTD approach. The complication can be avoided, however, by returning to the constitutive relations from which the dielectric tensor is derived [*Budden*, 1966],

$$q\vec{E} + \frac{1}{N_e}\frac{\partial \vec{P}}{\partial t} \times \vec{B}_E = \frac{m_e}{N_e q}\left(\frac{\partial^2 \vec{P}}{\partial t^2} + \nu \frac{\partial \vec{P}}{\partial t}\right) \tag{1}$$

which relates the forces on a charged plasma (here assumed to be the ionospheric electrons) to the plasma acceleration. We have included in (1) the force on a charge due to the applied field of our wave of interest and the external geomagnetic field $\vec{B}_E$ responsible for magneto-ionic splitting. The collisional forces responsible for signal absorption are incorporated through the electron collision frequency ν in the last term. Equation (1) has been written in terms of the electric polarization $\vec{P}$. Our approach is to discretize (1) on the FDTD grid and solve for the polarization P at time step n in terms of the polarization and field at previous time steps. We then use the relation $\vec{D} = \epsilon_o \vec{E} + \vec{P}$ in the FDTD versions of the Maxwell curl equations (with $\vec{B} = \mu_o \vec{H}$)

$$\frac{\partial \vec{B}}{\partial t} + \nabla \times \vec{E} = 0 \tag{2}$$

$$\frac{\partial \vec{D}}{\partial t} - \nabla \times \vec{H} = 0 \tag{3}$$

The interlaced electric-magnetic grid of Yee is employed [*Yee*, 1966], providing excellent numerical stability.

The above method for incorporating dispersion in the time domain solution of the Maxwell equations was developed by us a few years ago during initial investigations into the feasibility of using the Connection Machine to solve realistic ionospheric propagation problems [*Nickisch and (Minthorn) Calvert*, 1988; *Minthorn, et al.*, 1989]. During these investigations we were surprised to discover that this fundamental problem of dispersion did not appear to have been seriously addressed in previous FDTD analysis. Our initial approach involved the use of the inverse dielectric tensor acting on the electric displacement, and analytical barriers which had previously prohibited time domain dispersion calculations were successfully removed. The resulting expressions, however, proved to be too cumbersome for efficient application. The elegant method described above seems fairly obvious in retrospect, and proves to be both efficient and accurate.

An alternative to the coupled Maxwell curl equations is found in the vector wave equation. This equation is obtained by applying the curl operator to Equation (2) and using Equation (3). The result is

$$\frac{1}{c^2}\frac{\partial^2 \vec{E}}{\partial t^2} = \nabla^2 \vec{E} - \vec{\nabla}(\vec{\nabla}\cdot\vec{E}) - \mu_\circ \frac{\partial^2 \vec{P}}{\partial t^2} \tag{4}$$

Equation (4) can be discretized in the finite difference sense and solved in a manner similar to the coupled Maxwell curl equations. We have done so, and the results prove to be equivalent to the previously described method. There is some advantage to the use of the vector wave equation approach in that only one grid is required for the calculation rather than the two displaced grids used in the Maxwell curl equation approach. There is also a small advantage in the memory requirements in that magnetic field quantities are not computed, although this is partially offset by the need to retain two previous time steps of the electric field in memory so that the finite difference second temporal derivatives can be computed.

Examples of FDTD propagation in ionospheric plasma

We now show several examples of our FDTD method for treating the dispersive ionosphere. While our code accurately incorporates a nonzero geomagnetic field strength (anisotropic effects) and nonzero electron collision frequency (absorption), space does not allow consideration of these effects here. Thus in the examples to follow, $|\vec{B}_E| = 0$ and $\nu = 0$ in Equation (1). However both dispersion and polarization coupling will be manifested.

The accuracy of the FDTD method for an ionospheric plasma is apparent in the example shown in Figure 1. Here a single frequency sinusoid has been introduced from the left into a region consisting of free space to the left and a linear ramp of electron density to the right. The FDTD code was allowed to run until the solution attained steady state. Extremely accurate boundary conditions were employed at the left edge of the grid to account for the field leaving the grid (to be expanded upon in a forthcoming publication). This special case provides an exact analytic solution in the frequency domain, expressed in terms of Airy functions. To compare to this frequency domain solution, the time domain field was demodulated. Figure 1 compares the FDTD result (dots) to the analytic result (solid curve). The agreement is rather impressive.

The real efficiency of the FDTD method is, of course, for pulse propagation since a frequency domain solution requires a spectral decomposition, a solution for a sufficiently dense set of spectral components, and subsequent pulse reconstruction. Figure 2 shows a gaussian pulse at a carrier frequency of 9.375 MHz impinging from the left on a gaussian electron density distribution with peak plasma frequency 9.3 MHz. The pulse is partially reflected and significantly dispersed in accordance with expectations. In Figure 3, the same gaussian pulse is incident on a square plasma barrier of plasma frequency 9.3 MHz.

Dispersion is evident in the transmitted wave as a shortening of the wavelength with depth into the medium. The higher frequency components of a signal travel faster in the ionospheric plasma. Close inspection of Figure 3 reveals very low amplitude high frequency components well ahead of the main transmitted pulse.

Figure 4 shows three snapshots of a two-dimensional gaussian pulse (predominantly y-polarized) impinging on a two-dimensional gaussian electron density enhancement. The y-component of the field is shown in the left hand column (symmetric about the propagation axis) and the x-component is shown in the right hand column (anti-symmetric about the propagation axis). Contours of plasma frequency are also shown (1, 3, 5, 7, 9 MHz), and the pulse width was chosen so that the center frequency of the pulse is just below that of the peak of the gaussian electron density bump. These figures were generated by a 2-D vector wave code. A similar 2-D code solving the coupled Maxwell curl equations produced similar results. Note the strong conversion of energy from the y-polarization to the x-polarization evident at the last time step displayed, caused by polarization coupling in the plasma. Figure 5 is similar to Figure 4, but with the medium replaced by a 1-dimensional gaussian ridge with superimposed random structure (a 2-component power-law spectrum of irregularities with parameters chosen to provide strong scatter within the space of the computational grid). The incident field in this case is a 1-dimensional y-polarized gaussian pulse (no x-component is required to maintain the incident pulse in this case). Once again, a strong conversion to the cross-polarization is evident.

References

Budden, K. G., Radio Waves in the Ionosphere, Cambridge University Press, 1966.

Minthorn, P. A., C. H. Liu, and V. Sparrow, "Numerical Full-Wave Solutions to the Maxwell Equations Applied to Propagating Through an Ionospheric Medium," Program and Abstracts of the National Radio Science Meeting, January 1989.

Nickisch, L. J. and P. (Minthorn) Calvert, "Numerical Full-Wave Solutions to the Maxwell Equations in Continuously Random Media," Program and Abstracts of the National Radio Science Meeting, January 1988.

Taflove, Allen and Korada R. Umashankar, "Finite-Difference Time-Domain (FD-TD) Modeling of Electromagnetic Wave Scattering and Interaction Problems," IEEE Antennas and Propagation Society Newsletter, April 1988.

Yee, Kane S., "Numerical Solution of Initial Boundary Value Problems Involving Maxwell's Equations in Isotropic Media," IEEE Transactions on Antennas and Propagation, Vol. AP-14, No. 3, May 1966.

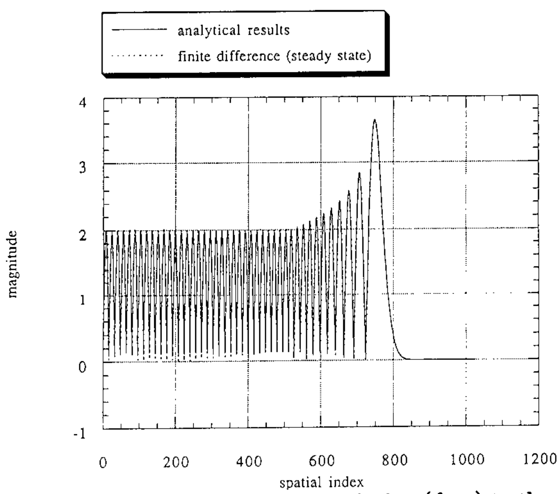

Figure 1: Comparison of the steady state FDTD solution (dots) to the exact Airy function solution (solid curve) for single frequency sinusoidal propagation in a region with free space on the left and a linear ramp of electron density on the right.

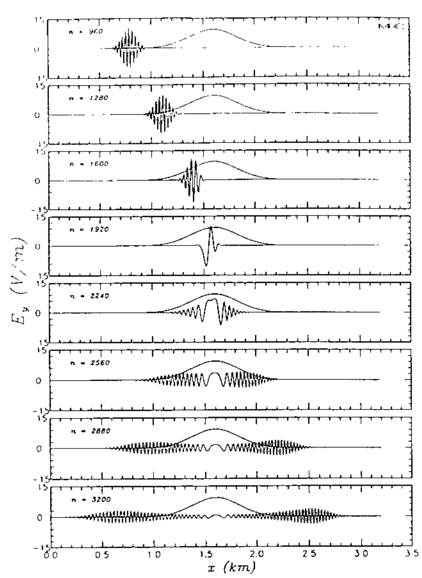

Figure 2: A 9.375 MHz gaussian pulse impinging on a gaussian electron density distribution of peak plasma frequency 9.3 MHz.

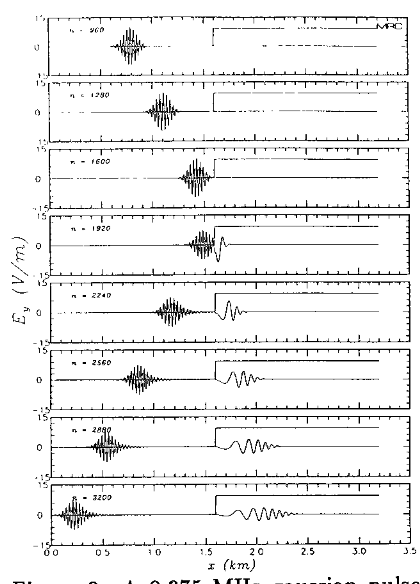

Figure 3: A 9.375 MHz gaussian pulse impinging on a square electron density barrier of plasma frequency 9.3 MHz.

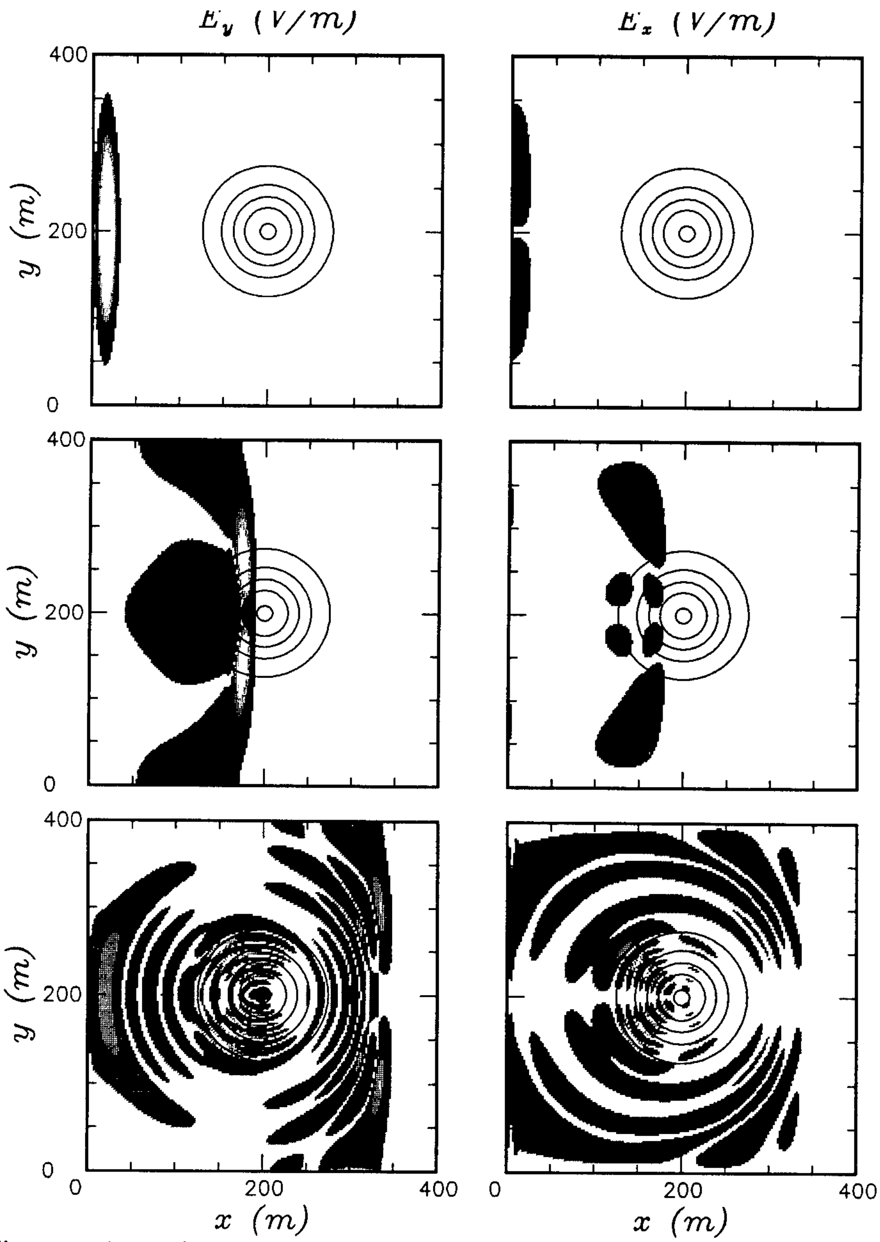

Figure 4: A two-dimensional gaussian pulse impinging on a two-dimensional gaussian electron density distribution. Contours of 1, 3, 5, 7, 9 MHz plasma frequency are shown.

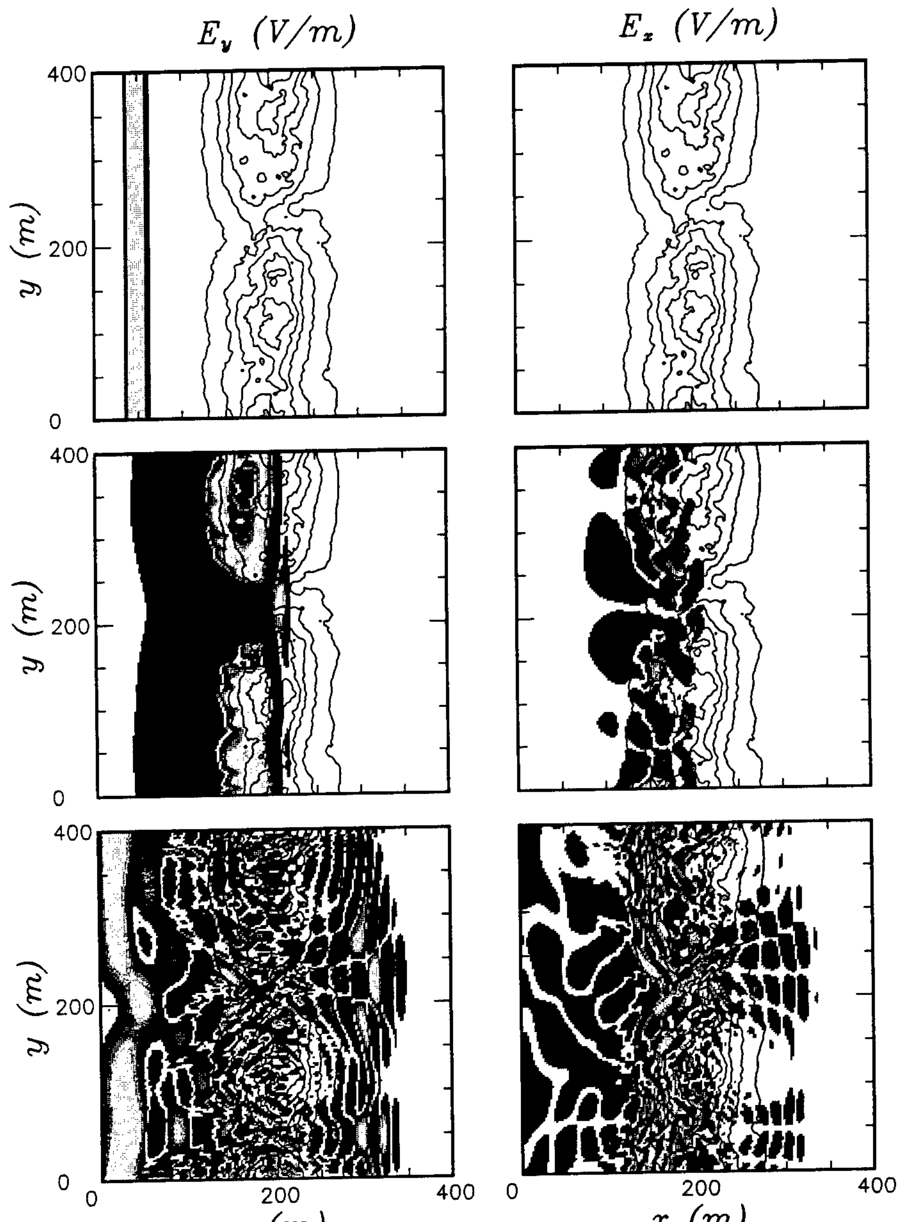

Figure 5: A one-dimensional gaussian pulse impinging on a one-dimensional gaussian ridge with superimposed random structure (structure generated with a two-component power law PSD). Contours of 1, 3, 5, 7, 9 MHz plasma frequency are shown.

SESSION 12 - "TRANSMISSION LINE MATRIX"

Moderator: Lloyd Riggs

DEVELOPMENTS IN THE TRANSMISSION LINE MODELLING (TLM) METHOD

Prof C Christopoulos and J L Herring
Numerical Modelling Laboratory
Department of Electrical and Electronic Engineering
University of Nottingham
Nottingham NG7 2RD
UK

Abstract

The transmission line modelling (TLM) method and its applications are described. Developments to the original symmetrical condensed node with stubs to increase efficiency and accuracy are presented. The manner in which wires and fine structures may be described by the hybrid variable mesh and, in particular, by the multigrid mesh are discussed. The effectiveness of these techniques in improving the description of open boundaries, increasing spatial resolution without significantly increasing the size of the computation and in describing lossy materials is demonstrated by simulation examples of antenna radiation patterns, radiation from equipment apertures and damping of screened room resonances.

Introduction

Electromagnetic simulation at high frequencies is becoming increasingly important since problems in microwave circuits, antenna and RCS studies and electromagnetic compatibility present many challenges to the designer. Practical problems are characterised by:

- complexity eg. wire looms, tracks on printed circuit boards
- large differences in spatial scale eg. thin wires in a large equipment cabinet or in free space
- large differences in time scale eg. between propagation times in typical systems and the diffusion time through partially conducting panels
- material non-uniformities eg. air-dielectric boundaries in microstrip circuits
- coupling between different regions of space through apertures and conducting penetrations

Numerical simulation in this environment therefore requires computer based tools which are versatile, easy to apply and can deal with general configurations of materials of different shapes and properties. Inevitably, simulation of complex systems necessitates the making of assumptions and simplifications and it always leads to better modelling if the models used are physically transparent.

The purpose of this paper is to describe developments to transmission line modelling (TLM) and to present results illustrating its range of applications and accuracy. A brief introduction to the essential features of TLM is given below followed by sections giving details of recent improvements.

In TLM, space is modelled by a network of transmission lines. The point at which transmission lines intersect is referred to as a node and the most commonly used node for three-dimensional simulation is the symmetrical condensed node first described by *Johns 1987*. A schematic diagram of this node is shown in *fig. 1*. There are twelve ports, two for each polarisation corresponding to the six surfaces of a cube. The structure of the node and the parameters of the twelve transmission lines are chosen so that the voltages and currents on them give information about the electric and magnetic field in each part of space. The TLM algorithm is particularly simple to implement. At each time step, *k*, voltage pulses $[{}_kV^i]$ are incident on the node from each of the twelve transmission lines. These are scattered to produce a set of scattered voltages $[{}_kV^s]$ which become incident on adjacent nodes at the next time step. The processes of scattering $[{}_kV^s] = [S][{}_kV^i]$ and connection $[{}_{k+1}V^i] = [C][{}_kV^s]$ are repeated for as many time steps as

required. The electric and magnetic fields at each node and at every time step may be obtained directly from the voltage pulses. The scattering matrix [S] is simple and may be obtained by imposing the usual conservation laws - namely by forcing [S] to be unitary.
Further details may be found in the paper by *Johns 1987*.

The TLM algorithm is explicit, computationally simple and has a high degree of parallelism and hence has been identified as a powerful numerical tool in electromagnetics. The manner in which computation in TLM is implemented can lead to considerable improvements in efficiency as described by *Tong and Fujino 1991*. The TLM model is unconditionally stable since it is a passive network which is solved exactly. A further useful feature is that the transmission lines can be considered as distributed models of capacitors, inductors and resistors. The user therefore has a good grasp of the properties and behaviour of the model, the nature and significance of errors and the manner in which material properties may be introduced. In the next section recent improvements to the basic symmetrical condensed node with stubs are described.

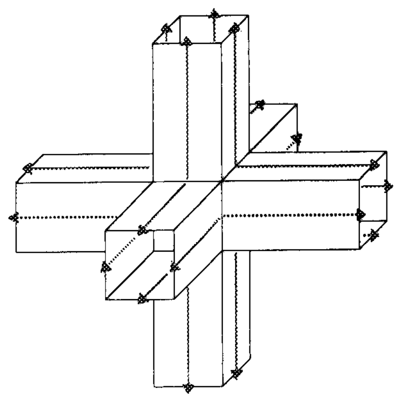

Fig. 1 The Symmetrical Condensed Node

Variable mesh and multigrid techniques

The regular TLM node shown in *fig. 1* can model a cubic volume of space of any dimensions. In electromagnetic simulation three additional features are often required:

- It is desirable for a single node to represent non-cubic volumes eg. a long thin node for describing wire-like structures. However, in such a node propagation times are different in each direction and so pulses will arrive at adjacent nodes after different time intervals. Such loss of synchronism renders the technique impractical.
- It is necessary in many problems to account for material non-uniformities. Nodes on either side of the boundary between two different materials must reflect the material properties. If the velocities of propagation are different then different space discretisation lengths must be used if synchronism is to be maintained. This leads to a lack of connectivity between nodes on each side of the boundary. Conversely, if space connectivity is enforced there will be a loss of synchronism.
- In many practical problems there are regions in which fields vary rapidly and hence a fine spatial description is necessary. In regions of slow field variation a coarse description is adequate and desirable since, in a large three-dimensional problem, a fine spatial resolution cannot be applied throughout the problem space. Also, there are often regions of space in which an accurate knowledge of the field is not necessary eg. the space near numerical boundaries in open boundary problems. At the interface between a coarse and fine mesh issues of connectivity and synchronism arise as described earlier.

The traditional approach to the modelling of irregular shapes and material non-uniformities is the stub loaded node described by *Johns 1987*. In this approach the twelve link transmission lines have the same impedance and propagation time irrespective of the shape of the node or the material properties. Free space parameters are normally chosen for these lines. Any deficiencies in capacitance or inductance needed to account for material properties or for an irregularly shaped node are added to the node in the form of capacitive and inductive stubs. A maximum of three capacitive and three inductive stubs are required to account for variations in each coordinate direction. In this manner synchronism and connectivity are maintained whilst a range of shapes and material properties can be described. To ensure unconditional stability, both the capacitive and inductive stubs must represent passive

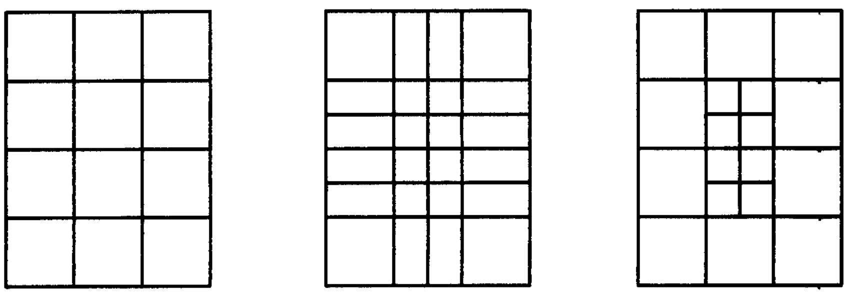

Fig. 2a Uniform mesh *Fig. 2b Variable mesh* *Fig. 2c Multigrid mesh*

components. This condition imposes a limit on the maximum time step that may be employed. In many applications this value is too small resulting in a lengthy computation.

An improved node leading to a hybrid variable mesh has been described recently by *Scaramuzza and Lowery 1990*. In this node all of the inductance is incorporated into the twelve link lines (which therefore have different impedances). The capacitance associated with the link lines is chosen to maintain synchronism and capacitive stubs are added at the node to make good any deficit. The hybrid node has the advantage over the stub loaded node of fewer stubs (three instead of six) and it can be operated with a much large time step. It also appears to have better dispersive properties and is much more efficient in run-time requirements. Further details may be found in papers by *Scaramuzza and Christopoulos 1991* and *Scaramuzza et al 1991*.

The division of space using a regular node is shown schematically in *fig. 2a*. One way of dividing space when a variable or graded mesh is used (stub loaded or hybrid) is shown in *fig. 2b*. A feature of the variable mesh is that the region of fine spatial description cannot be completely localised if connectivity between adjacent nodes is to be maintained. An alternative to the variable mesh is the multigrid mesh described by *Herring and Christopoulos 1991*. The division of space using this technique is shown in *fig. 2c* in which a well defined part of the space is described by a finer mesh. Across the interface separating the fine from the coarse mesh there is neither connectivity nor synchronism. It is therefore necessary to implement space and time approximations, subject to appropriate constraints, to pass information across the interface. The problems associated with the interface have been discussed by *Naylor and Christopoulos 1989* and *Herring and Christopoulos 1991*.

Consider a multigrid model in which there is a 2:1 reduction between the fine and coarse regions. Each coarse mesh link line is connected to four fine mesh link lines (two in each direction). If the time step in the coarse mesh is twice that in the fine mesh then each voltage pulse incident upon the interface from the coarse mesh must be converted into eight fine mesh pulses and each group of eight pulses from the fine mesh must be converted into a single coarse mesh pulse. Ideally, the implementation of the conversion process should be subject to the following constraints:

- pulses must pass through the interface without reflection
- the field associated with a group of pulses must be constant across the interface
- the energy associated with a group of pulses must be constant across the interface
- the velocity of energy transport must be unaffected by the interface

Obviously, when converting several pulses from the fine mesh into a single coarse mesh pulse it is not possible to satisfy all constraints. In the conversion method described below energy conservation has not

been enforced and the interface behaves as a low pass filter (when converting pulses from the fine mesh to the coarse mesh). Tests on a loss-less cavity in which one half of the volume is modelled using a coarse mesh and the other half with a fine mesh show that the loss of energy is not significant for frequencies within the working range of a uniform coarse mesh. The maximum frequency at which results from a uniform mesh are used is generally taken to be that corresponding to a wavelength of 10Δl. The multigrid technique, in this case, gives an increase in spatial resolution but no increase in the maximum working frequency.

A general conversion formula may be derived in which pulses from an integral number of link lines from one region are converted into pulses travelling into an integral number of link lines in another region. Let l_1 lines from region *1* be connected to l_2 lines from region 2, in each direction, and let n_1 and n_2 be the total number of pulses to be converted in each region. Let Δl be a base value for the node spacing common to both regions. If the average electric field is to be constant across the interface then

$$\frac{1}{n_1}\sum_{i=1}^{n_1}\frac{V_{1i}}{(\Delta l\,/\,l_1)} = \frac{1}{n_2}\sum_{j=1}^{n_2}\frac{V_{2j}}{(\Delta l\,/\,l_2)}$$

For the conversion of pulses from region *2* to pulses in region *1* and if all pulses into region *1* are set to be equal then

$$V_{1i} = \left(\frac{l_2}{n_2\,l_1}\right)\sum_{j=1}^{n_2} V_{2j}$$

For example, if region *1* is the coarse mesh then, for a 2:1 reduction ratio, l_1=1, n_1=1, l_2=2 and n_2=8. Eight fine mesh pulses are converted into a single coarse mesh pulse, $V_c=\frac{1}{4}\Sigma V_f$, and a single coarse mesh pulse is converted into eight identical fine mesh pulses, $V_f=\frac{1}{2}V_c$.

The points in the calculation at which the conversion between pulses in each region is performed are selected to minimise the delay in transferring information across the interface in both directions. A plane wave propagating through a uniform coarse mesh will therefore be unaffected by the inclusion of a fine mesh region extending across the whole cross-section. If the fine mesh region only partly fills the cross-section then some dispersion will occur.

Open boundaries

Open boundaries may be approximated by terminating the transmission lines adjacent to the boundary with a matched load. This method works perfectly when a plane wave is normally incident upon the boundary but works less well for waves incident at an angle. To minimise the effects of imperfect numerical boundaries the volume modelled may be increased so that the boundaries are distant from the region of interest. This approach is however limited due to computer storage and run-time restrictions. With the multigrid technique a layer of coarse mesh nodes may be placed between the region of interest and the numerical boundary. This allows the boundaries to be placed further away without a significant increase in computer resources. A more sophisticated approach to the open boundary problem, not considered here, is to use time-domain diakoptics as described by *Eswarappa et al 1990*.

As an example, consider the field profile around a spherical dipole antenna in free space. The dipole consists of two hemispheres, 10 cm in diameter, separated by a small gap. It is convenient to use a cartesian coordinate system so that plane surfaces can be introduced into the model if required. For these simulations three symmetry planes were used and the dipole was modelled within a 20×20×20 node fine mesh with a 0.5 cm node spacing. This was then placed within a 50×50×50 node mesh with a 1 cm node spacing. The details of the feed arrangement inside the dipole significantly affect the frequency response but not the field profile. In this model, two solid hemispheres were used with a

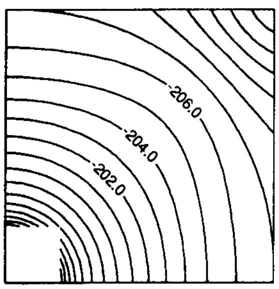

(a) 500 MHz, no border

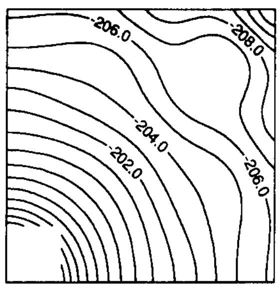

(b) 1 GHz, no border

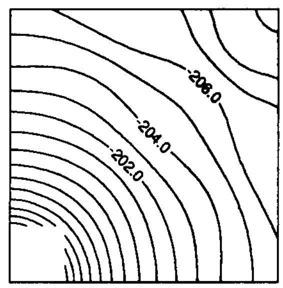

(c) 1 GHz, 5 nodes, 2:1 reduction

Fig. 3 Field profile around spherical dipole with various boundary layers

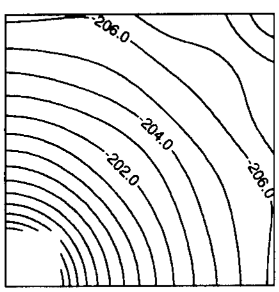

(d) 1 GHz, 5 nodes, 3:1 reduction

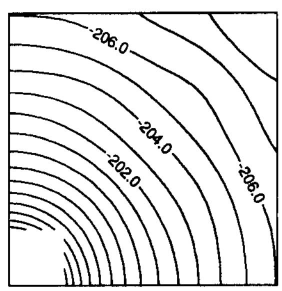

(e) 1 GHz, 80^3 node mesh

short-circuit node at the centre. The field profile around the dipole, on a 50 cm^2 plane, is shown in *fig. 3* at *(a)* 500 MHz and *(b)* 1 GHz. The dipole is in the bottom left corner and the contours, which should be a set of concentric circles, are lines of constant electric field magnitude spaced at intervals of 1 dB. The effect of the numerical boundaries can be seen in the top right corner, particularly at the higher frequency. The results obtained at 1 GHz when 5 node layers of *(c)* 2 cm and *(d)* 3 cm node spacings are introduced before the numerical boundary are also shown. *Fig. 3e* shows the field profile when a 80×80×80 node mesh is substituted for the 50×50×50 node mesh. A comparison of the computer requirements is shown below.

Boundary layer	Relative storage	Relative run-time
(a),*(b)* no border	1.00	1.00
(c) 5 nodes, 2:1 reduction	1.20	1.04
(d) 5 nodes, 3:1 reduction	1.14	1.08
(e) 80^3 node mesh	3.91	3.76

The field profiles obtained with the coarse node layers are similar to those obtained with a uniform mesh of the same spatial extent. The last example shows that boundary effects are apparent even in a problem employing in excess of 500,000 nodes.

Fine features

The modelling of fine features within a large space is difficult since a uniform fine mesh can rarely be employed throughout the entire problem space. As an example, consider a representative device under test (DUT) used for electromagnetic compatibility studies. The DUT measures 48×48×12 cm^3 and is designed to imitate, in a simplified manner, the way in which a real electronic device would radiate into

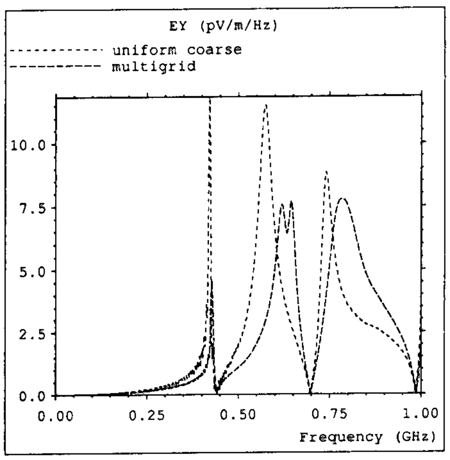

Fig. 4a DUT front slot mode

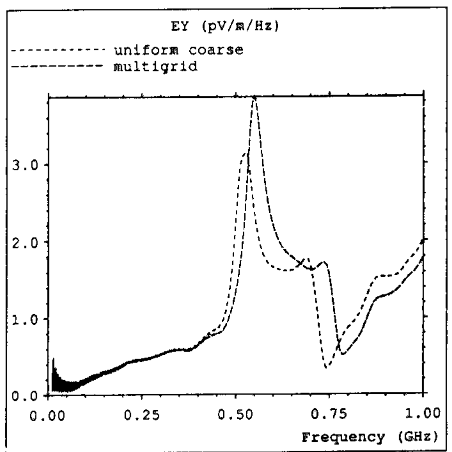

Fig. 4b DUT top gap mode

either free space or a screened room. It consists of a closed box which can be made to radiate in a number of ways by removing panels to reveal slots (slot modes) or by adding panels parallel to the existing surfaces (gap modes). A signal is then applied either across the slot or between the DUT body and the raised panel. *Fig. 4a* shows the electric field at a distance of 1 m from the centre of the DUT in free space for the case when the front slot (measuring 16×4 cm^2) is excited. For the first curve, a uniform mesh with a node spacing of 4 cm was used. The second curve was obtained when a fine mesh of 2 cm node spacing was used to describe the DUT. The physical volume of the fine mesh region was 1.3% of the coarse mesh volume. The curves are similar but features in the multigrid curve occur at higher frequencies and the central peak is resolved into two. Results obtained from a smaller physical volume indicate that the multigrid result is consistent with that obtained from a uniform fine mesh. The uniform coarse result might be expected to be inaccurate since the slot is only a single node across. *Fig. 4b* shows the corresponding curves for the case when an additional panel is placed 4 cm above the DUT. Again, higher frequencies are observed in the multigrid curve. The multigrid technique can also be used to model thin wires by describing them in fine mesh regions placed within a much larger coarse mesh.

Losses

Both electric and magnetic losses have been incorporated into the TLM model by *Naylor and Desai 1990* and *German et al 1990*. A node incorporating electric losses and an appropriate value of relative permittivity can be used to model radiation absorbing material (RAM). The addition of RAM inside a screened room results in a reduction of the Q-factor of resonances and therefore in a more uniform field distribution. Simulations have been performed to determine the optimum material properties of a RAM block, placed centrally inside a screened room, to damp a specific resonance. Consider a 1m^3 block placed within a screened room of dimensions $6.1\times4.8\times2.4$ m^3. *Fig. 5a* shows the magnitude of the electric field for five values of resistivity and a relative permittivity of unity in the frequency range about the first resonance. Optimum damping occurs with a resistivity of about 60 Ωm. If the resistivity is reduced further then a new resonance is established at a slightly lower frequency. The frequency range about the second resonance is shown in *fig. 5b*. This time the frequency is shifted up as the resistivity is reduced. 60 Ωm no longer produces the optimum damping although it is the best of the curves shown.

When the electric field component parallel to the shortest side is excited in the above screened room four resonances are observed in the frequency range 0 - 100 MHz as shown by the first curve in *fig. 6a*. When

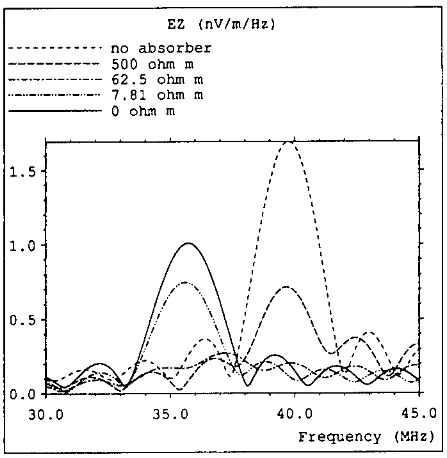

Fig. 5a 1m³ block, ε_r=1, first resonance

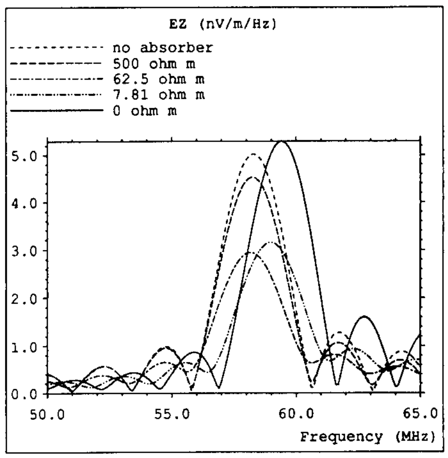

Fig. 5b 1m³ block, ε_r=1, second resonance

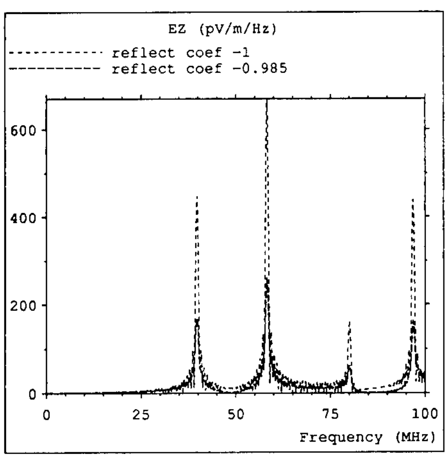

Fig. 6a Resonances in empty screened room

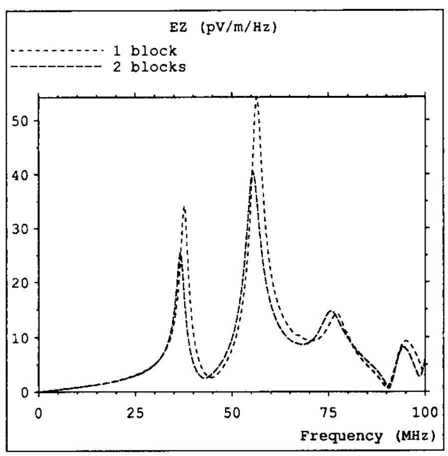

Fig. 6b Resonances in screened room with RAM blocks

lossy walls are introduced the second curve is obtained. The wall reflection coefficient was chosen so that the Q-factor of the first resonance was similar to that obtained experimentally, although this meant that the Q-factor of the second resonance differed somewhat from the experimental value. This discrepancy may be attributed to the simple model used to represent the room walls. *Fig. 6b* shows the curves obtained when one and then two RAM blocks measuring $3.0\times0.6\times0.6\ m^3$ are inserted into the room. A comparison of the TLM and experimental results for resonant frequency and Q-factor are shown in the table below for the first two resonances. Some error may be attributed to the values of resistivity and permittivity used in the model which may not properly represent the actual material properties. The results show that placing one or more RAM blocks at strategic points inside a screened room can be effective in suppressing low frequency resonances. High frequency resonances can then be

suppressed by placing a modest amount of RAM on the walls of the room.

No. Blocks	TLM Freq (MHz)	TLM Q-factor	Expt Freq (MHz)	Expt Q-factor
0	39.8	76	39.6	70
0	58.2	109	57.2	68
1	37.6	25	37.0	31
1	56.4	22	54.2	22
2	36.6	23	36.2	28
2	55.4	18	53.7	20

Conclusions

The description of open boundaries may be improved by inserting a layer of coarse nodes between the main mesh and the numerical boundary. Fine features can be described using the multigrid technique with an accuracy equivalent to that obtained from a uniform fine mesh. The incorporation of losses allows modelling of RAM so that optimum material properties and block location can be determined. The results shown demonstrate the effectiveness of TLM as a general simulation method.

Acknowledgements

The authors acknowledge financial support from the MoD Procurement Executive and wish to thank the National Physical Laboratory (UK) for supplying the experimental results.

References

1. Eswarappa, Costache G I and Hoefer W J R (1990) : "Transmission line matrix modeling of dispersive wide-band absorbing boundaries with time-domain diakoptics for S-parameter extraction", IEEE Trans, **MTT-38**, pp 379-385

2. German F J, Gothard G K and Riggs L S (1990) : "Modelling of materials with electric and magnetic losses with the symmetrical condensed TLM method", Electr Letts, **26**, pp 1307-1308

3. Herring J L and Christopoulos C (1991) : "Multigrid transmission-line modelling method for solving electromagnetic field problems", Electr Letts, **27**, pp 1794-1795

4. Johns P B (1987) : "A symmetrical condensed node for the TLM method", IEEE Trans, **MTT-35**, pp 370-377

5. Naylor P and Christopoulos C (1989) : "A comparison between time-domain and frequency-domain diakoptic methods of solving field problems by transmission-line modelling", Int Jrnl Num Mod, **2**, pp 17-30

6. Naylor P and Desai R A (1990) : "New three dimensional symmetrical condensed lossy node for solution of electromagnetic wave problems by TLM", Electr Letts, **26**, pp 492-494

7. Scaramuzza R A and Christopoulos C (1991) : "Developments in transmission-line modelling and its applications in electromagnetic field simulation", Proc Int Symp on EM Fields in Electrical Eng, Sept 18-20 1991, Southampton, pp 65-68

8. Scaramuzza R and Lowery A J (1990) : "Hybrid symmetrical condensed node for the TLM method", Electr Letts, **26**, pp 1947-1949

9. Scaramuzza R A, Naylor P and Christopoulos C (1991) : "Numerical simulation of field-to-wire coupling problems using transmission-line modelling", Proc Int Conf on Computation in Electromagnetics, Nov 25-27 1991, London, IEE Conf Publ 350, pp 63-66

10. Tong C E and Fujino Y (1991) : "An efficient algorithm for transmission line matrix analysis of electromagnetic problems using the symmetrical condensed node", IEEE Trans, **MTT-39**, pp 1420-1424

An X-Windows Previewer for GTEC Input Data

M.E.G. Upton[1] and S.J. Kubina

Electromagnetic Compatibility Laboratory,
Concordia University,
7141 Sherbrooke Street West,
Montréal, Québec,
CANADA. H4B 1R6.

Abstract

This paper describes an X-Windows program, *Xact*, which graphically previews input files for the TLM code GTEC. In *Xact* a three-dimensional TLM mesh is displayed as a series of two-dimensional projections. Using two-dimensional slices through the mesh allows the user to obtain fine detail of even very complex structures. The salient features of the *Xact* user interface are described, along with the major limitations of the code.

Introduction

The TLM code GTEC has been developed at Auburn University over the past few years, and its application to electromagnetics has been described at previous ACES conferences [1, 2, 3]. The code is freely available and already a number of companies and organisations are using it. One of the main disadvantages of GTEC is the complex data input format which makes it very difficult to detect errors. Even for very simple structures it is often not possible to visualize whether parameters have been set correctly.

This paper describes an X-Windows program, *Xact*, which graphically previews input files to GTEC. The program gives three two-dimensional views of the TLM mesh, one for each of the coordinate planes. A larger workspace window is available for expanded views of any one of the three coordinate planes. This workspace can also be used to display slices through the mesh of just one layer of cells to obtain fine detail of a structure. The properties of any cell within the TLM mesh can be displayed in a pop-up menu simply by pressing a mouse button on the appropriate cell. The properties which can be set for each node are:

[1]Dr. Upton is supported by SERC/NATO Postdoctoral Fellowship no. B/90/ITF/307

1. Upper boundary reflection coefficients in each plane.
2. The permittivity, permeability and conductivity of the node.
3. The type and magnitude of any excitation.
4. Whether the node is an output point.

The user interface to *Xact* is totally mouse-driven making it very easy to use. The X-Windows interface uses only the standard Xlib function calls to maintain portability. The whole program is written in C under Unix and will run on most Unix-based workstations. The program is designed to be used on colour terminals, due to the complexity of information available at each mesh cell, but it will work satisfactorily on a monochrome terminal.

In the rest of this paper, we will briefly describe how to execute *Xact*, along with specific details of all the elements of the user interface. The major limitations of *Xact* will also be described.

The User Interface

The command line for running *Xact* is;

```
Xact
```

in its simplest form. Two command line options are available to make it compatible with other X-Windows applications;

`-geometry` or `-g` to change the width, height and position of the application window.

`-display` or `-d` to change the default display on which the window appears.

See an X-Windows manual, such as [4] for a complete guide to these options. A third option, `-f`, changes the default input file. If no file name is specified, *Xact* attempts to display the input file `tlm3d.in`, which is the default input for GTEC.

For example, to run *Xact* with display on a local machine called 'donald', with the geometry set to 900 pixels by 1000 and the input file set to `test.in`, would require the following command line:

```
Xact -d donald:0 -g 900x1000 -f test.in
```

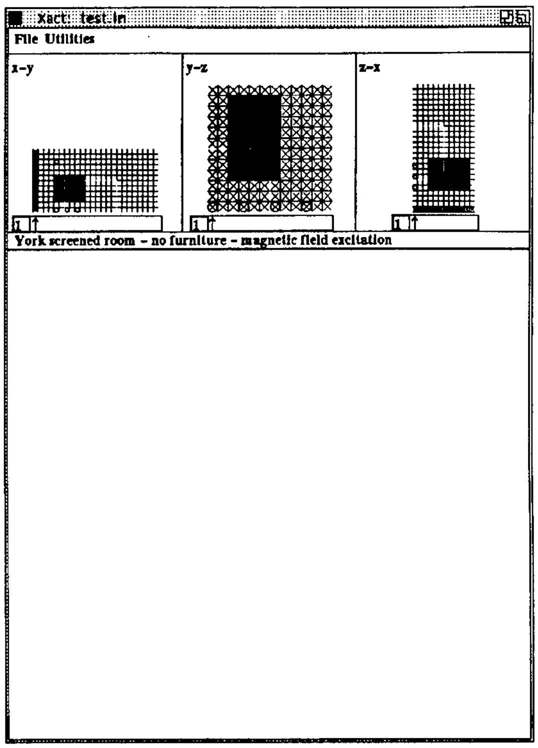

Figure 1: Overview of the *Xact* window.

When *Xact* has been executed, the user will see the display given in fig.1. This consists of a number of elements:

- A title bar giving the program name and the name of the file being viewed (in this case `test.in`).
- A menu bar containing two options for pulldown menus; "File" and "Utilities."
- Three "plane" windows giving two-dimensional projections of the three coordinate planes.
- Each plane window has an associated scroll bar to determine where slices are taken for projections in the workspace window.
- A comment window, giving the comment that appears in the GTEC input file.

- A workspace to hold expanded views of one of the plane windows and display properties of the mesh.

The use of the major elements is as given below. In each case, only brief details are given as more detail is available in the manual for *Xact* [5].

The Plane Windows

In the plane windows, the third dimension of the mesh is represented as a depth. For example, in the x-y plane the z axis is away from the viewer into the page, with $z = 1$ closest to the observer. The mesh is drawn as a series of slices of constant z, starting from the highest value of z and dropping to $z = 1$, with mesh objects closer to the observer overlaying those behind. The following objects are drawn in a cell if they are present, otherwise the cell is left empty.

- An $\times$ to show an excitation node. in the mesh.
- An ○ to represent an output point.
- A filled block to represent dielectric or lossy parameters.
- Inverted or coloured lines to display boundaries along mesh lines.

The x-y plane window from fig.1 is shown in more detail in fig.2. All the basic elements can be seen here, with a line of excitations at $x = 1$, four output points and a mesh block. Boundaries are present around three sides of the overall mesh, as well as three boundaries within the mesh that form a rectangle.

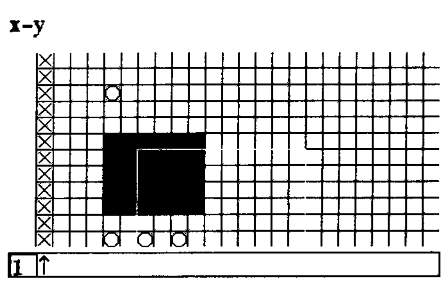

Figure 2: Detail of the x-y plane window.

Once drawn for a particular input file, the contents of the plane windows are fixed. Expanded views of the mesh, as well as slices through the mesh are drawn in the workspace (see below).

The Scrollbar

Each plane window contains a scrollbar which is used to determine how much of a particular 2D projection is displayed in the workspace window. The user moves the arrow in the scrollbar by grabbing the arrow with the mouse. A read-out of the coordinate position of the arrow is given in the box at the left of the scrollbar.

The Workspace

The function of the workspace window is to display an expanded view of one of the plane windows, allowing the user to examine the properties of individual cells. Drawing in the workspace is updated by clicking the mouse button on a plane window. The view drawn in the workspace is controlled by the scrollbar setting in the plane window clicked on and the options selected in the "Utilities" menu.

There are two modes of viewing the mesh in the workspace. Either a single layer of cells can be viewed, or the full depth of the mesh can be drawn. The latter is similar to the way the mesh is drawn in the plane windows. The switch between these two methods is enabled via an option in the "Utilities" menu. The "Single Plane" mode is useful for obtaining fine detail of a structure, whilst the "Full Depth" mode can be used to check the alignment of objects in the mesh.

Once something has been drawn in the workspace, it is possible to display the properties of a given cell by pressing the mouse button on that cell. A pop-up information box will appear describing the properties as they are defined in the GTEC input file. An example is shown in fig.3.
For all the cells the following information is displayed:

- The mesh dimensions.
- The coordinates of the current cell.
- The upper boundary reflection coefficients.
- The properties of the cell (permeability etc.).

In addition, the following information is displayed if relevant:

- The polarisation and magnitude of the cell excitation.
- If the cell is an output point.

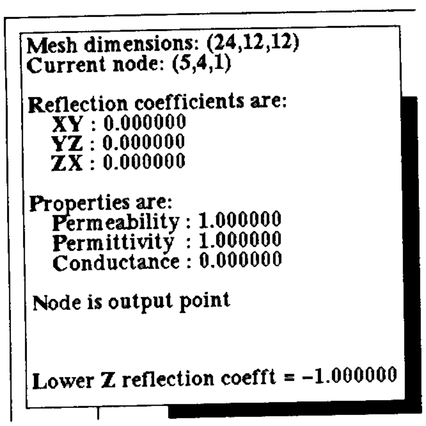

Figure 3: The workspace pop-up menu giving details of the cell properties.

- Lower boundary reflection coefficients if the cell is next to one of the coordinate planes.

The Utilities Menu

There are three options on the "Utilities" menu as shown in fig.4. Each option is a toggle option, whereby releasing the mouse button whilst the option is highlighted will invert its value. For example, "Full Depth" becomes "Single Plane" but will revert to "Full Depth" if selected again. The "Facing Planes" option enables the drawing of boundaries in the mesh that lie in the plane of the screen. Normally, these are omitted as they clutter the picture. The "Offset" option is used to view facing planes when there is also a mesh block defined in the cell. In normal operation, the latter will overlay the former but this option suppresses mesh block drawing in the cell closest to the viewer.

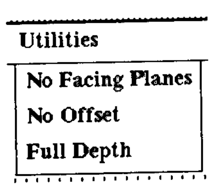

Figure 4: The "Utilities" menu.

The File Menu

There are three options in this menu; "Open...", "Start Print" and "Quit". The "Quit" option terminates *Xact* and deletes the window. The "Open" option allows the user to read in another file using a pop-up menu to display the file name. The initial file name that appears in this menu is the same as the current file to allow the user to quickly view any changes in the current file. The "Start Print" option saves the next update of the workspace in PostScript format in a file `xact.ps`. Greyscales are used to represent the colours and the output is scaled to give a reasonable size on the standard A4/8.5"×11" paper.

Limitations

Xact is designed to be a general application viewer for GTEC input files. As such it is not necessarily capable of handling every conceivable input file combination. The main limitations are:

1. It is not possible to view graded meshes with the present version of the code.
2. Very large meshes may be slow to draw because the program stores the mesh as a four-dimensional array of data. If not enough memory is available, the mesh has to be stored on disk which is very slow. Similar problems occur if other memory intensive programs are running at the same time as *Xact*.
3. Meshes with any one dimension particularly large, say > 150, are difficult to draw because the individual mesh cells become less than one pixel wide on the screen. This is largely a problem in the plane windows.

Conclusions

The main features of the X-Windows program *Xact* have been described. *Xact* is used to graphically preview input files for the TLM program GTEC and allows the user to view just one layer of cells in the TLM mesh if such fine detail is necessary. The program overcomes one of the main disadvantages of GTEC which is its complex data input format.

Xact is designed to be portable, using standard C and Xlib calls, and should run on most Unix based machines. The program performs extensive error checking on the GTEC input file (much more than GTEC itself) although these checks

have not been described in this paper due to space limitations. Although the program is designed to run with GTEC, the "input format" specific parts of the code are limited to one sub-program which should enable the user to adapt it to serve as a previewer for other TLM input data. Both the source code and the manual [5] are freely available from the authors.

References

[1] German, F.J., Gothard, G.K., Riggs, L.S., *The Modeling of Lossy Materials with the Symmetrical Condensed Node TLM Method*, Proceedings of the Seventh Annual ACES Conference, Monterey, California, March 1991.

[2] Gothard, G.K., German, F.J., Riggs, L.S., *Analysis of Radar Absorbent Material (RAM) Coated HF Wire Rope Antennas Using the TLM Method*, Proceedings of the Sixth Annual ACES Conference, Monterey, California, March 1990.

[3] German, F.J., Riggs, L.S., Baginski, M.E., *Electromagnetic Analysis by the Transmission Line Modelling (TLM) Method*, Proceedings of the Fourth Annual ACES Conference, Monterey, California, March 1988.

[4] Barkakati N., *X Window System Programming*, SAMS/Macmillan, 1990.

[5] Upton, M. and Braybrooke, S., *Xact* – X All Colour TLM. A User's Manual. Publication TN-EMC-91-03. EMC Laboratory, Concordia University.

The application of transmission line matrix modelling to a microwave heating applicator

Ian J. Dilworth B.Sc Ph.D, Senior Lecturer, Dept. Of Electronic Systems Engineering, University of Essex, Colchester, Essex. UK. CO4 3SQ

Abstract
A microwave heating system for use in a demanding environment in the nuclear industry is described. After describing the problem the time related heating profile of a phantom nuclear liquor suspension is analysed by means of a simple 2-D transmission line matrix (TLM) model which is used indirectly to obtain the temperature profile of the heated sample. The results of the modelling calculations are compared to measurements. The conclusion is made that useful qualitative data are possible using the technique and this is sufficient in this particular industrial application. It is noted however that to obtain more accurate data the modelling procedure is readily expandable to three dimensions.

Introduction
This paper attempts to outline the design and evaluation of a heating system for use in a demanding environment in the nuclear industry.

In order to perform chemistry on small quantities of nuclear liquor use has been made of RF microwave heating. There are two main problems associated in applying the technique. The first is actually getting relatively high power RF energy into the highly active nuclear chamber used for experimentation and the second is in the design of the applicator itself. With the former the only practicable means to get energy into the chamber is to site the power generation outside the chamber and feed in the RF power via a special coaxial cable. The reason for this is that any items introduced into the system become forever afterward highly active and consequently very expensive to dispose of and in addition the physical size of items for disposal is severely limited. For practical reasons easy access to the heating area is required since relatively crude mechanical 'arms' are used to manipulate the highly active liquors into place. This means that heating applicator needs to be simple and unobstructed, it is not practical to simply introduce a microwave multimode or single mode cavity into the chamber. Thus the microwave power is supplied via a coaxial cable and a (nominally) dominant mode waveguide applicator. Due to the constraints within the nuclear chamber and the desire for calibratable and repeatable liquor heating close design of the fields applied is desired. It was therefore necessary to model the effects of the changing dielectric constant with temperature and find the distribution of liquor temperature with time.

TLM modelling is well developed e.g. (1),(3),(4),(5),(6) and was chosen for the modelling because in concept it relates nicely to the physical propagation process, it is simple enough that the writer thinks he understands it, it is unconditionally stable and the calculations required are relatively straighforward and lend themselves to a computer based calculation. TLM modelling has been applied here to describe the field and hence the resultant temperature distribution in the nuclear liquor suspension. The basic idea of TLM has been described elsewhere (e.g. (11)) very briefly the idea is that a Cartesian mesh is set up (in 1-D, 2-D or 3-Dimensions) to discretise space. Then transmission lines are used to model the media and to connect the mesh, The transmission lines meet at crossing points called nodes which communicate with immeadiate neighbours - 4 in the case of a 2-D mesh. In this application such a mesh is applied. The scattering from the adjacent nodes is illustrated in figure(1).

System and modelling

The dielectric constant of the nuclear liquor is to a first approximation similar to *conductive* water although no direct measurement has yet been made of the suspensions to be used. There remains the possibility of a positive $d\varepsilon''_{eff}/dT$ characteristics in the various liquors to be experimented upon and hence the need to predict the effect this could have, should this be the case, to avoid the possibility of thermal runaway. However it was assumed for the initial model that as with non-ionic water a negative variation of dielectric properties with temperature occurs, the real $\varepsilon'$and imaginary part ε''_{eff} of the dielectric constant varies from about [80 - j12] to [50 - j2] over a temperature range of 25 to 95 degrees centigrade[8,2].

From the practical standpoint the frequency of operation of the system was chosen so that the dimensions of the heating applicator would be minimised, to allow disposal from the highly active chamber whilst, on the other hand, the lowest frequency was sought so that the special coaxial cable could handle the power and have tolerably low loss. Conveniently, the standard microwave heating frequency of 2.45GHz. at a wavelength of 12.25 cm was found to just meet both requirements.

In this engineering project it was desired to minimise, as far as possible, the design effort for the applicator although it was specifically not intended to rely on a totally empirical design. The volumetric heating is the important quantity required viz: $\varpi\varepsilon_o\varepsilon''_{eff} E^2_{rms}$ this is a straightforward quantity to calculate provided one has knowledge of the electric field magnitude within and throughout the sample. However as is well known from Maxwells equations ε, μ and σ are functions of

temperature and hence of the applied E and H fields. The nuclear liquor sample requires to be heated uniformly, as far as possible, and therefore it remains to examine whether a simple heater system used here will be adequate. By starting with a nominal (25°C) temperature for the liquor the E field distribution is found by a TLM model and hence the total power density is obtained. Then assuming for simplicity that no thermal radiation, convection or conductive loss occurs and that there is *no* significant mass transfer in the time interval considered, the total power absorbed can be used to obtain the new liquor temperature distribution by solving the standard heat transfer equation after a time period δt:

$$\delta T/\delta t = d_c \, 2 \, \delta T/\delta x^2 + \delta P/\rho\kappa$$

where P is the power, d_c is the temperature diffusivity constant, T is the temperature, t the time, ρ the density and κ the specific heat. Hence the new dielectric constant etc. can be found (interpolated from data in ref. [8]). The time period is then incremented - in small enough periods that the parameters change little, and the new TLM nodes are recalculated. The process is then iterated so that the dynamic temperature profile may be derived. The problem thus amounts to the calculation of the electric fields at the matrix nodes which is done, parametrically, for the expected variation of dielectric constant with temperature.

Starting the modelling from scratch the intention was to use, at least initially, just a two dimensional TLM mesh to try and get an intuitive 'feel' for the heating process. In the initial evaluation this appeared justifiable since the system operates nominally in the TE_{10} mode and so the maximum field interaction is at the centre of the applicator. Since the sample is symmetric and of relatively small volume then to a first approximation a 2-dimensional TLM model is considered adequate to yield useful qualitative information.,

The TLM model employed follows that of Johns and Beurle[1] and employs a Cartesian mesh of 0.05λ (0.1λ is the minimum requirement[1]) ~0.68mm spacing in the dielectric. The dielectric is accounted for in the mesh by a two dimensional transmission line network consisting of 'shunt' and 'series' nodes. The sample container is of square cross-section and of small enough 'x' dimension to allow a plane wave to be set up by applying a pulse to the adjacent leading edge matrix nodes with reasonable accuracy compared to the actual physical arrangement. The radiation and scattering from the nuclear liquor sample boundaries and the edges of the mesh are modelled as free space with zero reflection coefficients. The waveguide aperture is assumed perfectly matched to the surround by employing suitable transmission

lines at the matrix nodes. In fact measurements made using a reflectometer showed that the return loss from the surround (without the liquor absent) was about -23dB. Reflections from the nuclear liquor everywhere except directly back into the applicator are assumed to be perfectly absorbed. Measured reflections from the liquor directly back into the applicator were of course of interest. The resultant standing wave pattern can be calculated and compared to measured values although this has only so far been done at room temperature (~25°C).

Results

Each of the mesh nodes yields a value of the electric field which is in turn proportional to the square root of power density at that position. i.e. $|E| = (P/\sigma)^{1/2}$ thus the incident field and hence power along the space above the plate may be calculated and used in the procedure outlined. The calculations can be compared with measurements of the temperature of the sample after fixed periods of RF heating exposure at various positions on the support plate assuming that the mass heated is well mixed and that the average temperature is related to the integrated temperature distribution. In figure(2), which indicates the two dimensional x,z plane for a given y cut which in this case is modelled for the maximum field i.e. in the centre of the sample space, the calculated initial field and that after 20 seconds of heating is shown. In figure(3) the derived temperature distribution after 20 seconds is shown compared with the distribution obtained by linear calculation.

Conclusions

This investigation was essentially practical in that it was required to find the dynamic temperature profile for the heating of a nuclear liquor by microwaves. The modelled data were compared with measurements to confirm that a TLM model could be used to derive the volumetric temperature more accurately than a linear model. It turned out that after about 20 seconds of heating, mass transfer of the heat within the relatively small sample volume used in experimentation quickly produced a homogeneous temperature. The fact appears that some heat transfer due to the nuclear liquor suspension in (thermally induced) motion must be occurring after only a few seconds of heating. This meant that the direct comparison of the TLM derived temperature profile with actual measurements was not strictly possible. Nevertheless the trend of averaged temperatures so modelled agreed with actual measurements within about +/-15%. More accurate modelling would require a 3-D mesh and or a
more detailed heat transfer model.

References

(1) P.B Johns and R.L Beurle, "Numerical solution of 2-dimensional scattering problems using transmission line matrix", Proc. IEE, 118 (9), Sept. 1971.
(2) Metaxas and Meredith, "Industrial microwave heating", P.Peregrinus, 1988.
(3) D de Cogan M. Henini, " TLM modelling of the thermal behaviour of conducting films on insulating substrates" J. Physics D, applied phys, 20, 1987, 1445-1450.
(4) P.B Johns, " A Symmetrical condensed node for the TLM method", IEEE Trans., MTT-35, 1987, pp370-377.
(5) S. Akhtarzad and P.B Johns "The solution of Maxwells equations in three space dimensions and time by the TLM method of numerical analysis", proc. IEE, 122, 1975, pp1344-1348.
(6) C. Christopoulos and P. Naylor, "Coupling between EM fields and multiconductor transmission systems using TLM", Int. Journal of Numerical Modelling, 1,1988, pp31-43.
(7) 'Radioisotope review sheet - radiation stability of materials', Isotope Research Division, AERE, Harwell, Oxon, UK.
(8) Von Hippel 1954.
(9) Z. Shouzheng and J.B. Davies "Non-linear modelling of Microwave heating problem". Int conf. on Computation in Electromagnetics, IEE, Nov 1991. pp 86- 89.
(10) S.H.Pulko and P.B. Johns, "Modelling of thermal diffusion in 3-D by the TLM method....." Comms in Appl. Numerical methods, 3, 1987, pp 571-579.
(11) W.J.R. Hoefer, "The transmission line matrix method, theory and applications",IEEE Trans MTT, no 10, Oct 1985, pp 882-893.

Figure(1)

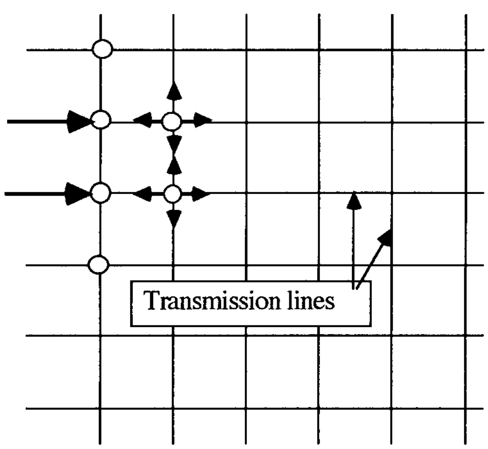

The TLM scattering process. An incident wavefront can be constructed at adjacent nodes, as for example shown with the two large left side arrows. The transmitted pulse are scattered into four connected transmission lines routed to the next nodes. Kirchoffs laws are applied to describe the reflected and incident voltages and currents. A reflection coefficient of -0.5 results from the 1/3 Z impedance 'seen' by the pulse incident on a node.

Figure(2) shows the x,z plane, y amplitude plot of the calculated initial field and the field after 20 seconds of heating.

Figure (2)

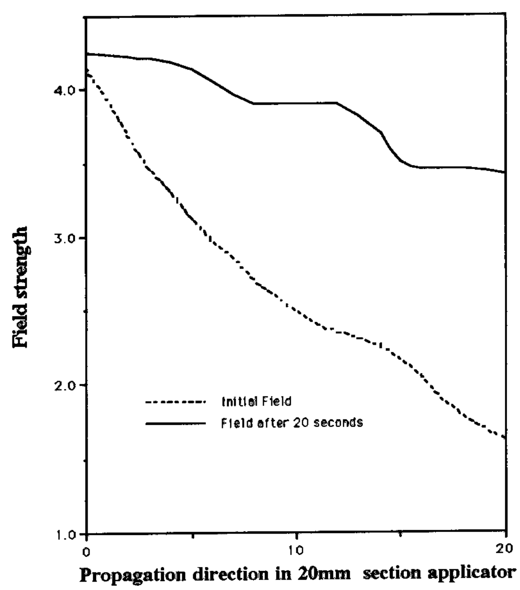

Figure(3) shows the derived temperature distribution after 20 seconds assuming a sinusoidal variation in the x direction of the field, compared with the distribution obtained by linear calculation.

Figure(3)

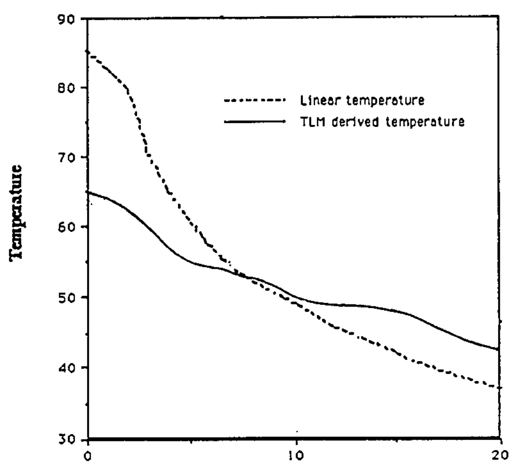

Z direction (mm) along sample space

SESSION 13 - "FINITE DIFFERENCE TIME DOMAIN"

(Part 2)

Moderator: Karl Kunz

A Dedicated VLSI Architecture for Finite-Difference Time Domain Calculations

J. Raley Marek, Mark A. Mehalic, Andrew J. Terzuoli, Jr.
School of Engineering
Air Force Institute of Technology
Wright-Paterson AFB, Ohio 45433

Abstract

This study investigated increasing the speed of Finite-Difference Time Domain (FDTD) cell calculations through a special purpose, Very Large Scale Integration (VLSI) architecture. A VHSIC Hardware Description Language (VHDL) simulation of the proposed chip established design feasibility and provided performance estimates: 350 ns to generate the first cell value, 200 ns thereafter (30 MFLOPS maximum double-precision). This study also implemented boundary conditions in hardware as well. No new hardware was designed; instead, the algorithm was translated into microcode for use by the AFIT Floating-Point Application Specific Processor (FPASP). The first boundary value is computed in 850 ns, with successive results following every 300 ns (43 MFLOPS maximum double-precision). Execution times of standard FDTD FORTRAN codes were compared to times of modified codes simulating the presence of the above hardware. On a 66 cubic-cell, free-space computational domain, these chips reduced total FDTD code execution time by a factor of 4.9, and cell and boundary calculation time by a factor of 9.5 [1].

I. Study Definition

The objective of this study was to speed up FDTD cell calculations through the use of VLSI. This paper presents a design of such a circuit and investigates how it might improve the run times of FDTD computer programs. Furthermore, the possibilities of speeding up the boundary value calculations are also presented. This study assumes that data is in IEEE 754-1985 double-precision format, and that suitable interface circuitry and high-speed RAM are available (1-Mbit 20-ns static RAM chips are already available for under \$100, and 4-Mbit RAMs are soon to come [2]).

II. FDTD Algorithm

Maxwell's curl equations are approximated by centered differences, with H-field values offset by one-half intervals from E-field values in both space and time [3]. The method solves alternately for E and H as time is incremented in one-half time steps. Note that all of the FDTD cell equations can all be represented in the following form:

$$Field_{next} = K1 \times Field_{prev} + K2 \times \begin{bmatrix} Dual_1 - Dual_2 \\ + Dual_3 - Dual_4 \end{bmatrix} \tag{1}$$

The constants are defined for E-field calculations as follows:

$$K1(i,j,k) = \frac{1 - \dfrac{\sigma(i,j,k)}{2\varepsilon(i,j,k)}}{1 + \dfrac{\sigma(i,j,k)}{2\varepsilon(i,j,k)}} \tag{2}$$

$$K2(i,j,k) = \frac{\Delta t}{\varepsilon(i,j,k)\delta} * \frac{1}{1 + \dfrac{\sigma(i,j,k)}{2\varepsilon(i,j,k)}} \tag{3}$$

where δ is the lattice spacing increment, Δt is the time step increment, ε is the real, dielectric permittivity of the material at a particular location, σ is the conductivity of the material at a particular location , and *Dual* is the dual of the field being calculated [4] (see Figure 1). Constants for the H-field are similar expressions. This simplified form leads to a straightforward method to compute these fields in hardware.

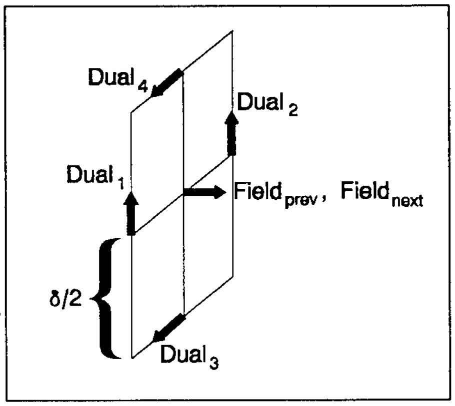

Figure 1 -- Modified Names

The second-order Mur radiation boundary condition equations require a total of sixteen adds and seven multiplies to generate a value (the leading terms of each multiply turn out to be constant for a particular problem) when computed as originally presented [5]. Combining terms to decrease the number of operations, gives (x=0 face):

$$\begin{aligned}E_z^{n+1}(0,j,k+\tfrac{1}{2}) = &-E_z^{n-1}(1,j,k+\tfrac{1}{2}) \\ &+K1*\{E_z^{n+1}(1,j,k+\tfrac{1}{2})+E_z^{n-1}(0,j,k+\tfrac{1}{2})\} \\ &+K2*\{E_z^{n}(0,j,k+\tfrac{1}{2})+E_z^{n}(1,j,k+\tfrac{1}{2})\} \\ &+K3*\begin{bmatrix} E_z^n(0,j+1,k+\tfrac{1}{2})+E_z^n(0,j-1,k+\tfrac{1}{2}) \\ +E_z^n(1,j+1,k+\tfrac{1}{2})+E_z^n(1,j-1,k+\tfrac{1}{2}) \\ +E_z^n(0,j,k+1\tfrac{1}{2})+E_z^n(0,j,k-\tfrac{1}{2}) \\ +E_z^n(1,j,k+1\tfrac{1}{2})+E_z^n(1,j,k-\tfrac{1}{2}) \end{bmatrix}\end{aligned} \tag{4}$$

where

$$K1=\frac{c\Delta t-\delta}{c\Delta t+\delta} \tag{5}$$

$$K2=\frac{2\delta^2-4c\Delta t^2}{c\Delta t+\delta} \tag{6}$$

$$K3=\frac{(c\Delta t)^2}{2\delta(c\Delta t+\delta)} \tag{7}$$

This expression now contains only twelve adds and three multiplies. This equation was also simulated in hardware, laying the groundwork for a complete, single-board FDTD computational engine, capable of calculating cell and boundary field values.

III. Design and Architecture of the FDTD Chip

This is a single-chip design containing five registers, one multiplier, and one adder, all double-precision. Data enters the chip via a 64-bit data bus, which is multiplexed to output the calculated result when completed (multiplexing keeps the pin-count low). Numbers are read into the chip, one at time, instead of in parallel. This increases the amount of time it takes to input data, but keeps the data bandwidth at 320 Mbytes/sec.

Since this chip would serve as an FDTD vector processor, care was exercised to ensure that maximum processing efficiency was obtained when calculating streams of data elements.

Even as computations are continuing on one set of data, new data is simultaneously being read in and processed. Operating in this capacity, the interface logic external to the chip must be capable of generating pointers to the addresses of at least eight different locations in memory to access all of the operands and specify a location to store the result (see Equation (1)). Also this logic must possess a counter that would signal the output of the last result and halt the FDTD chip.

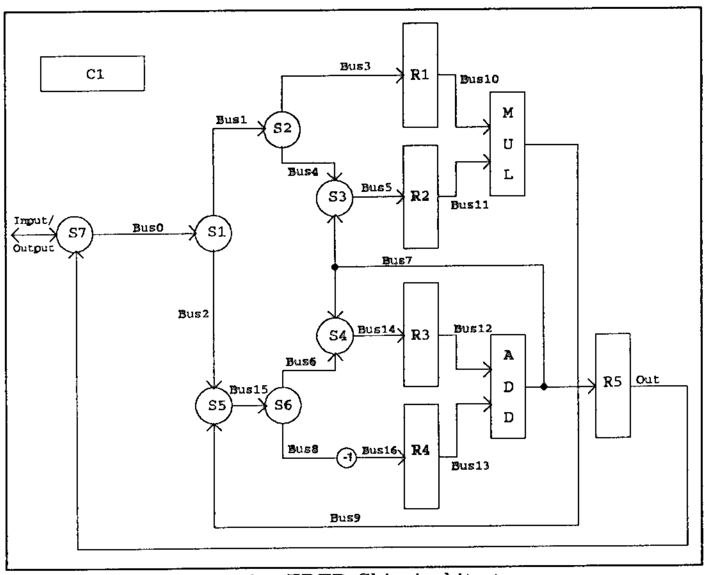

Figure 2 -- FDTD Chip Architecture

Figure 2 shows the overall layout of the FDTD chip design . Two of the five 64-bit registers are the input registers to the multiplier (R1,R2), two are input registers to the adder (R3,R4), and the last holds the computed result until it is time for output (R5). Of the six bus switches, three are one bus to two bus selectors (S1,S2,S6) and three are two bus to one bus multiplexers (S3,S4,S5). A special multiplexed bus switch (S7), connected to the input/output pins, is used to route incoming data into the chip and outgoing data from the result register. The multiplier (MUL) and adder (ADD) take two cycles to calculate results. There are a total of eighteen different 64-bit buses running between the switches, registers, and floating point units. An eight-state sequencer (C1) controls the operation of the above hardware (signals omitted from the figure for clarity). A reset signal clears the registers and sets the sequencer to state zero. The only IEEE exception support provided is for overflow. This signal is made available outside the chip but has no effect on operation. The signal is cleared by a non-overflowing calculation or a reset signal.

The first data elements (the first two of the four dual-field components, the E_{prev} field value, the third dual-field component and the constant K1) are sent into the chip during cycles t_0 to t_4 (and latched at the beginning of t_1 to t_5, see Figure 3). During t_5, the result is made available to the off-chip circuitry. No data is output during the first occurrence of t_5, however, since all of the data is not yet entered and the calculations are not complete until the next occurrence of t_5. During t_6, the last dual-field component is entered and the last constant, K2, is loaded during t_7, the final clock cycle in the sequence. A new data set is entered beginning with t_0. During the next occurrence of t_5, the result from the previous data set is output. Thus, the output of the first data result occurs after 14 clock cycles, with subsequent results following in 8 cycle intervals.

The critical path involves the addition of the four dual-fields, their multiplication by K2 and addition to K1*$Field_{Prev}$. Since each multiplication and addition lasts two clock cycles, the fastest time possible to achieve a result is ten clock cycles for the math operations, plus two to read in the first two operands, plus one to output the result or 13 cycles. This

design arrives at the first result in fourteen clock cycles. The fourteenth clock cycle provides a gap in the sequence of operations to output a result from the previous data set. After the first result is output, the input/output bus is continuously transferring data and answers are generated every eight cycles.

The VHDL timing results showed that the first output of the FDTD chip occurred at 350 ns when reset fell at the leading edge of the clock pulse, and at 375 ns when reset fell anywhere else within the clock pulse. Subsequent outputs occur at 200 ns intervals. These numbers correspond to 14 cycles for the first output and eight cycles for every output thereafter, given a 25 ns clock.

To characterize the impact an FDTD chip would have on electromagnetic analysis, it was necessary to obtain an FDTD FORTRAN code and make time measurements. (All measurements were made on SPARCstation 2 workstations). First, the code was run as provided, with no changes at all. Next, the code was modified to reflect the presence of a FDTD chip that would perform the FDTD cell equations. This was simulated by assignment statements specifying the locations of the vectors of data to be processed, as well as the number of sets of data and the location where the results were to be stored. Note that the FDTD chip calculation times are for double-precision while the FDTD code uses only single-precision.

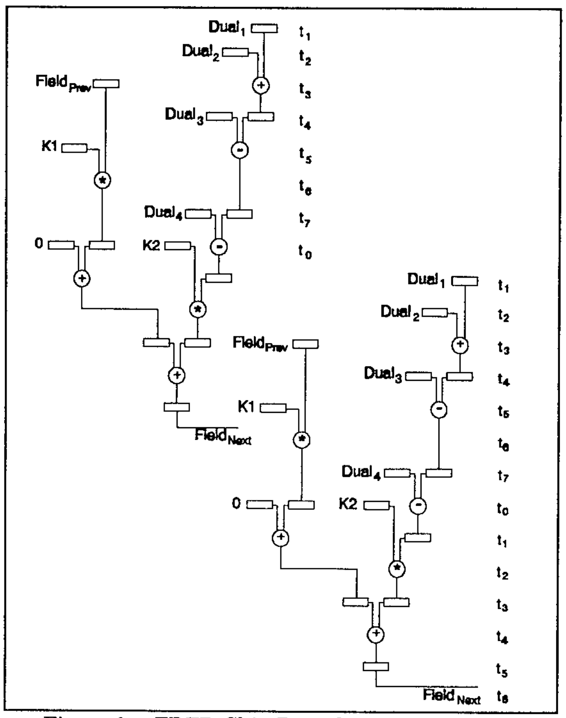

Figure 3 -- FDTD Chip Data Sequence Diagram

The original code configuration ran in 2 hours and 17 minutes. The vectorized code ran in 28 minutes. This time is increased by the estimated calculation time of the FDTD chip operating on the vectors. The run time of the FDTD chip can be expressed by the following (in ns):

$$\textit{FDTD Chip Run Time} = n \times 200 + 150 \tag{8}$$

where n is the number of values (results) to be calculated. Each full time step requires 12,545 calculations of vectors 64 elements in length and 12,416 calculations of vectors 65 elements in length. With 1024 total time steps, the full calculation time of the FDTD chip is 5.56 minutes. Therefore, the total run time of the problem with the FDTD chip is 33.6 minutes, a factor of four reduction in the original execution time of 137 minutes.

In order to see the actual benefits of the FDTD chip with respect to just the calculation time of the FDTD problem (and not the problem setup, initialization, and data reduction time), the original code was modified to exclude all of the cell and boundary condition calculations. The run time for this "overhead" was 15 minutes. Subtracting this overhead from both configurations, the original possesses 122 minutes of single-precision FDTD calculations, while the FDTD chip configuration possesses only 18.6 minutes of double-

ny precision FDTD calculations, a speed-up of a factor of over 6.5 in the actual FDTD algorithm calculation process.

IV. A Radiation Boundary Condition Evaluator Using the FPASP

Due to the complexity of the second-order Mur expression, it was decided to implement the boundary value algorithm in microcode using AFIT's FPASP. The FPASP is, in its simplest form, a ROM-microcoded, high-speed floating-point processor design, capable of performing one double-precision multiplication and one double-precision addition every two clock cycles. (See Figure 4 for a simplified diagram of the FPASP [6].) Both of the floating point units are pipelined so that a maximum of two double-precision results are generated every clock cycle (80 MFLOPS with a 40 MHz clock). The chip possesses several 32-bit registers, including 25 general-purpose double-precision registers, four incrementable registers, and memory pointers. In contrast to the FDTD chip described earlier, the FPASP requires little outside logic since pointers, counters, and memory signal drivers are all located on the chip. Since the control resides in programmable read only memory, FPASPs can be cheaply produced in mass numbers and microprogrammed by the individual users, each according to his needs.

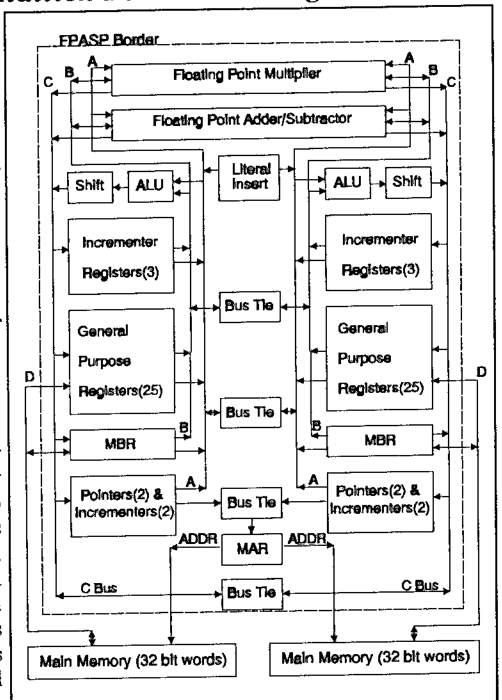

Figure 4 -- FPASP Architecture

As with the FDTD chip, this FPASP boundary condition evaluator microcode was designed to operate exclusively in double-precision. Care was taken to keep the floating-point adder as busy as possible since additions are the predominate operation in evaluating the expression (Equation (4)). Multiplies were worked into time slots during the additions. The microcoded algorithm was condensed down to a total of twelve additions and three multiplies. This result is available after 32 clock cycles. Thereafter, only ten additions and three multiplies are required. These results are available every ten cycles after the first (note that an addition is performed every clock cycle). This data is based on VHDL simulations of the FPASP using the developed microcode.

In order to assess the impact of the FPASP boundary condition solver, the FDTD code was modified to simulate the ability of the chip to process vectors of data elements. Again, this was done by simulating the passing of a pointer to a data array with an assignment. Since the microcode for this study was completed before receipt of an actual FDTD code, it did not incorporate all pointers necessary to access all data structures as written in the FORTRAN. However, this necessitates, at most, the addition of two microcode lines. This means the first result is available after 34 clock cycles and following results are available at 12 cycle intervals, and can be represented by the following relation:

$$\textit{Boundary Condition Calc Time} = n{\times}300{+}550 \tag{9}$$

where n is the number of data sets in the vector and the time is in nanoseconds.

The FORTRAN code was modified by removing the innermost loop in the radiation subroutines. The remaining variables simply specify the location of the data vector. The data must be stored in the proper order to ensure that data is accessed correctly as the FPASP chip progresses down the vector of data. (This was not specifically accomplished in our simulations, but could be accomplished by re-indexing the equations which appear at the tail of each of the radiation subroutines in the FDTD code.)

Recall, the time to run the original FDTD code was 2 hours and 17 minutes. The time to run the modified program simulating both the FPASP and FDTD chips was 22 minutes. To this is added the processing times of the FDTD chip (5.56 minutes) and the FPASP chip. The FPASP must compute 124 vectors of length 61, 370 vectors of length 62, and 248 vectors of length 63 every time step for 1024 time steps (an execution time of 14.6 seconds). The total execution time is therefore 27.8 minutes. Given the original code had a run time of 137 minutes, this dual chip engine reduced execution time by a factor of 4.9. In order to isolate the actual effect of the chips on just FDTD calculations, the overhead is subtracted from both calculations, giving a calculation time of 122 for the original FDTD code calculations, and 12.8 for the calculation time for the FDTD engine. These numbers reveal a speed-up of 9.5 for just the calculation of the FDTD cell and radiation boundary condition equations alone. This is still conservative considering that problems involving magnetic or electric loss would slow down the FDTD code, but would have no effect on the calculation time of the FDTD chip. Figure 5 shows summary of the times discussed above (data in Table 1 of the Appendix). These comparisons are made for the different cases that were discussed earlier.

These results apply to the speed-up that one might expect on a high-performance SPARC2 workstation. For a person running FDTD on a Macintosh or IBM PC, the speed-ups would most likely be even more substantial. Since the FDTD and FPASP chips would be performing the majority of the numerical operations, the total run times on these machines would compare favorably to those of the SPARC2/FDTD system. For an idea on the greatest possible improvements, the upper limits for the speed-up in overall run time is about 9.1, assuming zero calculation time, while the upper limit for the speed-up in calculation time alone is about 21, assuming the measured time is 15 minutes (all overhead, no "Code Time").

VI. Future Outlook

A likely parallel architecture features several of the FDTD boards plugged into the bus of a host workstation. These would possess the same features of the board described in this study as well as a DMA communications controller. This controller would be used to connect all of the boards together in the form of a 2-D or 3-D grid, perhaps using optical fiber technology. The problem space would be allocated to the memory of each of the boards, perhaps through the system bus or through the DMA communications chip connected to dedicated disks. The geometry of the partitioning would depend on several factors, especially communication time. Directions on which operations to perform would come from the host. With sixteen nodes, one could expect to solve a problem with 132 cells by 132 cells by 264 cells in about 27.8 minutes (as above) plus communication time.

For comparison, increasing the number of iterations from 1024 to 1800 (a factor of 1.76 times everything but the overhead) results in a run time of 37.5 minutes (plus communication time) to solve a problem with 27 million vector field unknowns. Cray Research reports solving a FDTD problem with 23 million vector unknowns after 1800 time steps on a Cray Y-MP/8 in 3 minutes and 40 seconds [7]. Assuming the FDTD boards could be produced for under $20,000 each, a sixteen node FDTD accelerator could solve Cray size problems for $320,000, less than 10 times slower but 100 times cheaper (assuming a $30 million Cray cost). Defining a performance metric as the cost of a computer, times the problem run-time (1800 time steps), divided by the number of cells in the problem (time cost per cell), we can see the performance of the FDTD engine versus other computers (including the Wavetracer, an FDTD-specific, massively parallel computer) in Figure 6 (data in Table 2 of the Appendix).

As should be the case, the FDTD specific machines offer lower time costs per cell than the general-purpose machines. Note that the FDTD engine is better than the Cray by a factor of 10 and the Wavetracer by a factor of 3.5. The SPARC2 is limited by the relatively small problem size it can handle in main (RAM) memory and the Cray by the initial cost. The FDTD engine, on the other hand, is scalable in small dollar increments ($20,000) so that one could start small and upgrade as budget permits and problem demands. This scalability is virtually limitless since the grid communication scheme requires that each node communicate only with nearest neighbors during computations. (Of course, only a limited number of nodes can be controlled through a simple bus architecture, so some other means of control would be implemented for large numbers).

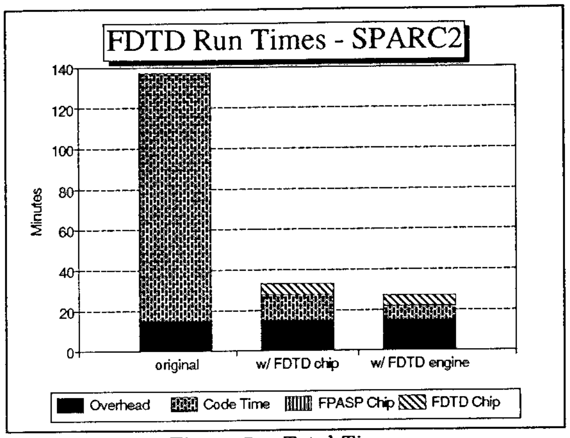

Figure 5 -- Total Times

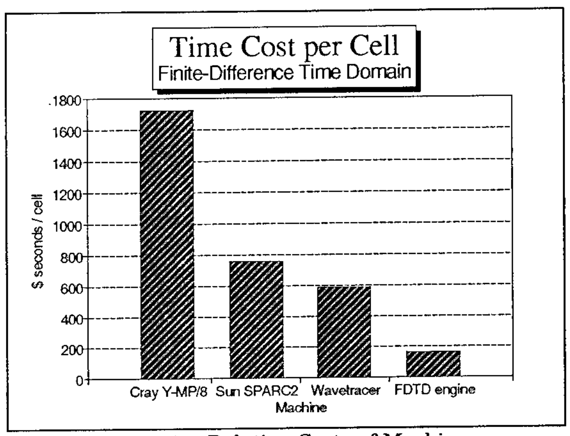

Figure 6 -- Relative Costs of Machines

VII. Conclusions

This study demonstrated the feasibility of a chip design which would directly and exclusively compute the FDTD cell field expressions. It also developed an FPASP microcode algorithm for the evaluation of second-order Mur radiation conditions at FDTD problem space boundaries. This study sought to further demonstrate the impact of these designs on typical FDTD codes and problems. These designs appear to speed up computational time by factors of 9.5 and corresponding total run times by a factor of 4.9. Given these designs could be fully implemented for under $20,000, they form the basis of an FDTD machine running at the speed and power of ten fully parallel SPARC2s for the price of just over two. In the area of architecture, this research has demonstrated the ability of the FPASP to adeptly handle workloads other than those related to signal processing, the FPASP program's original design objective. It also appears to be quite possible that the FPASP could perform the FDTD cell calculations just as well as the dedicated architecture described in this study. Both algorithms could be microcoded in the FPASP and called by the host according to the computation to be performed at that time. Due to the ability of the FPASP to maintain and modify pointers to memory locations, much of the interface hardware required by the FDTD chip could be eliminated, simplifying board design, freeing valuable board area, and lowering costs. Given the FPASP would be produced in much larger numbers than the FDTD chip, the costs associated with a special purpose architecture would be eliminated, further lowering the price of the final product.

Appendix -- Data for Performance Comparison

Table 1 -- Execution Times of Codes

CODE	MINUTES
ORIGINAL	137
VECTORIZED CELLS	28
ALL EQUATIONS VECTORIZED	22
OVERHEAD	15

Table 2 -- Data for Figure 5

	cost	time (secs)	number of cells
Cray Y-MP/8	$30 Million	220	3,833,000
SPARC2	$15,000	13,767	287,500
Wavetracer	$400,000	1,530	1,049,000
16 node FDTD engine and host	$340,000	2,220	4,600,000

Acknowledgements

The authors thank Dr. Raymond Luebbers of Pennsylvania State University for the use of his FDTD FORTRAN code.

References

[1] Marek, Capt James Raley. *An Investigation of a Design for a Finite-Difference Time Domain (FDTD) Hardware Accelerator*. MS Thesis, AFIT/GE/ENG/91D-38. School of Engineering, Air Force Institute of Technology (AU), Wright-Patterson AFB OH, December 1991.

[2] Child, Jeffrey. "256-kbit SRAMs provide many choices, while 1-Mbit chips gain speed," *Computer Design* (30: 99-105) April 1, 1990.

[3] Yee, Kane S. "Numerical Solution of Initial Boundary Value Problems Involving Maxwell's Equations in Isotropic Media," *IEEE Transactions on Antennas and Propagation*, 14: 302-307 (May 1966).

[4] Taflove, Allen, and Morris E. Brodwin. "Numerical Solution of Steady-State Electromagnetic Scattering Problems Using the Time-Dependent Maxwell's Equations," *IEEE Transactions on Microwave Theory and Techniques*, 23: 623-630 (August 1975).

[5] Mur, Gerrit. "Absorbing Boundary Conditions for the Finite-Difference Approximation of the Time-Domain Electromagnetic-Field Equations," *IEEE Transactions on Electromagnetic Compatibility*, 23: 377-382 (November 1981).

[6] Comtois, Capt John Henry. *Architecture and Design for a Laser Programmable Double Precision Floating Point Application Specific Processor*. MS Thesis, AFIT/GE/ENG/88-5. School of Engineering, Air Force Institute of Technology (AU), Wright-Patterson AFB OH, December 1988.

[7] Katz, Daniel S. and Allen Taflove. "Large-scale Methods in Computational Electromagnetics," *Cray Channels*, 13: 16-19 (Spring 1991).

"FDTD CALCULATIONS OF MICROWAVE ABSORPTION IN THE HUMAN HEAD"

P J Dimbylow

National Radiological Protection Board, Chilton, Didcot,
Oxon, OX11 0RQ, United Kingdom

Abstract

This paper describes how the finite-difference time-domain (FDTD) method can be used to calculate the absorption of power in a fine-scaled, heterogeneous, realistic model of the head. Exposure from plane wave and dipole sources are considered.

1. Introduction

All biological objects exhibit a resonant behaviour, marked by a significant increase in absorbed energy per unit incident energy when the wavelength of the incident radiation is comparable to the object dimensions. A heterogeneous object such as the head can also undergo a layer resonance, a focusing effect which causes an enhanced power transmission through the surface layers. Hence, there is a concern with power deposition in the head, particularly, in the eyes and the brain at rf and microwave frequencies.

This paper describes how the FDTD can be used to calculate the specific energy absorption rate (SAR) in a fine-scaled, heterogeneous, realistic model of the head for plane wave and dipole sources. The phantom has been derived from an atlas of cross-sectional anatomy. The 126,000-cell head model comprises of brain, bone/fat, muscle skin, blood, air and eye humour, lens and sclera.

2. Theory

The Finite-Difference Time-Domain (FDTD) method is inherently suitable for and is being increasingly used in calculating the interaction of electromagnetic fields with complex, 3-D, lossy dielectric bodies (e.g. Chen and Gandhi, 1989; Dimbylow, 1990). The underlying theory has been well documented (e.g. Taflove and Umashankar, 1990) and only a brief description is given here.

The computational domain is divided into a three-dimensional lattice of cells which are assigned individual electrical properties. Time-stepping for the FDTD method is accomplished by an explicit finite-difference procedure due to Yee (1966). For a cubic-cell space lattice, this procedure involves positioning the components of E on the middle of the edges and the components of H at the centre of the faces on a unit cell of the lattice. The calculation then leap-frogs, evaluating E and H at alternate half-time steps. In this manner, centred difference expressions can be used for both the space and time derivatives to attain second-order accuracy. To ensure the stability of the time-stepping algorithm Δt is chosen to be $\Delta t = \Delta/2c$ so as to

satisfy the inequality $c\ \Delta t \leq \Delta/\sqrt{3}$ where c is the speed of light. Time-stepping proceeds until equilibrium has been reached. A domain enclosing the target and a boundary condition on the surface of the domain must be chosen to numerically mimic the unbounded region outside the domain by absorbing the outgoing scattered waves. A finite difference scheme for a second order absorbing boundary condition has been devised by Mur (1981). The scheme does not work near edges where planes meet because it will require points outside the domain. To overcome this problem it was assumed that the scattered wave propagated from a point origin with a l/r dependence, where r is the distance from the origin, and that the field at the edges was related to adjacent fields by a propagation delay (Taflove and Umashankar, 1990). A Faraday's Law contour path was used to derive the circumferential H fields immediately adjacent to the wire (Taflove et al., 1988) when a dipole source was modelled. This approach allows the incorporation of near-fields physics into the time-stepping relationships. The dipole was excited by driving a voltage across the central gap.

3. Head Model

The model of the head was derived from the whole body phantom developed at the University of Utah (Sullivan et al, 1987). The anatomy of the human body was taken from Eycleshymer and Schoemaker (1911) which contains cross-sectional diagrams of horizontal sections with a spacing of about one inch in human cadavers. The data base consists of 6.35 mm (¼") square grids for each horizontal section. Each cell of the grid is assigned a number corresponding to its tissue type. Since the sections are for somewhat variable separations, typically, 2.3-2.7 cm, a new set of equispaced layers at 6.35 mm intervals was defined to construct a head model with cubical cells. As the frequency increases the cell size must decrease to remain less than a quarter of a wavelength. Taking a relative permittivity of $\varepsilon_r \sim 50$ leads to a maximum frequency of 1.67 GHz for $\Delta = 6.35$ mm. Therefore, the cell size was halved to $\Delta = 3.17$ mm to enable the exploration of higher frequencies. This results in an eight-fold increase in the number of cells in the head to

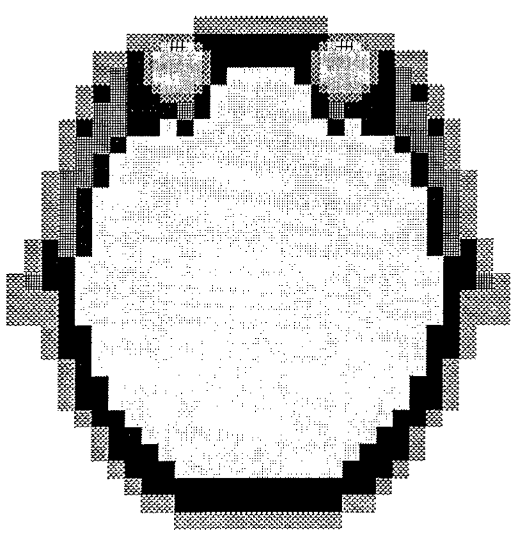

1. Horizontal cross-section through the anatomical model of the head at the eye

126,000. This increased resolution has enabled a more detailed structure of the eye to be included. The eye is modelled as a sphere 8 cells in diameter and has 4 types of tissue. These are lens, humour, a composite lens/humour and a composite sclera/humour. Figure 1 is a horizontal section showing the model structure through the centre of the eye.

4. Results

The specific absorption rate, SAR is defined as

$$SAR = \frac{\sigma |\tilde{E}|^2}{\rho}$$

where σ is the electrical conductivity, ρ the density and $\tilde{E}$ is the root-mean square (rms) electric field.

Figure 2 shows a histogram of the SAR across the section through the eyes, depicted in figure 1, for AP irradiation of the adult at 800 MHz. The front of the head faces the top righthand corner. Energy is preferentially absorbed in the high conductivity tissues such as the eye, brain, muscle and skin. The maximum absorption occurs in the eyes. Bone has a low conductivity resulting in lower power deposition in the skull. The absorption in the brain reveals a complex standing wave pattern with a strong local maximum in the centre. A detailed description of these plane-wave exposure calculations can be found in Dimbylow and Gandhi (1991), where irradiation from the front and side of an adult and an infant are considered for frequencies ranging from 600 MHz to 3 GHz.

Calculations have also been performed on the coupled head-dipole system. The absorbing boundary was placed 10 cells from the nearest anatomical feature or 20 cells from the dipole whichever was farthest. Figure 3 shows an example of the SAR distributions produced in an infant head for a 900 MHz resonant half-wave dipole. The adult steplength of 3.17 mm was linearly scaled by a factor of 0.7, derived from surface area data for a 1-year old compared with an adult from ICRP (1975), for the infant head model. The resultant steplength is 2.22 mm and the volume is a third of that for the adult. The centre of the vertical dipole is in line with the middle of the left eye and the separation is 16 cells which is 3.5 cm. This position results in a total of 950,000 cells in the calculation domain.

5. Prospectus

Future work will concentrate on the development of more detailed phantoms from serial medical imagining data and their application to consider the energy deposition from portable communication equipment.

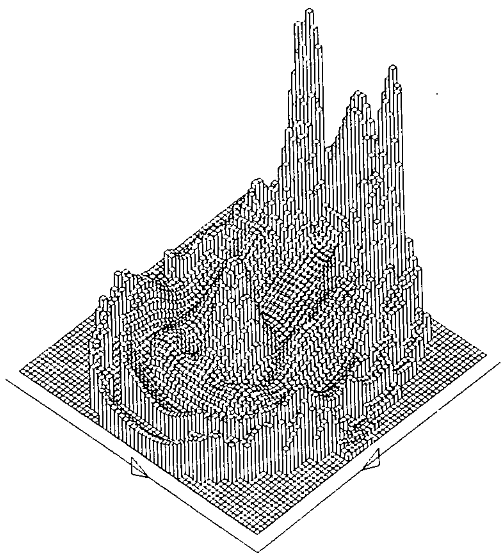

2. A histogram of the SAR across the section through the eyes, depicted in figure 1, for AP irradiation of the adult at 800 MHz. The front of the head faces the top right-hand corner. The heights are relative, normalised to the highest value in the section.

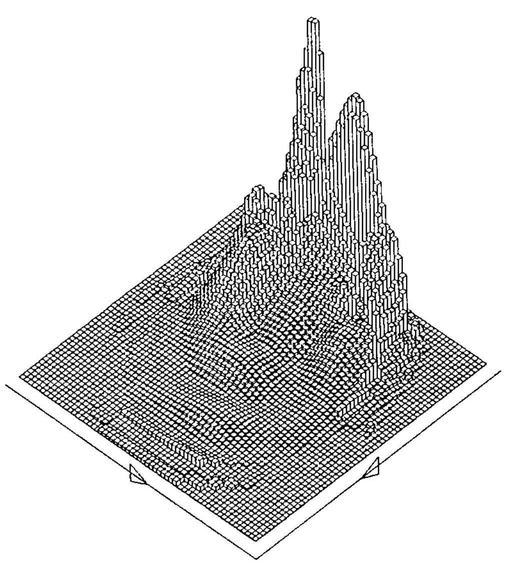

3. The SAR across the section through the eyes for irradiation of the infant head by a 900 MHz dipole. The centre of the dipole is aligned with the middle of the left eye and the separation is 3.5 cm

References

Chen, J-Y and Gandhi, O P, 1989, RF currents induced in an anatomically-based model of a human for plane-wave exposures (20-100 MHz), Health Phys., 57 (1), 89-98.

Dimbylow, P J, 1990, Finite-difference time-domain calculations of absorbed power in the ankle for 10-100 MHz plane wave exposure, IEEE Trans BME, 38 (5), 423-428.

Dimbylow, P J and Gandhi, O P, 1991, Finite-difference time-domain calculations of SAR in a realistic heterogeneous model of the head for plane-wave exposures from 600 MHz to 3 GHz, Phys. Med. Biol., 36 (8), 1075-89.

Eycleshymer, A C, and Schoemaker, D M, 1911, A Cross-Section Anatomy, New York and London: Appleton.

ICRP, 1975, Report of the Task Group on Reference Man, ICRP Report 23, (Oxford: Pergamon).

Mur, G, 1981, Absorbing boundary conditions for the finite-difference approximation of the time-domain electromagnetic field equations, IEEE Trans, EMC-23, 377-382.

Sullivan, D M, Borup, D T, and Gandhi, O P, 1987, Use of the finite-difference time-domain method in calculating EM absorption in human tissues, IEEE Trans, BME-34(2), 148-157.

Taflove, A, Umashankar, K R, Beker B, Harfoush F and Yee K S, 1988, Detailed FD-TD analysis of electromagnetic fields penetrating narrow slots and lapped joints in thick conducting screens, IEEE Trans, AP-36, 247-257.

Taflove, A, and Umashankar, 1990. The finite-difference time-domain method for numerical modelling of electromagnetic wave interactions with arbitrary structures, 287-373 IN Finite Element and Finite Difference Methods in Electromagnetic Scattering, ed M A Morgan, Elsevier.

Yee, K S, 1966, Numerical solution of initial boundary value problems involving Maxwell's equations in isotropic media, IEEE Trans, AP-14, 302-307.

Computational trade-offs associated with the use of higher-order interpolation functions in finite element modeling

Andrew F. Peterson
School of Electrical Engineering
Georgia Institute of Technology
Atlanta, GA 30332-0250

Abstract: An appealing aspect of finite element modeling is the ease with which simple linear polynomial interpolation functions may be replaced with higher-order polynomials. The improvement in accuracy resulting from higher-order functions has been well documented for traditional scalar finite elements such as Lagrangian interpolation functions. Little has been published to date, however, on the vector interpolation functions recently proposed for electromagnetic applications. In addition, few studies have considered the computational trade-offs arising from the use of higher-order functions with a particular sparse matrix solution algorithm, even in the scalar case. In this paper, the accuracy and efficiency arising from the use of higher-order scalar and vector functions will be considered for resonant cavity and open-region scattering applications. The performance of a sparse matrix solver (Y12M) will also be reported. The results suggest that higher-order functions have much to offer and should be used whenever possible.

1. Introduction

Finite element modeling has been used for static and quasi-static electromagnetic applications for more than 25 years, and during the last decade has become popular for high-frequency applications such as waveguide analysis and electromagnetic scattering. An appealing aspect of finite element modeling is the ease with which simple linear polynomial interpolation functions may be replaced with higher-order polynomials. The improvement in accuracy resulting from higher-order functions has been well documented [1-2] for traditional scalar finite elements such as Lagrangian interpolation functions, which are often used to discretize the scalar equations describing electrostatic or two-dimensional (2D) applications. Recently, vector finite elements have been proposed for use with more general applications [3-5]. Vector interpolation functions may also be extended in a systematic fashion to higher polynomial orders [6-7]. The purpose of this paper is to consider the computational trade-offs (accuracy, memory requirements, and computational efficiency) associated with the use of higher-order functions for resonant cavity and open-region scattering applications in 2D. For the scattering formulations, the performance of a particular sparse matrix solution algorithm (Y12M [8-9]) will be reported.

2. Scalar (Lagrangian) Finite Elements

Scalar Lagrangian interpolation functions complete to polynomial order p on triangular cells are well-established and described in a number of texts [2]. If these functions are used to discretize Laplace's equation constrained by Dirichlet or Neumann boundary conditions, the error in the primary unknown is essentially proportional to the interpolation error, which is known to be [1]

$$O(h^{p+1}) \qquad (1)$$

as $h \to 0$, where h is the length of the longest side of any triangle in the model. It has been shown that this same behavior is observed when using the scalar Helmholtz equation with a local radiation boundary condition, even in regions containing inhomogeneous materials [10-11]. An increase in polynomial order is accompanied by a reduction in matrix sparsity, suggesting a computational trade-off which in turn depends on the specific matrix solution algorithm employed to solve the sparse system of equations. (In other words, more computation will be required to treat the denser matrices associated with higher-order polynomials.) However, it is fairly obvious from (1) that increasing the polynomial order p of the expansion functions will reduce the error more rapidly for a given computational effort than reducing the grid size. Furthermore, the matrix condition number arising from such a discretization typically behaves as [1]

$$O(h^{-2}) \tag{2}$$

Since the matrix condition number is primarily a function of grid size, increasing the polynomial order is a more stable approach for improved accuracy than reducing the grid size in practice [1].

To illustrate the relative accuracy of interpolation functions with different polynomial order, consider a lossy circular dielectric cylinder of size ka=2 and relative permittivity ε_r=2.56–j2.56 illuminated by a plane wave having the electric field aligned parallel to the cylinder axis. We employ the formulation of Peterson and Castillo, which uses the scalar Helmholtz equation

$$\nabla \cdot \left(\frac{1}{\mu_r} \nabla E_z \right) + k^2 \varepsilon_r E_z = 0 \tag{3}$$

in conjunction with the second-order Bayliss-Turkel radiation boundary condition [12]. Table 1 shows the interior E_z-field obtained using linear and quadratic Lagrangian expansion functions, for a mesh containing 1480 triangular cells. The linear expansion involves one unknown for each of the 781 corner nodes in the mesh, yielding a density within the cylinder of 105 nodes/λ_d^2. For the quadratic expansion functions, the additional mid-side nodes bring the total to 3041 unknowns. The second-order Bayliss-Turkel RBC is imposed on a circular boundary having radius ρ=0.98 λ_0, approximately three times the cylinder radius. Despite the fact that the RBC is approximate, excellent accuracy is obtained with quadratic functions.

To illustrate the relative computational cost of linear and quadratic functions, Figure 1 shows the number of nonzero entries in the sparse matrix after LU factorization was performed using a complex-valued adaptation of the program Y12M [8-9]. Although the matrix arising from the quadratic functions contains approximately three times as many nonzero entries prior to factorization, a similar degree of sparsity is present after factorization. These data suggest that the total memory requirements are comparable for an equal number of linear and quadratic basis functions, despite the initial loss of sparsity associated with the quadratic functions. This is a surprising result, and may be due in part to the specific cylinder models employed for these examples. Although the formulations are developed for completely unstructured triangular-cell models, those employed in this work are primarily semi-annular conforming meshes. In any case, these observations suggest that quadratic elements may require very little additional overhead compared to linear elements.

Table 1

E_z-field produced by an incident TM plane wave along a y=0 cut through the center of a circular, homogeneous dielectric cylinder having ka=2 and relative permittivity ϵ_r=2.56–j2.56. Results obtained from the scalar finite element formulation described in [12] using linear and quadratic expansion functions with the identical 1480-cell model are compared with the exact solution. The numerical solutions were obtained with the second-order Bayliss-Turkel RBC imposed at ρ=0.98 λ_0.

x	linear	quadratic	exact
	magnitude of E_z		
–0.319	0.7163	0.7046	0.7039
–0.255	0.5683	0.5568	0.5566
–0.191	0.4508	0.4388	0.4386
–0.128	0.3568	0.3445	0.3443
–0.064	0.2902	0.2768	0.2767
0.0	0.2414	0.2276	0.2274
0.064	0.1962	0.1833	0.1831
0.128	0.1837	0.1698	0.1696
0.191	0.2412	0.2237	0.2235
0.255	0.3169	0.2964	0.2961
0.319	0.3511	0.3303	0.3299
	phase of E_z		
–0.319	123.75°	123.28°	123.32°
–0.255	83.39	82.32	82.35
–0.191	43.13	41.62	41.64
–0.128	1.80	0.05	0.07
–0.064	–40.65	–42.66	–42.63
0.0	–82.36	–84.81	–84.78
0.064	–126.16	–129.01	–128.98
0.128	178.41	178.09	178.12
0.191	139.68	135.48	135.50
0.255	120.23	116.14	116.15
0.319	115.98	112.54	112.57

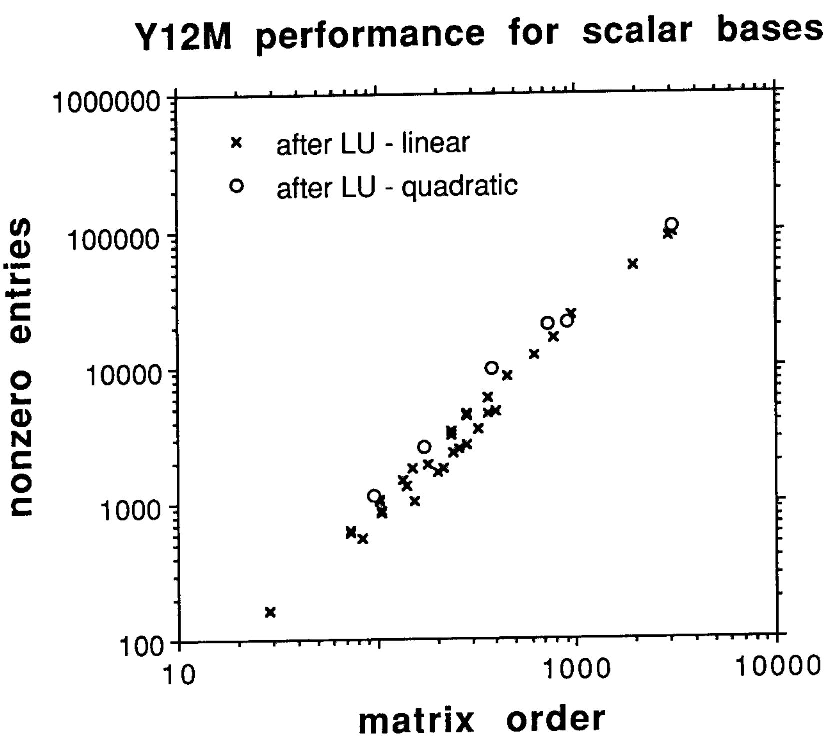

Figure 1. Number of nonzero entries in the finite element system after LU factorization, as a function of matrix order and the polynomial degree of the expansion functions.

3. Vector interpolation functions on triangular cells

Recently, vector interpolation functions (also known as "edge elements") have been proposed for finite element implementation [3-7]. On triangular cells, these functions permit a systematic realization of the mixed-order function spaces introduced by Nedelec in 1980 [13], and prescribe the proper continuity of tangential field components at interfaces. When used to discretize the curl-curl form of the vector Helmholtz equation, these basis functions separate the nullspace of the operator from the desired solutions and therefore eliminate "spurious modes" in eigenvalue problems. Although the lowest-order tangential-edge vector basis functions have zero divergence, this is not a general property of the class of interpolation functions and is not directly related to the ability to eliminate spurious modes. The following comparisons will use the quadratic tangential-edge vector basis functions recently proposed by Lee, Sun and Cendes [6-7].

To demonstrate that vector basis functions satisfying Nedelec's constraints can eliminate spurious modes, consider a 2D cavity with resonant frequencies described by the eigenvalue equation

$$\nabla \times \left(\frac{1}{\mu_r} \nabla \times \bar{E} \right) = k^2 \varepsilon_r \bar{E} \tag{4}$$

subject to the Dirichlet boundary condition $\bar{E}^{tan}=0$ on the perfect electric walls of the cavity. If discretized to form a generalized matrix eigenvalue equation, values of the eigenvalue k^2 are readily determined using standard software libraries such as EISPACK. The relative accuracy possible with linear and quadratic edge elements can be inferred from Table 2, which compares numerical and exact results for the resonant TE wavenumbers of a homogeneous circular cavity. The lower-order wavenumbers produced by the quadratic expansion are accurate to 3-4 decimal places. There appear to be no spurious nonzero wavenumbers.

Table 2

Resonant TE wavenumbers for a homogeneous circular cavity of unit radius produced by a discretization of Equation (4). Linear and quadratic tangential-vector "edge" basis functions were used. The cavity model consisted of a triangular-cell mesh with 55 nodes and 138 edges, yielding an order-114 system for the linear elements and a order-396 system for the quadratic elements. The resonant wavenumbers are listed in order of increasing values with their degree of multiplicity in parenthesis.

mode	linear	quadratic	exact
	0.00 (31)	0.000 (145)	
TE_{11}	1.85 (2)	1.841 (2)	1.8412 (2)
TE_{21}	3.08 (2)	3.054 (2)	3.0542 (2)
TE_{02}	3.84 (1)	3.833 (1)	3.8317 (1)
TE_{31}	4.24 (2)	4.201 (2)	4.2012 (2)
TE_{41}	5.34 (2)	5.319 (2)	5.3176 (2)
TE_{12}	5.37 (2)	5.336 (2)	5.3314 (2)
TE_{51}	6.48 (2)	6.423 (2)	6.4156 (2)
	•	•	•
	•	•	•
	•	•	•
	23.5	49.3	

Linear vector basis functions have been previously used within a 2D scattering formulation combining the curl-curl form of the Helmholtz equation with a local radiation boundary condition [14-15]. Recently, this approach was extended to incorporate quadratic edge elements. To illustrate the accuracy possible with these basis functions, Figure 2 compares the magnitude and phase produced by the numerical formulation with the exact solution for a two-layer circular dielectric cylinder. The inner cylinder has radius 0.093946 λ_0 and relative permittivity ε_r=10-j5,

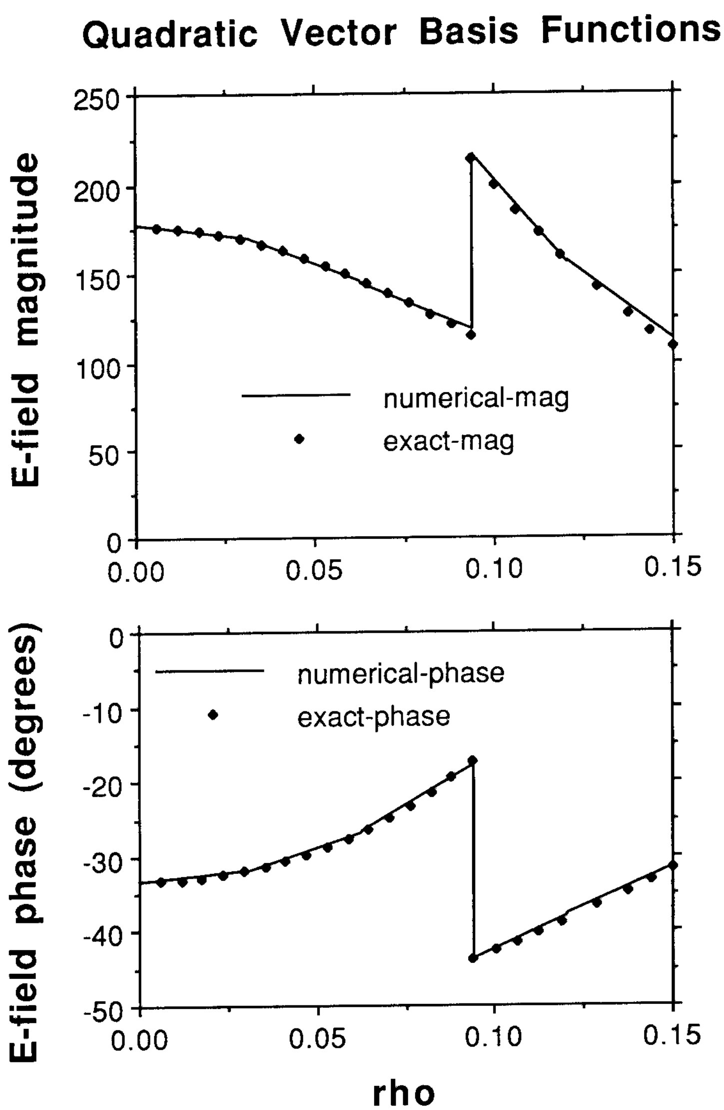

Figure 2. Magnitude and phase of the electric field along a cut through a coated circular dielectric cylinder. The numerical result obtained using quadratic vector basis functions exhibits excellent agreement with the exact analytical solution.

while the dielectric cladding has outer radius 0.15 λ_0 and ε_r=6. A local RBC was imposed at a radius of ρ=0.41 λ_0. Fields are shown as a function of ρ along a ϕ=90° cut, for an incident plane wave traveling in the ϕ=0° direction. Excellent agreement is observed between the exact and numerical results. A potential drawback of these vector basis functions is that the normal component at cell boundaries is discontinuous, and might produce fictitious discontinuities within homogeneous regions. However, as illustrated in Figure 2, our numerical solution appears to properly model the continuous field and accurately track the jump discontinuity at the interface between the two media.

Figure 3 demonstrates the performance of Y12M when used to solve the sparse system of equations arising from the 2D vector scattering formulation. In common with the scalar formulation, the systems arising from linear and quadratic vector elements require a comparable amount of storage after LU factorization — again, suggesting that there is very little additional cost in using quadratic basis functions instead of linear.

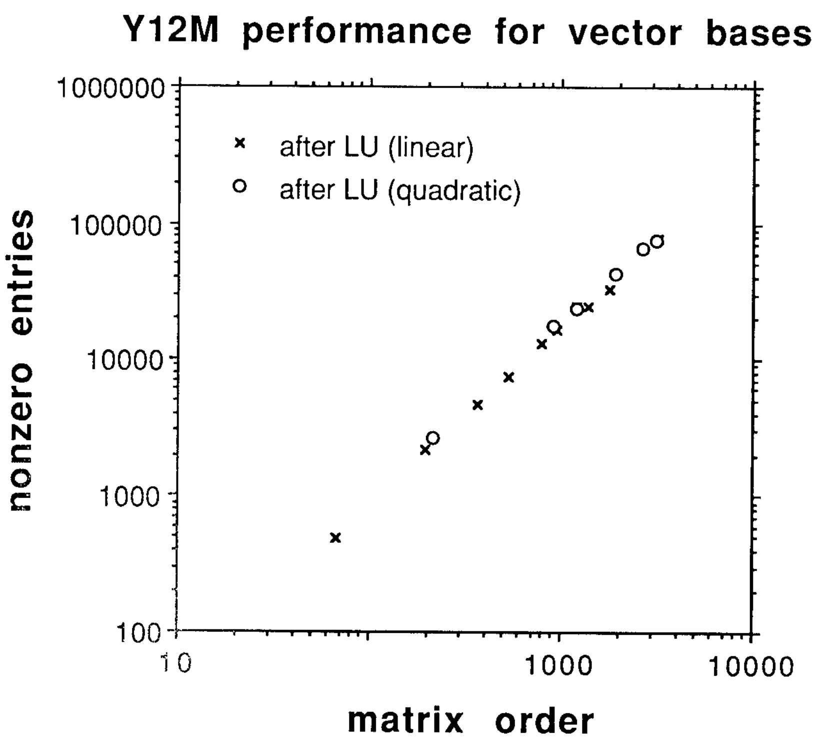

Figure 3. Number of nonzero entries in the finite element system after LU factorization, as a function of matrix order and the polynomial degree of the expansion functions.

4. Conclusions

Scalar (Lagrangian) interpolation functions and tangential-vector (edge) basis functions of various polynomial order can be systematically incorporated into finite element codes for electromagnetic applications. We have demonstrated that the use of quadratic basis functions can lead to substantial improvements in accuracy compared to linear functions, and with little additional computational cost in many cases.

References

[1] G. Strang and G. J. Fix, *An Analysis of the Finite Element Method.* Englewood Cliffs: Prentice-Hall, 1973.

[2] P. P. Silvester and R. L. Ferrari, *Finite Elements for Electrical Engineers.* Cambridge: Cambridge University Press, 1990.

[3] A. Bossavit and J. C. Verite, "A mixed FEM-BIEM method to solve 3D eddy current problems," *IEEE Trans. Magnetics*, vol. MAG-18, pp. 431-435, March 1982.

[4] M. L. Barton and Z. J. Cendes, "New vector finite elements for three-dimensional magnetic field computation," *J. Appl. Phys.*, vol. 61, pp. 3919-3921, April 1987.

[5] D. R. Tanner and A. F. Peterson, "Vector expansion functions for the numerical solution of Maxwell's equations," *Microwave and Optical Technology Letters*, vol. 2, pp. 331-334, Sept. 1989.

[6] J. -F. Lee, D. -K. Sun, and Z. J. Cendes, "Full-wave analysis of dielectric waveguides using tangential vector finite elements," *IEEE Trans. Microwave Theory Tech.*, vol. 39, pp. 1262-1271, Aug. 1991.

[7] Z. J. Cendes, "Vector finite elements for electromagnetic field computation," *IEEE Trans. Magnetics*, vol. 27, pp. 3958-3966, Sept. 1991.

[8] Z. Zlatev, J. Wasniewski, and K. Schaumburg, *Y12M – Solution of Large and Sparse Systems of Linear Algebraic Equations.* Berlin: Springer-Verlag, 1981.

[9] O. Osterby and Z. Zlatev, *Direct Methods for Sparse Matrices.* Berlin: Springer-Verlag, 1983.

[10] A. Bayliss, C. I. Goldstein, and E. Turkel, "On accuracy conditions for the numerical computation of waves," *J. Comp. Phys.*, vol. 59, pp. 396-404, 1985.

[11] L. J. Bahrmasel and R. A. Whitaker, "Convergence of the finite element method as applied to electromagnetic scattering problems in the presence of inhomogeneous media," *IEEE Trans. Magnetics*, vol. 27, pp. 3845-3847, Sept. 1991.

[12] A. F. Peterson and S. P. Castillo, "A frequency-domain differential equation formulation for electromagnetic scattering from inhomogeneous cylinders," *IEEE Trans. Antennas Propagat.*, vol. 37, pp. 601-607, May 1989.

[13] J. C. Nedelec, "Mixed finite elements in R3," *Numer. Math.*, vol. 35, pp. 315-341, 1980.

[14] A. F. Peterson, "Finite element solution of the vector wave equation using divergenceless basis functions," *Digest of the 1989 IEEE Antennas and Propagation Society International Symposium*, San Jose, CA, pp. 1624-1627, June 1989.

[15] J. Parker, R. D. Ferraro, and P. C. Liewer, "A comparison of isoparametric edge elements and DnEt elements for 3D electromagnetic scattering problems," *Abstracts of the URSI Radio Science Meeting*, Dallas, TX, p. 377, May 1990.

AN EFFICIENT FINITE ELEMENT ANALYSIS OF MICROWAVE CAVITIES AND WAVEGUIDES USING EDGE ELEMENTS

PICHON L. - RAZEK A.

Laboratoire de Génie Electrique de Paris
URA D0127 CNRS
Ecole Supérieure d'Electricité
Universités Paris 6 et Paris 11
Plateau du Moulon
91 192 Gif sur Yvette Cédex France

Abstract

In this paper we solve Maxwell's equations in microwave devices using edge elements . These finite elements whose degrees of freedom are associated with the edges of the mesh have two main advantages : they imply the right continuity for the fields and avoid "spurious modes", the non-physical numerical fields obtained from the solution of eigenvalue problems. The presented results involve the computation of cut-off frequencies in waveguides (2D problems) and the computation of resonant frequencies in microwave cavities (3D problems). Comparisons with analytical values or previously published results are performed.

Introduction

The finite element method is now found to be an efficient tool for electromagnetic computations in microwave structures such as waveguides and cavities. Solving Maxwell's equations leads to vector boundary value problems. Most current techniques are based on classical finite elements, obtained by interpolation (linear interpolation in the simplest case) from nodal values of vector components. This method can be easily extended from methods developed for scalar functions but has two serious drawbacks. The first drawback is that it has difficulties to account for particular physical properties of the fields : it implies full continuity at material interfaces whereas for example the electric field has tangential continuity but may have normal discontinuity. The second drawback is that nodal elements are known to give

"spurious" numerical fields (non-physical fields) when solving vectorial eigenvalue problems. Many attempts were performed to circumvent these unwanted solutions but none of them seems both satisfactory and straightforward [1]-[3].

In [4] Bossavit showed that the edge element is an efficient finite element for electromagnetic field computations in high frequency problems. In particular he explained the reason for which edge elements will not generate "spurious modes".

A model based on edge elements has been recently studied and developed by the authors [5][6].

In this paper we show that this technique provides an efficient way for the analysis of both waveguides (2D) and cavities (3D) with complex geometries and containing dielectric material.

Basic formulation

We deal with Maxwell's time harmonic equations in a bounded domain Ω surrounded by a perfect conductor and containing lossless materials :

$$\text{curl } e = - i \, \omega \, \mu_0 h \tag{1}$$

$$\text{curl } h = i \, \omega \, \epsilon_0 \epsilon_r \, e \tag{2}$$

where e and h are the complex electric and magnetic fields, ϵ_0 and μ_0 are respectively the permittivity and permeability of vacuum, ϵ_r is the relative permittivity and ω is the angular frequency.

The condition on the boundary Γ of Ω is :

$$e \wedge n = 0 \tag{3}$$

where n is the outward normal vector.

Substituting (1) into (2), we deduce the following eingenvalue problem expressed in terms of the electric field:

$$\left\{ \begin{array}{l} \text{curl (curl } e) - \epsilon_r \epsilon_0 \mu_0 \, \omega^2 \, e = 0 \\ \\ e \wedge n = 0 \end{array} \right. \tag{4}$$

A weak formulation of (4) holds in $H_0(\text{curl})$:

$$\int_\Omega \text{curl } e. \text{ curl } e' \, dx - k^2 \int_\Omega \epsilon_r \, e.e' \, dx = 0 \quad \forall \, e' \in H_0(\text{curl}) \tag{5}$$

where

$$H_0(\text{curl}) = \left\{ e \in [L^2(\Omega)]^3 \text{ , curl } e \in [L^2(\Omega)]^3 \text{ , } e \wedge n = 0 \text{ on } \Gamma \right\}$$

and where the values of k ($k^2 = \epsilon_0 \mu_0 \ \omega^2$) are the wavenumbers.

Finite element approximation

Edge elements are used for the numerical approximation of (5). These particular finite elements are a class Whitney elements introduced by Bossavit [7] and correspond to a class of mixed finite elements introduced by Nédélec [8].

Let Ω_h be a tetrahedral mesh of Ω . For one edge "a" containing the two nodes "i" and "j" we have a vector field w_a defined in terms of the barycentric functions as follows :

$$w_a(x) = \lambda_i(x) \text{ grad } \lambda_j(x) - \lambda_j(x) \text{ grad } \lambda_i(x) \qquad (6)$$

Figure 1 shows the general shape of the function w_a relevant to the edge "a".

This vector field has two properties which can be verified with easy computations :

- the circulation of w_a along edge a (from node "i" to node "j") is equal to 1 , and to 0 along other edges.

- w_a is not continuous over Ω_h but its tangential part is continuous across facets of the mesh. This type of continuity is exactly what is needed to represent the electric field vector.

Let us call E_{0h} the space spanned by linear combinations of the w_a's. This space E_{0h} is imbedded in $H_0(\text{curl})$. The electric field e will be expressed as :

$$e(x) = \sum e_a \ w_a(x) \qquad (7)$$

where the degrees of freedom e_a are the circulations of the field along the edges of the mesh.

Rewriting (7) in (5) and taking the w_a's as weighting vectors e', the approached problem leads to a generalized eigenvalue problem of the form :

$$[A] \ [e] = k^2 \ [B] \ [e] \qquad (8)$$

where the dimension of A ("stiffness matrix") and B ("mass matrix") is the number of edges in Ω_h .

Spurious modes

The searched resonant fields ($\omega > 0$) are theoritically divergence free since e is a curl. The trouble arises when discretizing (5) with classical (for example nodal) vector

elements. The eigenvalue 0 is a highly degenerate eigenvalue whose eigenspace is spanned by the gradient fields. These gradient fields can't be approximated with nodal elements and the numerical approximation of $k^2 = 0$ are then difficult to distinguish from the meaningful lowest non-zero eigenvalues ($k^2 > 0$) ; especially when the number of degrees of freedom increases. Most of them do not satisfy the divergence free condition and then are unacceptable as solutions of Maxwell's equations. the resulting set of solutions is a mixture of physical modes and numerical spurious ones.

With edge elements such a situation doesn't occur since all the gradient fields can be chosen as admissible test fields [4].

Numerical results

a) Waveguides

Our numerical approach was first used in two dimensions. Solving Maxwell's equations in a waveguide using the transversal components of the electric field leads to an eigenvalue problem of the form (8). Hollow rectangular waveguides and hollow circular waveguides, whose analytical solutions are known, were first modelled to show the validity of the technique. Here two other examples are presented.

A rectangular waveguide partially filled with dielectric material was studied (figure 2). Table 1 shows the 5 lowest computed values of k_c (cut-off wavenumbers) for TE-mode. This table also shows previously published results [2] based on an indirect technique which needs a preliminary finite element calculation to determine a basis of divergence-free fields to solve the eigenvalue system. Direct solution is possible in our model due to edge elements and no spurious mode occured. Moreover dielectric discontinuity is exactly verified in the waveguide since edge elements allow the normal component of the electric field to be discontinuous at material interfaces.

Waveguides with reentrant corners present difficulties to be treated with numerical methods ; a great number of spurious modes appears and a classical approach can't give reasonnable results . In such cases the field is concentrated in the corners and its normal component is discontinuous near the angular points. These geometrical particularity can easily be treated with "edge elements". As an example, a double ridged waveguide was considered (figure 3). One quarter of the problem was analyzed with the Neumann boundary condition on the two axis of symmetry. The first 3 corresponding wavenumbers were computed and compared with [9] obtained with a nodal magnetic vector potential formulation (

table 2) where the geometrical difficulty is avoided for a price of a special treatment in the singular points.

b) Cavities

Several types of microwave cavities were analyzed with the presented model. Comparisons with analytical values for empty cavities of simple shapes have already shown the accuracy of the numerical approximation [5]. We present here two examples : the first one is a dielectrically-loaded cavity and the second one is a junction between the microwave cavity of a caesium beam frequency standard with a waveguide at cut-off.

The dielectrically-loaded cavity is a rectangular one with a dielectric block (figure 4-a). The quarter (figure 4-b) was modelled with 240 tetrahedra. No analytical result is available but comparison with already published computed values is possible ; results for the dominant mode are listed on table 3.All these results agree within roughly 10%. However the use of edge elements avoided all spurious modes and exactly imply the continuity of the tangential component of the electric field at dielectric interfaces. Figure 5 shows the electric field vectors in the quarter of the cavity.

The second resonator is a caesium beam frequency standard microwave cavity. The studied domain is the combination of a rectangular waveguide and a rectangular cavity (figure 6). The computed resonant frequency is 9.174 GHz. This value is to be compared to the resonant frequency without the waveguide (9.192 GHz) which is obtained analytically and numerically. The distribution of the electric field vectors is plotted on figure 7.

Conclusion

Edge elements have been used to model waveguides and cavities. It was shown that the method can accurately compute cut-off frequencies and resonant frequencies. It allowed to take dielectric discontinuities into account and numerical results do not include "spurious modes" which appear with conventional (nodal) elements. It allows a precise distribution of the field even in case of complicated geometries (reentrant corners and irregular boundaries).

References

[1] KONRAD A., "On the reduction of the number of spurious modes in the vectorial finite element solution of three dimensional cavities and waveguides", IEEE-MTT, 34, n°2, 1982, pp 224-227.

[2] KOBELANSKY A.J., WEBB J.P., "Eliminating spurious modes in finite element waveguide problems by using divergence free fields", Electronics Letters, Vol 22, n°11, 1986, pp 569-570.

[3] WEBB J.P., "Efficient generation of divergence-free fields for the finite element analysis of 3D cavity resonances", IEEE-MAG, 33, n°1, 1988, pp 162-165.

[4] BOSSAVIT A., "Simplicial finite elements for scatterring problems in electromagnetism", Comp. Meth. Mech. Engng. ,76, 1989, pp 299-316.

[5] PICHON L., RAZEK A., "3D cavity resonances computations without spurious solutions", 4th International Symposium, Gratz, Austria, 10-12 Oct 1990.

[6] PICHON L., RAZEK A. ," Analysis of three diemensional dielectric loaded cavities with edge elements", to appear in ACES Journal.

[7] BOSSAVIT A., "A rationale for edge elements in 3D fields computations", IEEE-MAG, 24, n°1, 1988, pp 74-79.
[8] NEDELEC J.C. " Mixed finite elements in $\mathbb{R}^3$ ", Numer. Math., 35, 1980, pp 315-341.

[9] BARDI I. , "Finite element analysis of ridged waveguides", 4th International Symposium, Gratz, Austria, 10-12 Oct 1990.

[10] AKHTARZAD S., JOHNS P.B. , "Solution of Maxwell's equations in three space dimensions and time by the t.l.m method of numerical analysis", Proc IEE, 122, n°12, 1975, pp 1344-1348.

[11] ALBANI M., BERNADI P., "A numerical method based on the discretization of Maxwell equations in integral form, IEEE-MAG, 22, 1974, pp 446-450.

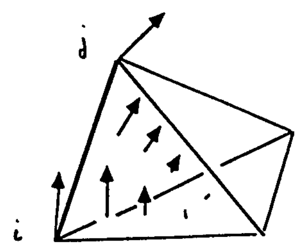

Figure 1 Shape function relevant to the edge {i,j}

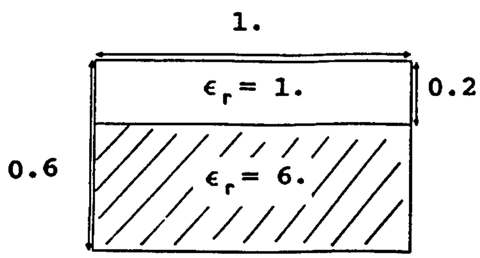

Figure 2 Partially filled dielectric waveguide

Mode	Edge Elements	Ref [2]
1	1.7652	1.7667
2	2.3151	2.3056
3	2.9580	2.9568
4	3.2939	3.3036
5	4.1239	4.1549

Table 1 Lowest values of k_c (dielectric waveguide)

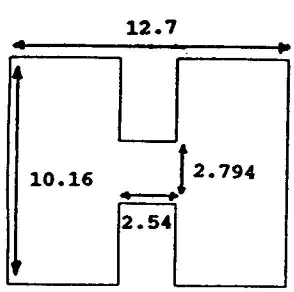

Figure 3 Double ridged waveguide

Mode	EdgeElements	Ref [9]
1	0.1401	0.1429
2	0.6021	0.6193
3	0.6688	0.6712

Table 2 Lowest wavenumbers k_c (ridged waveguide)

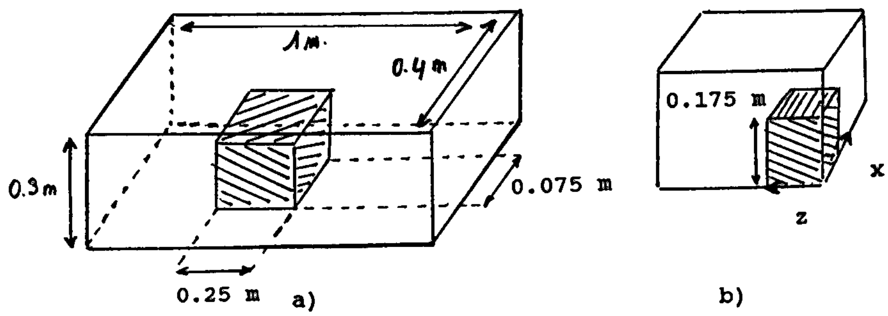

Figure 4 Cavity with dielectric block

Source	k (computed)
[3]	5.60
[10]	5.529
[11]	4.907
Edge Elements	5.102

Table 3 Computed eigenvalue (dominant mode)

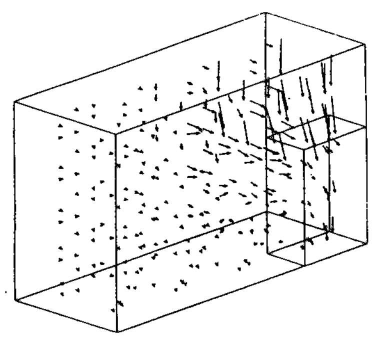

Figure 5 Electric field (dominant mode)

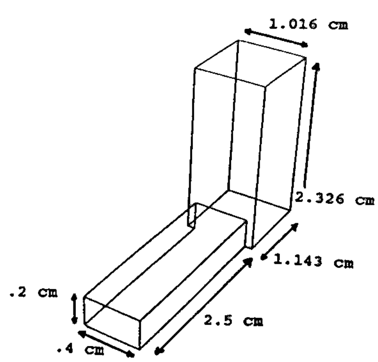

Figure 6 Microwave cavity of a caesium beam frequency standard (half shown)

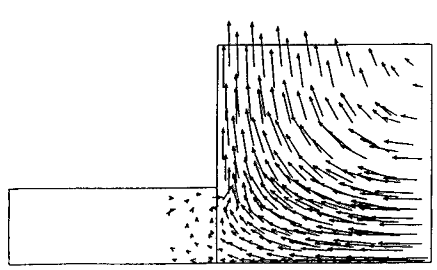

Figure 7 Distribution of magnetic field vectors

FINITE DIFFERENCE SOLUTION OF DIELECTRIC WAVEGUIDES CONTAINING ARBITRARILY NONLINEAR MATERIAL

J. R. Souza
Center for Telecommunication Studies - CETUC
Pontifical Catholic University of Rio de Janeiro - PUC/Rio
Rua Marquês de São Vicente, 225
22453 Rio de Janeiro - RJ, Brasil

ABSTRACT:

The propagation characteristics of electromagnetic waves in dielectric slab waveguides containing arbitrarily nonlinear material are investigated numerically using variational methods and finite difference techniques, and relying on an iterative scheme to arrive at self-consistent and stable solutions. For both TE and TM polarizations, the fundamental and higher order modes are considered, for different types of nonlinearities. It is observed that, for either polarization, the fundamental mode can exhibit hysteresis and bistability at low power levels, depending mostly on the slab thickness.

1. INTRODUCTION

Dielectric waveguides, or thin films, with nonlinear material have attracted considerable interest in recent years due to their unique, fascinating features, and potential application to devices for an all-optical signal processor, as well as for optical computers [1]. The knowledge of the propagation characteristics of electromagnetic waves in such structures is necessary not only to determine the feasibility of the suggested devices, but also to further the understanding of the physical phenomena associated with nonlinear guided waves systems. Only for certain types of nonlinearities, e. g. the Kerr-type, is this problem of nonlinear waveguides amenable to analytical solution [2],[3], which depends on the polarization and also on the waveguide configuration. The numerical solution presented in this paper allows arbitrary nonlinearities to be considered, as well as any type of distribution of the linear refractive index. With respect to other numerical solutions found in the literature [4],[5], the present one has the advantage of simpler formulation, and requires smaller amount of computer memory and processing time.

2. FORMULATION

Figure 1 shows the waveguides considered, where the three layers can be of nonlinear material.

For TE polarization, the nonlinear refractive index is written as [2]:

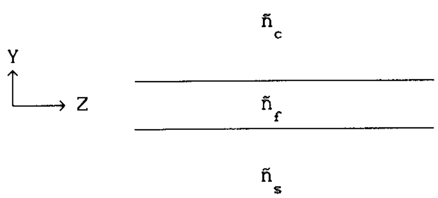

Figure 1: Nonlinear waveguide.

$$\tilde{n}_j^2 = n_j^2 + a_j f(S) \quad , \qquad j = s,\ f,\ c \tag{1}$$

where n_j represents the low power refractive index, which may be a function of y, a_j represents the nonlinear coefficient of medium j (j=s, f, c) and f(S), a function of the signal intensity S. For Kerr-type nonlinearity, $f(S) = |E|^2$, where E denotes the electric field. In this case, each coefficient a_j is then written as $n_j n_{2j} \varepsilon_o c_o$, n_{2j} being the nonlinear coefficient, ε_o the free space permittivity, and c_o the velocity of light in vacuum.

Assuming that the waveguide is composed of lossless media, and that $\partial/\partial X = 0$, considering wave propagation along the Z-direction, a variational expression for the propagation constant β for TE waves is written as [6]:

$$\beta^2 = \left[\int_{-\infty}^{\infty} [k_o^2 \tilde{n}^2 E_x^2 - (\frac{dE_x}{dy})^2] dy\right] \cdot \left[\int_{-\infty}^{\infty} E_x^2 dy\right]^{-1} \tag{2}$$

where E_x is the X-component of the electric field, k_o is the free space wavenumber, and the factor $\exp[j(\omega t - \beta z)]$ is implicit.

Next, the Y-axis is discretized, finite differences are used to evaluate the derivative in the expression for β^2, and the integrals in (2) are approximated in terms of the discretized field.

The stationary property of β^2 is then used through the differentiation of (2) with respect to each of the variables E_{xi}, where E_{xi} is the value of E_x at $y = y_i$, $i = 1, 2, \ldots, N$, E_{xo} and E_{xN+1} being set to zero. The following standard eigenvalue problem is arrived at:

$$[A] \cdot \{E_x\} = (\beta h)^2 \cdot \{E_x\} \tag{3}$$

where h is the distance between successive points along the Y-axis, [A] is a real, symmetrical and tridiagonal matrix, whose diagonal elements are given by:

$$A_{ii} = (k_o h)^2 \tilde{n}_i^2 - 2 \qquad (i=1,2,\ldots,N) \tag{4}$$

and the off-diagonal elements are all equal to unity.

The total guided power per unit length along the X-axis is calculated as:

$$P = \frac{\beta}{2k_o Z_o} \int_{-\infty}^{\infty} E_x^2 dy \tag{5}$$

where Z_o represents the intrinsic impedance of vacuum.

For TM polarization the nonlinear permittivity is written as [7]:

$$\begin{aligned} \varepsilon_{xj} &= n_j^2 \\ \varepsilon_{yj} &= \tilde{n}_{yj}^2 = n_j^2 + u_j f(E_y) + v_j f(E_z) \\ \varepsilon_{zj} &= \tilde{n}_{zj}^2 = n_j^2 + v_j f(E_y) + u_j f(E_z) \end{aligned} \tag{6}$$

where ε_{xj}, ε_{yj}, and ε_{zj} are diagonal elements of the permittivity tensor, n_j represents the low power refractive index of medium j. E_y and E_z are, respectively, the Y- and Z-components of the electric field. For Kerr-type nonlinearity, the coefficients u_j is written as $\varepsilon_o c n_o n_{2j}$, and $v_j = \gamma u_j$, where γ takes on different values, depending on the nonlinearity mechanism [7], and will here be fixed as 1.

As in the case of TE polarization, a variational expression is first developed for the propagation constant β [6]:

$$\beta^2 = \left[\int_{-\infty}^{\infty} \frac{1}{\varepsilon_z} (dH_x/dy)^2 dy - k_o^2 \int_{-\infty}^{\infty} H_x^2 \, dy \right] \cdot \left[\int_{-\infty}^{\infty} \frac{1}{\varepsilon_y} H_x^2 \, dy \right]^{-1} \tag{7}$$

Following the same steps as in the case of TE polarization, a standard eigenvalue problem is obtained:

$$[B] \cdot \{H_x\} = (\beta h)^2 \cdot \{H_x\} \tag{8}$$

where H_x is the X-component of the magnetic field, [B] is a real tridiagonal matrix, whose elements are given by:

$$\begin{aligned} B_{ii} &= \left(k_o^2 h^2 - \frac{1}{\varepsilon_{z\,i-1}} - \frac{1}{\varepsilon_{zi}} \right) \cdot \varepsilon_{yi} \\ B_{i,i+1} &= \varepsilon_{yi} (\varepsilon_{zi})^{-1} \\ B_{i-1,i} &= \varepsilon_{yi} (\varepsilon_{zi1})^{-1} \end{aligned} \tag{9}$$

The total guided power per unit length along the X-axis is calculated as:

$$P = \frac{1}{2} \cdot \frac{Z_o \beta}{k_o} \cdot \int_{-\infty}^{\infty} \frac{1}{\varepsilon_y} H_x^2 dy \tag{10}$$

The solution of the eigenvalue problems yields the propagation constant β and the electric field profile, in the case of TE waves, or the magnetic field profile, in the case of TM waves.

As in the presence of nonlinearity the refractive index distribution depends on the local field intensity, an iterative scheme is used in the solution of the eigenvalue problems (3) and (8). For each polarization,

the eigenvalue problem is initially solved assuming negligible power level. The resulting electric (or magnetic) field is then scaled to the required power level, and used to update the refractive index distribution due to the nonlinear contributions, and the eigenvalue problem is solved again. This iterative scheme continues until consistent solutions are obtained. The propagation mode to be considered is determined by selecting a particular eigenvalue among all that emerge from the solution of (3) or (8). For example, the highest order eigenvalue corresponds to the fundamental mode (TE_0 or TM_0), the next eigenvalue corresponds to the first higher order mode (TE_1 or TM_1), and so on.

The discretization along the Y-axis has the extra advantage that no restriction is imposed on the type of the nonlinearity, nor on the distribution of the linear (low power) refractive index, which can be either of the step- or the gradual-type, thus allowing a flexibility of analysis that is not matched by analytical solutions.

3. RESULTS

Initially, a waveguide with linear refractive index distribution of the step-type, in which both the substrate and cladding were nonlinear, with Kerr-type characteristics, was considered.

Figure 2 shows the variation of the fundamental mode TE_0 effective refractive index β/k_0 with the guided wave power for a structure composed of a linear film, whose thickness is 1.25μm and refractive index is 1.57, bounded by identical, semi-infinite nonlinear substrate and cladding, with a low power refractive index of 1.55, and nonlinear coefficient of $1.0\times10^{-9}m^2/W$. The wavelength is 0.515μm.

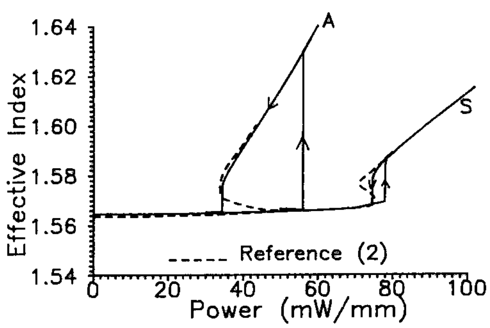

Figure 2: Variation of the TE_0 effective refractive index with guided wave power.

This fundamental mode presents two solutions: one, with a symmetrical electric field distribution with respect to the X-axis, that evolves from the corresponding solution in a similar, linear waveguide. This solution is represented by curve S in Figure 2. For power levels above a certain value, a second solution appears, in which the electric field distribution is asymmetrical with respect to the X-axis, curve A in Figure 2. It was observed that, for power levels where the asymmetrical solution exists, the symmetrical solution is unstable, i.e. it is not maintained along the iterative scheme. This behaviour is in accordance with the stability theory of reference [8]. The symmetrical solution could only be calculated

by the present algorithm enforcing symmetry boundary conditions. Figure 2 also shows results as read from reference [2], which presents an analytical, stationary solution for the nonlinear, one-dimensional wave equation. The results are seen to agree very well. In Figure 2 it can be seen that hysteresis takes place, represented by a sudden change of the effective index as the guided wave power is increased, which is associated with a sudden change from guided to surface wave, i.e. the electric field maximum moves from the film to one of the nonlinear media. It was observed [6], that this effect is determined mainly by the film thickness, and that it can occur at low power levels. Such effect has potential application in fast optical switches or memory loops [1].

Figure 3 shows, for the TM_0 mode, the variation of the effective refractive index with guided wave power in a structure with the same parameters as that of Figure 2, with the exception of the film thickness and wavelength, which are now 1.0μm and 0.5145μm, respectively.

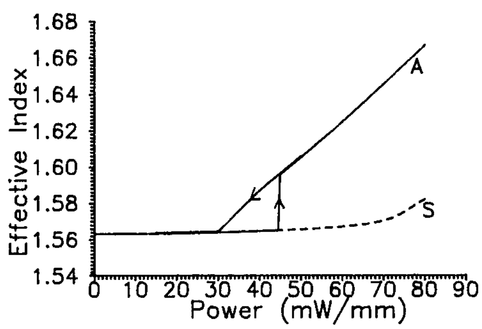

Figure 3: Variation of the TM_0 effective refractive index with guided wave power.

Again, as the structure is physically symmetrical, two solutions are possible, one symmetrical and one asymmetrical. As in the case of the TE_0 mode, the symmetrical solution is unstable for power levels where the asymmetrical solution exists.

In physically asymmetrical structures, only one solution exists, for both TE_0 and TM_0 modes, which is stable for all power levels [2], [8]. In asymmetrical structures the occurrence of hysteresis is also possible, determined mainly by the film thickness [6].

Next, saturable Kerr-like nonlinearity was considered for TE polarization, in which the nonlinear dielectric constant is written as [3]:

$$\tilde{\varepsilon}_j = \varepsilon_{Lj} + \varepsilon_{jsat} \cdot \left[1 - \exp\left(- \frac{c_o \varepsilon_o \varepsilon_{Lj} n_{2j}}{\varepsilon_{jsat}} \cdot |E|^2\right)\right] \qquad (11)$$

where ε_{Lj} is the linear (low power) dielectric constant of medium j.

Figure 4 shows the variation of the effective refractive index for both TE_0 and TE_1 in a waveguide whose parameters are: n_f=1.57, n_{2f}=0, n_s=n_c=1.55, n_{2s}=2x10^{-9}m^2/W, n_{2c}=0, t=2.0μm, and the wavelength is 0.515μm. In Figure 4, the parameter n_{sat} is obtained from $(\varepsilon_{Lj}+\varepsilon_{jsat})^{1/2}=n_j+n_{jsat}$. It was observed that, for the TE_0 mode, the effect of the saturation was to decrease the area of the hysteresis loop, when compared with the

Kerr-law nonlinearity (nsat=∞). Figure 4 also shows results for the TE_1 mode as read from reference [3], with good agreement.

Figure 5 shows results for a waveguide with the same parameter as in Figure 4, except that a power-law nonlinearity is now considered, where

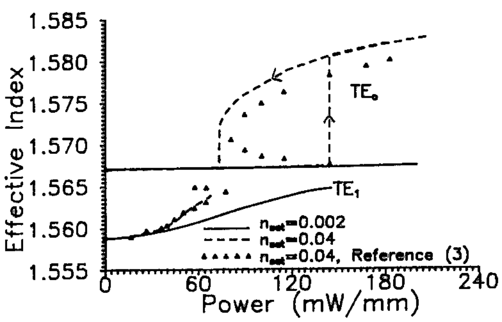

Figure 4: Variation of the effective index with guided wave power for a waveguide with linear film and cladding, and a saturable nonlinear substrate.

the nonlinear dielectric constant is given by [3]:

$$\tilde{\varepsilon}_j = \varepsilon_{Lj} + c_o \varepsilon_o \varepsilon_{Lj} n_{2j} |E|^p \tag{12}$$

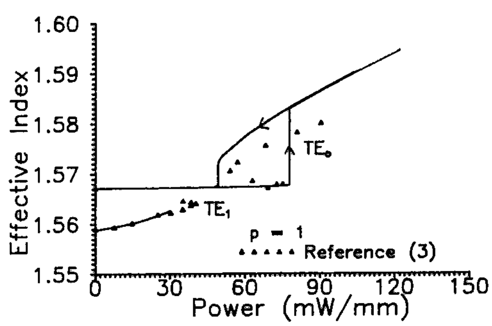

Figure 5: Variation of the effective index with guided wave power for a waveguide with linear film and cladding, and a power-law nonlinear substrate.

Again, the results showed good agreement with other ones in the literature [3].

Next, a waveguide was considered, in which the linear medium had Gaussian-profile refractive index distribution, and the nonlinear medium was of the Kerr-type, the complete refractive index distribution being given by [9]:

$$\tilde{n}^2(y) = \begin{cases} n_c^2 + c_o \varepsilon_o n_c^2 n_{2c} |E|^2, & y<0 \\ n_b^2 + (n_s^2 - n_b^2)\exp[-(y/a)^2], & y>0 \end{cases} \tag{13}$$

The following parameters were used, at a wavelength of 0.515μm: $n_s=1.57$, $n_c=n_b=1.55$, $n_{2c}=10^{-9}m^2/W$, a=2.0μm. Figure 6 shows the variation of the effective index with guided power, for both TE_0 and TE_1 modes. Also shown are results as read from reference [9], with good agreement.

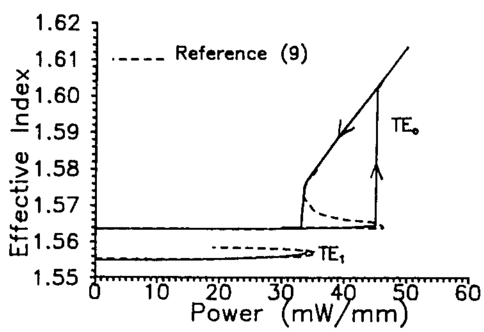

Figure 6: Variation of the effective index with guided wave power in a gradual-index waveguide.

It is worth mentioning that the first higher order TE_1 mode as calculated by the present algorithm showed a somewhat different behaviour than that obtained by the stationary solutions of references [2], [3], [9], as shown in Figures 4 to 6. According to these references, this mode propagates only for power levels below a certain value, with the effective index following a sort of u-turn curve, i.e., it exhibits a peak, near which two different values of effective index occur for the same power level. With the present solution and independent of the type of nonlinearity, it was observed that for power levels above a certain value the algorithm failed to converge to a single value of effective index (and electric field profile), but multiple values were obtained, which were periodic with respect to the iterations and the period doubled as the guided-wave power increased, until the periodicity disappeared, suggesting a transition to chaos through period doubling [10], [11]. The same behaviour was observed with TM_1 mode. Investigations are being carried out in order to determine whether this is a physical phenomenon or induced by the numerical algorithm.

4. CONCLUSION

A numerical solution was developed and applied to the analysis of the fundamental and higher order TE and TM modes in waveguides containing arbitrarily nonlinear material. For the fundamental TE_o and TM_o modes it was observed that hysteresis can occur depending mainly on the film thickness. It was also observed that in physically symmetrical structures, the symmetrical solution is unstable. Results obtained for the first higher order TE_1 mode indicate that it propagates in a stable manner only for limited values of power, but further investigations are required in order to determine its behaviour at higher power levels.

The present solution can be applied to non Kerr-type nonlinearities, as well as to structures with a gradual low power refractive index distribution. It can also be applied to multilayered structures.

Although results were presented mostly for TE polarization, calculations were also performed for TM polarization for different types of nonlinearities, and the results showed good agreement with other ones in the literature, when available.

ACKNOWLEDGEMENT: This work was supported by TELEBRÁS through the contract PUC-TELEBRÁS 415/91.

REFERENCES

1 - C. T. Seaton, Xu Mai, G. I. Stegeman, e H. G. Winful, *Optical Engineering*, Vol. 24, 1985, pp. 593-599.

2 - C. T. Seaton, J. Valera, R. L. Shoemaker, G. I. Stegeman, J. Chilwell, and S. D. Smith, *IEEE J. Quantum Electron.*, Vol. QE-21, 1985, pp. 774-783.

3 - G. I. Stegeman, E. M. Wright, C. T. Seaton, J. V. Maloney, T. Shen, A. A. Maradudin, and R. F. Wallis, *IEEE J. Quantum Electron.*, Vol. QE-22, 1986, pp. 977-982.

4 - B. M. A. Rahman, J. R. Souza, and J. B. Davies, *IEEE Photonics Technol. Lett.*, Vol. 2, 1990, pp. 265-267.

5 - K. Hayata, M. Nagai, and M. Koshiba, *IEEE Trans. Microwave Theory Techn.*, Vol. MTT-36, 1988, pp. 1207-1215.

6 - A. C. P. Zabeu and J. R. Souza, *Proc. 20th European Microwave Conference*, Budapest, Hungary, 1990, pp. 481-486.

7 - K. Ogusu, *IEEE Trans. Microwave Theory and Tech.*, vol. MTT-37, pp. 941-946, 1989.

8 - C. K. R. T. Jones and J. V. Moloney, *Phys. Lett.* A, Vol. 117, 1986, pp. 175-180.

9 - S. J. Al-Bader and H. A. Jamid, *J. Optical SOc. Am. A*, Vol. 5, 1988, pp. 374-379.

10 - A. C. P. Zabeu and J. R. Souza, *Microwave and Optical Technology Lett.*, Vol. 3, 1990, pp. 298-302.

11 - K. Hayata and M. Koshiba, *Opt. Lett.*, Vol. 13, 1988, pp. 1041-1043.

1992 ACES Symposium, Monterey, California, March 1992

ELECTROMAGNETIC PIC MODELLING IN ARBITRARY GEOMETRY

James W Eastwood and Wayne Arter

AEA Technology, Culham Laboratory,
Abingdon, Oxon. OX14 3DB, England

ABSTRACT

A new relativistic electromagnetic PIC algorithm for general three dimensional geometries is described. Correct choice between co- and contravariant field components and of weighting yields simple coordinate invariant numerical prescriptions. The combination of isoparametric hexahedral elements, generated by transfinite interpolation, and multiblock decomposition leads to algorithms ideally suited to MIMD computers.

1 INTRODUCTION

Virtual Particle (VP) particle-mesh algorithms are now established as an effective approach to obtaining numerical schemes for solving the relativistic Maxwell-Vlasov equations [1, 2, 3, 4]. Unlike conventional Particle-in-Cell (PIC) schemes, they are derived using finite elements in both space and time. Current is assigned from 'virtual particles' placed at points specially interpolated between positions at successive time levels, a procedure which automatically leads to charge conservation. Existing VP implementations use rectangular finite elements in two dimensional cartesian and polar geometries. Only a restricted class of device is well modelled in such circumstances, leading to the need to implement VP in more complex geometries. This paper shows how the VP method extends to general three dimensional body-fitted elements [5].

Section 2 shows that the derivation in general curvilinears is similar to that for orthogonal coordinate systems, differing only in that tensor components are used in the action integral expression for the Maxwell-Vlasov equations. The resulting expressions for current assignment, charge assignment and particle motion are treated in Section 3, whilst Section 4 deals with the field equations and constitutive relationships. Section 5 discusses finite element net generation and efficient usage of Distributed Memory MIMD architecture computers.

2 VARIATIONAL FORMULATION

In general curvilinear coordinates $(\bar{x}^1,\ \bar{x}^2,\ \bar{x}^3)$ the action integral may be written

$$I = \int dt\ d\bar{x}^1\ d\bar{x}^2\ d\bar{x}^3 \sqrt{g} \left\{ \frac{1}{2}(E_i\ D^i - H_i\ B^i) + j^i\ A_i - \rho\phi \right\} + I_K \tag{1}$$

where I_K is the kinetic lagrangian and

$$E_k = -\frac{\partial \phi}{\partial \bar{x}^k} - \frac{\partial A_k}{\partial t} \tag{2}$$

$$B^i = \frac{\epsilon^{ijk}}{\sqrt{g}} \frac{\partial A_k}{\partial \bar{x}^j} \tag{3}$$

$$D^i = \epsilon_o E^i = \epsilon_o g^{ij} E_j \tag{4}$$

$$H_i = \frac{B_i}{\mu_o} = \frac{1}{\mu_o} g_{ij} B^j \tag{5}$$

If we further assume that the distribution function is represented by a set of sample points (ie 'superparticles'), then the source terms in the field lagrangian become

$$j^i = \sum_p \frac{q_p}{\sqrt{g}} \delta(\bar{x}^1 - \bar{x}^1_p)\delta(\bar{x}^2 - \bar{x}^2_p)\delta(\bar{x}^3 - \bar{x}^3_p)\dot{\bar{x}}^i \tag{6}$$

$$\rho = \sum_p \frac{q_p}{\sqrt{g}} \delta(\bar{x}^1 - \bar{x}^1_p)\delta(\bar{x}^2 - \bar{x}^2_p)\delta(\bar{x}^3 - \bar{x}^3_p) \tag{7}$$

and the kinetic lagrangian term becomes

$$I_K = -\int dt\ \sum_p \frac{Mc^2}{\gamma_p} \tag{8}$$

The sums in p are over particles, each with charge q_p. The metric tensor elements g_{ij} can be computed from the relationship between cartesian and the general curvilinear coordinates i.e. given

$$x^i = x^i(\bar{x}^1,\ \bar{x}^2,\ \bar{x}^3) \tag{9}$$

then

$$g_{ij} = \frac{\partial x^s}{\partial \bar{x}^i} \frac{\partial x^s}{\partial \bar{x}^j} \tag{10}$$

where $g = ||g_{ij}||$ and $g_{ij}g^{jk} = \delta^k_i$.

Treating I as a functional of the vector potential A_i, the scalar potential ϕ and particle coordinates $\{\mathbf{x}_p\}$ leads to Euler-Lagrange equations representing Maxwell's equations and relativistic particle motion; the discrete approximations to these differential equations are obtained by substituting test function approximations for ϕ, A_i and $\mathbf{x}_p$ and taking variations with respect to the nodal amplitudes. As will become apparent from the discussions below (Sections 3.1 and 4.1), it is advantageous to introduce weighted tensor flux and charge quantities, with the weighting factor $\sqrt{g}$, ie we introduce $b^i = \sqrt{g}B^i$, $d^i = \sqrt{g}D^i$, $J^i = \sqrt{g}j^i$ and $Q = \sqrt{g}\rho$.

3 PARTICLE EQUATIONS

The use of sample points ('superparticles') reduces the velocity space integrals to sums over particles, and transforms the Vlasov equation to the relativistic equations of motion for the superparticles. Source terms, Eqs (6) and (7), arise from variations with respect to potentials in the differential limit. These variations give the charge and current assignment schemes in the finite element case, as illustrated in Section 3.1. Section 3.2 shows that the assignment has the charge conserving property even for non-orthogonal element nets. In the differential limit, variation of the action with respect to particle coordinates gives the relativistic momentum equation. The treatment of the equations of motion is outlined in Section 3.3.

3.1 Assignment and Interpolation

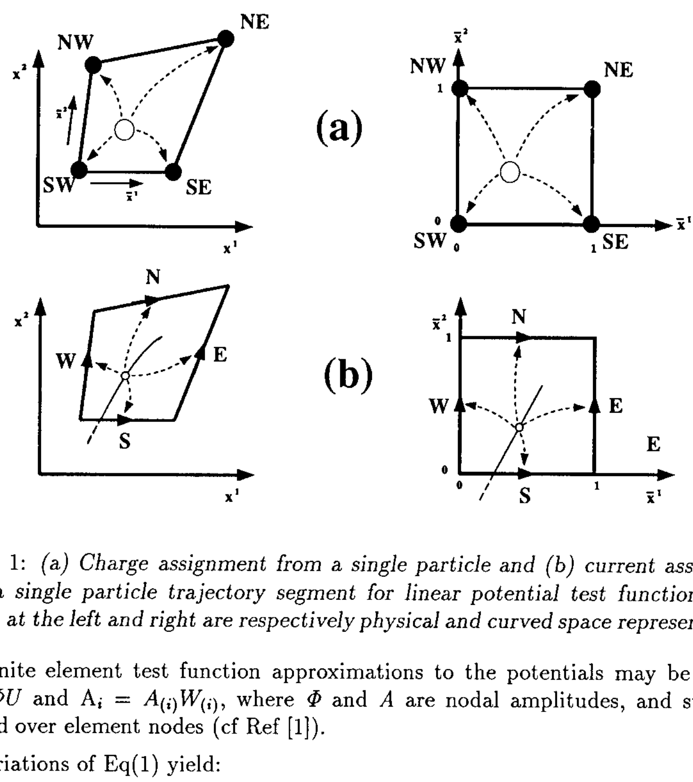

Figure 1: *(a) Charge assignment from a single particle and (b) current assignment from a single particle trajectory segment for linear potential test functions. The figures at the left and right are respectively physical and curved space representations.*

The finite element test function approximations to the potentials may be written $\phi = \Phi U$ and $A_i = A_{(i)}W_{(i)}$, where Φ and A are nodal amplitudes, and sums are implied over element nodes (cf Ref [1]).

Variations of Eq(1) yield:

$$\text{charge assignment}: \; Q \;=\; \int dt \sum_p q_p U((\bar{x}_p^1,\ \bar{x}_p^2,\ \bar{x}_p^3)(t), t) \qquad (11)$$

$$\text{current assignment : } J^i \;=\; \int dt \sum_p q_p \dot{\bar{x}}_p^{(i)} W_{(i)}((\bar{x}_p^1,\ \bar{x}_p^2,\ \bar{x}_p^3)(t), t) \tag{12}$$

The integrals for Q and J^i are evaluated in exactly the same manner as described in Ref [1]. For example, if in a general quadrilateral element U and W_i have the same linear / piecewise dependence as their cartesian counterpart [1, Section 4.3], then the fractions of the charge assigned from a unit charge at position $(\bar{x}^1, \bar{x}^2)$ (marked by open circles) to the four nodes at the corners of the element as shown in Figure 1(a) are given by

$$\begin{array}{ll} \delta Q_{NW} = (1-\bar{x}^1)\bar{x}^2 & \delta Q_{NE} = \bar{x}^1\bar{x}^2 \\ \delta Q_{SE} = \bar{x}^1(1-\bar{x}^2) & \delta Q_{SW} = (1-\bar{x}^1)(1-\bar{x}^2) \end{array} \tag{13}$$

Similarly, the contravariant current components from a trajectory segment from $(\bar{x}_i^1, \bar{x}_i^2)$ to $(\bar{x}_f^1, \bar{x}_f^2)$ are

$$\begin{array}{ll} \delta J_N = \bar{X}^2 \Delta\bar{x}^1 & \delta J_S = (1-\bar{X}^2)\Delta\bar{x}^1 \\ \delta J_E = \bar{X}^1 \Delta\bar{x}^2 & \delta J_W = (1-\bar{X}^1)\Delta\bar{x}^2 \end{array} \tag{14}$$

where $\bar{X}^k = (\bar{x}_f^k + \bar{x}_i^k)/2$, $\Delta\bar{x}^k = \bar{x}_f^k - \bar{x}_i^k$, where k=1 or 2. Coordinates $(\bar{x}_i^k, \bar{x}_i^k)$ and $(\bar{x}_f^k, \bar{x}_f^k)$ are respectively the start and end the trajectory segment (solid line in Figure 1(b)) in the finite element. Trajectory segments are assumed to be straight lines in the curved $(\bar{x}^1, \bar{x}^2)$ space. Figure 1(b) shows the position of the virtual particle at $(\bar{X}^k, \bar{X}^k)$ as a small open circle on the trajectory segment and labels the location of the current nodes referred to in Eq (14).

The example given here generalises straightforwardly to three dimensions, but then requires assignment from two rather than one 'virtual particle' per segment per element to ensure exact charge conservation.

3.2 Charge Conservation

Charge and current assignment are linear operations, so by linear superposition, conservation for one trajectory moving through a single time step implies the same for the sum of all trajectories. Summing all contributions to Eqs(14) from a single particle, gives the same as the difference of Eqs(13) at start and end points, ie the linear quadrilateral (hexahedral in three dimensions) element case satisfies

$$\partial_t Q = -\partial_k J^k \tag{15}$$

where the symbol ∂ denotes a centred difference arising from assembling the finite element contributions, and Q and J^k are nodal amplitudes. Equations of the form (15) can be shown to be generally satisfied for VP algorithms.

3.3 Particle Motion

The change in particle position is computed in exactly the same manner as the cartesian case. The change of position is computed from the leapfrog approximation to

$$\frac{d\bar{x}^k}{dt} = \bar{v}^k \tag{16}$$

The finite element approximation for the particle accelerations leads to unwieldy expressions; to avoid implicit formulae the time derivative of the momentum is lumped, which in effect replaces the time derivative by a finite difference. Treating the momentum equation in curved space introduces the Christoffel symbol Γ^l_{km} in the quadratic centripetal term:

$$\frac{d\bar{p}_k}{dt} - \Gamma^l_{km}\bar{v}^m\bar{p}_l = F_k = q(E_k + e_{klm}\bar{v}^l b^m) \tag{17}$$

A more straightforward generalisation of the cartesian leapfrog scheme for the momentum equation is obtained by reformulating Eq(17) in terms of the cartesian momentum components:

$$\frac{dp_i}{dt} = D^k_i F_k = qD^k_i(E_k + e_{klm}\bar{v}^l b^m) \tag{18}$$

where $\bar{v}^l = D^l_i p^i/\gamma = g^{lm}\bar{p}_m/\gamma$ and D^i_j is the deformation gradient tensor:

$$D^i_j = \frac{\partial \bar{x}^i}{\partial x^j} \tag{19}$$

Equation (18) leads to an integration scheme with leapfrog for the electric forces and an implicit scheme for Lorentz forces.

4 MAXWELL'S EQUATIONS

The principal difference between the cartesian and general curvilinear derivations of the field equations from the action integral (1) is the need for approximations to evaluate Eqs (4),(5) and (10) in the latter case. Approximation of Eq(10) is treated in Section 5. Choices of approximations to Eqs (4) and (5) lead to implicitness in computing either E_i from d^j for the circulation term in Faraday's Law or d^j from E_i in applying boundary conditions; the latter is favoured for computational simplicity.

4.1 Field Equations

Introducing the weighted fluxes b^i and d^i into Eq(1), taking variations with respect to the potential test function amplitude and assembling the element contributions gives, after a little algebra, approximations to Maxwell's Equations:

$$\partial_t \mathsf{b}^i = -e^{ijk}\partial_j \mathsf{E}_k, \quad \partial_i \mathsf{b}^i = 0 \tag{20}$$

$$\partial_t \mathsf{d}^i = e^{ijk}\partial_j \mathsf{H}_k - J^i, \quad \partial_i \mathsf{d}^i = Q \tag{21}$$

The precise relationship between quantities b^i,d^i, E_k,H_k and the nodal amplitudes depends on the approximations chosen for the constitutive relationships. In the lowest order lumped approximation they become the nodal amplitudes.

The analysis leading to Eqs (20) and (21) shows that the discrete VP equations in the quantities b^i,d^i, E_k,H_k,J^i and Q are identical in any coordinate system. Geometrical information appears, along with the permeability and permittivity tensors, only in the constitutive relations relating d^i to E_i and b^i to H_i.

4.2 Constitutive Equations

The weak approximations to Eqs (4) and (5), with lumped mass matrices give the simplest explicit expressions for E_i and H_i. If we denote the test function approximations $E_i = \bar{E}_{(i)}V_{(i)}$ and $H_i = \bar{H}_{(i)}X_{(i)}$, then Eqs (4) and (5) yield:

$$\langle \bar{E}_i V_{(i)}, V_{(i)}\rangle = \langle \frac{1}{\epsilon_0\sqrt{g}} g_{ij}\bar{d}^j V_{(j)}, V_{(i)}\rangle \qquad (\Rightarrow \mathsf{E}_i = \mathsf{G}^E_{ij}\mathsf{d}^j) \tag{22}$$

$$\langle \bar{H}_i X_{(i)}, X_{(i)}\rangle = \langle \frac{1}{\mu_0\sqrt{g}} g_{ij}\bar{b}^j X_{(j)}, X_{(i)}\rangle \qquad (\Rightarrow \mathsf{H}_i = \mathsf{G}^H_{ij}\mathsf{b}^j) \tag{23}$$

where the inner product is defined by

$$\langle a, b\rangle = \int_D dt\ d\bar{x}^1\ d\bar{x}^2\ d\bar{x}^3 a(\bar{x}^i, t) b(\bar{x}^i, t) \tag{24}$$

The integral forms of Eqs (22) and (23) are lumped to give the mesh forms shown in the brackets. Elements of the symmetric tensors G^E_{ij} and G^H_{ij} are sparse matrices.

4.3 Boundary Conditions

In orthogonal systems, boundary conditions are applied straightforwardly to the surface nodal values. In general curvilinears, there is the added complication that Eq (22) must be inverted to apply the conditions on E_i to d^i in Ampere's equation. Fortunately, the matrices involved are sparse and diagonally dominant, so a simple iterative scheme should be effective.

5 MESH GENERATION AND MIMD

A general curvilinear coordinate system arises naturally when we seek to represent awkwardly shaped devices. Transfinite interpolation [6] provides a coordinate system for any simply connected surface (in 2-D) or volume (in 3-D) provided the bounding curves or surfaces are not too convex or concave. Realistic microwave sources involve

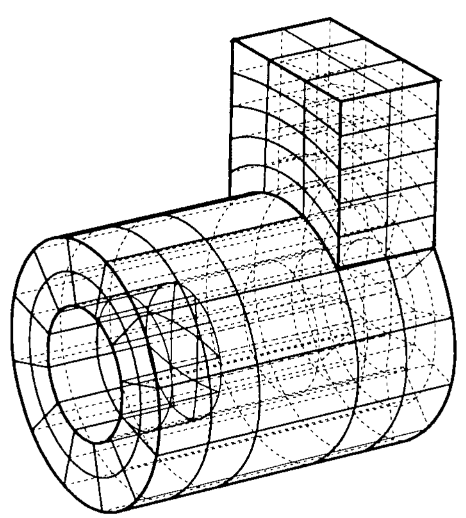

Figure 2: *An illustration of the meshing of the junction of a coaxial and rectangular guide.There are six blocks:the rectangular guide, the central cylinder and four in the annulus.*

cavities and waveguides of cylindrical and rectangular cross-section. Separate subdomains are therefore introduced to handle the various components and also axial effects. Figure 2 shows the multiblock representation of a cylindrical device with an attached waveguide. Each block is subdivided into elements, and the same parameterisation is used for the coordinate transformation as is employed for the scalar potential.

The multiblock subdivision of the computational domain minimises the amount of global data and interprocessor message passing, and simplifies load balancing across processors. Each slave block only requires data from its neighbours, and the master control program only requires information about the block surfaces ('glue patches') which join the slave blocks together. This arrangement offers the prospects of large computational intensity and a weak Amdahl limit to speedup on distributed memory MIMD computers. Moreover, the simple logical cube addressing within each block leads to fast serial processing.

Without compromising the subdivision of the spatial mesh into blocks to get efficient MIMD processing, one can further demand that boundary conditions *only* apply at the surfaces of blocks; this eliminates the addressing problems in embedding surfaces within blocks, and allows surface data to be passed to the control program through the 'glue patch' tables. Further saving of computer storage and time arise from keeping metric information and material property data only in those blocks where they are needed. When many small blocks are used to describe a complex

object, load balancing is achieved by assigning several blocks to one processor.

In summary, the efficient meshing strategy uses

- A multiblock spatial decomposition where segments of target surfaces and other boundaries are coincident with block surfaces.
- Indirect ('glue patch') addressing between blocks, and logical cube (i,j,k) element nets within blocks.
- Transfinite interpolation to divide the curvilinear hexahedral multiblocks into finite elements

6 FINAL REMARKS

This paper has outlined the extension of the VP algorithms to general geometry. The result is a particularly simple coordinate invariant form for the field equations *and* a current assignment scheme which has the same charge conserving property as its orthogonal counterpart.

The multiblock decomposition is ideal for distributed memory MIMD computers. The electromagnetic calculation can be statically load balanced, has little message passing between blocks and small scalar overheads.

We are currently developing general geometry software based on the scheme described herein in order to extend our capability for microwave tube modelling. However, the elegant body-fitting electromagnetic solver part of our PIC scheme can equally well be applied to the computationally simpler problems where free charges are absent; for example, to study waveguides and exterior scattering problems.

7 REFERENCES

[1] J W Eastwood, Comput Phys Commun **64**(1991)252.

[2] J W Eastwood, pp 655-660, Proc. 7th Ann Rev Prog App Computational Electromagnetics, Naval Postgraduate School, Monterey, Ca (Mar 1991).

[3] J W Eastwood, "Computer Modelling of Microwave Sources", *Proc 18th Annual Conf Plasma Phys*, IoP, Colchester (July 1991).

[4] N J Brealey, "Computer Simulation of Helix Travelling Wave Tubes", *Proc High Power Microwave generation and Applications*, Varenna, Italy (Sep 1991).

[5] W Arter and J W Eastwood, "Electromagnetic Modelling in Arbitrary Geometries by the Virtual Particle Particle-Mesh Method", Paper PWE15, *Proc 14th Int Conf Num Sim Plasmas*, APS, Annapolis (Sep 1991).

[6] W J Gordon and C A Hall, Int J Numer Meths Engng **7**(1973)461.

SESSION 14 - "TIME DOMAIN METHODS"

Moderator: Pat Foster

Programming a Portable GUI

Lee W. Henderson
The Ohio State University ElectroScience Lab
1320 Kinnear Rd.
Columbus OH, 43212

Abstract

This paper presents a functional programming model for developing software which will run, unmodified, on any of the popular windowing systems or graphics terminals. This is accomplished by defining a fixed programming model with standardized entry points, and a standard library of functions for controlling the GUI constructs (such as menus, dialogs, etc.), and a device dependent Interface Layer which sits between the windowing system and the program. All callback functions are are handled by this interface layer or passed to the standardized entry points. Graphics operations are handled by a standard graphics library such as GKS or PHIGS.

1 Introduction

In spite of all the talk of open systems, none of the three major windowing interfaces ("X" Windows, Microsoft Windows, and the Macintosh) support the same application programming interface (API). Thus software developers are forced to port their programs from system to system.

Programmers wishing to port electromagnetics codes to windowing systems must also deal with the language barrier. EM codes are generally written in FORTRAN, for a variety of good reasons. Standard FORTRAN 77, however, is ill suited to most window API's, where the language of choice is usually C. FORTRAN 90 has all of the capabilities needed to program for windows and is superior to C in most respects, but it will be some time before it is widely available. Thus most EM software developers will continue to use FORTRAN 77 for some time. Some FORTRAN compilers now allow programs to run in a pseudo terminal window, but this is clearly not the same as writing a FORTRAN program which makes use of the GUI functions of a windowing environment.

This paper presents a library of functions and programming methodology which will allow a program to be written (or modified) so that it can be transported to any windowing or non-windowing system. There are some commercial products (e.g. Aspect from Open Inc.) and a standards committee (Posix 1201.1) working to solve

the transportability problems, but these efforts aimed at the C programmer and are much broader in scope than the work presented here. Any program or library designed for maximum transportability must sacrifice some functionality. The success or failure of these efforts often rides on careful selection of these sacrifices.

The philosophy used in this paper is based on two requirements: (1) To employ a minimalist approach which will allow maximum functionality with minimum effort. (2) To generate a program which can be used on conventional graphics terminals as well as windowing systems. This is accomplished by distilling all of the features implied by the term "windowing system" into a few basic functions which capture the essence of a GUI. These functions constitute an interface layer as shown in figures 2 and 3. This interface layer maps the system dependent features of the particular windowing system into a standard interface for the user program as shown in the figures. Of course the interface layer is very system dependent, and must be implemented for each different system, but once written it can be used by any program on that system.

This is, of course, very similar to the way device independent graphics packages (such as GKS, PLOT10, DI3000, etc.) are written but with one important difference—programs written for windowing systems are based on an event driven model. Thus a standard programming interface must specify not only how the program will call the system, but how (and when) the system will call the program.

2 Event Driven Programming

"Conventional" programs are written on a procedural model. The operating system passes control to the program, which makes subroutine calls to the system or libraries. After each subroutine call, the system returns to the program at the point where the call occurred. When the program is finished it returns control to the system.

Windowing systems require that programs be written using an event driven model. The operating system passes control to the program which begins by initializing variables, creating windows, and allocating resources. The program also declares the names and locations of the various subroutines which will be used to handle events, an event being just about any interaction between the user and the computer such as moving the mouse, pressing a key, releasing a key, pressing a mouse button, releasing a mouse button, etc. The program then return control to the system. When an event occurs, the system calls the particular subroutine declared by the program to handle that type of event (or events).

3 Layers

As shown in figures 2 and 3, the programming environment consists of three layers: the system layer, the interface layer, and the user program layer.

3.1 System Layer

The system layer contains the operating system, the windowing system (if one exists), and any toolkits associated with the windowing system (such as MOTIF). For the purposes of this discussion, the hardware is also considered part of the system layer.

3.2 Interface Layer

The interface layer contains all of the system specific code necessary to implement the transportable interface. On most windowing systems it will be written in C, but all interactions between this layer and the user program layer must be compatible with FORTRAN.

For a window system, this layer has 6 major components: the initialize routine, dialog functions, menu functions, miscellaneous system functions, the window procedure, and the graphics library

3.2.1 The initialize routine

This is the main windows program. It receives control from the system and allocates resources. The user's initialize routine is called as a subroutine. When initialization is completed, control returns to the system. (Note: This is a slightly simplified explanation, in a real environment the initialize routine would also contain the message loop.)

3.2.2 Dialog Functions

This is where the greatest sacrifices must be made. On any windowing system, the construction of a dialog box is not difficult and the programmer is often provided with special editors and programming tools make the task even easier. The problem with dialogs is the differences that exist between the various windowing systems. These differences can be dealt with, but not with the minimalist approach used here. The short term solution to this problem is to define a standard set of dialogs from which the programmer must choose, then all of the system dependencies of implementing each dialog are buried in the interface layer. Through creative use of menus and the standard dialogs, the program can do a reasonable job interacting with the user. For example, instead of creating a dialog with many pushbuttons to select options, the

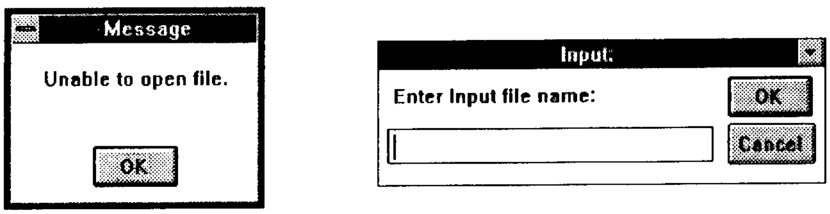

Figure 1: Message and input dialogs.

programmer can use menu items (with and without checkmarks) to control options. Each dialog is callable as a subroutine from the user layer. The standard dialogs are:

Function	Description
message	An output dialog which allows the programer to send a message to the user (figure 1)
input	An input dialog which allows the user to input a string (or press a button) in response to a prompt (figure 1).
open	A standard file "open" dialog. The exact format is system dependent, but usually contains file filter, a list of files, and an input area where the user can type a file name.
save as	A standard file "save as" dialog, similar to the "open" dialog.

3.2.3 Menu Functions

Menus are much simpler to define than dialog boxes because their appearance is usually controlled entirely by the window manager. The only real restriction to be placed on menus is that they must contain simple text strings, no bitmaps, icons, or other exotic constructs. The functions necessary for manipulating menus are:

Function	Description
create menu	Create a new pull down menu. The new menu is either attached to the menu bar at the top of the window or to a line in an existing menu.
enable/disable menu	Set the operational status of a pull down menu.
gray/ungray menu	Set the appearance of a pull down menu.
delete menu	Remove a pull down menu from the system.
insert separator	Insert a separator line between items in a pull down menu.
create item	Add a new line item to a pull down menu.
gray/ungray item	Change the display appearance of an item in a pull down menu.
check/uncheck item	Add or remove a checkmark next to an item in a pull down menu.
enable/disable item	Set the operational status of an item in a pull down menu.
delete item	Remove a line item from the system.

3.2.4 Miscellaneous System Functions

Several functions which don't fall into specific categories but must be provided are:

Function	Description
date/time	return current system date and time
release	return control to the operating system temporarily (necessary for non-preemptive multitasking systems such as Microsoft windows and the Macintosh Multifinder)
mouse cursor	Switches mouse cursor to a different symbol (such as an hourglass) to indicate that the program is working hard.
terminate	Interface layer releases all allocated resources, and terminates the program.

3.2.5 The window procedure

This routine is the "command center" for the interface layer. It coordinates all actions between the different libraries and the window system. Then the user picks a menu item, windows passes control to the window procedure which then passes control to the user program.

3.2.6 The graphics library

For this discussion we will assume that the graphics library is GKS, although any transportable graphics library, such as PHIGS, would work just as well.

GKS has many strengths and weaknesses but in this application it is appropriate, for the following reasons:

- It has a fortran binding.
- It provides a rich set of graphics primitives and operations.
- It is widely used in workstation and mainframe graphics applications (the popular NCAR graphics library is built on GKS).

Because of it's size and complexity, GKS has found limited use in the world of the PC, however, this should change with the increasing power of the PC and blurring of the line between PC's and workstations. The Microsoft Windows and X windows API show strong GKS influences both in terminology and functions. In many cases there is a one to one correspondence between GKS routines the API routines. The main weakness of GKS for window applications is it's limited support for bitmap and pixel operations.

3.3 User Program Layer

The user program is, in many respects, just a typical FORTRAN program. This is possible because the interface layer hides most of the complexity of windows from the user layer. However, there are a few programming rules which must be absolutely followed for the system to function:

- The program must have three entry points with specific names and arguments so that the interface layer can call the user program. The entry points are
  1. Initialize: This entry point is called by the init routine in the interface layer.
  2. Menu Select: This entry point is called by the window procedure whenever a menu item has been selected. An argument in the call window for this entry point specifies which item was chosen.
  3. Exit: This entry point is called by the window procedure whenever windows has determined that the program should be terminated.

- The program must never use the FORTRAN statements STOP or PAUSE. Both of these statements have unpredictable side effects on different windowing systems. Any use will seriously affect the transportability of the program. When the program is finished, it must call the appropriate interface layer routine to exit.

- The program must **never** do any terminal IO. The only IO operations permitted are those that go directly to and from a disk. Any attempt to perform non-disk IO, such as READ(*,), WRITE(*,), WRITE(6,), READ(5,), etc. will have disastrous consequences. All terminal IO must be done through the dialog functions. This restriction will cause the greatest problems for those programmers wishing to convert an existing program, but there is no other way to ensure portability.

4 Styles

Designers of a windowing system expect all program written for that system to have a similar look and feel, and all windowing systems have style documents which describe how programs are supposed to work [1],[2],[3]. These documents specify things like standard dialogs, menus, accelerator keys, etc. The appearance of dialogs is controlled by the interface layer. The menus are built by the user's program and it is the programmers responsibility to ensure that the standard menus are properly constructed. Fortunately there is so little difference among the popular windowing systems that this is not a serious problem.

References

[1] Open Software Foundation, "OSF/MOTIF Style Guide", Prentice–Hall, Englewood–Cliffs NJ, 1990

[2] IBM "SAA Common User Access Advanced Interface Design Guide", IBM corp., 1989

[3] Sun Microsystems Inc., "OPEN LOOK, Graphical User Interface Application Style Guide, Addison–Wesley, Reading, MA, 1990

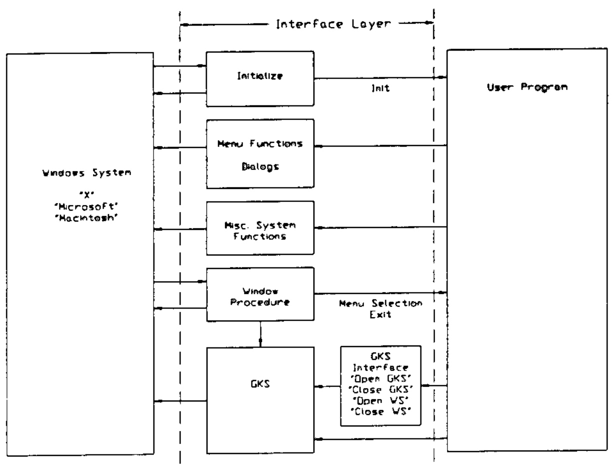

Figure 2: Programming model for a portable GUI based on a windowing system.

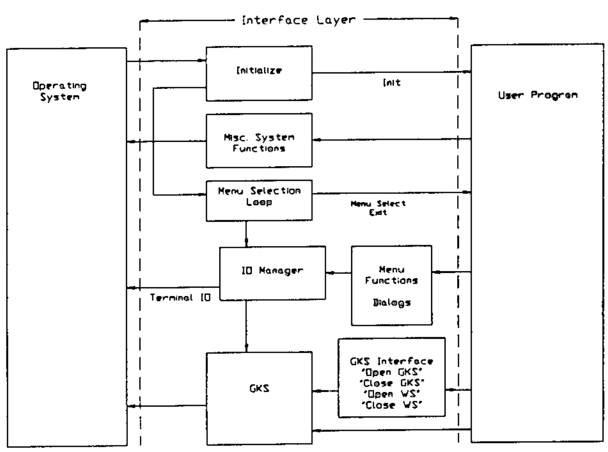

Figure 3: Programming model for a portable GUI based on a non-windowing system such as a graphics terminal.

A Graphical Language Interpreter for the Input of Geometrical Data

A. Genon, A. Nicolet, N. Bamps, W. Legros
University of Liège, Dept of Electrical Engineering, Institut Montefiore
B28, Sart Tilman, B-4000, Liège, Belgium

ABSTRACT

This paper presents a software tool for the input of geometrical data needed in numerical computations. Unlike the majority of similar tools, this one is not interactive. The basic concept is to program the structure using features such as parametrization, procedures, and control structures. The syntax of the particular language is first described and then it is illustrated by an example.

INTRODUCTION

Nowadays interactive graphical data input are very fashionable (Gardan 84). Nevertheless, if they are very convenient for the novice, they may be less attractive to a more skilled user at ease with programming and who needs to input several times the same structures with small modifications (e.g. for optimization purposes). The graphical language interpreter for the input of geometrical data in numerical modelling is aimed at this latter kind of users.

Its characteristics and advantages are the following ones:

- Its syntax is very close to that of classical structured languages and is consequentely very easy to learn for anyone already familiar with such a language.
- The full parametrization together with the possibility of using variables, arrays, arithmetic expressions and classical functions (trigonometric and inverse trigonometric, log, exp ...) make data input and modification very easy.
- The instructions generating graphics are: PT (point), DR (line segment), DT (tangent segment), CH (clockwise circle), CA (counterclockwise circle), CT (tangent circle).
- There are some facilities for the definition of coordinates: tangency points may be automatically computed, relative and absolute coordinates may be mixed in any expression, rectangular and cylindrical coordinates, symmetries, rotations and translations may be used.

GEOMETRICAL DATA INPUT SOFTWARE TOOL

The geometry definition tool LIGS (Langage Interprété Générateur de Structures) has the following characteristics (Nicolet 91):

• the user first writes a file containing the instructions necessary to generate the geometry; this may be done using his usual text editor; those instructions constitute a **program;**

• this file is then submitted to LIGS that interprets the program, i.e. verifies syntax, executes instructions and creates output files containing the description of the structure in the form of line segments and arcs of circle with numerical coordinates; those files may be easily used by drawing or meshing software tools (Bamps 91).

Before examining the particular syntax of the language, some objects are described whose definitions are almost the same as in FORTRAN 77 (some differences are underlined):

• a real: all the reals in LIGS correspond to double precision reals of FORTRAN;

• an integer;

• an array: the dimension must be declared, indices must be integer expressions between square brackets and separated by semicolon, e.g. a[i ; j ; k] ;

• an expression: the four operations +, -, *, / are allowed, together with the functions LOG (natural logarithm), EXP (exponential), ABS (absolute value), SIN (sine), COS (cosine), ASIN (inverse sine), ACOS (inverse cosine), TAN (tangent), ATAN (inverse tangent), SQR (square), SQRT (square root);

• a logical expression: the operators .LE. (Less or Equal), .LT. (Less Than), .GE. (Greater or Equal), .GT. (Greater Than), .EQ. (EQual), .NE. (Not Equal) are allowed;

• an identifier: the underscore (_) is allowed, a block identifier has a maximum length of 12 characters, a parameter identifier has a maximum length of 4 characters (extra characters are allowed but are meaningless).

Comments may be inserted in any line of the program: any text after an exclamation mark (!) is not taken into account in the interpretation.

For the description of the syntax, the Backus-Naur notation (Graham 75) is used i.e. the following meta-symbols:

|	alternative
[ ]	option
{ }	possible repetition
' '	litteral value (**keyword**)
:=	partial or complete definition
( )	*comment*

<u>Geometry definition</u>

geometry := **'$geo'**
{head}
{block}
{domain}
'$end geo'

head := {global declaration}
{initialization}

global declaration := **'glo real'** parameter list
:= **'glo integer'** parameter list

initialization := parameter identifier '=' expression

<u>Block definition</u>

block without parameter := **'bloc'** block identifier '( )'
[{declaration}]
[{instruction}]
'end'

block := block without parameter
:= **'bloc'** block identifier '(' parameter list ')'
[{declaration}]
[{instruction}]
'end'

parameter list := parameter identifier
[{ ',' parameter identifier}]

declaration := **'par integer'** parameter list
:= **'par real'** parameter list
(all the local variables and transmitted parameters must be declared using this command)

coordinates	:=	coord ',' coord	*(rectangular coordinates)*
	:=	distance ',' angle	*(polar coordinates)*
coord	:=	expression	*(absolute coordinates)*
	:=	'$' expression	*(relative coordinates)*
angle	:=	expression	*(angle)*
distance	:=	coord	
segmentation	:=	expression	*(element discretization)*
boundary condition	:=	expression	*(boundary condition number)*

element data := coordinates
:= coordinates ',' segmentation [',' boundary condition]
:= coordinates ',,' boundary condition

instruction	:=	**'pt'** coordinates	*(define a point)*
	:=	**'dr'** element data	*(define a line segment between the last point and the specified point)*
	:=	**'ch'** element data	*(define an arc of clockwise circle between two points. The specified coordinates are those of the center of the circle)*

:= **'ca'** element data *(define an arc of counterclockwise circle between two points. The specified coordinates are those of the center of the circle)*

:= **'dt'** element data *(define a line segment tangent to the following and/or to the preceding circle and passing by the specified point)*

:= **'ct'** real |
'ct' real ',' segmentation [','boundary condition] |
'ct' real ',,' boundary condition
(tangent circle of given radius)

*(- Only the instructions **dr**, **dt**, **ch**, **ca**, **ct** lead to the creation of contour elements.*

*- Only the instructions **pt**, **dr**, **dt** modify the definition of the current point, i.e. the point taken into account in the next instruction.*

*- The succession order of the various instructions **pt**, **dr**, **ch**, **ca**, **dt** and **ct** is not completely free. It must lead to well-defined geometrical elements.)*

:= **'print'** parameter identifier *(print the value of the local parameter during the interpretation of the file)*

:= parameter identifier '=' expression *(allocation)*

:= **'if** (' logical expression ')' *(control structure : if(condition) ... else ...)*
{instruction}
['**else**'
{instruction}]
'**fi**'

:= **'do** (' logical expression ')' *(control structure: while (condition) ...)*
{instruction}
'**od**'

:= **'call'** block identifier
'(' [expression [{',' expression }]] ')'
['>' (' parameter list ')']
(call a block (=subroutine), possibly recursively; possible modification of some parameters (=side effect) of the calling block (option '>'))

:= **'set'** setparameter
(define symmetries,rotations, etc ...)

setparameter := **'pol'** | **'rec'**
(flag for polar or rectangular coordinates)

:= **'order** [' orderparameter ']'
(evaluation order for symmetries, rotations, translations)

:= **'rot** [' expression ',' expression ',' expression ']'
(rotation: centre of rotation + angle of rotation)

:= **'sym** [' expression ',' expression
',' expression ',' expression']'
(symmetry: two points of the axis)

:= **'tran** [' expression ',' expression ']'
(translation: translation vector)

:= **'norot'** *(no rotation)*

:= **'nosym'** *(no symmetry)*

:= **'notran'** *(no translation)*

orderparameter := **'rot,sym,tran'** | **'rot,tran,sym'** |
'tran,rot,sym' | **'tran,sym,rot'** |
'sym,rot,tran' | **'sym,tran,rot'**
(various orders for the evaluation of symmetries, rotations and translations)

Domain definition

domain := **'dom'** integer ':' ['-']block identifier
[{ '/' ['-']block identifier }] ';'
(Only blocks without parameter must be used in the definition of the domains. The minus sign in front of a block means that this block must be reversed)

EXAMPLE

As an example, consider the stator of an electric motor whose teeth are similar. The natural description of this structure consists of a procedure that gives a parametric description of the generic tooth. The set of teeth is generated by a loop calling the tooth procedure and performing a rotation. If a computation involving a similar stator must be done, it is very easy to change the structure by modifying the radius, the characteristics of the generic tooth or the number of teeth.

Table 1 gives the example of a data file for LIGS describing a stepping motor. Figure 1 shows the corresponding geometry.

```
$geo

glo real       pi,th0,rr,sir,ser,pr,ps,p1,p2,p3
glo integer    nrot,nsta

th0   =   0.                              ! rotor angular position
nrot  =   18                              ! number of rotor poles
nsta  =   8                               ! number of stator poles
rr    =   0.25                            ! rotor radius (m)
pr    =   20.                             ! rotor pole height (%)
ser   =   0.7                             ! stator external radius (m)
ps    =   81.4                            ! stator internal radius (%)
sir   =   ps*ser/100.
p1    =   75.4                            ! parameters
p2    =   63.2                            ! of stator
p3    =   56.1                            ! teeth
pi    =   3.141592654

bloc rotor( )
      par integer   i
      par real      b,p
      set pol                             ! polar coordinates
      b     =     360./nrot               ! pole magnitude
      p     =     pr*rr/100               ! pole height
      i     =     1
      do    (i.le.nrot)                   ! for all the poles
            set rot[0.,0.,(1-i)*b]        ! rotate
            call pole_rotor(th0,b,rr,p)   ! define a pole
            i=i+1                         ! next pole
      od
end

bloc pole_rotor(th0,beta,rad,p)
      par real      th0,beta,rad,p
      pt    rad    , th0                  ! initial point
      ch    0.     , 0.     , 2           ! clockwise circle
      pt    rad    , th0-beta/2.
      dr    rad+p  , th0-beta/2.   , 2    ! line segment
      ch    0.     , 0.2
      pt    rad+p  , th0-beta
      dr    rad    , th0-beta      , 2
end
```

Table 1: data file for the description of a stepping motor

```
bloc int_sta()
        par integer     i
        par real        b,r1,r2,r3
        b       =       360./nsta               ! pole magnitude
        r1      =       (1.-p1/100.)*sir        ! pole
        r2      =       (1.-p2/100.)*sir        !
        r3      =       (1.-p3/100.)*sir        ! depth
        set pol
        i       =       1
        do      (i.le.nsta)                     ! for all the poles
                set rot[0.,0.,(1-i)*b]          ! rotate
                call pole_stator(b,sir,r1,r2,r3) ! define a pole
                i=i+1                           ! next pole
        od
end

bloc pole_stator(beta,rad,p1,p2,p3)
        par real        beta,p1,p2,p3,b
        b       =       beta/4.
        pt      rad     , 0.
        ca      0.      , 0.    , 5             ! counterclockwise circle
        pt      rad     , 3.*b
        dr      rad-p1  , 3.*b  , 3
        ch      0.      , 0.    , 2
        pt      rad-p1  , 2.*b
        dr      rad-p3  , 2.*b  , 2
        ca      0.      , 0.    , 2
        pt      rad-p3  , 3.*b
        dr      rad-p2  , 3.*b
        ca      0.      , 0.    , 2
        pt      rad-p2  , 4.*b
        dr      rad-p3  , 4.*b
        ca      0.      , 0.    , 2
        pt      rad-p3  , 5.*b
        dr      rad-p1  , 5.*b  , 2
        ca      0.      , 0.    , 2
        pt      rad-p1  , 4.*b
        dr      rad     , 4.*b  , 3
end

bloc ext_stator()
        set rec                                 ! back to rectangular coordinates
        pt      ser     , 0.
        ch      0.      , 0.    , 40
        pt      ser     , 0.
end
```

Table 1: data file for the description of a stepping motor (continued)

```
dom 1 :    -ext_stator ;
dom 2 :    int_sta / ext_stator ;
dom 3 :    -rotor / -int_sta ;
dom 4 :    rotor ;

$ end geo
```

Table 1 : data file for the description of a stepping motor (continued)

CONCLUSION

The graphical interpreter is an alternative to common interactive geometrical data inputs. One interesting possibility is to describe the whole problem in only one file i.e. to use other fields than '$geo' to describe material properties, boundary conditions, electrical excitations ... Note that the definition of an element allows references to boundary condition and segmentation.

The graphical interpreter may also be used to construct 3D structures. In this case, the elementary geometric building blocks are directly the finite elements. New keywords such as 'crno' to create a node and 'crel' to create an element are introduced.

REFERENCES

Bamps, N., Hedia, H., Genon, A., Legros, W., Nicolet, A., Umé, M.,
Graphical Language Interpreter and Meshing Tool for Electromagnetic Computations
COMPUMAG 91, Sorrento, Italy, July 1991, to appear

Gardan, Y., Lucas, M., Interactive Graphics in CAD, Kogan Page, London, 1984.

Graham R. M., Principles of Systems Programming, Wiley, New York, 1975.

Nicolet, A., Ph. D. Thesis, University of Liège, Liège, May 1991.

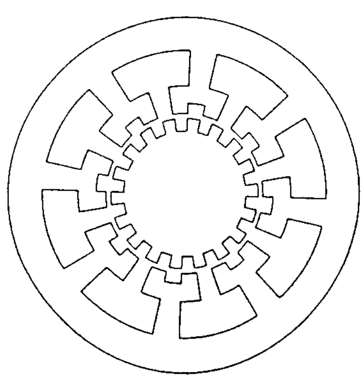

Figure 1 : stepping motor

Using Commercial CAD Packages to Interface with 3D EM Modeling Codes

T. H. Hubing and G. K. Bhat
University of Missouri-Rolla
Rolla, MO 65401

Abstract

Generating input files for three-dimensional EM modeling codes can be very difficult without the aid of a graphical user interface. This paper describes how an inexpensive commercial CAD program for PC's was used to provide a graphical user interface for a finite element modeling code. The same principles could be applied to other CAD programs and the procedure would work equally well with other three-dimensional EM modeling software including moment-method and finite-difference time-domain codes.

Introduction

Many useful three-dimensional electromagnetic modeling codes are distributed in the form of source code. A single Fortran or C source listing can be compiled to run on a wide range of systems from PCs to supercomputers. Hence, source code is perhaps the most convenient way to distribute a program to a wide variety of users.

Unfortunately graphical input/output procedures tend to vary considerably from one machine to another. Therefore, in order to compile a source code listing correctly on a variety of computers, input and output must generally be restricted to ASCII text. Simple three-dimensional configurations can usually be created using a text editor to build an input data file. Data files for large complex configurations however, can be difficult to build in this way and errors in such a data file are difficult to locate.

In order to combat this problem, many EM modelers have developed graphical front-ends for their source code programs. Graphical representations of the configuration being modeled help the user to build complex, error-free inputs. Graphical front-ends tend to be machine dependent and are rarely distributed with the rest of the code. They are usually complex programs that are difficult to develop, and relatively few non-commercial graphical front-ends are available.

This paper describes how an inexpensive, commercial CAD program (DesignCAD 3-D) is used to create input data files for a non-commercial finite element program. No modifications to the CAD program were necessary. Instead, rules were developed for identifying source parameters, material constants, and other non-geometric parameters within the CAD drawing. A simple utility converts the output from the CAD program into a suitable data input file for the EM modeling program.

DesignCAD 3-D

DesignCAD 3-D is an inexpensive, relatively easy to learn, three-dimensional drawing program that runs on personal computers. It uses a mouse and/or the keyboard with built-in drawing tools for making lines, arcs, circles, rectangles, boxes, cones, cylinders, spheres, and hemispheres. All objects are drawn in color on a resizable grid. There is one main viewing window and three smaller views that are constantly displayed. The object can be easily rotated or shifted while it is being drawn. Text labels and shading are also features of the program.

The Translation Code

DesignCAD 3-D saves all of the information describing a particular drawing in an ASCII text file. It was a simple matter to write a short *translation code* that reads the DesignCAD text file and converts it to an input file for our finite element program.

If a CAD drawing is going to be used to provide input to an EM modeling code, all of the necessary input information must be contained in the drawing. The geometry of the configuration is obtained from the dimensions of the drawing. Material properties, source fields, mesh densities, and other information can be stored in the drawing by taking advantage of color, special objects, text, or a combination of these features. The basic information required by our three-dimensional finite element code is

- the location of every mesh node
- the material coefficients at every mesh node
- whether a node is a boundary node and the orientation of the boundary
- the value of any source parameters at the node.

Since our code employs a uniform rectangular grid, it is a simple matter to designate the CAD program's grid points to be the mesh nodes. The *snap-to-grid* feature of the CAD program helps to ensure that nodes lie on material boundaries as much as possible.

A uniform rectangular grid is not a prerequisite for obtaining input from a CAD program. Finite element codes that employ more sophisticated mesh generating algorithms could still find all the input information they need in the CAD drawing. In this case, setting the grid points equal to mesh nodes was a matter of convenience.

Colors are used to define the material coefficients at every mesh node. For example, green is defined by our translation code to represent a lossless dielectric with a relative permittivity, $\varepsilon_r = 3$. Other colors represent other materials with different properties. White is different from other colors in that white objects have perfectly conducting walls and hollow interiors. This is a convenient way of defining the outer boundary of many problems. Although this particular finite element code

doesn't support infinite elements, representing infinite elements by a specific color would be a straight forward extension of the translation code.

Arrows are used to set the electric field at a specific node to a fixed non-zero value. The base of the arrow is located on the node associated with that field value. The direction of the arrow indicates the direction of the field. The magnitude of the field is represented by the color of the arrow. The length of the arrow and the size of the arrow head can be used to convey additional information about the field.

The translation code is relatively simple. The boundary of the configuration is specified in the first line of the CAD program's text file. Beginning with the first node (i.e. grid point), the code sets all electric field values to *free* and the material coefficients to free space values. Then the code checks to see if the node is on the boundary of a white object. If it is, the tangential components of electric field are set to zero. Next, the code checks to see if the node is within or on the boundary of a colored object. If so, the material coefficients are set to the values corresponding to that color. Finally, the code checks for the presence of an arrow at that node. If there is an arrow, the components of electric field corresponding to the arrow's direction are set to a fixed value based on the color of the arrow. The translation code cycles through every node in this manner until every node in the object has been described. The output of the translation code is an ASCII text file that can be read directly by the finite element code.

Example

The shorted rectangular waveguide illustrated in Figure 1 took only a few minutes to draw using the CAD program. The 4×11×16 node waveguide was drawn in white with the *box* tool. The dielectric block in the middle of the waveguide was drawn using the same tool in green. The arrows

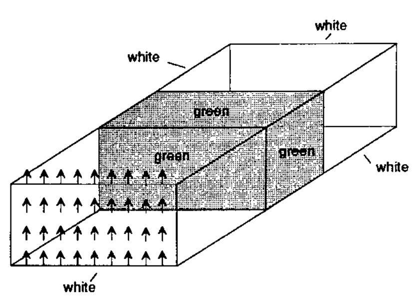

Figure 1: Shorted waveguide with dielectric loading

on the front end represent the source field. In this case, the source was a field consistent with TE_{10} mode propagation. The arrow colors change from red to blue moving from the innermost to outermost positions horizontally.

The text file generated by the CAD program is 203 lines long. There are four types of lines in the file; a header line, command lines, point lines and system parameters. The header line gives the overall dimensions of the drawing in screen units. Command lines are used to describe individual parts of the drawing such as lines, planes, arrows, etc. Point lines locate individual points using screen coordinates. System parameter lines serve a number of purposes the most important of which is to state the user drawing size. The user drawing size is used to convert between screen coordinates and grid coordinates.

The file generated by the translation code for input to the finite element program has a short header plus one line for each of the 704 nodes. Prior to developing the CAD interface, this input was generated by a number of subroutines. These subroutines had to be modified for each new configuration and there was no graphical feedback to alert the code user of an error in the input. The CAD interface has made it considerably easier to model new objects with fewer opportunities for mistakes.

Summary

By adopting an inexpensive commercial CAD program as our graphical user interface, we have greatly simplified the process of defining input for a three-dimensional finite element code. Writing a translation code to convert a DesignCAD 3-D output file into a finite element input file was a fairly straight forward task.

A similar procedure could be used to translate DesignCAD 3-D files to input suitable for other three-dimensional electromagnetic modeling codes such as NEC or TSAR. We chose this CAD program because of its price, performance, ease of use, and because it runs on a PC. Any CAD program that creates a readable description file could have been used.

In general, CAD programs are easier to use than code-specific graphical front-ends. CAD programs have a wider user base and there are usually a number to choose from for any given platform. The use of commercial CAD programs saves code developers from having to write their own graphical front-ends. This saves time and allows them to write truly portable codes. It also gives code users a professional graphical interface well suited to their needs and their particular platform.

Parallelization of the Numerical Electromagnetic Code – Basic Scattering Code (NEC-BSC) for the Intel iPSC/2 and iPSC/860 Hypercubes*

Paul R Work, Scott Suhr, Gary B. Lamont, and Andrew J. Terzuoli
Dept of Electrical and Computer Engineering
Air Force Institute of Technology
WPAFB, OH 45433

Abstract

This paper discusses the continuing development of parallelizing high frequency electromagnetic scattering code. The process of transforming serial computer codes for use in a concurrent processing environment is explained, and the results achieved through porting the NEC-BSC sequential FORTRAN source code to the Intel iPSC©/2 and iPSC©/860 hypercubes are presented. The sequential code is examined and modified incrementally, attempting to minimize the changes to the program interface in both input and output while maximizing performance. The final application is very efficient for problems with a moderate amount of complexity, even with large numbers of processors. This effectiveness is compared to results from serial machines, namely VAX serial benchmarks.

1 Introduction

Government agencies and academic and industrial institutions are very interested in reducing the computer processing time required to perform computational simulations by using the power available in the latest generation of parallel computers. Many applications in this field already exist for conventional serial computers, and most parallel computers cannot run unmodified off-the-shelf (dusty deck) serial programs. This research demonstrates the feasibility of modifying existing serial programs (whose data sets contain independent data items) for execution in a concurrent processing environment. An electromagnetic scattering prediction code known as NEC-BSC is incrementally modified to enable the code to execute on the Intel iPSC©series of hypercubes. NEC-BSC was originally developed for the VAX minicomputer and was written in FORTRAN-77 for portability to most standard mainframe computers.

*sponsored by the Target Recognition Branch, Avionics Directorate, Wright Laboratories, WPAFB, OH

2 Parallel Computers

The term "parallel computer" encompasses a wide range of different architectures. Some computers have a single block of memory that all the processors can access. Such computers are called "shared memory" machines. Other architectures reserve a section of memory for an individual processor, and no other processor can directly access that memory. Machines which use this kind of memory scheme are referred to as "distributed memory" computers.

Communication between processors is an important part of a parallel computer, and shared memory machines accomplish this through exchanging data through the common memory. Distributed memory computers communicate by sending "messages" back and forth through "ports" on an interconnection network. Within the realm of distributed computing, several different interconnection schemes have been developed. Two examples are a simple two-dimensional mesh, and a hypercube interconnect.

In a generic two-dimensional mesh, each processor is connected to exactly four other processors, one in each "direction" (North, South, East, and West) [3]. Other interconnection schemes are possible, and three-dimensional meshes have also been developed. With a mesh, however, the number of connections to one processor remains the same, no matter how many processors are in the machine. Recently, Intel announced the Paragon XP/S computer which uses a modification of a mesh interconnect [1].

The hypercube interconnect is a compromise architecture with a high degree of flexibility. A hypercube of dimension d has 2^d processors (or nodes), each of which is connected to d other processors (or neighbors) [3]. Parallel computers have been constructed with as many as 4,096 processors ($d = 12$) using a hypercube interconnect. This research uses the Intel iPSC series parallel computers which employ a hypercube interconnect with distributed memory.

3 Parallelization of Serial Code

Computer programs written specifically for one parallel machine normally do not run on another similar machine, much less one with a different architecture. Serial programs, for the most part, also cannot be executed on the current generation of parallel computers without some modification. Therefore, if an application is to be run on a parallel computer, it must be converted, or ported to the parallel machine in question. When converting a serial program to run on a parallel message passing architecture, two approaches are typically used: data decomposition and control decomposition.

3.1 Data Decomposition

In many programs, the individual items of data to be processed have, by design, a built in independence. This independence allows separate items of data to be processed simultaneously and eliminates side effects which data dependencies can cause. For example, consider a loop in a section of serial code where the results of the data processed in each pass do not depend on earlier

calculations or comparisons. With a data decomposition, every processor could have a complete copy of the code to be executed and process only a portion of the entire data set.

3.2 Control Decomposition

Sometimes, data dependencies do not allow partitioning the data set among the processors since such a decomposition would result in side effects or prohibitive communication costs. In such cases it may be more advantageous to divide up the various tasks among the processors. In other words, distribute the different task modules in the program among the available processors. This kind of decomposition is similar to a task scheduling problem, and care must be taken to assign the modules in an efficient and effective manner. Communication is required to pass parameters back and forth, but this cost is normally less than that of a data decomposition of the same problem. Instead of sending messages about every item of data to be processed (to determine the effects other items of data have on the current item of data), only the important parameters need to be communicated. This type of implementation is called a control decomposition, when each node has a unique set of code to be executed. One example of control decomposition is task scheduling on multiple processors; each node has a unique set of code (its current task) and performs the processing that corresponds to that task. In more involved cases, the tasks become interrelated modules of the same program, and additional communication is required. This additional communication, however, is normally only a moderate amount.

4 Load Balancing

When converting a serial program to run in a distributed memory environment, it is very possible for some processors to finish before others complete their part of the data. The overall execution time is then controlled by the *slowest* processor, and all other processors wait until the last one finishes. Since this idle time can be very detrimental to the overall efficiency of an application, this should be avoided if at all possible. Theoretically, each processor should do exactly the same amount of work in order to achieve maximum efficiency and the best possible speedup. In other words, the work load needs to be balanced among the active processors. Static load balancing is a technique where the programmer hard codes the division of labor among the nodes, specifying exactly what each node will do before the program is executed. Dynamic load balancing occurs when the program itself divides up the work according to heuristics that have been written into the balancing routine.

4.1 Static Load Balancing

When a software engineer uses static load balancing in order to efficiently partition the work, some prior knowledge of the complexity of the data set is required in order to make a good estimate of the workload. A simple scheme for static load balancing (when the data is handled in a loop from 1 to N) is to let each node do $x = N/n$ items of data; each node handling the items from

ix to $ix + x$ (i representing the current node number) in the data set where n is the number of nodes. This approach may not yield an efficient implementation, however, if some of the data items require more processing than others. Another approach has each node iterate through the entire data set with an increment equal to the number of nodes. Thus each node would process data items i, $n+i$, $2n+i$, $3n+i$, ... , $N-n+i$ (where i is the individual node number). This approach attempts to compensate for an unequal amount of processing by assuming that neighboring items have a similar amount of complexity associated with their computation. By assigning neighboring items to different processors, those items with more complexity are spread out among the available processors, and similarly the less complex items are also spread out evenly among the nodes.

4.2 Dynamic Load Balancing

Dynamic load balancing occurs as the program is running and can compensate for differing levels of complexity throughout the data set. One type of dynamic load balancing divides the available nodes into two groups by purpose: master and slave nodes, also known as controller and worker nodes. Each worker node receives a relatively small data set to operate on, and when done, it then notifies its controller node that it is ready to operate on another set of data. Here, the generic term "set of data" can be thought of as either individual data items, or possibly separate tasks that are to be executed. The master (or controller) node then determines the contents of the next set of data that the requesting slave (or worker) node should execute, and forwards that information to the requesting node. This process repeats itself until the global data set has been entirely processed. With a centralized list, one master controller (also known as a supervisor) maintains the global data set and distributes the work among the worker nodes.

4.3 Efficient Dynamic Load Balancing

Normally, dynamic load balancing has some overhead associated with implementing the heuristics and message passing. The Direct Connect Module in the Intel iPSC/2 and iPSC/860 hypercubes, however, has an inherent feature that allows much of this overhead to be "hidden". The DCM uses a message-passing protocol which allows a short message ($<$ 100 bytes) to be stored in a preallocated buffer at the receiving node [2]. The sending node then continues on with the next portion of its code. This happens even if the receiving node has not yet executed a receive instruction in its code. As long as the number of preallocated buffers has not been exhausted, the sending node is not blocked from further execution. This approach is a recent development and currently only two applications are known to use a some form of this technique [4] [8].

4.4 Implementation

NEC-BSC [5], A ray tracing program in electromagnetic scattering simulation, was chosen to implement both a statically and a dynamically balanced, data decomposed, conversion to the Intel iPSC/2 and iPSC/860 hypercubes. NEC-BSC calculates the electric and magnetic field strengths as well as the total power in a given direction away from a target geometry (called the scene) and

can calculate these values at any angle up to the precision limitations of floating point arithmetic. It can also calculate these same values for a range of angles separated by a finite difference, again limited only by the precision of floating point arithmetic. In NEC-BSC each angle to be processed is treated as a final ray. Based on the position of one or more sources, each object or combination of objects in the scene is examined for many possible interactions which could result in a ray with the desired final direction. Possible interactions are a combination of up to three reflections and up to two diffractions. Each permutation (of three interactions) is called a UTD term, but the current set of UTD terms examined by NEC-BSC does not contain all possible permutations of size three or less. If an interaction (described by a UTD term) between a source and an object or group of objects results in a ray in the desired final direction, the contribution of that interaction is added to a running subtotal. Once all the objects have been processed for all angles and UTD terms, the final totals are written to disk for later use in either plotting or other analysis means.

The parallel versions of NEC-BSC have more than 26,000 lines of code divided into several files. These versions have duplicate copies of some of the code with modifications as necessary to allow the necessary passing of messages. On the iPSC series hypercubes, a host computer controls what program the node processors execute and collects the data at the end. Accordingly, it needs a copy of some of the subroutines with its own unique functions inserted for its operation. The node processors also have a copy of the program with some functions added to allow execution and message passing.

The initial parallel version of NEC-BSC used interleaved static load balancing to develop a data decomposed version [6], and the next version incorporated a dynamic load balancing algorithm. The dynamic load balanced version used the communications abilities of the DCM discussed earlier, resulting in a variation (of the node execution times) of less than 0.5%. In this adaptation, rays are dispatched for processing in groups of four, and the slave nodes send a message requesting the next group of rays after the third ray in the current set had been processed. This implementation runs on up to 64 nodes. The number of rays to be calculated must exceed four times the number of nodes so that each node has at least one data set to process. If the number of rays should be less than this amount, then a smaller cube must be used to process the data. The maximum number of rays that NEC-BSC can calculate is currently limited to 1801, representing a full 360 degree scan with a step of 0.2 degrees between the rays. The number of objects allowed in the scene geometry is also limited to 36. These limitations come from the original serial version and are based on the limited amount of memory available in earlier serial computers. Later parallel versions of NEC-BSC could easily expand this number further, taking advantage of the larger memory available in the current generation of parallel machines. As the number of nodes used to process a data set increases, the division of labor among the nodes can become less balanced as each node processes fewer rays. In the extreme case, using 128 nodes and 1801 rays, each node would process (on the average) about 14 rays. This gives rise to a greater possibility of an uneven work load.

5 Results

Suhr [7] measured the execution time of the serial version of NEC-BSC for several platforms including the VAX 11/780, a microvax, the iPSC/2 (single node only, no communications), and the

iPSC/860 (also single node, no communications). This is used as a reference for the parallel versions when comparing run times. Table 1 shows these values, indicating an improvement of the iPSC/860 over the VAX 11/780 of approximately 6.1.

Table 1: Comparison of serial execution times

Run time (sec) for a simple example (ex1c)				
	VAX 11/780	μVAX	iPSC/2	iPSC/860
Time:	143	38	33.4	23.3
Speedup:	1.0	3.8	4.3	6.1

The execution time for NEC-BSC also varies with the number of angles calculated. Table 2 indicates how this execution time varies as the number of rays increases. This shows that the increase in elapsed time is fairly linear, allowing for distribution among the nodes.

Table 2: Execution time as a function of the number of rays

iPSC/860, time for one node in msec		
Number of rays	static	dynamic
10	18,068	26,247
40	44,221	64,363
160	155,120	257,877
640	599,698	1,033,499

Another factor that can influence the execution time of an application is the problem size. Table 3 shows that the execution time varies as the number of plates increases. This indicates that the execution time is not linear with respect to the number of objects in the scene geometry. Since NEC-BSC treats all objects in the same way, this means that the execution time can become exhorbitant if the number of objects is large.

Another result shown by Tables 2 and 3 is that the dynamic version of NEC-BSC has considerably longer execution times than the static version. This may be the result of the increased overhead associated with dynamic load balancing. Current investigations indicated inconclusive results [8]

Finally, Table 4 indicates that multiple processors can reduce the overall run time for an application. This table shows that both the static and dynamic versions of NEC-BSC performed well with respect to the execution time on one node. This means that reasonable gains can be expected if one wished to employ more processors than had been previously used. The reason for the difference between the static and dynamic is unknown at present, but is being investigated. In spite of this handicap, the dynamic version ran on the greatest number of nodes, and showed an efficiency (versus its own one node time) slightly better than that of the static version. It is expected that the static version would show similar performance improvements on large numbers of nodes.

Table 3: Execution time as a function of the number of objects

iPSC/860, time for one node in msec		
Number of plates	static	dynamic
8	61,586	94,383
16	213,364	337,313
24	314,022	603,726
32	674,686	1,186,464

Table 4: Execution time versus number of nodes (32 plates)

	Static Load Balancing			Dynamic Load Balancing		
Num Nodes	Efficiency	Speedup	Time (msec)	Efficiency	Speedup	Time (msec)
1	100.00	1.00	1,035,545	100.00	1.00	2,363,036
2	97.44	1.95	531,373	97.63	1.95	1,210,133
4	92.42	3.70	280,112	93.35	3.73	632,812
8	80.93	6.47	159,945	86.66	6.93	340,853
16	67.41	10.79	96,011	73.96	11.83	199,694
32	—	—-	—0	56.67	18.14	130,300
64	—	—-	—0	36.64	23.45	100,767

6 Conclusions

Data decomposition lends itself well to problems that have a large data set of independent items. For this application, static load balancing has been shown to be more effective in performing the work to be done. Theoretically, the dynamically balanced version should have been similar to the static version in performance, but unknown factors have caused a large difference between the two. Assuming a similar performance improvement for the static version of NEC-BSC (to that achieved by the dynamic version), the iPSC/860 is capable of improving the execution time of a sample problem by a factor of approximately 143 (6.1 x 23.45) when compared to the VAX 11/780. This reduces a two-hour problem to less than one minute! Such performance improvements are possible with the current generation of parallel computers, and future generations promise even more computing power.

Efficient parallelization of existing serial programs is possible by tailoring the parallel implementation to the characteristics of both the target machine and the program's structure. A good match of load balancing, decomposition technique, and target machine performance characteristics can result in efficient applications. The iPSC version of NEC-BSC with dynamic load balancing and data decomposition showed overall efficiencies greater than 50% (on the iPSC/860) for moderately complex problems (far zone calculations for 32 plates).

No performance data for the iPSC/2 was shown, but from the earlier comparison results some

inferences can be made. First, since the iPSC/2 (one node, no communication) demonstrated a longer execution time for the serial version than the iPSC/860, the run time for the iPSC/2 is also longer for both parallel versions with all other factors being the same. Since both the iPSC/2 and the iPSC/860 share the same interconnect and communications systems (with minor differences), the overall efficiencies for the iPSC/2 are greater than those of the iPSC/860 (with all other factors the same). This was also demonstrated by Suhr [6].

References

[1] Bernhardt, Mike, et al. "Paragon Supercomputer/IS-446." Intel Announces the Paragon XP/S Supercomputer; Parallel Architecture Scalable to TeraFLOPS, November 1991.

[2] Bernhardt, Mike, et al. "1990 Gordon Bell Prize/IS-436." 1990 Gordon Bell Prize Awarded to Scientists Using Intel iPSC/860 Parallel Supercomputer.

[3] DeCegama, Angel L. *Parallel Processing Architectures and VLSI Hardware*. Englewood Cliffs NJ: Prentice Hall, 1989.

[4] Gustafson, John L. and others. "A Radar Simulation Program for a 1024-Processor Hypercube." *Proceedings of Supercomputing*. 1989.

[5] Marhefka, Ronald J. *Numerical Electromagnetic Code - Basic Scattering Code User's Manual.* Ohio State University Electroscience Laboratory.

[6] Suhr, Scott. *High Frequency Scattering Code in a Distributed Processing Environment.* MS thesis, Air Force Institute of Technology, 1991.

[7] Suhr, Scott, et al. "High Frequency Electromagnetic Scattering Code in a Distributed Processing Environment." *Proceedings of the Seventh Annual Review of Progress in Applied Computational Electromagnetics*. March 1991.

[8] Work, Paul R. *Parallelizing Serial Code for a Distributed Processing Environment with an Application to High Frequency Electromagnetic Scattering*. MS thesis, Air Force Institute of Technology, 1991.

Virtual Memory Implementation of a 2-D Finite Element Eddy Current Simulation Program on a Personal Computer

D. E. Madle, A. Mahmood, Q. H. Nguyen, L. D. Philipp, D. J. Lynch
Washington State University at Tri-Cities, Richland, WA 99352

ABSTRACT

The use of Eddy currents in non-destructive examination of materials is a useful and proven technique. It has been successfully employed in identifying flaws in steam generator tubes. A 2-D Finite element based program (EDDY-2D) that allows the simulation of a tube/support plate using differential coils had been developed on mainframe computers by Lord and his associates [2-3] at Colorado State University. This code was developed to predict the resulting impedance of an Eddy current test probe, based on the presence of well defined system defects.

In this paper, we describe the conversion of the EDDY-2D program to a PC (PCEDDY-2D) focusing on the virtual memory part. The virtual memory development on a PC was necessary to overcome the 640 Kbyte addressable memory limitation imposed by DOS. Without such a system, a finite element mesh size of only 2600 elements (using less than 1400 nodes) is the maximum problem size possible. After virtual memory implementation, we have been able to successfully run Finite element mesh sizes of 10,680 elements with 5451 nodes.

During the performance testing of the PCEDDY-2D program, many system parameters were analyzed in an attempt to decrease the overall execution time. These included; page replacement algorithms, organization of virtual storage, size of RAM page etc. The best scheme employing a pseudo random page replacement algorithm resulted in a hit ratio of 98.9%.

1.0 Introduction

Finite element analysis has been used in the development of the EDDY-2D (two dimensional Eddy Current) computer program [1-3]. This program was developed to predict the resulting impedance of an Eddy current test probe based on the presence of well-defined system defects. The basic governing equation used in the development of the Eddy current technique is the linear, two-dimensional (Eddy current) diffusion equation.

$$\frac{1}{\mu}\left(\frac{\partial^2 \overline{A}}{\partial x^2}+\frac{\partial^2 \overline{A}}{\partial y^2}\right)=-\overline{J}_s+j\omega\sigma\overline{A} \tag{1}$$

where:

A = magnetic vector potential (Webers/m)

The finite element method can be used to solve the above differential equation for the vector potential A. The test space, made up of a pipe section, a coil and support plate are divided in two-dimensional space, into small triangular regions. Matrix equations are developed for each node and then combined into a global matrix equation of the form:

$$[G]\ \{A\} = \{Q\} \tag{2}$$

where the global matrix [G] is of dimension NxN for a mesh comprised of N nodes and is symmetrically banded. {A} is an Nx1 vector representing the unknown vector potential A. {Q} is an Nx1 vector specifying the boundary conditions. This global matrix equation is solved for the vector potential {A} using the LU decomposition technique. Finally from this vector potential at each node, the normalized impedance of a test coil can be calculated. A more detailed analysis of the finite element eddy current model can be found in [1-3].

The PC-based version (PCEDDY-2D) of the EDDY-2D program was implemented by converting the FORTRAN code to "C" at Washington State University at Tri-cities [4]. In the development of the PC version, one of the important goals was to devise an efficient virtual memory scheme to allow the addressing of data beyond the 640 Kbyte DOS limit such that large problems can be simulated. In the following section, we will describe the development and optimization of the virtual memory scheme for the PCEDDY-2D program.

2.0 Virtual Memory Development for PCEDDY-2D

The PC operating system DOS allows less than 640 Kbyte addressable RAM to the programs. This severely limits the size of Eddy current simulation problems that can be run on a PC. Thus a virtual memory system needs to be developed which also provides efficiency in terms of execution speed. In a virtual memory system, only part of the total data (and/or program code) resides in (DOS addressable) RAM at any given time. The remainder of the data is located on either the hard disk or the RAM disk if available. As new data is needed by the program which is not currently in RAM, a section known as a "page" of RAM data not currently needed is swapped with the desired data page on the disk. In the case of the EDDY-2D code, the storage of the global matrix data required a majority of the available memory space. The memory requirements for a 2600 element problem and a larger 5280 element (2745 nodes, semi-bandwidth 46) problem are summarized below:

	2600 Elements	5280 Elements
Available RAM (with DOS resident)	553 Kbytes	553 Kbytes
Executable code (DIFFRNT.EXE)	171 Kbytes	171 Kbytes
Program Data (excl. global matrix)	60 Kbytes	86 Kbytes
Global Matrix Data	313 Kbytes	988 Kbytes

Table 1. EDDY-2D Memory Requirements

Based on the above example, the virtual memory system for the EDDY-2D simulation program only needs to store the global matrix data on the hard disk. If program data in addition to the global matrix data were stored in the virtual memory, this would greatly increase program complexity as well as execution time, and thus is not implemented in our system.

A specific function called VIRTUAL() was developed to handle all of the memory management tasks associated with reading and writing global matrix data elements. The basic tasks performed by VIRTUAL() are shown in Figure 1 in the form of a flow chart.

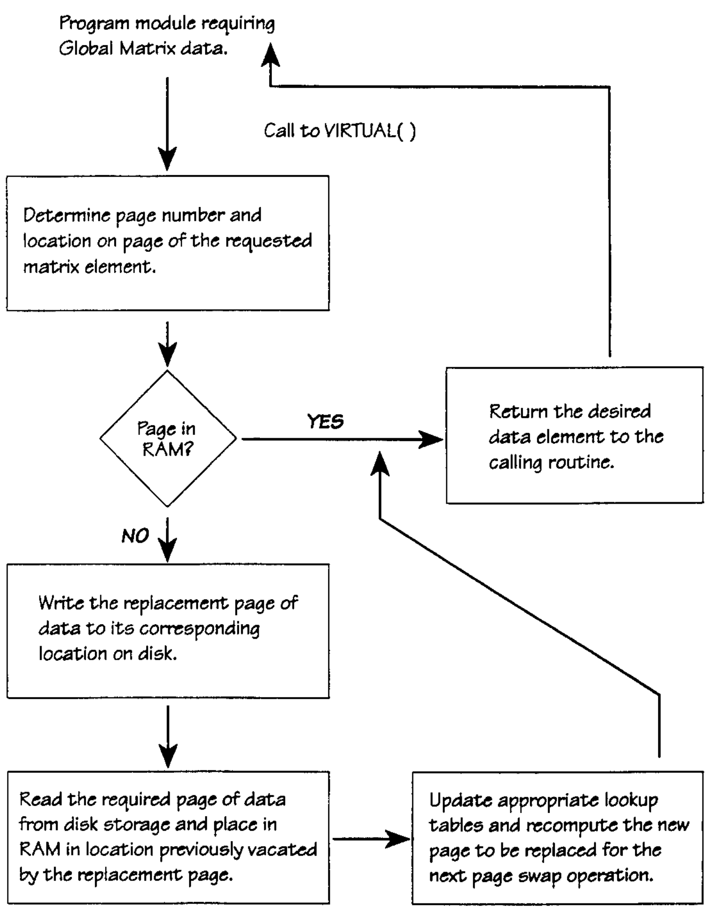

Figure 1. Virtual Memory System Flowchart.

The program module VIRTUAL.C was written to replace a typical variable assignment as:

Non-Virtual

```
A(complex) = G[row][column];       READ G(x,y)
G[row][column] = A(complex);       WRITE G(x,y)
```

Virtual

```
VIRTUAL("r",row,column,buffer address);    READ G(x,y)
VIRTUAL("w",row,column,buffer address);    WRITE G(x,y)
```

where "buffer address" points to a variable location where G(x,y) will be stored for a read, or points to the value to be written to G(x,y) for a write.

Therefore, throughout the PCEDDY-2D program, when an element of the global matrix is required, a call to the function VIRTUAL is inserted to store or retrieve the necessary value.

A major consideration in the development of VIRTUAL.C was the "page replacement" algorithm. This algorithm is the method the program uses in determining which page in RAM will be moved to the disk to make room for the desired data page. There were three page replacement algorithms considered:

Least recently used:	This method keeps track of which page(s) have been stored in RAM the longest period of time since it was last requested.
Pseudo Random:	The replacement page is determined by some simple function such as a continuous counter which approximates a random selection.
Random:	The replacement page is determined by some function which generates a random number between 0 and (number of pages in RAM - 1).

Further details of these algorithms can be found in [5]. In the case of PCEDDY-2D, the pseudo-random replacement algorithm gave the best performance. The least recently used algorithm produced the best hit ratio but the added overhead of tracking the current replacement page made the overall execution time slower. The pseudo-random replacement algorithm used for the PCEDDY-2D program maintained a counter which stored a value between 0 and (number of pages in RAM - 1). Every time a miss occured, the counter was incremented until it reached (number of RAM pages - 1) at which point it was reset back to 0. The count indicated which page in RAM would be replaced upon the next miss. This technique required very little overhead and though it did not produce the best hit ratio, it provided the best overall execution time.

The results of the different replacement algorithms are shown in figure 2. Figure 3 shows the hit ratio as the number of

total pages in RAM is varied for a test case using 1680 elements, 899 nodes, a semi-bandwidth of 32, a virtual page size of 200 elements using a pseudo-random replacement algorithm.

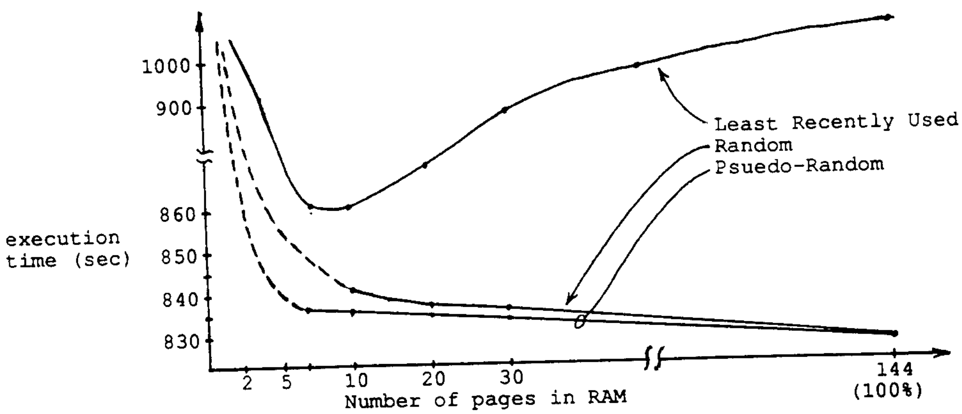

Figure 2. Page Replacement Algorithm Program Performance

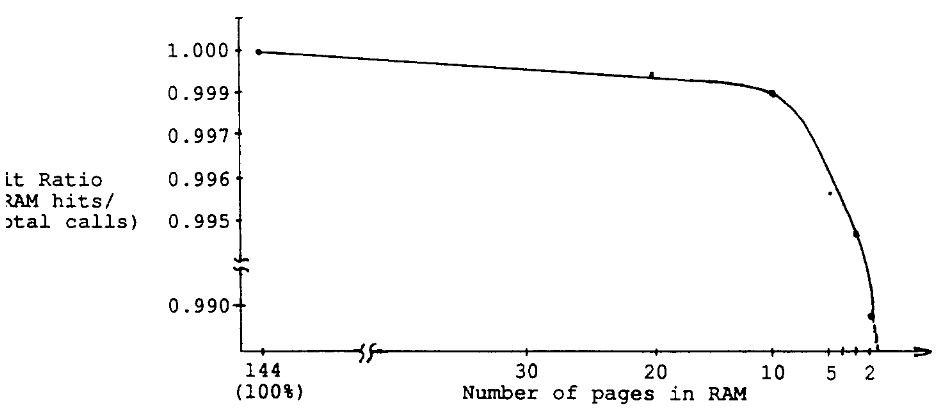

Figure 3. Effect of RAM Pages on Hit Ratio

2.1 Optimization of Virtual Memory: To optimize the virtual memory implementation, the following parameters were extensively tested to yield the best performance:

1) Virtual memory page size.
2) Global matrix data organization on disk.

The optimum page size for the PCEDDY-2D program was found to be 400 elements or 3200 bytes per page. Smaller page sizes increased the execution time since virtual() is called many more times even though the time to read/write smaller page sizes is less.

The global matrix data storage was examined for row-wise and a column-wise storage. After analyzing data from several different problem sizes using a column-wise storage, it was noticed that the execution time increased dramatically when a certain minimum number of pages in RAM were used. This minimum number of pages occurs near the semi-bandwidth of the problem. It then becomes clear due to the nature of the matrix solution program that if the data were organized in a row-wise format, the use of data by the matrix solution program results in very few RAM misses. Thus a row-wise storage of global matrix data was chosen.

3.0 Conclusions

The development of virtual memory for the PCEDDY-2D program allows a user to be able to run large simulation problems without having any additional RAM (extended memory) requirement in a PC. The virtual memory system was specially optimized for the eddy current simulation problem. A pseudo random algorithm with a page size of 3200 bytes, and a row-wise storage of the global matrix data resulted in the best execution speed.

4.0 References

[1] Q. H. Nguyen, "Verification of the EPRI Two-Dimensional Finite Element Computer Code for Eddy-Current Testing," Master's project report, Washington State University at Tri-cities, May 1987.

[2] Lord, W.,"Development of a Finite Element Model for Eddy-Current NDT Phenomena," EPRI report NP2026, 1981.

[3] Palanisamy, R. and W. Lord,"Finite Element Analysis of Eddy Current Phenomena," Materials Evaluation, Oct. 1980.

[4] D. E. Madle,"Personal Computer Implementation and Performance Analysis of an Eddy Current Non-Destructive Examination (NDE) Simulation Program," Master's project report, Washington State University at Tri-cities, March 1991.

[5] F. J. Hill, and D. O. Peterson, "Digital Systems, Hardware, Organization and Design," John Wiley and sons, 1987.

Implementation of EM-WAVETRACER in the Data Transport Computer

Check F. Lee and Robert L. Utzschneider
Wavetracer, Inc.
289 Great Road, Acton MA 01720

January 16, 1992

Abstract - The implementation of EM-WAVETRACER software is discussed. EM-WAVETRACER is designed to analyze problems of electromagnetic scattering and radiation. Its implementation makes use of the architectural advantages of the Data Transport Computer (DTC), which is a single instruction, multiple data (SIMD) 3-D parallel computer. The maximum configuration of the DTC contains 16,384 processors and 512 megabytes of memory. These processors are arranged in either a 3-D or a 2-D mesh. The methodologies behind EM-WAVETRACER are the finite-difference time-domain (FD-TD) technique and the method of moments (MOM). By taking advantage of the 3-D mesh and SIMD architecture, the implementation of the FD-TD algorithm greatly reduces the computational overhead associated with memory seeking and increases the parallelism of the computation. The implementation of the MOM algorithm is in block format, which uses the DTC-workstation hybrid configuration. With this approach, the degree of parallelism is high, while the number of floating operations remains unchanged as compared with known implementations. The application of these two algorithms to scattering and radiation problems achieves exceptional computational speed and price/performance.

I. Introduction

The engineering requirements for computer memory and floating point operations in computational electromagnetics are enormous. In the FD-TD analysis, for example, the memory requirement and the number of floating point operations per time step are proportional to the number of discretization nodes in the computational volume. In the MOM analysis, the memory requirement is proportional to the square of the number of unknowns, and the number of floating point operations is proportional to the cube of the number of unknowns. Clearly, the applicabilities of the FD-TD and the MOM algorithms to engineering problems are determined by the performance and the capacity of computers.

Parallel computing technology is rapidly become the future technology of supercomputers. Because of their large memory bandwidth and peak MFLOPs, parallel computers have gained ground in many scientific applications. There are two major parallel computing architectures: the multiple instruction, multiple data (MIMD) computer and the single instruction, multiple data (SIMD) computer. MIMD computers usually contain from several to a few hundred processors; each of these processors may execute different instructions on different data. SIMD computers are usually massively parallel computers containing thousands of processors. Each processor executes an identical instruction on different data simultaneously. MIMD computers are more flexible in some applications, due to their multiple instruction programming. SIMD computers offer simpler programming in both the development and application environments.

In this article, the parallel implementation of EM-WAVETRACER on the DTC is discussed. EM-WAVETRACER contains two algorithms: the FD-TD technique and the MOM. In section II, the architecture and the software technology of the DTC are discussed. In section III, the implementation of the FD-TD algorithm is discussed with focus on data communication and memory sharing. In section IV, the implementation of the MOM is discussed with focus on maximizing the parallelism using the DTC-workstation hybrid configuration. Finally, we will conclude this article with a brief note on applications in section V and a summary in section VI.

II. Data Transport Computer

The DTC is a 3-D SIMD massively parallel computer. It is supported by a data parallel C programming language (multiC).

The DTC consists of control and array modules. The array modules are controlled by the control module which is controlled by the host workstation through the SCSI interface (Figure 1). The SCSI interface is used primarily for instructions and commands. DTC Models contain from 4,096 processors with 128 megabytes of memory (DTC-4) to 16,384 processors with 512 megabytes of memory (DTC-16). Each of these processor elements is a single-bit computer with six data paths in *x, y* and *z* directions. These processors are arranged in a 3-D lattice, so that each processor has direct access to its six nearest neighbors. Alternatively, this 3-D lattice can be unfolded to 2-D for 2-D applications, so that each processor has direct access to its four nearest neighbors. The unfolding of the array is totally controlled by user software.

This 3-D architecture eases the inefficiencies associated with mapping 3-D data into linear memory (conventional computers) or planar memory (2-D computers). At the same time, it maximizes memory bandwidth by providing every processor element with its own path to a neighboring processor or to its memory; hence, there is no need for data path multiplexing. The DTC provides very high I/O rates. As shown in Figure 2, the 3-D array allows data movement through the edge and face of the cube. With these, the DTC-16 can achieve peak I/O throughputs of 1,024 megabytes/second. Because of these features, the DTC delivers a large percentage of its peak performance on complex multidimensional applications.

The multiC programming language is an extension of ANSI C to provide instructions for parallel operations on 2-D and 3-D data structures. It thereby eliminates many of the loops found in traditional programming while retaining all the familiar features of the C language.

When a multiC program is being executed, the portions of the program which do not contain parallel data are executed in the workstation and the remaining portions are executed in the DTC. This hybrid configuration allows users to fully exploit the computing powers of both the DTC and the workstation.

The DTC processor array can be configured dynamically to form a much larger 2-D or 3-D virtual processor array. The virtual array can be sized to fit a particular problem. Once the size is determined, the virtual processing occurs transparently to the user. It should be pointed out that although the size of the virtual array can be very large, the maximum distance between any two processors is limited by the physical size of the array.

III. Implementation of the FD-TD Algorithm

The FD-TD algorithm is a parallel version of the conventional FD-TD algorithm [4], and they share similar applicability, accuracy and limitations. This parallel FD-TD algorithm is implemented using the multiC language and optimized in the DTC environment to reduce memory related overhead and to obtain maximum parallelism.

For homogeneous medium with relative permeability μ_r , dielectric constant ε_r , and conductivity σ, Maxwell's equations are

$$\nabla\times \bar{E} = -\mu_0\mu_r\frac{\partial\bar{H}}{\partial t} \tag{1}$$

$$\nabla\times \bar{H} = \sigma\bar{E}+\varepsilon_0\varepsilon_r\frac{\partial\bar{E}}{\partial t} \tag{2}$$

where μ_0 and ε_0 are free space permeability and permittivity, respectively. For the purpose of illustration, let us focus on the x component in Eq. (1):

$$\frac{\partial E_z}{\partial y}-\frac{\partial E_y}{\partial z} = -\mu_0\mu_r\frac{\partial H_x}{\partial t}. \tag{3}$$

In order to apply the finite difference approximation, the 3-D computational volume is partitioned into many cells, represented by nodes. The discretized electric and magnetic fields of a node are placed in a staggered manner (Figure 3). Assuming the temporal discretization of the electric and magnetic fields are in half-integer (n+1/2) and integer (n) time steps, the difference equation corresponding to Eq. (3) is used to update H_x at all nodes, as shown below.

For (i=1 to I, j=1 to J, and k=1 to K):

$$H_{x(i,j+1/2,k+1/2)}^{(n+1)} = H_{x(i,j+1/2,k+1/2)}^{(n)}$$

$$-\frac{\Delta_t}{\mu_0\mu_r}\left[\frac{E_{z(i,j+1,k+1/2)}^{(n+1/2)} - E_{z(i,j,k+1/2)}^{(n+1/2)}}{\Delta_y} - \frac{E_{y(i,j+1/2,k+1)}^{(n+1/2)} - E_{y(i,j+1/2,k)}^{(n+1/2)}}{\Delta_z}\right] \quad (4)$$

in which I, J and K are the number of nodes along the *x*, *y* and *z* directions of the computational volume, respectively. Δ_y, Δ_z are the sizes of the cell along the *y* and *z* directions. Δ_t is the size of the time step. A close examination of Eq. (4) reveals that only neighboring data are needed for field updating. We represent each of these cells by a processor (virtual processor if necessary) in a 3-D array with address *(i,j,k)*. Electric field components of $E_{x(i+1/2,j,k)}$, $E_{y(i,j+1/2,k)}$, $E_{z(i,j,k+1/2)}$ and magnetic field components of $H_{x(i,j+1/2,k+1/2)}$, $H_{y(i+1/2,j,k+1/2)}$, $H_{z(i+1/2,j+1/2,k)}$ are assigned and stored in the memory associated with processor *(i,j,k)*. Using the multiC construct, the updating scheme of H_x becomes:

$$H_x -= \left(\frac{\Delta_t}{\mu_0\mu_r}\right)\left[\frac{[0;1;0]\,E_z - E_z}{\Delta_y} - \frac{[0;0;1]\,E_y - E_y}{\Delta_z}\right]. \quad (5)$$

In this scheme, E_z, E_y and H_x represent all discretized values of the correspondent fields. Therefore, H_x in the entire computational domain is updated in one DTC step. In Eq. (5), the square brackets imply communication. For example, [0;1;0]E_z implies moving E_z at *(i,j+1,k)* node to *(i,j,k)* node. Clearly the execution of Eq. (5) is very efficient in the DTC, and there is no need for memory seeking or mapping.

The absorbing boundary condition [5] is implemented in a similar manner to that of Eq. (4). Since the data required to update the boundary field come from different directions depending on the face of the boundary, for parallel updating of the boundary fields, appropriate fields are shifted according to their relative position with respect to the boundary face. The numerical operations to update the boundary fields are then executed in parallel.

For scattering and radiation, the existence of the absorbing boundary condition creates imbalance in memory allocations between the interior and the boundary nodes. Roughly speaking, there are three electric field and three magnetic field components associated with each interior node. For the boundary nodes, assuming the second order boundary condition is imposed, there are additionally six field variables (2 for each field component). Since a variable in the SIMD computer represents parallel data, this arrangement would potentially waste memory. There are a number of implementation techniques to resolve this problem. In EM-WAVETRACER the parallel data is shared. For regions within the scattered object, the excess memory is used to store material properties. For the region outside the scattered object and inside the boundary, the excess memory is used to store the complex tangential fields for post processing of the bistatic scattered fields. Eight floating point variables are needed for each frequency (4 complex tangential electric and magnetic fields). As a result, the excess memory of every four layers are used to store complex fields of three frequencies (Figure 4). At every time step, the integrations for calculating the complex fields are evaluated in parallel.

IV. Implementation of the MOM Algorithm

The MOM algorithm developed for the DTC is a parallel version of the MOM algorithm suggested in [6]. This MOM code analyzes the scattering of arbitrarily 3-D conducting objects. The surface geometries of these objects are described by triangular patches. The bi-triangular basis and testing functions are used. The parallel calculations of the matrix elements are implemented in a block manner. Matrix solutions are obtained by using the parallel block Gaussian elimination method.

The electric field integral equation of conducting objects in free space is

$$-\bar{E}_{i\,(\tan)} = \iint dS\, i\omega\mu_0\, \bar{\bar{G}}(\bar{r},\bar{r}') \cdot \bar{J}(\bar{r}')\,|_{(\tan)}, \tag{6}$$

where ω is the angular frequency, μ_0 is the free space permeability, $\bar{J}$ is the unknown current distribution, and $\bar{\bar{G}}$ is the dyadic Green's function

$$\bar{\bar{G}}(\bar{r},\bar{r}') = \left[\bar{\bar{I}} + \frac{\nabla\nabla}{k^2}\right] \frac{e^{ik|\bar{r}-\bar{r}'|}}{4\pi|\bar{r}-\bar{r}'|}, \tag{7}$$

with free space wave number k. Expanding the current distribution by the bi-triangular basis function $\bar{f}_n$ [6] and unknown coefficients, and following the MOM procedure, the EFIE is converted to a matrix form:

$$\bar{\bar{Z}} \cdot \bar{I} = \bar{V}, \tag{8}$$

where

$$V_m = -\iint_{T_m^{\pm}} dS_m \bar{f}_m(\bar{r}) \cdot \bar{E}_i(\bar{r})$$

$$Z_{mn} = \iint_{T_m^{\pm}} dS_m \bar{f}_m(\bar{r}_m) \cdot \iint_{T_n^{\pm}} dS_n\; \bar{\bar{G}}(\bar{r}_m,\bar{r}_n) \cdot \bar{f}_n(\bar{r}_n). \tag{9}$$

In Eq. (9), $T_m^{\pm}$ and $T_n^{\pm}$ represent observation and source triangle pairs. Evaluating the matrix element is time consuming. A parallel implementation of the MOM would be based on the edge-to-edge pair. That is, each matrix element is evaluated by a processor element. An implementation based on the patch-to-patch pair, however, can reduce the number of floating point operations by 7 to 8 times. As a result, the patch-to-patch pair approach is used. In this approach, the DTC is configured as a 2-D array of number of patches by number of patches. The coordinates of the vertices of the patch are spread both vertically and horizontally into the array, and integrations corresponding to a pair of patches are calculated in one step. The matrix elements are obtained by combining the appropriate integrations; this is difficult since it requires complex interprocessor communication. We resolve this problem by using the workstation for the final matrix element assembly. It turns out that only an insignificant amount of calculations is needed for this step. There are approximately 72 complex floating point operations for each matrix

element. For a 2 complex MFLOP workstation, a 1,000 unknowns matrix assembly takes about a half of a minute, and a portion of this time is overlapped with the DTC computation time in block implementation.

The idea of block implementation is based on the fact that special numerical operations are needed when the observation and source patches are the same. As seen from the dyadic Green's function, singularity appears when observation and source points coincide. Numerical integration with a singular integrand demands significantly more operations than without singularity. In the block implementation, the DTC-16/DTC-8 is configured as a 128 by 128 array (64 by 64 for the DTC-4). That is, the entire integration is partitioned into blocks of 128 by 128. Since singularity appears only along the diagonal blocks, special calculations are applied in those blocks (Figure 5). An additional advantage of this implementation is that, after integration of each block is finished, the matrix element assembly in the workstation and the DTC calculation on the next block proceed as if they are independent.

Finding a solution for a matrix equation is a major task. In sequential computers, LU decomposition is often used. For parallel computers, however, Gaussian-Jordan elimination is more suitable, but this algorithm requires more floating point operations. To avoid this shortcoming, the block Gaussian elimination is used. As in the matrix generation, the entire matrix is partitioned into blocks of either 128 by 128 or 64 by 64 depending on the DTC model. Each block is treated as a super matrix element; hence Gaussian elimination is applied to eliminate the lower blocks (Figure 6). For the diagonal blocks Gaussian-Jordan elimination is applied, since for these blocks there is no timing difference between the two algorithms and Gaussian-Jordan elimination simplifies the back substitution.

V. Brief Summary of the Application

The parallel version of the FD-TD algorithm has been applied to a number of problems such as scattering, radiation, microstrip line characterizations, and coplanar wave guide characterizations. The geometrical description for EM-WAVETRACER is in the form of a triangular list, which approximates the surface (conductor and coating) geometry of a target. This list of triangles can easily be extracted from a number of CAD tools. The conversion from the list to the rectangular cell description in the FD-TD algorithm is based on the minimum distance criteria and is fully automated. The computational speed is application dependent. In general, about 1 to 2 seconds per time step of a million node problem is achieved. For example, 0.85 second per time step per million node is obtained for a three gridding zone FD-TD analysis of a print wire board through-hole problem. Furthermore, the DTC can easily host problems with multimillion discretization nodes.

The parallel MOM code has been applied to a number of geometries; accurate radar cross sections are obtained. The geometrical description has the same format as the FD-TD code. This geometrical description (triangular list) is fed to a translation program and is converted to a file suitable for the MOM code. Reasonable computation speeds are obtained in both the matrix fill and solution steps. For instance, for 1,200 by 1,200 matrix fill, the DTC-16 spends 5 minutes in quadruple integral mode and the workstation (Sun Sparc 2) spends about 1 minute. (The MOM code has both double and quadruple integral modes; in some cases, the quadruple mode provides noticeably better results than that of the double integral mode.) For the block Gaussian elimination, with 128 right-hand-

sides of a 1,200 by 1,200 matrix, it takes about 5 minutes on a DTC-16 with double precision.The implementation of the block Gaussian elimination, as stated in section IV, is optimal for minimizing the number of operations, but it is not optimal for communication. The average communication distance, in the 2-D mode, is about 128/2 for DTC-16. Currently, a 3-D version of the block Gaussian elimination is being implemented; the average communication distance is about 16, and a very significant speed improvement is expected.

VI. Summary

This article summarizes the implementations of the FD-TD and MOM algorithms on the DTC. The DTC is a 3-D SIMD massively parallel computer. This computer is supported by the multiC language which extends the C language to include data-parallel programming. The implementation of the FD-TD algorithm uses the 3-D virtual processing and local connectivity features of the DTC, and parallel data is shared to minimize memory requirement. The block implementation technique is used for the MOM algorithm. For this approach, the 2-D unfolding feature and the workstation are used. These programs are applied to many scattering and radiation problems and very cost-effective performance is achieved.

References

[1] J. H. Jackson, "The Data Transport Computer: A 3-dimensional massively parallel SIMD computer," *IEEE CONPCOM* Symposium, Comp. Society Press, 264-269, 1991.

[2] Wavetracer, Inc., *The multiC Programming Language*, Version 1.0, Wavetracer, Inc., Acton, MA., 1991.

[3] Wavetracer, Inc., *EM-WAVETRACER Electromagnetic Modeling Package*, Version 1.0, Wavetracer, Inc., Acton, MA., 1991.

[4] K. S. Yee, "Numerical solution of initial boundary value problems involving Maxwell's equation in isotropic media," *IEEE* Trans. Ant. Prop., Vol. AP-14, 302-307, May 1966.

[5] G. Mur, "Absorbing boundary conditions for the finite difference approximation of the time domain electromagnetic field equations," *IEEE* Trans. Elec. Comp., Vol. EMC-23, Nov. 1981.

[6] S. M. Rao, D. R. Wilton, and A. W. Glisson, "Electromagnetic scattering by surface of arbitrary shape," *IEEE* Trans. Ant. Prop., AP-30, 409-418, May 1982.

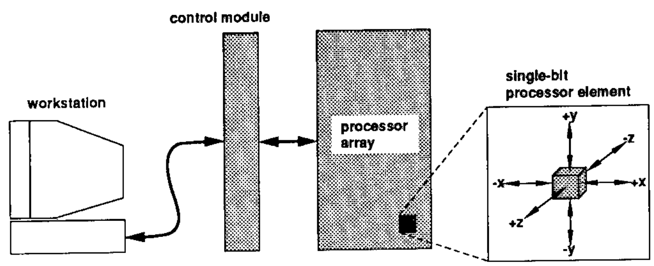

Figure 1: DTC hardware environment

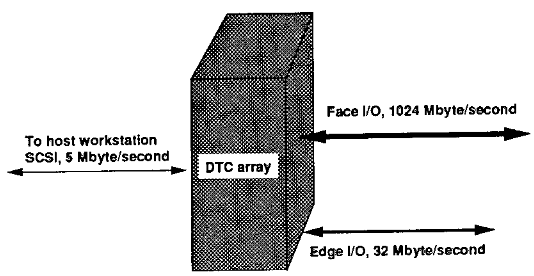

Figure 2: I/O ports of Data Transport Computer

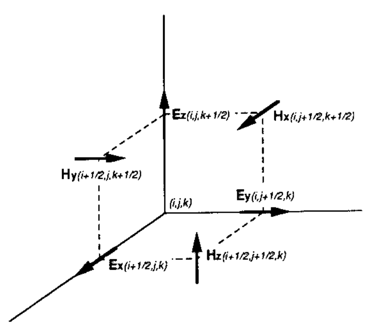

Figure 3: Staggered grid cell

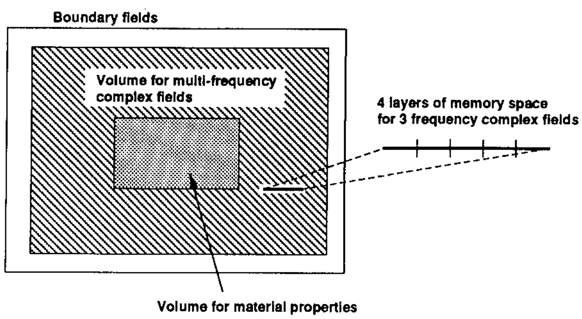

Figure 4: Sharing of parallel data in FD-TD algorithm

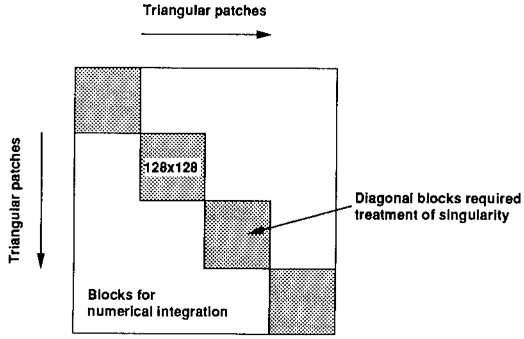

Figure 5: Block implementation of the parallel MOM algorithm

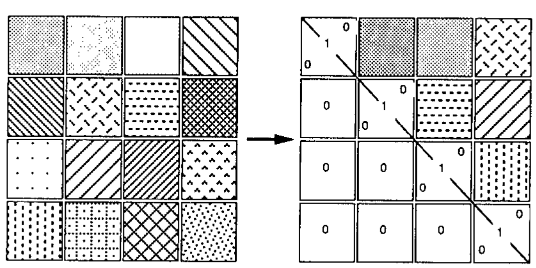

Figure 6: Block Gaussian elimination

Notes